Finite Element Method in GEO5 FEM
Theoretical manual

Theoretical manual

January 22, 2025

Contents

Chapter 1

Basic notation, invariant stress and strain measures, Hooke's law

The present chapter introduces the basic notation adopted in the formulation of material models implemented in the GEO5 FEM software. Unlike the results displayed by the program the formulations presented in this manual consider **standard elasticity sign convention with tension being positive**. Both tensor and matrix-vector notation is used with matrices defined as capital bold letters **A** and vectors defined as small italic letters $\boldsymbol{a}$. Standard indicial notation is used to identify 4th order A_{ijkl}, 2nd order a_{ij} and 1st order a_i, respectively with $i, j, k, = 1, 2, 3$.

1.1 Cartesian stresses and strains

In general three-dimensional stress space (3D) the stress and strain fields associated with standard Cartesian coordinated system x, y, z can be presented in terms of

- Stress and strain tensors

$$
[\sigma_{\mathsf{ij}}] \;=\; \begin{bmatrix} \sigma_{xx} & \tau_{xy} & \tau_{xz} \\ \tau_{yx} & \sigma_{yy} & \tau_{yz} \\ \tau_{zx} & \tau_{zy} & \sigma_{zz} \end{bmatrix} = \begin{bmatrix} \sigma_{11} & \sigma_{12} & \sigma_{13} \\ \sigma_{21} & \sigma_{22} & \sigma_{23} \\ \sigma_{31} & \sigma_{32} & \sigma_{33} \end{bmatrix} \tag{1.1}
$$

$$
[\varepsilon_{\mathsf{ij}}] \;=\; \begin{bmatrix} \varepsilon_{xx} & \varepsilon_{xy} & \varepsilon_{xz} \\ \varepsilon_{yx} & \varepsilon_{yy} & \varepsilon_{yz} \\ \varepsilon_{zx} & \varepsilon_{zy} & \varepsilon_{zz} \end{bmatrix} = \begin{bmatrix} \varepsilon_{11} & \varepsilon_{12} & \varepsilon_{13} \\ \varepsilon_{21} & \varepsilon_{22} & \varepsilon_{23} \\ \varepsilon_{31} & \varepsilon_{32} & \varepsilon_{33} \end{bmatrix} \tag{1.2}
$$

$$
\sigma_{ij} = \sigma_{ji}, \qquad \varepsilon_{ij} = \varepsilon_{ji} \tag{1.3}
$$

- Stress and strain vectors

$$
\boldsymbol{\sigma}^{\mathsf{T}} \;=\; \{\sigma\}^{\mathsf{T}} = \{\sigma_x, \sigma_y, \sigma_z, \tau_{yz}, \tau_{zx}, \tau_{xy}\} \tag{1.4}
$$

$$
\boldsymbol{\varepsilon}^{\mathsf{T}} \;=\; \{\varepsilon\}^{\mathsf{T}} = \{\varepsilon_x, \varepsilon_y, \varepsilon_z, \gamma_{yz}, \gamma_{zx}, \gamma_{xy}\} \tag{1.5}
$$

$$
\gamma_{ij} = 2\varepsilon_{ij} \quad \text{for } i \neq j \tag{1.6}
$$

where σ_i, ε_i represent the normal stress and strain components and τ_{ij} and γ_{ij} stand form shear stresses and engineering strains, respectively. In GEO5 FEM the analysis is performed assuming either plane-strain or axisymmetric state of stress. To this end, the x, z coordinate system is adopted to represent the two-dimensional (2D) solution plane so that

$$
\boldsymbol{\sigma}^{\mathsf{T}} \;=\; \{\sigma\}^{\mathsf{T}} = \{\sigma_x, \sigma_z, \tau_{yz}, \sigma_y\} \tag{1.7}
$$

$$
\boldsymbol{\varepsilon}^{\mathsf{T}} \;=\; \{\varepsilon\}^{\mathsf{T}} = \{\varepsilon_x, \varepsilon_z, \gamma_{xz}\} \tag{1.8}
$$

1.2   Principal stresses and principal strains

It is often desirable to introduce the principal stresses and strains acting on the planes on which the shear stress and strain components are zero. The principal stresses $\sigma_1, \sigma_2, \sigma_3$ in particular are solution of the eigenvalue problem

$$\det\left[\sigma_{ij} - \sigma_k\delta_{ij}\right] = \begin{vmatrix} \sigma_{11} - \sigma_k & \sigma_{12} & \sigma_{13} \\ \sigma_{21} & \sigma_{22} - \sigma_k & \sigma_{23} \\ \sigma_{31} & \sigma_{32} & \sigma_{33} - \sigma_k \end{vmatrix} = 0 \tag{1.9}$$

Usually, the principal stresses are ordered to satisfy $\sigma_1 \geq \sigma_2 \geq \sigma_3$ and are found from the solution of the following cubic equation

$$-\sigma_k^3 + I_{1\sigma}\sigma_k^2 - I_{2\sigma}\sigma_k + I_{3\sigma} = 0 \tag{1.10}$$

where $I_{1\sigma}$, $I_{2\sigma}$ and $I_{3\sigma}$ are stress invariants introduced in Section 1.5.

The principal strains can be derived similarly and for linear elastic and isotropic materials their direction coincides with the direction of the principal stresses.

1.3   Volumetric and deviatoric stresses and strains

Volumetric σ_m, ε_v and deviatoric s_{ij}, e_{ij} stresses and strains are introduced to describe deformations associated with the change in volume and shape, respectively, and are defined as

- Mean stress

$$\sigma_m = \frac{1}{3}\sigma_{ii} = \frac{1}{3}\left(\sigma_x + \sigma_y + \sigma_z\right) = \frac{1}{3}\left(\sigma_1 + \sigma_2 + \sigma_3\right) = \boldsymbol{m}^\mathsf{T}\boldsymbol{\sigma} \tag{1.11}$$

- Volumetric strain

$$\varepsilon_v = \varepsilon_{ii} = \varepsilon_x + \sigma_y + \varepsilon_z = \varepsilon_1 + \varepsilon_2 + \varepsilon_3 = 3\boldsymbol{m}^\mathsf{T}\boldsymbol{\varepsilon} \tag{1.12}$$

- Deviatoric stresses

$$\begin{aligned} s_{ij} &= \sigma_{ij} - \sigma_m\delta_{ij} & \text{(1.13)} \\ \boldsymbol{s} &= \boldsymbol{\sigma} - 3\boldsymbol{m}\sigma_m = \mathbf{PQ}\boldsymbol{\sigma} & \text{(1.14)} \\ I_{1s} &= s_{ii} = s_x + s_y + z_z = 0 & \text{(1.15)} \end{aligned}$$

- Deviatoric strains

$$\begin{aligned} e_{ij} &= \varepsilon_{ij} - \frac{1}{3}\varepsilon_v\delta_{ij} & \text{(1.16)} \\ \boldsymbol{e} &= \boldsymbol{\varepsilon} - \boldsymbol{m}\varepsilon_v = \mathbf{PQ}\boldsymbol{\varepsilon} & \text{(1.17)} \\ I_{1e} &= e_{ii} = e_x + e_y + e_z = 0 & \text{(1.18)} \end{aligned}$$

where δ_{ij} is the Kronecker symbol ($\delta_{ij} = 1$ if $i = j$ and $\delta_{ij} = 0$ otherwise) and I_{1s}, I_{1e} are the first deviatoric stress and strain invariants. The operators $\mathbf{P}, \mathbf{Q}, \boldsymbol{m}$ are defined as

- Operator matrix $\mathbf{P}$

$$\mathbf{P} = [\mathsf{P}] = \begin{bmatrix} 2/3 & -1/3 & -1/3 & 0 & 0 & 0 \\ -1/3 & 2/3 & -1/3 & 0 & 0 & 0 \\ -1/3 & -1/3 & 2/3 & 0 & 0 & 0 \\ 0 & 0 & 0 & 2 & 0 & 0 \\ 0 & 0 & 0 & 0 & 2 & 0 \\ 0 & 0 & 0 & 0 & 0 & 2 \end{bmatrix} \tag{1.19}$$

- Operator matrix $\mathbf{Q}$

$$\mathbf{Q} \;=\; [\mathsf{Q}] \;=\; \begin{bmatrix} 1 & 0 & 0 & 0 & 0 & 0 \\ 0 & 1 & 0 & 0 & 0 & 0 \\ 0 & 0 & 1 & 0 & 0 & 0 \\ 0 & 0 & 0 & 1/2 & 0 & 0 \\ 0 & 0 & 0 & 0 & 1/2 & 0 \\ 0 & 0 & 0 & 0 & 0 & 1/2 \end{bmatrix} \tag{1.20}$$

- Operator vector $\boldsymbol{m}$

$$\boldsymbol{m}^{\mathsf{T}} = \left\{ \frac{1}{3}, \frac{1}{3}, \frac{1}{3}, 0, 0, 0 \right\} \tag{1.21}$$

- Mutual relations

$$\boldsymbol{m}^{\mathsf{T}}\mathbf{Q}\boldsymbol{m} = \boldsymbol{m}^{\mathsf{T}}\boldsymbol{m} = \frac{1}{3} \quad \mathbf{PQP} = \mathbf{P} \quad \mathbf{PQ} = \mathbf{QP} \rightarrow \mathbf{Q}^{-1}\mathbf{PQ} = \mathbf{P} \quad \mathbf{PQ}\boldsymbol{m} = \mathbf{P}\boldsymbol{m} = \mathbf{0} \tag{1.22}$$

Note that these operators attain a slightly different forms when adopted with Eqs. (1.7), (1.8) in 2D analyses.

1.4 Deviatoric stress and strain invariants

The following deviatoric stress and strain measures called invariants (do not depend on the choice of the coordinate system) prove useful in the formulation of nonlinear material models used in GEO5 FEM.

- 2nd order stress invariants (equivalent deviatoric stress measures)

$$J \;=\; \sqrt{I_{2s}} = \sqrt{J_2} = \sqrt{\frac{1}{2} s_{ij} s_{ij}} = \sqrt{\frac{1}{2} \boldsymbol{s}^{\mathsf{T}} \mathbf{Q}^{-1} \boldsymbol{s}} = \sqrt{\frac{1}{2} \boldsymbol{\sigma}^{\mathsf{T}} \mathbf{P} \boldsymbol{\sigma}} \tag{1.23}$$

$$\;=\; \frac{1}{\sqrt{6}} \left[(\sigma_1 - \sigma_2)^2 + (\sigma_1 - \sigma_3)^2 + (\sigma_2 - \sigma_3)^2 \right]^{\frac{1}{2}} \tag{1.24}$$

$$q \;=\; \sqrt{3} J \tag{1.25}$$

Note that:

$$\frac{\partial J}{\partial \boldsymbol{s}} = \frac{\mathbf{Q}^{-1}\boldsymbol{s}}{2J} = \frac{\mathbf{Q}^{-1}\mathbf{PQ}\boldsymbol{\sigma}}{2J} = \frac{\mathbf{P}\boldsymbol{\sigma}}{2J} = \frac{\partial J}{\partial \boldsymbol{\sigma}} \tag{1.26}$$

- 3rd order deviatoric stress invariant

$$I_{3s} = \det [\mathsf{s}] \tag{1.27}$$

- 2nd order strain invariants (equivalent deviatoric strain measures)

$$E_d \;=\; \sqrt{2 e_{ij} e_{ij}} = \sqrt{2 \boldsymbol{e}^{\mathsf{T}} \mathbf{Q} \boldsymbol{e}} = \sqrt{2 \boldsymbol{\varepsilon}^{\mathsf{T}} \mathbf{QPQ} \boldsymbol{\varepsilon}} \tag{1.28}$$

$$\;=\; \frac{2}{\sqrt{6}} \left[(\varepsilon_1 - \varepsilon_2)^2 + (\varepsilon_1 - \varepsilon_3)^2 + (\varepsilon_2 - \varepsilon_3)^2 \right]^{\frac{1}{2}} \tag{1.29}$$

$$\gamma_{eq} \;=\; \sqrt{3} E_d \tag{1.30}$$

$$\gamma_s \;=\; \frac{1}{2}\gamma_{eq} = \frac{\sqrt{3}}{2} E_d \tag{1.31}$$

1.5   Cartesian stress invariants

Apart from already introduced deviatoric invariant stress measures the 1st $(I_{1\sigma})$, 2nd $(I_{3\sigma})$, and 3rd $(I_{3\sigma})$ stress invariants expressed in terms of Cartesian stresses will also appear in some definitions. These are given by

$$
\begin{aligned}
I_{1\sigma} &= \sigma_{ii} = \sigma_{11} + \sigma_{22} + \sigma_{33} && (1.32) \\
I_{2\sigma} &= \frac{1}{2}\left(I_{1\sigma}^2 - \sigma_{ij}\sigma_{ij}\right) = && (1.33) \\
&= \frac{1}{2}\left[(\sigma_{11} + \sigma_{22} + \sigma_{33})^2 - \left[\sigma_{11}^2 + \sigma_{22}^2 + \sigma_{33}^2 + 2\sigma_{12}^2 + 2\sigma_{13}^2 + 2\sigma_{23}^2\right]\right] \\
I_{3\sigma} &= \det[\boldsymbol{\sigma}] && (1.34)
\end{aligned}
$$

The introduced stress measures σ_m, J_2, I_{3s} can be written in terms of the above invariants as

$$
\begin{aligned}
\sigma_m &= \frac{1}{3}I_{1\sigma} && (1.35) \\
J_2 &= \frac{1}{3}I_{1\sigma}^2 - I_{2\sigma} && (1.36) \\
I_{3s} &= \frac{2}{27}I_{1\sigma}^3 - \frac{1}{3}I_{1\sigma}I_{2\sigma} + I_{3\sigma} && (1.37)
\end{aligned}
$$

1.6   Lode's angle θ

It will be seen that a given stress state can be visualized in the principal stress space with the help of the mean stress σ_m, the equivalent deviatoric stress J and so called Lode's angle provided by

$$
\theta = \tan^{-1}\left[\frac{1}{\sqrt{3}}\left(2\frac{\sigma_2 - \sigma_3}{\sigma_1 - \sigma_3} - 1\right)\right] = -\frac{1}{3}\arcsin\left(\frac{3\sqrt{3}}{2}\frac{I_{3s}}{J^3}\right) \tag{1.38}
$$

It ranges from $-30°$ to $30°$. The limiting values correspond to states of triaxial extension and compression.

1.7   Principal stresses in terms of σ_m, J_2, θ

It is seen in Fig. 1.1 that the conveniently chosen stress measures σ_m, J_2, θ have geometric meaning in the principal stress space. It is now clear that Lode's angle defines the orientation of the current stress state in the deviatoric plane. Note that most of the nonlinear models implemented in GEO5 FEM show dependency on Lode's angle θ. Because σ_m is a measure of the distance along the hydrostatic
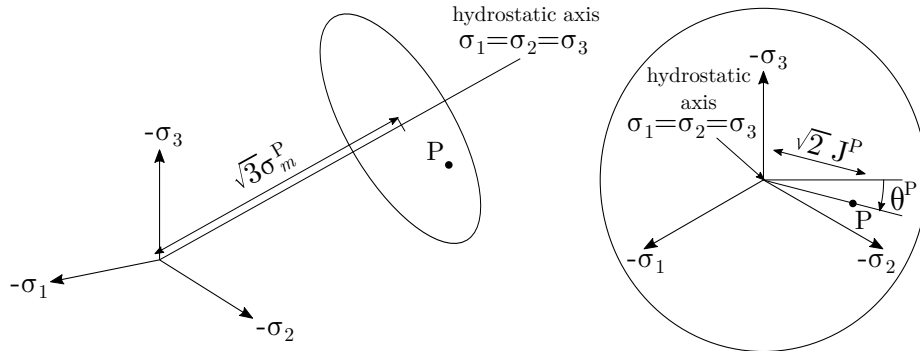
Figure 1.1: Graphical representation of stress point $P[\sigma_1, \sigma_2, \sigma_3]$ in deviatoric plane

axis (space diagonal) and J measures the distance from the hydrostatic axis in the deviatoric plane it

becomes possible to express the principal stresses as

$$\sigma_1 = \sigma_m + \frac{2}{\sqrt{3}}J\sin\left(\theta + \frac{2\pi}{3}\right)$$

$$\sigma_2 = \sigma_m + \frac{2}{\sqrt{3}}J\sin\left(\theta\right)$$

$$\sigma_3 = \sigma_m + \frac{2}{\sqrt{3}}J\sin\left(\theta - \frac{2\pi}{3}\right)$$

$$\sigma_1 > \sigma_2 > \sigma_3$$

1.8 Linear elastic constitutive law - Hooke's law

All material models implemented in GEO5 FEM assume isotropic materials that can described by only two material parameters such as Young's modulus E and Poisson's ratio ν. The linear elastic stress-strain relationship (Hooke's law) can be written as

$$
\begin{Bmatrix} \varepsilon_x \\ \varepsilon_y \\ \varepsilon_z \\ \gamma_{yz} \\ \gamma_{zx} \\ \gamma_{xy} \end{Bmatrix} =
\begin{bmatrix}
\frac{1}{E} & -\frac{\nu}{E} & -\frac{\nu}{E} & 0 & 0 & 0 \\
-\frac{\nu}{E} & \frac{1}{E} & -\frac{\nu}{E} & 0 & 0 & 0 \\
-\frac{\nu}{E} & -\frac{\nu}{E} & \frac{1}{E} & 0 & 0 & 0 \\
0 & 0 & 0 & \frac{2(1+\nu)}{E} & 0 & 0 \\
0 & 0 & 0 & 0 & \frac{2(1+\nu)}{E} & 0 \\
0 & 0 & 0 & 0 & 0 & \frac{2(1+\nu)}{E}
\end{bmatrix}
\begin{Bmatrix} \sigma_x \\ \sigma_y \\ \sigma_z \\ \tau_{yz} \\ \tau_{zx} \\ \tau_{xy} \end{Bmatrix}
\tag{1.39}
$$

where the 6×6 matrix is termed the compliance matrix and is usually denoted as **C**. An inverse relationship in terms of the stiffness matrix $\mathbf{D} = \mathbf{C}^{-1}$ attains the form

$$
\begin{Bmatrix} \sigma_x \\ \sigma_y \\ \sigma_z \\ \tau_{yz} \\ \tau_{zx} \\ \tau_{xy} \end{Bmatrix} =
\frac{E}{(1+\nu)(1-2\nu)}
\begin{bmatrix}
1-\nu & \nu & \nu & 0 & 0 & 0 \\
\nu & 1-\nu & \nu & 0 & 0 & 0 \\
\nu & \nu & 1-\nu & 0 & 0 & 0 \\
0 & 0 & 0 & \frac{1-2\nu}{2} & 0 & 0 \\
0 & 0 & 0 & 0 & \frac{1-2\nu}{2} & 0 \\
0 & 0 & 0 & 0 & 0 & \frac{1-2\nu}{2}
\end{bmatrix}
\begin{Bmatrix} \varepsilon_x \\ \varepsilon_y \\ \varepsilon_z \\ \gamma_{yz} \\ \gamma_{zx} \\ \gamma_{xy} \end{Bmatrix}
\tag{1.40}
$$

Employing tonsorial notation the above equations receive the following forms

$$\varepsilon_{ij} = C_{ijkl}\sigma_{kl} \tag{1.41}$$

$$C_{ijkl} = \frac{1+\nu}{E}\left[\delta_{ik}\delta_{jl} - \frac{\nu}{1+\nu}\delta_{ij}\delta_{kl}\right] \tag{1.42}$$

$$\sigma_{ij} = D_{ijkl}\varepsilon_{kl} \tag{1.43}$$

$$D_{ijkl} = \frac{E\nu}{(1+\nu)(1-2\nu)}\delta_{ij}\delta_{kl} + \frac{E}{2(1+\nu)}\left[\delta_{ik}\delta_{jl} + \delta_{il}\delta_{jk}\right] \tag{1.44}$$

It is often more convenient to introduce another two parameters, namely the bulk modulus K and the shear modulus G. The following mutual relationships can be established

$$
\begin{aligned}
G &= \frac{E}{2(1+\nu)} = \frac{3(1-2\nu)}{2(1+\nu)}K = \frac{3KE}{9K-E} \\
K &= \frac{E}{3(1-2\nu)} = \frac{GE}{3(3G-E)} = \frac{2(1+\nu)}{3(1-2\nu)}G \\
E &= 2G(1+\nu) = 3K(1-2\nu) = \frac{9KG}{3K+G} \\
\nu &= \frac{E}{2G}-1 = \frac{3K-2G}{2(3K+G)} = \frac{3K-E}{6K}
\end{aligned}
$$

This allows us to write the stiffness matrix $\mathbf{D}$ in terms of K and G as

$$
\mathbf{D} =
\begin{bmatrix}
K+\dfrac{4}{3}G & K-\dfrac{2}{3}G & K-\dfrac{2}{3}G & 0 & 0 & 0 \\[2mm]
K-\dfrac{2}{3}G & K+\dfrac{4}{3}G & K-\dfrac{2}{3}G & 0 & 0 & 0 \\[2mm]
K-\dfrac{2}{3}G & K-\dfrac{2}{3}G & K+\dfrac{4}{3}G & 0 & 0 & 0 \\[2mm]
0 & 0 & 0 & G & 0 & 0 \\
0 & 0 & 0 & 0 & G & 0 \\
0 & 0 & 0 & 0 & 0 & G
\end{bmatrix}
\tag{1.45}
$$

When splitting the Cartesian stresses and strains into their deviatoric and volumetric parts we arrive at relatively simple forms of Hook's law

$$
\begin{aligned}
s_{ij} &= 2Ge_{ij} & (1.46) \\
\boldsymbol{s} &= 2G\mathbf{Q}e & (1.47) \\
\sigma_m &= K\varepsilon_v = 3K\boldsymbol{m}^\mathsf{T}\boldsymbol{\varepsilon} & (1.48)
\end{aligned}
$$

The following relationships between deviatoric invariant stress and strain measures are also available

$$
\begin{aligned}
J &= GE_d & (1.49) \\
q &= G\gamma_{eq} & (1.50) \\
q &= 2G\gamma_s & (1.51)
\end{aligned}
$$

Recall also the strain energy defined as

$$
\begin{aligned}
W(\boldsymbol{\varepsilon}) &= \frac{1}{2}\sigma\varepsilon = \frac{1}{2}\{\sigma\}^\mathsf{T}\{\varepsilon\} = \frac{1}{2}\left(JE_d + \sigma_m\varepsilon_v\right) \\
&= \frac{1}{2}E\varepsilon^2 = \frac{1}{2}\{\varepsilon\}^\mathsf{T}[\mathrm{D}]\{\varepsilon\} = \frac{1}{2}\left(GE_d^2 + K\varepsilon_v^2\right)
\end{aligned}
\tag{1.52}
$$
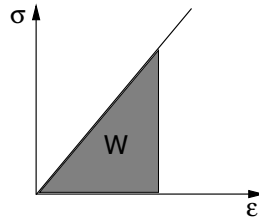
Figure 1.2: One-dimensional representation of strain energy density $W(\varepsilon)$

1.9 Depth dependent stiffness

Various models in GEO5 FEM allow for adjusting the soil stiffness with depth as

$$E_h = E + k_d h \tag{1.53}$$

where E is the originally assigned Young's modulus of a given soil and k_d is the rate with which the soil stiffness increases with depth. The depth h is the vertical distance from the terrain surface. This option is not available to Hardening soil, Soft soil, Modified Cam-clay, Generalized Cam-clay, and Hypoplastic models where the stiffness evolves with the current value of the mean effective stress σ_m.

1.10 Special stress and strain states assuming linear elasticity

As two illustrative examples we present some specific stress-strain relationships associated with basic laboratory tests such as drained triaxial compression and oedometric compression.

1.10.1 Triaxial compression

Consider the following two loading steps:

1. Isotropic compression: $\sigma_1 = \sigma_2 = \sigma_3 = \sigma_m = \sigma_m^0$

2. Triaxial compression: $\Delta\sigma_3 = -\Delta\sigma_v \neq 0, \Delta\sigma_1 = \Delta\sigma_2 = \Delta\sigma_r = 0$
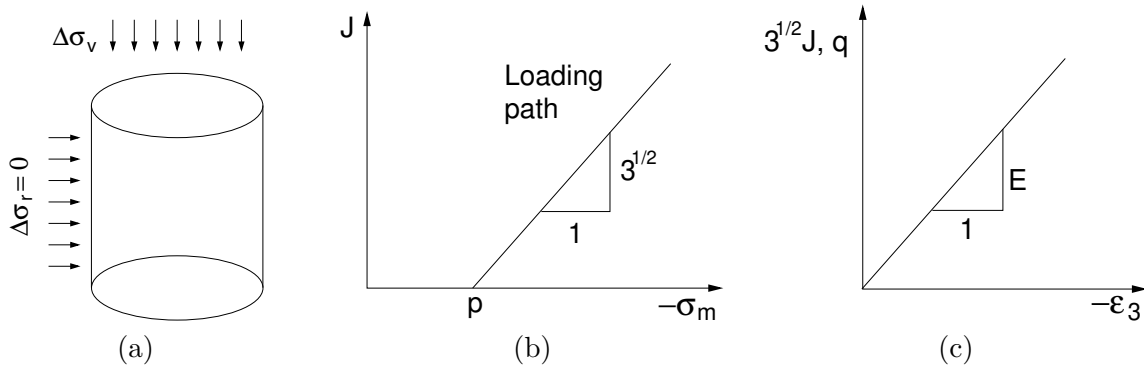
Figure 1.3: a) Triaxial compression step, b) loading path, c)Hooke's law

The triaxial compression step in Fig. 1.3 generates the following state of stress and strain

$$\sigma_m = \frac{1}{3}(2\sigma_1 + \sigma_3) \tag{1.54}$$

$$\varepsilon_v = 2\varepsilon_1 + \varepsilon_3 \tag{1.55}$$

$$J = \frac{\sqrt{3}}{3}(\sigma_1 - \sigma_3) = \frac{1}{\sqrt{3}}q \tag{1.56}$$

$$E_d = \frac{2\sqrt{3}}{3}(\varepsilon_1 - \varepsilon_3) = \frac{1}{\sqrt{3}}\gamma_{eq} = \frac{2}{\sqrt{3}}\gamma_s \tag{1.57}$$

$$\sigma_3 = -p + \Delta\sigma_3, \quad \sigma_1 = \sigma_2 = -p, \quad \Delta\sigma_1 = \Delta\sigma_2 = 0 \tag{1.58}$$

$$\tag{1.59}$$

Because

$$J^{i+1} = \frac{\sqrt{3}}{3}(\sigma_1^i - \sigma_3^i - \Delta\sigma_3) = J^i + \Delta J \tag{1.60}$$

$$E_d^{i+1} = \frac{2\sqrt{3}}{3}(\varepsilon_1^i + \Delta\varepsilon_1 - \varepsilon_3^i - \Delta\varepsilon_3) = E_d^i + \Delta E_d \tag{1.61}$$

we get the stress and strain increments in the form

$$\Delta\sigma_m = \frac{\Delta\sigma_3}{3} \tag{1.62}$$

$$\Delta J = -\sqrt{3}\Delta\sigma_m \tag{1.63}$$

$$\Delta\varepsilon_v = 2\Delta\varepsilon_1 + \Delta\varepsilon_3 = \frac{\Delta\sigma_m}{K} = -\frac{\Delta J}{\sqrt{3}K} \tag{1.64}$$

$$\Delta E_d = \frac{\Delta J}{G} = \frac{3}{2\sqrt{3}G}\frac{1}{(\Delta\varepsilon_1 - \Delta\varepsilon_3)} \tag{1.65}$$

Combing Eqs. (1.64) and (1.65) provides

$$\sqrt{3}\Delta J = -\frac{9KG}{3K+G}\Delta\varepsilon_3 = -E\Delta\varepsilon_3 = \Delta q \tag{1.66}$$

1.10.2   Oedometric compression

Consider the following loading and constrain conditions:

- Prescribed loading: $-\Delta\sigma_3 = \Delta\sigma_v \neq 0$

- Prescribed constraints: $\Delta\varepsilon_1 = \Delta\varepsilon_2 = 0$

- Measured and computed variables: $-\Delta\varepsilon_3 = \varepsilon_v \neq 0, \Delta\sigma_1 = \Delta\sigma_2 \neq 0$
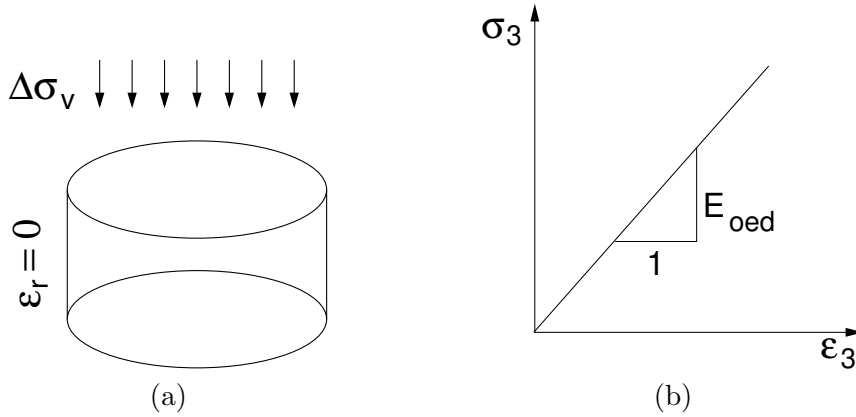
Figure 1.4: a) Oedometric test setup, b) Hooke's law

Adopting Eq. (1.40) and setting $\sigma_x = \sigma_1, \sigma_y = \sigma_2, \sigma_z = \sigma_3, \varepsilon_z = \varepsilon_3$ we get

$$\Delta\sigma_1 = \frac{\nu E}{(1+\nu)(1-2\nu)}\Delta\varepsilon_3 \tag{1.67}$$

$$\Delta\sigma_2 = \frac{\nu E}{(1+\nu)(1-2\nu)}\Delta\varepsilon_3 \tag{1.68}$$

$$\Delta\sigma_3 = \frac{(1-\nu)E}{(1+\nu)(1-2\nu)}\Delta\varepsilon_3 = \left(K + \frac{4}{3}G\right)\varepsilon_3 = E_{oed}\Delta\varepsilon_3 \tag{1.69}$$

where E_{oed} is the oedometric modulus when limiting attention to elasticity. Inverting the above equations or simply using Eq. (1.39) gives

$$\sigma_1 = \sigma_2 = \frac{\nu}{1-\nu}\sigma_3 = K_0\sigma_3 \tag{1.70}$$

where K_0 is the lateral earth pressure at rest. Note that in most practical applications the elastic coefficient of lateral earth pressure at rest is replaced by Jaky's formula

$$K_0 = 1 - \sin\varphi \tag{1.71}$$

where φ is the angle of internal friction. For overconsolidated soils the following representation is also available in GEO5 FEM

$$K_0 = 0.5(OCR)^{0.5} \tag{1.72}$$

where OCR is the overconsolidation ratio described in Section 1.13.

1.11   Void ratio e

An important parameter in soil mechanics which also appears in the formulation of several advanced constitutive models is the void ratio. The evolution of this parameter can be tied to the evolution of the volumetric strain. It represents the current state of soil and is defined as the ratio of the volume of pores Ω_p and the volume of the solid phase (grains/matrix) Ω_m

$$e = \frac{\Omega_p}{\Omega_m} \tag{1.73}$$

where $\Omega = \Omega_p + \Omega_m = \Omega_m(1 + e)$ is the total volume of the porous skeleton, where $(1 + e)$ is called the specific volume. Assuming incompressibility of the solid phase, i.e., $\dot{\Omega}_m = 0$, we write the change in void ratio as

$$\dot{e} = \frac{\dot{\Omega}_p}{\Omega_m} = (1 + e)\frac{\dot{\Omega}_p}{\Omega} \tag{1.74}$$

Because of incompressibility of the solid phase ($\dot{\Omega}_p = \dot{\Omega}$) Eq. (1.74) rewrites as

$$\frac{\dot{e}}{1 + e} = \frac{\dot{\Omega}}{\Omega} = \dot{\varepsilon}_v \tag{1.75}$$

Integrating Eq. (1.75) yields

$$\varepsilon_v - \varepsilon_v^{in} = \ln\left(\frac{1 + e_{in}}{1 + e}\right) \tag{1.76}$$

Assuming small strain theory the term on the right-hand side of equation(1.76) can be linearized via Taylor series to get

$$\varepsilon_v - \varepsilon_v^{in} \approx \frac{e - e_{in}}{1 + e_{in}} \tag{1.77}$$

To update the initial void ratio, the GEO5 FEM program assumes $\varepsilon_v^{in} = \varepsilon_v^{1^{st}stage}$ (the volume strain at the end of the 1st calculation stage, which is assumed to set the initial stress state) so that

$$e = (1 + e_{in})(\varepsilon_v - \varepsilon_v^{1^{st}stage}) + e_{in} \tag{1.78}$$

where e_{in} is the initial void ratio assumed again at the end of the 1st calculation stage. Providing the initial void ratio is not specified, neither inputted nor calculated in dependence of the selected constitutive model, the value of $e = 0$ is considered. When the initial void ratio e_{in} is specified and the soil is introduced already in the 1st calculation stage, we keep $e = e_{in}$ within this stage.

1.12   Dilation angle ψ

The angle of dilation controls an amount of plastic volumetric strain developed during plastic shearing and is assumed constant during plastic yielding. The value of $\psi = 0$ corresponds to the volume preserving deformation while in shear.

Clays (regardless of overconsolidated layers) experience a relatively low dilation ($\psi \approx 0$). As for sands, the angle of dilation depends on the angle of internal friction. For non-cohesive soils (sand, gravel) with the angle of internal friction $\varphi > 30°$ the value of dilation angle can be estimated as $\psi = \varphi - 30°$. A negative value of dilation angle is acceptable only for rather loose sands. In most cases, however, the assumption of $\psi = 0$ can be adopted.

The value of dilation angle ψ can also be estimated from Rowe's dilation theory as

$$\sin\psi_m = \frac{\sin\varphi - \sin\varphi_{cv}}{1 - \sin\varphi\sin\varphi_{cv}} \tag{1.79}$$

where φ is the peak angle of internal friction and φ_{cv} represents the angle of internal friction at critical state. Such an approach is adopted for example in the formulation of Hardening soil model where φ_{cv} is derived from

$$\sin\varphi_{cs} = \frac{\sin\varphi - \sin\psi}{1 - \sin\varphi\sin\psi} \tag{1.80}$$

where ψ is the peak dilation angle. Because the soil cannot expand its volume infinitely, the dilation is typically terminated when the current void ration e exceeds an allowable limit e_{max}.

1.13   Overconsolidaion ratio OCR and preoverburden pressure POP

The concept of overconsolidation ratio allows us to take into consideration the stress history, e.g., unloading-reloading. In one-dimensional consolidation such as oedometer test it is commonly observed that the response of a soil at the initial stage of loading is considerably stiffer in comparison to a normally consolidated soil. Such a soil is termed overconsolidated and can be characterized by a overconsolidation ratio OCR given by

$$OCR = \frac{\sigma_z^{pc}}{\sigma_z^0} \tag{1.81}$$

where σ_z^0 is the current in-situ stress, e.g., the initial geostatic stress introduced via the K_0 procedure and σ_z^{pc} is the preconsolidation vertical stress, i.e., the maximum vertical stress the soil has witnessed in the past. For constant OCR the evolution of preconsolidation stress σ_z^{pc} appears in Fig. 1.5. The value of σ_z^{pc} can also be determined via a preoverburden pressure POP as

$$\sigma_z^{pc} = \sigma_z^0 - POP, \quad \text{assuming } \sigma_z^0 < 0, POP > 0 \tag{1.82}$$

as shown in Fig. 1.5. When computing the preconsolidation stress σ_z^{pc} from POP we arrive at a variable OCR profile as plotted in Fig. 1.5(c). An illustrative example is presented in Fig. 1.6 for five
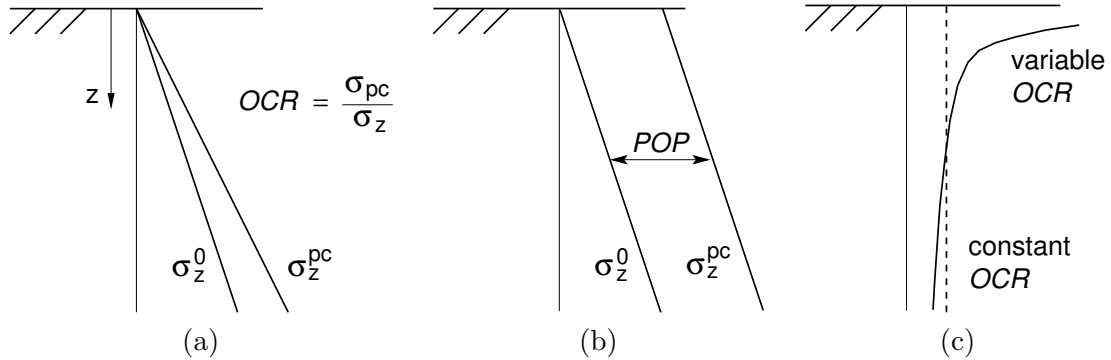
Figure 1.5: Vertical preconsolidation stress based on: a) overconsolidation ratio OCR, b) preoverburden pressure POP, c) Variation of OCR with depth

different values of POP. The current in-situ stress σ_z^0 is derived from gravity loading as

$$\sigma_z^0 = -\gamma z \tag{1.83}$$

where γ is the self-weight of the soil set equal to 20kN/m^3 in the present example and z is the vertical coordinate shown in Fig. 1.5(a).

As an example of application of in-situ measurements we present for illustration two expressions derived from a dilatometer test

$$\begin{aligned} OCR &= (0.5K_D)^{1.56}, \text{ for } I_D < 1.2, \quad \text{Totani et al. [77]} &\tag{1.84}\\ OCR &= 0.225K_D^{1.35\div1.67}, \quad\quad\quad\quad \text{Lacasse and Lunne [48]} &\tag{1.85} \end{aligned}$$
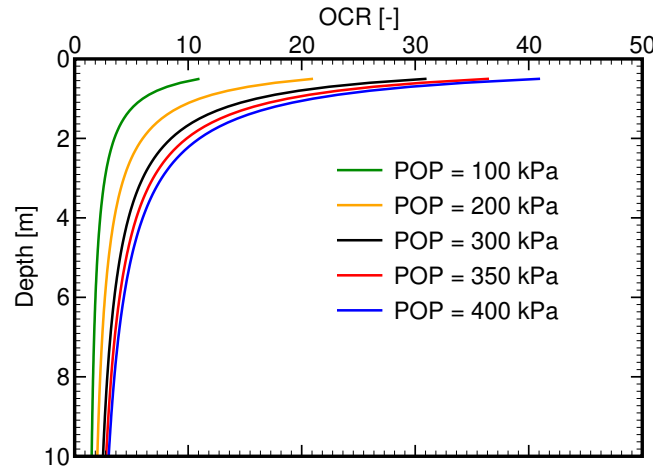
Figure 1.6: Variation of OCR derived from application of Eqs. (1.81) and (1.82) for five different values of POP

where K_D is the measured horizontal stress index.

In GEO5 FEM program the overconsolidation ratio serves to adjust the initial value of preconsolidation pressure characterizing the evolution of a cap yield surface in advanced plasticity models, i.e., the Modified Cam-clay, Generalized Cam-clay, Hardening soil and Soft soil models. This option, however, is available to initial stress states generated with the help of the K_0 procedure, see Section 1.14. To this end we start from the definition of a one-dimensional preconsolidation stress using either Eq. (1.81) or Eq. (1.82) with the in-situ vertical stress σ_z^0 provided by Eq. (1.83). Because the preconsolidation stress state is expected to be reached through a normal consolidation, the corresponding horizontal stress σ_x^{pc} is provided by

$$\sigma_x^{pc} = K_0^{NC}\sigma_z^{pc} \tag{1.86}$$

$$\sigma_3^{pc} = \sigma_z^{pc}, \ \sigma_1^{pc} = \sigma_2^{pc} = \sigma_x^{pc}, \quad \text{recall Eq. (1.70)} \tag{1.87}$$

where K_0^{NC} is the K_0 value of a normally consolidated soil. As mentioned in Section 1.14, this value should be specified when defining an arbitrary material model to be adopted in the K_0 procedure. In material models where K_0^{NC} is one of the model parameters, e.g., the Soft soil model or potentially the Hardening soil model, this value is automatically accepted by the model. For the Modified and Generalized cam clay models, the value of K_0^{NC} can be estimated from Eq. (1.92).

In light of one-dimensional (oedometer) consolidation we get the preconsolidation mean σ_m^{pc}, Eq. (1.54), and equivalent deviatoric J^{pc}, Eq. (1.56), stresses in the form

$$\sigma_m^{pc} = \frac{1}{3}\left(1 + 2K_0^{NC}\right)\sigma_z^{pc} \tag{1.88}$$

$$J^{pc} = \frac{\sqrt{3}}{3}|\sigma_x^{pc} - \sigma_z^{pc}| \tag{1.89}$$

The above two definitions of invariant stress measures can be then substituted into the cap failure criteria of advanced plasticity models to give the preconsolidation pressure p_c. Referring to Chapters, 8, 9, 11 and 12 the following results are obtained

1. **Hardening Soil model** - K_0^{NC} is either directly specified as one of the input parameters, thus known, or can be estimated based on the Jaky formula (1.105) as the peak angle of internal friction φ is one of the input parameters.

   - Cap yield surface

$$f = \frac{3(J^{pc})^2}{\chi^2 M^2} + (\sigma_m^{pc})^2 - p_c^2 = 0, \quad \chi = 1 \text{ in } K_0 \text{ procedure} \tag{1.90}$$

- Preconsolidation pressure

$$p_c = \sqrt{\frac{3(J^{pc})^2}{M^2} + (\sigma_m^{pc})^2} \tag{1.91}$$

2. **Soft soil model** - K_0^{NC} is one the input parameters, the model parameter M is provided by Brinkgreve [70] as

$$M = \sqrt{3} \sqrt{\frac{(1 - K_0^{NC})^2}{(1 + 2K_0^{NC})^2} + \frac{(1 - K_0^{NC})(1 - 2\nu)\left(\frac{\lambda^*}{\kappa^*} - 1\right)}{(1 + 2K_0^{NC})(1 - 2\nu)\frac{\lambda^*}{\kappa^*} - (1 - K_0^{NC})(1 + \nu)}} \tag{1.92}$$

where ν is the Poisson ratio and κ^*, λ^* are stiffness parameters all stored in the list of input parameters, see Chapter 9 for further details.

- Cap yield surface

$$f = \frac{(J^{pc})^2}{\chi^2 M^2} + (\sigma_m^{pc} - c\cot\varphi)(\sigma_m^{pc} + p_c) = 0, \quad \chi = 1 \text{ in } K_0 \text{ procedure} \tag{1.93}$$

where c, φ are the cohesion and angle of internal friction, respectively.

- Preconsolidation pressure

$$p_c = -\frac{(J^{pc})^2}{M^2(\sigma_m^{pc} - c\cot\varphi)} - \sigma_m^{pc} \tag{1.94}$$

3. **Modified Mohr-Coulomb model** - formulation of the cap yield surface is identical to that in the Soft soil model.

4. **Modified Cam-clay model** - the slope of the critical state line M_{cs} is one of the input parameters so that the associated value of K_0^{NC}, if not directly inputted, might be calculated from Eq. (1.92) while setting $M = M_{cs}$ and subsequently used to setup the K_0 procedure.

- Cap yield surface

$$f = \frac{(J^{pc})^2}{M_{cs}^2} + (\sigma_m^{pc})^2 + (\sigma_m^{pc})p_c = 0 \tag{1.95}$$

- Preconsolidation pressure

$$p_c = -\frac{(J^{pc})^2}{M_{cs}^2 \sigma_m^{pc}} - \sigma_m^{pc} \tag{1.96}$$

5. **Generalized Cam-clay model** - the model parameter $M_{\varphi_{cs}}$ is provided by

$$M_{\varphi_{cs}} = \frac{2\sqrt{3}\sin\varphi_{cs}}{3 - \sin\varphi_{cs}} \tag{1.97}$$

where φ_{cs} is the critical angle of internal friction. The value of K_0^{NC} can be either inputted, or again estimated, similarly to the Modified Cam-clay model, from Eq. (1.92) when setting $M = M_{\varphi_{cs}}$. One may also adopt the Jaky formula (1.105) as the peak angle of internal friction φ is one of the input parameters.

- Cap yield surface

$$f = \frac{(J^{pc})^2}{\chi^2 M_{\varphi_{cs}}^2} + (\sigma_m^{pc})^2 + \sigma_m^{pc}p_c, \quad \chi = 1 \text{ in } K_0 \text{ procedure} \tag{1.98}$$

- Preconsolidation pressure

$$p_c = -\frac{(J^{pc})^2}{M_{\varphi_{cs}}^2 \sigma_m^{pc}} - \sigma_m^{pc} \tag{1.99}$$

1.14 K_0 procedure to generate initial (geostatic) stress state

It is often desirable to generate an initial stress state that differs from the one provided by standard elasticity analysis. It is a well known fact that in rock analysis the lateral earth pressure often exceeds the vertical stress as a consequence of various deformation processes that took place in the past. Such a stress state, however, cannot be attained for a general class of materials when adopting classical constitutive equations of elasticity. Recall that in the case of linear elasticity and assuming standard boundary conditions ($\varepsilon_x = 0$ in the case of a homogeneous stress state) the following relation holds

$$\sigma_x = \frac{\nu}{1 - \nu}\sigma_z \tag{1.100}$$

where σ_x and σ_z represent the lateral and vertical normal stress, respectively, and ν is the Poisson ratio. Equation (1.100) can be generalized to get

$$\sigma_x = K_0\sigma_z \tag{1.101}$$

where K_0 is known as the coefficient of lateral earth pressure at rest introduced already in Section 1.10.2. Thus setting

$$K_0 = \frac{\nu}{1 - \nu} \tag{1.102}$$

corresponds to a standard elasticity approach. In the plane strain and axisymmetric analyses the third principal stress follows from the geometrical symmetry

$$\sigma_y = \sigma_x = K_0\sigma_z. \tag{1.103}$$

The stress τ_{xy} is obviously zero.

Adopting Eq. (1.102) the K_0 variable may in general attain values ranging from 0 to 1. To overcome this limitation most geotechnical software products offer an option called the K_0 procedure that allows an arbitrary selection of K_0 when generating an initial geostatic stress state prior to any construction stage (stress state that exists in the earth body prior to any mankind activities).

For normally consolidated soils the value of $K_0 = K_0^{NC}$. The most common approximation is the Jaky formula [39]

$$K_0^{NC} = \frac{1 - \sin\varphi}{1 + \sin\varphi}\left(1 + \frac{2}{3}\sin\varphi\right) \tag{1.104}$$

assumed usually in the form

$$K_0^{NC} = 1 - \sin\varphi \tag{1.105}$$

where φ is the effective angle of internal friction. Another estimate available in [75, 74] reads

$$K_0^{NC} = \frac{\sqrt{2} - \sin\varphi}{\sqrt{2} + \sin\varphi} \tag{1.106}$$

For overconsolidated soils a general form of K_0 is provided by, recall Eq. (1.72),

$$\begin{aligned}
K_0 &= K_0^{NC}OCR^\alpha \tag{1.107}\\
\alpha &= 0.5, \quad \text{Meyerhof [56]}\\
\alpha &= \sin\varphi, \quad \text{Mayne\&Kulhawy [54]}
\end{aligned}$$

where OCR is the overconsolidation ratio described in Section 1.13. Experimental evidence for the $K_0 - OCR$ relationship can be found for example in [76]. Similarly to Section 1.13, the dilatometer measurements can be exploited to estimate the value of K_0 employing the measured horizontal stress index K_D as

$$\begin{aligned}
K_0 &= \frac{K_D}{1.5}^{0.47} - 0.6, \quad \text{Marchetti [53]} \tag{1.108}\\
K_0 &= 0.34K_D^{0.44\div0.64}, \quad \text{Lacasse and Lunne [47]} \tag{1.109}
\end{aligned}$$

Such a test was numerically simulated in [12]. As a general conclusion for a reliable determination of the K_0 value the authors recommend combination of laboratory tests, field measurements and numerical analysis. While this may play a significant role for cohesive soils such as stiff clays, the cohesionless soils such as sands are usually assumed normally consolidated, i.e., $OCR = 1, K_0 = K_0^{NC}$.

PLAXIS [63] finite element program offers a simple two-step loading/unloading procedure with the assumption of an elastic behavior to estimate the horizontal overconsolidated stress σ_x^0 associated with the in-situ vertical stress σ_z^0:

1. The soil is first normally consolidated to a stress σ_z^{pc}, i.e., $\sigma_x^{pc} = K_0^{NC}\sigma_z^{pc}$

2. Next, the soil is elastically unloaded, i.e., $\Delta\sigma_x = \dfrac{\nu}{1-\nu}\Delta\sigma_z$, to an overconsolidated state σ_x^0, σ_z^0
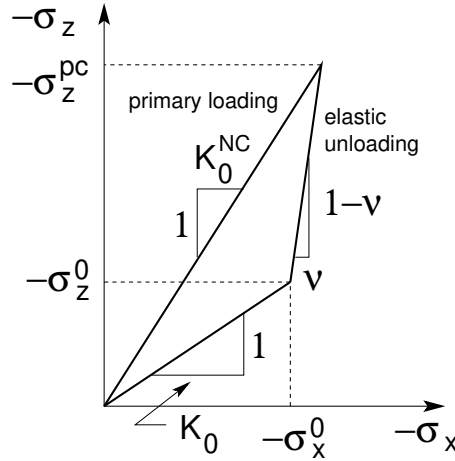
Figure 1.7: Loading/unloading sequence to define overconsolidated state of stress

A graphical presentation of individual steps is plotted in Fig. 1.7. As suggested in Section 1.13 there are two options to generate the overconsolidated state of stress:

1. **Using OCR** - consider the unloading path together with Eqs. (1.81) and (1.86) to get

$$\frac{\Delta\sigma_x}{\Delta\sigma_z} = \frac{\nu}{1-\nu} = \frac{\sigma_x^{pc} - \sigma_x^0}{\sigma_z^{pc} - \sigma_z^0} = \frac{K_0^{NC}OCR\sigma_z^0 - \sigma_x^0}{(OCR - 1)\sigma_z^0} \tag{1.110}$$

$$\sigma_x^0 = \underbrace{\left(K_0^{NC}OCR - \frac{\nu}{1-\nu}(OCR - 1)\right)}_{K_0}\sigma_z^0 \tag{1.111}$$

2. **Using POP** - consider the unloading path together with Eqs. (1.82) and (1.86) to get

$$\frac{\Delta\sigma_x}{\Delta\sigma_z} = \frac{\nu}{1-\nu} = \frac{\sigma_x^{pc} - \sigma_x^0}{\sigma_z^{pc} - \sigma_z^0} = \frac{K_0^{NC}(\sigma_z^0 + POP) - \sigma_x^0}{(\sigma_z^0 + POP) - \sigma_z^0} \tag{1.112}$$

$$\sigma_x^0 = K_0^{NC}\sigma_z^0 + POP\left(K_0^{NC} - \frac{\nu}{1-\nu}\right) \tag{1.113}$$

Notice that both expressions (1.111) and (1.113) reduce to $\sigma_x^0 = K_0^{NC}\sigma_z^0$ for normally consolidated soils with $OCR = 1, POP = 0$. Point out that in GEO5 FEM the value of K_0^{NC} is introduced when setting up the material model within the K_0 **procedure**. The Jaky formula (1.105) is usually adopted for non-cohesive soils, while cohesive soils typically assume the value of K_0^{NC} based on Eq. (1.102). When the peak angle of internal friction φ is not one of the input parameters, such as the Modified Cam-clay model, the value of K_0^{NC} can be estimated by solving Eq. (1.92).

1.14.1 Restriction on combination of parameters K_0^{NC}, K_0, OCR

As pointed out in the previous Section 1.13 the degree of overconsolidation is projected into the definition of preconsolidation pressure p_c determining the initial size of the compression cap in advanced plasticity models. This step requires introduction of the coefficient of lateral earth pressure at rest of a normally consolidated soil K_0^{NC} and one of the two overconsolidation parameters, either OCR or POP. The structure of governing equations makes this procedure applicable only when generating the initial stress state $\boldsymbol{\sigma}_0$ with the K_0 procedure. Note that one of the options in GEO5 FEM is to specify both OCR and K_0 arbitrarily without considering their mutual relation, e.g., through Eq. (1.107) or (1.111), which may lead to an unacceptable stress state. Such a stress state might be identified with the preconsolidation pressure $p_c(K_0^{NC}, OCR)$ pertinent to the original normally consolidated soil, recall Section 1.13, being smaller than the preconsolidation pressure $p_c^0(K_0)$ associated with the overconsolidated soil, e.g., a soil underwenting some sort of unloading from the original normally consolidated state.

It turns out that regardless of the material model an allowable stress state requires

$$|\sigma_m^{pc}| \geq |\sigma_m^0| \tag{1.114}$$

where σ_m^{pc} and σ_m^0 are the mean effective stresses associated with normally consolidated and overconsolidated stress states, respectively. In light of K_0 procedure and the notation introduced in previous sections they read

$$\sigma_m^{pc} = \frac{1}{3}\left(1 + 2K_0^{NC}\right)OCR\,\sigma_y^0 \tag{1.115}$$

$$\sigma_m^0 = \frac{1}{3}\left(1 + 2K_0\right)\sigma_y^0 \tag{1.116}$$

where σ_y^0 is the initial vertical stress given, e.g., by Eq. (1.83). These definitions when introduced into Eq. (1.114) thus provide some restrictions on the combination of parameters K_0^{NC}, K_0 and OCR expressed as follows

$$K_0 \leq \frac{1}{2}\left(\left(1 + 2K_0^{NC}\right)OCR - 1\right) \quad \text{or} \quad OCR \geq \frac{1 + 2K_0}{1 + 2K_0^{NC}} \tag{1.117}$$

While these inequalities should be satisfied in general, they are checked in GEO5 FEM only for advanced constitutive models with the compression cap including the Hypoplastic clay model.

As an illustrative example we now present application of Eq. (1.117)$_1$ to the Modified Cam-clay model. Recall Eqs. (1.96) to write the preconsolidation pressures associated with the mean stresses in Eqs. (1.115) and (1.115) as

$$p_c = -\frac{(J^{pc})^2}{M_{cs}^2\sigma_m^{pc}} - \sigma_m^{pc} \tag{1.118}$$

$$p_c^0 = -\frac{(J^0)^2}{M_{cs}^2\sigma_m^0} - \sigma_m^0 \tag{1.119}$$

where the equivalent deviatoric stresses are, with reference to Eqs. (1.89) and (1.86), provided by

$$J^{pc} = \frac{\sqrt{3}}{3}|\left(K_0^{NC} - 1\right)OCR\,\sigma_y^0| \tag{1.120}$$

$$J^0 = \frac{\sqrt{3}}{3}|\left(K_0 - 1\right)\sigma_y^0| \tag{1.121}$$

Adopting Eq. (1.117)$_1$ and setting, e.g., $K_0^{NC} = 0.5$ and $OCR = 2$ gives $K_0 \leq 1.5$. The corresponding stresses are listed Table 1.1 for a specific choice of $M_{cs} = 1, \sigma_y^0 = -100\text{kPa} \rightarrow \sigma_m^{pc} - 133.3\,\text{kPa}, J^{pc} = 86.6\,\text{kPa}, p_c^{pc} = 189\,\text{kPa}$.

Table 1.1: Testing influence of condition $(1.117)_1$

K_0	σ_m^0	J^0	p_c^0
1	-100	0	100$< p_c^{pc}$
2	-166.7	100	**200**$> p_c^{pc}$

It is clear that setting $K_0 = 2$ violates Eq. $(1.117)_1$ and thus also Eq. (1.114) suggesting in turn an unacceptable initial geostatic stress state $\boldsymbol{\sigma}^0$. A graphical representation is plotted in Fig. 1.8, where p_c^1, p_c^2 represent p_c^0 for $K_0 = 1$ and $K_0 = 2$, respectively.
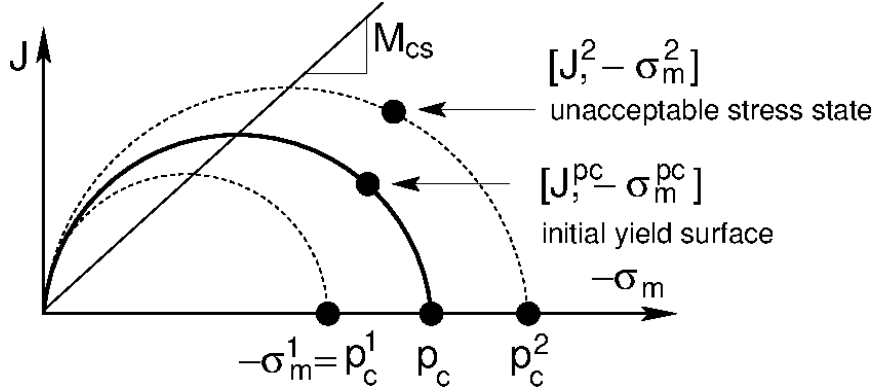
Figure 1.8: Example of acceptable $(\sigma_m^0 = \sigma_m^1)$ and unacceptable $(\sigma_m^0 = \sigma_m^2)$ initial stress state

1.15   Mobilized shear strength R_{mob}

Next to the equivalent deviatoric plastic strain E_d^{pl} the mobilized shear strength R_{mob} is another parameter to provide a graphical testimony about accessibility of a structure to a catastrophic failure. It gives the degree of shear strength mobilization in light of the critical or limit shear yield surface.

Considering models of the Mohr-Coulomb type this parameter is given by

$$R_{mob} = \frac{M_{\varphi_m}}{M_\varphi} \times 100 \; [\%] \tag{1.122}$$

where M_φ represents the slope of the yield surface projected into the meridian plane and M_{φ_m} is the slope associated with currently mobilized angle of internal friction φ_m, which in turn depends on the current stress state $[\sigma_m^c, J^c]$, see Fig. 1.9.
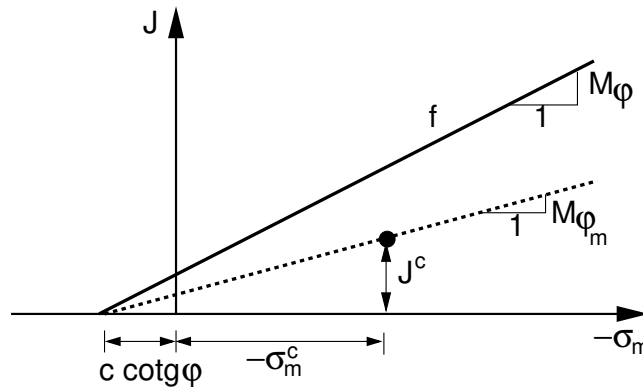
Figure 1.9: Graphical representation of mobilized shear strength

Similarly we proceed with the Modified and Generalized Cam-clay models where the slope M_φ is now replaced with the slopes representing the critical state M_{cs} and g in Figs. 11.2 and 12.1,

respectively. These figures also suggest that the mobilized shear strength may exceed 100% if the material point is found above the critical state line within the supercritical region. At critical state we get $R_{mob} = 100\%$.

When the limit shear yield surface is formulated on the basis of Matsuoka-Nakai failure criterion is appears advantageous to compute the mobilized shear strength directly in terms of the mobilized friction angle as

$$R_{mob} = \frac{\sin \varphi_m}{\sin \varphi} \times 100 \ [\%] \tag{1.123}$$

where φ is the peak friction angle and φ_m is the mobilized friction angle associated with, see ahead Eq. (8.48),

$$\sin \varphi_m = \sqrt{I_\sigma^c} \tag{1.124}$$

where the current value of I_σ^c follows from Eqs. (8.24) - (8.27). Such a formulation is adopted for the Hardening soil, Soft soil, and Hypoplastic clay models. In the latter model the peak internal friction is replaced with the critical state friction angle φ_{cs}.

In some applications, e.g., when performing the analysis in undrained conditions, the undrained angle of internal friction $\varphi_u = 0$. This is the case of Mises and Tresca material models where the mobilized shear strength is then provided by

$$R_{mob} = \frac{J^c}{J_f} \times 100 \ [\%] \tag{1.125}$$

where J_f represents the value of equivalent deviatoric stress for a material point sitting on the yield surface. This formulation is also adopted for the Hoek-Brown model where J_f is derived for the current value of mean stress σ_m^c.

Chapter 2

Material models and analyses types

The material models implemented in GEO5 FEM are classified in light of the type of analysis as

- **Stress-strain analysis**

  1. ***Elastic models*** can be used to perform standard elastic analysis with no account for evolution of plastic strains. Therefore, these models are typically employed to check the computational model, i.e., geometry, finite element mesh, boundary conditions, construction sequence, etc. Further details are provided in Chapter 3
     - Linear elastic (elastic), Section 3.1
     - Bilinear elastic (elastic modified), Section 3.2

  2. ***Basic plastic models*** fall into the category of elastic perfectly plastic materials of the Mohr-Coulomb type. They are characterized by a linear elastic response within the yield surface with potential variation of elastic stiffness as a function of depth. In isotropic compression their behavior is purely elastic. Their application is expected in a structural analysis where potential failure is driven by shear.
     - Drucker-Prager (Mises used with undrained analysis in total stresses), Chapter 4
     - Mohr-Coulomb (Tresca used with undrained analysis in total stresses), Chapter 5
     - Hoek-Brown, Chapter 6
     - Hoek-Brown modified, Chapter 7

  3. ***Elasto-plastic models with hardening/softening*** fall into the category of advanced plasticity models taking into account potential evolution of yield surfaces with plastic strains. Apart from shear yield surface the evolution of plastic strains in isotropic compression is monitored by the cap yield surface. In both shear and compression the yield surfaces assume Matsuoka-Nakai projection into the deviatoric plane. Nonlinear elastic response with stress dependent stiffness is allowed with some models. A better prediction of settlement in comparison to basic plastic models can therefore be expected.
     - Hardening soil, Chapter 8
     - Soft soil, Chapter 9
     - Modified Mohr-Coulomb, Chapter 10

  4. ***Critical state models*** are advanced constitutive models particularly suitable in applications where a correct prediction of settlement plays a crucial role. Their formulation allows for representation of most of the features of soils observed experimentally such as nonlinear elastic response with stress dependent stiffness, dependence of soil response on porosity, possibility to define a limit surface in the stress and porosity space, etc.
     - Modified Cam clay, Chapter 11
     - Generalized Cam clay, Chapter 12
     - Hypoplastic clay, Chapter 13
     - Hypoplastic sand, Chapter 14

- **Water flow analysis**

  To represent the water flow in partially saturated zones in both steady state and transient seepage analyses the program GEO5 FEM introduces three material models for the prediction of relative permeability and degree of saturation. Details can be found in Chapter 16.

  - Log-linear
  - Gardner
  - van Genuchten

2.1   Drained and undrained conditions in stress-strain analysis

When performing standard time independent stress-strain analysis the program GEO5 FEM offers two options to treat the presence of ground water in subsoil. In particular, the two boundary states in more general consolidation problem, see Section 17.4.5, are represented by

- **Drained boundary conditions** corresponding to steady state of pore pressure attained at the end of consolidation for time $t \to \infty$.

- **Undrained boundary conditions** corresponding to the onset of consolidation at time $t = 0$. The analysis thus generates transient pore pressures to be dissipated in the consolidation step.

To introduce the subject we imagine soil as a partially saturated three-phase porous medium consisting of grains (a solid phase s) and pores filled with liquid water (w) and moist air (g) as sketched in Figure 2.1.
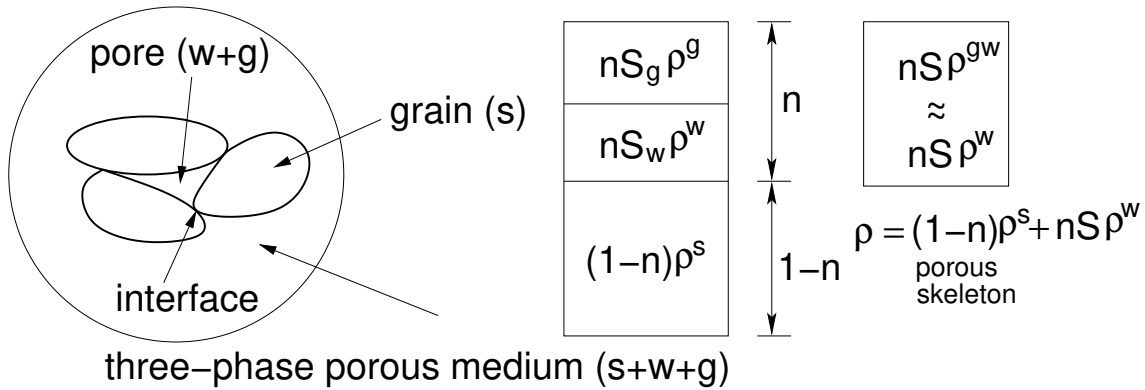
Figure 2.1: Simplified definition of a two-phase medium

The pore pressure p^s acting on a solid phase can be then expressed as

$$p^s = S_w p^w + S_g p^g \tag{2.1}$$

where p^w, p^g are the pressures in liquid and gaseous phase, respectively, S_w, S_g are corresponding degrees of saturation satisfying $S_w + S_g = 1$. Point out that the pore pressure is assumed positive when in compression while negative value represents suction. The saturation S_w can also be expressed in terms of the volumetric water content θ [m^3/m^3]

$$\theta = \frac{\Omega_w}{\Omega} \tag{2.2}$$

as

$$S_w = \frac{\Omega_w}{\Omega_p} = \frac{\Omega_w}{n\Omega} = \frac{\theta}{n} \tag{2.3}$$

where $\Omega = \Omega_m + \Omega_w + \Omega_g$ is the total volume equal to the sum of the volume of solid phase Ω_m, volume of water Ω_w and volume of air space Ω_g with $\Omega_p = \Omega_w + \Omega_g$ be the volume of pores, and n is the porosity typically written in terms of the void ratio e introduced in Section 1.11 as

$$n = \frac{\Omega_w + \Omega_g}{\Omega} = \frac{e}{1 + e}, \qquad e = \frac{\Omega_w + \Omega_g}{\Omega_m} = \frac{\Omega_p}{\Omega_m} = \frac{n}{1 - n} \tag{2.4}$$

To simplify the model it is often assumed that during the flow the moist air remains at atmospheric pressure. Next, taking the atmospheric pressure as the reference pressure gives $p^g = 0$ so that, see also [45],

$$p^s = S_w p^w = Sp \tag{2.5}$$

The effective mass density ρ is then given by

$$\rho = (1 - n)\rho^s + nS\rho^w \tag{2.6}$$

Note that in GEO5 FEM the effective mass density $\rho = \rho_{dry}$ or $\rho = \rho_{sat}$ depending on whether the macroscopic point is found above or below the ground water table. Such a simplification of the two-phase model, which essentially treats the liquid and gaseous phases as the mixture of a one-phase compressible fluid moving throughout the porous skeleton (Figure 2.1) is adopted in GEO5 FEM. Readers interested in a more general description of moisture and heat transfer in porous media are referred to [50, 45].

A standard volume averaging already employed to define the effective mass density in Eq. (2.6) of the porous medium filled with fluid phases allows us to write the total stress $\boldsymbol{\sigma}$ in terms of the stress $\boldsymbol{\sigma}^m$ developed in the solid phase and the stress Sp transmitted by the pores as

$$\boldsymbol{\sigma} = (1 - n)\boldsymbol{\sigma}^m - 3\boldsymbol{m}(nSp) = \underbrace{(1 - n)(\boldsymbol{\sigma}^m + 3\boldsymbol{m}Sp)}_{\boldsymbol{\sigma}^{eff}} - 3\boldsymbol{m}Sp \tag{2.7}$$

where the operator $\boldsymbol{m}$ is defined by Eq. (1.21). Recall that $\boldsymbol{\sigma}^{eff}$ represents the effective stresses between the grains. Taking on the other hand the strains in the bulk material due to changes of the pore pressure Sp into account yields the constitutive equation (1.40) in a slightly modified format

$$\boldsymbol{\sigma}^{eff} = \mathbf{D}(\boldsymbol{\varepsilon} - \boldsymbol{m}\varepsilon_v^p) \tag{2.8}$$

where $\mathbf{D}$ is the elastic stiffness matrix of the porous skeleton, recall Eq. (1.45) and

$$\varepsilon_v^p = -\frac{Sp}{K_m} \tag{2.9}$$

represents the volumetric strain of the solid phase due to changes of the pore pressure Sp with K_m being the bulk modulus of the solid phase. Following [10, 50, 45] allows us to rewrite Equation (2.7) as

$$\boldsymbol{\sigma} = \mathbf{D}\boldsymbol{\varepsilon} - \alpha 3\boldsymbol{m}Sp = \boldsymbol{\sigma}_\varepsilon - \alpha 3\boldsymbol{m}Sp \tag{2.10}$$

where the Biot constant α reads

$$\alpha = \boldsymbol{m}^\mathsf{T} \left(\mathbf{I} - \frac{\mathbf{D}}{3K_m}\right) 3\boldsymbol{m} = 1 - \frac{K_{sk}}{K_m} < 1 \tag{2.11}$$

and K_{sk} is the bulk modulus of the porous skeleton. For a material without any pores we get $K_{sk} = K_m$. For cohesive soils we typically have $K_{sk} << K_m$ and $\alpha = 1$.

2.1.1 Drained conditions

In GEO5 FEM suction in standard stress-strain analysis is neglected. Thus for drained analysis we set saturation $S = 0$ for the stress point found above the ground water table and $S = 1$ for the stress point located below the ground water table to modify Eq. (2.10) accordingly. The analysis is carried out in effective stresses using effective strength parameters when applicable, i.e., effective cohesion c and effective angle of internal friction φ. The steady state pore pressure p is prescribed and does not change with the deformation of porous skeleton.

2.1.2   Undrained conditions

When running undrained analysis with GEO5 FEM the soil is considered fully saturated in the entire solution domain with $S = 1$. Three options to address undrained conditions are available

1. Analysis in effective stresses (φ_{eff}, c_{eff})

2. Analysis in effective stresses (S_u)

3. Analysis in total stresses (S_u)

Type (1): Analysis in effective stresses (φ_{eff}, c_{eff})

This type of undrained analysis is essentially a solution of a coupled problem where evolution of excess pore pressure results from deformation of the porous skeleton. In undrained analysis this boils down to finding a relationship between the increment of excess pore pressure Δp and the increment of volumetric strain $\Delta\varepsilon_v$. The volume averaging renders the latter quantity in the form

$$\Delta\varepsilon_v = (1-n)\frac{\Delta\Omega_m}{\Omega_m} + n\frac{\Delta\Omega_w}{\Omega_w} \tag{2.12}$$

Combining Eqs. (2.7) - (2.9) allows us to write the change in volume of the solid phase as

$$\frac{\Delta\Omega_m}{\Omega_m} = \frac{\Delta\sigma_m^m}{K_m} = -\frac{\Delta p}{K_m} + \frac{\Delta\sigma_m^{eff}}{(1-n)K_m} = -\frac{1}{1-n}\left[\frac{\alpha-n}{K_m}\Delta p + (\alpha-1)\Delta\varepsilon_v\right] \tag{2.13}$$

The mass conservation of the liquid phase gives

$$\frac{\Delta\Omega_w}{\Omega_w} = -\frac{\Delta p}{K_w} \tag{2.14}$$

Equations (2.13) and (2.14) can be now introduced back to Eq. (2.12) to get

$$\Delta\varepsilon_v = -\frac{1}{\alpha}\left(\frac{\alpha-n}{K_m} + \frac{n}{K_w}\right)\Delta p = -\frac{1}{\alpha M}\Delta p \tag{2.15}$$

where M is known as the Biot modulus.

To proceed we write the increment of virtual work done by internal forces, Eq. (17.2), in the form

$$\delta E_i = \int_V \delta\Delta\boldsymbol{\varepsilon}^\mathsf{T}\left(\mathbf{D}\Delta\boldsymbol{\varepsilon} - \alpha 3\boldsymbol{m}\Delta p\right)\,\mathrm{d}V \tag{2.16}$$

which upon substitution for Δp from Eq. (2.15) modifies Eq. (2.16) as

$$\delta E_i = \int_V \delta\Delta\boldsymbol{\varepsilon}^\mathsf{T}\left(\mathbf{D} + \alpha^2 M 9\boldsymbol{m}\boldsymbol{m}^\mathsf{T}\right)\Delta\boldsymbol{\varepsilon}\,\mathrm{d}V = \int_V \delta\Delta\boldsymbol{\varepsilon}^\mathsf{T}\mathbf{D}_{eff}\Delta\boldsymbol{\varepsilon}\,\mathrm{d}V \tag{2.17}$$

where V is the volume of the analysis domain and $\mathbf{D}_{eff}$ is effective stiffness matrix. With the application of plastic models the elastic stiffness matrix $\mathbf{D}$ can be replaced by an elastoplastic (algorithmic) tangent stiffness matrix $\mathcal{D}$, recall Section 17.1.

Once $\Delta\boldsymbol{\varepsilon}$ is known from the solution of the system of global equations of equilibrium the unknown increment of excess pore pressure Δp then readily follows from Eq. (2.15). Numerical experiments suggest that reasonable predictions of excess pore pressure distributions are obtained providing the Biot modulus is sufficiently large, say

$$M = (100 \div 1000)K_{sk} \tag{2.18}$$

As evident from the above formulations the analysis employs effective stresses, effective stiffness and effective shear strength parameters c_{eff}, φ_{eff} in models where applicable. The total pore pressure $p = p^{ss} + p^{ex}$, were p^{ss}, p^{ex} stand for the steady state and excess pore pressure, respectively.

With this option:

- All material models formulated in the framework of standard plasticity can be adopted.
- Advanced models are expected to perform better in comparison to elastic-perfectly plastic models such as the Mohr-Coulomb model.
- With simple elastic-perfectly plastic models it is desirable to check the generated undrained shear-strength as this might be overestimated owing to an incorrectly predicted effective stress path. The GEO5 FEM program provides a graphical representation of a numerically predicted mobilized undrained shear strength $S_u^m = J \cos \theta \leq S_u$ where S_u is the actual undrained shear strength and J and θ are the computed equivalent deviatoric stress and Lode 's angle, respectively.
- The dilatancy angle ψ (as well as the mobilized dilatancy angle ψ_m in the case of Hardening soil model), if specified, is set to zero.

Type (2): Analysis in effective stresses (S_u)

Only models of the Mohr-Coulomb type without compressive cap are permitted with this option. Similarly to the previous option the analysis adopts the effective stiffness and generates the excess pore pressure via Eq. (2.15). On the contrary, the effective shear strength parameters are replaced by undrained shear strength S_u, i.e., $c \to S_u, \varphi = 0$. With this option:

- Mohr-Coulomb and Drucker-Prager models perform as the elastic-perfectly plastic Tresca and Mises models, respectively.
- Modified Mohr-Coulomb model is assumed in the form of elastic-perfectly plastic model so that its hardening-softening feature is turned off. The model performs as the Mises model.
- The dilatancy angle ψ, if specified, is set to zero .
- Unlike the previous option the undrained shear strength S_u is not affected, as it is one of the input parameters.
- Distinction is again made between the effective and total stresses via the total pore pressure $p = p^{ss} + p^{ex}$. Note, however, that the pore pressures and thus the effective stresses might not be predicted entirely correctly.

Type (3): Analysis in total stresses (S_u)

Only models of the Mohr-Coulomb type without compressive cap are permitted with this option. The analysis is performed in total stresses exploiting again the total shear strength S_u. In addition, this option requires inputting undrained Young's modulus E_u and undrained Poisson's ration $\nu_u = (0.495 - 0.499)$. Because standard elements are used, care must be taken when choosing the Poisson ratio $\nu_u \to 0.5$ which may cause oscillation of the mean stresses and consequently yield convergence problems. With this option:

- Mohr-Coulomb and Drucker-Prager models perform as the elastic-perfectly plastic Tresca and Mises models, respectively.
- Modified Mohr-Coulomb model is assumed in the form of elastic-perfectly plastic model so that its hardening-softening feature and the compressive cap are turned off. The model performs as the elastic-perfectly plastic Mises model.
- No distinction is made between the effective and total stresses so that all stresses are treated as the total stresses. The effective stresses are therefore assigned the values of the total stresses prior to calculation phase. Both the steady state (p^{ss}) and excess (p^{ex}) pore pressures are set equal to zero, so they are not reflected in the analysis.
- If undrained conditions are replaced by drained conditions in subsequent calculation stage, the model behaves like undergoing dissipation of (unknown) excess pore pressure without altering the current state of deformation. Such a modeling strategy should by approached with caution in general it is not recommended.
- The value of K_0 if used with the K_0-procedure to generate initial stresses refers to total rather then effective stresses.

Chapter 3

Elastic models

The GEO5 FEM program offers two variants of elastic models, the basic lienear elastic model (elastic) and the bilinear elastic model (elastic modified) in particular.

3.1 Linear elastic model (elastic)

Table 3.1 lists material parameters needed by the linear elastic model.

Table 3.1: Parameters of linear elastic constitutive model

Symbol	Units	Description
E	[MPa]	Modulus of elasticity
ν	[-]	Poisson's ratio
α	[1/℃]	Coefficient of thermal expantion

The linear elastic model is the basic model assuming proportional change in stress $\boldsymbol{\sigma}$ as a function strain $\boldsymbol{\varepsilon}$ as plotted in Fig. 3.1 .
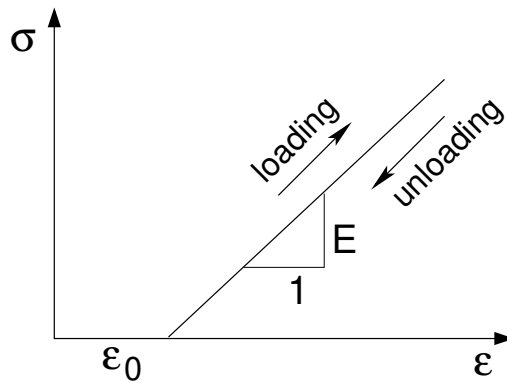
Figure 3.1: Linear elastic Hooke's law

When loading due to temperature change $\Delta\theta$ is considered, the Hooke law is provided by

$$\boldsymbol{\sigma} = \mathbf{D}(\boldsymbol{\varepsilon} - \boldsymbol{\varepsilon}_0) \tag{3.1}$$

where $\mathbf{D}$ is the elastic stiffness matrix given by Eq. (1.45) and $\boldsymbol{\varepsilon_0}$ is the initial strain written as

$$\boldsymbol{\varepsilon}_0 = \alpha\Delta\theta\boldsymbol{m} \tag{3.2}$$

where the operator $\boldsymbol{m}$ is given by Eq. (1.21).

3.2 Bilinear elastic model (elastic modified)

Table 3.2 lists material parameters needed by the bilinear elastic model.

Table 3.2: Parameters of bilinear elastic constitutive model

Symbol	Units	Description
E	[MPa]	Modulus of elasticity
E_{ur}	[MPa]	Modulus of elasticity in unloading/realoading
ν	[-]	Poisson's ratio
α	[1/℃]	Coefficient of thermal expantion

The bilinear elastic model represents an extention of the linear elastic model by assuming different stiffness in primary loading represented by Young's modulus E and in unloading/realoding given by unloading/realoding modulus E_{ur} as plotted in Fig. 3.2.
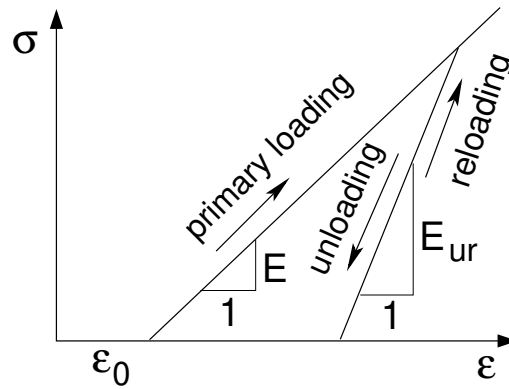
Figure 3.2: Bilinear elastic Hooke's law

The stress-strain relation is provided by Eq. (3.1) while properly accounting for a particular loading path. Note that upon unloding the sudden change in stiffness may result in several iterations of global equations equilibrium for a given load step.

Chapter 4

Drucker-Prager model

The Drucker-Prager (DP) model implemented in GEO5 FEM is assumed in the form of elastic-perfectly plastic material. If omitting thermal effects such a material response is schematically plotted in Fig. 4.1, σ_y identifies transition from an elastic into a plastic behavior in uniaxial tension.
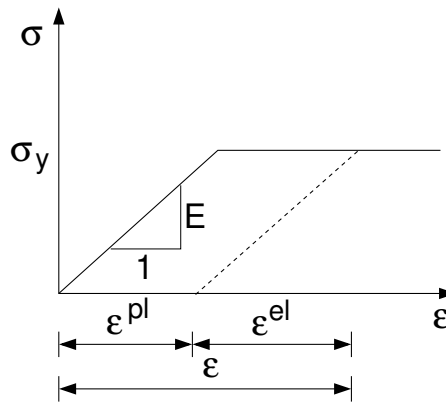
Figure 4.1: Elastic-perfectly plastic material law

In the DP model such a transition is controlled by the effective shear strength parameters, cohesion c_{eff} and angle of internal friction φ_{eff}. Because the undrained shear strength is denoted by S_u we shall drop the subscript (eff) and denote these parameters as c, φ henceforth. The list of material parameters needed by the DP model is available in Table 4.1.

Table 4.1: Parameters of Drucker-Prager plasticity model

Symbol	Units	Description
E	[MPa]	Modulus of elasticity
E_{ur}	[MPa]	Modulus of elasticity in unloading/realoading
ν	[-]	Poisson's ratio
c	[kPa]	Effective cohesion
φ	[°]	Effective angle of internal friction
ψ	[°]	Angle of dilation
e^{in}	[-]	Initial void ratio
e^{max}	[-]	Maximum void ratio to terminate dilation
α	[1/°C]	Coefficient of thermal expansion

Figure 4.2: Drucker-Prager yield function: a) plot in effective principal stress space, b) plot in meridian plane, c) plot in deviatoric plane

4.1 Formulation of Drucker-Prager failure criterion

When introduced in space of effective principal stresses the DP yield function plots as a cylindrical cone, see Fig. 4.2(a). Projections into meridian and deviatoric plane are displayed in Figs. 4.2(b,c). Following [65] the Drucker-Prager yield criterion then assumes the form

$$f^{DP} = J + (\sigma_m - c \cot \varphi) M_\varphi = 0 \tag{4.1}$$

where J and σ_m are given by Eqs. (1.24) and (1.11), respectively. The slope M_φ can be defined by matching the Drucker-Prager and Mohr-Coulomb yield surfaces as illustrated in Fig. 4.2(c). Three alternative Drucker-Prager circles are shown. Assuming that both surfaces match at $\theta = 30^0$ (triaxial compression we arrive at the Drucker-Prager circle circumscribed to the Mohr-Coulomb function (solid circle in Fig. 4.2(c)). The corresponding value of M_φ reads

$$M_\varphi^{\theta=+30^\circ} = \frac{2\sqrt{3}\sin\varphi}{3 - \sin\varphi} \tag{4.2}$$

If we desire that the Drucker-Prager circle touches the Mohr-Coulomb hexagon at $\theta = -30^0$ (triaxial extension) we set the value of M_φ to

$$M_\varphi^{\theta=-30^\circ} = \frac{2\sqrt{3}\sin\varphi}{3 + \sin\varphi} \tag{4.3}$$

Finally, the inscribed circle is found, see [65] for more details, when setting

$$M_\varphi^{ins} = \frac{\sin\varphi}{\cos\theta^{ins} - \dfrac{\sin\theta^{ins}\sin\varphi}{\sqrt{3}}} \tag{4.4}$$

with

$$\theta^{ins} = \arctan\frac{\sin\varphi}{\sqrt{3}} \tag{4.5}$$

Point out that in GEO5 FEM the 2nd option, fitting the DP model to the Mohr-Coulomb irregular hexagon at triaxial extension, is implemented. The model is completed by adopting a plastic potential function of the form

$$g^{DP} = J + (\sigma_m - a_{pp}) M_\psi = 0 \tag{4.6}$$

where a_{pp} follows from Fig. 4.2(b) when matching f^{DP} and g^{DP} for the current value of stress $\boldsymbol{\sigma}$ (σ_m^c). This gives

$$-a_{pp} = -\sigma_m^c + (\sigma_m^c - c \cot \varphi)\frac{M_\varphi}{M_\psi} \tag{4.7}$$

After substituting a_{pp} into Eq. (4.6) the plastic potential can be written in the form

$$g^{DP} = J + \left(\sigma_m - \sigma_m^c + (\sigma_m^c - c\cot\varphi)\frac{M_\varphi}{M_\psi} \right) M_\psi = 0 \tag{4.8}$$

where M_ψ is the slope of the plastic potential function in $J - \sigma_m$ space (see Fig 4.2(b)). For associated plasticity we set $M_\psi = M_\varphi$. The term M_ψ can be expressed in terms of the angle ψ, by substituting ψ for φ in Eqs. (4.2)–(4.4).

The above formulation suggests:

- The shear strength parameters c, φ remain constant throughout the analysis.

- The DP model is independent of the Lode angle θ.

4.2 Stress return mapping

When loading the material point beyond elasticity the constitutive law takes into account the evolution of plastic strains as, recall Fig. 4.1. In light of nonlinear analysis we write this stress-strain relationship in terms of stress and strain increments as

$$\Delta\boldsymbol{\sigma} = \mathbf{D}(\Delta\boldsymbol{\varepsilon} - \Delta\boldsymbol{\varepsilon}^{pl}) \tag{4.9}$$

To derive the increment of plastic strain $\Delta\boldsymbol{\varepsilon}^{pl}$ we invoke the plastic flow rule by assuming that the components of plastic strain evolve in the direction normal to the plastic potential g^{DP}. This gives

$$\Delta\varepsilon_v^{pl} = \Delta\lambda\frac{\partial g^{DP}}{\partial \sigma_m} = \Delta\lambda M_\psi \tag{4.10}$$

$$\Delta\boldsymbol{e}^{pl} = \Delta\lambda\frac{\partial g^{DP}}{\partial \boldsymbol{s}} = \Delta\lambda\frac{\mathbf{Q}^{-1}\boldsymbol{s}}{2J} \tag{4.11}$$

$$\Delta E_d^{pl} = \Delta\lambda\frac{\partial g^{DP}}{\partial J} = \Delta\lambda \tag{4.12}$$

where $\Delta\lambda$ is the plastic strain increment. Recall also Chapter 1 for the definition of operator matrix $\mathbf{Q}$, volumetric strain ε_v, deviatoric stresses $\boldsymbol{s}$, deviatoric strains $\boldsymbol{e}$, and equivalent deviatoric strain measure E_d.

To proceed, consider an equilibrium state at the end of the i-th load increment. Equations (4.10) - (4.12) allow us to the corresponding stresses at the end of the $(i+1)$ load increment as

$$\sigma_m^{i+1} = \sigma_m^{tr} - KM_\psi\Delta\lambda \tag{4.13}$$

$$\boldsymbol{s}^{i+1} = \boldsymbol{s}^{tr} - 2G\Delta\lambda\frac{\boldsymbol{s}^{i+1}}{2J^{i+1}} = \frac{\boldsymbol{s}^{tr}}{1 + \dfrac{\mu\Delta\lambda}{J^{i+1}}} = \boldsymbol{s}^{tr}\left(1 - \frac{\mu\Delta\lambda}{J^{tr}}\right) \tag{4.14}$$

$$J^{i+1} = J^{tr} - G\Delta\lambda, \quad J^{tr} = \sqrt{\frac{1}{2}(\boldsymbol{s}^{tr})^\mathsf{T}\mathbf{Q}^{-1}\boldsymbol{s}^{tr}} = \left[J_2^i + 2G\Delta\boldsymbol{e}^\mathsf{T}\boldsymbol{s}^i + G^2\Delta E_d^2\right]^{\frac{1}{2}} \tag{4.15}$$

where K and G are the bulk modulus and shear modulus, respectively, and the trial stresses follow from standard predictor step as, recall Eqs. (1.48) and (1.47),

$$\sigma_m^{tr} = \sigma_m^i + K\Delta\varepsilon_v \tag{4.16}$$

$$\boldsymbol{s}^{tr} = \boldsymbol{s}^i + 2G\mathbf{Q}\Delta\boldsymbol{e} \tag{4.17}$$

The required plastic strain increment is found by satisfying Eq. (4.1) at the end of $(i+1)$ load increment. Because the present elastic-perfectly plastic DP model is linear in $J - \sigma_m$ space we get

$$\Delta\lambda = \frac{f^{DP}(\boldsymbol{\sigma}^{tr})}{\left(\dfrac{\partial f^{DP}(\boldsymbol{\sigma}^{tr})}{\partial \boldsymbol{\sigma}}\right)^\mathsf{T}\mathbf{D}\left(\dfrac{\partial g^{DP}(\boldsymbol{\sigma}^{tr})}{\partial \boldsymbol{\sigma}}\right)} = \frac{f^{DP}(\boldsymbol{\sigma}^{tr})}{\boldsymbol{n}^\mathsf{T}\mathbf{D}\boldsymbol{n}_g} \tag{4.18}$$

4.3   Algorithmic tangent stiffness matrix

Given the volumetric-deviatoric split $\boldsymbol{\sigma} = 3\boldsymbol{m}\sigma_m + \boldsymbol{s}$ we may write the algorithmic tangent stiffness matrix $\boldsymbol{\mathcal{D}}$ at a given material point as

$$\boldsymbol{\mathcal{D}} = \frac{\mathrm{d}\boldsymbol{\sigma}^{i+1}}{\mathrm{d}\boldsymbol{\varepsilon}^{i+1}} = 3\boldsymbol{m}\left(\frac{\mathrm{d}\sigma_m^{i+1}}{\mathrm{d}\boldsymbol{\varepsilon}^{i+1}}\right)^{\mathsf{T}} + \frac{\mathrm{d}\boldsymbol{s}^{i+1}}{\mathrm{d}\boldsymbol{\varepsilon}^{i+1}} \tag{4.19}$$

where in light of Eqs. (4.13) - (4.17) it holds

$$\frac{\mathrm{d}\sigma_m}{\mathrm{d}\boldsymbol{\varepsilon}} = \frac{\partial\sigma_m}{\partial\boldsymbol{\varepsilon}} + \frac{\partial\sigma_m}{\partial\Delta\lambda}\frac{\partial\Delta\lambda}{\partial\boldsymbol{\varepsilon}} = a_1\boldsymbol{m} + a_2\frac{\partial\Delta\lambda}{\partial\boldsymbol{\varepsilon}} \tag{4.20}$$

$$\frac{\mathrm{d}\boldsymbol{s}}{\mathrm{d}\boldsymbol{\varepsilon}} = \frac{\partial\boldsymbol{s}}{\partial\boldsymbol{\varepsilon}} + \frac{\mathrm{d}\boldsymbol{s}}{\mathrm{d}\Delta\lambda}\left(\frac{\partial\Delta\lambda}{\partial\boldsymbol{\varepsilon}}\right)^{\mathsf{T}} = \mathsf{E} + \boldsymbol{q}\left(\frac{\partial\Delta\lambda}{\partial\boldsymbol{\varepsilon}}\right)^{\mathsf{T}} \tag{4.21}$$

where we dropped the script $(i+1)$ for the sake of clarity. The partial and total derivatives in above equations are

$$\frac{\partial\sigma_m}{\partial\boldsymbol{\varepsilon}} = 3K\boldsymbol{m} = a_1\boldsymbol{m} \tag{4.22}$$

$$\frac{\partial\sigma_m}{\partial\Delta\lambda} = -KM_\psi = a_2 \tag{4.23}$$

$$\frac{\partial\boldsymbol{s}}{\partial\boldsymbol{\varepsilon}} = \left[\frac{\partial\boldsymbol{s}}{\partial\Delta\boldsymbol{e}} + \frac{\partial\boldsymbol{s}}{\partial J}\left(\frac{\partial J}{\partial\Delta\boldsymbol{e}}\right)^{\mathsf{T}}\right]\frac{\partial\Delta\boldsymbol{e}}{\partial\boldsymbol{\varepsilon}} = \mathsf{E} \tag{4.24}$$

$$\frac{\partial\boldsymbol{s}}{\partial\Delta\boldsymbol{e}} = \frac{2G\mathbf{Q}}{1 + \dfrac{G\Delta\lambda}{J}} \tag{4.25}$$

$$\frac{\partial\boldsymbol{s}}{\partial J} = \frac{\boldsymbol{s}^i + 2G\mathbf{Q}\Delta\boldsymbol{e}}{\left(1 + \dfrac{G\Delta\lambda}{J}\right)^2}\frac{G\Delta\lambda_s}{J^2} = \frac{\boldsymbol{s}}{(-)}\frac{G\Delta\lambda_s}{J^2} \tag{4.26}$$

$$\frac{\partial J}{\partial\Delta\boldsymbol{e}} = \frac{\partial J}{\partial J^{tr}}\frac{\partial J^{tr}}{\partial\Delta\boldsymbol{e}} = G\frac{\boldsymbol{s}^{tr}}{J^{tr}} = G\frac{\boldsymbol{s}}{J} \tag{4.27}$$

$$\frac{\partial\Delta\boldsymbol{e}}{\partial\boldsymbol{\varepsilon}} = \mathbf{PQ} \tag{4.28}$$

$$\frac{\mathrm{d}\boldsymbol{s}}{\mathrm{d}\Delta\lambda} = \frac{\partial\boldsymbol{s}}{\partial\Delta\lambda} + \frac{\partial\boldsymbol{s}}{\partial J}\frac{\partial J}{\partial\Delta\lambda} = \boldsymbol{q} \tag{4.29}$$

$$\frac{\partial\boldsymbol{s}}{\partial\Delta\lambda} = -\frac{\boldsymbol{s}^i + 2G\mathbf{Q}\Delta\boldsymbol{e}}{\left(1 + \dfrac{G\Delta\lambda}{J}\right)^2}\frac{G}{J} = -\frac{\boldsymbol{s}}{(-)}\frac{G}{J} \tag{4.30}$$

$$\frac{\partial J}{\partial\Delta\lambda} = -G \tag{4.31}$$

It now remains to determine $\dfrac{\partial\Delta\lambda}{\partial\boldsymbol{\varepsilon}}$ from consistency condition as proposed, e.g., in [14]. The consistency condition states that

$$\frac{\mathrm{d}f^{DP}}{\mathrm{d}\boldsymbol{\varepsilon}} = \frac{\partial f^{DP}}{\partial J}\frac{\mathrm{d}J}{\mathrm{d}\boldsymbol{\varepsilon}} + \frac{\partial f^{DP}}{\partial\sigma_m}\frac{\mathrm{d}\sigma_m}{\mathrm{d}\boldsymbol{\varepsilon}} = \left[\frac{\mathrm{d}\boldsymbol{s}}{\mathrm{d}\boldsymbol{\varepsilon}}\right]^{\mathsf{T}}\boldsymbol{j} + a_3\frac{\mathrm{d}\sigma_m}{\mathrm{d}\boldsymbol{\varepsilon}} = 0 \tag{4.32}$$

where we found convenient to write

$$\frac{\mathrm{d}J}{\mathrm{d}\boldsymbol{\varepsilon}} = \left[\left(\frac{\partial J}{\partial\boldsymbol{s}}\right)^{\mathsf{T}}\frac{\mathrm{d}\boldsymbol{s}}{\mathrm{d}\boldsymbol{\varepsilon}}\right]^{\mathsf{T}} = \left[\frac{\mathrm{d}\boldsymbol{s}}{\mathrm{d}\boldsymbol{\varepsilon}}\right]^{\mathsf{T}}\frac{\partial J}{\partial\boldsymbol{s}} \tag{4.33}$$

$$\frac{\partial J}{\partial\boldsymbol{s}} = \frac{1}{2J}\mathbf{Q}^{-1}\boldsymbol{s} = \frac{1}{2J}\mathbf{P}\boldsymbol{\sigma} = \boldsymbol{j} \tag{4.34}$$

$$\frac{\partial f^{DP}}{\partial\sigma_m} = M_\varphi = a_3 \tag{4.35}$$

Substituting Eqs. (4.20), (4.21), and (4.33) gives the consistency condition (4.32)in the form

$$\frac{\mathrm{d}f^{DP}}{\mathrm{d}\varepsilon} = \left[\frac{\mathrm{d}s}{\mathrm{d}\varepsilon}\right]^{\mathsf{T}} \boldsymbol{j} + a_3 \left(a_1 \boldsymbol{m} + a_2 \frac{\partial \Delta \lambda}{\partial \varepsilon}\right) \tag{4.36}$$

$$= \left(\mathsf{E}^{\mathsf{T}} + \frac{\partial \Delta \lambda}{\partial \varepsilon} \boldsymbol{q}^{\mathsf{T}}\right) \boldsymbol{j} + a_3 \left(a_1 \boldsymbol{m} + a_2 \frac{\partial \Delta \lambda}{\partial \varepsilon}\right) \tag{4.37}$$

$$= \mathsf{E}^{\mathsf{T}} \boldsymbol{j} + a_3 a_1 \boldsymbol{m} + \left(\boldsymbol{q}^{\mathsf{T}} \boldsymbol{j} + a_3 a_2\right) \frac{\partial \Delta \lambda}{\partial \varepsilon} = \boldsymbol{g} + b \frac{\partial \Delta \lambda}{\partial \varepsilon} = 0 \tag{4.38}$$

which provides

$$\frac{\partial \Delta \lambda}{\partial \varepsilon} = -\frac{1}{b} \boldsymbol{g} \tag{4.39}$$

Finally, introducing the vector $\dfrac{\partial \Delta \lambda}{\partial \varepsilon}$ into Eqs. (4.20) and (4.21) provides Eq. (4.19) in the form

$$\mathcal{D} = 3a_1 \boldsymbol{m}\boldsymbol{m}^{\mathsf{T}} + \mathsf{E} - \frac{1}{b} \left(3a_2 \boldsymbol{m} + \boldsymbol{q}\right) \boldsymbol{g}^{\mathsf{T}} \tag{4.40}$$

4.4 Return to apex

The stress return algorithm described in Section 4.2 is applicable providing the trial stress when brought back to the yield surface in the direction of the plastic strain rate vector (following inclination of the boundary of K_ε cone) is found on the boundary of cone K_σ representing the admissible stress domain, Fig. 4.3(a) (note that the vector $\boldsymbol{n}_g$ stores components of the normal to the plastic potential surface, recall Eq. (4.18)). Such a condition is met for point 1 in Fig. 4.3(b) but violated when referring to point 2. In the latter case the standard stress point return algorithm locates the stress point on the boundary of dual cone (point 2" in Fig. 4.3(b)) thus violating the yield condition. Such a situation
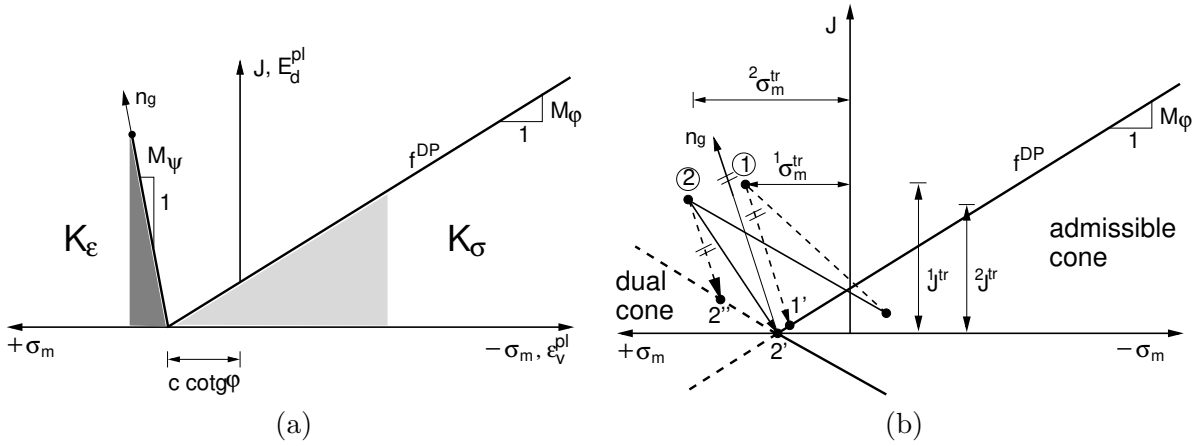
Figure 4.3: Apex problem: (a) Admissible regions for stresses and plastic strain rates, (b) Regular and singular return.

can be referred to as an "apex problem", since in this particular case the stress update is simply a return mapping to the apex (point 2' in Fig. 4.3(b)) so that

$$\boldsymbol{\sigma}^{i+1} = 3c \cot \varphi \boldsymbol{m} \tag{4.41}$$

Note that the non-associated flow rule restricts the plastic strain increment to belong to the cone K_ε, see also [29]. The admissibility condition for plastic strain rates is therefore given by, recall Fig. 4.3(a),

$$\dot{\varepsilon}_v \geq M_\psi \dot{E}_d^{pl} \tag{4.42}$$

In [29] the authors introduced a variational form of the flow rule to show through the concept of bi-potentials that the vector of plastic strain increments for the apex problem is indeed provided by

$$\Delta \varepsilon_v^{pl} = \frac{1}{K} \left(\sigma_m^{tr} - c \cot \varphi\right) \tag{4.43}$$

under the condition

$$M_\psi \frac{J^{tr}}{G} - \frac{1}{K} \left(\sigma_m^{tr} - c \cot \varphi \right) < 0 \qquad (4.44)$$

Note that Eq. (4.44) is essentially a linearized form of Eq. (4.42) (recall Eqs. (4.12) and (4.15) and note that $J^{i+1} = 0$ at the end of the return step).

Also point out that when returning to apex we get the algorithmic tangent stiffness matrix in the form

$$\mathcal{D} = \mathbf{0} \qquad (4.45)$$

4.5 Undrained analysis in total stresses - Type (3)

When performing an undrained analysis in total stresses, type (3), the Drucker-Prager yield criterion turns into the most simple von Mises yield criterion, which plots as an infinite cylinder opened along the hydrostatic axis as shown in Fig. 4.4(a). This is because the undrained angle of internal friction $\varphi_u = 0$. The undrained cohesion c_u is replaced by the undrained shear strength S_u. The corresponding projections into deviatoric and meridian planes are shown in Fig. 4.4(b).
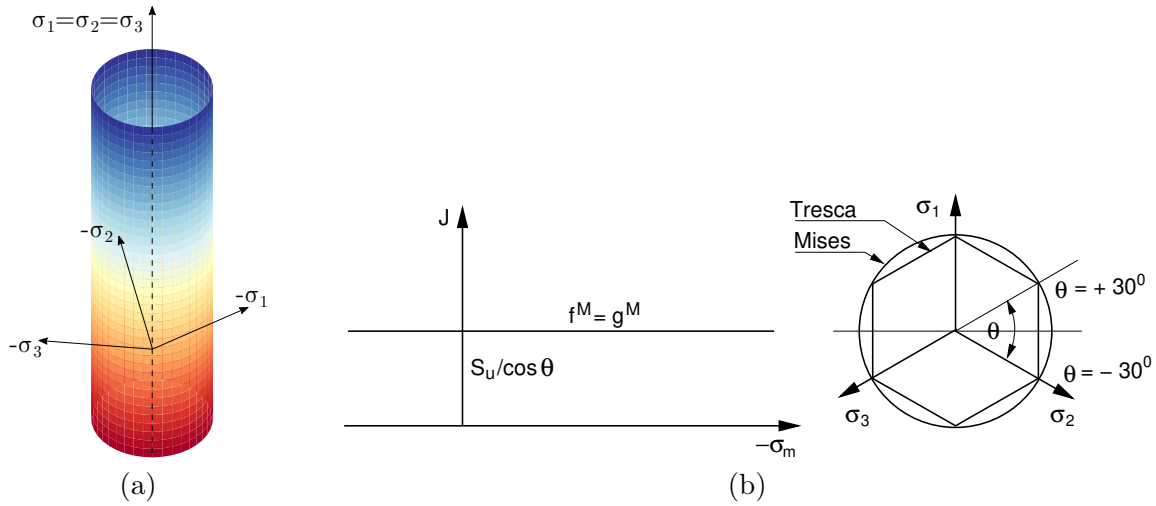
Figure 4.4: von Mises yield function: a) plot in total principal stress space, b) plot in meridian and deviatoric planes

Material parameters needed by the von Mises model are stored in Table 4.2.

Table 4.2: Parameters of von Mises plasticity model

Symbol	Units	Description
E_u	[MPa]	Undrained modulus of elasticity
S_u	[kPa]	Undrained shear strength
ν_u	[-]	Poisson's ratio assumed in the range of $(0.49 - 0.499)$
α	[1/K]	Coefficient of thermal expansion

The von Mises yield criterion is then defined by

$$f^M = J - \frac{S_u}{\cos \theta_{\pm 30}} \qquad (4.46)$$

where the Lode angle $\theta_{\pm 30} = \pm 30°$ resulting into a yield surface circumscribed to the Tresca model, see Fig. 4.4(b). As also evident from this figure the flow rule to derive increments of plastic strain is

associated suggesting

$$\Delta\varepsilon_v^{pl} = 0 \tag{4.47}$$

$$\Delta\boldsymbol{e}^{pl} = \Delta\lambda\frac{\partial f^M}{\partial \boldsymbol{s}} = \Delta\lambda\frac{\mathbf{Q}^{-1}\boldsymbol{s}}{2J} \tag{4.48}$$

$$\Delta E_d^{pl} = \Delta\lambda\frac{\partial f^M}{\partial J} = \Delta\lambda \tag{4.49}$$

so that

$$\sigma_m^{i+1} = \sigma_m^{tr} = \sigma_m^i + K\Delta\varepsilon_v \tag{4.50}$$

As indicated by Eqs. (4.48) and (4.49) the deviatoric stresses are updated with the help of Eqs. (4.14) and (4.15). Finally, following the same steps as in Section (4.3) we arrive at the algorithmic tangent stiffness matrix in the form, compare with Eq. (4.40) and note that $a_2 = a_3 = 0$,

$$\mathcal{D} = 9K\boldsymbol{m}\boldsymbol{m}^\mathsf{T} + \left(\mathbf{I} - \frac{\boldsymbol{q}\boldsymbol{j}^\mathsf{T}}{\boldsymbol{q}^\mathsf{T}\boldsymbol{j}}\right)\mathbf{E} \tag{4.51}$$

4.6 Testing implementation with simple laboratory tests

A convenient approach verify the ability of a given constitutive model to represent the soil behavior is to reproduce simple laboratory experiments numerically. Attention is then often limited to the behavior under one dimensional compression and under triaxial stress conditions when modeling the response in shear. Modeling such experiments is examined here mainly from educational perspectives. The material properties used in all simulations are stored in Table 4.3.

Table 4.3: Material properties of selected soil

$E = E_{ur}$ [MPa]	ν [-]	c [kPa]	φ [^{0}]	ψ [^{0}]	e^{in}	e^{max}
10	0.3	10	30	0-30	0.5	1

4.6.1 Oedometer test

The behavior of soils under one dimensional compression is usually investigated in an oedometer. Graphical representation of such a test from numerical stand point is displayed in Fig. 4.5. When assuming an ideal oedometer test, the loading and constraint conditions evident from Fig. 4.5(a) promote an evolution of uniform stresses and strains in the sample. Although a single quadrilateral element would be sufficient to model this numerically, a more complex mathematical model shown in Fig. 4.5(b) is considered, primarily in light of follow up simulations. As suggested, the analysis can be performed both in force and displacement loading regime.
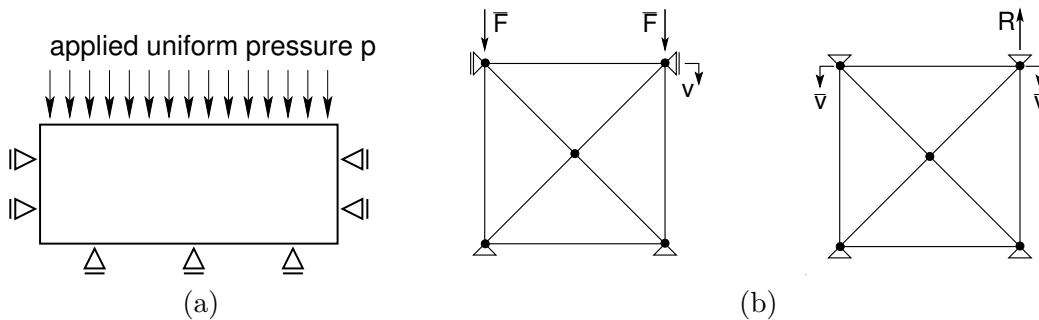
Figure 4.5: Ideal oedometer test: (a) uniform one-dimensional compression, (b) mathematical model

Referring to the specific boundary conditions the specimen is essentially loaded in triaxial compression resulting in a bilinear response plotted in Fig. 4.6. We identify to particular branches, the
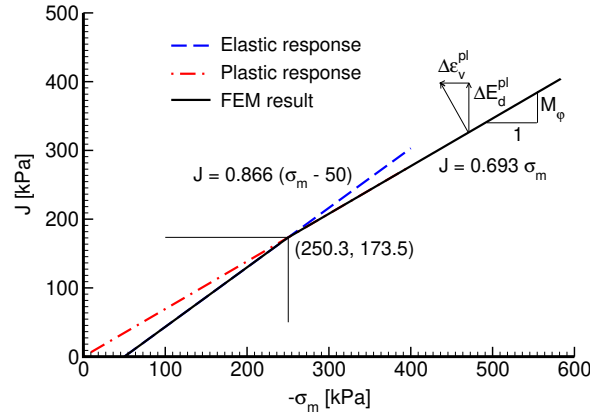
Figure 4.6: Predicted oedometer stress path

elastic one provided by

$$J = \frac{3(1-2\nu)}{\sqrt{3}(1+\nu)}(-\sigma_m + \sigma_m^{in}), \quad \sigma_m^{in} = -50 \text{ kPa in this example} \tag{4.52}$$

and the plastic one obtained from

$$\frac{\dfrac{\partial f^{DP}}{\partial \sigma_m}}{\dfrac{\partial f^{DP}}{\partial J}} = \frac{M_\varphi}{1} = \frac{J}{-\sigma_m} \tag{4.53}$$

An exact match with true solution is evident.

The analysis assumed no dilation to occur by setting $\psi = 0$. Real soil behavior, however, often deviates from such an assumption as evident from experimental measurements displayed in Fig. 4.7(a) for a variety of soils. We note in advance that dilation described by the Mohr-Coulomb model with constant dilation angle ψ may provide a reasonable estimate of such a behavior. This is visualized in Fig. 4.7(b). Note that infinite dilation would be predicted if no action is taken. As the soil eventually reaches the critical state with no volume changes with further shearing, it is advisable to introduce a certain condition to terminate plastic dilation. A reasonable condition is suggested in [63] where the maximum angle of dilation is linked to critical volume or the maximum voids ratio e^{max} the soil can experience, recall Table 4.1. Dilation cut-off can therefore be turned on when such a state is reached as indicated in Fig. 4.7(b).
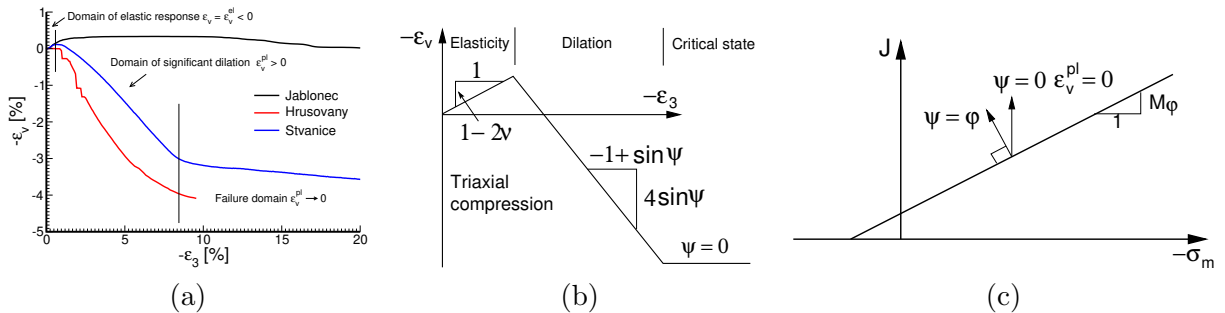
Figure 4.7: Treating dilatancy: a) Experimental observation, b) idealized prediction by Mohr-Coulomb model with dilation cut-off, c) direction of plastic strain increment comparing associated and non-associated flow rule

To appreciate the effect of dilation in numerical simulations we consider two limiting values of $\psi = 0$ (non-associated flow rule and critical state condition) and $\psi = \varphi$ (associated flow rule). The corresponding directions of the plastic strain increment is illustrated in Fig. 4.7(c). Note that for sands the typical value of ψ can be assumed equal to $\psi = \varphi - 30^0$ while $\psi = 0$ is usually set for clays.

To receive more complex response the FEM model in Fig. 4.8(a) is adopted. The results are plotted in Fig. 4.8(b,c). Variation of the total volumetric strain and its plastic component as a function of
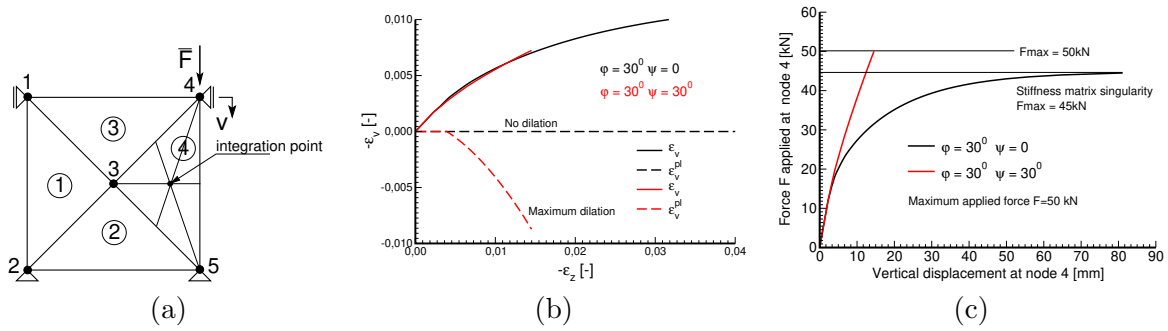
Figure 4.8: Comparing associated and non-associated flow rule: a) FEM model, b) evolution of volumetric plastic strain, c) effect of dilation on prediction of collapse load

vertical strain is evident from Fig. 4.8(b). As expected, no dilation is predicted for $\psi = 0$, while an excessive amount of dilation is predicted when assuming associated plasticity, $\psi = \varphi$. It is also useful to point out a rather constrained plastic deformation due to dilation. Such a behavior is further confirmed in Fig. 4.8(c) suggesting the collapse load being predicted only when keeping the dilation angle equal to zero. The results derived for an elastic-perfectly plastic material and associated plasticity are presented for further comparison.

4.6.2 Triaxial test

Drained or undrained triaxial compression tests are perhaps the most common experimental tests performed in the laboratory, Fig. 4.9(a). The computational model plotted in Fig. 4.9(b) is assumed here to simulate such an experiment. Again, drained conditions are assumed. In 2D environment, such a test is conveniently modeled using axisymmetric elements.

Unlike an ideal oedometer test, the triaxial test can be considered as a statically determinate problem with no additional constraints. Due to uniform stresses and strains developed inside the specimen, the structural analysis thus essentially reduces to the analysis of a material point. Hence, simple elastic rigid plastic material models must fail when loading the material beyond its elastic limit. This is demonstrated in Fig. 4.10. In particular, the use of a tangent stiffness matrix in the full Newton-Raphson method results in a singular stiffness matrix at a structural level as the yield condition is violated in all elements at the same time, Fig. 4.10(c). On the other hand, employing an elastic material stiffness matrix in the modified Newton-Raphson method gives a convergence error evident from Fig. 4.10(c). To overcome this drawback the analysis can be driven by the prescribed vertical displacements instead of tractions, recall Fig. 4.5(b), or by employing the Arc-length method introduced in Section 17.2.6. The former method option is used herein.

To compare the results of numerical simulations with analytical solutions we consider for simplicity a soil with zero cohesion as shown in 4.10(a). Other material parameters in Table 4.3 remain the same with $\psi = 0$. As evident 4.10(a) the soil is first compressed isotropically to arrive at the chamber pressure $\sigma_m^0 = -50$ kPa and than sheared in triaxial compression. The initial yield condition and the loading path are given by

$$J + \sigma_m M_\varphi = 0, \quad \text{onset of yielding} \tag{4.54}$$

$$J + \sqrt{3}(50 + \sigma_m) = 0, \quad \text{loading path} \tag{4.55}$$

and therefore

$$\sigma_m^e = \frac{50\sqrt{3}}{M_\varphi - \sqrt{3}} = -83.33 \text{ kPa}, \quad J^e = 57.73 \text{ kPa}, \quad E_d^e = \frac{J^0}{G} = 0.015 \tag{4.56}$$

$$\sigma_3 = -\sqrt{3}J^e + \sigma_1 = -150 \text{ kPa}, \quad \sigma_1 = \sigma_2 = -50 \text{ kPa} \tag{4.57}$$

As seen in 4.10(b) the analytical results are matched by simulations rather well. Point out that a relatively small loading step was used to obtain such a smooth transition from an elastic to a plastic response.
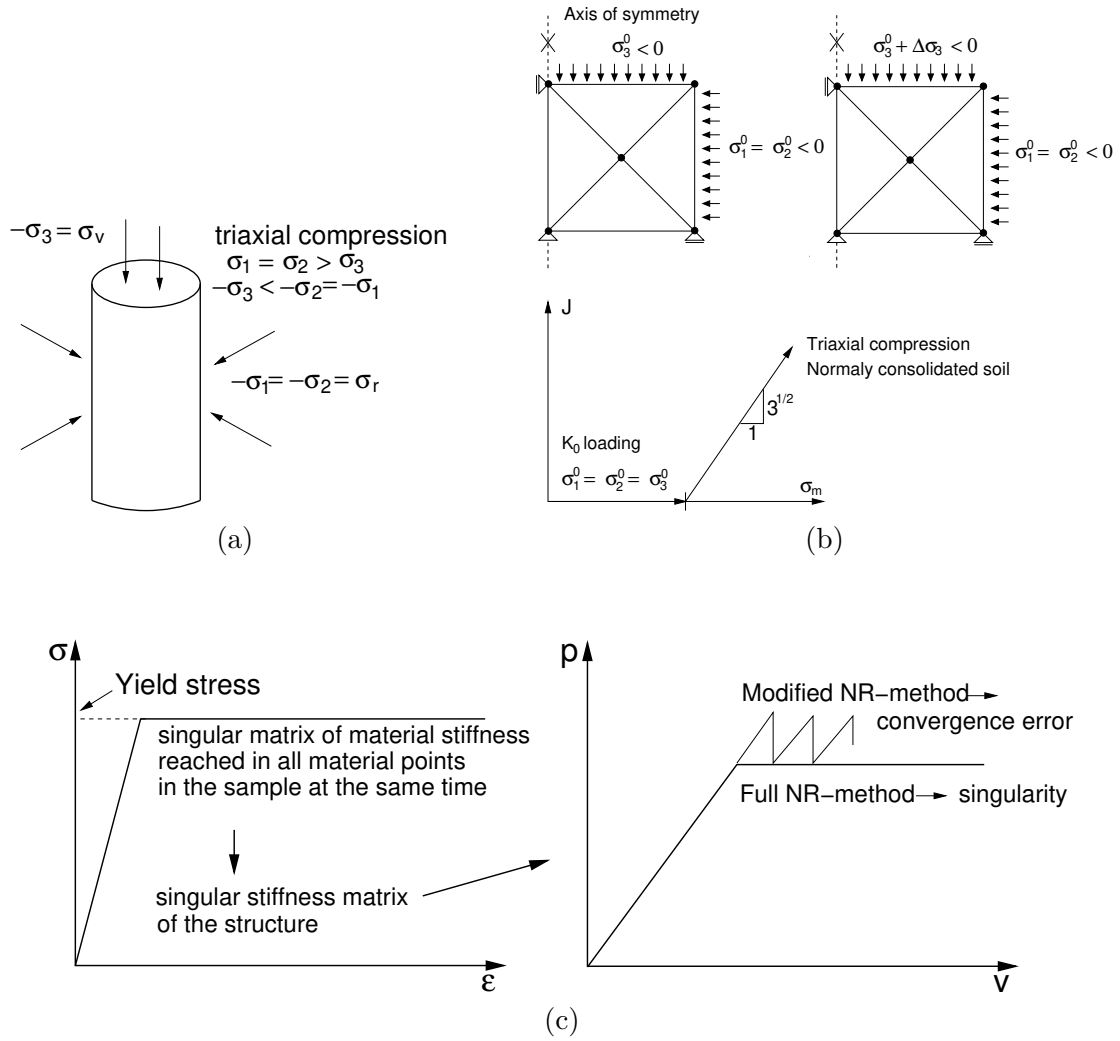
Figure 4.9: Numerical simulation of triaxial: a) loading conditions, b) finite element model and loading path for triaxial compression, c) lack of convergence for elastic-perfectly plastic material with full NR-method and stress control loading at the onset of yielding
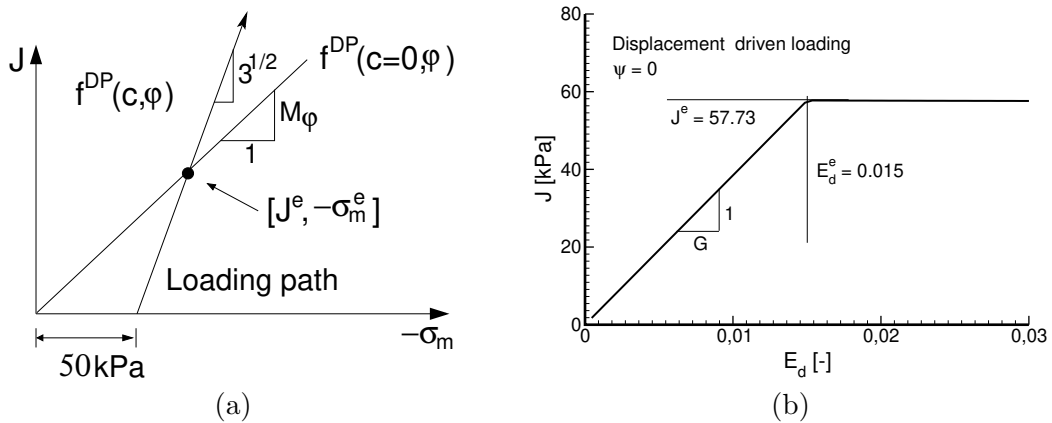
Figure 4.10: Drained triaxial compression: a) initial conditions and loading path, b) predicted stress-strain curve

Chapter 5

Mohr-Coulomb model

The Mohr-Coulomb (MC) failure criterion is perhaps the most well-known and understood soil failure model in geotechnical engineering. The model is very simple and unites the concepts of Mohr's circle and Coulomb's failure criterion. Unlike the models based on the J_2 plasticity concept, e.g., the Drucker-Prager model in Chapter 4, the formulation is presented in the principal stress space. Nevertheless, the material parameters describing the MC model are identical to the DP model extended to take into account the possibility of tension cut-off. Their summary is available in Table 5.1.

Table 5.1: Parameters of Mohr-Coulomb plasticity model

Symbol	Units	Description
E	[MPa]	Modulus of elasticity
E_{ur}	[MPa]	Modulus of elasticity in unloading/reloading
ν	[-]	Poisson's ratio
c	[kPa]	Effective cohesion
φ	[°]	Effective angle of internal friction
ψ	[°]	Angle of dilation
e^{in}	[-]	Initial void ratio
e^{max}	[-]	Maximum void ratio to terminate dilation
σ_t	[kPa]	Maximum allowable tensile strength
TsRF	[-]	Tensile strength reduction factor
α	[1/℃]	Coefficient of thermal expansion

Similarly to DP model the MC model belongs to the category of elastic-perfectly plastic models, recall Fig. 4.1. This is also illustrated in Fig. 5.1(c) showing the response in $q-\gamma_s$ space for the case of triaxial compression, remember definitions of the selected equivalent stress and strain measures given in Section 1.4. In Section 4.6 this response was investigated numerically, see Fig. 4.10(b). Compare to the smooth DP model the MC model plots in the effective principal stress space as an irregular cone opened along the hydrostatic axis as evident in Fig. 5.1(a). Singularities observed along the edges, see also the sharp corners in the deviatoric plane projection in Fig. 5.1(b), bring about some issues associated with a numerical implementation. These are described in details in subsequent sections.

5.1 Formulation of Mohr-Coulomb failure criterion

Consider the results of a triaxial test being plotted as Mohr's circles and the failure envelope drawn as shown in Fig. 5. Numerically, this Coulomb's failure criterion can be stated as

$$|\tau_f| = c - \sigma_{nf} \tan \varphi \tag{5.1}$$

Equation (5.1) defines a 'failure envelope' that is essentially a yield function, see Fig 5. It has exactly the same properties and characteristics as a yield function. Stresses below the envelope lie in the
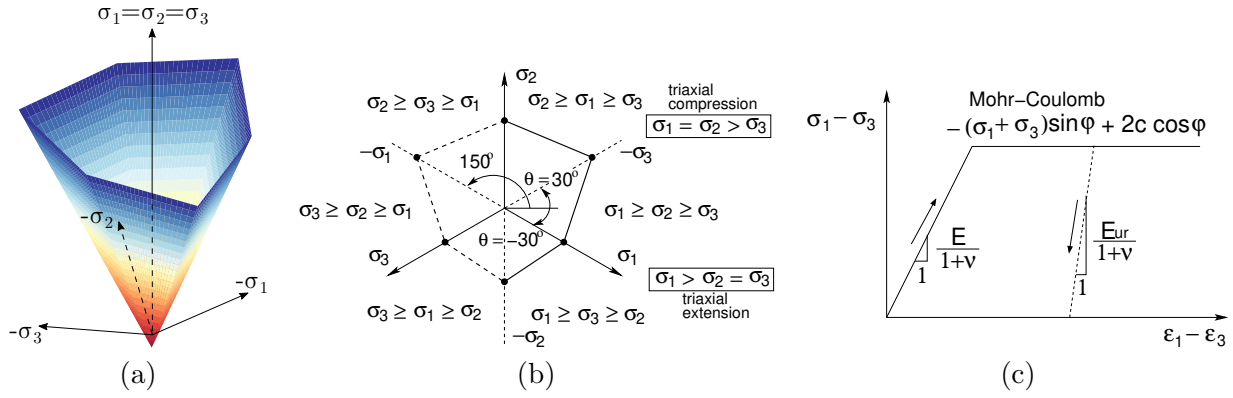
Figure 5.1: Mohr-Coulomb yield function: a) plot in effective principal stress space, b) plot in deviatoric plane, c) elastic perfectly plastic stress-strain law
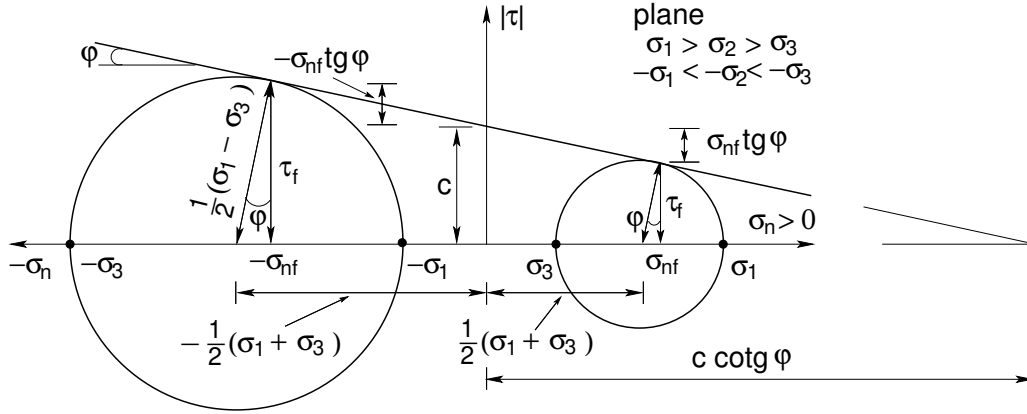
Figure 5.2: Coulomb's failure criterion

elastic regime. On the envelope surface plastic failure occurs. A stress state in the soil above the yield surface is not possible. Using the elementary trigonometric identity one can further state that

$$\tau_f = \frac{1}{2}(\sigma_1 - \sigma_3)\cos\varphi \tag{5.2}$$

$$\sigma_{nf} = \frac{1}{2}(\sigma_1 + \sigma_3) + \frac{1}{2}(\sigma_1 - \sigma_3)\sin\varphi \tag{5.3}$$

which upon substitution into Eq. (5.1) gives the Mohr-Coulomb failure criterion, which in the present model is adopted as the yield function

$$f^{MC}(\sigma_1, \sigma_3) = \frac{1}{2}(\sigma_1 - \sigma_3) + \frac{1}{2}(\sigma_1 + \sigma_3)\sin\varphi - c\cos\varphi = 0 \tag{5.4}$$

Plotting Mohr's circles essentially gives us a graphical way to obtain the shear strength parameters for the soil. They could equally be obtained from the numerical results of two triaxial tests. The stress values for each test could be placed into Eq. (5.4) setting up two simultaneous equations which would be solved for the shear strength parameters. Alternatively if one knows the shear strength parameters and either the major or minor principal stress in the soil the other principal stress at the failure condition can be calculated.

A limitation to using the Mohr-Coulomb failure criterion is that it is independent of the intermediate principal stress. The same failure stress values are predicted for all values of intermediate principal stress. In triaxial testing the intermediate principal stress is always equal to the minor principal stress and the shear strength parameters are obtained for these values. In real world geotechnical problems the magnitudes of the intermediate and the minor principal stresses may be different. Some experimental evidence has shown that intermediate stress values can influence the failure condition for soils and this should be appreciated every time an engineer uses any Mohr-Coulomb based models, see e.g. [65, Chapter 4].

It is evident from Fig. 5.1(b) that the six-fold symmetry arises from possible permutations of principal stresses. It may therefore appear more convenient, if confining our attention to plane $\sigma_1 > \sigma_2 > \sigma_3$, to rewrite Eq. (5.4) in terms of stress invariants σ_m, J, θ, see Sections 1.3 and 1.4 for their definition. Recall Section 1.7 to write the principal stresses terms of stress invariants as

$$\sigma_I = \sigma_m + \frac{2}{\sqrt{3}} J \sin\left[\theta - (I-2)\frac{2\pi}{3}\right], \qquad I = 1, 2, 3 \tag{5.5}$$

Note that the maximum shear stress τ_{max} and the center of Mohr-Coulomb's circle, Fig. 5, are then provided by

$$\frac{1}{2}(\sigma_1 - \sigma_3) = \tau_{max} = J \cos\theta \tag{5.6}$$

$$\frac{1}{2}(\sigma_1 + \sigma_3) = \sigma_m - \frac{J}{\sqrt{3}} \sin\theta \tag{5.7}$$

Introducing these equations into Eq. (5.4) then yields

$$f^{MC}(J, \sigma_m, \theta) = J(\cos\theta + \frac{1}{\sqrt{3}} \sin\theta \sin\varphi) + \sigma_m \sin\varphi - c \cos\varphi = 0 \tag{5.8}$$

Next define

$$g(\theta) = \frac{\sin\varphi}{\cos\theta + \frac{1}{\sqrt{3}} \sin\theta \sin\varphi} \tag{5.9}$$

to finally get upon introducing Eq. (5.9) into (5.8) and rearranging

$$f^{MC}(J, \sigma_m, \theta) = J + (\sigma_m - c \cot\varphi) g(\theta, \varphi) = 0 \tag{5.10}$$

Observe similarity of Eq. (5.10) with Eq. (4.1). In the former case, however, the projection of MC model into the meridian plane (see, e.g., Fig. 4.2(b)) depends on Lode's angle. Unfortunately, Eq. (5.10) may no longer be applicable when moving along the triaxial compression or triaxial extension lines as suggested in Fig. 5.1(b). In either case, at least two segments of the Mohr-Coulomb hexagon then become active. Writing out the respective yield surfaces in terms of principal stresses then becomes more convenient. In particular, the following three segments of the yield surface might be needed when returning the stress point violating the yield criterion back to the yield surface

$$f_1^{MC}(\sigma_1, \sigma_3, c, \varphi) = \frac{1}{2}(\sigma_1 - \sigma_3) + \frac{1}{2}(\sigma_1 + \sigma_3)\sin\varphi - c\cos\varphi = 0, \quad \sigma_1 \geq \sigma_2 \geq \sigma_3 \tag{5.11}$$

$$f_2^{MC}(\sigma_2, \sigma_3, c, \varphi) = \frac{1}{2}(\sigma_2 - \sigma_3) + \frac{1}{2}(\sigma_2 + \sigma_3)\sin\varphi - c\cos\varphi = 0, \quad \sigma_2 \geq \sigma_1 \geq \sigma_3 \tag{5.12}$$

$$f_3^{MC}(\sigma_1, \sigma_2, c, \varphi) = \frac{1}{2}(\sigma_1 - \sigma_2) + \frac{1}{2}(\sigma_1 + \sigma_2)\sin\varphi - c\cos\varphi = 0, \quad \sigma_1 \geq \sigma_3 \geq \sigma_2 \tag{5.13}$$

with corresponding plastic potential surfaces

$$g_1^{MC}(\sigma_1, \sigma_3, \psi) = \frac{1}{2}(\sigma_1 - \sigma_3) + \frac{1}{2}(\sigma_1 + \sigma_3)\sin\psi \tag{5.14}$$

$$g_2^{MC}(\sigma_2, \sigma_3, \psi) = \frac{1}{2}(\sigma_2 - \sigma_3) + \frac{1}{2}(\sigma_2 + \sigma_3)\sin\psi \tag{5.15}$$

$$g_3^{MC}(\sigma_1, \sigma_2, \psi) = \frac{1}{2}(\sigma_1 - \sigma_2) + \frac{1}{2}(\sigma_1 + \sigma_2)\sin\psi \tag{5.16}$$

where ψ is the familiar dilation angle. Similarly to the DP model from Chapter 4 the formulation thus assumes in general a non-associated plasticity with $\psi \neq \varphi$ to allow for a better control of potential dilation. When setting $\psi = \varphi$ the concept of associated plasticity is recovered. Also notice that compare to the DP model the formulation of the plastic potential surface (Eq. (4.6) for DP model) was somewhat simplified taking advantage of the fact that the evolution of dilation is driven only by the slope of $g^{MC}(g^{DP})$ in the meridian plane.

In view of the stress return algorithm presented next it becomes convenient to define vectors normal to the yield ($\boldsymbol{n}$) and plastic potential ($\boldsymbol{n}_g$) surfaces. These are derived as partial derivatives of the yield and plastic potential surfaces with respect to principal stress components. Given the above definitions of f^{MC} and g^{MC} they are constant independent of stresses and are given by

- segment $\sigma_1 \geq \sigma_2 \geq \sigma_3$ (f_1^{MC}, g_1^{MC})

$$\boldsymbol{n}^1 = \frac{\partial f_1^{MC}}{\partial \boldsymbol{\sigma}} = \frac{1}{2}\{1 + \sin\varphi, 0, -1 + \sin\varphi\}^\mathsf{T} \tag{5.17}$$

$$\boldsymbol{n}_g^1 = \frac{\partial g_1^{MC}}{\partial \boldsymbol{\sigma}} = \frac{1}{2}\{1 + \sin\psi, 0, -1 + \sin\psi\}^\mathsf{T} \tag{5.18}$$

- segment $\sigma_2 \geq \sigma_1 \geq \sigma_3$ (f_2^{MC}, g_2^{MC})

$$\boldsymbol{n}^2 = \frac{\partial f_2^{MC}}{\partial \boldsymbol{\sigma}} = \frac{1}{2}\{0, 1 + \sin\varphi, -1 + \sin\varphi\}^\mathsf{T} \tag{5.19}$$

$$\boldsymbol{n}_g^2 = \frac{\partial g_2^{MC}}{\partial \boldsymbol{\sigma}} = \frac{1}{2}\{0, 1 + \sin\psi, -1 + \sin\psi\}^\mathsf{T} \tag{5.20}$$

- segment $\sigma_1 \geq \sigma_3 \geq \sigma_2$ (f_3^{MC}, g_3^{MC})

$$\boldsymbol{n}^3 = \frac{\partial f_3^{MC}}{\partial \boldsymbol{\sigma}} = \frac{1}{2}\{1 + \sin\varphi, -1 + \sin\varphi, 0\}^\mathsf{T} \tag{5.21}$$

$$\boldsymbol{n}_g^3 = \frac{\partial g_3^{MC}}{\partial \boldsymbol{\sigma}} = \frac{1}{2}\{1 + \sin\psi, -1 + \sin\psi, 0\}^\mathsf{T} \tag{5.22}$$

5.2   Stress return mapping

Consider first a "working sector" defined by a domain such that $\sigma_1 \geq \sigma_2 \geq \sigma_3$, Fig. 5.1(b). A brief comment on the concept of the working sector is appropriate as the implementation of the entire model is centered around this idea. The loading that is applied to the soil is increased in increments from the initial conditions. An "elastic prediction" is used to estimate the stress state in the material at the end of each loading increment. However, when the material is no longer elastic the actual magnitude of stress in the material after this plastic flow would be lower than that forecast by the elastic prediction. As a result the elastic prediction corresponds to a stress point that violates the yield surface. The stress return scheme is then implemented and the stress state gets returned back to the yield surface, recall Section 17.2.9. The idea of the working sector originates from the order in which the model calculates the relevant values. If plasticity is detected, the model makes the elastic prediction in terms of the six components of the stress vector. After this the model then calculates the magnitude and orientation of the principal stresses based on the elastic prediction stress values. The elastic guess can then be plotted in principal stress space. The model calculates the principal stresses such that $\sigma_1 \geq \sigma_2 \geq \sigma_3$ and since the conversion from six dimensional stress space to three dimensional principal stress space is based on the elastic prediction stress values, the elastic prediction itself must lie in the sector where $\sigma_1 \geq \sigma_2 \geq \sigma_3$. This is defined as the working sector and the elastic prediction stress will always lie in this domain due to the orientation of the principal stress axes being based on the values of the elastic prediction stress.

Upon bringing the elastic guess back to the yield surface the following two scenarios as plotted in Fig. 5.3 may occur. First, refer to Figs. 5.3(a),(b) demonstrating a successful return back to the "working sector" thus employing only a single yield function f_1^{MC}. The return algorithm, however, failed in the example plotted in Fig. 5.3(c). Although bringing the initial elastic guess back to the assumed active yield function f_1^{MC}, dashed line, the resulting stress state violates the yield function f_2^{MC}. It is interesting to note that if reordering the principal stresses in the definition of Lode's angle such that $\sigma_2 \geq \sigma_1 \geq \sigma_3$, the algorithm returns the stress back to function f_2^{MC}, dot-dashed line. This particular situation suggests that more than one yield function may be active at the same time.
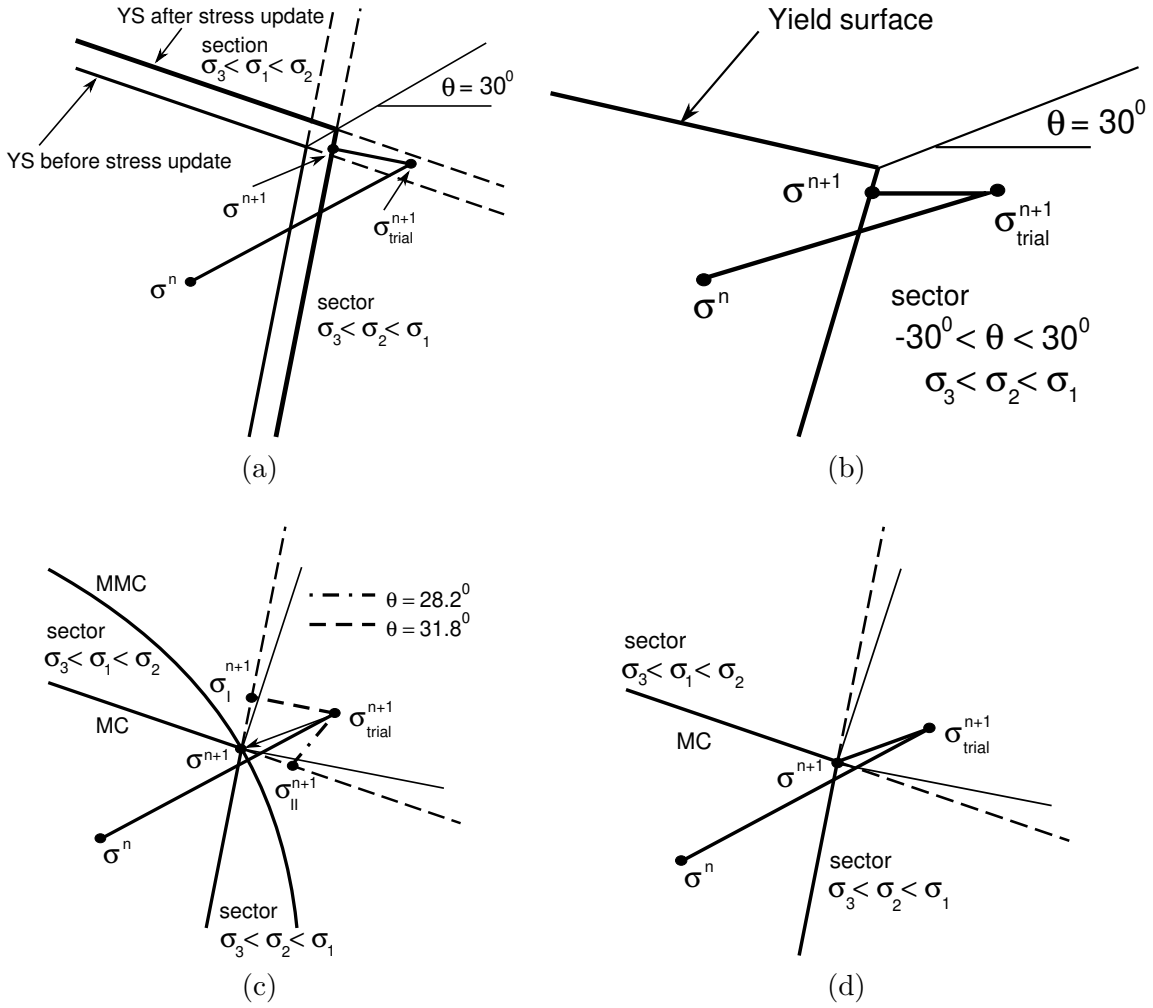
Figure 5.3: a) Successful return to working sector $\psi = \varphi$, b) successful return to working sector $\psi = 0$, c) failure to return to working sector $\psi = 0$, d) successful return to triaxial compression cone $\psi = 0$

To provide some explanation observe that where arbitrary two planes of the Mohr-Coulomb hexagon intersect, the yield functions are not smoothly defined and a set of edges are formed. If the stress state of the material is such that it lies on one of these vertices, two yield functions are simultaneously active and have values equal to zero. The problem arises of determining the direction and magnitude of the incremental plastic strains in this situation. As both yield functions are simultaneously active, the incremental plastic strains must be related to both the plastic potential functions of the violated yield functions. Koiter [43] showed that for associated plasticity the incremental plastic strains can be determined from the plastic flow rule as

$$\varepsilon^{pl} = \sum_{j=1}^{m} \Delta\lambda_j \frac{\partial f_j^{MC}}{\partial \boldsymbol{\sigma}} \tag{5.23}$$

for m active yield functions f_j^{MC}, where λ_j are the plastic multipliers and $\Delta\varepsilon^{pl}$ and $\boldsymbol{\sigma}$ are the incremental plastic strain and accumulated stress vectors, respectively. Hence the total incremental plastic strains are the summed contributions of the incremental plastic strains related to each of the active yield surfaces.

Using the concept of multi-surface plasticity the plastic corrector algorithm then returns the stress to the common intersection of the two active surfaces as plotted in Fig. 5.3(d). It should be noted, however, that violating both yield functions at the elastic predictor stage does not necessarily imply that both yield conditions are active as evident from Fig. 5.3(a). To determine whether a single or multiple yield surfaces are active one may appreciate a set of singularity indicators developed, e.g. in [60]. Here, a rather simplistic approach for identification of multi-surface plasticity return based on

the Lode angle stress invariant is employed. The Lode angle θ specifies the orientation of any stress state on the deviatoric plane and can be stated in principal stresses as

$$\theta = \arctan\left(\frac{1}{\sqrt{3}}\left(2\frac{(\sigma_2 - \sigma_3)}{(\sigma_1 - \sigma_3)} - 1\right)\right) \tag{5.24}$$

The procedure starts from performing a single surface plasticity stress return from the elastic prediction stress. The Lode angle is then calculated for the returned stress. If the value lies within the limits $-30° \leq \theta \leq 30°$, then the stress return is successful. This situation is indicated in Fig. 5.3(b). If another stress return is considered, this time when the element is placed under triaxial compression, Fig. 5.3(c), upon calculating the Lode angle one will find that it lies outside the limits $-30° \leq \theta \leq 30°$. In this situation one can see that one yield function remains violated after the stress return consequently indicating that a multi-surface plasticity stress return is required from the elastic prediction stress. This is then performed and the stress path is that indicated by Fig. 5.3(d) returning the stress state to the apex of the two yield functions as shown.

A special situation arises, see also [60], when returning the stress to the apex of the combined Mohr-Coulomb yield surface. In such a case all six planes are active. Nevertheless, as discussed in [60], the set of six equations corresponding to six yield functions Fig. 5.1(b) are linearly dependent and rank deficient by three. Therefore, only three arbitrary yield functions, say $f_1^{MC}, f_2^{MC}, f_3^{MC}$ in Eqs. (5.11) - (5.13), are needed in the plastic corrector stage. A word of caution is required, however, when applying the procedure with non-associated plasticity with the dilation angle ψ equal to zero. The resulting system of equations is then singular. Fortunately, to avoid such a situation we may always set $\psi = \varphi$ to perform the apex return.

The single yield surface and multi-surface plasticity concepts will be now discussed separately.

5.2.1   Single yield surface plasticity

Consider again the "working sector" $\sigma_1 \geq \sigma_2 \geq \sigma_3$ with the corresponding yield and plastic potential functions f_1^{MC} and g_1^{MC} and normal vectors $\boldsymbol{n}^1, \boldsymbol{n}_g^1$ represented by Eqs. (5.11), (5.14), (5.17), (5.18). The consistency condition becomes, see [10] for a general definition,

$$\Delta f_1^{MC} = \left(\frac{\partial f_1^{MC}}{\partial \boldsymbol{\sigma}}\right)^\mathsf{T} \Delta \boldsymbol{\sigma} = 0 \tag{5.25}$$

$$\Delta \boldsymbol{\sigma} = \mathbf{D}\Delta\varepsilon - \Delta\lambda \mathbf{D} \boldsymbol{n}_g^1 \tag{5.26}$$

where $\mathbf{D}$ is the elastic 3×3 material stiffness matrix. Combining Eqs. (5.25) - (5.26) yields the desired plastic multiplier in the form

$$\Delta\lambda = \frac{\left(\boldsymbol{n}^1\right)^\mathsf{T} \mathbf{D}\Delta\varepsilon}{\left(\boldsymbol{n}^1\right)^\mathsf{T} \mathbf{D}\boldsymbol{n}_g^1} = \frac{\left(\boldsymbol{n}^1\right)^\mathsf{T} \Delta\boldsymbol{\sigma}^{tr}}{\left(\boldsymbol{n}^1\right)^\mathsf{T} \mathbf{D}\boldsymbol{n}_g^1} \tag{5.27}$$

where $\Delta\boldsymbol{\sigma}^{tr} = \mathbf{D}\Delta\varepsilon$ is the elastic trial stress increment, recall Fig. 17.11 and Eq. (17.82). Note that condition (5.25) is identical to

$$(f_1^{MC})^{n+1}(\boldsymbol{\sigma}^{n+1}) = 0 = \overbrace{(f_1^{MC})^n}^{=0} + \overbrace{\frac{1}{2}\left(\Delta\sigma_1^{tr} - \Delta\sigma_3^{tr}\right) + \frac{1}{2}\left(\Delta\sigma_1^{tr} + \Delta\sigma_3^{tr}\right)\sin\varphi}^{\boldsymbol{n}^\mathsf{T}\Delta\boldsymbol{\sigma}^{tr}} \tag{5.28}$$

$$- \underbrace{\Delta\lambda\left[\frac{1}{2}\left(D_{11}n_{g1}^1 - D_{33}n_{g3}^1\right) + \frac{1}{2}\left(D_{11}n_{g1}^1 + D_{33}n_{g3}^1\right)\sin\varphi\right]}_{\left(\boldsymbol{n}^1\right)^\mathsf{T}\mathbf{D}\boldsymbol{n}_g^1}$$

which allows for evaluation of $\Delta\lambda$. In Eq. (5.29) $(f_1^{MC})^n$ and $(f_1^{MC})^{n+1}$ refer to the values of f_1^{MC} at the n-th and $(n+1)$-th load increments, respectively. Also note that a diagonal material stiffness matrix was assumed for simplicity. Also note that

$$\boldsymbol{n}^\mathsf{T}\Delta\boldsymbol{\sigma}^{tr} = (f_1^{MC})^{n+1}(\boldsymbol{\sigma}^{tr})$$

which confirms analogy with the cutting plane algorithm [59, 23] that offers the plastic strain increment $\Delta\lambda$ in the form

$$\Delta\lambda = \frac{(f_1^{MC})^{n+1}(\boldsymbol{\sigma}^{tr})}{(\boldsymbol{n}^1)^{\mathsf{T}}\mathbf{D}\boldsymbol{n}_g^1} \tag{5.29}$$

Therefore, either of the three Eqs. (5.27) - (5.29) can be used in the plastic corrector stage.

5.2.2 Multi-yield surface plasticity

Although the procedure discussed henceforth can be generalized to any number of active yield surfaces, the attention will be limited for the sake of clarity to only two arbitrary yield functions simultaneously active with the notation adopted from [65, Section 8.4].

As an example consider the case of triaxial compression already examined in Figs. 5.3. One can then show how the plastic multipliers are calculated to enable the determination of the incremental plastic strains. The derivation is very similar to obtaining the plastic multipliers for single surface plasticity except that in this case, to obtain both plastic multipliers, a pair of simultaneous equations need to be solved. Initially, separate the incremental strains $\Delta\boldsymbol{\varepsilon}$ into their elastic $\Delta\boldsymbol{\varepsilon}^{el}$ and plastic $\Delta\boldsymbol{\varepsilon}^{pl}$ components. The plastic strains are then sub-divided into the contributions from each violated yield surface $\Delta\boldsymbol{\varepsilon}^{p1}$, $\Delta\boldsymbol{\varepsilon}^{p2}$ such that the total incremental plastic strain $\Delta\boldsymbol{\varepsilon}$ is

$$\Delta\boldsymbol{\varepsilon} = \Delta\boldsymbol{\varepsilon}^{el} + \Delta\boldsymbol{\varepsilon}^{p1} + \Delta\boldsymbol{\varepsilon}^{p2} \tag{5.30}$$

The incremental stresses $\Delta\boldsymbol{\sigma}$ are again related to the incremental elastic strains by the elastic constitutive matrix $\mathbf{D}$ in the following way

$$\Delta\boldsymbol{\sigma} = \mathbf{D}\Delta\boldsymbol{\varepsilon}^{el} \tag{5.31}$$

Combining Eqs. (5.30) and (5.31) gives

$$\Delta\boldsymbol{\sigma} = \mathbf{D}(\Delta\boldsymbol{\varepsilon} - \Delta\boldsymbol{\varepsilon}^{p1} - \Delta\boldsymbol{\varepsilon}^{p2}) \tag{5.32}$$

The flow rule is now written for each of the plastic potential functions

$$\Delta\boldsymbol{\varepsilon}^{p1} = \Delta\lambda_1 \frac{\partial g_1^{MC}}{\partial\boldsymbol{\sigma}} \tag{5.33}$$

$$\Delta\boldsymbol{\varepsilon}^{p2} = \Delta\lambda_2 \frac{\partial g_2^{MC}}{\partial\boldsymbol{\sigma}} \tag{5.34}$$

Substitution of Eqs. (5.33) and (5.34) into Eq. (5.32) provides

$$\Delta\boldsymbol{\sigma} = \mathbf{D}\Delta\boldsymbol{\varepsilon} - \Delta\lambda_1\mathbf{D}\frac{\partial g_1^{MC}}{\partial\boldsymbol{\sigma}} - \Delta\lambda_2\mathbf{D}\frac{\partial g_2^{MC}}{\partial\boldsymbol{\sigma}} \tag{5.35}$$

Before we proceed any further with the development of this derivation look at the structure of Eq. (5.35) If one were to multiply through by $\mathbf{D}^{-1}$ and then rearrange you would obtain the following

$$-\mathbf{D}^{-1}\Delta\boldsymbol{\sigma} + \Delta\boldsymbol{\varepsilon} = \Delta\boldsymbol{\varepsilon}^{pl} = \Delta\lambda_1\frac{\partial g_1^{MC}}{\partial\boldsymbol{\sigma}} + \Delta\lambda_2\frac{\partial g_2^{MC}}{\partial\boldsymbol{\sigma}}. \tag{5.36}$$

Observing Eq. (5.36) one can clearly see that Koiter's generalization [43] can be extended for non-associated plasticity behavior by replacing the yield functions with their respective plastic potential functions. Thus Eq. (5.36) verifies

$$\Delta\boldsymbol{\varepsilon}^{pl} = \sum_{j=1}^{m} \Delta\lambda_j \frac{\partial g_j^{MC}}{\partial\boldsymbol{\sigma}} = \sum_{j=1}^{m} \Delta\lambda_j\boldsymbol{n}_g^j \tag{5.37}$$

Hence one can use the flow rule to obtain the total incremental plastic strains when using multi-surface plasticity if the contribution of each plastic potential function is summed. One still needs to calculate the plastic multipliers. This is done by acknowledging that when both yield surfaces are active, the

values of both of them is zero, and the consistency condition is satisfied. Using the chain rule on this observation gives

$$\Delta f_1^{MC} \quad = \quad \left(\frac{\partial f_1^{MC}}{\partial \boldsymbol{\sigma}} \right)^{\mathsf{T}} \Delta \boldsymbol{\sigma} = \left(\boldsymbol{n}^1 \right)^{\mathsf{T}} \Delta \boldsymbol{\sigma} = 0 \tag{5.38}$$

$$\Delta f_2^{MC} \quad = \quad \left(\frac{\partial f_2^{MC}}{\partial \boldsymbol{\sigma}} \right)^{\mathsf{T}} \Delta \boldsymbol{\sigma} = \left(\boldsymbol{n}^2 \right)^{\mathsf{T}} \Delta \boldsymbol{\sigma} = 0 \tag{5.39}$$

Substitution of Eq. (5.35) into (5.38) and (5.39) yields

$$\Delta f_1^{MC} \quad = \quad \left(\boldsymbol{n}^1 \right)^{\mathsf{T}} \mathbf{D} \Delta \boldsymbol{\varepsilon} - \Delta \lambda_1 \left(\boldsymbol{n}^1 \right)^{\mathsf{T}} \mathbf{D} \boldsymbol{n}_g^1 - \Delta \lambda_2 \left(\boldsymbol{n}^1 \right)^{\mathsf{T}} \mathbf{D} \boldsymbol{n}_g^2 = 0 \tag{5.40}$$

$$\Delta f_2^{MC} \quad = \quad \left(\boldsymbol{n}^2 \right)^{\mathsf{T}} \mathbf{D} \Delta \boldsymbol{\varepsilon} - \Delta \lambda_1 \left(\boldsymbol{n}^2 \right)^{\mathsf{T}} \mathbf{D} \boldsymbol{n}_g^1 - \Delta \lambda_2 \left(\boldsymbol{n}^2 \right)^{\mathsf{T}} \mathbf{D} \boldsymbol{n}_g^2 = 0 \tag{5.41}$$

A set of simultaneous equations are now set in place and are solved for the plastic multipliers. Equations (5.40) and (5.41) can now be written in a simplified form as

$$\Delta \lambda_1 L_{11} + \Delta \lambda_2 L_{12} \quad = \quad q_1 \tag{5.42}$$

$$\Delta \lambda_1 L_{21} + \Delta \lambda_2 L_{22} \quad = \quad q_2 \tag{5.43}$$

where

$$L_{11} \quad = \quad \left(\boldsymbol{n}^1 \right)^{\mathsf{T}} \mathbf{D} \boldsymbol{n}_g^1 \tag{5.44}$$

$$L_{22} \quad = \quad \left(\boldsymbol{n}^2 \right)^{\mathsf{T}} \mathbf{D} \boldsymbol{n}_g^2 \tag{5.45}$$

$$L_{12} \quad = \quad \left(\boldsymbol{n}^1 \right)^{\mathsf{T}} \mathbf{D} \boldsymbol{n}_g^2 \tag{5.46}$$

$$L_{21} \quad = \quad \left(\boldsymbol{n}^2 \right)^{\mathsf{T}} \mathbf{D} \boldsymbol{n}_g^1 \tag{5.47}$$

$$q_1 \quad = \quad \left(\boldsymbol{n}^1 \right)^{\mathsf{T}} \mathbf{D} \Delta \boldsymbol{\varepsilon} \tag{5.48}$$

$$q_2 \quad = \quad \left(\boldsymbol{n}^2 \right)^{\mathsf{T}} \mathbf{D} \Delta \boldsymbol{\varepsilon}. \tag{5.49}$$

Thus the plastic multipliers are calculated as

$$\Delta \lambda_1 \quad = \quad \left(L_{22} q_1 - L_{12} q_2 \right) / \left(L_{11} L_{22} - L_{12} L_{21} \right) \tag{5.50}$$

$$\Delta \lambda_2 \quad = \quad \left(L_{11} q_2 - L_{21} q_1 \right) / \left(L_{11} L_{22} - L_{12} L_{21} \right) \tag{5.51}$$

These are then used in Eq. (5.36) or (5.37) to calculate the incremental plastic strains. This process can be easily extended using the same concepts when one has more than two surface multi-surface plasticity such as the apex problem or the Mohr-Coulomb yield surface combined with a tension cut-off problem. This concept is outlined in Section 5.4.

5.3   Algorithmic tangent stiffness matrix

As for the algorithmic tangent stiffness matrix $\boldsymbol{\mathcal{D}}$ its derivation may proceed along the same lines as discussed in [10] for standard elastoplastic stiffness matrix $\mathbf{D}^{ep}$ as these to matrices are identical owing to the constant values of $\boldsymbol{n}_g$. To that end, we substitute from Eqs. (5.50) and (5.51) into Eq. (5.35) to get after rearranging, see also [65],

$$\boldsymbol{\mathcal{D}} \quad = \quad \mathbf{D} - \frac{\mathbf{D}}{\Omega} \left[\boldsymbol{n}_g^1 \left(\boldsymbol{b}_1 \right)^{\mathsf{T}} + \boldsymbol{n}_g^2 \left(\boldsymbol{b}_2 \right)^{\mathsf{T}} \right] \mathbf{D} \tag{5.52}$$

$$\Omega \quad = \quad L_{11} L_{22} - L_{12} L_{21}$$

$$\boldsymbol{b}_1 \quad = \quad L_{22} \boldsymbol{n}^1 - L_{12} \boldsymbol{n}^2$$

$$\boldsymbol{b}_2 \quad = \quad L_{11} \boldsymbol{n}^2 - L_{21} \boldsymbol{n}^1$$

A similar procedure can be applied when more than two yield surfaces are active. Recall, e.g. the apex problem, where all three surfaces $f_1^{MC}, f_2^{MC}, f_3^{MC}$ are simultaneously active. In fact, all six
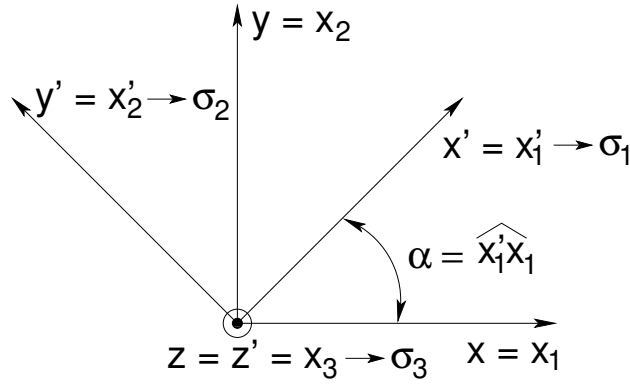
Figure 5.4: Transformation of coordinates for plane strain and axisymmetric problems

surfaces shown in Fig. 5.1(b) are active, but only three are needed to bring the stress to their common point of intersection [60]. Such a situation will also arise in Section 5.4 that outlines tension cut-off extension of the original Mohr-Coulomb formulation. While it is shown that four yield surfaces may become active at the same time, again only three of them can be chosen in the multi-surface plasticity stress update procedure if limiting attention to isotropic materials.

In every case, assuming perfect plasticity, the following generalization of Eqs. (5.38) - (5.52) applies. Suppose that N yield surfaces are active. The increments of plastic multipliers then follow from

$$\Delta\boldsymbol{\lambda} = \mathbf{L}\boldsymbol{q} \tag{5.53}$$

where the components of $N \times N$ matrix $\mathbf{L}$ and $N \times 1$ vector $\boldsymbol{q}$ are provided by

$$L_{ij} = \left(\boldsymbol{n}^i\right)^{\mathsf{T}} \mathbf{D}\boldsymbol{n}_g^j \tag{5.54}$$

$$q_i = \left(\boldsymbol{n}^i\right)^{\mathsf{T}} \mathbf{D}\Delta\varepsilon \tag{5.55}$$

The algorithmic tangent stiffness matrix then becomes

$$\boldsymbol{\mathcal{D}} = \mathbf{D} - \mathbf{D}\left[\sum_{i=1}^{N} \boldsymbol{n}_g^i \left(\boldsymbol{b}_i\right)^{\mathsf{T}}\right]\mathbf{D} \tag{5.56}$$

$$\boldsymbol{b}_i = \sum_{j=1}^{N} L_{ij}^{-1}\boldsymbol{n}^j$$

5.3.1 Algorithmic tangent stiffness matrix in the Cartesian coordinate system

The principal stress space was adopted throughout this section to develop the general framework for the implementation of the Mohr-Coulomb constitutive model. On the other hand, the derivation of the finite element stiffness matrices presented in Section 17.1 assumes a material point to be placed in a certain global Cartesian coordinate system. The algorithmic tangent stiffness matrices that appear in Eqs. (5.52) and (5.56) thus require some transformation as demonstrated in Fig. 5.4 For further reference these matrices will be provided with subscript I while their cartesian counterparts will be denoted by subscript g. The same notation is reserved also for respective stress and strain vectors.

The transformation law is usually found through equality of increments of work in both coordinate spaces written as

$$\left(\Delta\varepsilon_g\right)^{\mathsf{T}} \boldsymbol{\mathcal{D}}_g \Delta\varepsilon_g = \left(\Delta\varepsilon_I\right)^{\mathsf{T}} \boldsymbol{\mathcal{D}}_I \Delta\varepsilon_I \tag{5.57}$$

To continue, introduce a certain 3×6 transformation matrix $\mathbf{T}_I^{\varepsilon}$ (note that the general six-dimensional cartesian stress space is temporarily assumed)

$$\mathbf{T}_I^{\varepsilon} = \begin{bmatrix} n_{11}n_{11} & n_{12}n_{12} & n_{13}n_{13} & n_{12}n_{13} & n_{11}n_{13} & n_{11}n_{12} \\ n_{21}n_{21} & n_{22}n_{22} & n_{23}n_{23} & n_{22}n_{23} & n_{21}n_{23} & n_{21}n_{22} \\ n_{31}n_{31} & n_{32}n_{32} & n_{33}n_{33} & n_{32}n_{33} & n_{31}n_{33} & n_{31}n_{32} \end{bmatrix} \tag{5.58}$$

where n_{ij} represent components of 3×3 orthogonal rotation matrix $\mathbf{T}$ giving the relation between coordinates in individual spaces in the form

$$\boldsymbol{x}_I = \mathbf{T}\boldsymbol{x}_g \tag{5.59}$$

Limiting attention to plane-strain or axisymmetric analysis with the computational model sitting in the xy-plane for illustration the matrix $\mathbf{T}$ arrives simply from the rotation about the z-axis as displayed in Fig. 5.4

$$\mathbf{T} = \begin{bmatrix} \cos\alpha & \sin\alpha & 0 \\ -\sin\alpha & \cos\alpha & 0 \\ 0 & 0 & 1 \end{bmatrix} \tag{5.60}$$

In general, individual rows in $\mathbf{T}$ correspond to principal directions of stresses $\sigma_1, \sigma_2, \sigma_3$. The matrix $\mathbf{T}_I^\varepsilon$ then rotates the cartesian strain components into the principal stress space such that

$$\Delta\boldsymbol{\varepsilon}_I = \mathbf{T}_I^\varepsilon \Delta\boldsymbol{\varepsilon}_g \tag{5.61}$$

Substitution of Eq. (5.61) into Eq. (5.57) yields

$$\boldsymbol{\mathcal{D}}_g = \left(\mathbf{T}_I^\varepsilon\right)^{\mathsf{T}} \boldsymbol{\mathcal{D}}_I \mathbf{T}_I^\varepsilon \tag{5.62}$$

Note that for plane strain and axisymmetric problems the general 6×6 material stiffness matrix $\boldsymbol{\mathcal{D}}_g$ in Eq. (5.62) must be reduced into 4×4 matrix and suitably augmented to comply with the notation introduced in Section 17.1. Finally, it is perhaps interesting to point out the relation between stress vectors

$$\Delta\boldsymbol{\sigma}_g = \mathbf{T}_g^\sigma \Delta\boldsymbol{\sigma}_I \tag{5.63}$$

where

$$\mathbf{T}_g^\sigma = \left(\mathbf{T}_I^\varepsilon\right)^{\mathsf{T}} \tag{5.64}$$

5.4   Mohr-Coulomb model with tension cut-off

The standard Mohr-Coulomb model allows for certain amount of tension that is in general proportional to the soil strength parameters c, φ such that its maximum value cannot exceed $\sqrt{3}\,c\cot\varphi$, see Fig. 5.5(a). In reality, however, the soil can sustain almost none or very small values of these stresses. Also, the tension carrying capacity of soils is not commonly relied upon as it is typically extremely variable and unpredictable in real soils. It is therefore desirable to either avoid tension completely or to limit its magnitude by a specific value of the ultimate tensile stress σ_t the material can sustain before plastic failure.

   This can be achieved by introducing three additional tension cut-off yield surfaces of the Rankine type Figs. 5.5(b)(c), in the form

$$\begin{aligned} f_1^R(\sigma_1, \sigma_t) &= \sigma_1 - \sigma_t = 0 & (5.65) \\ f_2^R(\sigma_2, \sigma_t) &= \sigma_2 - \sigma_t = 0 & (5.66) \\ f_3^R(\sigma_3, \sigma_t) &= \sigma_3 - \sigma_t = 0 & (5.67) \end{aligned}$$

The model assumes the material to have isotropic properties and hence the ultimate tensile strength σ_t is the same in all orientations. Furthermore, an associated plastic flow rule is adopted in conjunction with tension cut-off. The tensile yield surfaces plot as a regular triangular pyramid in principal stress space, see Fig. 5.5(b).

   The shear and tension yield surfaces intersect in the tensile domain of the principal stress space. As a result, the tension yield surfaces "cut-off" the shear yield surfaces leading to the effect of the material being able to ultimately sustain lower tensile stresses than those predicted as being possible by the Mohr-Coulomb model alone, Fig. 5.5(d). Note that point B in Fig. 5.5(d) corresponds to a point of intersection of the Mohr-Coulomb f^{MC} and the tension cut-off f^R yield surfaces. Should the
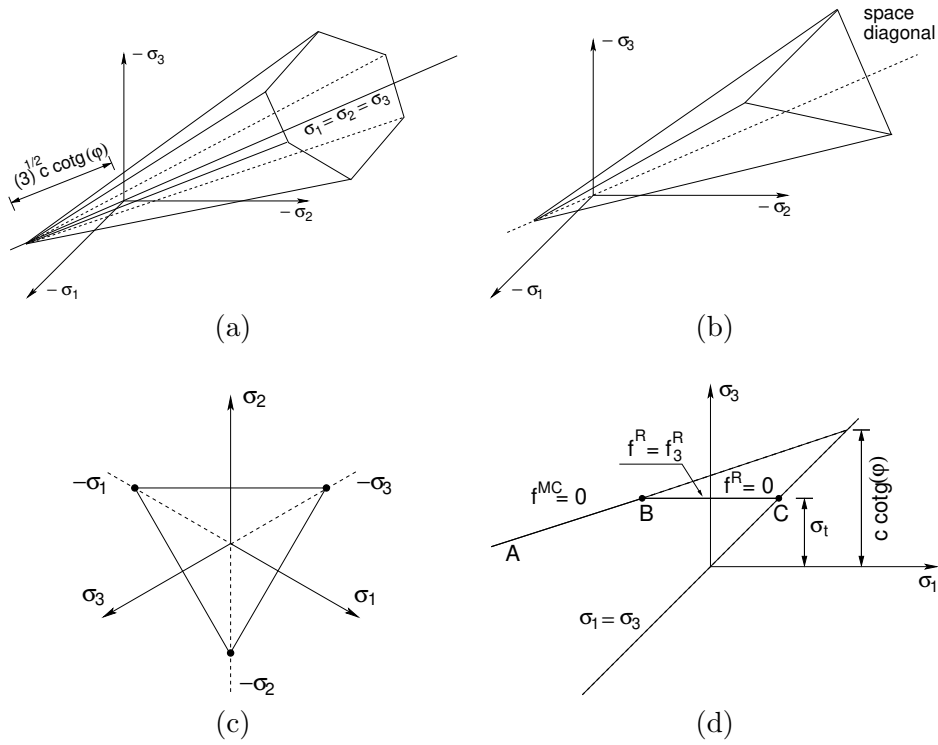
Figure 5.5: Mohr-Coulomb model extended by tension cut-off: a) 3D plot of Mohr-Coulomb model in principal stress space, b) 3D plot of tension cut-off yield surface in principal stress space, c) projection of tension cut-off surface into deviatoric plane, d) projection of the combined Mohr-Coulomb and tension cut-off yield surfaces into $\sigma_1 - \sigma_3$ stress space

line A-C represent an edge of two planes of the Mohr-Coulomb yield surfaces, then there would be at least three simultaneously active yield surfaces.

If the material element were placed under triaxial tension then the stress path during the increase in loading would follow the space diagonal towards the apex of the tension cut-off pyramid. As the failure criterion would now map out as a regular triangular pyramid rather than an irregular hexagonal pyramid the number of surfaces violated when the element reached the plastic state would be three as in the case of the pure Mohr-Coulomb failure criterion.

5.4.1 Operation of the proposed model

Once the tension cut-off yield functions had been introduced to the model the use of the Lode angle as a singularity indicator was no longer possible. A situation could arise whereby an elastic guess causes one shear and one tensile yield surface to become active. Both surfaces would lie in the same "working sector" where the Lode angle would lie in between the limits $-30° \leq \theta \leq 30°$. Hence the Lode angle would not be useful in detecting the need for a multi-surface plasticity stress return when the above mentioned condition arose. As a consequence a new singularity indicator or singularity detection procedure needed to be developed. An important point to note is that if multiple yield surfaces are active, the violation of a specific yield function at the elastic prediction stage does not necessarily imply that the yield condition is active [60].

The structure of the proposed model allows for this observation by attempting first to find a stress return using single surface plasticity, even if multiple yield surfaces are active after the elastic prediction is calculated. After each attempted stress return, all yield functions are checked to see if any are violated. If none are violated then the solution to the stress return is found. If one or more are still found to be violated after the single surface plasticity stress return, another stress return is attempted using the plastic potential function of one of the other yield surfaces that was violated at the elastic prediction stage. Only when all of the yield surfaces that were violated at the elastic prediction stage have been tested for a single surface plasticity return does the model move on to attempting to use two surface multi-surface plasticity to find a successful stress return solution.

If the model determines that multi-surface plasticity is required it will first attempt to find a solution using two surface multi-surface plasticity. Similarly to the previous procedure, the model will now test stress returns using combinations of pairs of yield functions that are violated at the elastic prediction stage. The return scheme is based upon the idea of two surface multi-surface plasticity and satisfies Koiter's generalization [43]. Two plastic multipliers are determined and used in the flow rule to direct the stress point back onto the intersection vertex of the two yield functions under consideration. If the stress return is successful the solution is found. If unsuccessful the model tests a different pair of yield functions that were violated by the elastic prediction. The process is repeated until either a successful stress return is obtained or all different combinations of pairs of violated yield functions have been tested. If the later is the case then three surface multi-surface plasticity is used in the same way to obtain the correct stress return solution.

To accelerate the searching process and at the same time to ensure the selection of a proper pair or a proper triplet of the violated yield surfaces a singularity indicator distinguishing the stress return along either the triaxial compression or extension lines is added. In fact, it is sufficient to check whether the argument in Eq. (5.24) receives, up on returning to the yield surface f_1^{MC} (the first yield surface being checked), a positive value (return along the triaxial compression line) or a negative value (return along the triaxial extension line). Moreover, when three surface multi-surface plasticity stress return is suggested without having a specific apex singularity indicator at hand it is vital to proceed first with the return towards the apex of the tension cut-off pyramid.

5.4.2   Testing implementation of Mohr-Coulomb model with tension cut-off

The testing consisted of checking that the model performed as expected for every possible combination of one, two, three and four yield surface violations. As in Section 4.6 two simple models were used to test all the above mentioned violations, see Fig 5.6.
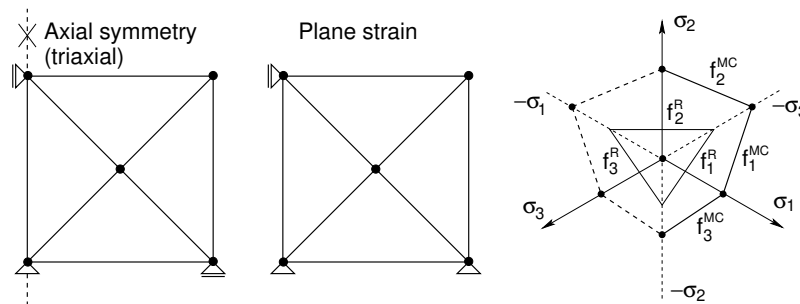
Figure 5.6: The two simple models used in testing and labeling of yield surfaces

One of the models used a plane strain assumption that allowed the testing of the working sector shear and tension single yield surface violations as plotted in Fig. 5.7.

The remaining tests were carried out assuming the axisymmetric model, Figs. 5.8 - 5.9 where the stress path followed one of the lines defining the edge of the working sector until the vertex of two yield surfaces were met. This replicated the conditions of typical triaxial compression and extension tests, Fig. 5.8.

Testing of the combination of the working sector shear and tension yield surface violation was then performed by applying tensile forces. To ensure that the three or four surface violation occurred, the magnitude of the maximum tensile strength σ_t was varied, thus moving the the tension cut-off yield surface to the desired position that caused the violation as displayed in Fig. 5.9(a)(b).

The apex violations of both the tension cut-off pyramid and the shear yield surface pyramid were tested using an axisymmetric model that placed the soil into triaxial tension. Note that if the ultimate tensile strength of the soil was larger than the $c \cot \varphi$ value then the governing apex is defined by the six shear yield surface intersection. During the testing, both apex violations were checked. The two different cases were produced by varying the ultimate tensile strength parameter so that it was above and below the $c \cot \varphi$ value for the separate tests. Whilst it is appreciated that the shear yield function violation is in fact of six yield surfaces, the violation of the three shear surfaces F1, F2 and F3 would

(a)

(b)
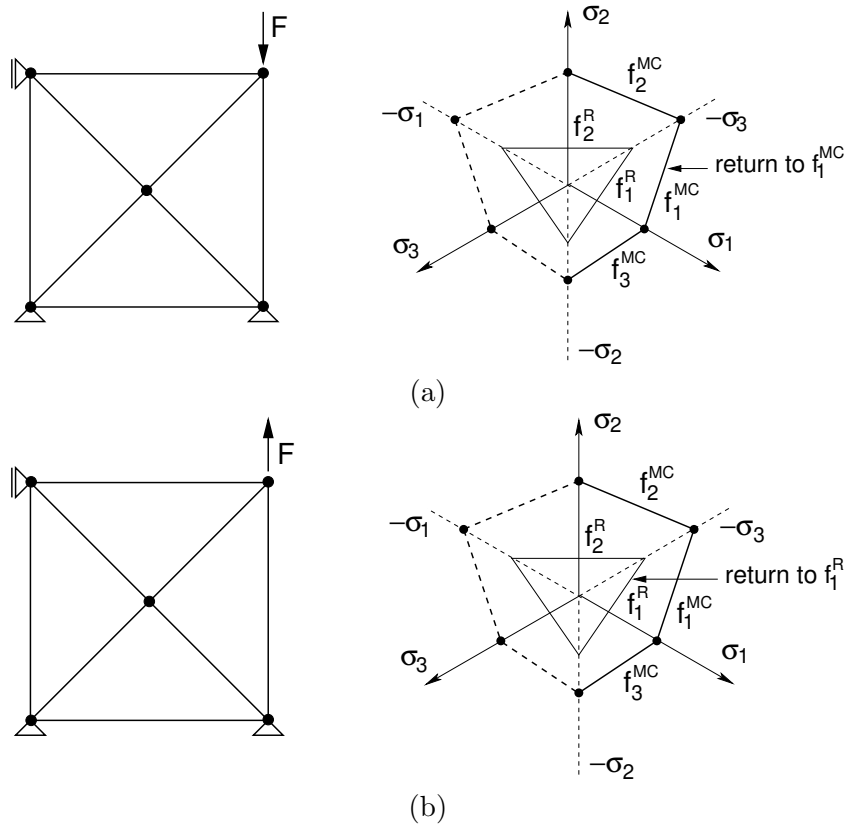
Figure 5.7: Summary of the simple element models used to test single yield surface violations: (a) return to f_1^{MC} yield surface, (b) return to f_1^R yield surface

also indicate that the stress point was in the space where an apex return is necessary. This procedure has previously been implemented by Pankaj and Bićanić [60] in their 'inverted apex pyramid'. The testing of the shear yield surface apex caused problems when assuming a non-associated flow rule with a dilation angle $\psi = 0$ rendering the matrix **L** in Eq. (5.53) singular. Note, however, that the actual value of ψ is not important when solving the apex problem. Thus setting $\psi = \varphi$ appears as a natural choice to arrive at a successful apex return.

During all the tests the computer code was incrementally stepped through with all the local variables observed at each step. The code was checked to see that it identified the correct violation case and then that the stress return scheme did in fact take the stress back to the yield surface(s).

Multi-surface plasticity

The assumptions inherent to the model were found to imply that even though a case could arise where four yield functions were violated by the elastic prediction, only a three surface multi-surface plasticity stress return was required to obtain a successful solution. Whilst there were problems implementing this with the shear yield surface apex, this procedure was found to be true for the violation where two tension and two shear yield surfaces became active. The observation can be explained by the particular way in which the yield surfaces intersect. A specific point is defined at the location where four yield surfaces intersect and would be the position that the stress state would return to if a four surface multi-surface plasticity stress return was used. However, the point is still defined by the intersection of just three of the yield function planes. Therefore using three surface multi-surface plasticity returns the stress state to exactly the same point as a four surface return would. Hence the model which tests firstly single surface, then two and finally three surface multi-surface plasticity stress returns finds a solution to the above mentioned situations without using a four surface multi-surface plasticity return. The reason for this behavior is that the forth plane intersects the other three at the same point (defined by the three surfaces intersection). A similar observation has been documented by Pankaj and Bićanić [60] where in their proposed "inverted apex pyramid" six yield surfaces simultaneously

(a)

(b)
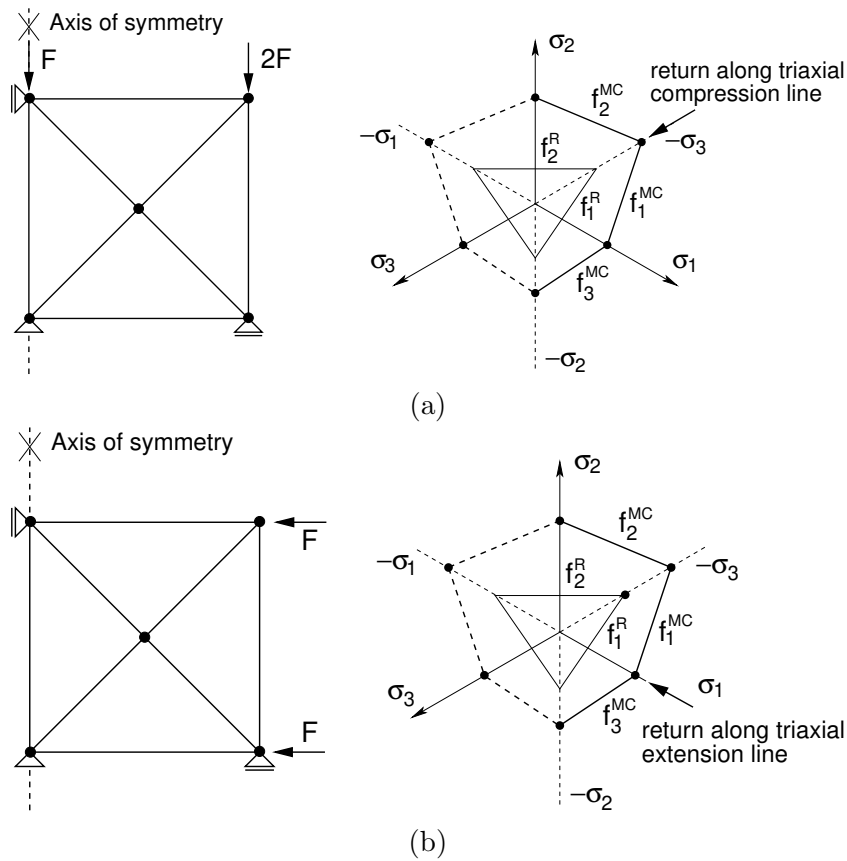
Figure 5.8: Summary of the simple element models used to test two surface violations: (a) return to $f_1^{MC} f_2^{MC}$ yield surfaces along the triaxial compression line, (b) return to $f_1^{MC} f_3^{MC}$ yield surfaces along the triaxial extension line

intersect. They found that a three surface return was always adequate in returning to the apex of the pyramid.

It should also be stated that any combination of three out of the four yield surfaces in these locations can be used for the stress return; the stress state will always return to the same point. This has been verified for the two shear, two tensile surface violation when the model was tested. If anisotropic tensile behavior was assumed then four surface multi-surface plasticity would need to be incorporated into the model as there would be no defined points where four yield surfaces simultaneously intersect.

Effect of varying the size of the elastic prediction

During development of the model it was hypothesized that by varying the magnitude of the elastic guess, one could obtain different successful stress return routines. When traveling along the same stress path, situations arise where different sizes of elastic guess result in different stress return routines being the appropriate course of action to obtain a successful solution. Consider an element being loaded nearly in triaxial compression as shown is Figure. 5.10.

Principal stress space is plotted with the six shear yield surfaces. The thicker dashed lines represent the "singularity cone" where if the elastic predicted stress lies in the domain between these lines a multi-surface plasticity stress return is required. The stress state at the end of the previous loading increment is denoted by point A. This point lies inside the elastic domain. The elastic prediction moves the stress point in the direction of the arrows shown towards points B and C. Consider using a relatively small elastic guess where the elastic predicted stress is point B. The correct stress return for this situation would be a single surface plasticity return to the f_1^{MC} yield surface, see Fig. 5.7 for labeling of the yield surfaces. If a larger elastic guess had been used, (still along the same loading path direction) and the elastic predicted stress was that corresponding to point C, one would use a two surface multi-surface plasticity stress return to come back to the corner where the yield surfaces

(a)

(b)

(c)
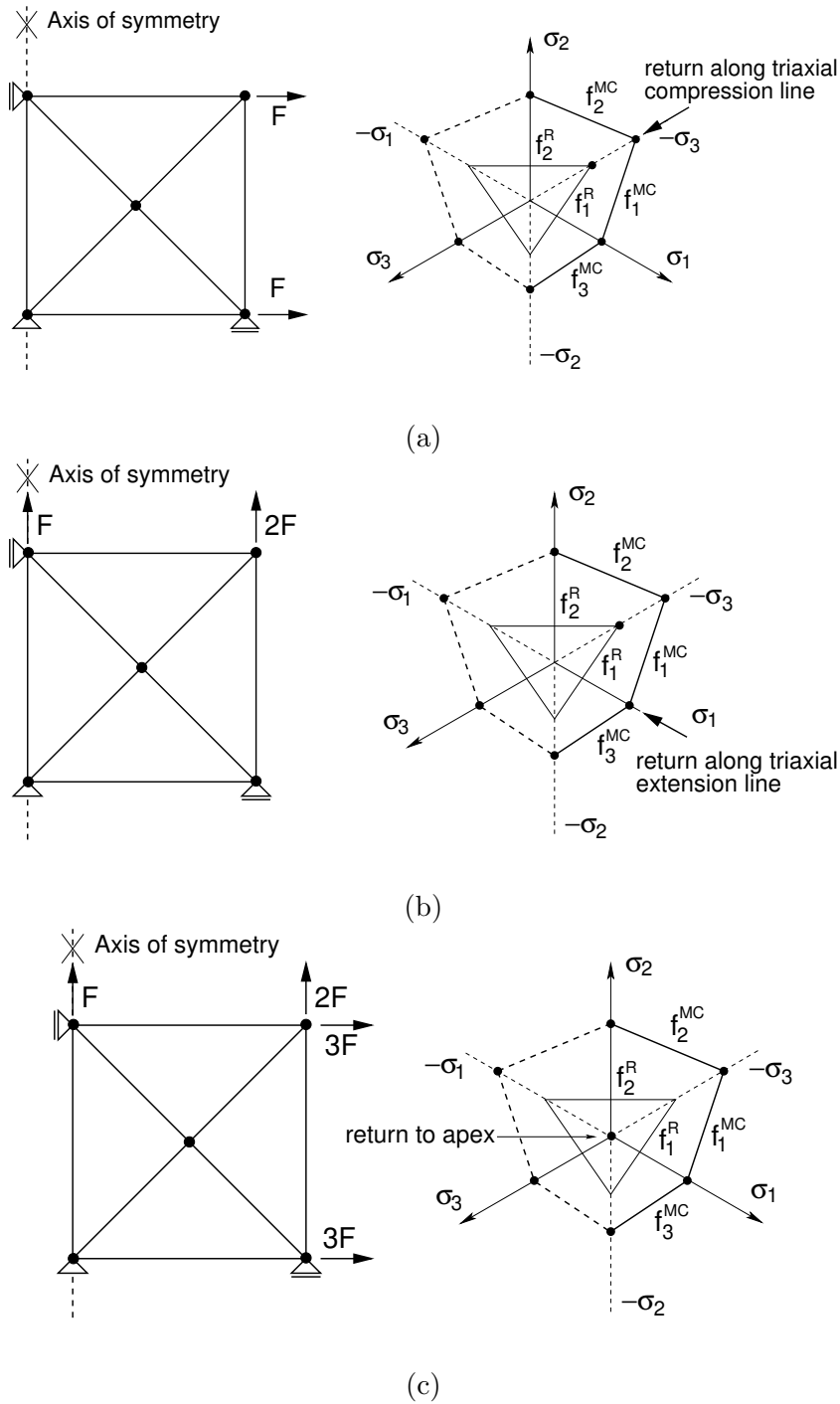
Figure 5.9: Summary of the simple element models used to test two, three or four surface violations including the apex problem: (a) return to $f_1^{MC} f_2^{MC}$, $f_1^R f_2^R$ yield surfaces along the triaxial compression line or to a point intercept of the four yield surfaces $f_1^{MC} f_2^{MC} f_1^R f_2^R$, (b) return to f_1^R yield surface or $f_1^{MC} f_3^{MC}$ yield surfaces along the triaxial extension line or to a point intercept of the three yield surfaces $f_1^{MC} f_3^{MC} f_1^R$, (c) return to the apex of either Mohr-Coulomb or tension cut-off yield surfaces

f_1^{MC} and f_2^{MC} intersect. Therefore in this simple case one obtains two different values for the stress state of the element at the end of the loading increment by using different sizes of elastic prediction. As the magnitude of the elastic guess is increased the probability of a multi-surface stress return being required rises. If one takes the view that the correct stress return is related to where the elastic prediction stress path crosses the yield surface(s) then unless the element is in pure triaxial compression or extension (neglecting tension yield surfaces for this argument) then a single surface plasticity return would always be appropriate. If elastic guesses were infinitesimally small the stress state would only enter the singularity cone when the element was in pure triaxial compression or
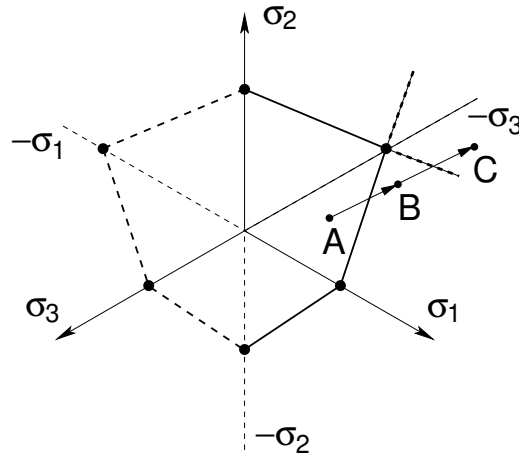
Figure 5.10: Effect of varying the magnitude of the elastic guess

extension. Thus by increasing the size of the elastic guess one increases the likelihood of obtaining a multi-surface plasticity solution and hence a different stress state at the end of the loading increment.

Nevertheless, for various reasons one can propose that these potential inaccuracies are negligible in real world finite element code implementation. In reality the number of occasions when a multi-surface plasticity solution is used is relatively low. Near or pure triaxial compression or extension conditions typically do not arise very commonly in real world problems and hence when considering the stress field of the entire problem domain the small inaccuracies would have a negligible effect. The same phenomenon could happen around the intersection of the shear and tension yield surfaces. The same reasoning as mentioned above could justify neglecting the effects in this case.

Whilst generally negligible in real world problems these observations should be appreciated from an academic perspective and were successfully observed when the model was tested. By varying the magnitude of the elastic prediction different stress return routines and different stress fields were seen to occur.

Proposed singularity indicator for triaxial conditions where two tension yield surfaces become simultaneously active

Whilst the overall efficiency of the new model in terms of computing resources is not expected to be a problem, the model could be adapted to use singularity indicators that would immediately identify which stress return procedure was required for any given elastic prediction. Pankaj and Bićanić [60] have identified singularity indicators for the two surface multi-surface plasticity occurrences in the Mohr-Coulomb model in the form of inequalities that are functions of the elastic prediction in terms of principal stresses. These singularity indicators assume that the shear yield functions of the Mohr-Coulomb model have associated plasticity and hence would need to be adjusted to account for non-associated plasticity to be incorporated into the new model. However, with the addition of the tension cut-off yield surfaces in the new model, a number of new single, two, three and four yield surface violation combinations arise for which singularity indicators would need to be developed. It is hypothesized that if one were able to create singularity indicators for all the combinations of single and two surface violations, then the three and four surface violations could be detected by using the singularity indicators in combination with one another.

Hereafter, a singularity indicator is proposed to detect when the triaxial two tension yield surface violation occurs by manipulating the ideas presented in [60]. Firstly plot the shear and tension yield surfaces in principal stress space, see Fig. 5.11.

A singular region is defined in the working sector as the area where an elastic prediction would violate both the f_1^R and f_2^R tension yield surfaces and a two surface stress return would be required. Incidentally, two other singular regions are defined where two shear yield surfaces are violated. Singularity indicators for these areas are documented in [60] for associated plasticity.

The proposed singularity indicator works on the following simple principle. If a single surface
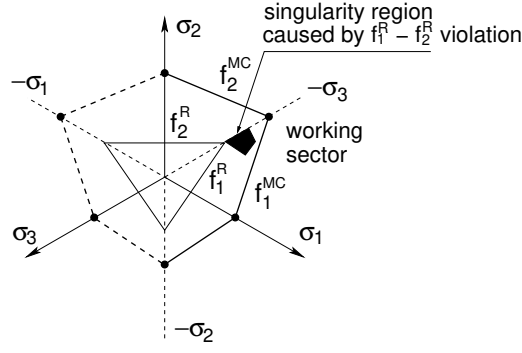
Figure 5.11: Shear and tension yield surfaces plotted in deviatoric stress space

stress return using the f_1^R yield surface places the returned stress outside the working sector then the trial stress must have been inside the singularity area. Therefore the singularity indicator is formed by representing the final stress values after a single surface f_1^R stress return in terms of the elastic trial stress values. If these final returned stresses lie outside the working sector then a multi-surface plasticity solution is needed. To develop the singularity indicator for the $f_1^R - f_2^R$ yield surface violation case one first needs to develop a few relationships. Noting that for the tensile yield surfaces associated plasticity is assumed, the normal to the f_1^R yield function is

$$\frac{\partial f_1^R}{\partial \boldsymbol{\sigma}} = \{1,\, 0,\, 0\}^\mathsf{T} \tag{5.68}$$

For a linearly elastic material the elastic matrix is defined as

$$\mathbf{D} = B \begin{bmatrix} 1-\nu & \nu & \nu \\ \nu & 1-\nu & \nu \\ \nu & \nu & 1-\nu \end{bmatrix} \tag{5.69}$$

where

$$B = \frac{E}{(1+\nu)(1-2\nu)} \tag{5.70}$$

with a familiar notation for ν and E being Poisson's ratio and Young's modulus, respectively. Using the cutting plane algorithm one obtains an expression for the incremental plastic multiplier

$$\Delta\lambda = \frac{f_1^R(\sigma_1^{tr})}{\left(\dfrac{\partial f_1^R}{\partial \boldsymbol{\sigma}}\right)^{\mathsf{T}} \mathbf{D} \dfrac{\partial f_1^R}{\partial \boldsymbol{\sigma}}} \tag{5.71}$$

where (tr) denotes again that the value is with respect to the elastic prediction trial stress. Again, an elastic rigid-plastic material response in tension is adopted for simplicity. Upon substitution of Eq. (5.68) into Eq. (5.71) one obtains

$$\Delta\lambda = \frac{f_1^R(\sigma_1^{tr})}{B(1-\nu)} \tag{5.72}$$

Using Koiter's generalization [43] one can obtain the incremental plastic strains as

$$\Delta\varepsilon^{pl} = \Delta\lambda \frac{\partial f_1^R}{\partial \boldsymbol{\sigma}} = \frac{f_1^R(\sigma_1^{tr})}{B(1-\nu)} \begin{Bmatrix} 1 \\ 0 \\ 0 \end{Bmatrix} \tag{5.73}$$

Now the final corrected stress $\boldsymbol{\sigma}^F$, once the single surface return has been performed, will take the form

$$\boldsymbol{\sigma}^F = \boldsymbol{\sigma}^{tr} - \mathbf{D}\Delta\varepsilon^{pl} \tag{5.74}$$

Hence the final principal stresses can be written as

$$\left\{ \begin{array}{c} \sigma_1^F \\ \sigma_2^F \\ \sigma_3^F \end{array} \right\} = \left\{ \begin{array}{c} \sigma_1^{tr} \\ \sigma_2^{tr} \\ \sigma_3^{tr} \end{array} \right\} - \frac{f_1^R(\sigma_1^{tr})}{(1-\nu)} \left\{ \begin{array}{c} 1-\nu \\ \nu \\ \nu \end{array} \right\} \tag{5.75}$$

Eq. (5.75) gives the final principal stresses if a single surface plasticity stress return was attempted using the f_1^R yield surface. If the elastic prediction stress lies in the singularity area then the single surface stress return would place the stress point outside the working sector. In this case the stress point would satisfy $\sigma_1^F > \sigma_2^F > \sigma_3^F$ and thus $\sigma_1^F - \sigma_2^F > 0$. Using this relationship with Eq. (5.75) one can obtain the singularity indicator

$$\sigma_1^{tr} - \sigma_2^{tr} + \frac{f_1^R(\sigma_1^{tr})(2\nu - 1)}{(1-\nu)} > 0 \tag{5.76}$$

If Eq. (5.76) is satisfied then the elastic prediction stress is in the singular area and a two surface multi-surface plasticity stress return is required.

5.5 Undrained analysis in total stresses - Type (3)

Performing the analysis in total stresses, type (3) approach, was already elaborated in Section 4.5 in conjunction with the Drucker-Prager plasticity model. Considering the same material parameters as stored in Table 4.2 with the Mohr-Coulomb model we arrive at the Tresca model seen in Fig. 4.4(b). The model is implemented in GEO5 FEM to solve this particular task by suitably adjusting the Mohr-Coulomb model. As with the DP model the undrained stiffness ($E_u, \nu_u \in (0.49 - 0.499)$) and undrained shear strength parameters ($c_u = S_u, \varphi_u = 0$) are used.

5.6 Comparing performance of Mohr-Coulomb model against real soil behavior

Implementation of a given material model is usually verified by comparing numerical predictions with experimental measurements. However, the laboratory measurements may also serve to expose potential deficiencies of the model. This exercise is examined here by plotting the Mohr-Coulomb predictions against data measured for three different sandy soils.

Table 5.2: Material parameters of selected sandy soils

Soil	USCS classification	E_{oed} [MPa]	Peak		Residual	
			c [kPa]	φ [°]	c [kPa]	φ [°]
Štvanice	SM	16.2	10	40	0	35
Hrušovany	SW	24.9	12	43	0	36.5
Jablonec	SM	18.8	8	44	0	41

Table 5.2 stores the values of oedometric modulus E_{oed} and shear strength parameters, cohesion c and angle of internal friction φ. For illustration, the results from the associated laboratory tests are plotted for the Hrušovany soil in Fig. 5.12(a,b). While a standard oedometric test was adopted to estimate the soil stiffness, the shear strength parameters were acquired from a triaxial test considering three chamber pressures $\sigma_m^0 = -(50, 100, 200)$ kPa, in particular. The resulting stress strain curves for $\sigma_m^0 = -50$ kPa are displayed in Fig. 5.13. To appreciate the effect of initial stress we also plot the evolution of dilation at two different chamber pressures for all soils in Fig. 5.12(c).

When assuming standard triaxial compression with Lode's angle $\theta = 30°$ we may derive the Mohr-Coulomb predictions analytically. First recall Fig. 5.1(b) to see that in this particular case the

(a) (b) (c)
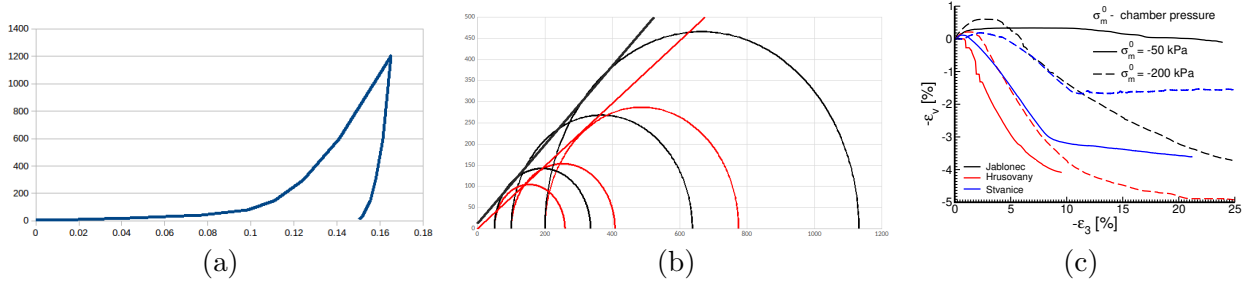
Figure 5.12: a) Oedometer test (Hrušovany soil), b) Estimated shear strength parameters (Hrušovany soil), c) Evolution of dilation for selected soils

f_1^{MC} and f_2^{MC} yield surfaces become active. The corresponding plastic strains are obtained from Eqs. (5.23), (5.18), and (5.20) as

$$\Delta \boldsymbol{\varepsilon}^{pl} = \Delta\lambda_1 \frac{\partial g_1^{MC}}{\partial \boldsymbol{\sigma}} + \Delta\lambda_2 \frac{\partial g_2^{MC}}{\partial \boldsymbol{\sigma}} = \Delta\lambda \left(\boldsymbol{n}_{g,1} + \boldsymbol{n}_{g,2} \right) \tag{5.77}$$

$$\boldsymbol{n}_{g,1}^{\mathsf{T}} = \frac{1}{2} [1 + \sin\psi, 0, -1 + \sin\psi] \tag{5.78}$$

$$\boldsymbol{n}_{g,2}^{\mathsf{T}} = \frac{1}{2} [0, 1 + \sin\psi, -1 + \sin\psi] \tag{5.79}$$

Employing the values of individual components of the plastic strain increment

$$\Delta\varepsilon_1^{pl} = \Delta\varepsilon_2^{pl} = \frac{\Delta\lambda}{2} (1 + \sin\psi) \tag{5.80}$$

$$\Delta\varepsilon_3^{pl} = \Delta\lambda(-1 + \sin\psi) \tag{5.81}$$

provides the volumetric and deviatoric plastic strain measures in the form

$$\Delta\varepsilon_v^{pl} = \Delta\varepsilon_1^{pl} + \Delta\varepsilon_3^{pl} + \Delta\varepsilon_3^{pl} = 2\Delta\lambda \sin\psi \tag{5.82}$$

$$\Delta E_d^{pl} = \frac{2}{\sqrt{3}}(\Delta\varepsilon_1^{pl} - \Delta\varepsilon_2^{pl}) = \frac{\Delta\lambda}{\sqrt{3}}(3 - \sin\psi) \frac{\Delta\varepsilon_v^{pl}}{\Delta E_d^{pl}} = \frac{2\sqrt{3}\sin\psi}{3 - \sin\psi} \tag{5.83}$$

$$\Delta\varepsilon_s^{pl} = \frac{1}{\sqrt{3}}\Delta E_d^{pl} = \frac{\Delta\lambda}{3}(3 - \sin\psi) \longrightarrow \frac{\Delta\varepsilon_v^{pl}}{\Delta\varepsilon_s^{pl}} = \frac{6\sin\psi}{3 - \sin\psi}, \quad (JE_d = q\varepsilon_s) \tag{5.84}$$

Linear elastic Hooke's, Eq. (1.39), together with Eqs. (5.81) and (5.82) give the slopes of lines in Fig. 4.7(b) as

$$\frac{\varepsilon_v^{el}}{\varepsilon_3^{el}} = 1 - 2\nu \tag{5.85}$$

$$\frac{\varepsilon_v^{pl}}{\varepsilon_3^{pl}} = \frac{4\sin\psi}{-1 + \sin\psi} \tag{5.86}$$

to address the evolution of volumetic strains both in elastic and plastic response. Finally we recall the failure condition in Eq. (5.10) together with the elastic response associated with the triaxial compression loading path given by Eq. (1.66) to write

$q = -E\varepsilon_3$ Elastic branch for triaxial compression

$J + (\sigma_m - c\cot\varphi) \, g(\varphi, \theta = 30°) = 0$ Failure condition, see also Fig. 5.1(c)

$J + \sqrt{3}(50 + \sigma_m) = 0$ Loading path assuming chamber pressure $\sigma_m^0 = -50$ kPa

$\sqrt{3}J = \sigma_1 - \sigma_3 = q, \quad \sigma_1 = -50\text{kPa}$

The values at the onset of yielding satisfying the failure condition are stored in Table 5.3. Recall that arriving at this condition numerically in stress control loading regime would terminate the analysis

Table 5.3: Stress values at failure

	Peak			Residual		
Soil	σ_m^e [kPa]	J^e [kPa]	σ_3^e [kPa]	σ_m^e [kPa]	J^e [kPa]	σ_3^e [kPa]
Štvanice	-124.3	128.7	-272.9	-94.8	77.6	-184.4
Hrušovany	-139.9	155.7	-319.7	-98.9	84.7	-196.7
Jablonec	-138.4	153.1	-315.2	-113.6	110.2	-240.9

because of singularity of the algorithmic tangent stiffness matrix. To continue shearing beyond this point requires exploiting the displacement control simulation as used already in Section 4.6, recall Fig. 4.10(b). Graphically, the failure condition is plotted for individual soils in Fig. 5.13 showing also the effect of Poisson's ratio which was used to calculate Young's modulus E from oedometric modulus E_{oed} according to Eq. (1.69).
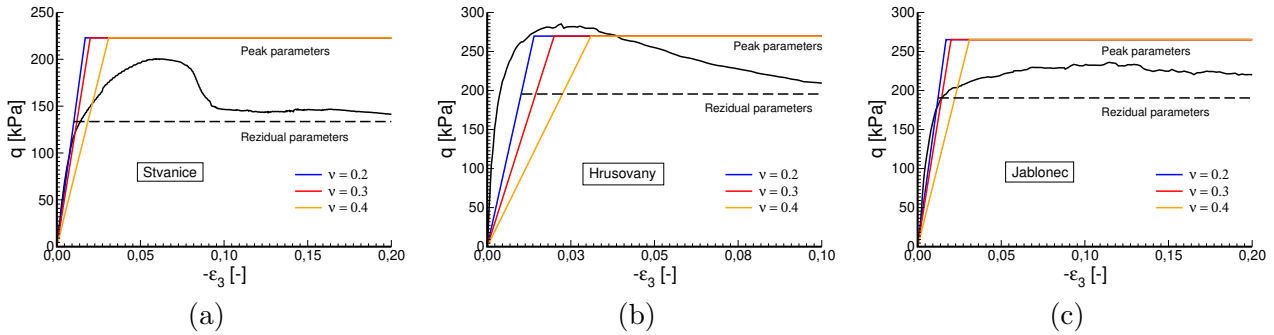
Figure 5.13: Application of Mohr-Coulomb model to predict failure in triaxial compression for chamber pressure $\sigma_m^0 = -50$ kPa: a) Štvanice, b) Hrušovany, c) Jablonec

Figure 5.14 finally compares evolution of dilation for two values of dilation angle $\psi = 5°, 20°$, in particular. The slopes corresponding to elastic and plastic branches are derived from Eqs. (5.85) and (5.86), respectively.
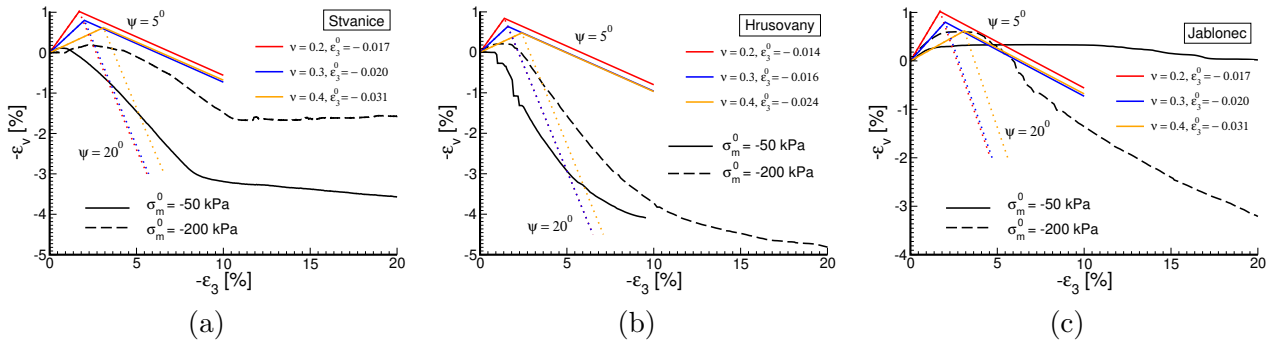
Figure 5.14: Application of Mohr-Coulomb model to predict dilation: a) Štvanice, b) Hrušovany, c) Jablonec

5.7 Mohr-Coulomb model in undrained analysis

Chapter 6

Hoek-Brown model

Similarly to the Mohr-Coulomb (MC) model the Hoek-Brown (HB) model falls into the category of elastic-perfectly plastic material models. At present the HB model is the most commonly used failure criterion to describe the strength of rock masses. It is purely empirical and the original formulation [30] was expected to address the behavior of an intact rock. To extend its applicability the authors in [31] and later in [32] provided a generalized version capable of describing rock masses of a variable quality. The list of model parameters is available in Table 6.1. The essential parameters are the Geological strength index GSI, which quantifies the quality of the rock mass structure and the amount of discontinuities (the value of GSI=100 corresponds to an intact rock and decreases to zero with worsening of the rock quality) and the disturbance factor D, which takes into account prior underground activities including mining and excavation (the value of D=0 corresponds to an intact rock and the maximum degree of damage is represented by the value of D=1). The strength of an intact rock is represented by the uniaxial compressive strength σ_{ci} and by the Hoek-Brown constant m_i both determined from a triaxial test. Figure 6.1 illustrates their influence on the shape of the HB

Table 6.1: Parameters of Hoek-Brown plasticity model

Symbol	Units	Description
E_{rm}	[MPa]	Modulus of elasticity of rock mass
ν	[-]	Poisson's ratio
σ_{ci}	[MPa]	Uniaxial compressive strength
m_i	[-]	Hoek-Brown constant
GSI	[-]	Geological strength index
D	[-]	Disturbance factor
ψ_0	[°]	Initial angle of dilation
m_b	[-]	Reduced Hoek-Brown constant
s, a	[-]	Material constants
σ_t	[kPa]	Maximum allowable tensile strength
TsRF	[-]	Tensile strength reduction factor
σ_ψ	[kPa]	Threshold value of confining stress for application of dilatancy

failure criterion as well as location of the apex i.e., the physically acceptable maximum value of the prescribed tensile strength $\sigma_t \leq \overline{\sigma}_t$ given by

$$\overline{\sigma}_t = \frac{s\sigma_{ci}}{m_b} \tag{6.1}$$

where the reduced Hoek-Brown constant is written in terms of GSI and D as

$$m_b = m_i \exp\frac{\text{GSI} - 100}{28 - 14\text{D}} \tag{6.2}$$

Note that for an intact rock we get $m_b = m_i$.
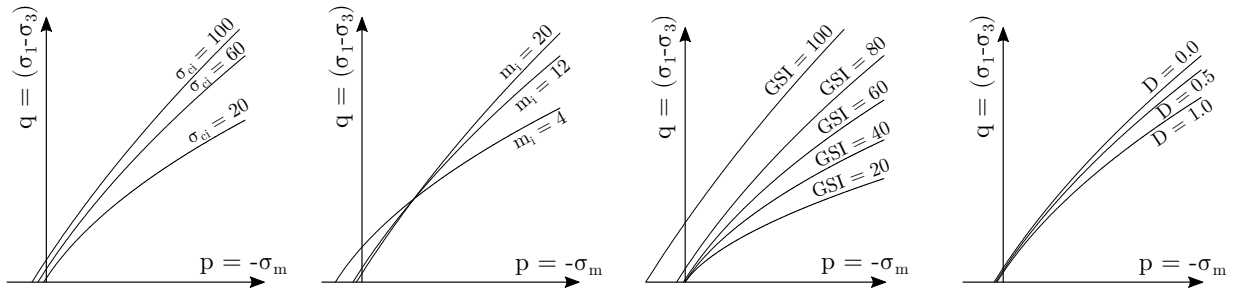
Figure 6.1: Influence of Hoek-Brown parameters on shape of yield criterion: a) uniaxial compressive strength of intact rock, b) Hoek-Brown constant of intact rock, c) Geological strength index, d) disturbance factor
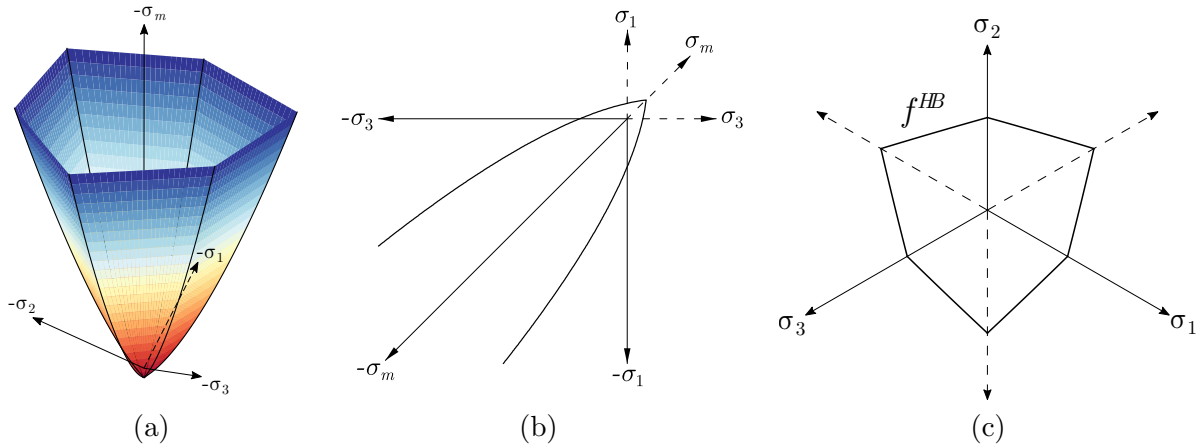
Figure 6.2: Hoek-Brown yield function: a) plot in effective principal stress space, b) plot in plane of maximum and minimum principal stress, c) plot in deviatoric plane

These basic parameters can also be exploited to estimate the rock mass stiffness represented by the modulus of elasticity E_{rm}. As an example we provide one particular formulation presented in [32], see also [33] for other options,

$$E_{rm}\,[\text{GPa}] \;=\; \left(1 - \frac{\text{D}}{2}\right)\sqrt{\frac{\sigma_{ci}}{100}}\,10^{(\text{GSI}-10)/40}, \quad \sigma_{ci} \le 100\,\text{MPa} \tag{6.3}$$

$$E_{rm}\,[\text{GPa}] \;=\; \left(1 - \frac{\text{D}}{2}\right)10^{(\text{GSI}-10)/40}, \qquad\qquad \sigma_{ci} > 100\,\text{MPa} \tag{6.4}$$

Similarly to the Mohr-Coulomb model, the Hoek-Brown model plots as an irregular hexagonal pyramid in the principal stress space, see Fig. 6.2(a). While the edges of the MC surface are linear, the HB model experiences curvature along both edges and surfaces, see also projection into $\sigma_1 - \sigma_3$ plane displayed in Fig. 6.2(b). Although not evident from Fig. 6.2(c), individual sectors of the HB failure criterion are also slightly curved when projected into a deviatoric plane.

6.1   Formulation of Hoek-Brown failure criterion

In analogy with the Mohr-Coulomb model described in Chapter 5 we start from the assumption that the response at failure is independent of the intermediate principal stress. The three main sectors

representing the yield surface, recall Fig. 5.1(b), now receive the form

$$f_1^{HB}(\sigma_1, \sigma_3) \;=\; \sigma_1 - \sigma_3 - \sigma_{ci}\left(s - m_b\frac{\sigma_1}{\sigma_{ci}}\right)^a, \quad \sigma_1 \geq \sigma_2 \geq \sigma_3 \tag{6.5}$$

$$f_2^{HB}(\sigma_2, \sigma_3) \;=\; \sigma_2 - \sigma_3 - \sigma_{ci}\left(s - m_b\frac{\sigma_2}{\sigma_{ci}}\right)^a, \quad \sigma_2 \geq \sigma_1 \geq \sigma_3 \tag{6.6}$$

$$f_3^{HB}(\sigma_1, \sigma_2) \;=\; \sigma_1 - \sigma_2 - \sigma_{ci}\left(s - m_b\frac{\sigma_1}{\sigma_{ci}}\right)^a, \quad \sigma_1 \geq \sigma_3 \geq \sigma_2 \tag{6.7}$$

where parameters s, a follow from empirical relations

$$s \;=\; \exp\frac{\text{GSI} - 100}{9 - 3\text{D}}, \tag{6.8}$$

$$a \;=\; \frac{1}{2} + \frac{1}{6}\left(\exp\frac{-\text{GSI}}{15} - \exp\frac{-20}{3}\right) \tag{6.9}$$

so that for an intact rock we see that $s = 1$, $a = 0.5$. The stress return mapping is driven by a non-associated flow rule with the plastic potential functions associated with the three potentially active sectors written as

$$g_1^{HB}(\sigma_1, \sigma_3) \;=\; \sigma_1\frac{1 + \sin\psi_m}{1 - \sin\psi_m} - \sigma_3 \tag{6.10}$$

$$g_2^{HB}(\sigma_2, \sigma_3) \;=\; \sigma_2\frac{1 + \sin\psi_m}{1 - \sin\psi_m} - \sigma_3 \tag{6.11}$$

$$g_3^{HB}(\sigma_1, \sigma_2) \;=\; \sigma_1\frac{1 + \sin\psi_m}{1 - \sin\psi_m} - \sigma_2 \tag{6.12}$$

where ψ_m is the mobilized angle of dilation. Grounding on experimental evidence, see also [52], the dilation angle is expected to evolve according to Fig. 6.3 where σ_ψ is a certain threshold value of the
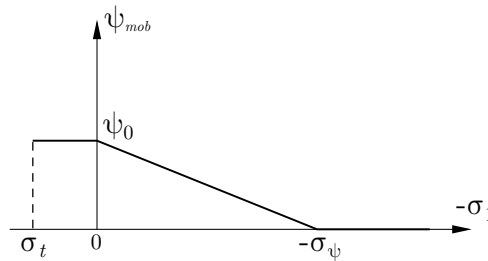
Figure 6.3: Graphical representation of the adopted dilatancy rule

confining pressure σ_1 beyond which the dilation can be neglected. In the space of positive tensile stresses the dilation angle is assumed constant. This simple bilinear variation is mathematically expressed as

$$\psi_m(0 \leq \sigma_1 \leq \sigma_t) \;=\; \psi_0 \tag{6.13}$$

$$\psi_m(\sigma_\psi < \sigma_1 < 0) \;=\; \frac{\sigma_\psi + \sigma_1}{\sigma_\psi}\psi_0 \tag{6.14}$$

$$\psi_m(\sigma_1 \leq \sigma_\psi) \;=\; 0 \tag{6.15}$$

where ψ_0 is the initial value which is also allowed to remain constant regardless of Eq. (6.14) in dependence on the analysis setting in GEO5 FEM.

6.2 Hoek-Brown model with tension cut-off

Equation (6.1) introduced a physically acceptable value of a biaxial tensile strength $\bar{\sigma}_t$ obtained by setting $\sigma_3 = \sigma_1 = \bar{\sigma}_t$ in Eq. (6.5). Note that deriving a uniaxial tensile strength would require an

iterative procedure. This promotes application of a limiting tensile stress $\sigma_t < \overline{\sigma}_t$. From a physical point view this might be supported by a very low tensile strength of weak rock masses. But what appears even more crucial is the application of limiting tensile strength in the return mapping procedure. To see this recall definition of the Hoek-Brown yield function via Eq. (6.5). Because the exponent a ranges from 0.5 to 0.666 (corresponds to GSI=0), setting $\sigma_1 > \overline{\sigma}_t$ generates a negative value within parentheses of Eqs. (6.5) - (6.5) of a given yield function and hence the corresponding failure criterion cannot be evaluated for trial principle stresses falling beyond the apex. A remedy is provided by introducing a tension cut-off failure criterion which allows us to move from this inadmissible stress space as described in Section 6.3.1. To this end, the Rankine failure criterion introduced already in Section 5.4 is adopted. For the sake of completeness we recall the three yield functions representing projections of the Rankine failure criterion in the deviatoric plane, see Figs. 5.5(b,c),

$$f_1^R(\sigma_1, \sigma_t) \quad = \quad \sigma_1 - \sigma_t = 0 \tag{6.16}$$

$$f_2^R(\sigma_2, \sigma_t) \quad = \quad \sigma_2 - \sigma_t = 0 \tag{6.17}$$

$$f_3^R(\sigma_3, \sigma_t) \quad = \quad \sigma_3 - \sigma_t = 0 \tag{6.18}$$

An associated flow rule is again exploited to receive directions of plastic strain increments in the form

$$\boldsymbol{n}_t^1 = \frac{\partial f_1^R}{\partial \boldsymbol{\sigma}} = \{1, 0, 0\}^\mathsf{T} \tag{6.19}$$

$$\boldsymbol{n}_t^2 = \frac{\partial f_2^R}{\partial \boldsymbol{\sigma}} = \{0, 1, 0\}^\mathsf{T} \tag{6.20}$$

$$\boldsymbol{n}_t^3 = \frac{\partial f_3^R}{\partial \boldsymbol{\sigma}} = \{0, 0, 1\}^\mathsf{T} \tag{6.21}$$

6.3   Stress return mapping

Stress return mapping is based on the same concept of working sectors as in the case of MC model. Typically, the elastic trial stress violating the HB failure criterion is brought back to the main sector where $\sigma_1 > \sigma_2 > \sigma_3$. Nevertheless, situations may arise, e.g., the case of triaxial compression or extension, which calls for application of a multi-surface return mapping since more than one yield surface become simultaneously active as outlined in Section 6.3.2. See also Section 5.2.2 for more details. As already pointed out, a particular attention deserves the case where an inadmissible trial stress does not allow for evaluation of the HB yield function. This issue is treated next in Section 6.3.1 addressing a two-step return approach to the HB yield surface over the Rankine yield surface. Because we may identify a close similarity with the Mohr-Coulomb model, we limit our discussion to most essential topics pertinent to the HB model and refer the interested reader to Section 5.2 and [83] for further reading.

6.3.1   Single yield surface plasticity

Unlike the MC model the HB yield surface is nonlinear which requires adopting the Newton-Raphson (NR) iterative method within the return mapping algorithm to give the searched increment of the plastic strain multiplier $\Delta\lambda$ allowing in turn for the evaluation of plastic strain increment as

$$\Delta\boldsymbol{\varepsilon}^{pl} = \Delta\lambda\frac{\partial g_1^{HB}}{\partial\boldsymbol{\sigma}} = \Delta\lambda\boldsymbol{n}_g^1 \tag{6.22}$$

where the normal to the plastic potential function $\boldsymbol{n}_g^1$ reads

$$(\boldsymbol{n}_g^1)^\mathsf{T} = \left\{\frac{1 + \sin\psi_m}{1 - \sin\psi_m}, 0, -1\right\} \tag{6.23}$$

The stress at the end of the $(i + 1)$ load increment is then provided by

$$\boldsymbol{\sigma}^{i+1} = \boldsymbol{\sigma}^{tr} - (\Delta\lambda)^{k+1}\mathbf{D}\boldsymbol{n}_g^1 \tag{6.24}$$

where $\boldsymbol{\sigma}^{tr} = \boldsymbol{\sigma}^i + \mathbf{D}\Delta\boldsymbol{\varepsilon}$ is the trial stress and $\mathbf{D}$ is the 3×3 elastic stiffness matrix, recall Eq. (5.69). Clearly, the above equations represent the case of a successful return to the main sector for which the iterative NR scheme reads

$$(\Delta\lambda)^{k+1} = (\Delta\lambda)^k - \frac{(f_1^{HB})^k}{\left(\mathrm{d}f_1^{HB}\right)^k} \tag{6.25}$$

where $\mathrm{d}f_1^{HB}$ is the derivative of the yield function evaluated at the and the $(i+1)$ load increment with respect to $\Delta\lambda$. Note that ψ_m is considered to remain constant during the return mapping and is updated at the end of the stress update for the converged stress state. This makes $\Delta\lambda$ the only variable in the local iteration scheme (6.25). Writing the direction of principal plastic corrector as

$$\mathbf{D}^{el}\boldsymbol{n}_g^1 = \boldsymbol{\sigma}^{pl} = \left\{\sigma_1^{pl}, \sigma_2^{pl}, \sigma_3^{pl}\right\}^{\mathsf{T}} \tag{6.26}$$

gives

$$\sigma_1(\Delta\lambda) = \sigma_1^{tr} - \Delta\lambda\sigma_1^{pl} \tag{6.27}$$

$$\sigma_2(\Delta\lambda) = \sigma_2^{tr} - \Delta\lambda\sigma_2^{pl} \tag{6.28}$$

$$\sigma_3(\Delta\lambda) = \sigma_3^{tr} - \Delta\lambda\sigma_3^{pl} \tag{6.29}$$

Substituting Eqs. (6.27)-(6.29) into Eq. (6.5) gives the yield function f_1^{HB} in Eq. (6.25) in the form

$$f_1^{HB}(\Delta\lambda^k) = (\sigma_1^{tr} - \sigma_3^{tr}) - \Delta\lambda^k(\sigma_1^{pl} - \sigma_3^{pl}) - \sigma_{ci}\left[s - \frac{m_b}{\sigma_{ci}}\left(\sigma_1^{tr} - \Delta\lambda^k\sigma_1^{pl}\right)\right]^a \tag{6.30}$$

and the corresponding derivative with respect to $\Delta\lambda$ as

$$\mathrm{d}f_1^{HB}(\Delta\lambda^k) = \sigma_3^{pl} - \sigma_1^{pl} - am_b\sigma_1^{pl}\left[s - \frac{m_b}{\sigma_{ci}}\left(\sigma_1^{tr} - \Delta\lambda^k\sigma_1^{pl}\right)\right]^{a-1} \tag{6.31}$$

To initiate the iterative scheme we simply set $\Delta\lambda^0 = 0 \rightarrow \boldsymbol{\sigma}^0 = \boldsymbol{\sigma}^{tr}$. The iteration process is terminated when $f_1^{HB} < \epsilon$, where ϵ is an acceptable convergence error.

Return to Rankine yield surface

Return to the Rankine yield surface f_1^R follows the same minimization procedure. The tensile yield surface defined in terms of the plastic multiplier is given by

$$f_1^R = \sigma_1^{tr} - \Delta\lambda\sigma_1^{pl} - \sigma_t \tag{6.32}$$

and the derivative with respect to $\Delta\lambda$ is therefore

$$\mathrm{d}f_1^R = -\sigma_1^{pl} \tag{6.33}$$

Returning from the trial stress space violating the Rankine failure criterion considers two scenarios:

- *Correct return to the HB yield surface is expected*: This is a two-step return where bringing an inadmissible stress back to the Rankine yield surface is performed first assuming the direction of plastic corrector given by the HB model, i.e., $\boldsymbol{\sigma}^{pl} = \mathbf{D}^{el}\boldsymbol{n}_g^1$ (non-associated flow rule). The procedure then continues with the second step bringing the stresses back onto the HB yield surface along the same direction, see Fig. 6.4. The total plastic strain increment is then the sum of plastic strain increments generated by both steps

$$\boldsymbol{\varepsilon} = (\Delta\lambda_R + \Delta\lambda_{HB})\boldsymbol{n}_g^1 \tag{6.34}$$

  where $\Delta\lambda_R, \Delta\lambda_{HB}$ correspond to the two consecutive return steps, i.e., return to the Rankine and HB yield surfaces, respectively.

- *Correct return to the Rankine yield surface is expected:* This is a one-step return along the direction given by $\boldsymbol{\sigma}^{pl} = \mathbf{D}^{el}\boldsymbol{n}_t^1$ (associated flow rule) so that

$$\boldsymbol{\varepsilon} = \Delta\lambda_R \boldsymbol{n}_t^1 \tag{6.35}$$

As the two vectors, $\boldsymbol{n}_g^1$ and $\boldsymbol{n}_t^1$, are constant within the stress return, the correct increment of the plastic strain is found in one iteration step for both cases using

$$\Delta\lambda_R = -\frac{f_1^R}{\mathrm{d}f_1^R} \tag{6.36}$$
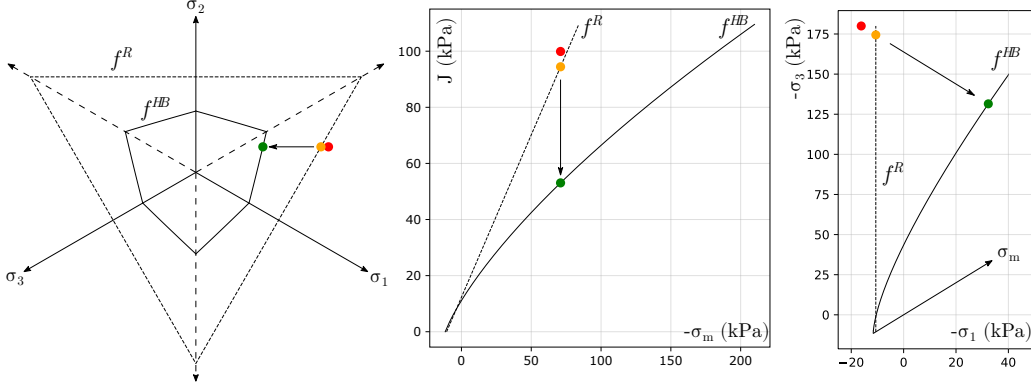
Figure 6.4: Non-associated return to the HB surface from trial stress violating f_1^R in two consecutive steps (plotted for $\psi_0 = 0$): first - from trial stress (red point) onto the Rankine yield surface (orange point), second - from Rankine surface to HB surface (green point) plotted in the deviatoric plane (left), $\sigma_m - J$ plane (middle), $\sigma_1 - \sigma_3$ plane (right).

6.3.2   Multi-surface plasticity stress return

Two active sectors of the HB yield surface apply both to the state of triaxial compression (f_1^{HB} and f_2^{HB}) and triaxial extension (f_1^{HB} and f_3^{HB}). Therefore, two additional directions of plastic yielding are required in accordance with active plastic potential functions (6.11) and (6.12) written as

$$\boldsymbol{n}_g^2 = \frac{\partial g_2^{HB}}{\partial\boldsymbol{\sigma}} = \left\{0, \frac{1+\sin\psi_m}{1-\sin\psi_m}, -1\right\}^{\top} \tag{6.37}$$

$$\boldsymbol{n}_g^3 = \frac{\partial g_3^{HB}}{\partial\boldsymbol{\sigma}} = \left\{\frac{1+\sin\psi_m}{1-\sin\psi_m}, -1, 0\right\}^{\top} \tag{6.38}$$

Next, consider a triaxial stress state in compression which gives the NR iterative scheme in the form

$$\left\{\begin{array}{c} \Delta\lambda_1 \\ \Delta\lambda_2 \end{array}\right\}^{k+1} = \left\{\begin{array}{c} \Delta\lambda_1 \\ \Delta\lambda_2 \end{array}\right\}^{k} - (\mathbf{H}^{-1})^k \left\{\begin{array}{c} f_1^{HB} \\ f_2^{HB} \end{array}\right\}^{k} \tag{6.39}$$

where the Jacobian matrix $\mathbf{H}$ is composed of partial derivatives of the yield functions with respect to two plastic multipliers $\Delta\lambda_1$ and $\Delta\lambda_2$. Therefore

$$\mathbf{H} = \begin{bmatrix} \dfrac{\mathrm{d}f_1^{HB}}{\mathrm{d}(\Delta\lambda_1)} & \dfrac{\mathrm{d}f_1^{HB}}{\mathrm{d}(\Delta\lambda_2)} \\[3mm] \dfrac{\mathrm{d}f_2^{HB}}{\mathrm{d}(\Delta\lambda_1)} & \dfrac{\mathrm{d}f_2^{HB}}{\mathrm{d}(\Delta\lambda_2)} \end{bmatrix} \tag{6.40}$$

The vector of updated principle stresses for the current iterative step is given by

$$\boldsymbol{\sigma}^{i+1} = \boldsymbol{\sigma}^{tr} - (\Delta\lambda_1)^{k+1}\mathbf{D}^{el}\boldsymbol{n}_g^1 - (\Delta\lambda_2)^{k+1}\mathbf{D}^{el}\boldsymbol{n}_g^2 \tag{6.41}$$

Vectors providing the direction of the plastic corrector are defined as

$$\boldsymbol{\sigma}_1^{pl} = \mathbf{D}^{el}\boldsymbol{n}_g^1 = \left\{\sigma_{1,1}^{pl}, \sigma_{1,2}^{pl}, \sigma_{1,3}^{pl}\right\}^{\top} \tag{6.42}$$

$$\boldsymbol{\sigma}_2^{pl} = \mathbf{D}^{el}\boldsymbol{n}_g^2 = \left\{\sigma_{2,1}^{pl}, \sigma_{2,2}^{pl}, \sigma_{2,3}^{pl}\right\}^{\top} \tag{6.43}$$

and individual components of the stress vector for $j = 1, 2, 3$

$$\sigma_j(\Delta\lambda_1, \Delta\lambda_2) = \sigma_j^{tr} - \Delta\lambda_1\sigma_{1,j}^{pl} - \Delta\lambda_2\sigma_{2,j}^{pl} \tag{6.44}$$

Writing, e.g., the yield function f_1^{HB} in terms of two plastic multipliers yields

$$f_1^{HB}(\Delta\lambda_1^k, \Delta\lambda_2^k) = (\sigma_1^{tr} - \sigma_3^{tr}) - \Delta\lambda_1(\sigma_{1,1}^{pl} - \sigma_{1,3}^{pl}) - \Delta\lambda_2^k(\sigma_{2,1}^{pl} - \sigma_{2,3}^{pl}) - $$
$$- \sigma_{ci}\left[s - \frac{m_b}{\sigma_{ci}}\left(\sigma_1^{tr} - \Delta\lambda_1^k\sigma_{1,1}^{pl} - \Delta\lambda_2^k\sigma_{2,1}^{pl}\right)\right]^a \tag{6.45}$$

The corresponding partial derivatives become

$$\mathbf{H}_{11} = \sigma_{1,3}^{pl} - \sigma_{1,1}^{pl} - am_b\sigma_{1,1}^{pl}\left[s - \frac{m_b}{\sigma_{ci}}\left(\sigma_1^{tr} - \Delta\lambda_1^k\sigma_{1,1}^{pl} - \Delta\lambda_2^k\sigma_{2,1}^{pl}\right)\right]^{a-1} \tag{6.46}$$

$$\mathbf{H}_{12} = \sigma_{2,3}^{pl} - \sigma_{2,1}^{pl} - am_b\sigma_{2,1}^{pl}\left[s - \frac{m_b}{\sigma_{ci}}\left(\sigma_1^{tr} - \Delta\lambda_1^k\sigma_{1,1}^{pl} - \Delta\lambda_2^k\sigma_{2,1}^{pl}\right)\right]^{a-1} \tag{6.47}$$

The second yield function f_2^{HB} and components $\mathbf{H}_{2,1}, \mathbf{H}_{2,2}$ of the Jacobian matrix $\mathbf{H}$ are derived similarly. The same approach is applied when addressing the state of triaxial extension with sectors f_1^{HB} and f_3^{HB} being simultaneously active.

Attention should be also paid to the triaxial corner of the tensile yield surface. In this case, the proposed approach is adopted for the intersection of the yield functions f_1^R and f_2^R. Similarly to a single surface plasticity return only one iteration is needed to perform this step. Again, both non-associated and associated plasticity is considered in return mapping scheme depending on whether the stress is expected to be brought back to HB model or directly to the Rankine yield surface, recall the last paragraph in the previous section. A graphical representation is provided in Fig. 6.5. For a general framework comprising all potential stress return options we refer the reader to [83].

Apex return

When returning to apex, three sectors of the yield surface are simultaneously active. In the framework of the proposed tension cut-off, these three functions correspond to the linear Rankine criterion. Hence the solution does not require an iterative procedure. Equations (6.16) - (6.18) must be satisfied at the end of the stress update procedure and the associated flow rule applies. Return to apex is carried out only providing all other tested cases of return mapping fail.

6.4 Algorithmic tangent stiffness matrix

A robust implementation of the HB model into finite element method requires formulation of the tangent operator consistent with the stress update procedure. In analogy with Section 4.3 an algorithmic tangent operator can be defined as

$$\boldsymbol{\mathcal{D}} = \frac{\mathrm{d}\boldsymbol{\sigma}^{i+1}}{\mathrm{d}\boldsymbol{\varepsilon}^{i+1}} \tag{6.48}$$

where $\boldsymbol{\sigma}$ represents implicit functions of the updated principle stress. Before proceeding it becomes useful to introduce the elastic stiffness matrix with reference to Eq. (5.69) in the form

$$\mathbf{D} = \begin{bmatrix} d_1 & d_2 & d_2 \\ d_2 & d_1 & d_2 \\ d_2 & d_2 & d_1 \end{bmatrix} \tag{6.49}$$
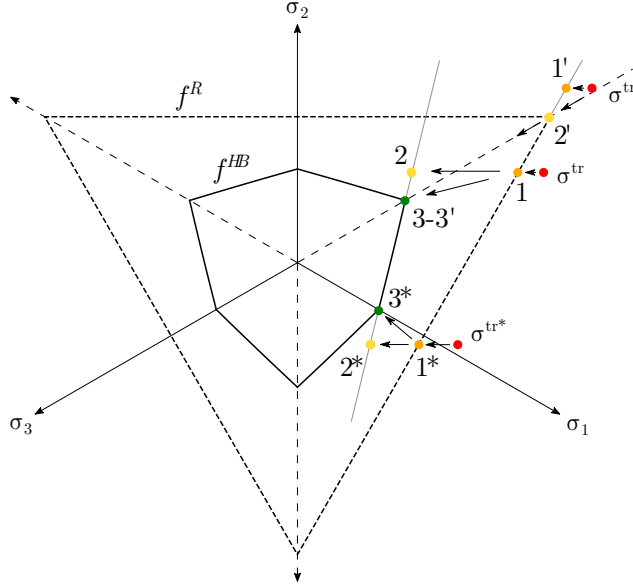
Figure 6.5: Demonstration of the return to the triaxial corners of the HB yield surface from trial stress violating tensile yield condition ($\psi_0 = 0$ is assumed): $\boldsymbol{\sigma}^{tr}$ violates f_1^R condition (TC corner), $\boldsymbol{\sigma}^{tr'}$ violates both f_1^R, f_2^R conditions (TC corner), $\boldsymbol{\sigma}^{tr*}$ violates f_1^R condition (TE corner)

and the direction of plastic yielding with reference to Eq. (6.23) as

$$\boldsymbol{n}_g^1 = \{\Psi, 0, -1\}^{\mathsf{T}} \tag{6.50}$$

This allows us to write the trial principal stresses $\boldsymbol{\sigma}^{tr} = \boldsymbol{\sigma}^i + \mathbf{D}\Delta\boldsymbol{\varepsilon}$ as

$$\sigma_1^{tr} = \sigma_1^i + d_1\Delta\varepsilon_1 + d_2(\Delta\varepsilon_2 + \Delta\varepsilon_3) \tag{6.51}$$
$$\sigma_2^{tr} = \sigma_2^i + d_1\Delta\varepsilon_2 + d_2(\Delta\varepsilon_1 + \Delta\varepsilon_3) \tag{6.52}$$
$$\sigma_3^{tr} = \sigma_3^i + d_1\Delta\varepsilon_3 + d_2(\Delta\varepsilon_1 + \Delta\varepsilon_2) \tag{6.53}$$

and when substituted into Eq. (6.24) to provide the implicit stress functions for a single surface plasticity in the form

$$\sigma_1^{i+1} = \sigma_1^{tr} - \Delta\lambda(d_1\Psi - d_2) = \sigma_1^i + d_1\Delta\varepsilon_1 + d_2(\Delta\varepsilon_2 + \Delta\varepsilon_3) - \Delta\lambda(d_1\Psi - d_2) \tag{6.54}$$
$$\sigma_3^{i+1} = \sigma_3^{tr} - \Delta\lambda(d_2\Psi - d_1) = \sigma_3^i + d_1\Delta\varepsilon_3 + d_2(\Delta\varepsilon_1 + \Delta\varepsilon_2) - \Delta\lambda(d_2\Psi - d_1) \tag{6.55}$$

The yield function f_1^{HB} associated with the main sector of the HB surface then becomes

$$(f_1^{HB})^{i+1} = \sigma_1^i - \sigma_3^i + (\Delta\varepsilon_1 - \Delta\varepsilon_3)(d_1 - d_2) - \Delta\lambda(d_1 - d_2)(\Psi + 1) - \sigma_{ci}\tilde{f}_1(\Delta\boldsymbol{\varepsilon}, \Delta\lambda) \tag{6.56}$$

where

$$\tilde{f}_1(\Delta\boldsymbol{\varepsilon}, \Delta\lambda) = \left\{ s - \frac{m_b}{\sigma_{ci}} \left[\sigma_1^i + d_1\Delta\varepsilon_1 + d_2(\Delta\varepsilon_2 + \Delta\varepsilon_3) - \Delta\lambda(d_1\Psi - d_2) \right] \right\}^a \tag{6.57}$$

Because the direction of plastic corrector is independent of the strain increment $\Delta\boldsymbol{\varepsilon}$ and since $\boldsymbol{\varepsilon}^{i+1} = \boldsymbol{\varepsilon}^i + \Delta\boldsymbol{\varepsilon}$, we may expand Eq. (6.48) as (index $i + 1$ was dropped for the sake of simplicity)

$$\boldsymbol{\mathcal{D}} = \mathbf{D} - \frac{\partial\Delta\lambda}{\partial\boldsymbol{\varepsilon}}\mathbf{D}\boldsymbol{n}_g^1 \tag{6.58}$$

where the derivative of plastic strain increment follows from consistency condition written as

$$\frac{\mathrm{d}f_1^{HB}}{\mathrm{d}\boldsymbol{\varepsilon}} = \frac{\partial f_1^{HB}}{\partial\boldsymbol{\varepsilon}} + \frac{\partial f_1^{HB}}{\partial\Delta\lambda}\frac{\partial\Delta\lambda}{\partial\boldsymbol{\varepsilon}} = 0 \tag{6.59}$$

to get

$$\frac{\partial \Delta \lambda}{\partial \varepsilon} = -\left(\frac{\partial f_1^{HB}}{\partial \varepsilon}\right)\left(\frac{\partial f_1^{HB}}{\partial \Delta \lambda}\right)^{-1} \tag{6.60}$$

$$= -\left\{ \begin{array}{c} (d_1 - d_2) + am_b d_1 (\tilde{f}_1)^{a-1} \\ am_b d_2 (\tilde{f}_1)^{a-1} \\ (d_2 - d_1) + am_b d_2 (\tilde{f}_1)^{a-1} \end{array} \right\} \left[(d_2 - d_1)(\Psi + 1) - m_b a(d_1 \Psi - d_2)(\tilde{f}_1)^{a-1} \right] \tag{6.61}$$

Equation (6.61) can be now substituted back to Eq. (6.58) to finally get the searched algorithmic tangent stiffness matrix $\mathcal{D}$.

It can also be shown that

$$\frac{\partial \Delta \lambda}{\partial \varepsilon} = \frac{n_1^\mathsf{T} \mathbf{D}}{n_1^\mathsf{T} \mathbf{D} n_g^1} \tag{6.62}$$

where the normal n_1 to the yield surface f_1^{HB} is provided by, see Eq. (6.5),

$$n_1 = \frac{\partial f_1^{HB}(\sigma_1, \sigma_3)}{\partial \sigma} \tag{6.63}$$

which renders the matrix $\mathcal{D}$ as

$$\mathcal{D} = \mathbf{D} - \frac{\mathbf{D} n_g^1 n_1^\mathsf{T} \mathbf{D}}{n_1^\mathsf{T} \mathbf{D} n_g^1} \tag{6.64}$$

It is worth mentioning that Eq. (6.64) is consistent with the formulation of standard elasto-plastic tangent stiffness matrix $\mathbf{D}^{ep}$, see, e.g., [10] Eq. (1.66). This suggests that the derivation of algorithmic tangent stiffness matrix for the case of a multi-surface plasticity return may proceed along the same lines as presented in Section 5.3 including the transformation from a principal stress space to a general cartesian stress space as outlined in Section 5.3.1.

6.5 Analogy with Mohr-Coulomb model

The similarity of HB and MC models has already been mentioned. Application of the MC model is common when addressing for example the slope stability analysis, which typically provides the factor of safety defined in terms of effective shear strength parameters, cohesion c and angle of internal friction φ. To identify equivalency between the two models in practical engineering thus appears useful. This issue was examined by Hoek et al. in [31, 32] in order to derive the equivalent shear strength parameters controlling the MC failure criterion defined in the form

$$\sigma_3 = -\sigma_{cm} + k\sigma_1, \tag{6.65}$$

where σ_{cm} is the uniaxial compressive strength of the rock mass and k is the slope of the MC line plotted in the σ_3 and σ_1 stress space, see Fig. 6.6.

The values of effective shear strength parameters c, φ are then given by

$$c = \frac{\sigma_{cm}}{2\sqrt{k}}, \quad \sin \varphi = \frac{k-1}{k+1} \tag{6.66}$$

Comparing Eq. (6.65) and the HB criterion written as

$$\sigma_3 = \sigma_1 - \sigma_{ci}\left(s - m_b \frac{\sigma_1}{\sigma_{ci}}\right)^a \tag{6.67}$$

it is seen that no mathematical relationship between the two models can be determined. To that end, an iterative approach balancing the area above and below the MC model, see Fig. 6.6, was developed in [32] to get

$$c = \frac{\sigma_{ci}[(1+2a)s + (1-a)\,m_b\sigma_{1n}](s + m_b\sigma_{1n})^{a-1}}{A\sqrt{1 + (6am_b(s + m_b\sigma_{1n})^{a-1})/A}} \tag{6.68}$$

$$A = (1+a)(2+a)$$

$$\sin \varphi = \left[\frac{6am_b(s + m_b\sigma_{1n})^{a-1}}{2(1+a)(2+a) + 6am_b(s + m_b\sigma_{1n})^{a-1}}\right] \tag{6.69}$$
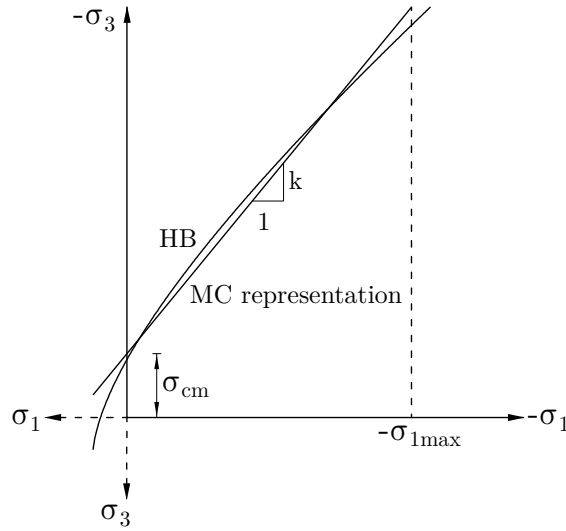
Figure 6.6: Comparison of nonlinear Hoek-Brown criterion and equivalent Mohr-Coulomb model in $\sigma_1 - \sigma_3$ plane

for the range of confining stress of $\overline{\sigma}_t > \sigma_1 > \sigma_{1,max}$, where $\sigma_{1n} = |\sigma_{1,max}|/\sigma_{ci}$ depends on the upper limit $\sigma_{1,max}$ seen in Fig. 6.6.

Application of the MC model in slope stability analysis requires setting the value of $\sigma_{1,max}$ to estimate the shear strength parameters. By performing a large parametric study on a variety of slope geometries and rock mass properties using Bishop's limit state analysis, Hoek et al. [32] proposed the following relationship for $\sigma_{1,max}$

$$|\sigma_{1max}| = 0.72\sigma_{cm} \left(\frac{\sigma_{cm}}{\gamma H} \right)^{-0.91} \tag{6.70}$$

where H is the height of the slope, γ is the unit weight of the rock mass and σ_{cm} is the rock mass strength defined by Eq. (6.66)

$$\sigma_{cm} = \frac{2c \cos \varphi}{1 - \sin \varphi} \tag{6.71}$$

The rock mass strength expressed using parameters of the Hoek-Brown model is then given by substituting Eqs. (6.68) and (6.69) into Eq. (6.71). It holds

$$\sigma_{cm} = \sigma_{ci} \frac{(m_b + 4s - a(m_b - 8s))(m_b/4 + s)^{a-1}}{2(1 + a)(2 + a)} \tag{6.72}$$

Reliability of the proposed approach strongly depends on a suitable choice of range of confining pressure, see [64] and also Section 6.7.2 for further details. As the determined pair of equivalent shear strength parameters is independent of the current stress state, the accuracy of equivalency differs at each integration point. Therefore, the method addressed in the next section proves more appropriate.

6.6   Application of Hoek-Brown model in slope stability analysis

The factor of safety is defined as the ratio of the current shear strength parameter, e.g. cohesion, to the minimum one for which the convergence of the nonlinear problem still exists. This approach is thus not directly applicable to the HB model. However, the authors in [8] introduced an elegant way to overcome this obstacle. So the method of solving the slope stability employing directly of the HB model in GEO5 FEM proceeds in their footsteps.

The approach outlined in [8] builds upon a gradual reduction of the strength of a rock mass by modifying the yield function as

$$f(\sigma_1, \sigma_3) = \sigma_1 - \sigma_3 - \frac{\sigma_{ci}}{\eta} \left(s - m_b \frac{\sigma_1}{\sigma_{ci}} \right)^a \tag{6.73}$$

where η is the reduction factor. A different reduction factor is introduced to reduce the shear strength parameters φ, c as

$$\tan \varphi_d = \frac{\tan \varphi_c}{\gamma}, \quad c_d = \frac{c_c}{\gamma} \tag{6.74}$$

where φ and c are the actual strength parameters of the subsoil material and γ is the reduction factor common to both strength parameters. The objective now is to determine the relationship between the two reduction factors η and γ.

This is achieved by constructing a tangent to the Hoek-Brown yield function at the current state of stress sitting on the yield function and comparing this slope to the slope of the MC yield surface to get

$$\eta = \frac{1}{2} \left(\gamma \left(2 - \tilde{f}' \right) \sqrt{1 + \frac{\left(\frac{1}{\gamma^2} - 1 \right) \left(-\tilde{f}' \right)^2}{\left(2 - \tilde{f}' \right)^2}} + \tilde{f}' \right) \tag{6.75}$$

where

$$\tilde{f}' = \frac{\partial \tilde{f}(\sigma_1)}{\partial \sigma_1} = -m_b a \left(s - m_b \frac{\sigma_1}{\sigma_{ci}} \right)^{a-1} \tag{6.76}$$

Notice that η is a function of the current stress state and must be evaluated for every integration point in the the finite element mesh in every iteration step of the global NR method separately. For complete derivation of Eq. (6.75) we refer the interested reader to [8].

6.7   Testing implementation with simple laboratory tests

The basic laboratory tests mentioned already in Section 1.10 are used again to test numerical implementation of the Hoek-Brown model. Attention is also accorded to a possible replacement of the HB model with the MC model as outlined in Section 6.5. All simulations adopt the material data listed in Table 6.2. Recall that parameters E_{rm}, m_b, s, a are back calculated employing Eq. (6.3), (6.2) (6.8) and (6.9).

Table 6.2: Parameters of Hoek-Brown plasticity model taken from [31]

Symbol	Units	Magnitude
E_{rm}	[MPa]	1414.20
ν	[-]	0.3
σ_{ci}	[MPa]	20.0
m_i	[-]	8.0
GSI	[-]	30
D	[-]	0.0
ψ	[°]	0
m_b	[-]	0.656680
s	[-]	0.000419
a	[-]	0.52234

As suggested in [31] to receive a reasonable approximation of the Hoek-Brown model by the Mohr-Coulomb failure criterion a set of triaxial tests with the minor principal stress ranging in the interval of $(0, 0.25\sigma_{ci})$ should be carried out. Considering the maximum value of the minor principal stress $\sigma_{1,max} = -5$ MPa we get the parameter $\sigma_{1n} = |\sigma_{1,max}|/\sigma_{ci} = 0.25$ which, when substituted in Eqs. (6.68) and (6.69), gives the equivalent Mohr-Coulomb strength parameters c, φ as

$$c = 649 \text{ kPa}, \quad \varphi = 22.8°$$

6.7.1   Triaxial loading conditions

With reference to Section 1.10 a two dimensional axisymmetric computational model consisting of two constant strain triangular elements is constructed, see Fig. 6.8(a), to predict the sample response both in triaxial compression and extension. A schematic representation of these stress states is displayed in Fig. 6.7. Following the initial isotropic consolidation phase, Fig. 6.8(a), the corresponding kinematic boundary conditions appear in Fig. 6.8(b) and Fig. 6.8(c), respectively. The displacement control loading regime is chosen on purpose to avoid termination of the analysis when exceeding the failure criterion, recall specific discussion on this subject in Section 4.6.2 with reference to a triaxial test.
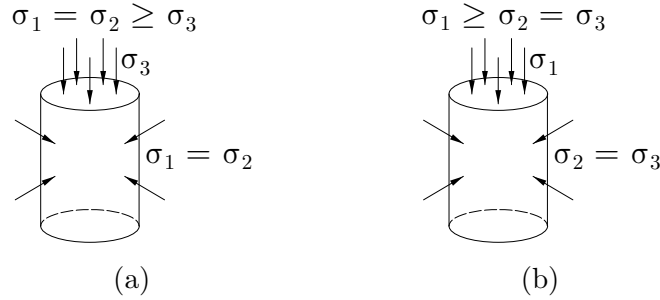
Figure 6.7: a) Triaxial compression, b) Triaxial extension
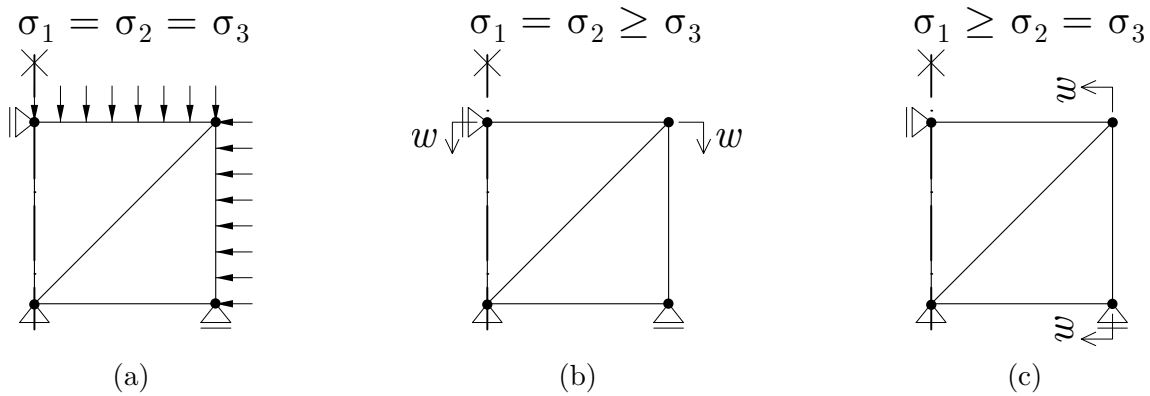
Figure 6.8: Numerical model of triaxial assuming axisymmetric stress state: a) initial isotropic compression, b) loading in triaxial compression, c) loading in triaxial extension

Figure 6.9 shows plots of the HB and MC yield surfaces (solid lines) in the meridian plane for the case of triaxial compression ($\theta = +30°$) and triaxial extension ($\theta = -30°$), respectively. The corresponding loading path is also displayed for the sake of convenience. It is seen that the numerically derived stress states at the onset of failure (stars) match the yield surfaces for all selected chamber pressures $((\sigma_m^0)_i, i = 1, \ldots, 8)$ well. One particular value of $(\sigma_m^0)_8 = -5$ MPa which yields the stress state at failure marked as 8 is shown for illustration.

Remember that the parameter σ_{n1} which identifies the range of applicability of the MC failure criterion was calculated for the largest expected value of the minimum principal stress (the chamber pressure) $\sigma_{1,max} = -5$ MPa. It is seen that the degree of sameness depends on the actual stress state and because of constant values of shear strength parameters ($c = 649$ kPa, $\varphi = 22.8°$) assumed for this particular stress range and it is not the same for all considered chamber pressures.

Two particular stress states marked as 6 and 8 are examined in more details in Fig. 6.10. The analytically derived stress states at failure corresponding to these to points are stored in Table 6.3 and replotted in Figs. 6.10(a) and 6.11(a). These figures show a gradual evolution of chamber pressure during the initial stage of isotropic consolidation followed by triaxial compression loading stage. Because of elastic-perfectly plastic character of both the HB and MC models the mean stress σ_m as well as the equivalent deviatoric stress J do not evolve further once arriving at the corresponding yield surface. Also recall the dilation angle $\psi = 0$ which suggests no evolution of volumetric strains with
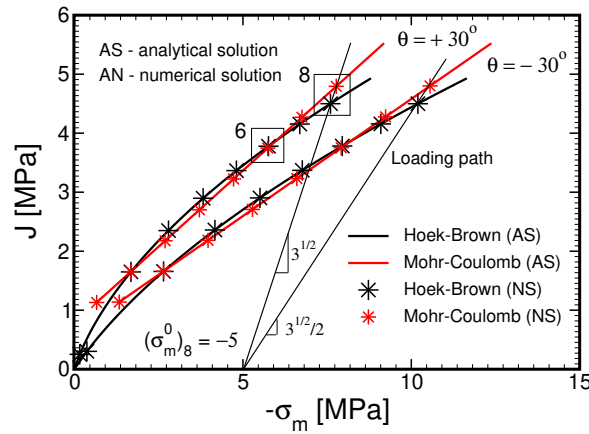
Figure 6.9: Analytical representation of Hoek-Brown and Mohr-Coulomb plasticity models and numerical predictions of failure stresses for triaxial compression ($\theta = +30°$) and extension ($\theta = -30°$)

Table 6.3: Analytically derived stress values at failure for two selected chamber pressures, points 6 and 8 in Fig. 6.9

Chamber pressure	$\sigma_m^0 = -3.57$ MPa (6)		$\sigma_m^0 = -5$ MPa (8)	
Model	σ_m^e [MPa]	J^e [MPa]	σ_m^e [MPa]	J^e [MPa]
Hoek-Brown	-5.73	3.75	-7.77	4.79
Mohr-Coulomb	-5.75	3.78	-7.60	4.45

further shearing. Thus only the $J - E_d$ stress-strain law is plotted in Figs. 6.10(b) and 6.11(b) further confirming the assumption of elastic-perfectly plastic material model. We also see the difference between the HB and MC predictions for the two selected points evident already in Fig. 6.9.

Before proceeding it is perhaps worth reminding a well known shortcoming of the *FULL* Newton-Raphson iteration scheme when combined with the elastic-perfectly plastic material and traction control loading regime in triaxial setting. Figures 6.10(b) and 6.11(b) suggest a zero stiffness at the onset of failure which yields singularity of the *FULL* Newton-Raphson method as demonstrated in Fig. 4.9(c). A potential remedy, if not using the kinematic boundary conditions, is provided via application of the Arc-length method. This solution strategy is examined in Section 11.5.2 and the interested reader is referred therein.

Testing multi-surface plasticity return

A thorough investigation of multi-surface plasticity return has been carried out in Section 5.4.2 with application to the Mohr-Coulomb failure criterion. Herein, attention is limited to triaxial compression for which the return to intersection of sectors represented by f_1^{HB} and f_2^{HB} yield surfaces has already been put forward in Fig. 5.8(a), recall also Section 6.3.2. The loading scenario appears in Fig. 6.12 suggesting again the triaxial compression loading stage being analyzed with the help of kinematic boundary conditions.

Following the initial isotropic compression calculation stage, see Fig. 6.12(a), the triaxial compression stage is examined for a single load step caused by the prescribed vertical displacement $w = 1$ cm, see Fig. 6.12(b) which amounts to major principal stress $\sigma_3 \approx -15$ MPa. A graphical representation of the return mapping procedure is displayed in Figs. 6.14 and 6.14.

The implemented algorithm, similarly to the Mohr-Coulomb model, starts from testing the main sector $\sigma_1 \geq \sigma_2 \geq \sigma_3$ (recall Fig. 5.1(b)) for violating the yield conditions, i.e., $f_1^{HB} > 0$. In such a case it attempts to bring the stress point back to the yields surface to satisfy $f_1^{HB} \leq \epsilon$. This step is visualized in Figs. 6.14(a,c,e), where Fig. 6.14(a) also shows linearization within individual steps of the Newton-Raphson iteration scheme, recall Section 6.3.1 and Eq. (6.36) in particular. Figure 6.14 displays in

(a)   (b)
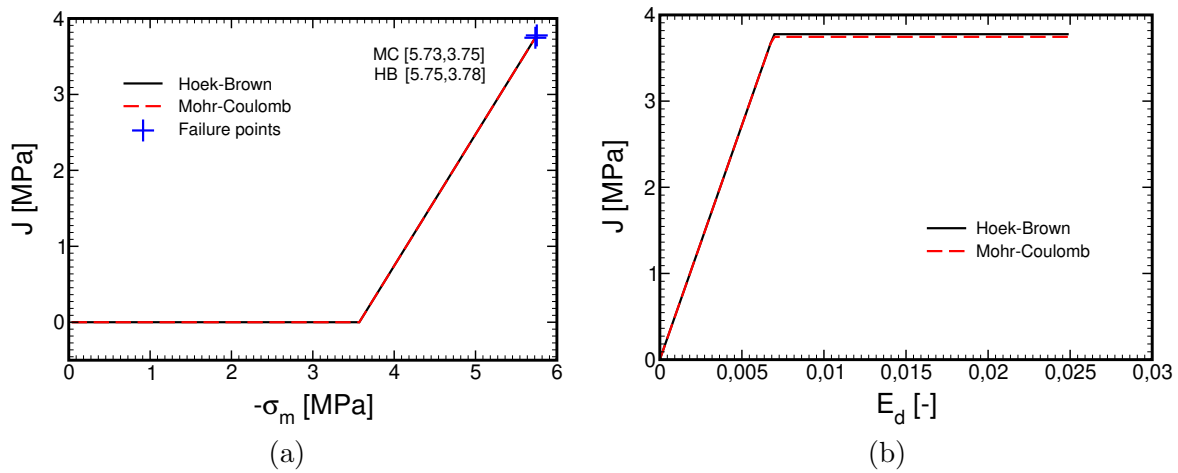
Figure 6.10: Comparing Hoek-Brown and Mohr-Coulomb prediction of failure assuming triaxial compression and chamber pressure $\sigma_m^0 = -3.57$ MPa (point 6 in Fig. 6.9): a) loading path, stress-strain response

(a)   (b)
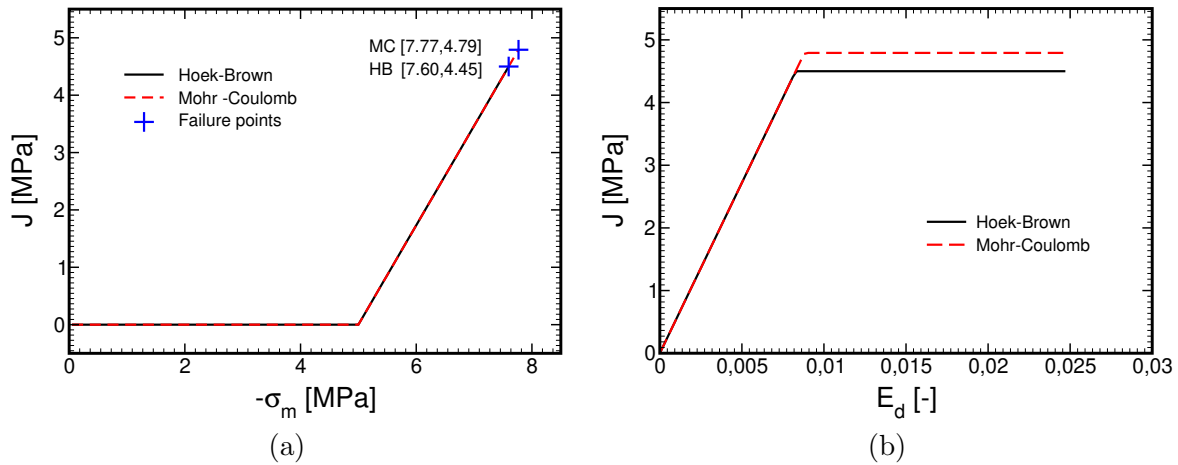
Figure 6.11: Comparing Hoek-Brown and Mohr-Coulomb prediction of failure assuming triaxial compression and chamber pressure $\sigma_m^0 = -5$ MPa (point 8 in Fig. 6.9): a) loading path, stress-strain response

(a)   (b)
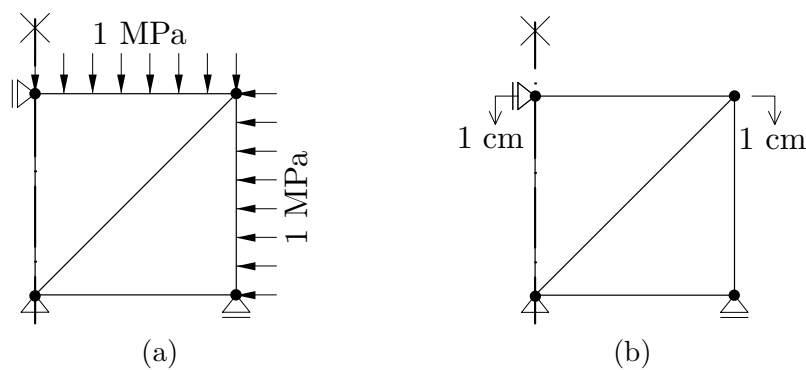
Figure 6.12: Numerical model to test stress return mapping algorithm: a) initial isotropic compression stage, b) triaxial compression stage

turn the course of return mapping in the $\sigma_2 - \sigma_3$ space. Note that the value of an intermediate stress σ_2 does not change and when completing the iteration process we observe violation of the yield condition for sector $\sigma_2 \geq \sigma_1 \geq \sigma_3$ (recall Fig. 5.1(b)), i.e., $f_2^{HB} > 0$, see also Fig. 6.13(a). Owing to the assumed value of the dilation angle $\psi = 0$ the mean stress σ_m does not change during the return process. This is apparent in Fig. 6.14(c) showing the stress return along the J-axis when plotting individual steps
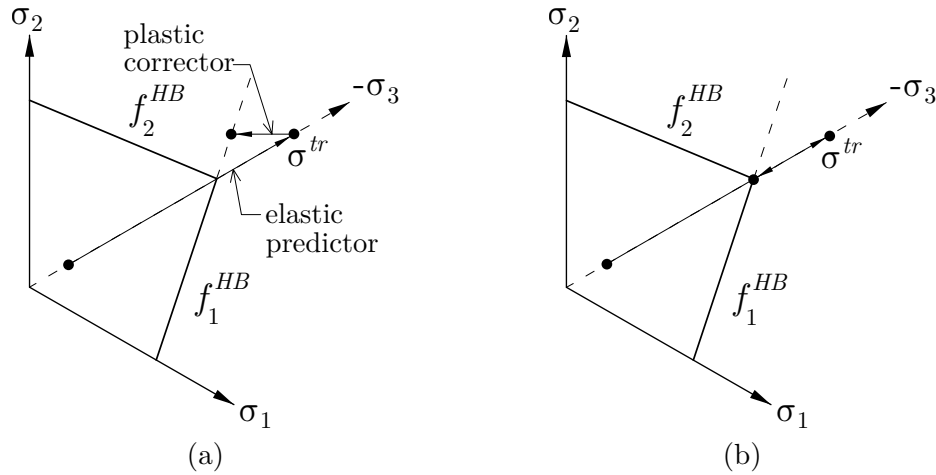
Figure 6.13: Visualization of stress return mapping algorithm in principal stress space: a) considering the main sector f_1^{HB} only, b) return to singularity edge represented by intersection of f_1^{HB} and f_2^{HB} sectors

of the return mapping algorithm in the meridian plane.

Returning into an inadmissible stress space in the first attempt invites application of a multi-surface plasticity return described in Section 6.3.2 to enforce satisfying the two yield conditions $f_1^{HB} \leq \epsilon$ and $f_2^{HB} \leq \epsilon$ simultaneously. The mathematical formulation of this process given by Eqs. (6.39) is corresponds graphically to return along the triaxial compression line as shown in Fig. 6.13(b). Individual steps of this process are plotted in Figs. 6.14(b,d,f). The linearization within the Newton-Raphson method is evident in Fig. 6.14(b). Because of solving a set of two equations the return direction obviously differs from the previous case owing to the evolution of all three principal stresses as documented in Figs.6.14(b,d). Figure 6.14(f) further confirms a successful return both yield surfaces when visualized in the meridian plane again with no change in the mean stress σ_m due to $\psi = 0$.

6.7.2 Oedometer test

The main objective is to further investigate the relevance of simulating the response of a rock mass with the Mohr-Coulomb failure criterion. Recall that the equivalent shear strength properties strongly depend on the expected stress range. While in a triaxial test the stress state is prescribed, the determination of parameter $\sigma_{n1} = |\sigma_{1,max}|/\sigma_{ci}$ is not so straightforward and it can be ordained only approximately. For simplicity, the plane strain state of stress will be considered henceforth. The corresponding numerical model in Fig. 6.15, now consisting of two 3-node plane strain triangles, is used in all simulations. Because of lateral constraints, no difficulties should be encountered with the application of *FULL* Newton-Raphson method even combined with elastic-perfectly plastic material, recall Section 4.6.1. Therefore, both traction and displacement control loading conditions in Figs. 6.15(a,b) can be adopted without any restrictions.

Assuming elasticity the stress state in oedometer is given by

$$\sigma_1 = \sigma_2 = \frac{v}{1-\nu}\sigma_3 \tag{6.77}$$

where $-\sigma_3$ is the applied vertical stress in Fig. 6.15(a). Substituting Eq. (6.77) into the yield criterion (6.5) allows us to determine the maximum vertical stress at the onset of failure. In particular,

$$\frac{\nu}{1-\nu}\sigma_3 - \sigma_3 - \sigma_{ci}\left(s - m_b\frac{\sigma_1}{\sigma_{ci}}\right)^a = 0 \tag{6.78}$$

which for the assumed parameters in Table 6.2 gives $\sigma_3 = -16.165$ MPa. If loading beyond this stress level considering, e.g., the loading scenario in Fig. 6.15(c) the stress point moves up the yield surface with continuously increasing values of lateral stresses σ_1, σ_2, thus also the mean and equivalent deviatoric stress measures σ_m and J. This supports already mentioned difficulty is estimating a "correct" value of σ_{n1}.
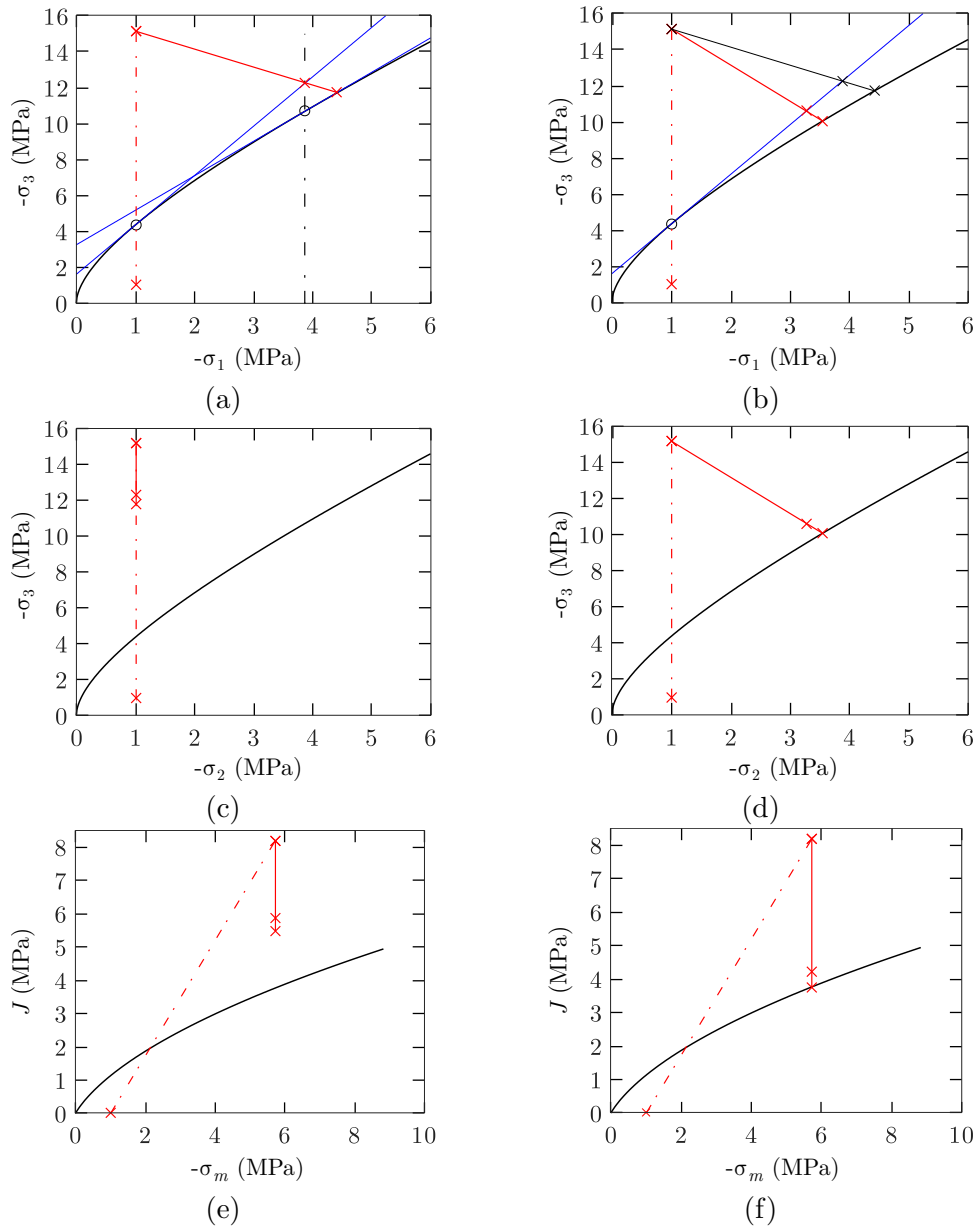
Figure 6.14: Graphical representation of stress return mapping algorithm: (a,c,e) - considering the main sector f_1^{HB} only, (b,d,f) return to singularity edge represented by intersection of f_1^{HB} and f_2^{HB} sectors
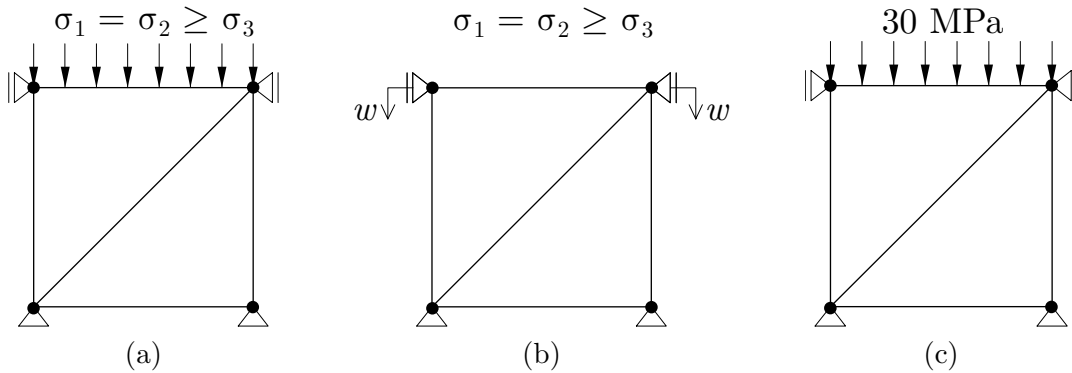
Figure 6.15: Numerical model of oedometer assuming plane strain state of stress: a) loading driven by prescribed tractions, b) loading driven by prescribed displacement, c) loading driven by prescribed tractions generating inadmissible stress state

To examine a consequence of an improperly chosen stress range in estimating the equivalent shear strength parameters c, φ of the MC model we consider two particular cases:

1. The value of σ_{n1} is set the same as in the triaxial test, i.e., $\sigma_{n1} = 0.25$.

2. The maximum value of the minimum principal stress $\sigma_{1,max}$ is derived numerically at end of simulation for the suggested maximum applied tractions, see Fig. 6.15(c), while using the HB model. For the selected $\sigma_3 = -30$ MPa we obtained $\sigma_{1,max} = \sigma_{2,max} = -15.975$ MPa which subsequently gives $\sigma_{n1} = |\sigma_{1,max}|/\sigma_{ci} = 0.79$. Point out that the corresponding maximum mean stress $\sigma_{m,max} = -20.53$ MPa.

The results appear in Fig. 6.16. Figure 6.16(a) examines the first case suggesting an improperly selected range of expected stresses. In other words, the assumed $\sigma_{1,max} = -5$ MPa is too low thus largely overestimating the onset of failure provided by the Mohr-Coulomb, see the failure point on the dashed red line. Clearly, as confirmed in Fig. 6.16(a), the MC model predicts elastic behavior over the entire range of the expected stress range, say in the interval of $\sigma_m \in (0, \sigma_{m,max} = -20.53)$ MPa. On the contrary, inspecting the results for the second case in Figs. 6.16(b,d) the intentionally selected stress range accompanied by a reasonable value of σ_{n1} might support applicability of the MC model in place of more complex, at least from the implementation point view, HB model. Although for specific classes of problems such as slope stability or ground excavation the authors in [32] recommend a way of setting a suitable value of σ_{n1}, see also Section 6.5, the decision of accepting the MC model should be approached with caution as the actual stress state, being considerably affected by plastic deformation, is generally not known.
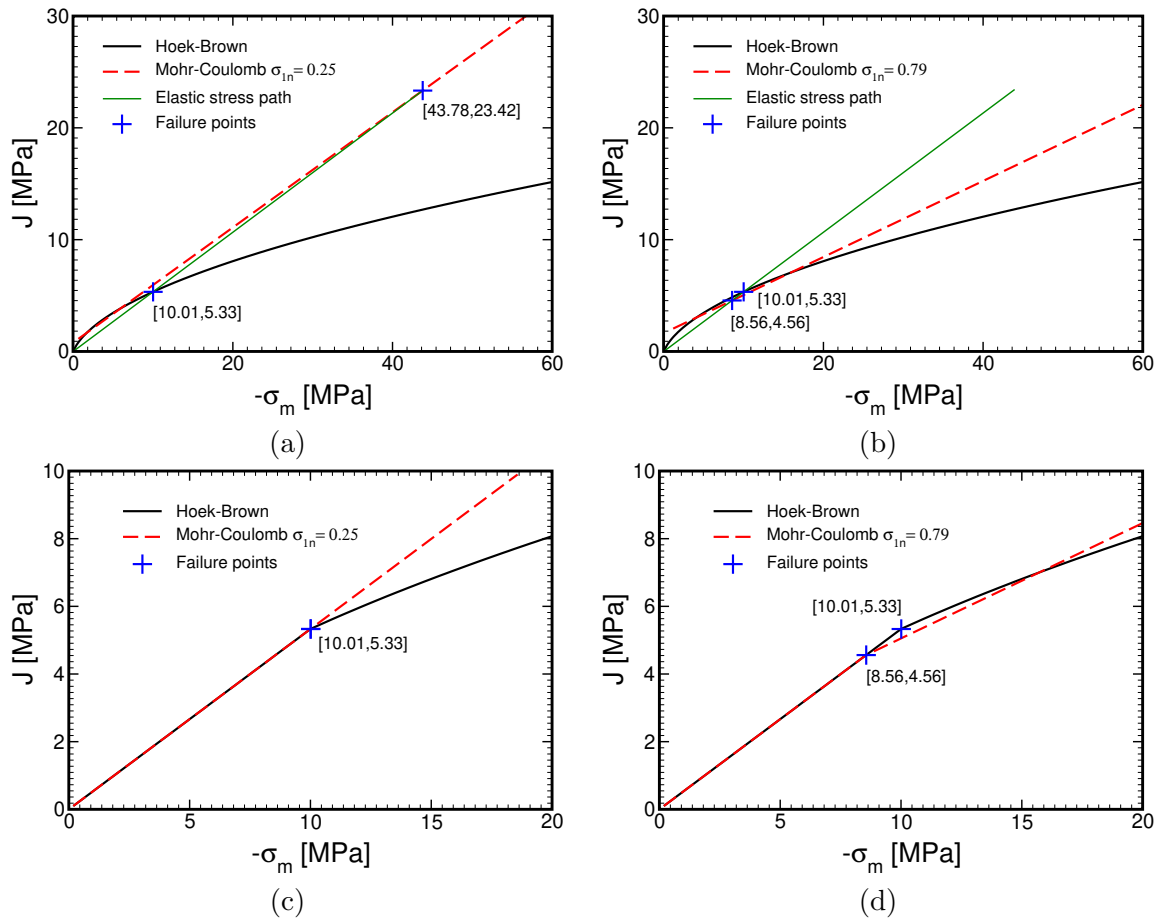
Figure 6.16: Comparing Hoek-Brown and Mohr-Coulomb prediction of failure assuming oedometric compression and variable parameter σ_{n1} to estimate shear strength parameter of Mohr-Coulomb model: (a,c) $\sigma_{n1} = 0.25$, (b,d) $\sigma_{n1} = 0.79$.

Chapter 7

Modified Hoek-Brown model

This model is under current development. The theoretical formulation grounds on the work of [85]. Unlike the standard Hoek-Brown failure criterion the Modified Hoek-Brown yield surface is presented in an invariant stress space thus taking into account the effect of an intermediate principal stress. In the deviatoric plane the model takes the form of the Matsuoka-Nakai yield surface. Tension cutoff is introduced in the framework of the I_3-generalization of the Galileo-Rankine tension criterion [49]. The model is expected to appear in the fall release of 2025.

Chapter 8

Hardening soil model

The Hardening soil model (HS) was first introduced by Schanz et al. [70] and ever since it has been implemented in a number of commercial geotechnical software including PLAXIS [63, 1] and ZSoil [52, 58]. The present formulation, implemented in GEO5 FEM, proceeds in the footsteps of Benz [9] and introduces several modifications mainly in the definition of yield surface and stress dependent stiffness. This is also why the predictions provided by the PLAXIS and GEO5 FEM programs for the same set of material parameters may not fully match. While a simple tool integrated in the ExCalibre software [25] is provided to convert the values of some of the material parameters from PLAXIS to GEO5 FEM, we strongly recommend the user to calibrate the GEO5 version of HS model based on her/his own laboratory measurements with the help of ExCalibre.

The essential difference between PLAXIS and GEO5 FEM is seen in the formulation of the yield surface. Unlike PLAXIS where the formulation is presented in the principal stress space, the formulation in GEO5 the three basic invariant stress measures J, σ_m, θ, recall Chapter 1. Thus the projection of the yield surface into a deviatoric plane moves from that of the Mohr-Coulomb type (irregular hexagon) to a smooth variant formulated here in light of the Matsuoka-Nakai yield surface as plotted in Fig. 8.1(a). Figure 8.1(b) then shows the projection of the failure criterion into a meridian plane
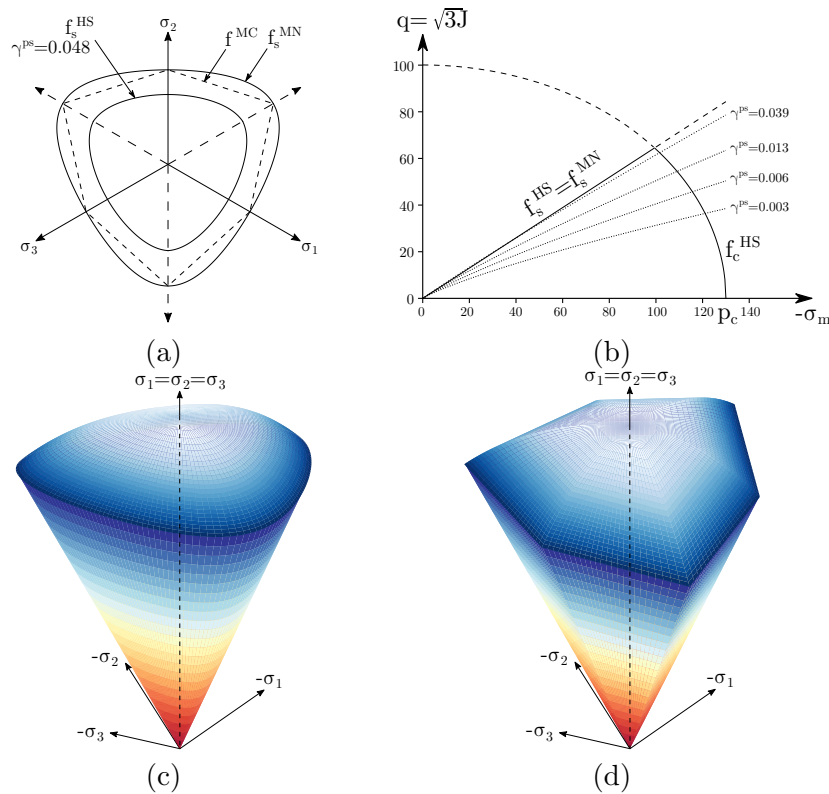
Figure 8.1: Yield surface: a) plot in deviatoric plane, b) plot in meridian plane, c) plot in principal stress space (GEO5 FEM), d) plot in principal stress space (PLAXIS)

clearly identifying two yield surfaces. The evolution of hardening shear yield surface f_s^{HS} is presented as a function of the accumulated equivalent deviatoric plastic shear strain κ. This evolution is bounded by the Matsuoka-Nakai limit yield surface f_s^{MN} defined in terms of the peak values of cohesion c and angle of internal friction φ. The cap yield surface f_c^{HS} is introduced to control the volumetric plastic mechanism in the spirit of the critical state models described in Chapters 11 and 12. Its evolution, similar to the Modified Cam-clay model in Chapter 11, is controlled by the current value of the pre-consolidation pressure p_c. Introducing the cap yield surface allows for representing a gradual evolution of stiffness in compression for normally consolidated and lightly overconsolidated soils. For further details on this subject we refer the reader to Section 11.1. Both shear and cap yield functions are smoothed and their plot in principal stress space is displayed in Fig. 8.1(c). The three-dimensional plot of failure criterion implemented in PLAXIS is showed in Fig. 8.1(d) for illustration. The list of material parameters entering the formulation of HS model is available in Table 8.1.

Table 8.1: Parameters of Hardening soil plasticity model

Symbol	Units	Description
$E_i^{p,ref}$	[MPa]	Secant modulus of elasticity
$E_{ur}^{p,ref}$	[MPa]	Modulus of elasticity in unloading/reloading
ν_{ur}	[-]	Poisson's ratio
σ_m^{ref}	[kPa]	Reference mean stress
m_p	[-]	Exponent for power law
σ_m^{L}	[kPa]	Limiting mean value of mean stress to avoid zero stiffness
R_f	[-]	Failure ratio
c	[kPa]	Effective peak cohesion
φ	[°]	Effective peak angle of internal friction
ψ	[°]	Angle of dilation
K_0^{NC}	[-]	Coefficient of lateral earth pressure for normal consolidation
E_{oed}^{ref}	[MPa]	Tangent oedometric modulus
σ_{oed}^{ref}	[kPa]	Reference vertical stress to specify E_{oed}^{ref}
e_{in}	[-]	Initial void ratio
e_{max}	[-]	Maximum void ratio to terminate dilation
OCR	[-]	Overconsolidation ratio
POP	[kPa]	Preoverburden pressure
α	[1/°C]	Coefficient of thermal expansion
K_s/K_c	[-]	Bulk stiffness ratio
M	[-]	Model parameter to define shape of cap yield function, inputted or calculated
$H^{p,ref}$	[kPa]	Hardening modulus, inputted or calculated
p_c	[kPa]	Preconsolidation pressure ($p_c^{min} = 1$kPa), calculated

8.1   Shear yield surface of GEO5 HS model

Formulation of the shear hardening yield function is founded on the assumed hyperbolic approximation of the soil response in drained triaxial compression plotted in $q-\varepsilon_3$ space[1] in Fig. 8.2, where $q = \sigma_1 - \sigma_3$ is the deviatoric stress, recall Eq. (1.56), and ε_3 is the vertical compressive strain. Note that in the formulation of the shear failure criterion the asymptotic value of the deviatoric stress q_a is replaced by a certain limit value $q_f = R_f q_a (R_f \in (0,1\rangle)$, where q_f is associated with the limit failure criterion. With reference to Mohr-Coulomb failure criterion given by Eq. (5.4) we may express q_f in terms of minor principal stress σ_1 and shear strength parameters c, φ by first setting $q_f = \sigma_1 - \sigma_3$ which upon substituting in Eq. (5.4) provides

$$q_f = \frac{2\sin\varphi}{1-\sin\varphi}\left(-\sigma_1 + c\cot\varphi\right) \tag{8.1}$$

---

[1]Remember that standard elasticity sign convention is used throughout this text so $\sigma_1 = \sigma_2 < 0$ represent the confining pressure and $\sigma_3 \le \sigma_1 (|\sigma_3| \ge |\sigma_1|)$ is the vertical compressive stress.
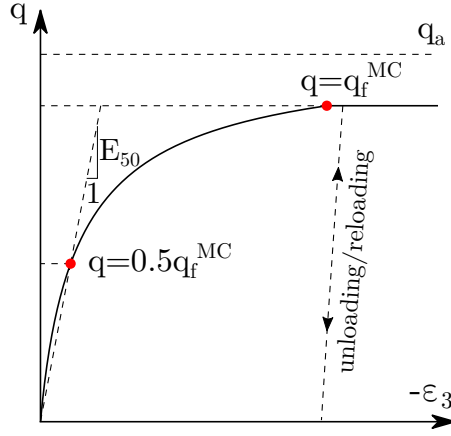
Figure 8.2: Hyperbolic stress-strain law

The secant Young modulus E_{50}, which corresponds to 50% of the value of q_a, differs from the unloading/reloading modulus $E_{ur} \approx 3E_{50}$, which in turn governs the elastic response. To see how the secant modulus E_{50} enters the formulation of HS model we start from the hyperbolic equation written as

$$q = \frac{\varepsilon_3}{b\varepsilon_3 - a} \tag{8.2}$$

Following [44] the parameters a and b are given by $a = \dfrac{1}{2E_{50}}, b = \dfrac{1}{q_a}$ which gives

$$-\varepsilon_3 = \frac{q_a}{2E_{50}} \frac{q}{q_a - q} \tag{8.3}$$

As described in [70] the elastic-plastic split of ε_3 can be written as

$$\varepsilon_3 = \varepsilon_3^{el} + \varepsilon_3^{pl} = -\frac{q}{E_{ur}} + \varepsilon_3^{pl} = \frac{q_a}{2E_{50}} \frac{q}{q_a - q} \tag{8.4}$$

To identify the plastic strain ε_3^{pl} Schanz et al. [70] proposed a yield function while introducing a plastic strain hardening parameter γ^{ps}. Considering triaxial compression this parameter is written as

$$\gamma^{ps} = 2\varepsilon_1^{pl} - \varepsilon_3^{pl} \tag{8.5}$$

Assuming incompressibility of the plastic volumetric strain in the contractancy domain $(2\varepsilon_1^{pl} + \varepsilon_3^{pl} = 0)$ gives

$$\gamma^{ps} = -2\varepsilon_3^{pl} \tag{8.6}$$

Combining Eqs. (8.4) and (8.4) renders the shear hardening yield function in the form

$$f_s^{HS}(q, \gamma^{ps}) = \frac{q_a}{E_{50}} \frac{q}{q_a - q} - \frac{2q}{E_{ur}} - \gamma^{ps} = 0 \tag{8.7}$$

Note that for triaxial compression the equivalent strain measures γ_s^{pl}, recall Eq. (1.31), receives the form

$$\gamma_s^{ps} = \varepsilon_1^{pl} - \varepsilon_3^{pl} = -\frac{3}{2}\varepsilon_3^{pl} \tag{8.8}$$

where the aforementioned incompressibility condition was taken into account. Comparison with Eq. (8.6) readily provides

$$\gamma_s^{ps} = \frac{3}{4}\gamma^{ps} \tag{8.9}$$

With reference to Eq. (8.1) we may write the current deviatoric stress q in terms of the mobilized angle of internal friction φ_m associated with a given yield loci in Fig. 8.1(b) as

$$q = \frac{2\sin\varphi_m}{1 - \sin\varphi_m}(-\sigma_1 + c\cot\varphi) \tag{8.10}$$

Because $q_f = Rq_a$ we get

$$\frac{q}{q_a} = \frac{R_f q}{q_f} = R_f \left(\frac{1 - \sin \varphi}{\sin \varphi} \right) \left(\frac{\sin \varphi_m}{1 - \sin \varphi_m} \right) = \frac{b}{a} \tag{8.11}$$

Introducing Eq. (8.11) into (8.7) together with Eq. (8.9) yields

$$f_s^{HS} = \frac{3}{2} \frac{q}{2E_{50}} \frac{a}{a - b} - \frac{3}{2} \frac{q}{E_{ur}} - \gamma_s^{ps} \tag{8.12}$$

To avoid singularity at $a \to b$ it was proposed in [19] to rewrite this equation as

$$f_s^{HS} = \frac{3}{2} \frac{q}{2E_{50}} - \frac{a - b}{a} \left(\frac{3}{2} \frac{q}{E_{ur}} + \gamma_s^{ps} \right) \tag{8.13}$$

Figure 8.3 compares evolution of function f_s^{HS} provided by Eqs. (8.12) and (8.13) assuming the following set of parameters: $c = 0, \varphi = 30°, E_{50}^{p,ref} = 30$ [MPa], $E_{ur}^{p,ref} = 90$ [MPa], $\sigma_m^{ref} = -100$ [kPa], $R_f = 0.9, m_p = 0.55, \gamma_s^{ps} = 0.0005$ [-]. It should be mentioned that stiffness $2E_{50} = E_i$ and E_{ur} evolve in accordance with Eqs. (8.16) and (8.17).
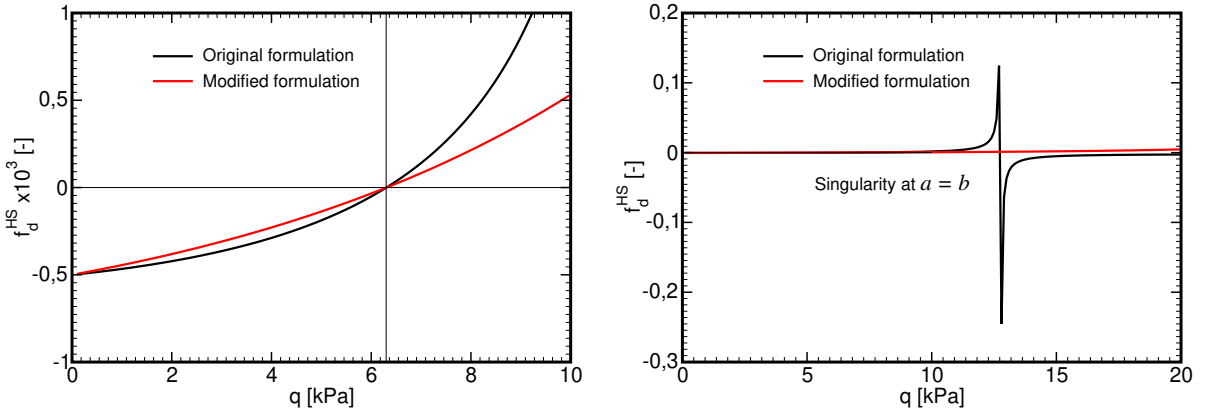
Figure 8.3: Evolution of yield function f_s^{HS} in triaxial compression for fixed σ_m: a) identifying common point of interaction at $f_s^{HS} = 0$, b) identifying singularity

Note that function the above function is not defined along the hydrostatic axis for which $q = 0, \sin \varphi_m = 0$. To this end we introduce an additional modification which gives the shear hardening yield surface as

$$f_s^{HS} = \frac{3}{2} \frac{q}{2E_{50}} - (1 - b\tilde{a}) \left(\frac{3}{2} \frac{q}{E_{ur}} + \gamma_s^{ps} \right) \tag{8.14}$$

$$b = R_f \frac{1 - \sin \varphi}{\sin \varphi}, \quad \tilde{a} = \frac{\sin \varphi_m}{1 - \sin \varphi_m}$$

To be consistent with formulations presented in other chapters we finally rewrite this function as, recall Eqs. (1.25) and (1.31),

$$f_s^{HS} = J - (1 - b\tilde{a}) \left(\frac{E_i^{p,ref}}{E_{ur}^{p,ref}} J + \frac{E_i}{3} \kappa_s \right) \tag{8.15}$$

where the transition from $2E_{50}$ to E_i was proposed in [9]. The reference moduli $E^{p,ref}$ are introduced in the next section whereas the hardening parameter κ_s, which replaces γ_s, is defined later in Section 8.3.

8.1.1   Stiffness evolution in GEO5 HS model

In GEO5 FEM the Janbu [40] stiffness power law, originally written in terms of the minor principal stress which remains constant in plastic shearing in triaxial compression, is rephrased in terms of the

mean effective stress σ_m as

$$E_i(\sigma_m) \;=\; E_i^{\mathrm{p,ref}} \left(\frac{\widehat{\sigma}_m}{\widehat{\sigma}_m^{\mathrm{ref}}} \right)^{m_p} \tag{8.16}$$

$$E_{ur}(\sigma_m) \;=\; E_{ur}^{\mathrm{p,ref}} \left(\frac{\widehat{\sigma}_m}{\widehat{\sigma}_m^{\mathrm{ref}}} \right)^{m_p} \tag{8.17}$$

$$\widehat{\sigma}_m \;=\; \sigma_m^* - c \cot \varphi \tag{8.18}$$

$$\widehat{\sigma}_m^{\mathrm{ref}} \;=\; \sigma_m^{\mathrm{ref}} - c \cot \varphi \tag{8.19}$$

$$\sigma_m^* \;=\; \max\left(\sigma_m, \sigma_m^{\mathrm{L}} \right) \ \text{ for } c = 0, \ \ \sigma_m^{\mathrm{L}} < 0$$

$$\sigma_m^{\mathrm{L}} \;-\; \text{Limiting mean stress to avoid zero stiffness}$$

$$\text{By default } \sigma_m^{\mathrm{L}} = -10 \text{ kPa in GEO5 FEM}$$

Such a formulation avoids spurious oscillations of stiffness moduli as mentioned in [58]. On the contrary, the stiffnesses E_i and E_{ur} are not directly identifiable from triaxial compression test as the mean effective stress σ_m varies. It is worth mentioning that in PLAXIS the stiffness evolution is controlled by the minor principal stress which precludes a direct translation of model parameters between PLAXIS and GEO5 FEM. To this end, as has already been mentioned, the user may either exploit the calibration software ExCalibre [25] or adopt a simple conversion tool integrated in ExCalibre to adjust the model parameters $m_p, E^{\mathrm{p,ref}} : m \to m_p, E^{\mathrm{ref}} \to E^{\mathrm{p,ref}}$. Note that the ExCalibre software provides the model parameters such as to match the experimental curves computationally. In triaxial compression this match is strongly controlled by the reference stiffness $E_i^{\mathrm{p,ref}}$. A reasonable point of departure is provided by

$$E_i^{\mathrm{p,ref}} = \frac{2 E_{50}^{\mathrm{p,ref}}}{2 - R_f} \tag{8.20}$$

A significant deviation can be expected for smaller Poisson ratios. Point out that the minor stress (σ_1) dependence assumes the form

$$E = E^{\mathrm{ref}} \left(\frac{\sigma_1 - c \cot \varphi}{\sigma_1^{\mathrm{ref}} - c \cot \varphi} \right)^{m} \tag{8.21}$$

Limiting attention to elasticity and triaxial compression while taking into account the elasticity sign convention we get

$$\sigma_m \;=\; \frac{(1 + 2K_0)\sigma_3}{3} \qquad \sigma_1 = K_0 \sigma_3 \qquad K_0 = \frac{\nu}{1 - \nu}$$

$$\nu \;=\; 0.2 \to \sigma_m = 0.50\sigma_3, \sigma_1 = 0.25\sigma_3$$

$$\nu \;=\; 0.4 \to \sigma_m = 0.78\sigma_3, \sigma_1 = 0.67\sigma_3$$

8.1.2 Matsuoka-Nakai limit yield function and mobilized angle of internal friction

As described, for example, in [5] the Matsuoka-Nakai yield surface can be written in terms of three basic stress invariants, recall Eqs. (1.32) - (1.34), as

$$f^{MN}(I_{1\sigma}, I_{2\sigma}, I_{3\sigma}, c, \varphi) = I_{1\sigma} I_{2\sigma} - \eta(\varphi) I_{3\sigma} = 0, \quad \eta(\varphi) = \frac{9 - \sin^2 \varphi}{1 - \sin^2 \varphi} \tag{8.22}$$

or upon rearranging in the form

$$f^{MN}(I_{1\sigma}, I_{2\sigma}, I_{3\sigma}, c, \varphi) = I_{\sigma} - \sin^2 \varphi = 0 \tag{8.23}$$

where

$$I_\sigma = \frac{9 - \dfrac{I_{1\sigma}I_{2\sigma}}{I_{3\sigma}}}{1 - \dfrac{I_{1\sigma}I_{2\sigma}}{I_{3\sigma}}} = \frac{9I_{3\sigma} - I_{1\sigma}I_{2\sigma}}{I_{3\sigma} - I_{1\sigma}I_{2\sigma}} \tag{8.24}$$

$$I_{1\sigma} = 3\widehat{\sigma}_m \tag{8.25}$$

$$I_{2\sigma} = 3\widehat{\sigma}_m^2 - J_2 = 3\widehat{\sigma}_m^2 - J^2 \tag{8.26}$$

$$I_{3\sigma} = \widehat{\sigma}_m^3 - \widehat{\sigma}_m J_2 + I_{3s} = \widehat{\sigma}_m^3 - \widehat{\sigma}_m J^2 + I_{3s} \tag{8.27}$$

$$\widehat{\sigma}_m = \sigma_m - c\cot\varphi \tag{8.28}$$

and c, φ are the peak shear strength parameters. The other stress invariants, σ_n, J_2, I_{3s} in particular, are defined in Section 1.3. Point out that such a formulation of the yield surface introduces the dependence on the 3rd stress invariant θ in the deviatoric plane, recall Fig. 8.1(a). To see this we limit our attention, without loss of generality, the case of zero cohesion. Then, substituting Eqs. (8.25) - (8.27), while dropping the "bar" notation, into Eq. (8.22) gives

$$(9 - \eta)\sigma_m^3 + (\eta - 3)\sigma_m J^2 - \eta I_{3s} = 0 \tag{8.29}$$

Next, multiply the above equation by $\dfrac{3\sqrt{3}}{2}\dfrac{1}{J^3}$ to get after some manipulation

$$\left(\frac{\sigma_m}{J}\right)^3 - \left(\frac{\eta - 3}{\eta - 9}\right)\left(\frac{\sigma_m}{J}\right) - \frac{2\sqrt{3}}{3}\frac{\eta}{\eta - 9}\sin 3\theta = 0 \tag{8.30}$$

Finally, multiply this equation by $\left(\dfrac{J}{\sigma_m}\right)^3$ to obtain

$$-\frac{2\sqrt{3}}{9}\eta\sin 3\theta \left(\frac{J}{\sigma_m}\right)^3 - (\eta - 3)\left(\frac{J}{\sigma_m}\right)^2 - (\eta - 9) = 0 \tag{8.31}$$

Note that Eq. (8.31) complies with standard elasticity sign convention, i.e., $\sigma_m < 0$ in compression.

In the spirit of Drucker-Prager model we may now rewrite the Matsuoka-Nakai yield surface, while still keeping $c = 0$, as

$$f^{MN}(J, \sigma_m, \theta, \varphi) = J + \sigma_m g(\theta, \varphi) = 0 \tag{8.32}$$

$$g(\theta, \varphi) = \chi(\theta\varphi)M_\varphi^{TC}(\varphi), \quad M_\varphi^{TC} = \frac{2\sqrt{3}\sin\varphi}{3 - \sin\varphi} \tag{8.33}$$

Note that setting $\chi = 1$ recovers the Drucker-Prager fit to the Mohr-Coulomb yield surface in triaxial compression (TC), recall Eqs. (4.1) and (4.3). To solve for function $g(\theta, \varphi) = -\dfrac{J}{\sigma_m}$ from Eq. (8.30) we proceed along steps presented in [85] and set $\dfrac{1}{g(\theta, \varphi)} = a = r\sin\beta$. Equation (8.30) now becomes

$$\sin^3\beta - \frac{1}{r^2}\frac{\eta - 3}{\eta - 9}\sin\beta - \frac{1}{r^3}\frac{2\sqrt{3}}{9}\frac{\eta}{\eta - 9}\sin 3\theta = 0 \tag{8.34}$$

which resembles similarity with the following trigonometric function

$$\sin^3\beta - \frac{3}{4}\sin\beta - \frac{1}{4}\sin 3\beta = 0 \tag{8.35}$$

Comparing the above two equations suggests

$$r = \frac{2}{\sqrt{3}}\sqrt{\frac{\eta - 3}{\eta - 9}} \tag{8.36}$$

$$\sin 3\beta = -\eta\sqrt{\frac{\eta - 9}{(\eta - 3)^3}}\sin 3\theta = B\sin 3\theta \tag{8.37}$$

$$\beta = \frac{1}{3}\sin^{-1}(B\sin 3\theta) \tag{8.38}$$

The three roots of Eq. (8.30) are then provided by

$$a_1 = r\sin\beta = \frac{2}{\sqrt{3}}\sqrt{\frac{\eta-3}{\eta-9}}\sin(\frac{1}{3}\sin^{-1}(B\sin 3\theta)) \tag{8.39}$$

$$a_2 = r\sin\left(\beta+\frac{2\pi}{3}\right) = \frac{2}{\sqrt{3}}\sqrt{\frac{\eta-3}{\eta-9}}\sin\left(\frac{1}{3}\sin^{-1}(B\sin 3\theta)+\frac{2\pi}{3}\right) \tag{8.40}$$

$$a_3 = r\sin\left(\beta-\frac{2\pi}{3}\right) = \frac{2}{\sqrt{3}}\sqrt{\frac{\eta-3}{\eta-9}}\sin\left(\frac{1}{3}\sin^{-1}(B\sin 3\theta)-\frac{2\pi}{3}\right) \tag{8.41}$$

Keeping in mind the standard elasticity sign convention we notice that only the 3rd root represents the true solution as $\frac{\sigma_m}{J} = a_3 < 0$.

Since used later in the definition of cap yield surface in Section 8.2 it becomes useful to compare the previous formulation with Lode angle θ dependent representation of function $\chi(\theta,\varphi)$ in Eq. (8.33) known as LMN dependence. This function is presented in [5]. The variant that complies with the adopted elasticity sign convention reads

$$\chi(\theta,\varphi) = \frac{\sqrt{3}\beta}{2\sqrt{\beta^2-\beta+1}}\frac{1}{\cos\vartheta} \tag{8.42}$$

$$\beta = \frac{3-\sin\varphi}{3+\sin\varphi} \tag{8.43}$$

$$\alpha = \frac{1}{6}\arccos\left(-1+\frac{27\beta^2(1-\beta)^2}{2(\beta^2-\beta+1)^3}\sin^2(3\theta)\right) \tag{8.44}$$

$$\vartheta = \alpha(\theta), \qquad \text{for } \theta \le 0 \tag{8.45}$$

$$\vartheta = \frac{\pi}{3}-\alpha(\theta), \quad \text{for } \theta > 0 \tag{8.46}$$

For illustration we compare the solution of cubic equation (8.30) with function $\chi(\theta,\varphi)$. To this end we first scale function $g(\theta,\varphi = \frac{1}{a_3}$, recall Eq. (8.41), with the solution pertinent to triaxial compression identified with $\theta = 30°$. This yields

$$g_c(\varphi,\theta) = \frac{a_3(\theta=30^0)}{a_3} = \frac{\sin\left(\frac{1}{3}\sin^{-1}(B)-\frac{2\pi}{3}\right)}{\sin\left(\frac{1}{3}\sin^{-1}(B\sin 3\theta)-\frac{2\pi}{3}\right)} \tag{8.47}$$

As evident from Fig. 8.4(a) the two functions perfectly match. The Matsuoka-Nakai and the Mohr-Coulomb projections into the deviatoric plane are finally compared for the sake of completeness.
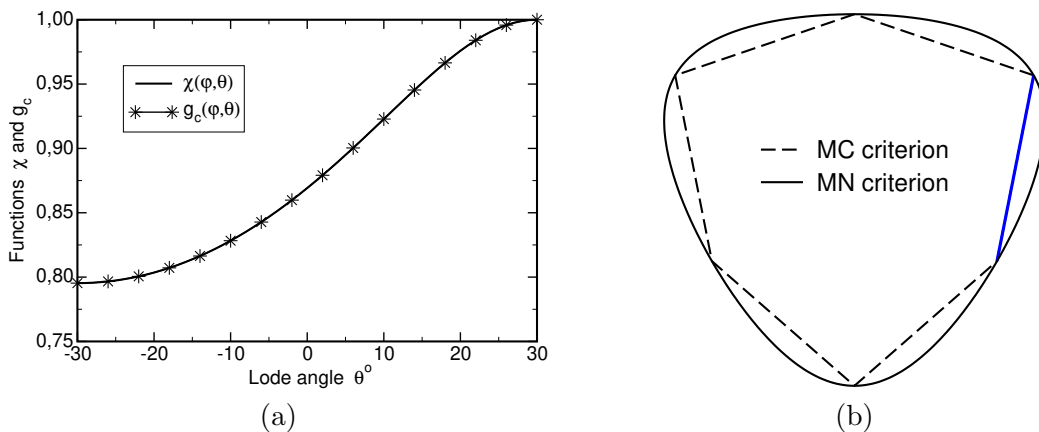
Figure 8.4: a) Comparing functions $\chi(\varphi,\theta)$ and $g_c(\varphi,\theta)$ b) Mohr-Coulomb (MC) and Matsuoka-Nakai (MN) yield surfaces in deviatoric plane

It remains to determine the mobilized friction angle φ_m. This can be easily accomplished by replacing the peak friction angle in Eq. (8.23) by the mobilized friction angle φ_m to obtain

$$\sin\varphi_m = \sqrt{I_\sigma} \tag{8.48}$$

8.1.3   Rowe's dilatancy theory

To introduce the subject we first present the flow in the form presented already for the Mohr-Coulomb yield criterion in Section 5.1. To this end, consider the case of triaxial compression and recall the plastic potential functions given by Eqs. (5.14) and (5.15)

$$g_1(\sigma_1, \sigma_3, \psi) = \frac{1}{2}(\sigma_1 - \sigma_3) + \frac{1}{2}(\sigma_1 + \sigma_3)\sin\psi_m \tag{8.49}$$

$$g_2(\sigma_2, \sigma_3, \psi) = \frac{1}{2}(\sigma_2 - \sigma_3) + \frac{1}{2}(\sigma_2 + \sigma_3)\sin\psi_m \tag{8.50}$$

where ψ_m is the mobilized dilation angle. The plastic strain increments follow from the flow rule, Eq. (5.36) ($\Delta\boldsymbol{\varepsilon}^{pl} = \Delta\boldsymbol{\varepsilon}^{p1} + \Delta\boldsymbol{\varepsilon}^{p1}$), as

$$\boldsymbol{n}_g^1 = \frac{\partial g_1}{\partial\boldsymbol{\sigma}} = \left\{\frac{1}{2}(1 - \sin\psi_m), 0, \frac{1}{2}(-1 - \sin\psi_m)\right\}^\mathsf{T} \tag{8.51}$$

$$\boldsymbol{n}_g^2 = \frac{\partial g_2}{\partial\boldsymbol{\sigma}} = \left\{\frac{1}{2}(1 - \sin\psi_m), \frac{1}{2}(-1 - \sin\psi_m), 0\right\}^\mathsf{T} \tag{8.52}$$

$$\Delta\varepsilon_v^{pl} = \Delta\varepsilon_1^{pl} + \Delta\varepsilon_2^{pl} + \Delta\varepsilon_3^{pl} = -2\Delta\lambda\sin\psi_m \tag{8.53}$$

$$\Delta\gamma_s^{pl} = \Delta\varepsilon_1^{pl} - \Delta\varepsilon_3^{pl} = \Delta\lambda \tag{8.54}$$

where $\boldsymbol{n}_g^i$ represents the normal to a given plastic potential surface and $\Delta\varepsilon_v^{pl}$ and $\Delta\gamma_s$ are the increments of plastic volumetric strain and plastic equivalent shear strain, respectively, written in terms of plastic multiplier $\Delta\lambda$. Hence

$$\Delta\varepsilon_v^{pl} = -2\Delta\gamma_s^{pl}\sin\psi_m \tag{8.55}$$

Evolution of the mobilized dilation angle ψ_m is described by the Rowe [69] dilatancy theory

$$\sin\psi_m = 0, \qquad\qquad\qquad \text{for}\ \ \varphi_m < \varphi_{cs} \tag{8.56}$$

$$\sin\psi_m = \frac{\sin\varphi_m - \sin\varphi_{cs}}{1 - \sin\varphi_m\sin\varphi_{cs}}, \qquad \text{for}\ \ \varphi_m > \varphi_{cs} \tag{8.57}$$

$$\sin\psi_m = 0, \qquad\qquad\qquad \text{for}\ \ e \geq e_{max} \tag{8.58}$$

where φ_{cs} is the angle of internal friction at critical state provided by

$$\sin\varphi_{cs} = \frac{\sin\varphi - \sin\psi}{1 - \sin\varphi\sin\psi} \tag{8.59}$$

At critical state the increment of volumetric plastic strain becomes zero (plastic incompressibility, $\sin\psi_m = 0$) and $\varphi_m = \varphi_{cs}$. Within the context of Mohr-Coulomb failure criterion the mobilized friction angle φ_m, recall also Eq. (8.48), reads (remember the adopted elasticity sign convention)

$$\sin\varphi_m = \frac{\sigma_1 - \sigma_3}{-(\sigma_1 + \sigma_3) + 2c\cot\varphi} \tag{8.60}$$

It is seen from Eq. (8.56) that in contractancy domain, see Fig. 8.5(a) [58], no volumetric plastic strain is allowed to occur, which provides a partial remedy of the original formulation [9]. The ultimate dilation angle ψ follows from the maximum slope in the $\varepsilon_1 - \varepsilon_v$ curve, see Fig. 8.5(b)[2], as

$$\frac{\mathrm{d}\varepsilon_v^{pl}}{\mathrm{d}\varepsilon_1^{pl}} = -\frac{4\sin\psi}{1 - \sin\psi} \tag{8.61}$$

Additional cut-off criterion given by Eq. (8.58) is introduced to avoid an excessive dilation for large shear strains once at critical state. Therein, e and e_{max} are the current and the maximum void ratio to terminate dilatation, respectively, recall Eq. (1.78).

---

[2]Strictly speaking, Fig. 8.5(b) applies to formulations which assume constant dilation angle, such as the Drucker-Prager and Mohr-Coulomb failure criteria.
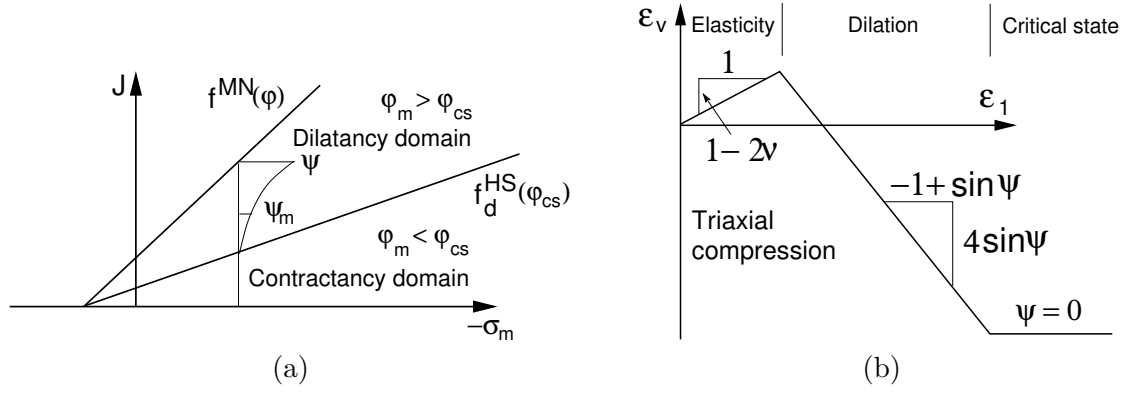
Figure 8.5: Rowe's dilatancy theory: a) graphical explanation of mobilized dilation angle ψ_m (adopted from [58]), b) strain curve for standard triaxial drained compression test with the dilatancy cut-off

8.2 Cap yield surface in GEO5 HS model

The present formulation follows closely the one developed in Benz [9] to give the cap yield function as

$$f_c^{HS} = \frac{3J^2}{\chi^2(\theta, \varphi)M^2} + \sigma_m^2 - p_c^2 \tag{8.62}$$

where the LMN function χ is introduced Section 8.1.2 via Eq. (8.42), M is the model parameter to define the shape of the yield surface, and p_c is the hardening parameter termed the preconsolidation pressure, recall Fig. 8.1(b).

In the spirit of Cam clay model described in Chapter 11 the increment of plastic volumetric strain $\Delta\varepsilon_v^{pl}$ is provided by, see the derivation of Eq. (11.14) in Section 11.1.1 where also the meaning of parameters κ^* and λ^* is explained in detail,

$$\begin{aligned}
\dot{\varepsilon}_v^{pl} &= -(\lambda^* - \kappa^*)\frac{\dot{p}_c}{p_c} = -\left(\frac{\lambda^*}{p_c} - \frac{\kappa^*}{p_c}\right)\dot{p}_c = -\left(\frac{1}{K_c} - \frac{1}{K_s}\right)\dot{p}_c = -\left(\frac{K_s - K_c}{K_c K_s}\right)\dot{p}_c \\
&= -\frac{\frac{K_s}{K_c} - 1}{K_s}\dot{p}_c = -\frac{1}{H}\dot{p}_c
\end{aligned} \tag{8.63}$$

or in incremental form

$$\Delta\varepsilon_v^{pl} = \Delta\kappa_c = -\frac{1}{H}\Delta p_c \tag{8.64}$$

where H is the hardening modulus. Point out that the bulk moduli ratio $\dfrac{K_s}{K_c}$ is

$$\frac{K_s}{K_c} = \frac{K_s^{\text{ref}}}{K_c^{\text{ref}}} = \frac{K_s^{\text{p,ref}}}{K_c^{\text{p,ref}}} \tag{8.65}$$

where the swelling bulk modulus in unloading/reloading K_s^{ref} ($K_s^{\text{p,ref}}$) is related to $E_{ur}^{\text{ref}}(E_{ur}^{\text{p,ref}}), \nu_{ur}$ through standard elasticity relation for isotropic materials as

$$K_s^{\text{ref}} = \frac{E_{ur}^{\text{ref}}}{3(1 - 2\nu_{ur})}, \quad K_s^{\text{p,ref}} = \frac{E_{ur}^{\text{p,ref}}}{3(1 - 2\nu_{ur})} \tag{8.66}$$

To provide an approximation to Eq. (8.65) we consider a primary loading in oedometer and approximate the elasto-plastic bulk modulus[3] as

$$K_c^{\text{ref}} \approx \frac{\dot{\sigma}_m}{\dot{\varepsilon}_v}|_{\sigma_m = \sigma_m^{\text{ref}}} = \frac{1}{3}(1 + 2K_0^{NC})\frac{\dot{\sigma}_3}{\dot{\varepsilon}_3}|_{\sigma_3 = \sigma_3^{\text{ref}}} = \frac{1}{3}(1 + 2K_0^{NC})E_{oed}^{\text{ref}} \tag{8.67}$$

---

[3]Note that K_c is considered for a normally consolidated soil in isotropic compression

When substituting from Eqs. (8.66) and (8.67) back into Eq. (8.65) we obtain

$$\frac{K_s}{K_c} \approx \frac{E_{ur}^{\text{ref}}}{E_{oed}^{\text{ref}}} \frac{1}{(1 + 2K_0^{NC})(1 - 2\nu_{ur})} \tag{8.68}$$

The relationship to E_{oed}^{ref} allows us to consider the bulk moduli ratio in Eq. (8.65) as internal parameters. Similarly we treat the model parameter M, which can be related to K_0^{NC}. Determination of cap model parameters M, H is described in detail in Section 8.5.3.

8.3 Stress return mapping

We begin with the summary of yield surfaces presented in the previous section accompanied by the corresponding plastic potentials to provide increments of plastic strains.

- **Shear hardening yield surface f_s^{HS}**
  The implemented shear hardening yield is provided by Eq. (8.15)

$$f_s^{HS}(\boldsymbol{\sigma}, c, \varphi, \varphi_{cs}, \kappa_s) = J - (1 - b\tilde{a}) \left(\frac{E_i^{\text{p,ref}}}{E_{ur}^{\text{p,ref}}} J + \frac{E_i}{3} \kappa_s \right) \tag{8.69}$$

The plastic potential attains the form of the Drucker-Prager model. Therefore, the dilation angle $\psi_m(\boldsymbol{\sigma}) = \tilde{\psi}_m(\boldsymbol{\sigma})$ is assumed constant when deriving the direction of the plastic strain increments, i.e., there is no derivative of M_ψ with respect to $\boldsymbol{\sigma}$. Considering triaxial compression gives

$$g_s^{HS}(\boldsymbol{\sigma}, \tilde{\psi}_m) \;=\; J + \widehat{\sigma}_m M_\psi(\tilde{\psi}_m), \quad M_\psi = \frac{2\sqrt{3}\sin\tilde{\psi}_m}{3 - \sin\tilde{\psi}_m} \tag{8.70}$$

- **Matsuoka-Nakai yield surface f_s^{HS}**
  As suggested by Eq. (8.23) the Matsuoka-Nakai yield surface is fixed in stress based assuming elastic perfectly plastic material

$$f_s^{MN} = I_\sigma(\boldsymbol{\sigma}, c, \varphi) - \sin^2\varphi \tag{8.71}$$

The plastic potential is taken the same as in the case of hardening shear yield surface, Eq. (8.70)

$$g_s^{MN} = g_s^{HS}(\boldsymbol{\sigma}, \tilde{\psi}_m) \tag{8.72}$$

- **Cap yield surface f_c^{HS}**
  The extended version of the cap yield surface, Eq. (8.62), reads

$$f_c^{HS}(\boldsymbol{\sigma}, \varphi, p_c) = \frac{3J^2}{\chi^2(\theta, \varphi)M^2} + \sigma_m^2 - p_c^2 = \frac{3}{2}\frac{\boldsymbol{s}^\mathsf{T}\mathbf{Q}^{-1}\boldsymbol{s}}{\chi^2(\theta, \varphi)M^2} + \sigma_m^2 - p_c^2 \tag{8.73}$$

Referring to Benz [9] the plastic potential is assumed in the form

$$g_c^{HS}(\boldsymbol{\sigma}, \tilde{\theta}) = \frac{3J^2}{\tilde{\chi}^2(\tilde{\theta}, \varphi)M^2} + \sigma_m^2 - p_c^2 = \frac{3}{2}\frac{\boldsymbol{s}^\mathsf{T}\mathbf{Q}^{-1}\boldsymbol{s}}{\tilde{\chi}^2(\theta^{tr}, \varphi)M^2} + \sigma_m^2 - p_c^2 \tag{8.74}$$

keeping $\tilde{\chi}(\tilde{\theta}, \varphi)$ constant in the local stress update, where $\tilde{\theta} = \theta^{tr}$ is evaluated based on the trial stresses, recall Eq. (17.82). This allows for keeping the mean stress as the only stress-based primary variable.

In general, both the hardening shear (or Matsuoka-Nakai) and cap yield surface can be simultaneously active. To this end, the concept of multi-yield surface plasticity described in Section 5.2.2

can be exploited to give the increments of plastic strains in terms of stresses evaluated at $(i+1)$ load increment as

$$\Delta \varepsilon^{pl} = \Delta e^{pl} + m \Delta \varepsilon_v^{pl} \tag{8.75}$$

$$\Delta \varepsilon_v^{pl} = \Delta \lambda_s \frac{\partial g_s^{HS}}{\partial \sigma_m} + \Delta \lambda_c \frac{\partial g_c^{HS}}{\partial \sigma_m} = \Delta \lambda_s M_\psi(\tilde{\psi}(\boldsymbol{\sigma}^{i+1})) + 2\Delta \lambda_c \sigma_m^{i+1} \tag{8.76}$$

$$\Delta e^{pl} = \Delta \lambda_s \frac{\partial g_s^{HS}}{\partial s} + \Delta \lambda_c \frac{\partial g_c^{HS}}{\partial s} = \Delta \lambda \mathbf{Q}^{-1} s^{i+1} = \Delta \lambda \mathbf{P} \boldsymbol{\sigma}^{i+1} \tag{8.77}$$

$$\Delta \lambda = \frac{\Delta \lambda_s}{2J^{i+1}} + \frac{3\Delta \lambda_c}{\tilde{\chi}^2 M^2}, \quad s = \mathbf{P}\mathbf{Q}\boldsymbol{\sigma} = \mathbf{Q}\mathbf{P}\boldsymbol{\sigma} \tag{8.78}$$

where e and s are the deviatoric strains and stresses defined in Section 1.3.

The hardening parameter κ_s in Eq. (8.69) is defined in terms of the equivalent deviatoric plastic strain $\Delta E_{d,s}^{pl}$ linked to the hardening shear yield surface as

$$\Delta \kappa_s = \Delta E_{d,s}^{pl} = \Delta \lambda_s \longrightarrow \kappa_s = \sum \Delta \lambda_s \tag{8.79}$$

where

$$\Delta E_{d,s}^{pl} = \sqrt{2(\Delta \varepsilon_s^{pl})^\mathsf{T} \mathbf{Q}\mathbf{P}\mathbf{Q}\Delta \varepsilon_s^{pl}} = \sqrt{2(\Delta e_s^{pl})^\mathsf{T} \mathbf{Q}\Delta e_s^{pl}} = \Delta \lambda_s, \quad \Delta e_s^{pl} = \Delta \lambda_s \frac{\partial g_s^{HS}}{\partial s} \tag{8.80}$$

Similarly, the hardening parameter κ_c in Eq. (8.64) is evaluated as a function of the volumetric plastic strain associated with the cap yield surface as

$$\Delta \kappa_c = \Delta \varepsilon_{v,c}^{pl} = \Delta \lambda_c \frac{\partial g_c^{HS}}{\partial \sigma_m} = 2\Delta \lambda_c \sigma_m^{i+1} = -\frac{1}{H}\Delta p_c \rightarrow \Delta p_c = -2H\Delta \lambda_c \sigma_m^{i+1} \tag{8.81}$$

Recall also Eq. (8.63) to give the hardening modulus H in the form

$$H = \frac{K_s}{\frac{K_s}{K_c} - 1} = \frac{K_{ur}^{\mathrm{p,ref}}}{\frac{K_s}{K_c} - 1} \left(\frac{\widehat{\sigma}_m}{\widehat{\sigma}_m^{\mathrm{ref}}}\right)^{m_p} = H^{\mathrm{p,ref}} \left(\frac{\widehat{\sigma}_m}{\widehat{\sigma}_m^{\mathrm{ref}}}\right)^{m_p} \tag{8.82}$$

As described already in Section 4.2 for the Drucker-Prager model the return mapping algorithm assumes the standard volumetric-deviatoric split. Point out that the plastic potential functions are formulated such that the deviatoric stress s can be explicitly written in terms of the mean stress σ_m and increments of plastic strains $\Delta \lambda_s$ and $\Delta \lambda_c$. This provides the stresses and associated equivalent stress measures at the end of the $(i+1)$ load increment in the form

- Mean stress σ_m^{i+1}

$$\sigma_m^{i+1} = \sigma_m^i + K_{ur}(\widehat{\bar{\sigma}}_m)(\Delta \varepsilon_v - \Delta \lambda_s M_\psi(\boldsymbol{\sigma}^{i+1}) - 2\Delta \lambda_c \sigma_m^{i+1}) \tag{8.83}$$

Rearrange the above equation to get

$$\sigma_m^{i+1} = \frac{\sigma_m^i + K_{ur}(\widehat{\bar{\sigma}}_m)(\Delta \varepsilon_v - \Delta \lambda_s M_\psi(\boldsymbol{\sigma}^{i+1}))}{1 + 2K_{ur}(\widehat{\bar{\sigma}}_m)\Delta \lambda_c} = \bar{\sigma}_m(\sigma_m^{i+1}, \Delta \lambda_s, \Delta \lambda_c) \tag{8.84}$$

- Deviatoric stress s^{i+1}

$$s^{i+1} = s^i + 2G_{ur}(\widehat{\bar{\sigma}}_m)\mathbf{Q}\left(\Delta e - \left(\frac{\Delta \lambda_s}{2J^{i+1}} + \frac{3\Delta \lambda_c}{\tilde{\chi}^2 M^2}\right)\mathbf{Q}^{-1}s^{i+1}\right) \tag{8.85}$$

Rearrange the above equation to get

$$s^{i+1} = \frac{s^i + 2G_{ur}(\widehat{\bar{\sigma}}_m)\mathbf{Q}\Delta e}{1 + G_{ur}(\widehat{\bar{\sigma}}_m)\left(\frac{\Delta \lambda_s}{J^{i+1}} + \frac{6\Delta \lambda_c}{\tilde{\chi}^2 M^2}\right)} \tag{8.86}$$

Similarly we derive the equivalent deviatoric stress J^{i+1} as

$$J^{i+1} = \frac{J^{tr} - G_{ur}(\widehat{\overline{\sigma}}_m)\Delta\lambda_s}{1 + \dfrac{6G_{ur}(\widehat{\overline{\sigma}}_m)\Delta\lambda_c}{\tilde{\chi}^2 M^2}} \tag{8.87}$$

$$J^{tr} = \left[J_2^i + 2G_{ur}(\widehat{\overline{\sigma}}_m)\Delta\boldsymbol{e}^{\mathsf{T}}\boldsymbol{s}^i + (G_{ur}(\widehat{\overline{\sigma}}_m))^2\Delta E_d^2 \right]^{\frac{1}{2}} \tag{8.88}$$

As indicated in Section 8.1.1 the stiffness depends on the value of effective mean stress. While the initial modulus $E_i(\sigma_m^{i+1})$ is expected to depend on the stress σ_m^{i+1} at the end of the $(i+1)$ load increment, the *nonlinear elastic behavior* in the absence of plasticity is proposed in the form

$$\boldsymbol{\sigma}^{i+1} = \boldsymbol{\sigma}^i + \mathbf{D}^{el}\left(\frac{\sigma_m^i + \sigma_m^{i+1}}{2}\right)\Delta\boldsymbol{\varepsilon} = \boldsymbol{\sigma}^i + \mathbf{D}^{el}(\widehat{\overline{\sigma}}_m)\Delta\boldsymbol{\varepsilon} \tag{8.89}$$

where the elastic stiffness matrix for isotropic material $\mathbf{D}^{el} = \mathbf{D}^{el}(E_{ur}(\widehat{\overline{\sigma}}_m), \nu_{ur})$ is a function of unloading/reloading modulus $E_{ur}(\widehat{\overline{\sigma}}_m)$, or $K_{ur}(\widehat{\overline{\sigma}}_m)$ and $G_{ur}(\widehat{\overline{\sigma}}_m)$ entering Eqs. (8.84) - (8.88), and corresponding Poisson ration ν_{ur}. The selected definition of $\widehat{\overline{\sigma}}_m$ is in accord with PLAXIS and promotes evolution of stresses independent of the magnitude of load increment. Unlike PLAXIS, however, this stress dependency is also employed for *plastic loading*. Some particular observations are presented in Section 8.6. Therein, the implemented formulation will also be compared to a secant formulation (backward Euler) written as

$$\boldsymbol{\sigma}^{i+1} = \mathbf{D}^{el}(\sigma_m^{i+1})(\boldsymbol{\varepsilon}^i + \Delta\boldsymbol{\varepsilon}) \tag{8.90}$$

The two computational tasks, the nonlinear elastic step and the plastic step, will be now treated separately. But before proceeding, we mention the following notation adopted in subsequent formulations, compare also with Eqs. (8.16) - (8.19).

$$\widehat{\sigma}_m = \sigma_m^{i+1} - c\cot\varphi \tag{8.91}$$

$$\widehat{\overline{\sigma}}_m = \frac{\sigma_m^i + \sigma_m^{i+1}}{2} - c\cot\varphi \tag{8.92}$$

$$E_i = E_i^{\mathrm{p,ref}}\left(\frac{\widehat{\sigma}_m}{\widehat{\sigma}_m^{\mathrm{ref}}}\right)^{m_p} = E_i^{\mathrm{p,ref}} f_E \tag{8.93}$$

$$E_{ur} = E_{ur}^{\mathrm{p,ref}}\left(\frac{\widehat{\overline{\sigma}}_m}{\widehat{\sigma}_m^{\mathrm{ref}}}\right)^{m_p} = E_{ur}^{\mathrm{p,ref}}\widehat{f}_E, \quad G_{ur} = G_{ur}^{\mathrm{p,ref}}\widehat{f}_E, \quad K_{ur} = K_{ur}^{\mathrm{p,ref}}\widehat{f}_E \tag{8.94}$$

$$\Delta p_c = -2H^{\mathrm{p,ref}}\widehat{f}_E\Delta\lambda_c\sigma_m^{i+1} \tag{8.95}$$

8.3.1   Nonlinear elastic step

Apart from cases when the stress point is found inside the current yield envelope, this calculation step is performed at the beginning of each plastic step to provide trial stresses that satisfy Eq. (8.84) for zero plastic strain increments, i.e., $\sigma_m^{i+1} = \overline{\sigma}_m$ while $\Delta\lambda_s = \Delta\lambda_c = 0$. To this end, we introduce the first residuum

$$r_1 = \sigma_m^{i+1} - \overline{\sigma}_m(\sigma_m^{i+1}) \tag{8.96}$$

to be brought to zero via local Newton-Raphson iteration scheme

$$(\sigma_m^{i+1})_{j+1} = (\sigma_m^{i+1})_j - \frac{(r_1)_j}{\dfrac{\mathrm{d}(r_1)_j}{\mathrm{d}(\sigma_m^{i+1})_j}} \tag{8.97}$$

with the following initial conditions

$$(\sigma_m^{i+1})_0 = \sigma_m^i \tag{8.98}$$

$$(r_1)_0 = \sigma_m^i - (\sigma_m^i + K_{ur}(\sigma_m^i)\Delta\varepsilon_v) \longrightarrow (r_1)_0 = -K_{ur}(\sigma_m^i)\Delta\varepsilon_v \tag{8.99}$$

8.3.2 Plastic step

Because the hardening shear yield surface and the cap yield surface can be simultaneously active we revisit the concept of multi-yield surface plasticity and write the vector of residuals to be minimized as

$$\boldsymbol{r} = \left\{ \begin{array}{c} \sigma_m^{i+1} - \overline{\sigma}_m \\ f_s^{HS}(E_i^{i+1}, \boldsymbol{\sigma}^{i+1}, \kappa_s^{i+1}) \text{ or } f_s^{MN}(\boldsymbol{\sigma}^{i+1}) \\ f_c^{HS}(\boldsymbol{\sigma}^{i+1}, p_c^{i+1}) \end{array} \right\} = \boldsymbol{r}(\boldsymbol{a}(\boldsymbol{\varepsilon}), \boldsymbol{\varepsilon}) \tag{8.100}$$

The vector of primary variables reads

$$\boldsymbol{a}^\mathsf{T} = \left\{ \sigma_m^{i+1}, \Delta\lambda_s, \Delta\lambda_c \right\} \tag{8.101}$$

Similarly to the nonlinear elastic step the above system of implicit equations is solved by the Newton-Raphson method which now receives a more complex form

$$\boldsymbol{a}_{j+1}^{i+1} = \boldsymbol{a}_j^{i+1} - \mathbf{H}_j^{-1} \boldsymbol{r}_j \tag{8.102}$$

where the Jacobian matrix $\mathbf{H}$ is given by

$$\mathbf{H} = \frac{\partial \boldsymbol{r}}{\partial \boldsymbol{a}} + \frac{\partial \boldsymbol{r}}{\partial \boldsymbol{s}}\frac{\partial \boldsymbol{s}}{\partial \boldsymbol{a}} = \begin{bmatrix} \dfrac{\mathrm{d}r_1}{\mathrm{d}\sigma_m} & \dfrac{\mathrm{d}r_1}{\mathrm{d}\Delta\lambda_s} & \dfrac{\mathrm{d}r_1}{\mathrm{d}\Delta\lambda_c} \\[2mm] \dfrac{\mathrm{d}r_2}{\mathrm{d}\sigma_m} & \dfrac{\mathrm{d}r_2}{\mathrm{d}\Delta\lambda_s} & \dfrac{\mathrm{d}r_2}{\mathrm{d}\Delta\lambda_c} \\[2mm] \dfrac{\mathrm{d}r_3}{\mathrm{d}\sigma_m} & \dfrac{\mathrm{d}r_3}{\mathrm{d}\Delta\lambda_s} & \dfrac{\mathrm{d}r_3}{\mathrm{d}\Delta\lambda_c} \end{bmatrix} \tag{8.103}$$

Taking into account the solution of nonlinear elastic step that always precedes the plastic calculation step gives the initial values of $\boldsymbol{a}$ and $\boldsymbol{r}$ in the form

$$\boldsymbol{a}_0^\mathsf{T} = \left\{ \sigma_m^{tr}, 0, 0 \right\} \tag{8.104}$$

$$\boldsymbol{r}_0^\mathsf{T} = \left\{ 0, f_s^{HS}(\boldsymbol{s}^{tr}, \sigma_m^{tr}, \kappa_s^i) \text{ or } f_s^{MN}(\boldsymbol{s}^{tr}, \sigma_m^{tr}), f_c^{HS}(\boldsymbol{s}^{tr}, \sigma_m^{tr}, p_c^i) \right\} \tag{8.105}$$

where

$$\sigma_m^{tr} = \sigma_m^i + K_{ur}(\widehat{\overline{\sigma}}_m^{tr})\Delta\varepsilon_v \tag{8.106}$$

$$\boldsymbol{s}^{tr} = \boldsymbol{s}^i + 2G_{ur}(\widehat{\overline{\sigma}}_m^{tr})\mathbf{Q}\Delta e \tag{8.107}$$

remembering that σ_m^{tr} satisfies Eq. (8.96).

The components of matrix **H** are provided in the form of the following chain rules as

- **H_{1i}**

$$\frac{\mathrm{d}r_1}{\mathrm{d}\sigma_m} = \frac{\partial r_1}{\partial \sigma_m} + \frac{\partial r_1}{\partial K_{ur}}\frac{\partial K_{ur}}{\partial E_{ur}}\frac{\partial E_{ur}}{\partial \sigma_m} + \frac{\partial r_1}{\partial M_\psi}\frac{\partial M_\psi}{\partial \sin\psi_m}\frac{\partial \sin\psi_m}{\partial \sin\varphi_m}\frac{\mathrm{d}\sin\varphi_m}{\mathrm{d}\sigma_m} \tag{8.108}$$

$$\frac{\mathrm{d}r_1}{\mathrm{d}\Delta\lambda_s} = \frac{\partial r_1}{\partial \Delta\lambda_s} + \frac{\partial r_1}{\partial M_\psi}\frac{\partial M_\psi}{\partial \sin\psi_m}\frac{\partial \sin\psi_m}{\partial \sin\varphi_m}\frac{\mathrm{d}\sin\varphi_m}{\mathrm{d}\Delta\lambda_s} \tag{8.109}$$

$$\frac{\mathrm{d}r_1}{\mathrm{d}\Delta\lambda_c} = \frac{\partial r_1}{\partial \Delta\lambda_c} + \frac{\partial r_1}{\partial M_\psi}\frac{\partial M_\psi}{\partial \sin\psi_m}\frac{\partial \sin\psi_m}{\partial \sin\varphi_m}\frac{\mathrm{d}\sin\varphi_m}{\mathrm{d}\Delta\lambda_c} \tag{8.110}$$

- **H_{2i}**

  Hardening shear yield function

$$\frac{\mathrm{d}r_2}{\mathrm{d}\sigma_m} = \frac{\partial r_2}{\partial J}\frac{\partial J}{\partial \sigma_m} + \frac{\partial r_2}{\partial E_i}\frac{\partial E_i}{\partial \sigma_m} + \frac{\partial r_2}{\partial \sin\varphi_m}\frac{\mathrm{d}\sin\varphi_m}{\mathrm{d}\sigma_m} \tag{8.111}$$

$$\frac{\mathrm{d}r_2}{\mathrm{d}\Delta\lambda_s} = \frac{\partial r_2}{\partial J}\frac{\partial J}{\partial \Delta\lambda_s} + \frac{\partial r_2}{\partial \kappa_s}\frac{\partial \kappa_s}{\partial \Delta\lambda_s} + \frac{\partial r_2}{\partial \sin\varphi_m}\frac{\mathrm{d}\sin\varphi_m}{\mathrm{d}\Delta\lambda_s} \tag{8.112}$$

$$\frac{\mathrm{d}r_2}{\mathrm{d}\Delta\lambda_c} = \frac{\partial r_2}{\partial J}\frac{\partial J}{\partial \Delta\lambda_c} + \frac{\partial r_2}{\partial \sin\varphi_m}\frac{\mathrm{d}\sin\varphi_m}{\mathrm{d}\Delta\lambda_c} \tag{8.113}$$

  Matsuoka-Nakai yield function

$$\frac{\mathrm{d}r_2}{\mathrm{d}\sigma_m} = \frac{\mathrm{d}I_\sigma}{\mathrm{d}\sigma_m} \tag{8.113}$$

$$\frac{\mathrm{d}r_2}{\mathrm{d}\Delta\lambda_s} = \frac{\mathrm{d}I_\sigma}{\mathrm{d}\Delta\lambda_s} \tag{8.114}$$

$$\frac{\mathrm{d}r_2}{\mathrm{d}\Delta\lambda_c} = \frac{\mathrm{d}I_\sigma}{\mathrm{d}\Delta\lambda_c} \tag{8.115}$$

- **H_{3i}**

$$\frac{\mathrm{d}r_3}{\mathrm{d}\sigma_m} = \frac{\partial r_3}{\partial \sigma_m} + \frac{\partial r_3}{\partial J}\frac{\partial J}{\partial \sigma_m} +$$
$$+ \frac{\partial r_3}{\partial \chi}\frac{\partial \chi}{\partial \vartheta}\frac{\partial \vartheta}{\partial \sin 3\theta}\left(\frac{\partial \sin 3\theta}{\partial J}\frac{\partial J}{\partial \sigma_m} + \frac{\partial \sin 3\theta}{\partial I_{3s}}\frac{\mathrm{d}I_{3s}}{\mathrm{d}\sigma_m}\right) + \frac{\partial r_3}{\partial p_c}\frac{\mathrm{d}p_c}{\mathrm{d}\sigma_m} \tag{8.116}$$

$$\frac{\mathrm{d}r_3}{\mathrm{d}\Delta\lambda_s} = \frac{\partial r_3}{\partial J}\frac{\partial J}{\partial \Delta\lambda_s} + \frac{\partial r_3}{\partial \chi}\frac{\partial \chi}{\partial \vartheta}\frac{\partial \vartheta}{\partial \sin 3\theta}\left(\frac{\partial \sin 3\theta}{\partial J}\frac{\partial J}{\partial \Delta\lambda_s} + \frac{\partial \sin 3\theta}{\partial I_{3s}}\frac{\mathrm{d}I_{3s}}{\mathrm{d}\Delta\lambda_s}\right) \tag{8.117}$$

$$\frac{\mathrm{d}r_3}{\mathrm{d}\Delta\lambda_c} = \frac{\partial r_3}{\partial J}\frac{\partial J}{\partial \Delta\lambda_c} + \frac{\partial r_3}{\partial \chi}\frac{\partial \chi}{\partial \vartheta}\frac{\partial \vartheta}{\partial \sin 3\theta}\left(\frac{\partial \sin 3\theta}{\partial J}\frac{\partial J}{\partial \Delta\lambda_c} + \frac{\partial \sin 3\theta}{\partial I_{3s}}\frac{\mathrm{d}I_{3s}}{\mathrm{d}\Delta\lambda_c}\right) + \frac{\partial r_3}{\partial p_c}\frac{\partial p_c}{\partial \Delta\lambda_c} \tag{8.118}$$

where the total derivatives $\dfrac{\mathrm{d}\sin\varphi_m}{\mathrm{d}\sigma_m}, \dfrac{\mathrm{d}\sin\varphi_m}{\mathrm{d}\Delta\lambda_s}, \dfrac{\mathrm{d}\sin\varphi_m}{\mathrm{d}\Delta\lambda_c}, \dfrac{\mathrm{d}I_{3s}}{\mathrm{d}\sigma_m}, \dfrac{\mathrm{d}I_{3s}}{\mathrm{d}\Delta\lambda_s}, \dfrac{\mathrm{d}I_{3s}}{\mathrm{d}\Delta\lambda_c}, \dfrac{\mathrm{d}\boldsymbol{s}}{\mathrm{d}\sigma_m}, \dfrac{\mathrm{d}\boldsymbol{s}}{\mathrm{d}\Delta\lambda_s}, \dfrac{\mathrm{d}\boldsymbol{s}}{\mathrm{d}\Delta\lambda_c}$ are provided by

$$
\begin{aligned}
\frac{\mathrm{d}\sin\varphi_m}{\mathrm{d}\sigma_m} &= \frac{1}{2\sqrt{I_\sigma}}\frac{\mathrm{d}I_\sigma}{\mathrm{d}\sigma_m} = \frac{1}{2\sqrt{I_\sigma}}\left[\frac{\partial I_\sigma}{\partial I_{1\sigma}}\frac{\partial I_{1\sigma}}{\partial \sigma_m} + \frac{\partial I_\sigma}{\partial I_{2\sigma}}\left(\frac{\partial I_{2\sigma}}{\partial \sigma_m} + \frac{\partial I_{2\sigma}}{\partial J}\frac{\partial J}{\partial \sigma_m}\right) + \right. \\
&\quad \left. + \frac{\partial I_\sigma}{\partial I_{3\sigma}}\left(\frac{\partial I_{3\sigma}}{\partial \sigma_m} + \frac{\partial I_{3\sigma}}{\partial J}\frac{\partial J}{\partial \sigma_m} + \frac{\partial I_{3\sigma}}{\partial I_{3s}}\frac{\mathrm{d}I_{3s}}{\mathrm{d}\sigma_m}\right)\right]
\end{aligned}
\tag{8.119}
$$

$$
= \frac{\partial \sin\varphi_m}{\partial \sigma_m} + \frac{\partial \sin\varphi_m}{\partial J}\underbrace{\left(\frac{\partial J}{\partial \boldsymbol{s}}\right)^{\mathsf{T}}\frac{\mathrm{d}\boldsymbol{s}}{\mathrm{d}\sigma_m}}_{\frac{\partial J}{\partial \sigma_m}} + \frac{\partial \sin\varphi_m}{\partial I_{3s}}\underbrace{\left(\frac{\partial I_{3s}}{\partial \boldsymbol{s}}\right)^{\mathsf{T}}\frac{\mathrm{d}\boldsymbol{s}}{\mathrm{d}\sigma_m}}_{\frac{\partial I_{3s}}{\partial \sigma_m}}
\tag{8.120}
$$

$$
\begin{aligned}
\frac{\mathrm{d}\sin\varphi_m}{\mathrm{d}\Delta\lambda_s} &= \frac{1}{2\sqrt{I_\sigma}}\frac{\mathrm{d}I_\sigma}{\mathrm{d}\Delta\lambda_s} = \\
&= \frac{1}{2\sqrt{I_\sigma}}\left[\frac{\partial I_\sigma}{\partial I_{2\sigma}}\frac{\partial I_{2\sigma}}{\partial J}\frac{\partial J}{\partial \Delta\lambda_s} + \frac{\partial I_\sigma}{\partial I_{3\sigma}}\left(\frac{\partial I_{3\sigma}}{\partial J}\frac{\partial J}{\partial \Delta\lambda_s} + \frac{\partial I_{3\sigma}}{\partial I_{3s}}\frac{\mathrm{d}I_{3s}}{\mathrm{d}\Delta\lambda_s}\right)\right]
\end{aligned}
\tag{8.121}
$$

$$
\begin{aligned}
\frac{\mathrm{d}\sin\varphi_m}{\mathrm{d}\Delta\lambda_c} &= \frac{1}{2\sqrt{I_\sigma}}\frac{\mathrm{d}I_\sigma}{\mathrm{d}\Delta\lambda_c} = \\
&= \frac{1}{2\sqrt{I_\sigma}}\left[\frac{\partial I_\sigma}{\partial I_{2\sigma}}\frac{\partial I_{2\sigma}}{\partial J}\frac{\partial J}{\partial \Delta\lambda_c} + \frac{\partial I_\sigma}{\partial I_{3\sigma}}\left(\frac{\partial I_{3\sigma}}{\partial J}\frac{\partial J}{\partial \Delta\lambda_c} + \frac{\partial I_{3\sigma}}{\partial I_{3s}}\frac{\mathrm{d}I_{3s}}{\mathrm{d}\Delta\lambda_c}\right)\right]
\end{aligned}
\tag{8.122}
$$

$$
\frac{\mathrm{d}I_{3s}}{\mathrm{d}\sigma_m} = \left(\frac{\partial I_{3s}}{\partial \boldsymbol{s}}\right)^{\mathsf{T}}\frac{\mathrm{d}\boldsymbol{s}}{\mathrm{d}\sigma_m}
\tag{8.123}
$$

$$
\frac{\mathrm{d}I_{3s}}{\mathrm{d}\Delta\lambda_s} = \left(\frac{\partial I_{3s}}{\partial \boldsymbol{s}}\right)^{\mathsf{T}}\frac{\mathrm{d}\boldsymbol{s}}{\mathrm{d}\Delta\lambda_s}
\tag{8.124}
$$

$$
\frac{\mathrm{d}I_{3s}}{\mathrm{d}\Delta\lambda_c} = \left(\frac{\partial I_{3s}}{\partial \boldsymbol{s}}\right)^{\mathsf{T}}\frac{\mathrm{d}\boldsymbol{s}}{\mathrm{d}\Delta\lambda_c}
\tag{8.125}
$$

$$
\frac{\mathrm{d}\boldsymbol{s}}{\mathrm{d}\sigma_m} = \frac{\partial \boldsymbol{s}}{\partial \sigma_m} + \frac{\partial \boldsymbol{s}}{\partial J}\frac{\partial J}{\partial \sigma_m}
\tag{8.126}
$$

$$
\frac{\mathrm{d}\boldsymbol{s}}{\mathrm{d}\Delta\lambda_s} = \frac{\partial \boldsymbol{s}}{\partial \Delta\lambda_s} + \frac{\partial \boldsymbol{s}}{\partial J}\frac{\partial J}{\partial \Delta\lambda_s}
\tag{8.127}
$$

$$
\frac{\mathrm{d}\boldsymbol{s}}{\mathrm{d}\Delta\lambda_c} = \frac{\partial \boldsymbol{s}}{\partial \Delta\lambda_c} + \frac{\partial \boldsymbol{s}}{\partial J}\frac{\partial J}{\partial \Delta\lambda_c}
\tag{8.128}
$$

Note that all derivatives are taken with respect to variables evaluated at the end of the $(i+1)$ load increment. But this index was dropped from all expressions for the sake of clarity. So if not otherwise stated it holds $\sigma_m = \sigma_m^{i+1}, \boldsymbol{s} = \boldsymbol{s}^{i+1}, J = J^{i+1}, I_{3s} = I_{3s}^{i+1}$. Similar simplification is adopted for elastic moduli where we consider $E_{ur} = E_{ur}(\widehat{\overline{\sigma}}_m), K_{ur} = K_{ur}(\widehat{\overline{\sigma}}_m), G_{ur} = G_{ur}(\widehat{\overline{\sigma}}_m)$.

With this simplified notation the partial derivatives $\frac{\partial \boldsymbol{s}}{\partial J}, \frac{\partial \boldsymbol{s}}{\partial \Delta \lambda_s}, \frac{\partial \boldsymbol{s}}{\partial \Delta \lambda_c}, \frac{\partial \boldsymbol{s}}{\partial \sigma_m}, \frac{\partial J}{\partial \Delta \lambda_s}, \frac{\partial J}{\partial \Delta \lambda_c}, \frac{\partial J}{\partial \sigma_m}, \frac{\partial I_{3s}}{\partial \boldsymbol{s}}$ and ∂I_σ in Eqs. (8.111) - (8.128) become

$$\frac{\partial \boldsymbol{s}}{\partial J} = \frac{\boldsymbol{s}^i + 2G_{ur}\mathbf{Q}\Delta \boldsymbol{e}}{\left[1 + G_{ur}\left(\frac{\Delta \lambda_s}{J} + \frac{6\Delta \lambda_c}{\tilde{\chi}^2 M^2}\right)\right]^2}\frac{G_{ur}\Delta \lambda_s}{J^2} = \frac{\boldsymbol{s}}{[-]}\frac{G_{ur}\Delta \lambda_s}{J^2} \tag{8.129}$$

$$\frac{\partial \boldsymbol{s}}{\partial \Delta \lambda_s} = -\frac{\boldsymbol{s}^i + 2G_{ur}\mathbf{Q}\Delta \boldsymbol{e}}{\left[1 + G_{ur}\left(\frac{\Delta \lambda_s}{J} + \frac{6\Delta \lambda_c}{\tilde{\chi}^2 M^2}\right)\right]^2}\frac{G_{ur}}{J} = -\frac{\boldsymbol{s}}{[-]}\frac{G_{ur}}{J} \tag{8.130}$$

$$\frac{\partial \boldsymbol{s}}{\partial \Delta \lambda_c} = -\frac{\boldsymbol{s}^i + 2G_{ur}\mathbf{Q}\Delta \boldsymbol{e}}{\left[1 + G_{ur}\left(\frac{\Delta \lambda_s}{J} + \frac{6\Delta \lambda_c}{\tilde{\chi}^2 M^2}\right)\right]^2}\frac{6G_{ur}}{\tilde{\chi}^2 M^2} = -\frac{\boldsymbol{s}}{[-]}\frac{6G_{ur}}{\tilde{\chi}^2 M^2} \tag{8.131}$$

$$\frac{\partial \boldsymbol{s}}{\partial \sigma_m} = \frac{\partial \boldsymbol{s}}{\partial G_{ur}}\frac{\partial G_{ur}}{\partial E_{ur}}E_{ur}^{\text{p,ref}}\mathrm{d}\widehat{f}_E \tag{8.132}$$

$$\frac{\partial \boldsymbol{s}}{\partial G_{ur}} = \frac{2\mathbf{Q}\Delta \boldsymbol{e} - \left(\frac{\Delta \lambda_s}{J} + \frac{6\Delta \lambda_c}{\tilde{\chi}^2 M^2}\right)\boldsymbol{s}^i}{\left[1 + G_{ur}\left(\frac{\Delta \lambda_s}{J} + \frac{6\Delta \lambda_c}{\tilde{\chi}^2 M^2}\right)\right]^2} = \frac{2\mathbf{Q}\Delta \boldsymbol{e} - \left(\frac{\Delta \lambda_s}{J} + \frac{6\Delta \lambda_c}{\tilde{\chi}^2 M^2}\right)\boldsymbol{s}}{1 + G_{ur}\left(\frac{\Delta \lambda_s}{J} + \frac{6\Delta \lambda_c}{\tilde{\chi}^2 M^2}\right)} \tag{8.133}$$

$$\frac{\partial G_{ur}}{\partial E_{ur}} = \frac{1}{2(1 + \nu_{ur})} \tag{8.134}$$

$$\frac{\partial J}{\partial \Delta \lambda_s} = -\frac{G_{ur}}{1 + \frac{6G_{ur}\Delta \lambda_c}{\tilde{\chi}^2 M^2}} \tag{8.135}$$

$$\frac{\partial J}{\partial \Delta \lambda_c} = -\frac{J^{tr} - G_{ur}\Delta \lambda_s}{\left(1 + \frac{6G_{ur}\Delta \lambda_c}{\tilde{\chi}^2 M^2}\right)^2}\frac{6G_{ur}}{\tilde{\chi}^2 M^2} = -\frac{J}{1 + \frac{6G_{ur}\Delta \lambda_c}{\tilde{\chi}^2 M^2}}\frac{6G_{ur}}{\tilde{\chi}^2 M^2} \tag{8.136}$$

$$\frac{\partial J}{\partial \sigma_m} = \frac{\partial J}{\partial G_{ur}}\frac{\partial G_{ur}}{\partial E_{ur}}E_{ur}^{\text{p,ref}}\mathrm{d}\widehat{f}_E \tag{8.137}$$

$$\frac{\partial J}{\partial G_{ur}} = \frac{\frac{\partial J^{tr}}{\partial G_{ur}}\left(1 + \frac{6G_{ur}\Delta \lambda_c}{\tilde{\chi}^2 M^2}\right) - J^{tr}\frac{6\Delta \lambda_c}{\tilde{\chi}^2 M^2} - \Delta \lambda_s}{\left(1 + \frac{6G_{ur}\Delta \lambda_c}{\tilde{\chi}^2 M^2}\right)^2} \tag{8.138}$$

$$\frac{\partial J^{tr}}{\partial G_{ur}} = \frac{1}{J^{tr}}\left(\Delta \boldsymbol{e}^\mathsf{T}\boldsymbol{s}^i + G_{ur}\Delta E_d^2\right) \tag{8.139}$$

$$\frac{\partial I_{3s}}{\partial \boldsymbol{s}} = \left\{\begin{array}{c} s_y s_z - \tau_{yz}^2 \\ s_x s_z - \tau_{xz}^2 \\ s_x s_y - \tau_{xy}^2 \\ 2(\tau_{xy}\tau_{xz} - s_x\tau_{yz}) \\ 2(\tau_{xy}\tau_{yz} - s_y\tau_{xz}) \\ 2(\tau_{xz}\tau_{yz} - s_z\tau_{xy}) \end{array}\right\}\text{3D} \qquad \frac{\partial I_{3s}}{\partial \boldsymbol{s}} = \left\{\begin{array}{c} s_y s_z \\ s_x s_z \\ -2s_z\tau_{xy} \\ s_x s_y - \tau_{xy}^2 \end{array}\right\}\text{PStrain} \tag{8.140}$$

The derivatives ∂I_σ are

$$\frac{\partial I_\sigma}{\partial I_{1\sigma}} = \frac{8 I_{2\sigma} I_{3\sigma}}{(I_{3\sigma} - I_{1\sigma} I_{2\sigma})^2} \tag{8.141}$$

$$\frac{\partial I_\sigma}{\partial I_{2\sigma}} = \frac{8 I_{1\sigma} I_{3\sigma}}{(I_{3\sigma} - I_{1\sigma} I_{2\sigma})^2} \tag{8.142}$$

$$\frac{\partial I_\sigma}{\partial I_{3\sigma}} = -\frac{8 I_{1\sigma} I_{2\sigma}}{(I_{3\sigma} - I_{1\sigma} I_{2\sigma})^2} \tag{8.143}$$

$$\frac{\partial I_{1\sigma}}{\partial \sigma_m} = 3 \tag{8.144}$$

$$\frac{\partial I_{2\sigma}}{\partial \sigma_m} = 6\widehat{\sigma}_m \tag{8.145}$$

$$\frac{\partial I_{2\sigma}}{\partial J} = -2J \tag{8.146}$$

$$\frac{\partial I_{3\sigma}}{\partial \sigma_m} = 3\widehat{\sigma}_m^2 - J^2 \tag{8.147}$$

$$\frac{\partial I_{3\sigma}}{\partial J} = -2\widehat{\sigma}_m J \tag{8.148}$$

$$\frac{\partial I_{3\sigma}}{\partial I_{3s}} = 1 \tag{8.149}$$

The remaining partial derivatives that appear in Eqs. (8.108) - (8.118) are now presented in a sequel for individual residua $\dfrac{\partial r_i}{\partial a_j}$

- Partial derivatives $\dfrac{\partial r_1}{\partial a_j}, \dfrac{\partial r_1}{\partial K_{ur}}, \dfrac{\partial r_1}{\partial M_\psi}, \dfrac{\partial K_{ur}}{\partial E_{ur}}, \dfrac{\partial E_{ur}}{\partial \sigma_m}, \dfrac{\partial M_\psi}{\partial \sin \psi_m}, \dfrac{\partial \sin \psi_m}{\partial \sin \varphi_m}$

$$\frac{\partial r_1}{\partial \sigma_m} = 1 \tag{8.150}$$

$$\frac{\partial r_1}{\partial \lambda_s} = \frac{K_{ur} M_\psi}{1 + 2 K_{ur} \Delta\lambda_c} \tag{8.151}$$

$$\frac{\partial r_1}{\partial \lambda_c} = \frac{(\sigma_m^i + K_{ur}(\Delta\varepsilon_v - \Delta\lambda_s M_\psi)) 2 K_{ur}}{(1 + 2 K_{ur} \Delta\lambda_c)^2} = \frac{2 K_{ur} \sigma_m}{1 + 2 K_{ur} \Delta\lambda_c} \tag{8.152}$$

$$\frac{\partial r_1}{\partial K_{ur}} = \frac{-\Delta\varepsilon_v + M_\psi \Delta\lambda_s + 2\sigma_m^i \Delta\lambda_c}{(1 + 2 K_{ur} \Delta\lambda_c)^2} \tag{8.153}$$

$$\frac{\partial r_1}{\partial M_\psi} = \frac{K_{ur} \Delta\lambda_s}{1 + 2 K_{ur} \Delta\lambda_c} \tag{8.154}$$

$$\frac{\partial K_{ur}}{\partial E_{ur}} = \frac{1}{3(1 - 2\nu_{ur})} \tag{8.155}$$

$$\frac{\partial E_{ur}}{\partial \sigma_m} = E_{ur}^{\mathrm{p,ref}} \mathrm{d}\widehat{f}_E, \quad \mathrm{d}\widehat{f}_E = \frac{\partial \widehat{f}_E}{\partial \sigma_m} = \frac{1}{2} \frac{m_p}{\widehat{\sigma}_m^{\mathrm{ref}}} \left(\frac{\widehat{\sigma}_m}{\widehat{\sigma}_m^{\mathrm{ref}}} \right)^{m_p - 1} \tag{8.156}$$

$$\frac{\partial M_\psi}{\partial \sin \psi_m} = \frac{6\sqrt{3}}{(3 - \sin \psi_m)^2} \tag{8.157}$$

$$\frac{\partial \sin \psi_m}{\partial \sin \varphi_m} = \frac{1 - \sin^2 \varphi_{cs}}{(1 - \sin \varphi_m \sin \varphi_{cs})^2} \tag{8.158}$$

- Partial derivatives $\dfrac{\partial r_2}{\partial J}, \dfrac{\partial r_2}{\partial E_i}, \dfrac{\partial r_2}{\partial \kappa_s}, \dfrac{\partial r_2}{\partial \sin \varphi_m}, \dfrac{\partial E_i}{\partial \sigma_m}, \dfrac{\partial \kappa_s}{\partial \Delta \lambda_s}$

$$\frac{\partial r_2}{\partial J} = 1 - (1 - b\tilde{a}) \frac{E_i^{\mathrm{p,ref}}}{E_{ur}^{\mathrm{p,ref}}} \tag{8.159}$$

$$\frac{\partial r_2}{\partial E_i} = -(1 - b\tilde{a}) \frac{\kappa_s}{3} \tag{8.160}$$

$$\frac{\partial r_2}{\partial \kappa_s} = -(1 - b\tilde{a}) \frac{E_i}{3} \tag{8.161}$$

$$\frac{\partial r_2}{\partial \sin \varphi_m} = b \left(\frac{E_i^{\mathrm{p,ref}}}{E_{ur}^{\mathrm{p,ref}}} J + \frac{E_i}{3} \kappa_s \right) \frac{1}{(1 - \sin \varphi_m)^2} \tag{8.162}$$

$$\frac{\partial E_i}{\partial \sigma_m} = E_i^{\mathrm{p,ref}} \mathrm{d}\widehat{f}_E \tag{8.163}$$

$$\frac{\partial \kappa_s}{\partial \Delta \lambda_s} = 1 \tag{8.164}$$

- Partial derivatives $\dfrac{\partial r_3}{\partial \sigma_m}, \dfrac{\partial r_3}{\partial J}, \dfrac{\partial r_3}{\partial \chi}, \dfrac{\partial r_3}{\partial p_c}, \dfrac{\partial \chi}{\partial \vartheta}, \dfrac{\partial \vartheta}{\partial \sin 3\theta}, \dfrac{\partial \sin 3\theta}{\partial J}, \dfrac{\partial \sin 3\theta}{\partial I_{3s}}, \dfrac{\partial p_c}{\partial \Delta \lambda_s}, \dfrac{\partial p_c}{\partial \Delta \lambda_c}$

$$\frac{\partial r_3}{\partial \sigma_m} = 2\sigma_m \tag{8.165}$$

$$\frac{\partial r_3}{\partial J} = \frac{6J}{\chi^2 M^2} \tag{8.166}$$

$$\frac{\partial r_3}{\partial \chi} = -\frac{6J^2}{\chi^3 M^2} \tag{8.167}$$

$$\frac{\partial r_3}{\partial p_c} = -2p_c \tag{8.168}$$

$$\frac{\partial \chi}{\partial \vartheta} = \frac{\sqrt{3}\beta}{2\sqrt{\beta^2 - \beta + 1}} \frac{\sin \vartheta}{\cos^2 \vartheta} \tag{8.169}$$

$$\frac{\partial \vartheta}{\partial \sin 3\theta} = \pm \frac{1}{3} \frac{z \sin 3\theta}{\sqrt{1 - (-1 + z \sin^2 3\theta)^2}}, \quad z = \frac{27\beta^2 (1 - \beta)^2}{2(\beta^2 - \beta + 1)^3}$$

$$= -\frac{1}{3} \frac{\sqrt{z}}{\sqrt{2 - z \sin^2 3\tilde{\theta}}}, \quad \text{for } \theta \leq 0 \tag{8.170}$$

$$= +\frac{1}{3} \frac{\sqrt{z}}{\sqrt{2 - z \sin^2 3\tilde{\theta}}}, \quad \text{for } \theta > 0 \tag{8.171}$$

$$\frac{\partial \sin 3\theta}{\partial J} = \frac{9\sqrt{3}}{2} \frac{I_{3s}}{J^4} \tag{8.172}$$

$$\frac{\partial \sin 3\theta}{\partial I_{3s}} = -\frac{3\sqrt{3}}{2J^3} \tag{8.173}$$

$$\frac{\mathrm{d}p_c}{\mathrm{d}\sigma_m} = \frac{\partial p_c}{\partial \sigma_m} + \frac{\partial p_c}{\partial \widehat{f}_E} \frac{\partial \widehat{f}_E}{\partial \sigma_m} = -2H^{\mathrm{p,ref}} \Delta \lambda_c (\widehat{f}_E + \mathrm{d}\widehat{f}_E \sigma_m) \tag{8.174}$$

$$\frac{\partial p_c}{\partial \Delta \lambda_c} = -2H^{\mathrm{p,ref}} \widehat{f}_E \sigma_m \tag{8.175}$$

- Partial derivatives $\dfrac{\partial J}{\partial \boldsymbol{s}}, \dfrac{\partial r_3}{\partial \boldsymbol{s}}$

$$\frac{\partial J}{\partial \boldsymbol{s}} = \frac{1}{2J} \mathbf{Q}^{-1} \boldsymbol{s} = \frac{1}{2J} \mathbf{P}\boldsymbol{\sigma} \tag{8.176}$$

$$\frac{\partial r_3}{\partial \boldsymbol{s}} = \frac{3}{\chi^2 M^2} \mathbf{Q}^{-1} \boldsymbol{s} = \frac{3}{\chi^2 M^2} \mathbf{P}\boldsymbol{\sigma} \tag{8.177}$$

It can also be shown that the following relationships hold

$$\frac{\partial J}{\partial \sigma_m} = \left(\frac{\partial J}{\partial s}\right)^{\mathsf{T}} \frac{\mathrm{d}s}{\mathrm{d}\sigma_m} = \frac{\left(\frac{\partial J}{\partial s}\right)^{\mathsf{T}} \frac{\partial s}{\partial \sigma_m}}{1 - \left(\frac{\partial J}{\partial s}\right)^{\mathsf{T}} \frac{\partial s}{\partial J}} \tag{8.178}$$

$$\frac{\partial J}{\partial \Delta\lambda_s} = \left(\frac{\partial J}{\partial s}\right)^{\mathsf{T}} \frac{\mathrm{d}s}{\mathrm{d}\Delta\lambda_s} = \frac{\left(\frac{\partial J}{\partial s}\right)^{\mathsf{T}} \frac{\partial s}{\partial \Delta\lambda_s}}{1 - \left(\frac{\partial J}{\partial s}\right)^{\mathsf{T}} \frac{\partial s}{\partial J}} \tag{8.179}$$

$$\frac{\partial J}{\partial \Delta\lambda_c} = \left(\frac{\partial J}{\partial s}\right)^{\mathsf{T}} \frac{\mathrm{d}s}{\mathrm{d}\Delta\lambda_c} = \frac{\left(\frac{\partial J}{\partial s}\right)^{\mathsf{T}} \frac{\partial s}{\partial \Delta\lambda_c}}{1 - \left(\frac{\partial J}{\partial s}\right)^{\mathsf{T}} \frac{\partial s}{\partial J}} \tag{8.180}$$

$$\frac{\partial r_3}{\partial J} \frac{\partial J}{\partial \sigma_m} = \left(\frac{\partial r_3}{\partial s}\right)^{\mathsf{T}} \frac{\mathrm{d}s}{\mathrm{d}\sigma_m} = \frac{\partial r_3}{\partial J}\left(\frac{\partial J}{\partial s}\right)^{\mathsf{T}} \frac{\mathrm{d}s}{\mathrm{d}\sigma_m} = \frac{3}{\chi^2 M^2}\sigma^{\mathsf{T}}\mathbf{P}\frac{\mathrm{d}s}{\mathrm{d}\sigma_m} \tag{8.181}$$

$$\frac{\partial r_3}{\partial J} \frac{\partial J}{\partial \Delta\lambda_s} = \left(\frac{\partial r_3}{\partial s}\right)^{\mathsf{T}} \frac{\mathrm{d}s}{\mathrm{d}\Delta\lambda_s} = \frac{\partial r_3}{\partial J}\left(\frac{\partial J}{\partial s}\right)^{\mathsf{T}} \frac{\mathrm{d}s}{\mathrm{d}\Delta\lambda_s} = \frac{3}{\chi^2 M^2}\sigma^{\mathsf{T}}\mathbf{P}\frac{\mathrm{d}s}{\mathrm{d}\Delta\lambda_s} \tag{8.182}$$

$$\frac{\partial r_3}{\partial J} \frac{\partial J}{\partial \Delta\lambda_c} = \left(\frac{\partial r_3}{\partial s}\right)^{\mathsf{T}} \frac{\mathrm{d}s}{\mathrm{d}\Delta\lambda_c} = \frac{\partial r_3}{\partial J}\left(\frac{\partial J}{\partial s}\right)^{\mathsf{T}} \frac{\mathrm{d}s}{\mathrm{d}\Delta\lambda_c} = \frac{3}{\chi^2 M^2}\sigma^{\mathsf{T}}\mathbf{P}\frac{\mathrm{d}s}{\mathrm{d}\Delta\lambda_s} \tag{8.183}$$

8.4   Algorithmic tangent stiffness matrix

The point of departure in the derivation of algorithmic tangent stiffness matrix is Eq. (4.19). This formulation takes into account the volumetric-deviatoric split exploited already in the previous section and gives the algorithmic tangent stiffness matrix $\mathcal{D}$ in the form

$$\mathcal{D} = \frac{\mathrm{d}\sigma^{i+1}}{\mathrm{d}\varepsilon^{i+1}} = 3m\left(\frac{\mathrm{d}\sigma_m^{i+1}}{\mathrm{d}\varepsilon^{i+1}}\right)^{\mathsf{T}} + \frac{\mathrm{d}s^{i+1}}{\mathrm{d}\varepsilon^{i+1}} \tag{8.184}$$

Equation (8.184) suggests that the derivatives are evaluated at the end of the $(i+1)$ load increment. To simplify notation, however, we drop the superscript $(i+1)$ and consider all stress and strain quantities, if not otherwise stated, to correspond to the end of the $(i + 1)$ load increment. We shall also adopt the following notation

$$\Delta\varepsilon_v = 3m^{\mathsf{T}}\Delta\varepsilon = 3m^{\mathsf{T}}\left(\varepsilon^{i+1} - \varepsilon^i\right) \Rightarrow \frac{\partial\Delta\varepsilon_v}{\partial\varepsilon} = 3m \tag{8.185}$$

$$\Delta e = \mathbf{PQ}\Delta\varepsilon = \mathbf{PQ}\left(\varepsilon^{i+1} - \varepsilon^i\right) \Rightarrow \frac{\partial\Delta e}{\partial\varepsilon} = \mathbf{PQ} \tag{8.186}$$

and consider the following stress and strain dependencies

$$\sigma_m^{i+1} = f(K_{ur}(\sigma_m^{i+1}), M_\psi(\sin\psi_m^{i+1}), \Delta\lambda_s(\varepsilon), \Delta\lambda_c(\varepsilon), \Delta\varepsilon_v(\varepsilon)) \tag{8.187}$$

$$\sin\psi_m^{i+1} = f(\sigma_m^{i+1}, J^{i+1}(s^{i+1}), I_{3s}^{i+1}(s^{i+1})) \tag{8.188}$$

$$s^{i+1} = f(G_{ur}(\sigma_m^{i+1}), J^{i+1}, \Delta\lambda_s(\varepsilon), \Delta\lambda_c(\varepsilon), \Delta e(\varepsilon)) \tag{8.189}$$

$$J^{i+1} = f(J^{tr}, G_{ur}(\sigma_m^{i+1}), \Delta\lambda_s(\varepsilon), \Delta\lambda_c(\varepsilon)) \tag{8.190}$$

$$J^{tr} = f(G_{ur}(\sigma_m^{i+1}), \Delta e(\varepsilon)) \tag{8.191}$$

It is also worth mentioning that the hardening soil model is in general a multi-yield surface plasticity model which will have some impact in the derivation of $\mathcal{D}$.

Observing Eqs. (8.189) - (8.191) we start from writing the second term on the right hand side of Eq. (8.184) as

$$
\frac{\mathrm{d}s}{\mathrm{d}\varepsilon} = \frac{\partial s}{\partial \varepsilon} + \frac{\mathrm{d}s}{\mathrm{d}\tilde{\chi}}\left(\frac{\mathrm{d}\tilde{\chi}}{\mathrm{d}\varepsilon}\right)^{\mathsf{T}} + \frac{\mathrm{d}s}{\mathrm{d}\sigma_m}\left(\frac{\mathrm{d}\sigma_m}{\mathrm{d}\varepsilon}\right)^{\mathsf{T}} + \frac{\mathrm{d}s}{\mathrm{d}\Delta\lambda_s}\left(\frac{\partial\Delta\lambda_s}{\partial\varepsilon}\right)^{\mathsf{T}} + \frac{\mathrm{d}s}{\mathrm{d}\Delta\lambda_c}\left(\frac{\partial\Delta\lambda_c}{\partial\varepsilon}\right)^{\mathsf{T} } \tag{8.192}
$$

$$
= \mathbf{E}_1 + \mathbf{E}_2 + s_1\left(\frac{\mathrm{d}\sigma_m}{\mathrm{d}\varepsilon}\right)^{\mathsf{T}} + s_2\left(\frac{\partial\Delta\lambda_s}{\partial\varepsilon}\right)^{\mathsf{T}} + s_3\left(\frac{\partial\Delta\lambda_c}{\partial\varepsilon}\right)^{\mathsf{T}} \tag{8.193}
$$

where the derivatives $\dfrac{\mathrm{d}s}{\mathrm{d}\sigma_m} = s_1, \dfrac{\mathrm{d}s}{\mathrm{d}\Delta\lambda_s} = s_2, \dfrac{\mathrm{d}s}{\mathrm{d}\Delta\lambda_c} = s_3$ are provided by (8.126), (8.127), (8.128) and the matrices $\mathbf{E}_1$ and $\mathbf{E}_2$

$$
\mathbf{E}_1 = \frac{\partial s}{\partial \varepsilon} = \left[\frac{\partial s}{\partial \Delta e} + \frac{\partial s}{\partial J}\left(\frac{\partial J}{\partial \Delta e}\right)^{\mathsf{T}}\right]\frac{\partial \Delta e}{\partial \varepsilon} \tag{8.194}
$$

$$
\mathbf{E}_2 = \frac{\mathrm{d}s}{\mathrm{d}\tilde{\chi}}\left(\frac{\mathrm{d}\tilde{\chi}}{\mathrm{d}\varepsilon}\right)^{\mathsf{T}} \tag{8.195}
$$

Definition of both matrices deserves a considerable attention. We begin with the derivatives in Eq. (8.194) given by

$$
\frac{\partial s}{\partial \Delta e} = \frac{2G_{ur}\mathbf{Q}}{1 + G_{ur}\left(\dfrac{\Delta\lambda_s}{J} + \dfrac{6\Delta\lambda_c}{\tilde{\chi}^2 M^2}\right)}, \qquad \frac{\partial \Delta e}{\partial \varepsilon} = \mathbf{PQ} \tag{8.196}
$$

$$
\frac{\partial J}{\partial \Delta e} = \frac{\partial J}{\partial J^{tr}}\frac{\partial J^{tr}}{\partial \Delta e}
$$
$$
= \frac{G_{ur}(s^i + 2G_{ur}\mathbf{Q}\Delta e)}{\left(1 + \dfrac{6G_{ur}\Delta\lambda_c}{\tilde{\chi}^2 M^2}\right)J^{tr}} = \frac{G_{ur}}{1 + \dfrac{6G_{ur}\Delta\lambda_c}{\tilde{\chi}^2 M^2}}\frac{s^{tr}}{J^{tr}} = \frac{G_{ur}}{1 + \dfrac{6G_{ur}\Delta\lambda_c}{\tilde{\chi}^2 M^2}}\frac{s}{J} \tag{8.197}
$$

When addressing the derivatives in Eq. (8.194) we first notice that $\tilde{\chi} = \tilde{\chi}(\tilde{J}(\Delta e, \tilde{G}_{ur}(\tilde{\sigma}_m(\Delta\varepsilon_v))), \tilde{I}_{3s}(\tilde{s}(\Delta e, \tilde{G}_{ur}(\tilde{\sigma}_m(\Delta\varepsilon_v)))))$ depends on stresses at the end of the non-linear elastic step written as

$$
\tilde{\sigma}_m = \sigma_m^i + \tilde{K}_{ur}(\tilde{\sigma}_m)\Delta\varepsilon_v \tag{8.198}
$$
$$
\tilde{s} = s^i + 2\tilde{G}_{ur}(\tilde{\sigma}_m)\mathbf{Q}\Delta e \tag{8.199}
$$
$$
\tilde{J} = \left[J_2^i + 2\tilde{G}_{ur}(\tilde{\sigma}_m)\Delta e^{\mathsf{T}}s^i + (\tilde{G}_{ur}(\tilde{\sigma}_m))^2\Delta E_d^2\right]^{\frac{1}{2}} \tag{8.200}
$$

To expand Eq. (8.195) requires evaluating the total derivatives $\dfrac{\mathrm{d}\tilde{s}}{\mathrm{d}\varepsilon}$ and $\dfrac{\mathrm{d}\tilde{\sigma}_m}{\mathrm{d}\varepsilon}$ which attain the the following forms

$$
\frac{\mathrm{d}\tilde{s}}{\mathrm{d}\varepsilon} = \frac{\partial \tilde{s}}{\partial \varepsilon} + \frac{\mathrm{d}\tilde{s}}{\mathrm{d}\tilde{\sigma}_m}\left(\frac{\mathrm{d}\tilde{\sigma}_m}{\mathrm{d}\varepsilon}\right)^{\mathsf{T}} \tag{8.201}
$$

$$
\frac{\mathrm{d}\tilde{\sigma}_m}{\mathrm{d}\varepsilon} = \frac{\partial \tilde{\sigma}_m}{\partial \varepsilon} + \frac{\partial \tilde{\sigma}_m}{\partial \tilde{K}_{ur}}\frac{\partial \tilde{K}_{ur}}{\partial \tilde{E}_{ur}}\frac{\partial \tilde{E}_{ur}}{\partial \tilde{\sigma}_m}\frac{\mathrm{d}\tilde{\sigma}_m}{\mathrm{d}\varepsilon} \tag{8.202}
$$

Equation (8.202) can be further rearranged to get

$$
\frac{\mathrm{d}\tilde{\sigma}_m}{\mathrm{d}\varepsilon} = \frac{1}{1 - \dfrac{\partial \tilde{\sigma}_m}{\partial \tilde{K}_{ur}}\dfrac{\partial \tilde{K}_{ur}}{\partial \tilde{E}_{ur}}\dfrac{\partial \tilde{E}_{ur}}{\partial \tilde{\sigma}_m}}\frac{\partial \tilde{\sigma}_m}{\partial \varepsilon} = \frac{\tilde{a}_1}{1 - \tilde{a}_2} \tag{8.203}
$$

where

$$
\tilde{a}_1 = \frac{\partial \tilde{\sigma}_m}{\partial \varepsilon} = 3m\tilde{K}_{ur} \tag{8.204}
$$

$$
\tilde{a}_2 = \frac{\partial \tilde{\sigma}_m}{\partial \tilde{K}_{ur}}\frac{\partial \tilde{K}_{ur}}{\partial \tilde{E}_{ur}}\frac{\partial \tilde{E}_{ur}}{\partial \tilde{\sigma}_m} = \Delta\varepsilon_v\frac{1}{3(1 - 2\nu_{ur})}E_{ur}^{\mathrm{p,ref}}\,\mathrm{d}\widehat{f}_E \tag{8.205}
$$

The derivatives in Eq. (8.195) thus become

$$\frac{\mathrm{d}\boldsymbol{s}}{\mathrm{d}\tilde{\chi}} = \frac{\partial \boldsymbol{s}}{\partial \tilde{\chi}} + \frac{\partial \boldsymbol{s}}{\partial J}\frac{\partial J}{\partial \tilde{\chi}} \tag{8.206}$$

$$\frac{\mathrm{d}\tilde{\chi}}{\mathrm{d}\boldsymbol{\varepsilon}} = \left[\frac{\mathrm{d}\tilde{\boldsymbol{s}}}{\mathrm{d}\boldsymbol{\varepsilon}}\right]^{\mathsf{T}}\frac{\partial \tilde{\chi}}{\partial \tilde{\boldsymbol{s}}}, \text{(note similar definitions used in Eqs. (8.222), (8.223))} \tag{8.207}$$

$$\frac{\mathrm{d}\tilde{\boldsymbol{s}}}{\mathrm{d}\boldsymbol{\varepsilon}} = \frac{\partial \tilde{\boldsymbol{s}}}{\partial \Delta \boldsymbol{e}}\frac{\partial \Delta \boldsymbol{e}}{\partial \boldsymbol{\varepsilon}} + \frac{\partial \tilde{\boldsymbol{s}}}{\partial \tilde{G}_{ur}}\frac{\partial \tilde{G}_{ur}}{\partial \tilde{\sigma}_m}\left(\frac{\mathrm{d}\tilde{\sigma}_m}{\mathrm{d}\boldsymbol{\varepsilon}}\right)^{\mathsf{T}}, \text{ recall Eqs. (8.201), (8.203)} \tag{8.208}$$

$$\frac{\partial \tilde{\chi}}{\partial \tilde{\boldsymbol{s}}} = \frac{\partial \tilde{\chi}}{\partial \vartheta}\frac{\partial \vartheta}{\partial \sin 3\tilde{\theta}}\left(\frac{\partial \sin 3\tilde{\theta}}{\partial \tilde{J}}\frac{\partial \tilde{J}}{\partial \tilde{\boldsymbol{s}}} + \frac{\partial \sin 3\tilde{\theta}}{\partial \tilde{I}_{3s}}\frac{\partial \tilde{I}_{3s}}{\partial \tilde{\boldsymbol{s}}}\right) \tag{8.209}$$

$$\frac{\partial \boldsymbol{s}}{\partial \tilde{\chi}} = \frac{\boldsymbol{s}^i + 2G_{ur}\mathbf{Q}\Delta \boldsymbol{e}}{\left[1 + G_{ur}\left(\frac{\Delta \lambda_s}{J} + \frac{6\Delta \lambda_c}{\tilde{\chi}^2 M^2}\right)\right]^2}\frac{12G_{ur}\Delta \lambda_c}{\tilde{\chi}^3 M^2} = \frac{\boldsymbol{s}}{1 + G_{ur}\left(\frac{\Delta \lambda_s}{J} + \frac{6\Delta \lambda_c}{\tilde{\chi}^2 M^2}\right)}\frac{12G_{ur}\Delta \lambda_c}{\tilde{\chi}^3 M^2} \tag{8.210}$$

$$\frac{\partial J}{\partial \tilde{\chi}} = \frac{J^{tr} - G_{ur}\Delta \lambda_s}{\left(1 + \frac{6G_{ur}\Delta \lambda_c}{\tilde{\chi}^2 M^2}\right)^2}\frac{12G_{ur}\Delta \lambda_c}{\tilde{\chi}^3 M^2} = \frac{J}{1 + \frac{6G_{ur}\Delta \lambda_c}{\tilde{\chi}^2 M^2}}\frac{12G_{ur}\Delta \lambda_c}{\tilde{\chi}^3 M^2} \tag{8.211}$$

$$\frac{\partial \tilde{\boldsymbol{s}}}{\partial \Delta \boldsymbol{e}} = 2\tilde{G}_{ur}\mathbf{Q} \tag{8.212}$$

$$\frac{\partial \tilde{\boldsymbol{s}}}{\partial \tilde{G}_{ur}} = 2\mathbf{Q}\Delta \boldsymbol{e}, \quad \frac{\partial \tilde{G}_{ur}}{\partial \tilde{\sigma}_m} = G_{ur}^{\mathrm{p,ref}}\widetilde{\mathrm{d}\hat{f}_E} \tag{8.213}$$

to give the matrix $\mathbf{E}_2$ in the form

$$\mathbf{E}_2 = \frac{\mathrm{d}\boldsymbol{s}}{\mathrm{d}\tilde{\chi}}\left(\frac{\partial \tilde{\chi}}{\partial \tilde{\boldsymbol{s}}}\right)^{\mathsf{T}}\left[\frac{\partial \tilde{\boldsymbol{s}}}{\partial \Delta \boldsymbol{e}}\frac{\partial \Delta \boldsymbol{e}}{\partial \boldsymbol{\varepsilon}} + \frac{\partial \tilde{\boldsymbol{s}}}{\partial \tilde{G}_{ur}}\frac{\partial \tilde{G}_{ur}}{\partial \tilde{\sigma}_m}\left(\frac{\mathrm{d}\tilde{\sigma}_m}{\mathrm{d}\boldsymbol{\varepsilon}}\right)^{\mathsf{T}}\right] = \mathbf{E}_{21} + \mathbf{E}_{22} \tag{8.214}$$

$$\mathbf{E}_{21} = \frac{\mathrm{d}\boldsymbol{s}}{\mathrm{d}\tilde{\chi}}\left(\frac{\partial \tilde{\chi}}{\partial \tilde{\boldsymbol{s}}}\right)^{\mathsf{T}}\frac{\partial \tilde{\boldsymbol{s}}}{\partial \Delta \boldsymbol{e}}\frac{\partial \Delta \boldsymbol{e}}{\partial \boldsymbol{\varepsilon}} \tag{8.215}$$

$$\mathbf{E}_{22} = \frac{\mathrm{d}\boldsymbol{s}}{\mathrm{d}\tilde{\chi}}\left(\frac{\partial \tilde{\chi}}{\partial \tilde{\boldsymbol{s}}}\right)^{\mathsf{T}}\frac{\partial \tilde{\boldsymbol{s}}}{\partial \tilde{G}_{ur}}\frac{\partial \tilde{G}_{ur}}{\partial \tilde{\sigma}_m}\left(\frac{\mathrm{d}\tilde{\sigma}_m}{\mathrm{d}\boldsymbol{\varepsilon}}\right)^{\mathsf{T}} \tag{8.216}$$

With reference to Eqs. (8.187) and (8.188) the first total derivative on the right hand side of Eq. (8.184) becomes

$$\frac{\mathrm{d}\sigma_m}{\mathrm{d}\boldsymbol{\varepsilon}} = \frac{\partial \sigma_m}{\partial \boldsymbol{\varepsilon}} + \frac{\partial \sigma_m}{\partial K_{ur}}\frac{\partial K_{ur}}{\partial E_{ur}}\frac{\partial E_{ur}}{\partial \sigma_m}\frac{\mathrm{d}\sigma_m}{\mathrm{d}\boldsymbol{\varepsilon}} + \frac{\partial \sigma_m}{\partial M_\psi}\frac{\partial M_\psi}{\partial \sin \psi_m}\frac{\partial \sin \psi_m}{\partial \sin \varphi_m}\frac{\mathrm{d}\sin \varphi_m}{\mathrm{d}\boldsymbol{\varepsilon}} +$$
$$+ \frac{\partial \sigma_m}{\partial \Delta \lambda_s}\frac{\partial \Delta \lambda_s}{\partial \boldsymbol{\varepsilon}} + \frac{\partial \sigma_m}{\partial \Delta \lambda_c}\frac{\partial \Delta \lambda_c}{\partial \boldsymbol{\varepsilon}} \tag{8.217}$$

where the term $\dfrac{\mathrm{d}\sin \varphi_m}{\mathrm{d}\boldsymbol{\varepsilon}}$ expands as

$$\frac{\mathrm{d}\sin \varphi_m}{\mathrm{d}\boldsymbol{\varepsilon}} = \frac{\partial \sin \varphi_m}{\partial \sigma_m}\frac{\mathrm{d}\sigma_m}{\mathrm{d}\boldsymbol{\varepsilon}} + \frac{\partial \sin \varphi_m}{\partial J}\frac{\mathrm{d}J}{\mathrm{d}\boldsymbol{\varepsilon}} + \frac{\partial \sin \varphi_m}{\partial I_{3s}}\frac{\mathrm{d}I_{3s}}{\mathrm{d}\boldsymbol{\varepsilon}} \tag{8.218}$$

$$\frac{\partial \sin \varphi_m}{\partial \sigma_m} = \frac{1}{2\sqrt{I_\sigma}}\left[\frac{\partial I_\sigma}{\partial I_{1\sigma}}\frac{\partial I_{1\sigma}}{\partial \sigma_m} + \frac{\partial I_\sigma}{\partial I_{2\sigma}}\frac{\partial I_{2\sigma}}{\partial \sigma_m} + \frac{\partial I_\sigma}{\partial I_{3\sigma}}\frac{\partial I_{3\sigma}}{\partial \sigma_m}\right] = \frac{1}{2\sqrt{I_\sigma}}\frac{\partial I_\sigma}{\partial \sigma_m} \tag{8.219}$$

$$\frac{\partial \sin \varphi_m}{\partial J} = \frac{1}{2\sqrt{I_\sigma}}\left[\frac{\partial I_\sigma}{\partial I_{2\sigma}}\frac{\partial I_{2\sigma}}{\partial J} + \frac{\partial I_\sigma}{\partial I_{3\sigma}}\frac{\partial I_{3\sigma}}{\partial J}\right] = \frac{1}{2\sqrt{I_\sigma}}\frac{\partial I_\sigma}{\partial J} \tag{8.220}$$

$$\frac{\partial \sin \varphi_m}{\partial I_{3s}} = \frac{1}{2\sqrt{I_\sigma}}\frac{\partial I_\sigma}{\partial I_{3\sigma}}\frac{\partial I_{3\sigma}}{\partial I_{3s}} = \frac{1}{2\sqrt{I_\sigma}}\frac{\partial I_\sigma}{\partial I_{3s}} \tag{8.221}$$

It will prove useful to write the terms $\dfrac{\mathrm{d}J}{\mathrm{d}\varepsilon}$ and $\dfrac{\mathrm{d}I_{3s}}{\mathrm{d}\varepsilon}$ as

$$\frac{\mathrm{d}J}{\mathrm{d}\varepsilon} = \left[\left(\frac{\partial J}{\partial \boldsymbol{s}}\right)^{\mathsf{T}} \frac{\mathrm{d}\boldsymbol{s}}{\mathrm{d}\varepsilon}\right]^{\mathsf{T}} = \left[\frac{\mathrm{d}\boldsymbol{s}}{\mathrm{d}\varepsilon}\right]^{\mathsf{T}} \frac{\partial J}{\partial \boldsymbol{s}} \tag{8.222}$$

$$\frac{\mathrm{d}I_{3s}}{\mathrm{d}\varepsilon} = \left[\frac{\mathrm{d}\boldsymbol{s}}{\mathrm{d}\varepsilon}\right]^{\mathsf{T}} \frac{\partial I_{3s}}{\partial \boldsymbol{s}} \tag{8.223}$$

With the help of Eqs. (8.218), (8.222), (8.223) and (8.193), recall also Eq. (8.120), we rewrite Eq. (8.217) after some lengthy manipulation as

$$\frac{\mathrm{d}\sigma_m}{\mathrm{d}\varepsilon} = \boldsymbol{b}_1 + b_{2s}\frac{\partial \Delta\lambda_s}{\partial \varepsilon} + b_{2c}\frac{\partial \Delta\lambda_c}{\partial \varepsilon}, \quad \boldsymbol{b}_1 = \frac{\boldsymbol{a}_1}{1 - a_2}, \quad b_{2s} = \frac{a_{3s}}{1 - a_2}, \quad b_{2c} = \frac{a_{3c}}{1 - a_2} \tag{8.224}$$

$$\boldsymbol{a}_1 = \frac{\partial \sigma_m}{\partial \varepsilon} + \frac{\partial \sigma_m}{\partial M_\psi}\frac{\partial M_\psi}{\partial \sin\psi_m}\frac{\partial \sin\psi_m}{\partial \sin\varphi_m}\mathbf{E}^{\mathsf{T}}\left(\frac{\partial \sin\varphi_m}{\partial J}\frac{\partial J}{\partial \boldsymbol{s}} + \frac{\partial \sin\varphi_m}{\partial I_{3s}}\frac{\partial I_{3s}}{\partial \boldsymbol{s}}\right)$$

$$a_2 = \frac{\partial \sigma_m}{\partial K_{ur}}\frac{\partial K_{ur}}{\partial E_{ur}}\frac{\partial E_{ur}}{\partial \sigma_m} + \frac{\partial \sigma_m}{\partial M_\psi}\frac{\partial M_\psi}{\partial \sin\psi_m}\frac{\partial \sin\psi_m}{\partial \sin\varphi_m}\frac{\mathrm{d}\sin\varphi_m}{\mathrm{d}\sigma_m} = 1 - \frac{\mathrm{d}r_1}{\mathrm{d}\sigma_m}$$

$$a_{3s} = \frac{\partial \sigma_m}{\partial \Delta\lambda_s} + \frac{\partial \sigma_m}{\partial M_\psi}\frac{\partial M_\psi}{\partial \sin\psi_m}\frac{\partial \sin\psi_m}{\partial \sin\varphi_m}\left(\frac{\partial \sin\varphi_m}{\partial J}\left(\frac{\partial J}{\partial \boldsymbol{s}}\right)^{\mathsf{T}} + \frac{\partial \sin\varphi_m}{\partial I_{3s}}\left(\frac{\partial I_{3s}}{\partial \boldsymbol{s}}\right)^{\mathsf{T}}\right)\boldsymbol{s}_2$$

$$a_{3c} = \frac{\partial \sigma_m}{\partial \Delta\lambda_c} + \frac{\partial \sigma_m}{\partial M_\psi}\frac{\partial M_\psi}{\partial \sin\psi_m}\frac{\partial \sin\psi_m}{\partial \sin\varphi_m}\left(\frac{\partial \sin\varphi_m}{\partial J}\left(\frac{\partial J}{\partial \boldsymbol{s}}\right)^{\mathsf{T}} + \frac{\partial \sin\varphi_m}{\partial I_{3s}}\left(\frac{\partial I_{3s}}{\partial \boldsymbol{s}}\right)^{\mathsf{T}}\right)\boldsymbol{s}_3$$

$$\frac{\partial \sigma_m}{\partial \varepsilon} = \frac{\partial \sigma_m}{\partial \Delta\varepsilon_v}\frac{\partial \Delta\varepsilon_v}{\partial \varepsilon} = \frac{K_{ur}(\widehat{\overline{\sigma}}_m)}{1 + 2K_{ur}(\widehat{\overline{\sigma}}_m)\Delta\lambda_c}3\boldsymbol{m} \tag{8.225}$$

where $\mathbf{E} = \mathbf{E}_1 + \mathbf{E}_2$.

As evident from Eqs. (8.193) and (8.224) one still needs to determine the terms $\dfrac{\partial \Delta\lambda_s}{\partial \varepsilon}$ and $\dfrac{\partial \Delta\lambda_c}{\partial \varepsilon}$. Because both the shear and cap yield functions are equal to zero at the end of the local stress update and the consistency condition is satisfied, see also [14], we may write

$$\frac{\mathrm{d}r_i}{\mathrm{d}\varepsilon} = \boldsymbol{0} \tag{8.226}$$

$$r_2 = f_s^{HS} \text{ or } f_s^{MN}, \quad r_3 = f_c^{HS} \tag{8.227}$$

Starting from the hardening shear yield surface f_s^{HS} we get

$$\frac{\mathrm{d}r_2}{\mathrm{d}\varepsilon} = \frac{\partial r_2}{\partial J}\frac{\mathrm{d}J}{\mathrm{d}\varepsilon} + \frac{\partial r_2}{\partial E_i}\frac{\partial E_i}{\partial \sigma_m}\frac{\mathrm{d}\sigma_m}{\mathrm{d}\varepsilon} + \frac{\partial r_2}{\partial \sin\varphi_m}\frac{\mathrm{d}\sin\varphi_m}{\mathrm{d}\varepsilon} + \frac{\partial r_2}{\partial \kappa_s}\frac{\partial \kappa_s}{\partial \Delta\lambda_s}\frac{\partial \Delta\lambda_s}{\partial \varepsilon} = 0 \tag{8.228}$$

which upon substituting Eqs. (8.218), (8.222) and (8.223) rewrites as

$$\frac{\mathrm{d}r_2}{\mathrm{d}\varepsilon} = \left(\frac{\partial r_2}{\partial E_i}\frac{\partial E_i}{\partial \sigma_m} + \frac{\partial r_2}{\partial \sin\varphi_m}\frac{\partial \sin\varphi_m}{\partial \sigma_m}\right)\frac{\mathrm{d}\sigma_m}{\mathrm{d}\varepsilon} +$$

$$+ \left(\frac{\partial r_2}{\partial J} + \frac{\partial r_2}{\partial \sin\varphi_m}\frac{\partial \sin\varphi_m}{\partial J}\right)\left[\frac{\mathrm{d}\boldsymbol{s}}{\mathrm{d}\varepsilon}\right]^{\mathsf{T}}\frac{\partial J}{\partial \boldsymbol{s}} + \frac{\partial r_2}{\partial \sin\varphi_m}\frac{\partial \sin\varphi_m}{\partial I_{3s}}\left[\frac{\mathrm{d}\boldsymbol{s}}{\mathrm{d}\varepsilon}\right]^{\mathsf{T}}\frac{\partial I_{3s}}{\partial \boldsymbol{s}} +$$

$$+ \frac{\partial r_2}{\partial \kappa_s}\frac{\partial \kappa_s}{\partial \Delta\lambda_s}\frac{\partial \Delta\lambda_s}{\partial \varepsilon} \tag{8.229}$$

$$= c_1\frac{\mathrm{d}\sigma_m}{\mathrm{d}\varepsilon} + c_2\left[\frac{\mathrm{d}\boldsymbol{s}}{\mathrm{d}\varepsilon}\right]^{\mathsf{T}}\boldsymbol{j}_1 + c_3\left[\frac{\mathrm{d}\boldsymbol{s}}{\mathrm{d}\varepsilon}\right]^{\mathsf{T}}\boldsymbol{j}_2 + c_4\frac{\partial \Delta\lambda_s}{\partial \varepsilon} = \boldsymbol{0} \tag{8.230}$$

When the Matsuoka-Nakai yield surface is active we write Eq.(8.226) as

$$\frac{\mathrm{d}r_2}{\mathrm{d}\boldsymbol{\varepsilon}} = \frac{\partial I_\sigma}{\partial \sigma_m}\frac{\mathrm{d}\sigma_m}{\mathrm{d}\boldsymbol{\varepsilon}} + \frac{\partial I_\sigma}{\partial J}\frac{\mathrm{d}J}{\mathrm{d}\boldsymbol{\varepsilon}} + \frac{\partial I_\sigma}{\partial I_{3s}}\frac{\mathrm{d}I_{3s}}{\mathrm{d}\boldsymbol{\varepsilon}} \tag{8.231}$$

$$= \frac{\partial I_\sigma}{\partial \sigma_m}\frac{\mathrm{d}\sigma_m}{\mathrm{d}\boldsymbol{\varepsilon}} + \frac{\partial I_\sigma}{\partial J}\left[\frac{\mathrm{d}\boldsymbol{s}}{\mathrm{d}\boldsymbol{\varepsilon}}\right]^{\mathsf{T}}\frac{\partial J}{\partial \boldsymbol{s}} + \frac{\partial I_\sigma}{\partial I_{3s}}\left[\frac{\mathrm{d}\boldsymbol{s}}{\mathrm{d}\boldsymbol{\varepsilon}}\right]^{\mathsf{T}}\frac{\partial I_{3s}}{\partial \boldsymbol{s}} \tag{8.232}$$

$$= c_1\frac{\mathrm{d}\sigma_m}{\mathrm{d}\boldsymbol{\varepsilon}} + c_2\left[\frac{\mathrm{d}\boldsymbol{s}}{\mathrm{d}\boldsymbol{\varepsilon}}\right]^{\mathsf{T}}\boldsymbol{j}_1 + c_3\left[\frac{\mathrm{d}\boldsymbol{s}}{\mathrm{d}\boldsymbol{\varepsilon}}\right]^{\mathsf{T}}\boldsymbol{j}_2 + c_4(=0)\frac{\partial \Delta\lambda_s}{\partial \boldsymbol{\varepsilon}} \tag{8.233}$$

$$= \boldsymbol{g}_1 + (c_1 b_{2s} + c_4(=0) + d_1)\frac{\partial \Delta\lambda_s}{\partial \boldsymbol{\varepsilon}} + (c_1 b_{2c} + d_2)\frac{\partial \Delta\lambda_c}{\partial \boldsymbol{\varepsilon}} = \boldsymbol{0} \tag{8.234}$$

where the derivatives $\dfrac{\partial I_\sigma}{\partial \sigma_m}, \dfrac{\partial I_\sigma}{\partial J}, \dfrac{\partial I_\sigma}{\partial I_{3s}}$ were introduced in Eqs. (8.219), (8.220), (8.221). Finally, introducing Eqs. (8.193) and (8.224) into either Eq. (8.230) or Eq. (8.234) gives

$$\frac{\mathrm{d}r_2}{\mathrm{d}\boldsymbol{\varepsilon}} = \boldsymbol{g}_1 + h_{11}\frac{\partial \Delta\lambda_s}{\partial \boldsymbol{\varepsilon}} + h_{12}\frac{\partial \Delta\lambda_c}{\partial \boldsymbol{\varepsilon}} = \boldsymbol{0} \tag{8.235}$$

$$\boldsymbol{g}_1 = c_1\boldsymbol{b}_1 + \left(\mathbf{E}^{\mathsf{T}} + \boldsymbol{b}_1\boldsymbol{s}_1^{\mathsf{T}}\right)(c_2\boldsymbol{j}_1 + c_3\boldsymbol{j}_2)$$

$$h_{11} = c_1 b_{2s} + c_4 + d_1$$

$$h_{12} = c_1 b_{2c} + d_2$$

$$d_1 = (b_{2s}\boldsymbol{s}_1^{\mathsf{T}} + \boldsymbol{s}_2^{\mathsf{T}})(c_2\boldsymbol{j}_1 + c_3\boldsymbol{j}_2)$$

$$d_2 = (b_{2c}\boldsymbol{s}_1^{\mathsf{T}} + \boldsymbol{s}_3^{\mathsf{T}})(c_2\boldsymbol{j}_1 + c_3\boldsymbol{j}_2)$$

The second equation derives from the consistency condition pertinent to the cap yield surface provided by

$$\frac{\mathrm{d}r_3}{\mathrm{d}\boldsymbol{\varepsilon}} = \frac{\partial r_3}{\partial J}\frac{\mathrm{d}J}{\mathrm{d}\boldsymbol{\varepsilon}} + \frac{\partial r_3}{\partial \chi}\frac{\partial \vartheta}{\partial \vartheta}\frac{\partial \vartheta}{\partial \sin 3\theta}\frac{\mathrm{d}\sin 3\theta}{\mathrm{d}\boldsymbol{\varepsilon}} + \frac{\partial r_3}{\partial \sigma_m}\frac{\mathrm{d}\sigma_m}{\mathrm{d}\boldsymbol{\varepsilon}} + \frac{\partial r_3}{\partial p_c}\frac{\mathrm{d}p_c}{\mathrm{d}\boldsymbol{\varepsilon}} = \boldsymbol{0} \tag{8.236}$$

where the terms $\dfrac{\mathrm{d}\sin 3\theta}{\mathrm{d}\boldsymbol{\varepsilon}}$ and $\dfrac{\mathrm{d}p_c}{\mathrm{d}\boldsymbol{\varepsilon}}$ read

$$\frac{\mathrm{d}\sin 3\theta}{\mathrm{d}\boldsymbol{\varepsilon}} = \frac{\partial \sin 3\theta}{\partial J}\frac{\mathrm{d}J}{\mathrm{d}\boldsymbol{\varepsilon}} + \frac{\partial \sin 3\theta}{\partial I_{3s}}\frac{\mathrm{d}I_{3s}}{\mathrm{d}\boldsymbol{\varepsilon}} \tag{8.237}$$

$$\frac{\mathrm{d}p_c}{\mathrm{d}\boldsymbol{\varepsilon}} = \frac{\mathrm{d}p_c}{\mathrm{d}\sigma_m}\frac{\mathrm{d}\sigma_m}{\mathrm{d}\boldsymbol{\varepsilon}} + \frac{\partial p_c}{\partial \Delta\lambda_c}\frac{\partial \Delta\lambda_c}{\partial \boldsymbol{\varepsilon}} \tag{8.238}$$

In analogy with the previous steps we first substitute from Eqs. (8.237) and (8.238) into Eq. (8.236) while taking into account Eqs. (8.222) and (8.223) to get

$$\frac{\mathrm{d}r_3}{\mathrm{d}\boldsymbol{\varepsilon}} = \left(\frac{\partial r_3}{\partial \sigma_m} + \frac{\partial r_3}{\partial p_c}\frac{\mathrm{d}p_c}{\mathrm{d}\sigma_m}\right)\frac{\mathrm{d}\sigma_m}{\mathrm{d}\boldsymbol{\varepsilon}} +$$

$$+ \left(\frac{\partial r_3}{\partial J} + \frac{\partial r_3}{\partial \chi}\frac{\partial \vartheta}{\partial \vartheta}\frac{\partial \sin 3\theta}{\partial \sin 3\theta}\frac{\partial \sin 3\theta}{\partial J}\right)\left[\frac{\mathrm{d}\boldsymbol{s}}{\mathrm{d}\boldsymbol{\varepsilon}}\right]^{\mathsf{T}}\frac{\partial J}{\partial \boldsymbol{s}} + \frac{\partial r_3}{\partial \chi}\frac{\partial \vartheta}{\partial \vartheta}\frac{\partial \sin 3\theta}{\partial \sin 3\theta}\frac{\partial \sin 3\theta}{\partial I_{3s}}\left[\frac{\mathrm{d}\boldsymbol{s}}{\mathrm{d}\boldsymbol{\varepsilon}}\right]^{\mathsf{T}}\frac{\partial I_{3s}}{\partial \boldsymbol{s}} +$$

$$+ \frac{\partial r_3}{\partial p_c}\frac{\partial p_c}{\partial \Delta\lambda_c}\frac{\partial \Delta\lambda_c}{\partial \boldsymbol{\varepsilon}} \tag{8.239}$$

$$= c_5\frac{\mathrm{d}\sigma_m}{\mathrm{d}\boldsymbol{\varepsilon}} + c_6\left[\frac{\mathrm{d}\boldsymbol{s}}{\mathrm{d}\boldsymbol{\varepsilon}}\right]^{\mathsf{T}}\boldsymbol{j}_1 + c_7\left[\frac{\mathrm{d}\boldsymbol{s}}{\mathrm{d}\boldsymbol{\varepsilon}}\right]^{\mathsf{T}}\boldsymbol{j}_2 + c_8\frac{\partial \Delta\lambda_c}{\partial \boldsymbol{\varepsilon}} = \boldsymbol{0} \tag{8.240}$$

The final step again represents substitution Eqs. (8.193) and (8.224) into Eq. (8.240) to arrive at

$$\frac{\mathrm{d}r_3}{\mathrm{d}\boldsymbol{\varepsilon}} = \boldsymbol{g}_2 + h_{21}\frac{\partial \Delta\lambda_s}{\partial \boldsymbol{\varepsilon}} + h_{22}\frac{\partial \Delta\lambda_c}{\partial \boldsymbol{\varepsilon}} = \boldsymbol{0} \tag{8.241}$$

$$\boldsymbol{g}_2 = c_5\boldsymbol{b}_1 + \left(\mathbf{E}^{\mathsf{T}} + \boldsymbol{b}_1\boldsymbol{s}_1^{\mathsf{T}}\right)(c_6\boldsymbol{j}_1 + c_7\boldsymbol{j}_2)$$

$$h_{21} = c_5 b_{2s} + d_3$$

$$h_{22} = c_5 b_{2c} + c_8 + d_4$$

$$d_3 = (b_{2s}\boldsymbol{s}_1^{\mathsf{T}} + \boldsymbol{s}_2^{\mathsf{T}})(c_6\boldsymbol{j}_1 + c_7\boldsymbol{j}_2)$$

$$d_4 = (b_{2c}\boldsymbol{s}_1^{\mathsf{T}} + \boldsymbol{s}_3^{\mathsf{T}})(c_6\boldsymbol{j}_1 + c_7\boldsymbol{j}_2)$$

Several scenarios may now occur:

- **Both the shear and cap yield surfaces are simultaneously active**
  In such a case Eqs. (8.193) and (8.224) yield the system of equations

$$
\begin{bmatrix} h_{11} & h_{12} \\ h_{21} & h_{22} \end{bmatrix}
\left\{ \begin{array}{c} \left(\dfrac{\partial \Delta \lambda_s}{\partial \varepsilon}\right)^{\mathsf{T}} \\ \left(\dfrac{\partial \Delta \lambda_c}{\partial \varepsilon}\right)^{\mathsf{T}} \end{array} \right\}
= \left\{ \begin{array}{c} -\boldsymbol{g}_1^{\mathsf{T}} \\ -\boldsymbol{g}_2^{\mathsf{T}} \end{array} \right\}
\tag{8.242}
$$

  to be solved for $\dfrac{\partial \Delta \lambda_s}{\partial \varepsilon}$ and $\dfrac{\partial \Delta \lambda_c}{\partial \varepsilon}$ as

$$
\frac{\partial \Delta \lambda_s}{\partial \varepsilon} = \boldsymbol{q}_1 = \frac{1}{h_{11} h_{22} - h_{12} h_{21}} \left(-h_{22} \boldsymbol{g}_1 + h_{12} \boldsymbol{g}_2 \right)
\tag{8.243}
$$

$$
\frac{\partial \Delta \lambda_c}{\partial \varepsilon} = \boldsymbol{q}_2 = \frac{1}{h_{11} h_{22} - h_{12} h_{21}} \left(h_{21} \boldsymbol{g}_1 - h_{11} \boldsymbol{g}_2 \right)
\tag{8.244}
$$

  Introducing the vectors $\boldsymbol{q}_1$ and $\boldsymbol{q}_2$ into Eqs. (8.193) and (8.224) then gives the algorithmic tangent stiffness matrix $\boldsymbol{\mathcal{D}}$, Eq. (8.184), in the form

$$
\boldsymbol{\mathcal{D}} = \mathbf{E} + \mathbf{A} + \mathbf{B} + \mathbf{C}
\tag{8.245}
$$

  where

$$
\mathbf{A} = (3\boldsymbol{m} + \boldsymbol{s}_1)\boldsymbol{b}_1^{\mathsf{T}}
\tag{8.246}
$$

$$
\mathbf{B} = [(3\boldsymbol{m} + \boldsymbol{s}_1)b_{2s} + \boldsymbol{s}_2)]\boldsymbol{q}_1^{\mathsf{T}}
\tag{8.247}
$$

$$
\mathbf{C} = [(3\boldsymbol{m} + \boldsymbol{s}_1)b_{2c} + \boldsymbol{s}_3)]\boldsymbol{q}_2^{\mathsf{T}}
\tag{8.248}
$$

- **Only the hardening shear yield surface or the Matsuoka-Nakai yield surface is active**
  We then start from Eq. (8.235) while setting $\dfrac{\partial \Delta \lambda_c}{\partial \varepsilon} = 0$ to get

$$
\frac{\mathrm{d} r_2}{\mathrm{d} \varepsilon} = \boldsymbol{g}_1 + h_{11} \frac{\partial \Delta \lambda_s}{\partial \varepsilon} = \mathbf{0} \longrightarrow \frac{\partial \Delta \lambda_s}{\partial \varepsilon} = -\frac{1}{h_{11}} \boldsymbol{g}_1 = \boldsymbol{q}_1
\tag{8.249}
$$

  Substituting the vector $\boldsymbol{q}_1$ back into Eqs. (8.193) and (8.224) gives Eq. (8.184) in the form

$$
\boldsymbol{\mathcal{D}} = \mathbf{E} + \mathbf{A} + \mathbf{B}
\tag{8.250}
$$

  where

$$
\mathbf{A} = (3\boldsymbol{m} + \boldsymbol{s}_1)\boldsymbol{b}_1^{\mathsf{T}}
\tag{8.251}
$$

$$
\mathbf{B} = [(3\boldsymbol{m} + \boldsymbol{s}_1)b_{2s} + \boldsymbol{s}_2)]\boldsymbol{q}_1^{\mathsf{T}}
\tag{8.252}
$$

- **Only the cap yield surface is active**
  This is the case when $\dfrac{\partial \Delta \lambda_s}{\partial \varepsilon} = 0$ so Eq. (8.241) yields

$$
\frac{\mathrm{d} r_3}{\mathrm{d} \varepsilon} = \boldsymbol{g}_2 + h_{22} \frac{\partial \Delta \lambda_c}{\partial \varepsilon} = \mathbf{0} \longrightarrow \frac{\partial \Delta \lambda_c}{\partial \varepsilon} = -\frac{1}{h_{22}} \boldsymbol{g}_2 = \boldsymbol{q}_2
\tag{8.253}
$$

  Substituting the vector $\boldsymbol{q}_2$ back into Eqs. (8.193) and (8.224) gives Eq. (8.184) in the form

$$
\boldsymbol{\mathcal{D}} = \mathbf{E} + \mathbf{A} + \mathbf{C}
\tag{8.254}
$$

  where

$$
\mathbf{A} = (3\boldsymbol{m} + \boldsymbol{s}_1)\boldsymbol{b}_1^{\mathsf{T}}
\tag{8.255}
$$

$$
\mathbf{C} = [(3\boldsymbol{m} + \boldsymbol{s}_1)b_{2c} + \boldsymbol{s}_3)]\boldsymbol{q}_2^{\mathsf{T}}
\tag{8.256}
$$

- **Nonlinear elasticity**

  Adopting Eqs. (8.193) and (8.224) while setting $\dfrac{\partial \Delta \lambda_s}{\partial \varepsilon} = \dfrac{\partial \Delta \lambda_c}{\partial \varepsilon} = 0$ together with

  $$a_1 = 3K_{ur}(\widehat{\overline{\sigma}}_m)\boldsymbol{m} \tag{8.257}$$

  $$a_2 = \frac{\partial \sigma_m}{\partial K_{ur}}\frac{\partial K_{ur}}{\partial E_{ur}}\frac{\partial E_{ur}}{\partial \sigma_m} \tag{8.258}$$

  $$\tag{8.259}$$

  gives Eq. (8.184) in the form

  $$\boldsymbol{\mathcal{D}} = \mathsf{E} + \frac{9K_{ur}(\widehat{\overline{\sigma}}_m)}{1 - a_2}\boldsymbol{m}\boldsymbol{m}^\mathsf{T} \tag{8.260}$$

  $$\mathsf{E} = 2G_{ur}(\widehat{\overline{\sigma}}_m)\mathsf{Q}\mathsf{P}\mathsf{Q} \tag{8.261}$$

  Note that when setting $K_{ur}(\widehat{\overline{\sigma}}_m) = K_{ur}^{\mathrm{p,ref}}$ and $G_{ur}(\widehat{\overline{\sigma}}_m) = G_{ur}^{\mathrm{p,ref}}$ gives standard linear elastic stiffness matrix in the form

  $$[\mathcal{D}] = \mathsf{E} + 9K_{ur}^{\mathrm{p,ref}}\boldsymbol{m}\boldsymbol{m}^\mathsf{T} \tag{8.262}$$

  $$\mathsf{E} = 2G_{ur}^{\mathrm{p,ref}}\mathsf{Q}\mathsf{P}\mathsf{Q} \tag{8.263}$$

8.5 Note on numerical implementation

8.5.1 Initializing hardening parameters κ_s and p_c

In GEO5 FEM the initial values of hardening parameters κ_s^{in} and p_c^{in} are calculated on the basis of a given stress observed in the computational model at the time the Hardening soil model is introduced into the calculation step. There are several options which may potentially occur with the GEO5 FEM program, see also the discussion in Section 11.4:

1. Hardening parameters are set based on the geostatic stress provided by K_0 **procedure**, see Section 1.14. The hardening soil model can be introduced even in the 2nd calculation stage when replacing another material model considered in the K_0 **procedure** as therein the type of material model is irrelevant. When using the K_0 **procedure** the vertical σ_3, horizontal $\sigma_1 = \sigma_2$ and mean effective σ_m stresses together with the deviatoric stress measure J and the Lode angle θ are computed as

   $$\sigma_3 = -\gamma h, \quad \sigma_1 = \sigma_2 = K_0^{NC}\sigma_3 \tag{8.264}$$

   $$\sigma_m = \frac{1}{3}\left(1 + 2K_0^{NC}\right)\sigma_3 \tag{8.265}$$

   $$J = \frac{1}{\sqrt{3}}\left(\sigma_1 - \sigma_3\right) \tag{8.266}$$

   $$\theta = \tan^{-1}\left[\frac{1}{\sqrt{3}}\left(2\frac{\sigma_2 - \sigma_3}{\sigma_1 - \sigma_3} - 1\right)\right] \tag{8.267}$$

   where γ is the bulk unit weight, h is the actual depth of a stress point in the soil profile, and K_0^{NC} is the coefficient of lateral earth pressure at rest for normally consolidated soils. These stresses then allow us to define the hardening parameters κ_s^{in} and p_c^{in} such that both the hardening shear and cap yield criteria are satisfied, i.e., $f_s^{HS} = 0$ and $f_c^{HS} = 0$, recall Eqs. (8.15) and (8.62), respectively. This gives

   $$\kappa_s^{in} = \frac{3J}{E_i}\left(\frac{1}{1 - b\tilde{a}} - \frac{E_i^{\mathrm{p,ref}}}{E_{ur}^{\mathrm{p,ref}}}\right) \tag{8.268}$$

   $$p_c^{in} = \sqrt{\frac{3J^2}{\chi^2(\theta, \varphi)M^2} + \sigma_m^2} \tag{8.269}$$

   How to account for overconsolidation is described in Section 1.13.

2. Hardening parameters are set based on the geostatic stress derived by standard stress analysis while considering the **linearly elastic material model** in place of the Hardening soil model. The hardening soil model is introduced in the 2nd calculation stage and replaces the elastic material model adopted in the 1st calculation stage. The initial hardening parameters κ_s^{in} and p_c^{in} then from Eqs. (8.268) and (8.269). Also, with reference to Sections 1.13 and 1.14, the overconsolidation parameters $OCR = 1$ and $POP = 0$ are considered so the soil is assumed to be normally consolidated. To introduce overconsolidation a loading/unloading sequence would have to be introduced.

3. There is **zero initial stress** when introducing the hardening soil model into the analysis. In such a case the shear hardening parameter $\kappa_s^{in} = 0$ and the initial value of preconsolidation pressure $p_c^{in} = 1$ kPa are considered. The initial values of moduli E_i and E_{ur} follow from Eqs. (8.16) and (8.17), i.e., based on the values of cohesion c and angle of internal friction φ or the limiting value σ_L. The subsequent analysis evolution of κ_s and p_c derives from the standard plastic calculation step. Similarly to the previous item the overconsolidation parameters $OCR = 1$ and $POP = 0$ are considered so the soil is assumed to be normally consolidated. To introduce overconsolidation a loading/unloading sequence would have to be introduced.

Owing to the formulation of the Hardening soil model one may also encounter an inadmissible stress state that requires solving the apex problem. Because the plastic potential function is essentially the same as in the case of the Drucker-Prager model, compare Eqs. (4.6) with $a_{pp} = 0$ and (8.70), the procedure described in Section 4.4 is readily available. An indicator that promotes the solution of the apex problem is now given by

$$M_\psi(\sigma_m^{tr}) \frac{J^{tr}}{G(\widehat{\overline{\sigma}}_m^{tr})} - \frac{1}{K(\widehat{\overline{\sigma}}_m^{tr})}(\sigma_m^{tr} - c \cot \varphi) < 0 \tag{8.270}$$

where σ_m^{tr} is the mean stress at the end of the nonlinear elastic step.

8.5.2   Parameter migration between minor and mean stress stiffness formulations

Because of a long history of Hardening soil model and differences in the formulation of stiffness evolution based either on the minor principal stress σ_1 (PLAXIS) and the mean effective stress σ_m (GEO5 FEM) it appears useful to provide a certain conversion tool that transforms the stiffness parameters E^{ref}, m (PLAXIS) to $E^{\text{p,ref}}, m_p$ (GEO5 FEM). Following [58] such a tool could be designed as follows:

1. **Migration of E_{ur}^{ref} and m**
   Perform a simple linear regression to adjust $E_{ur}^{\text{p,ref}}$ and m_p by matching E_{ur} provided by the σ_1-formulation, Eq. (8.21), and σ_m-formulations, Eq. (8.17), respectively. This is mathematically written as

$$\min E_1 = \sum_i \left[\underbrace{E_{ur}^{\text{ref}} \left(\frac{\sigma_1^i - c \cot \varphi}{\sigma^{\text{ref}} - c \cot \varphi} \right)^m}_{y_i} - E_{ur}^{\text{p,ref}} \underbrace{\left(\frac{\sigma_m^i - c \cot \varphi}{\sigma_m^{\text{ref}} - c \cot \varphi} \right)^{m_p}}_{x_i} \right]^2 \tag{8.271}$$

using the least square method. To proceed, we first rewrite Eq. (8.271) as

$$\min E_2 = \sum_i \left[\underbrace{\log y_i}_{Y_i} - \underbrace{\log E_{ur}^{\text{p,ref}}}_{q} - m_p \underbrace{\log x_i}_{X_i} \right]^2 \tag{8.272}$$

Application of the least square method boils down to the solution of the following two algebraic equations

$$\frac{\partial E_2}{\partial q} = \sum_{i=1}^{N}(Y_i - q - m_p X_i) = 0 \tag{8.273}$$

$$\frac{\partial E_2}{\partial m_p} = \sum_{i=1}^{N}(Y_i - q - m_p X_i)X_i = 0 \tag{8.274}$$

so that

$$D = -\sum_{i=1}^{N}X_i\sum_{i=1}^{N}X_i + N\sum_{i=1}^{N}X_i^2 \tag{8.275}$$

$$m_p = \frac{1}{D}\left(-\sum_{i=1}^{N}X_i\sum_{i=1}^{N}Y_i + N\sum_{i=1}^{N}X_iY_i\right) \tag{8.276}$$

$$q = \frac{1}{D}\left(\sum_{i=1}^{N}X_i^2\sum_{i=1}^{N}Y_i - \sum_{i=1}^{N}X_i\sum_{i=1}^{N}X_iY_i\right) \longrightarrow E_{ur}^{\text{p,ref}} = 10^q \tag{8.277}$$

where N is the number of sampling points and σ_1^i and σ_m^i follow from Eqs. (8.264) and (8.265) for a given value of the prescribed vertical stress σ_3^i. Figure 8.6 compares evolution of unloading/reloading stiffness E_{ur} provided by the σ_1- and σ_m-formulations for three different values of K_0^{NC} while assuming $\sigma^{\text{ref}} = \sigma_m^{\text{ref}}$. Point out that $m_p = m$ for cohesion $c = 0$.
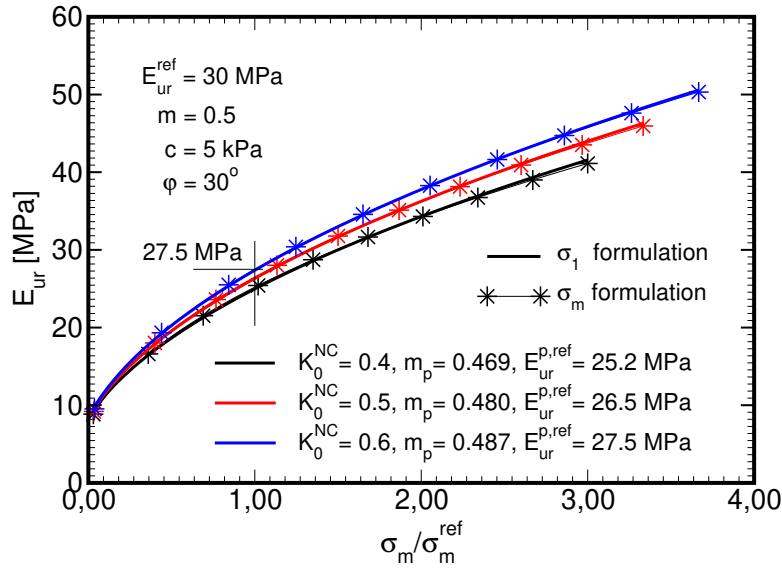
Figure 8.6: Determination of σ_m dependency of unloading/reloading stiffness E_{ur} from linear regression

2. **Migration of E_{50}^{ref}**
   The stiffness parameter $E_{50}^{\text{p,ref}}(E_i^{\text{p,ref}})$ is determined subsequently by matching predictions provided by the σ_1- and σ_m-formulations for the triaxial compression test while taking into account already derived parameters $E_{ur}^{\text{p,ref}}$ and m_p. This also requires the knowledge of $H^{\text{p,ref}}$. It can be estimated from Eq. (8.82) based on the provided ratio $\dfrac{K_s}{K_c}$ and the value of $E_{ur}^{\text{p,ref}}$. With this step the value of R_f can also be potentially adjusted as suggested in [58].

3. **Fine tuning of migrated parameters used in σ_m- formulation**
   One may perform an extra optimization step if starting from the data derived via first two steps and attempt to simultaneously match all three basic laboratory tests, i.e., isotropic compression, one-dimensional compression (oedometer), and triaxial compression, generated by the σ_1- and σ_m- formulations.

Clearly, steps 2 and 3 require having both formulations at hand.

8.5.3   Determining cap model parameters $M, H^{\mathrm{p,ref}}$ on basis of $K_0^{NC}, E_{oed}^{\mathrm{ref}}$

The two model parameters can be either considered directly as input parameters or generated on the basis of the specified values of K_0^{NC} and E_{oed}^{ref} determined at primary loading. The latter approach requires optimization which involves a numerical analysis of an oedometric test. The optimization process is terminated once, see [58],

- The value of K_0^{NC} derived numerically as $K_0^{NC} = \dfrac{\sigma_h}{\sigma_v}|_{\sigma_v=\sigma_{oed}^{\mathrm{ref}}}$ matches the one specified by the user, where $\sigma_{oed}^{\mathrm{ref}}$ represents the reference pressure at which the tangent oedometric modulus E_{oed}^{ref} is found experimentally, see Fig. 8.7(a), and $\sigma_h = \sigma_x, \sigma_v = \sigma_y$ are the horizontal and vertical stress components, respectively.

- The value of E_{oed} equals the value of E_{oed}^{ref} specified by the user.

The numerical experiment is performed in the displacement control regime by gradually increasing the vertical strain through small strain increments $\Delta\varepsilon_3$ until arriving at stress $\sigma_v = \sigma_{oed}^{ref}$ at which the oedometric tangent modulus is calculated as $E_{oed} = \dfrac{\Delta\sigma_3}{\Delta\varepsilon_3}$. The initial value of $H^{\mathrm{p,ref}}$ might be estimated from Eqs. (8.82) and (8.68), while the initial value of $M = 1$ could be assumed. The numerically calculated stress invariants σ_m^* and J^* at the end of optimization process should therefore satisfy

$$\sigma_m^* = \frac{1}{3}(1 + 2K_0^{NC})\sigma_{oed}^{ref} \tag{8.278}$$

$$J^* = -\frac{1}{\sqrt{3}}(1 - K_0^{NC})\sigma_{oed}^{ref}, \quad \sigma_{oed}^{ref} < 0 \tag{8.279}$$

where K_0^{NC} and $\sigma_{oed}^{\mathrm{ref}}$ are specified by the user, see Fig. 8.7(b).
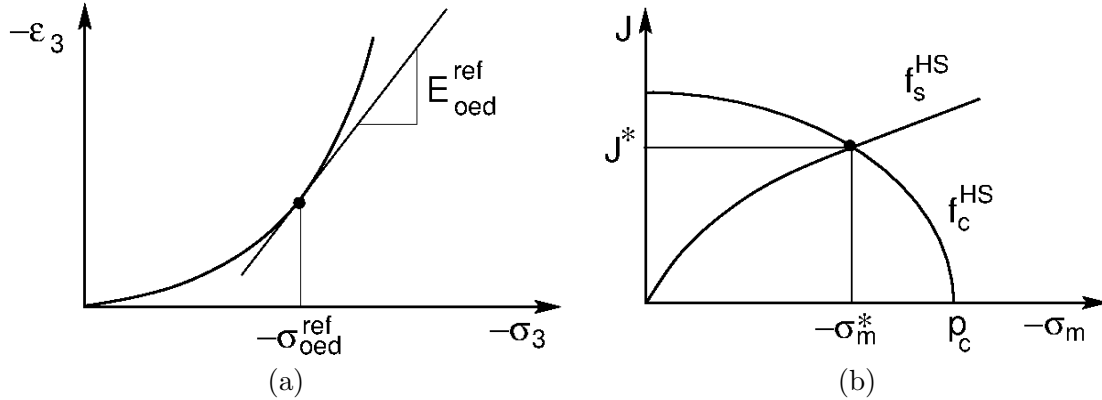
Figure 8.7: a) Graphical representation of reference oedometric modulus determined at reference stress b) Current stresses at the end of optimization process associated with $\sigma_{oed}^{\mathrm{ref}}$

8.6 Testing implementation with simple laboratory tests

Numerical simulation of three basic laboratory tests is performed in this section to examine and compare two potential formulations of nonlinear elasticity presented in Section 8.3, recall Eqs. (8.89) and (8.90). Hereinafter, these formulations will be termed incremental and secant, respectively, and for the sake of clarity both are now reviewed for the bulk response as

- Incremental formulation (currently implemented in GEO5 FEM)

$$\sigma_m^{i+1} = \sigma_m^i + K_{ur}(\widehat{\overline{\sigma}}_m)\Delta\varepsilon_v \tag{8.280}$$

- Secant formulation

$$\sigma_m^{i+1} = K_{ur}(\sigma_m^{i+1})(\varepsilon_v^i + \Delta\varepsilon_v) \tag{8.281}$$

The response derived from Eq. (8.280) will further be compared with that provided by PLAXIS where the unloading/realoding modulus $E_{ur} = E_{ur}(\widehat{\overline{\sigma}}_1)$ is function of the minor principal stress being σ_1 for the assumed standard elasticity sign convention.

In all cases, the computational model consists of two constant strain triangular elements. While the oedometric test is run in a plane strain regime, the axisymmetric state of stress is assumed for isotropic and triaxial compression. The loading and boundary conditions are displayed in Fig. 8.8 for individual cases. All simulations assumed zero initial stress. This is also why the non-zero values of $c = 10$ kPa and $\varphi = 30°$ are adopted together with $E_{ur}^{p,ref} = 30$ MPa and $\sigma_m^{ref} = -100$ kPa to set the initial stiffness of $E_{ur}(\sigma_m = 0)$ according to Eq. (8.17). The value of $m_p = 0.5$ was used. Note that the same values of $E_{ur}^{p,ref} = E_{ur}^{ref}, m_p = m, -\sigma_m^{ref} = p^{ref}$ were adopted also in PLAXIS simulations, recall Section 8.5.2.
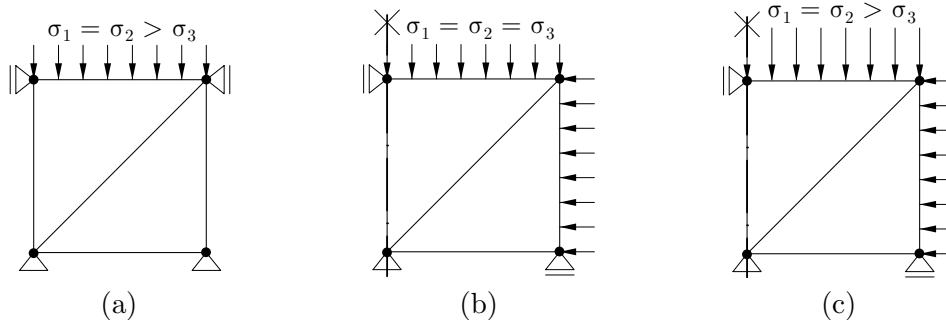
Figure 8.8: Computational models of simple laboratory tests: a) one-dimensional compression (oedometer), b) isotropic compression, c) drained triaxial compression.

We begin with the results that compare the two formulations of nonlinear elasticity. These are plotted for the case of isotropic and oedometric compression in Fig. 8.8. The observed difference between the two approaches is obvious as no adjustments to model parameters, the model parameter m_p in particular, was considered. What, however, is more interesting is the independence of secant formulation on the selected magnitude of load increment for both loading scenarios. Clearly, this is not the case of incremental formulations, being currently implemented in both PLAXIS and GEO5 FEM software. While for the case of isotropic compression this difference is almost negligible owing to a relatively small load step needed to solve Eq. (8.96), the oedometric compression test already reveals the expected load step size dependence. This observation should be taken into account in structural analyses, particularly when starting from a zero initial stress. This issue is addressed in more detail in Section 11.5.1.

Still within the nonlinear elasticity framework the second example aims at comparing the predictions provided by the two previously mentioned softwares. Fig. 8.10(a) shows a reasonable match of the predicted response for the case isotropic compression. This is obviously of no surprise as for this type of analysis the mean and minor principal stresses are the same so the modulus of elasticity E_{ur} evolves in both softwares identically. On the contrary, some differences should be expected for
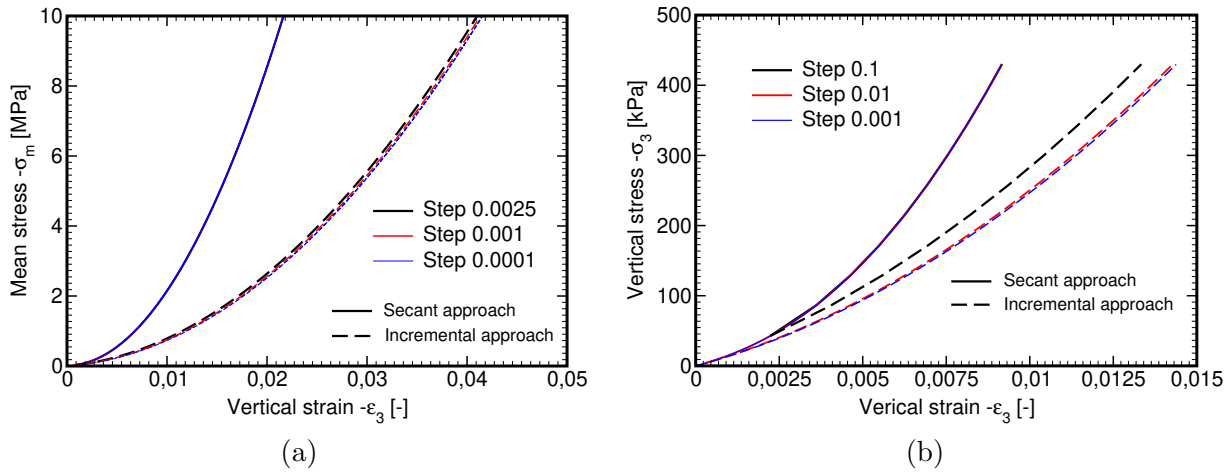
Figure 8.9: **Nonlinear elastic** response, influence of load step magnitude: a) isotropic compression, b) oedometric compression
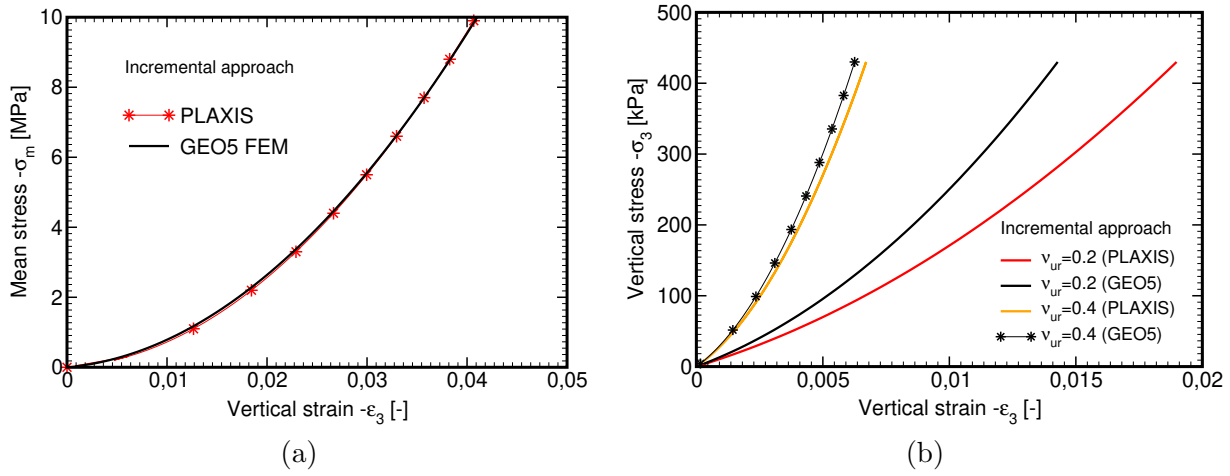
Figure 8.10: **Nonlinear elastic** response, comparing predictions provided by PLAXIS and GEO5 FEM for the same set of data: a) isotropic compression, b) oedometric compression

loading conditions where $\sigma_m \neq \sigma_1$ such as for example the case of oedometric compression presented in Fig. 8.10(b). As already mentioned in Section 8.1.1 this difference becomes less pronounced for larger Poisson ratios as also evident from the presented plots. How to bring these predictions close to each other via adjusting the model parameters $E_{ur}^{\mathrm{p,ref}}, m_p$ is described in Section 8.5.2.

Table 8.2: Material and model parameters [19, 9]. All stiffness and strength parameters are in [kPa] and correspond to σ_1-formulation

Soil	E_i^{ref}	E_{ur}^{ref}	ν_{ur} [-]	σ_m^{ref}	m	c	φ [^{0}]	ψ [^{0}]	M [-]	H^{ref}	R_f
1	18182	30000	0.2	-100	0.50	10	30	5	1.04	25836	0.9
2	54545	90000	0.25	-100	0.55	0	30	16	1.47	71229	0.9
3	3909	11500	0.20	-100	0.80	0	20	0	0.78	1699	0.9

Moving beyond the nonlinear behavior calls for the introduction of additional parameters, namely those defining the plastic potential and cap yield surfaces. The specific material data, adopted in the remaining simulations, are stored in Table 8.2. Note that all these parameters correspond to the σ_1-formulation. While **Soil 1** is taken from [19], **Soil 2**, representing a dense sand, and **Soil 3**, representing a clayey soil, are available in [9]. Here, H^{ref} was found from Eq. (8.82) for the given ratio $\dfrac{K_s}{K_c}$ when substituting $E_{ur}^{\mathrm{p,ref}}$ by E_{ur}^{ref} listed in Table 8.2.

To be consistent with the first set of examples we start from isotropic and oedometric loading
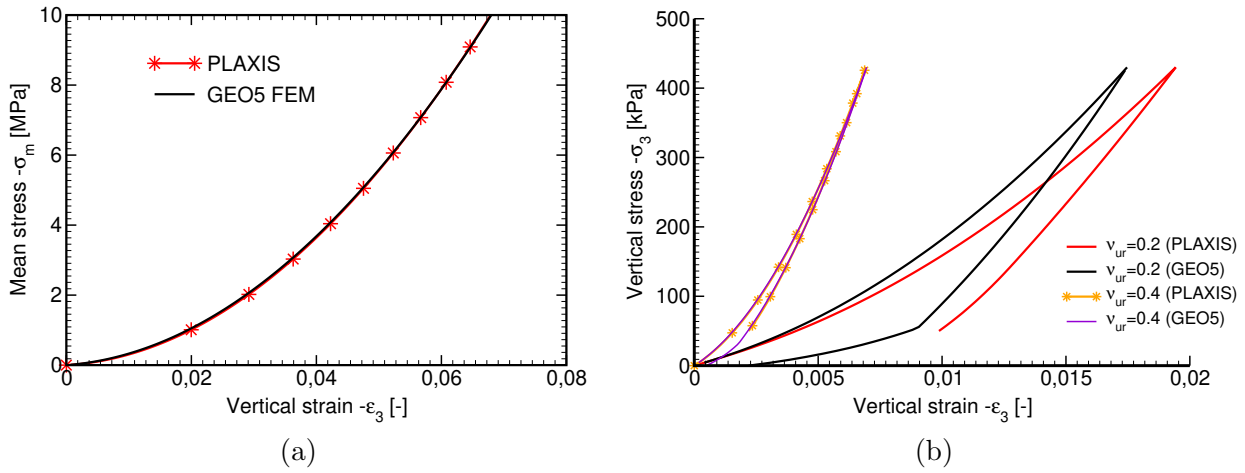
Figure 8.11: **Plastic** response, comparing predictions provided by PLAXIS and GEO5 FEM for the same set of data (**Soil 1**): a) isotropic compression, b) oedometric compression
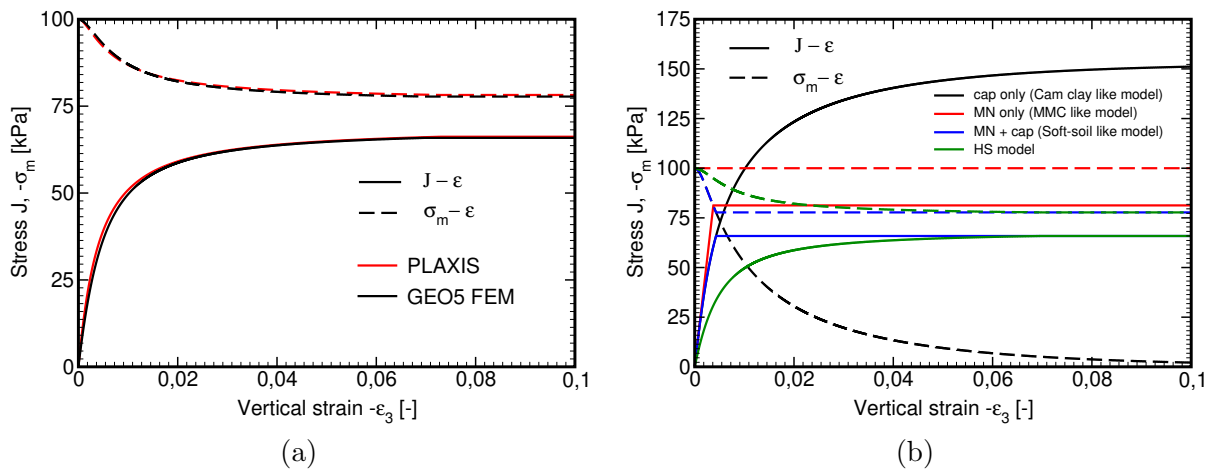
Figure 8.12: **Plastic** response in undrained triaxial compression: a) comparing predictions provided by PLAXIS and GEO5 FEM for the same set of data (**Soil 1**), b) comparing predictions associated with variable combination of active yield surfaces (**Soil 1**)

conditions. Figure 8.11 provides similar observation discussed in previous paragraphs also for plastic loading conditions. Since starting from zero initial stress, the hardening shear yield surface and the cap yield surface are simultaneously active already at the onset of loading. Nevertheless, the ultimate failure surface has not been reached in either of these examples even for relatively large stresses.

Thus to arrive at the Matsuoka-Nakai yield surface we performed yet another simulation pertinent to triaxial loading conditions. The resulting comparison appears in Fig. 8.12(a). Herein, the sample was first isotropically compressed to 100 kPa. Thus triaxial shearing started in both cases, given the data in Table 8.2, from the same stiffness $E_{ur} \approx 34$ MPa. While in PLAXIS this stiffness remained constant as a consequence of no evolution of minor principal stress σ_1, the elastic stiffness $E_{ur}(\sigma_m)$ in GEO5 FEM was gradually reduced as a function of evolving mean effective stress σ_m down to about $E_{ur} = 29$ MPa at the end of loading. This minor difference, however, caused essentially no significant difference in the predictions derived by individual softwares. Also note that in both cases we eventually arrived at an elastic perfectly plastic behavior. It is worth mentioning that in the present simulation of the undrained triaxial test we performed the finite element analysis in the displacement control loading regime by setting $\Delta u_h = -0.5\Delta u_v$ where Δu_h and Δu_v represent increments of the horizontal and vertical displacements, respectively. Given the 1m×1m domain dimensions and axisymmetric state of stress, recall Fig. 8.8(s), this setting maintains zero increment of the volumetric strain $\varepsilon_v = 0$ as required. This is also why the analysis was not terminated when reaching the Matsuoka-Nakai yield surface representing essentially an elastic perfectly plastic material, recall the discussion in Section 4.6.2.

The next example is concerned with the performance of individual facets of the hardening soil model. Figure 8.12(b) shows the performance of the model in undrained triaxial compression when allowing for either a single yield surface or a specific combination of yield surfaces to be active. For example, the red lines were obtained when turning off both the hardening shear and cap yield surfaces thus arriving at predictions identical to those one would obtain with the application of the standard Mohr-Coulomb model. The remaining examples are just for illustration as the present formulation of the cap yield surface is unique to the Hardening soil model. Nevertheless, one may still draw a parallel with, e.g., the Modified cam clay model when allowing for the cap yield surface only to drive the soil response. This prediction is represented by black lines in Fig. 8.12(b). One may identify the critical state which in this particular case corresponds to zero mean effective stress, recall Fig. 8.1(b). Similarly, a Soft soil like model, see Section 9 for its actual formulation, can be imagined if turning off the hardening shear yield surface. This is the case when the Matsuoka-Nakai and cap yield surfaces are only allowed to enter the analysis. This particular combination generates the blue lines in Fig. 8.12(b). As expected, these lines initially follow the black lines as only the cap yield surface is active at this stage of loading. The behavior then turns into the one corresponding to a perfectly plastic material once the Matsuoka-Nakai yield surface is reached.

The last example is devoted to the drained triaxial compression test. To properly arrive at a failure state given by Eq. (8.1) the analysis was carried out in the displacement control regime by prescribing vertical displacements u_v along the top boundary in Fig. 8.8(c) in place of the vertical pressure. Given the preceding isotropic compression stage to generate initial confinement stresses σ_0 equal to $50, 100, 200$ kPa the vertical displacements were set in turn to 0.1, 0.15, and 0.175 m, respectively.
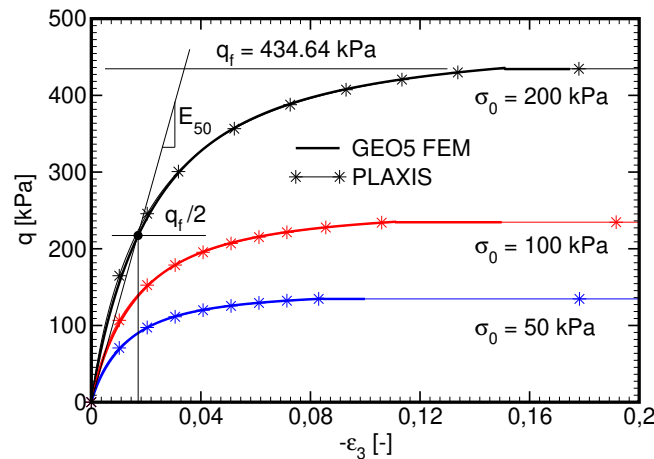
Figure 8.13: Drained triaxial test (**Soil 1**)

The resulting stress-strain curves for **Soil 1**, recall Table 8.2, are plotted in Fig. 8.13, whereas the results obtained for **Soils 2** and **Soil 3** are presented in Fig. 8.14. In all cases we eventually arrived at a failure deviatoric stress q_f. This state is manifested by increasing vertical strain $\varepsilon_3 = u_v$ at zero increment of Δq. Just for illustration we also show in Fig. 8.13 the failure stress associated with $\sigma_0 = -\sigma_1 = 200$ kPa together with $\frac{q_f}{2}$ and the corresponding modulus E_{50}. Recall that the solid lines were derived assuming the evolution moduli E_i and E_{ur} according to Eqs. (8.16) and (8.17), respectively. So in triaxial compression these moduli evolve in dependence on the evolution of mean effective stress σ_m. This is in contradiction to the original formulation implemented in PLAXIS where, in accord with Eq. (8.21), these moduli remain constant as the minor principal stress σ_1 does not change, recall the previous discussion devoted to the results derived for undrained conditions. Taking into account Eq. (8.20) the value of E_i in Table 8.2 gives $E_{50}^{p,ref} = 10$ MPa. Because the same data without any adjustments were adopted also in comparative simulations performed in PLAXIS we also have $E_{50}^{p,ref} = E_{50}^{ref}$. Equation (8.21) yields $E_{50} = 13.6$ MPa which is almost identical to the value of $E_{50} = 13.4$ MPa obtained from simulations via PLAXIS. On the other hand, GEO5 FEM gives the E_{50} modulus in the range of $13.6 - 17.4$ MPa. Nevertheless, the predictions provided by both

softwares are, similar to an undrained compression test, essentially indistinguishable for the **Soil 1** set of data. It is also worth mentioning that in this way one should recover $E_{50} = E_{50}^{\text{ref}}$ from Fig. 8.13 when considering the value of confining pressure $\sigma_0 = \sigma^{\text{ref}} = -100$ kPa and the σ_1−formulation (PLAXIS). As already mentioned this is the principal advantage of using the σ_1−formulation.
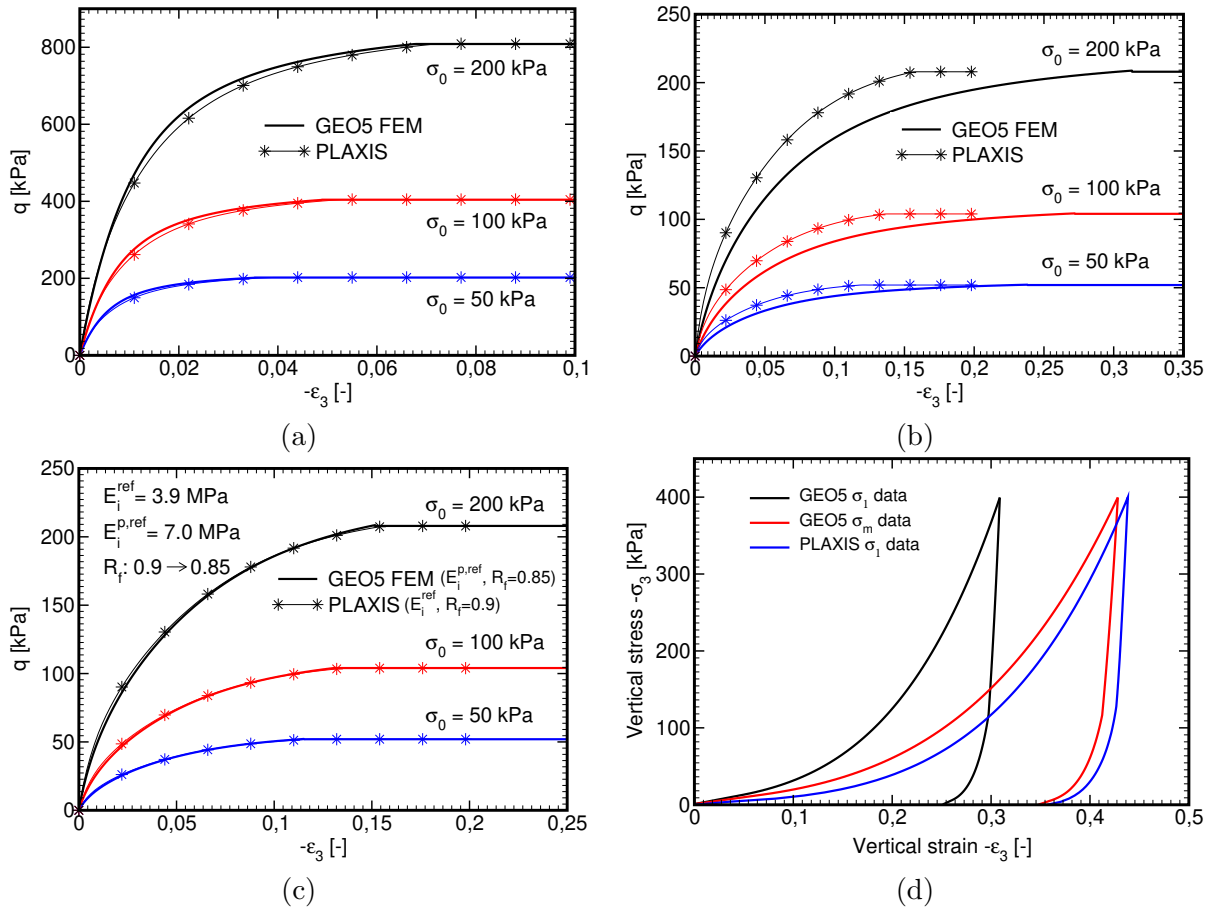
Figure 8.14: (a-c) Drained triaxial test: a) **Soil 2** with original parameters, b) **Soil 3** with original parameters, c) **Soil 3** with adjusted parameters $E_i^{\text{ref}} \rightarrow E_i^{\text{p,ref}}, R_f : 0.9 \rightarrow 0.85$, d) one-dimensional compression test (oedometer, **Soil 3**, for input data refer to Table 8.3)

To appreciate potential differences in the predictions provided by the σ_1− and σ_m− formulations for the same set of data we tested two more soils, one corresponding to a dense sand (**Soil 2**), and one representing a clayey soil (**Soil 3**). The results in Figs. 8.14(a,b) were derived assuming the data in Table 8.2 estimated such as to match laboratory measurements via simulations while adopting the σ_1−formulation [9]. Quite significant differences are observed for the clayey type of soil (**Soil 3**).

Table 8.3: Material and model parameters of **Soil 3**

Formulation	E_i^{ref}	E_{ur}^{ref}	ν_{ur} [-]	σ_m^{ref}	m	c	φ [^{0}]	ψ [^{0}]	M [-]	H^{ref}	R_f
σ_1 ($E^{\sigma,\text{ref}}, H^{\sigma,\text{ref}}$)	3909	11500	0.20	-100	0.80	0	20	0	0.78	1699	0.9
σ_m ($E^{\text{p,ref}}, H^{\text{p,ref}}$)	**7000**	8314	0.20	-100	0.80	0	20	0	0.78	1228	**0.85**

To reconcile the two approaches calls for adjusting the material parameters associated with the σ_m−formulation as described in Section 8.5.2. These are listed in the 3rd row of Table 8.3 denoted as σ_m and were used with GEO5 FEM, whereas the 2nd row collects the original data adopted with PLAXIS. Note that only the first 2 steps in the parameter migration procedure were exploited to derive the σ_m−data.

It is interesting to point out that in order to arrive at improved predictions with the σ_m−formulation in triaxial compression it is sufficient to adjust $E_i^{\text{p,ref}}$ together with R_f while keeping the other model

parameters unchanged as these two parameters play the decisive role in adjusting the shape of the stress-strain curve for this type of test. This was essentially tested and the results appear in Fig. 8.14(c) showing a reasonable match provided by the two simulations.

It has already been shown in Fig. 8.11 that a significant difference between the two formulations when considering the same set of data can be expected for the oedometric test. This is supported by the results plotted in Fig. 8.14(d). The black line was constructed using the σ_m- formulation while employing the data pertinent to the σ_1-formulation. When compared to PLAXIS prediction, the blue line, the difference is remarkable. A considerable improvement can be achieved by exploiting the material and model parameters adjusted with the help of the parameter migration procedure. The corresponding results are represented by the red line in Fig. 8.14(d). Further improvement might be expected if taking the present data as a point of departure and exercise the step 3 in Section 8.5.2 for finer tuning.

8.7   Hardening soil model in undrained analysis

8.8   Hardening soil model in stability analysis

This topic becomes relevant when running the stability analysis within a given calculation stage, providing the Hardening soil model was selected to represent the soil behavior in standard stress analysis. To this end, some action is required to allow for the application of standard shear strength parameters reduction procedure in stability analysis implemented in GEO5 FEM software. In particular, the Matsuoka-Nakai limit yield surface will be the only one potentially active yield surface throughout the analysis. The strength reduction procedure then corresponds to a simultaneous reduction of peak values of the cohesion c and the angle of internal friction φ. On the other hand, the unloading/reloading stiffness $E_{ur}(\widehat{\overline{\sigma}}_m) = \overline{\overline{E}}_{ur}$ equal to the one at the end of the preceding stress or earthquake analysis is kept constant within the reduction process.

Chapter 9

Soft soil model

The original formulation of the Soft soil (SS) model, also implemented in PLAXIS [63], was developed in [16]. But unlike PLAXIS, which grounds upon the application of the Mohr-Coulomb model, the present formulations, similarly to Chapter 8, is presented entirely in the invariant stress space combining the Matsuoka-Nakai yield surface introduced in Section 8.1.2 and the cap yield surface in the form of the Generalized Cam-clay (GCC) model described in detail in Section 12.1. The three-dimensional plot of the Soft soft model in the principal stress space appears in Fig. 9.1(a), whereas its projections into the meridian and deviatoric planes are displayed in Fig. 9.1(b) and Fig. 9.1(c), respectively.
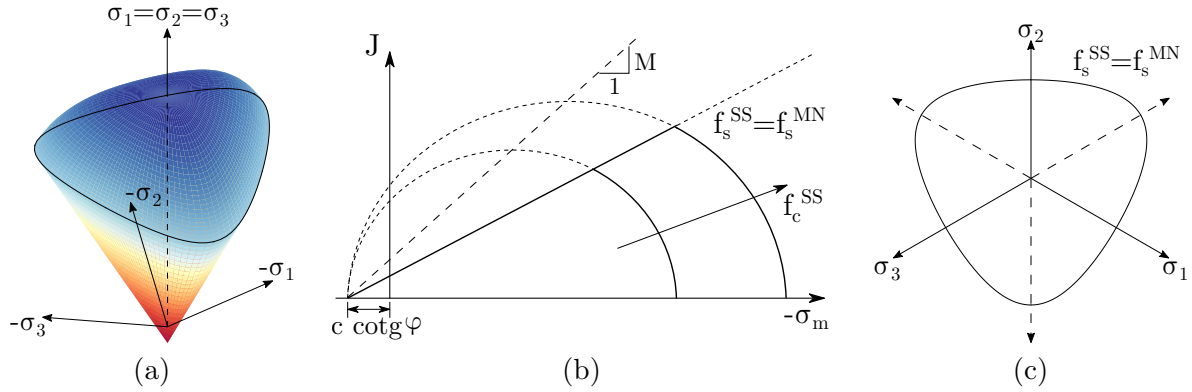
Figure 9.1: Yield surface: a) plot in principal stress space, b) plot in meridian plane, c) plot in deviatoric plane

Point out that in comparison to the cap yield surface in the GCC model the present formulation accounts for a non-zero cohesion c. Another modification is associated with the definition of the slope of critical state line $g(\theta, \varphi, M) = \chi(\theta, \varphi)M$. In the SS model the shape parameter M depends on the coefficient of lateral earth pressure for normally consolidated soils K_0^{NC} in the form, see [16] for detailed derivation,

$$M = \sqrt{3}\sqrt{\frac{(1-K_0^{NC})^2}{(1+2K_0^{NC})^2} + \frac{(1-K_0^{NC})(1-2\nu_{ur})\left(\frac{\lambda^*}{\kappa^*}-1\right)}{(1+2K_0^{NC})(1-2\nu_{ur})\frac{\lambda^*}{\kappa^*}-(1-K_0^{NC})(1+\nu_{ur})}} \tag{9.1}$$

$$\approx \frac{\sqrt{3}}{3}(3.0 - 2.8K_0^{NC}) \tag{9.2}$$

where

$$\kappa^* = \frac{\kappa}{1+e_{in}} \quad \text{and similarly} \quad \lambda^* = \frac{\lambda}{1+e_{in}} \tag{9.3}$$

are defined in terms of the slopes of swelling and normal consolidation lines κ and λ and the initial void ratio e_{in} given by Eq. (11.3) in terms of the maximum void ratio e_0. For a detailed description of these parameters we refer the reader to Section 11.1.1. The Poisson ratio ν_{ur} is identical to that introduced in Chapter 8 for the Hardening soil model and is typically in the range $(0.1 - 0.2)$.

While the Matsuoka-Nakai yield surface remains constant and in light of elastic-perfectly plastic material, recall Fig. 4.1, depends on the peak values of the effective angle of internal friction φ and effective cohesion c, the soil in compression may undergo hardening controlled by the evolution of cap yield surface as a function of the current value of the preconsolidation pressure p_c, see Figs. 11.2 and 11.3 in Section 11.1 for more details.

Similarly to critical state models, see ahead Chapters 11 and 12, the response inside the yield surface is assumed linear elastic with the bulk (K) and shear (G) moduli written as

$$\overline{K}_s = -\frac{\sigma_m^i}{\kappa^*} \tag{9.4}$$

$$\overline{G}_s = \frac{3(1 - 2\nu_{ur})}{2(1 + \nu_{ur})}\overline{K}_s = \zeta\overline{K}_s \tag{9.5}$$

where σ_m^i represents the mean effective stress at the beginning of the new load increment. This is consistent with the Modified and Generalized Cam-clay models formulated in the framework of constant elasticity return also implemented in the current version of GEO5 FEM, see for example Section 11.2.2.

The complete list of material parameters needed in the formulation of SS model is available in Table 9.1.

Table 9.1: Parameters of Soft soil plasticity model

Symbol	Units	Description
κ	[-]	Slope of swelling line (swelling modulus)
λ	[-]	Slope of normal consolidation line (isotropic NCL, compression modulus)
e_0	[-]	Maximum void ratio
ν_{ur}	[-]	Poisson's ratio
c	[kPa]	Effective peak cohesion
φ	[°]	Effective peak angle of internal friction
ψ	[°]	Angle of dilation
K_0^{NC}	[-]	Coefficient of lateral earth pressure for normal consolidation
e_{max}	[-]	Maximum void ratio to terminate dilation
OCR	[-]	Overconsolidation ratio
POP	[kPa]	Preoverburden pressure
α	[1/°C]	Coefficient of thermal expansion
M	[-]	Slope of critical state line at triaxial compression, calculated
p_c	[kPa]	Preconsolidation pressure ($p_c^{min} = 1$kPa), calculated

9.1   Formulation of Soft soil model

As already suggested in the previous section the Soft soil model combines two yield surfaces to overcome some of the drawbacks associated with the formulation of the Modified Cam-clay model as put forward in Chapters 11 and 12. Unlike the GCC model, however, the shear response is restricted by an independent failure criterion in the form of the Matsuoka-Nakai yield surface. Thus when compared to the Hardening soil model the soil hardening is limited to compression where the elastic behavior is bounded by a cap yield surface. Because at a point of intersection we wish to arrive at a smooth transition from one surface to the other, the projection of the cap yield surface into a deviatoric plane assumes the LMN dependence, recall Section 8.1.2. Thus except for the definition of the critical state line M_c and introduction of a non-zero cohesion c its formulation can be provided in the spirit of the subcritical part of the GCC model, see the definition of function f_c^{GCC} in Section 12.1.1, Eq. (12.3).

Mathematical formulation of these two functions is then provided by

$$f_s^{SS} = f_s^{MN} = I_\sigma - \sin^2 \varphi, \quad \text{recall Eq. (8.23)} \tag{9.6}$$

$$f_c^{SS} = \frac{J^2}{\chi^2(\theta, \varphi)M^2} + \widehat{\sigma}_m(\sigma_m + p_c), \quad \text{compare with Eq. (12.3)} \tag{9.7}$$

where, similar to Eq. (8.18),

$$\widehat{\sigma}_m = \sigma_m - c \cot \varphi \tag{9.8}$$

and I_σ and $\chi(\theta, \varphi)$ follow from Eqs. (8.24) and (8.42), respectively. Proceeding in the footsteps of the Drucker-Prager (or Hardening soil) and the Generalized Cam-clay models the plastic potential surfaces are assumed in the form

$$g_s^{SS} = g_s^{MN} = J + \widehat{\sigma}_m M_\psi, \quad \text{recall Eqs. (4.8) or (8.70)} \tag{9.9}$$

$$g_c^{SS} = \frac{J^2}{\widetilde{\chi}^2(\widetilde{\theta}, \varphi)M^2} + \widehat{\sigma}_m(\sigma_m + p_c), \quad \text{compare with Eq. (8.74) or (12.12)} \tag{9.10}$$

Remember that in accord with Eq. (8.74) we keep $\widetilde{\chi}(\widetilde{\theta}, \varphi)$ constant in the local stress update by setting $\widetilde{\theta} = \theta^{tr}$ where the Lode angle θ^{tr} is evaluated on the basis of trial stresses defined in Eq. (17.82).

In contrast to critical state models in Chapters 11 and 12 the Soft soil model allows for hardening only. This means that only the subcritical part of the Cam-clay model, recall Figs. 11.2(b) and 12.1(b), can be active. This in turn introduces certain restrictions on the magnitude of the angle of internal friction φ. To see this we first define

$$M_c = \chi(\theta, \varphi)M \tag{9.11}$$

$$M_s = \widehat{g}(\theta, \varphi) = -\frac{J}{\widehat{\sigma}_m} \tag{9.12}$$

where Eq. (8.32) was called to define the slope of the Matsuoka-Nakai yield surface M_s. To avoid potential softening within the cap model we must ensure that $M_c > M_s$-value should be larger than the slope of the Matsuoka-Nakai failure surface M_s. Recall that the value of M_s is found from the solution of cubic equation (8.34). While for triaxial compression (TC) the value of slope M_c is a function of K_0^{NC} ($\chi = 1$), the M_s-value depends solely on the value of peak effective friction angle and is written as

$$M_s^{TC} = \frac{2\sqrt{3}\sin \varphi}{3 - \sin \varphi} \tag{9.13}$$

Table 9.2 lists some specific values for three types of soil assuming three particular values of K_0^{NC} typically found in the range $(0.4 - 0.6)$.

Table 9.2: Slope of critical state line for triaxial compression $M_c = M, \theta = 30°, \chi = 1$

soil	κ	λ	e	λ/κ	K_0^{NC}	M	M^{approx}
1	0.0077	0.066	0.788	8.57	0.4/0.5/0.6	**1.130/0.940/0.774**	
2	0.0250	0.181	1.67	7.24	0.4/0.5/0.6	1.125/0.934/0.768	1.085/0.924/0.762
3	0.0164	0.106	0	6.45	0.4/0.5/0.6	1.121/0.930/0.763	

Similarly, the values of M_s for several angles of internal friction and three specific value of Lode's angle θ are provided in Table 9.3.

Finally, we consider soil 1 and the case of triaxial compression to illustrate the influence of both K_0^{NC} and φ on the M_c/M_s ratio listed in Table 9.4. It seen that for relatively large angles of internal friction and larger values of K_0^{NC} the M_c/M_s ration may drop below zero. As illustrated in Fig. 9.2(b) for the case of $\varphi = 40°$ and $K_0^{NC} = 0.6$, this suggests potential softening within the cap yield surface.

Table 9.3: Slope of Matsuoka-Nakai failure surface

φ	θ	χ	M_s
10	-30/0/**30**	0.812/0.937/**1**	0.190/0.196/**0.213**
20	-30/0/**30**	0.753/0.869/**1**	0.354/0.387/**0.446**
30	-30/0/**30**	0.693/0.801/**1**	0.495/0.555/**0.693**
40	-30/0/**30**	0.638/0.737/**1**	0.611/0.696/**0.945**

Table 9.4: Soil 1 - M_c/M_s ratio for triaxial compression

φ	M_c/M_s		
[°]	$K_0^{NC} = 0.4$	$K_0^{NC} = 0.5$	$K_0^{NC} = 0.6$
10	5.309	4.416	3.634
20	2.535	2.109	1.735
30	1.631	1.357	1.117
40	1.196	**0.995**	**0.819**

This is not allowed in the implemented version of the soft soil model. Thus considering the case of TC the following condition should be satisfied

$$\varphi < \arcsin\left(\frac{3M}{2\sqrt{3} + M}\right) \tag{9.14}$$

which is clearly not the case for $M(K_0^{NC} = 0.6) = 0.774$ which gives $\varphi_{max} = 33.2° < \varphi = 40°$.
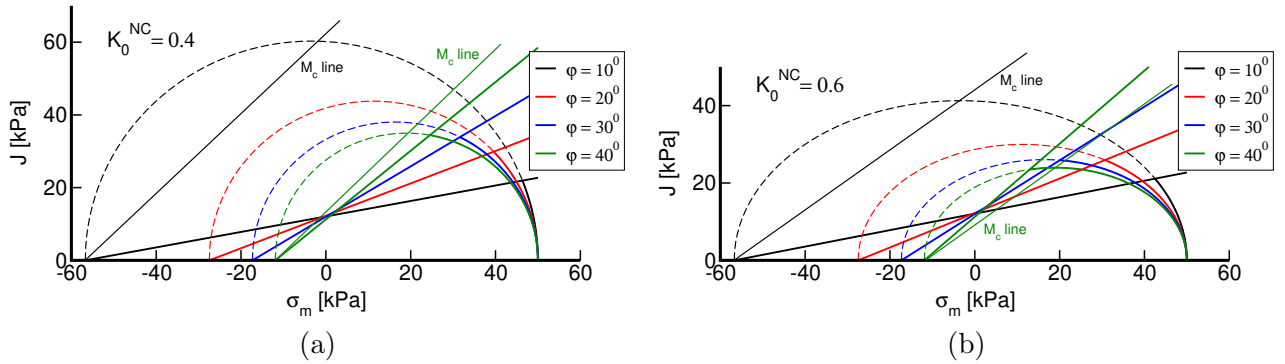
Figure 9.2: Cap and shear failure surfaces as a function of φ and K_0^{NC}: a) $K_0^{NC} = 0.4$, b) $K_0^{NC} = 0.6$

9.2   Stress return mapping

To open this section we consider the case when both yield surfaces are simultaneously active. With reference to Eqs. (9.9) and (9.10), recall also Eq. (1.26), the plastic strain increments attain the forms

$$\Delta\boldsymbol{\varepsilon}^{pl} = \Delta\boldsymbol{e}^{pl} + \boldsymbol{m}\Delta\varepsilon_v^{pl} \tag{9.15}$$

$$\Delta\varepsilon_v^{pl} = \Delta\lambda_s\frac{\partial g_s^{SS}}{\partial\sigma_m} + \Delta\lambda_c\frac{\partial g_c^{SS}}{\partial\sigma_m} = \Delta\lambda_s M_\psi + \Delta\lambda_c(2\sigma_m^{i+1} + p_c^{i+1} - c\cot\varphi) \tag{9.16}$$

$$\Delta\boldsymbol{e}^{pl} = \Delta\lambda_s\frac{\partial g_s^{SS}}{\partial\boldsymbol{s}} + \Delta\lambda_c\frac{\partial g_c^{SS}}{\partial\boldsymbol{s}} = \Delta\lambda\mathbf{Q}^{-1}\boldsymbol{s}^{i+1} = \Delta\lambda\mathbf{P}\boldsymbol{\sigma}^{i+1} \tag{9.17}$$

where the plastic multiplier $\Delta\lambda$ is given by

$$\Delta\lambda = \frac{\Delta\lambda_s}{2J^{i+1}} + \frac{\Delta\lambda_c}{\tilde{\chi}^2 M^2} \tag{9.18}$$

The interested reader may also compare this equation with Eq. (8.78). The superscript $(i+1)$ in the above equations states that all derivatives are taken with respect to stresses evaluated at the end of the $(i+1)$ load increment. It is also useful to provide the increment of the equivalent deviatoric plastic strain ΔE_d^{pl} as

$$\Delta E_d^{pl} = \sqrt{2(\Delta e^{pl})^\mathsf{T}\mathbf{Q}\Delta e^{pl}} = \Delta\lambda\sqrt{2(s^{i+1})^\mathsf{T}\mathbf{Q}^{-1}s^{i+1}} = 2\Delta\lambda J^{i+1} \tag{9.19}$$

Next, similar to PLAXIS, we assume that the elastic stiffness matrix is evaluated at the beginning of the new load increment and is kept constant throughout the local stress update, i.e., the bulk modulus $\overline{K}_s = K^i = -\frac{\sigma_m^i}{\kappa^*}$. This allows us, with the help of Eqs. (17.82), (9.16), (9.17) and (9.19), to write the stresses and associated equivalent stress measures at the end of the $(i+1)$ load increment as

- Mean stress σ_m^{i+1}

$$\sigma_m^{i+1} = \sigma_m^i + K^i(\Delta\varepsilon_v - \Delta\varepsilon_v^{pl}) = \sigma_m^{tr} - K^i(\Delta\lambda_s M_\psi + \Delta\lambda_c(2\sigma_m^{i+1} + p_c^{i+1} - c\cot\varphi)) \tag{9.20}$$

  Rearrange the above equation to get

$$\sigma_m^{i+1} = \frac{\sigma_m^{tr} - K^i(\Delta\lambda_s M_\psi + \Delta\lambda_c(p_c^{i+1} - c\cot\varphi))}{1 + 2K^i\Delta\lambda_c}, \quad \text{compare with Eq. (8.84)} \tag{9.21}$$

- Deviatoric stress s^{i+1}

$$s^{i+1} = s^i + 2G^i\mathbf{Q}\left(\Delta e - \left(\frac{\Delta\lambda_s}{2J^{i+1}} + \frac{\Delta\lambda_c}{\tilde{\chi}^2 M^2}\right)\mathbf{Q}^{-1}s^{i+1}\right) \tag{9.22}$$

  Rearrange the above equation to get

$$s^{i+1} = \frac{s^i + 2G^i\mathbf{Q}\Delta e}{1 + G^i\left(\dfrac{\Delta\lambda_s}{J^{i+1}} + \dfrac{2\Delta\lambda_c}{\tilde{\chi}^2 M^2}\right)} = \frac{s^{tr}}{1 + G^i\left(\dfrac{\Delta\lambda_s}{J^{i+1}} + \dfrac{2\Delta\lambda_c}{\tilde{\chi}^2 M^2}\right)}, \quad \text{compare with Eq. (8.86)} \tag{9.23}$$

- Equivalent deviatoric stress J^{i+1}

$$J^{i+1} = J^i + G^i(\Delta E_d - \Delta E_d^{pl}) = J^{tr} - G^i\Delta E_d^{pl} = J^{tr} - G^i\left(\frac{\Delta\lambda_s}{J^{i+1}} + \frac{2\Delta\lambda_c}{\tilde{\chi}^2 M^2}\right)J^{i+1} \tag{9.24}$$

  Rearrange the above equation to get

$$J^{i+1} = \frac{J^{tr} - G^i\Delta\lambda_s}{1 + \dfrac{2G^i\Delta\lambda_c}{\tilde{\chi}^2 M^2}}, \quad \text{compare with Eq. (8.87)} \tag{9.25}$$

Inspecting Eqs. (9.21), (9.23) and (9.25) suggests the vector of primary variables a in the form

$$a^\mathsf{T} = \{p_c^{i+1}, \Delta\lambda_s, \Delta\lambda_c\} \tag{9.26}$$

In the framework of multi-yield surface plasticity the vector of residuals to be minimized can be then written as

$$r = \left\{ \begin{array}{c} p_c^{i+1} - \overline{p}_c(\Delta\lambda_c, p_c^{i+1}) \\ f_s^{SS}(\sigma^{i+1}(\Delta\lambda_s, \Delta\lambda_c, p_c^{i+1})) \\ f_c^{SS}(\sigma^{i+1}(\Delta\lambda_s, \Delta\lambda_c, p_c^{i+1}), p_c^{i+1}) \end{array} \right\} = r(a(\varepsilon), \varepsilon) \tag{9.27}$$

Similarly to the Hardening soil model the preconsolidation pressure evolves only with the part of the volumetric plastic strain associated with the cap yield surface $\Delta\varepsilon_{vc}^{pl}$. Adopting Eqs. (9.16) and (9.21) then gives

$$
\begin{aligned}
\overline{p}_c &= p_c^i \exp\left[-\frac{\Delta\varepsilon_{vc}^{pl}}{\lambda^* - \kappa^*}\right] = p_c^i \exp\left[-\frac{\Delta\lambda_c(2\sigma_m^{i+1}(\Delta\lambda_s = 0) + p_c^{i+1} - c\cot\varphi)}{\lambda^* - \kappa^*}\right] \\
&= p_c^i \exp\left[-\frac{1}{\lambda^* - \kappa^*}\frac{\Delta\lambda_c(2\sigma_m^{tr} + p_c^{i+1} - c\cot\varphi)}{1 + 2K^i\Delta\lambda_c}\right], \quad \text{compare with Eq. (11.68)}
\end{aligned}
\tag{9.28}
$$

where we exploited Eq. (11.15) derived exhaustively in Section 11.1.1.

The system of nonlinear implicit equations (9.27) can be solved by employing the Newton-Raphson method

$$
\boldsymbol{a}_{j+1}^{i+1} = \boldsymbol{a}_j^{i+1} - \mathbf{H}_j^{-1}\boldsymbol{r}_j
\tag{9.29}
$$

where the Jacobian matrix $\mathbf{H}$ is provided by

$$
\mathbf{H} = \frac{\partial \boldsymbol{r}}{\partial \boldsymbol{a}} + \frac{\partial \boldsymbol{r}}{\partial \boldsymbol{s}}\frac{\partial \boldsymbol{s}}{\partial \boldsymbol{a}} = \begin{bmatrix} \dfrac{dr_1}{dp_c} & \dfrac{dr_1}{d\Delta\lambda_s} & \dfrac{dr_1}{d\Delta\lambda_c} \\[2ex] \dfrac{dr_2}{dp_c} & \dfrac{dr_2}{d\Delta\lambda_s} & \dfrac{dr_2}{d\Delta\lambda_c} \\[2ex] \dfrac{dr_3}{dp_c} & \dfrac{dr_3}{d\Delta\lambda_s} & \dfrac{dr_3}{d\Delta\lambda_c} \end{bmatrix}
\tag{9.30}
$$

To initialize Eq. (9.29) we assume

$$
\boldsymbol{a}_0^{\mathsf{T}} = \{p_c^i, 0, 0,\}
\tag{9.31}
$$
$$
\boldsymbol{r}_0^{\mathsf{T}} = \{0, f_s^{SS}(\boldsymbol{\sigma}^{tr}), f_c^{SS}(\boldsymbol{\sigma}^{tr}, p_c^i)\}
\tag{9.32}
$$

Employing standard differentiation of composite functions, while dropping out the superscript $(i+1)$ for the sake of simplicity, gives the components of the Jacobian matrix $\mathbf{H}$ in the form of chain rules as

- $\boldsymbol{H}_{1i}$

$$
H_{11} = \frac{dr_1}{dp_c} = 1 + \frac{\overline{p}_c}{\lambda^* - \kappa^*}\frac{\partial\Delta\varepsilon_{vc}^{pl}}{\partial p_c}
\tag{9.33}
$$

$$
H_{12} = \frac{dr_1}{d\Delta\lambda_s} = \frac{\overline{p}_c}{\lambda^* - \kappa^*}\frac{\partial\Delta\varepsilon_{vc}^{pl}}{\partial\Delta\lambda_s}
\tag{9.34}
$$

$$
H_{13} = \frac{dr_1}{d\Delta\lambda_c} = \frac{\overline{p}_c}{\lambda^* - \kappa^*}\frac{\partial\Delta\varepsilon_{cv}^{pl}}{\partial\Delta\lambda_c}
\tag{9.35}
$$

where

$$
\frac{\partial\Delta\varepsilon_{vc}^{pl}}{\partial p_c} = \frac{\Delta\lambda_c}{1 + 2K^i\Delta\lambda_c}
\tag{9.36}
$$

$$
\frac{\partial\Delta\varepsilon_{vc}^{pl}}{\partial\Delta\lambda_s} = 0
\tag{9.37}
$$

$$
\frac{\partial\Delta\varepsilon_{cv}^{pl}}{\partial\Delta\lambda_c} = \frac{2\sigma_m^{tr} + p_c^{i+1} - c\cot\varphi}{(1 + 2K^i\Delta\lambda_c)^2}
\tag{9.38}
$$

- $\boldsymbol{H}_{2i}$

$$\frac{\mathrm{d}r_2}{\mathrm{d}p_c} = \frac{\mathrm{d}I_\sigma}{\mathrm{d}p_c} = \frac{\partial I_\sigma}{\partial \sigma_m} \frac{\partial \sigma_m}{\partial p_c} \tag{9.39}$$

$$\frac{\mathrm{d}r_2}{\mathrm{d}\Delta\lambda_s} = \frac{\mathrm{d}I_\sigma}{\mathrm{d}\Delta\lambda_s} = \frac{\partial I_\sigma}{\partial \sigma_m} \frac{\partial \sigma_m}{\partial \Delta\lambda_s} + \frac{\partial I_\sigma}{\partial J} \frac{\partial J}{\partial \Delta\lambda_s} + \frac{\partial I_\sigma}{\partial I_{3s}} \frac{\mathrm{d}I_{3s}}{\mathrm{d}\Delta\lambda_s} \tag{9.40}$$

$$\frac{\mathrm{d}r_2}{\mathrm{d}\Delta\lambda_c} = \frac{\mathrm{d}I_\sigma}{\mathrm{d}\Delta\lambda_c} = \frac{\partial I_\sigma}{\partial \sigma_m} \frac{\partial \sigma_m}{\partial \Delta\lambda_c} + \frac{\partial I_\sigma}{\partial J} \frac{\partial J}{\partial \Delta\lambda_c} + \frac{\partial I_\sigma}{\partial I_{3s}} \frac{\mathrm{d}I_{3s}}{\mathrm{d}\Delta\lambda_c} \tag{9.41}$$

where

$$\frac{\partial I_\sigma}{\partial \sigma_m} = \frac{\partial I_\sigma}{\partial I_{1\sigma}} \frac{\partial I_{1\sigma}}{\partial \sigma_m} + \frac{\partial I_\sigma}{\partial I_{2\sigma}} \frac{\partial I_{2\sigma}}{\partial \sigma_m} + \frac{\partial I_\sigma}{\partial I_{3\sigma}} \frac{\partial I_{3\sigma}}{\partial \sigma_m} \tag{9.42}$$

$$\frac{\partial I_\sigma}{\partial J} = \frac{\partial I_\sigma}{\partial I_{2\sigma}} \frac{\partial I_{2\sigma}}{\partial J} + \frac{\partial I_\sigma}{\partial I_{3\sigma}} \frac{\partial I_{3\sigma}}{\partial J} \tag{9.43}$$

$$\frac{\partial I_\sigma}{\partial I_{3s}} = \frac{\partial I_\sigma}{\partial I_{3\sigma}} \frac{\partial I_{3\sigma}}{\partial I_{3s}} \tag{9.44}$$

- $\boldsymbol{H}_{3i}$

$$\frac{\mathrm{d}r_3}{\mathrm{d}p_c} = \frac{\partial r_3}{\partial p_c} + \frac{\partial r_3}{\partial \sigma_m} \frac{\partial \sigma_m}{\partial p_c} \tag{9.45}$$

$$\frac{\mathrm{d}r_3}{\mathrm{d}\Delta\lambda_s} = \frac{\partial r_3}{\partial J} \frac{\partial J}{\partial \Delta\lambda_s} + \frac{\partial r_3}{\partial \sigma_m} \frac{\partial \sigma_m}{\partial \Delta\lambda_s} +$$
$$+ \frac{\partial r_3}{\partial \chi} \frac{\partial \chi}{\partial \vartheta} \frac{\partial \vartheta}{\partial \sin 3\theta} \left(\frac{\partial \sin 3\theta}{\partial J} \frac{\partial J}{\partial \Delta\lambda_s} + \frac{\partial \sin 3\theta}{\partial I_{3s}} \frac{\mathrm{d}I_{3s}}{\mathrm{d}\Delta\lambda_s} \right) \tag{9.46}$$

$$\frac{\mathrm{d}r_3}{\mathrm{d}\Delta\lambda_c} = \frac{\partial r_3}{\partial J} \frac{\partial J}{\partial \Delta\lambda_c} + \frac{\partial r_3}{\partial \sigma_m} \frac{\partial \sigma_m}{\partial \Delta\lambda_c} +$$
$$+ \frac{\partial r_3}{\partial \chi} \frac{\partial \chi}{\partial \vartheta} \frac{\partial \vartheta}{\partial \sin 3\theta} \left(\frac{\partial \sin 3\theta}{\partial J} \frac{\partial J}{\partial \Delta\lambda_c} + \frac{\partial \sin 3\theta}{\partial I_{3s}} \frac{\mathrm{d}I_{3s}}{\mathrm{d}\Delta\lambda_c} \right) \tag{9.47}$$

where

$$\frac{\partial r_3}{\partial p_c} = \sigma_m - c \cot\varphi \tag{9.48}$$

$$\frac{\partial r_3}{\partial \sigma_m} = 2\sigma_m + p_c - c \cot\varphi \tag{9.49}$$

$$\frac{\partial r_3}{\partial J} = \frac{2J}{\chi^2 M^2} \tag{9.50}$$

$$\frac{\partial r_3}{\partial \chi} = -\frac{2J^2}{\chi^3 M^2} \tag{9.51}$$

$$\frac{\mathrm{d}I_{3s}}{\mathrm{d}\Delta\lambda_s} = \left(\frac{\partial I_{3s}}{\partial \boldsymbol{s}} \right)^\mathsf{T} \frac{\mathrm{d}\boldsymbol{s}}{\mathrm{d}\Delta\lambda_s} \tag{9.52}$$

$$\frac{\mathrm{d}I_{3s}}{\mathrm{d}\Delta\lambda_c} = \left(\frac{\partial I_{3s}}{\partial \boldsymbol{s}} \right)^\mathsf{T} \frac{\mathrm{d}\boldsymbol{s}}{\mathrm{d}\Delta\lambda_c} \tag{9.53}$$

$$\frac{\mathrm{d}\boldsymbol{s}}{\mathrm{d}\Delta\lambda_s} = \frac{\partial \boldsymbol{s}}{\partial \Delta\lambda_s} + \frac{\partial \boldsymbol{s}}{\partial J} \frac{\partial J}{\partial \Delta\lambda_s} \tag{9.54}$$

$$\frac{\mathrm{d}\boldsymbol{s}}{\mathrm{d}\Delta\lambda_c} = \frac{\partial \boldsymbol{s}}{\partial \Delta\lambda_c} + \frac{\partial \boldsymbol{s}}{\partial J} \frac{\partial J}{\partial \Delta\lambda_c} \tag{9.55}$$

Further details are available in Section 8.3.2. The derivatives not explicitly provided therein are

$$\frac{\partial \sigma_m}{\partial p_c} = -\frac{K^i \Delta\lambda_c}{1 + 2K^i \Delta\lambda_c} \tag{9.56}$$

$$\frac{\partial \sigma_m}{\partial \Delta\lambda_s} = -\frac{K^i M_\psi}{1 + 2K^i \Delta\lambda_c} \tag{9.57}$$

$$\frac{\partial \sigma_m}{\partial \Delta\lambda_c} = -\frac{K^i(2\sigma_m^{tr} + p_c - c\cot\varphi - 2K^i \Delta\lambda_s M_\psi)}{(1 + 2K^i \Delta\lambda_c)^2} \tag{9.58}$$

$$\frac{\partial J}{\partial \Delta\lambda_s} = -\frac{G^i}{1 + \dfrac{2G^i \Delta\lambda_c}{\tilde\chi^2 M^2}} \tag{9.59}$$

$$\frac{\partial J}{\partial \Delta\lambda_c} = -\frac{J^{tr} - G^i \Delta\lambda_s}{\left(1 + \dfrac{2G^i \Delta\lambda_c}{\tilde\chi^2 M^2}\right)^2} \frac{2G^i}{\tilde\chi^2 M^2} = -\frac{J}{1 + \dfrac{2G^i \Delta\lambda_c}{\tilde\chi^2 M^2}} \frac{2G^i}{\tilde\chi^2 M^2} \tag{9.60}$$

$$\frac{\partial \boldsymbol{s}}{\partial \Delta\lambda_s} = -\frac{\boldsymbol{s}^{tr}}{\left[1 + G^i\left(\dfrac{\Delta\lambda_s}{J} + \dfrac{2\Delta\lambda_c}{\tilde\chi^2 M^2}\right)\right]^2} \frac{G^i}{J} = -\frac{\boldsymbol{s}}{1 + G^i\left(\dfrac{\Delta\lambda_s}{J} + \dfrac{2\Delta\lambda_c}{\tilde\chi^2 M^2}\right)} \frac{G^i}{J} \tag{9.61}$$

$$\frac{\partial \boldsymbol{s}}{\partial \Delta\lambda_c} = -\frac{\boldsymbol{s}^{tr}}{\left[1 + G^i\left(\dfrac{\Delta\lambda_s}{J} + \dfrac{2\Delta\lambda_c}{\tilde\chi^2 M^2}\right)\right]^2} \frac{2G^i}{\tilde\chi^2 M^2} = -\frac{\boldsymbol{s}}{1 + G^i\left(\dfrac{\Delta\lambda_s}{J} + \dfrac{2\Delta\lambda_c}{\tilde\chi^2 M^2}\right)} \frac{2G^i}{\tilde\chi^2 M^2} \tag{9.62}$$

$$\frac{\partial \boldsymbol{s}}{\partial J} = \frac{\boldsymbol{s}^{tr}}{\left[1 + G^i\left(\dfrac{\Delta\lambda_s}{J} + \dfrac{2\Delta\lambda_c}{\tilde\chi^2 M^2}\right)\right]^2} \frac{G^i \Delta\lambda_s}{J^2} = \frac{\boldsymbol{s}}{1 + G^i\left(\dfrac{\Delta\lambda_s}{J} + \dfrac{2\Delta\lambda_c}{\tilde\chi^2 M^2}\right)} \frac{G^i \Delta\lambda_s}{J^2} \tag{9.63}$$

$$\tag{9.64}$$

Remember that all stresses including equivalent stress measure J and the preconsolidation pressure p_c are evaluated at the end of the $(i+1)$ load increment.

9.3   Algorithmic tangent stiffness matrix

A general framework for the derivation of algorithmic tangent stiffness matrix is presented in Section 8.4. Some specific issues related to the present version of the cap yield surface are addressed in Section 12.3.2. These two sections thus constitute the right springboard in succeeding formulations. We start from Eq. (8.184) and write the algorithmic tangent stiffness matrix $\boldsymbol{\mathcal{D}}$ as

$$\boldsymbol{\mathcal{D}} = \frac{\mathrm{d}\boldsymbol{\sigma}^{i+1}}{\mathrm{d}\boldsymbol{\varepsilon}^{i+1}} = 3\boldsymbol{m}\left(\frac{\mathrm{d}\sigma_m^{i+1}}{\mathrm{d}\boldsymbol{\varepsilon}^{i+1}}\right)^{\mathsf{T}} + \frac{\mathrm{d}\boldsymbol{s}^{i+1}}{\mathrm{d}\boldsymbol{\varepsilon}^{i+1}} \tag{9.65}$$

Expanding both terms on the right-hand side of Eq. (9.65) grounds on the following stress and strain dependencies, recall Eqs. (8.187) - (8.191),

$$p_c^{i+1} = f(p_c^{i+1}, \sigma_m^{tr}(\Delta\varepsilon_v(\boldsymbol{\varepsilon})), \Delta\lambda_s(\boldsymbol{\varepsilon}), \Delta\lambda_c(\boldsymbol{\varepsilon}), \Delta\varepsilon_v(\boldsymbol{\varepsilon})) \tag{9.66}$$

$$\boldsymbol{s}^{i+1} = f(J^{i+1}, \Delta\lambda_s(\boldsymbol{\varepsilon}), \Delta\lambda_c(\boldsymbol{\varepsilon}), \Delta\boldsymbol{e}(\boldsymbol{\varepsilon})) \tag{9.67}$$

$$J^{i+1} = f(J^{tr}(\Delta\boldsymbol{e}(\boldsymbol{\varepsilon})), \Delta\lambda_s(\boldsymbol{\varepsilon}), \Delta\lambda_c(\boldsymbol{\varepsilon})) \tag{9.68}$$

To simplify notation the superscript $(i+1)$ identifying the stresses and strains with the end of the $(i+1)$ load increment is left out in subsequent formulations. Also, the notation introduced in Eqs. (8.185) and (8.186) will be used. With this in mind we adopt Eq. (9.21) and write the term $\dfrac{\mathrm{d}\sigma_m}{\mathrm{d}\varepsilon}$ as

$$\frac{\mathrm{d}\sigma_m}{\mathrm{d}\varepsilon} = \frac{\partial \sigma_m}{\partial \varepsilon} + \frac{\partial \sigma_m}{\partial p_c}\frac{\mathrm{d}p_c}{\mathrm{d}\varepsilon} + \frac{\partial \sigma_m}{\partial \Delta\lambda_s}\frac{\partial \Delta\lambda_s}{\partial \varepsilon} + \frac{\partial \sigma_m}{\partial \Delta\lambda_c}\frac{\partial \Delta\lambda_c}{\partial \varepsilon} \tag{9.69}$$

$$= \frac{1}{1 + 2K^i\Delta\lambda_c}\left(3K^i\boldsymbol{m} - K^i M_\psi \frac{\partial \Delta\lambda_s}{\partial \varepsilon} - K^i\Delta\lambda_c\frac{\mathrm{d}p_c}{\mathrm{d}\varepsilon} - \frac{K^i(2\sigma_m^{tr} + p_c - c\cot\varphi - 2K^i\Delta\lambda_s M_\psi)}{1 + 2K^i\Delta\lambda_c}\frac{\partial \Delta\lambda_c}{\partial \varepsilon}\right)$$

where the term $\dfrac{\mathrm{d}p_c}{\mathrm{d}\boldsymbol{\varepsilon}}$ follows from Eq. (9.28) and is defined by

$$\frac{\mathrm{d}p_c}{\mathrm{d}\boldsymbol{\varepsilon}} = -\frac{p_c}{(\lambda^* - \kappa^*)(1 + 2K^i\Delta\lambda_c)}\left[6K^i\Delta\lambda_c\boldsymbol{m} + \Delta\lambda_c\frac{\mathrm{d}p_c}{\mathrm{d}\boldsymbol{\varepsilon}} + \frac{2\sigma_m^{tr} + p_c - c\cot\varphi}{1 + 2K^i\Delta\lambda_c}\frac{\partial\Delta\lambda_c}{\partial\boldsymbol{\varepsilon}}\right] \quad (9.70)$$

Rearranging Eq. (9.70) gives

$$\frac{\mathrm{d}p_c}{\mathrm{d}\boldsymbol{\varepsilon}} = a_4 3\boldsymbol{m} + a_5\frac{\partial\Delta\lambda_c}{\partial\boldsymbol{\varepsilon}} \quad (9.71)$$

$$a_4 = -\frac{2K^i\Delta\lambda_c p_c}{(\lambda^* - \kappa^*)(1 + 2K^i\Delta\lambda_c) + \Delta\lambda_c p_c} = -\frac{K^i}{a}\frac{2\Delta\lambda_c p_c}{\lambda^* - \kappa^*} \quad (9.72)$$

$$a_5 = -\frac{\left(\dfrac{2\sigma_m^{tr} + p_c - c\cot\varphi}{1 + 2K^i\Delta\lambda_c}\right)p_c}{(\lambda^* - \kappa^*)(1 + 2K^i\Delta\lambda) + \Delta\lambda_c p_c} = -\frac{p_c}{a}\frac{2\sigma_m^{tr} + p_c - c\cot\varphi}{(\lambda^* - \kappa^*)(1 + 2K^i\Delta\lambda_c)} \quad (9.73)$$

$$a = 1 + \frac{\Delta\lambda_c p_c}{\lambda^* - \kappa^*} + 2K^i\Delta\lambda_c \quad (9.74)$$

We may now substitute back from Eq. (9.71) to Eq. (9.69) to get

$$\frac{\mathrm{d}\sigma_m}{\mathrm{d}\boldsymbol{\varepsilon}} = a_1 3\boldsymbol{m} + a_2\frac{\partial\Delta\lambda_s}{\partial\boldsymbol{\varepsilon}} + a_3\frac{\partial\Delta\lambda_c}{\partial\boldsymbol{\varepsilon}} \quad (9.75)$$

$$a_1 = \frac{K^i}{1 + 2K^i\Delta\lambda_c}(1 - a_4\Delta\lambda_c) \quad (9.76)$$

$$a_2 = -\frac{K^i M_\psi}{1 + 2K^i\Delta\lambda_c} \quad (9.77)$$

$$a_3 = -\frac{K^i}{1 + 2K^i\Delta\lambda_c}\left(\frac{2\sigma_m^{tr} + p_c - c\cot\varphi - 2K^i\Delta\lambda_s M_\psi}{1 + 2K^i\Delta\lambda_c} + a_5\Delta\lambda_c\right) \quad (9.78)$$

Similarly to Section 8.4 the second term on the right-hand side of Eq. (9.65) receives the form, recall Eqs. (8.192) and (8.193),

$$\frac{\mathrm{d}\boldsymbol{s}}{\mathrm{d}\boldsymbol{\varepsilon}} = \frac{\partial\boldsymbol{s}}{\partial\boldsymbol{\varepsilon}} + \frac{\mathrm{d}\boldsymbol{s}}{\mathrm{d}\tilde{\chi}}\left(\frac{\mathrm{d}\tilde{\chi}}{\mathrm{d}\boldsymbol{\varepsilon}}\right)^{\mathsf{T}} + \frac{\mathrm{d}\boldsymbol{s}}{\mathrm{d}\Delta\lambda_s}\left(\frac{\partial\Delta\lambda_s}{\partial\boldsymbol{\varepsilon}}\right)^{\mathsf{T}} + \frac{\mathrm{d}\boldsymbol{s}}{\mathrm{d}\Delta\lambda_c}\left(\frac{\partial\Delta\lambda_c}{\partial\boldsymbol{\varepsilon}}\right)^{\mathsf{T}} \quad (9.79)$$

$$= \mathbf{E} + \boldsymbol{s_1}\left(\frac{\partial\Delta\lambda_s}{\partial\boldsymbol{\varepsilon}}\right)^{\mathsf{T}} + \boldsymbol{s_2}\left(\frac{\partial\Delta\lambda_c}{\partial\boldsymbol{\varepsilon}}\right)^{\mathsf{T}} \quad (9.80)$$

where the derivatives $\dfrac{\mathrm{d}\boldsymbol{s}}{\mathrm{d}\Delta\lambda_s} = \boldsymbol{s_1}, \dfrac{\mathrm{d}\boldsymbol{s}}{\mathrm{d}\Delta\lambda_c} = \boldsymbol{s_2}$ are provided by (9.54) and (9.55) and the matrix $\mathbf{E}$ reads

$$\mathbf{E} = \mathbf{E}_1 + \mathbf{E}_2 \quad (9.81)$$

$$\mathbf{E}_1 = \frac{\partial\boldsymbol{s}}{\partial\boldsymbol{\varepsilon}} = \left[\frac{\partial\boldsymbol{s}}{\partial\Delta\boldsymbol{e}} + \frac{\partial\boldsymbol{s}}{\partial J}\left(\frac{\partial J}{\partial\Delta\boldsymbol{e}}\right)^{\mathsf{T}}\right]\frac{\partial\Delta\boldsymbol{e}}{\partial\boldsymbol{\varepsilon}} \quad (9.82)$$

$$\mathbf{E}_2 = \frac{\mathrm{d}\boldsymbol{s}}{\mathrm{d}\tilde{\chi}}\left(\frac{\mathrm{d}\tilde{\chi}}{\mathrm{d}\boldsymbol{\varepsilon}}\right)^{\mathsf{T}} \quad (9.83)$$

with

$$\frac{\mathrm{d}\boldsymbol{s}}{\mathrm{d}\tilde{\chi}} = \frac{\partial\boldsymbol{s}}{\partial\tilde{\chi}} + \frac{\partial\boldsymbol{s}}{\partial J}\frac{\partial J}{\partial\tilde{\chi}} \quad (9.84)$$

$$\frac{\mathrm{d}\tilde{\chi}}{\mathrm{d}\boldsymbol{\varepsilon}} = \left[\frac{\mathrm{d}\tilde{\boldsymbol{s}}}{\mathrm{d}\boldsymbol{\varepsilon}}\right]^{\mathsf{T}}\frac{\partial\tilde{\chi}}{\partial\tilde{\boldsymbol{s}}} \quad (9.85)$$

$$\frac{\mathrm{d}\tilde{\boldsymbol{s}}}{\mathrm{d}\boldsymbol{\varepsilon}} = \frac{\partial\tilde{\boldsymbol{s}}}{\partial\Delta\boldsymbol{e}}\frac{\partial\Delta\boldsymbol{e}}{\partial\boldsymbol{\varepsilon}} \quad (9.86)$$

The remaining partial derivatives in Eqs. (9.82) - (9.86) are provided by

$$\frac{\partial \boldsymbol{s}}{\partial \Delta \boldsymbol{e}} = \frac{2G^i \mathbf{Q}}{1 + G^i \left(\dfrac{\Delta \lambda_s}{J} + \dfrac{2 \Delta \lambda_c}{\tilde{\chi}^2 M^2} \right)} \tag{9.87}$$

$$\frac{\partial J}{\partial \Delta \boldsymbol{e}} = \frac{\partial J}{\partial J^{tr}} \frac{\partial J^{tr}}{\partial \Delta \boldsymbol{e}} = \frac{G^i}{1 + \dfrac{2G^i \Delta \lambda_c}{\tilde{\chi}^2 M^2}} \frac{\partial \Delta E_d}{\partial \Delta \boldsymbol{e}}, \quad \frac{\partial \Delta E_d}{\partial \Delta \boldsymbol{e}} = \frac{\partial \sqrt{2 \Delta \boldsymbol{e}^\mathsf{T} \mathbf{Q} \Delta \boldsymbol{e}}}{\partial \Delta \boldsymbol{e}} = \frac{2 \mathbf{Q} \Delta \boldsymbol{e}}{\Delta E_d} = \frac{\boldsymbol{s}}{J} \tag{9.88}$$

$$\frac{\partial \boldsymbol{s}}{\partial \tilde{\chi}} = \frac{\boldsymbol{s}^{tr}}{\left[1 + G^i \left(\dfrac{\Delta \lambda_s}{J} + \dfrac{2 \Delta \lambda_c}{\tilde{\chi}^2 M^2} \right) \right]^2} \frac{4G^i \Delta \lambda_c}{\tilde{\chi}^3 M^2} = \frac{\boldsymbol{s}}{1 + G^i \left(\dfrac{\Delta \lambda_s}{J} + \dfrac{2 \Delta \lambda_c}{\tilde{\chi}^2 M^2} \right)} \frac{4G^i \Delta \lambda_c}{\tilde{\chi}^3 M^2} \tag{9.89}$$

$$\frac{\partial J}{\partial \tilde{\chi}} = \frac{J^{tr} - G^i \Delta \lambda_s}{\left(1 + \dfrac{2G^i \Delta \lambda_c}{\tilde{\chi}^2 M^2} \right)^2} \frac{4G^i \Delta \lambda_c}{\tilde{\chi}^3 M^2} = \frac{J}{1 + \dfrac{2G^i \Delta \lambda_c}{\tilde{\chi}^2 M^2}} \frac{4G^i \Delta \lambda_c}{\tilde{\chi}^3 M^2} \tag{9.90}$$

$$\frac{\partial \tilde{\chi}}{\partial \tilde{\boldsymbol{s}}} = \frac{\partial \tilde{\chi}}{\partial \vartheta} \frac{\partial \vartheta}{\partial \sin 3\tilde{\theta}} \left(\frac{\partial \sin 3\tilde{\theta}}{\partial \tilde{J}} \frac{\partial \tilde{J}}{\partial \tilde{\boldsymbol{s}}} + \frac{\partial \sin 3\tilde{\theta}}{\partial \tilde{I}_{3s}} \frac{\partial \tilde{I}_{3s}}{\partial \tilde{\boldsymbol{s}}} \right) \tag{9.91}$$

$$\frac{\partial \tilde{\boldsymbol{s}}}{\partial \Delta \boldsymbol{e}} = = 2G^i \mathbf{Q} \tag{9.92}$$

It is worth mentioning that $\tilde{\boldsymbol{s}} = \boldsymbol{s}^{tr}, \tilde{J} = J^{tr}, \tilde{I}_{3s} = I_{3s}^{tr}$

Similarly to Section 8.4 the unknown derivatives $\dfrac{\partial \Delta \lambda_s}{\partial \boldsymbol{\varepsilon}}$ and $\dfrac{\partial \Delta \lambda_c}{\partial \boldsymbol{\varepsilon}}$ are determined from the consistency condition, see Eq. (8.226), which in the case of Soft soil model reads

$$\frac{\mathrm{d} r_i}{\mathrm{d} \boldsymbol{\varepsilon}} = \mathbf{0} \tag{9.93}$$

$$r_2 = f_s^{SS}, \quad r_3 = f_c^{SS} \tag{9.94}$$

We begin with the Matsuoka-Nakai yield surface $f_s^{SS} \equiv f_s^{MN}$ and write the corresponding consistency condition in the form, recall Eqs. (8.222) and (8.223) to get the terms $\dfrac{\mathrm{d} J}{\mathrm{d} \boldsymbol{\varepsilon}}$, and $\dfrac{\mathrm{d} I_{3s}}{\mathrm{d} \boldsymbol{\varepsilon}}$,

$$\frac{\mathrm{d} r_2}{\mathrm{d} \boldsymbol{\varepsilon}} = \frac{\partial I_\sigma}{\partial \sigma_m} \frac{\mathrm{d} \sigma_m}{\mathrm{d} \boldsymbol{\varepsilon}} + \frac{\partial I_\sigma}{\partial J} \frac{\mathrm{d} J}{\mathrm{d} \boldsymbol{\varepsilon}} + \frac{\partial I_\sigma}{\partial I_{3s}} \frac{\mathrm{d} I_{3s}}{\mathrm{d} \boldsymbol{\varepsilon}} \tag{9.95}$$

$$= \frac{\partial I_\sigma}{\partial \sigma_m} \frac{\mathrm{d} \sigma_m}{\mathrm{d} \boldsymbol{\varepsilon}} + \frac{\partial I_\sigma}{\partial J} \left[\frac{\mathrm{d} \boldsymbol{s}}{\mathrm{d} \boldsymbol{\varepsilon}} \right]^\mathsf{T} \frac{\partial J}{\partial \boldsymbol{s}} + \frac{\partial I_\sigma}{\partial I_{3s}} \left[\frac{\mathrm{d} \boldsymbol{s}}{\mathrm{d} \boldsymbol{\varepsilon}} \right]^\mathsf{T} \frac{\partial I_{3s}}{\partial \boldsymbol{s}} \tag{9.96}$$

$$= c_1 \frac{\mathrm{d} \sigma_m}{\mathrm{d} \boldsymbol{\varepsilon}} + c_2 \left[\frac{\mathrm{d} \boldsymbol{s}}{\mathrm{d} \boldsymbol{\varepsilon}} \right]^\mathsf{T} \boldsymbol{j}_1 + c_3 \left[\frac{\mathrm{d} \boldsymbol{s}}{\mathrm{d} \boldsymbol{\varepsilon}} \right]^\mathsf{T} \boldsymbol{j}_2 = \mathbf{0}, \quad \text{compare with Eq. (8.234)} \tag{9.97}$$

where the derivatives $\dfrac{\partial I_\sigma}{\partial \sigma_m}, \dfrac{\partial I_\sigma}{\partial J}, \dfrac{\partial I_\sigma}{\partial I_{3s}}$ were introduced in are given by Eqs. (9.42), (9.43), (9.44). After substituting from Eqs. (9.75) and (9.80) back to Eq. (9.97) we arrive at

$$\frac{\mathrm{d} r_2}{\mathrm{d} \boldsymbol{\varepsilon}} = \boldsymbol{g}_1 + h_{11} \frac{\partial \Delta \lambda_s}{\partial \boldsymbol{\varepsilon}} + h_{12} \frac{\partial \Delta \lambda_c}{\partial \boldsymbol{\varepsilon}} = \mathbf{0} \tag{9.98}$$

$$\boldsymbol{g}_1 = c_1 a_1 3 \boldsymbol{m} + \mathbf{E}^\mathsf{T} (c_2 \boldsymbol{j}_1 + c_3 \boldsymbol{j}_2)$$

$$h_{11} = c_1 a_2 + \boldsymbol{s}_1{}^\mathsf{T} (c_2 \boldsymbol{j}_1 + c_3 \boldsymbol{j}_2)$$

$$h_{12} = c_1 a_3 + \boldsymbol{s}_2{}^\mathsf{T} (c_2 \boldsymbol{j}_1 + c_3 \boldsymbol{j}_2)$$

Next, consider consistency condition associated with the cap yield surface f_c^{SS} in the form

$$\frac{\mathrm{d}r_3}{\mathrm{d}\varepsilon} = \frac{\partial r_3}{\partial J}\frac{\mathrm{d}J}{\mathrm{d}\varepsilon} + \frac{\partial r_3}{\partial \chi}\frac{\partial \vartheta}{\partial \vartheta}\frac{\partial \vartheta}{\partial \sin 3\theta}\frac{\mathrm{d}\sin 3\theta}{\mathrm{d}\varepsilon} + \frac{\partial r_3}{\partial \sigma_m}\frac{\mathrm{d}\sigma_m}{\mathrm{d}\varepsilon} + \frac{\partial r_3}{\partial p_c}\frac{\mathrm{d}p_c}{\mathrm{d}\varepsilon} \tag{9.99}$$

$$= \frac{\partial r_3}{\partial \sigma_m}\frac{\mathrm{d}\sigma_m}{\mathrm{d}\varepsilon} +$$

$$+ \left(\frac{\partial r_3}{\partial J} + \frac{\partial r_3}{\partial \chi}\frac{\partial \vartheta}{\partial \vartheta}\frac{\partial \vartheta}{\partial \sin 3\theta}\frac{\partial \sin 3\theta}{\partial J}\right)\left[\frac{\mathrm{d}\boldsymbol{s}}{\mathrm{d}\varepsilon}\right]^{\mathsf{T}}\frac{\partial J}{\partial \boldsymbol{s}} +$$

$$+ \frac{\partial r_3}{\partial \chi}\frac{\partial \vartheta}{\partial \vartheta}\frac{\partial \vartheta}{\partial \sin 3\theta}\frac{\partial \sin 3\theta}{\partial I_{3s}}\left[\frac{\mathrm{d}\boldsymbol{s}}{\mathrm{d}\varepsilon}\right]^{\mathsf{T}}\frac{\partial I_{3s}}{\partial \boldsymbol{s}} +$$

$$+ \frac{\partial r_3}{\partial p_c}\frac{\mathrm{d}p_c}{\mathrm{d}\varepsilon} \tag{9.100}$$

$$= c_4\frac{\mathrm{d}\sigma_m}{\mathrm{d}\varepsilon} + c_5\left[\frac{\mathrm{d}\boldsymbol{s}}{\mathrm{d}\varepsilon}\right]^{\mathsf{T}}\boldsymbol{j}_1 + c_6\left[\frac{\mathrm{d}\boldsymbol{s}}{\mathrm{d}\varepsilon}\right]^{\mathsf{T}}\boldsymbol{j}_2 + c_7\frac{\mathrm{d}p_c}{\mathrm{d}\varepsilon} = \boldsymbol{0} \tag{9.101}$$

where

$$\frac{\mathrm{d}\sin 3\theta}{\mathrm{d}\varepsilon} = \frac{\partial \sin 3\theta}{\partial J}\frac{\mathrm{d}J}{\mathrm{d}\varepsilon} + \frac{\partial \sin 3\theta}{\partial I_{3s}}\frac{\mathrm{d}I_{3s}}{\mathrm{d}\varepsilon} \tag{9.102}$$

together with Eqs. (8.222) and (8.223) was exploited. Substituting from Eqs. (9.75), (9.80) and (9.71) to Eq. (9.101) finally yields

$$\frac{\mathrm{d}r_3}{\mathrm{d}\varepsilon} = \boldsymbol{g}_2 + h_{21}\frac{\partial \Delta\lambda_s}{\partial \varepsilon} + h_{22}\frac{\partial \Delta\lambda_c}{\partial \varepsilon} = \boldsymbol{0} \tag{9.103}$$

$$\boldsymbol{g}_2 = (c_4a_1 + c_7a_4)3\boldsymbol{m} + \mathbf{E}^{\mathsf{T}}(c_5\boldsymbol{j}_1 + c_6\boldsymbol{j}_2)$$

$$h_{21} = c_4a_2 + \boldsymbol{s}_1^{\mathsf{T}}(c_5\boldsymbol{j}_1 + c_6\boldsymbol{j}_2)$$

$$h_{22} = c_4a_3 + c_7a_5 + \boldsymbol{s}_2^{\mathsf{T}}(c_5\boldsymbol{j}_1 + c_6\boldsymbol{j}_2)$$

Proceeding in the footsteps of Section 8.4 we may now identify three potential scenarios:

- **Both the shear (Matsuoka-Nakai) and cap yield surfaces are simultaneously active**
  In this case of multi-yield surface plasticity the consistency conditions (9.98) and (9.103) can be now used to solve for $\dfrac{\partial \Delta\lambda_s}{\partial \varepsilon}$ and $\dfrac{\partial \Delta\lambda_c}{\partial \varepsilon}$ as

$$\underbrace{\begin{bmatrix} h_{11} & h_{12} \\ h_{21} & h_{22} \end{bmatrix}}_{\mathbf{H}}\left\{\begin{array}{c}\left(\dfrac{\partial \Delta\lambda_s}{\partial \varepsilon}\right)^{\mathsf{T}} \\ \left(\dfrac{\partial \Delta\lambda_c}{\partial \varepsilon}\right)^{\mathsf{T}}\end{array}\right\} = \left\{\begin{array}{c}-\boldsymbol{g}_1^{\mathsf{T}} \\ -\boldsymbol{g}_2^{\mathsf{T}}\end{array}\right\} \tag{9.104}$$

so

$$\frac{\partial \Delta\lambda_s}{\partial \varepsilon} = \boldsymbol{q}_1 = \frac{1}{h_{11}h_{22} - h_{12}h_{21}}(-h_{22}\boldsymbol{g}_1 + h_{12}\boldsymbol{g}_2) \tag{9.105}$$

$$\frac{\partial \Delta\lambda_c}{\partial \varepsilon} = \boldsymbol{q}_2 = \frac{1}{h_{11}h_{22} - h_{12}h_{21}}(h_{21}\boldsymbol{g}_1 - h_{11}\boldsymbol{g}_2) \tag{9.106}$$

Finally, introducing the vectors $\boldsymbol{q}_1, \boldsymbol{q}_2$ into Eqs. (9.75) and (9.80) gives Eq. (9.65) in the form

$$\mathcal{D} = \mathbf{E} + \mathbf{A} + \mathbf{B} + \mathbf{C} \tag{9.107}$$

where

$$\mathbf{A} = 9a_1\boldsymbol{m}\boldsymbol{m}^{\mathsf{T}} \tag{9.108}$$

$$\mathbf{B} = (3a_2\boldsymbol{m} + \boldsymbol{s}_1)\boldsymbol{q}_1^{\mathsf{T}} \tag{9.109}$$

$$\mathbf{C} = (3a_3\boldsymbol{m} + \boldsymbol{s}_2)\boldsymbol{q}_2^{\mathsf{T}} \tag{9.110}$$

- **Only the shear (Matsuoka-Nakai) yield surface is active**

  We start from Eq. (9.98) and set $\dfrac{\partial \Delta\lambda_c}{\partial\varepsilon} = 0$. This gives

$$\frac{\mathrm{d}r_2}{\mathrm{d}\varepsilon} \;=\; \boldsymbol{g}_1 + h_{11}\frac{\partial \Delta\lambda_s}{\partial\varepsilon} = \mathbf{0} \;\longrightarrow\; \frac{\partial \Delta\lambda_s}{\partial\varepsilon} = -\frac{1}{h_{11}}\boldsymbol{g}_1 = \boldsymbol{q}_1 \qquad (9.111)$$

  Substituting back to Eqs. (9.75) and (9.80) allows us to write Eq. (9.65) as

$$\mathcal{D} = \mathbf{E} + \mathbf{A} + \mathbf{B} \qquad (9.112)$$

  where the matrices **A** and **B** are provided by Eqs. (9.108) and (9.109), respectively.

- **Only the cap yield surface is active**

  The procedure is similar to the previous case but here we adopt Eq. (9.103) and set $\dfrac{\partial \Delta\lambda_s}{\partial\varepsilon} = 0$ instead to get

$$\frac{\mathrm{d}r_2}{\mathrm{d}\varepsilon} \;=\; \boldsymbol{g}_2 + h_{22}\frac{\partial \Delta\lambda_c}{\partial\varepsilon} = \mathbf{0} \;\longrightarrow\; \frac{\partial \Delta\lambda_c}{\partial\varepsilon} = -\frac{1}{h_{22}}\boldsymbol{g}_2 = \boldsymbol{q}_2 \qquad (9.113)$$

  After substituting back to Eqs. (9.75) and (9.80) we now receive Eq. (9.65) in the form

$$\mathcal{D} = \mathbf{E} + \mathbf{A} + \mathbf{C} \qquad (9.114)$$

  where the matrices **A** and **C** are provided by Eqs. (9.108) and (9.110), respectively.

9.4 Note on numerical implementation

Similarly to all plasticity models that include the hardening cap yield surface the issue of initial preconsolidation pressure p_c^{in} must be addressed. Because in the Soft soil model the cap yield surface closely resembles the formulation of the subcritical (compression) part of the Generalized cam clay model, this step is fully compatible with the discussion presented in Section 11.4 including the initial value of the bulk modulus $K^{in} = K^0$ for low initial stresses as this parameter is not included in the standard material setting of the Soft soil model. The only difference is thus the present formulation of the cap yield surface via Eq. (9.7) which, unlike the Generalized Cam-clay model, allows for a non-zero cohesion c. Using the notation from Section 11.4 the initial preconsolidation pressure p_c^{in} then becomes

$$p_c^{in} = -\frac{(\overline{J}^b)^2}{\chi^2(\overline{\theta}^b,\varphi)M^2\widehat{\sigma}_m(\overline{\sigma}_m^a)} - \overline{\sigma}_m^a \qquad (9.115)$$

Because of apex singularity the need for the solution of apex problem may arise for a certain inadmissible stress states. Observing a close similarity of the present plastic potential surface given by Eq. (9.9) with the one adopted in the Drucker-Prager model, recall Eq. (4.6), allows us to follow the discussion presented in Section 4.4. An indicator that calls for the solution of the apex problem is now given by

$$M_\psi \frac{J^{tr}}{G^i} - \frac{1}{K^i}\left(\sigma_m^{tr} - c\cot\varphi\right) < 0 \qquad (9.116)$$

where G^i, K^i are evaluated at the beginning of the new load increment.

9.5 Testing implementation with simple laboratory tests

Figure 9.3 shows simple finite element models to simulate an oedometric, isotropic, and triaxial compression test. The purpose of this section is to address an influence of the initial load step size when starting from zero initial stresses and some specific features related to the application of Soft soil model in drained triaxial compression. While the former issue is thoroughly examined with reference to the Modified Cam-clay model in Section 11.5.1, the latter one takes us back to the performance
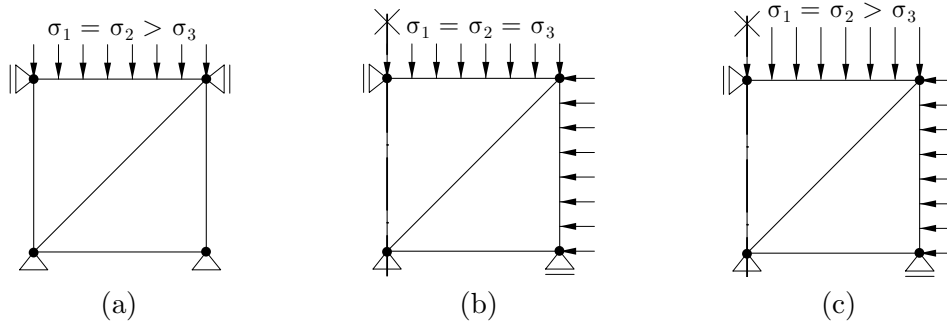
Figure 9.3: Computational models of simple laboratory tests: a) one-dimensional compression (oedometer), b) isotropic compression, c) drained triaxial compression.

Table 9.5: Material properties of Soft soil and Modified Cam-clay model used in numerical simulations

ν	κ	λ	e_{in}	$M_{cs} = M$	c	φ [°]	K_0^{NC}
0.26	0.025	0.181	1.67	1.146	0	20	0.4

of Drucker-Prager model discussed in Section 4.6.2. Table 9.5 stores the material parameters of the Soft soil and the Modified Cam-clay model employed in the presented simulations. The slope of the critical state line M_{cs} used in Eq. (11.17) was calculated on the basis of Eq. (9.1).

The results of one-dimensional compression test are plotted in Fig. 9.4(a). Because starting from zero initial stress the initial stiffness given by

$$K^0 = \frac{1}{\kappa^*}, \quad \text{recall Eq. (11.136)} \tag{9.117}$$

is relatively small yielding a large increment of strain for a relatively large initial load step ($\zeta = 0.1$) as observed in the black and red lines in 9.4(a). Reducing the initial load step size ($\zeta = 0.001$)provides a considerably improved prediction as indicated by the blue line in 9.4(a). A useful option how to arrive at realistic predictions with a relatively low number of load steps by gradually increasing the load step size ζ controlled by the minimum number of required iterations is addressed also in Section 11.5.1, see Fig. 11.7(b) in particular.
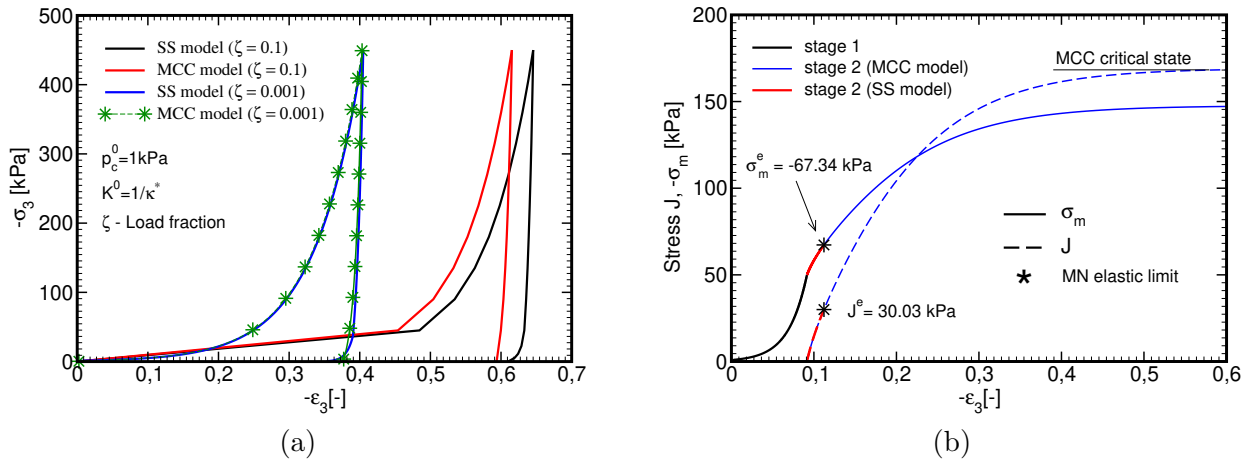
Figure 9.4: a) One-dimensional compression (oedometric) test: compering predictions provided by the Soft soil and Modified Cam-clay model, b) Isotropic compression (stage 1) followed by triaxial compression (stage 2)

Additionally, Figure 9.4(a) compares the predictions derived by the Soft soil (SS) and the Modified Cam-clay (MCC) models. Remember that in triaxial compression the Modified and Generalized Cam-clay models provide the same predictions because the LMN parameter χ in Eqs. (9.7) and (12.3) equals to 1 so the Lode angle dependence is irrelevant. Point out that with the Soft soil model both the

Matsuoka-Nakai and cap yield surfaces are simultaneously active during the loading stage so the stress point moves with the intersection of the two surfaces. This results in some differences in the predicted stress-strain curves. Upon unloading the stress point stays within the elastic region of the Modified Cam-clay model so upon unloading the response predicted by the MCC model is purely nonlinear elastic. On the contrary, the fact that at the end of unloading stage the response changes from triaxial compression to triaxial extension turns on the Matsuoka-Nakai yield surface thus generating additional plastic strains. This is demonstrated by an increased nonlinearity in the derived stress-strain curve, see, e.g., the black line in Fig. 9.4(a).

The second example is concerned with the performance of Soft soil model in drained triaxial compression. To this end, we would like to brink the reader attention to the discussion presented already in Section 4.6.2 for the elastic-perfectly plastic Drucker-Prager model.
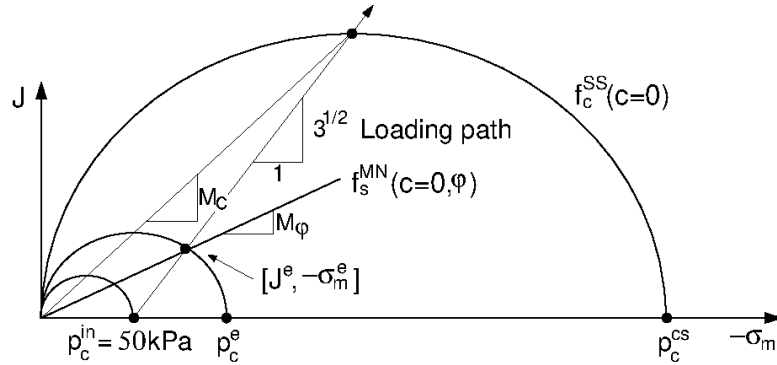
Figure 9.5: Drained triaxial compression: initial conditions and loading path identifying the elastic limit state associated with the Matsuoka-Nakai yield surface and the critical state predicted by the Modified Cam-clay model

Figure 9.5 shows the loading path in triaxial compression relating the increment of deviatoric stress ΔJ and the mean effective stress $\Delta\sigma_m$ as $\Delta J = -\sqrt{3}\Delta\sigma_m$. Also recall that the Matsuoka-Nakai yield surface in the Soft soil model grounds upon perfected plasticity so only the cap yield surface may expand (harden) with increasing volumetric plastic strains. In the first stage of loading, the case of isotropic compression, the cap yield surface thus gradually expands from $p_c = 1$ kPa to $p_c^{in} = 50$ kPa owing to the prescribed confining pressure of 50 kPa. The corresponding stress-strain curve appears as the black solid line in Fig. 9.4(b). In Fig. 9.5 the end point on this curve is manifested by the smallest ellipse being the initial cap yield surface prior to triaxial compression. In the second loading stage, the case of traxial compression, the stress point moves along the set loading path while the cap yield surface continues to expand until reaching the common point of intersection with the Matsuoka-Nakai yield surface. The associated stress-strain curves plot as the solid and dashed red curves in 9.4(b) with the star symbol identifying the common point of intersection of the two yield surfaces. We denote this point as the elastic limit given by the Matsuoka-Nakai yield surface to draw similarity with the Drucker-Prager model. We may now adopt Eq. (4.56) to give the associated stresses $J^e = 30.03$ kPa and $\sigma_m^e = -67.34$ kPa. The corresponding preconsolidation pressure is denoted as p_c^e in Fig. 9.5. Given the prescribed loading path and no hardening of the Matsuoka-Nakai yield the simulation carried out with the Soft soil model is terminated as the stress point cannot move beyond this limit stress state. It is worth mentioning that turning off the Matsuoka-Nakai yield surface, i.e., using purely the Modified Cam-clay model allows us to pass this point until arriving at the critical state predicted by the MCC model manifested by zero increments of plastic volumetric strains. This final cap yield surface is labeled with the preconsolidation pressure p_c^{cs} in Fig. 9.5. The corresponding stress strain curves are plotted as the blue solid and dashed curves in Fig. 9.4(b).

9.6 Soft soil model in stability analysis

Similarly to what was mentioned in Section 8.8 with reference to the Hardening soil model the Soft soil model may appear in stability analysis when performing this analysis within a given calculation stage only. In this case the cap yield surface is simply turned off so the plastic response is driven purely by the Matsuoka-Nakai shear yield surface. Standard shear strength parameters reduction procedure in stability analysis implemented in GEO5 FEM software is thus readily available with no additional actions required.

Chapter 10

Modified Mohr-Coulomb model

New version of the Modified Mohr-Coulomb (MMC) model is under current development and will appear in fall 2025. Apart from currently available features, the MCM model will allow to bound the plastic response along the hydrostatic axis by introducing a compression cap. In order to unite implementation of all model, the van Eckelen type of smoothing of the irregular Mohr-Coulomb hexagon will be replaced by the Matsuoka-Nakai yield surface. Basic information can be found in online manual.

Chapter 11

Modified Cam-clay model

The model belongs to the class of critical state a models and was proposed by Roscoe and his co-workers [68], who in an attempt of confirming the original findings of Hvorslev [38], introduced the concept of a critical void ratio state at which an unlimited deformation can take place without altering the current stress and void ratio state. Within this behavioral framework a strain-dependent yield surface controlling the progressive yielding of a material sample can be defined. Regardless of their point of departure all material points moving along a certain stress path with a progressively evolving yield surface eventually end at a unique critical void ratio line that belongs to a certain unique state boundary surface (SBS) when plotted in $J - \sigma_m - e$ space [68], where J is defined as the square root of the second invariant of deviatoric stress, σ_m is the mean effective stress and e stands for the void ratio, recall Chapter 1. Such a surface appears in Fig. 11.1 where CSL and NCL stand for the critical state line and normal consolidation line, respectively.
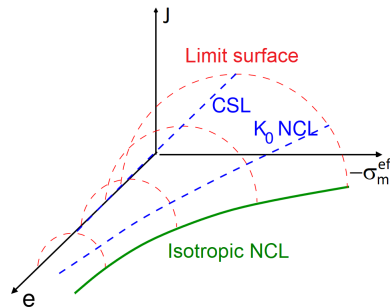
Figure 11.1: State boundary surface

The corresponding yield surface appears in Fig. 11.2. As suggested in Fig. 11.2(b) the yield surface may naturally expand (hardening) or shrink (softening) with the evolution of preconsolidation pressure p_c representing the maximum pressure a soil has witnessed ever before providing the isotropic consolidation conditions apply, e.g. setting $K_0 = 1$ in K_0 procedure described in Section 1.10.2. When projected to a deviatoric plane, the yield surface plots as a circle similarly to the Drucker-Prager model described in Chapter 4.

Table 11.1 provides the list of material parameters of the Modified Cam-clay model.

11.1 Formulation of Modified Cam-clay yield criterion

To begin with, consider projection of a state boundary surface into $e - \ln(-\sigma_m)$. Assuming isotropic loading conditions, $J = 0$ (isotropic compression), allows schematic projection of all points on this surface into a domain bounded by the $\sigma_m - e$ axis and the virgin or normal consolidation line (isotropic NCL) plotted in Fig. 11.3(a). As suggested in [68] this line represents a loosest packing or greatest void ratio for any given value of σ_m stress. Although theoretically acceptable ($e = 0$) a minimum value $e_{min} \neq 0$ of void ratio that the soil can experience is usually assumed. From the mathematical formulation the maximum value of void ratio e_0 will be hereafter associated with a
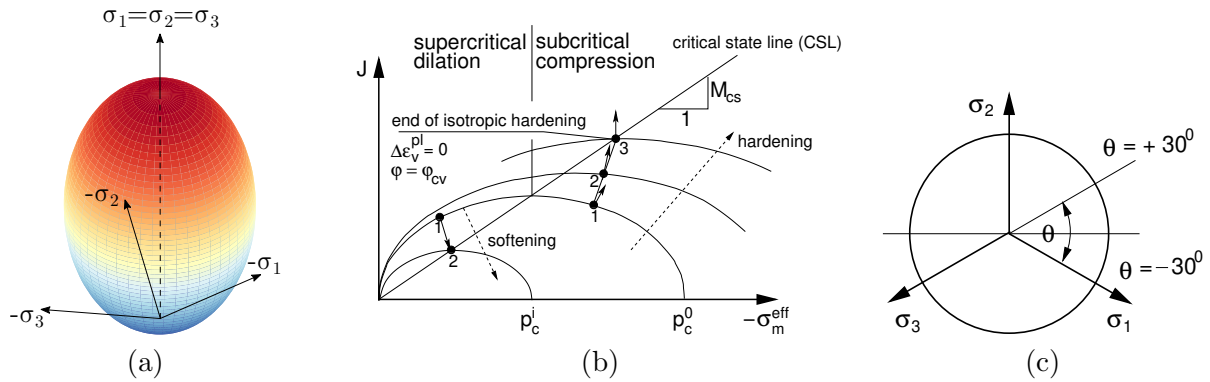
Figure 11.2: Modified Cam-clay yield surface: a) plot in effective principal stress space, b) plot in meridian plane, c) plot in deviatoric plane

Table 11.1: Parameters of Modified Cam-clay plasticity model

Symbol	Units	Description
κ	[-]	Slope of swelling line (swelling modulus)
λ	[-]	Slope of normal consolidation line (isotropic NCL, compression modulus)
e_0	[-]	Maximum void ratio
ν	[-]	Poisson's ratio
M_{cs}	[-]	Slope of critical state line
OCR	[-]	Overconsolidation ratio
POP	[kPa]	Preoverburden pressure
α	[1/°C]	Coefficient of thermal expansion
φ_{cs}	[°]	Critical state friction angle
p_c	[kPa]	Preconsolidation pressure ($p_c^{min} = 1$kPa), calculated

stress level $|\sigma_m| = 1$, Fig. 11.3(a). For a remoulded clay, the soil initially moves down the virgin consolidation line. When unloaded at a certain level of mean effective stress, e.g. p_c^1, it moves up the so called swelling line . When reloaded, it moves along the same line until it rejoins the normal consolidation line and when stressed even further, it follows this line again.
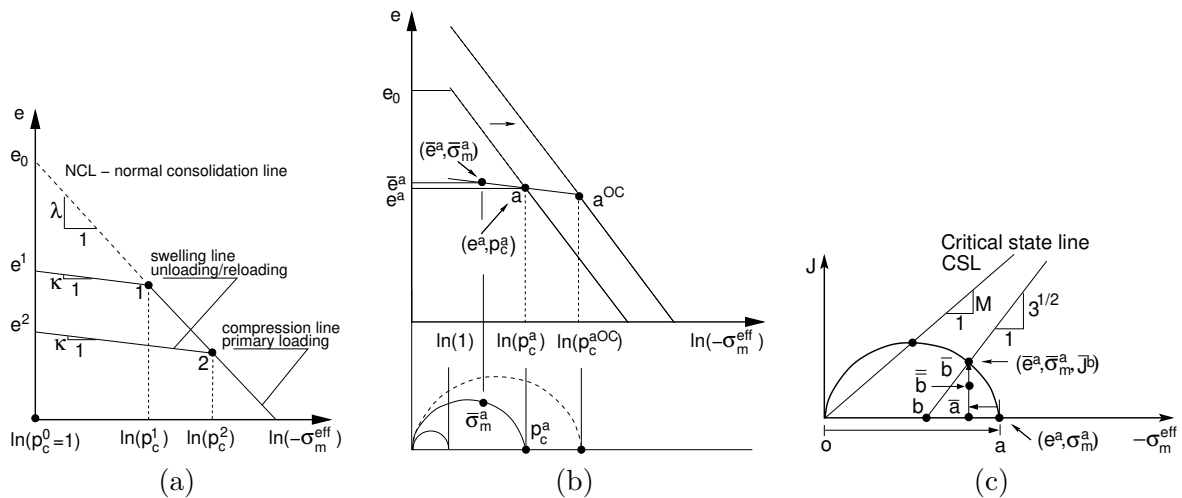
Figure 11.3: a,b) Behavior under isotropic compression, c) Initial state of stress

11.1.1 Constitutive law

Notice that both lines in Fig. 11.3(a) are assumed to be straight in $e - \ln(-\sigma_m)$ space. Introducing the so called compression and swelling moduli λ, κ, respectively, renders the following equations defining the two lines

$$e \;=\; e_0 - \lambda \ln(-\sigma_m) \quad \text{– virgin consolidation line} \tag{11.1}$$

$$e \;=\; e^i - \kappa \ln(-\sigma_m) \quad \text{– swelling line}, i = 1, 2, ... \tag{11.2}$$

While the values of e_0, κ, λ characterize a particular type of clayey soil, the value of initial void ratio e^i is linked to a specific swelling line, i.e., to a specific state of soil. At this point it appears useful to recall that in GEO5 FEM the zero state of deformation is assumed at the end of the 1st calculation stage, which in turn is expected to provide the state of geostatic or initial stress $\overline{\boldsymbol{\sigma}}^a$. As a point of departure in defining the evolution of void ratio it thus becomes desirable to identify the associated void ratio $\overline{e}^a$ in Fig. 11.3(b), which will be considered the initial void ratio e_{in} henceforth, see also Section 1.11. To proceed, imagine that the initial stress of a normally consolidated soil $\overline{\sigma}_m^a$ in Fig. 11.3(b) satisfies the yield condition, see also discussion in Section 11.4 addressing numerical implementation with reference to an initial stiffness and preconsolidation pressure. To arrive at a such stress state, we consider an illustrative example being represented by the $ob\overline{b}$ loading path in Fig. 11.3(c), where the specimen is first consolidated isotropically to point b and then loaded in triaxial compression to arrive at point $\overline{b}$. From void ratio point of view, such a stress state can be reached following the $oa\overline{a}\overline{b}$ loading path, i.e., isotropic loading to point a assuming normal consolidation - isotropic elastic unloading along the κ-line to arrive at point $\overline{a}$ representing essentially a certain overconsolidated stress state - shearing to point $\overline{b}$. The associated initial void ratio $\overline{e}^a$ is then provided by

$$\overline{e}^a = e_{in} = e_0 + (\kappa - \lambda) \ln(p_c^a) - \kappa \ln(-\overline{\sigma}_m^a) \tag{11.3}$$

The above procedure is thus applicable to both normally consolidated (the current stress point sits on the initial yield surface) and overconsolidated (the current stress point is found inside the initial yield surface, e.g., point $\overline{\overline{b}}$ in Fig. 11.1.1(c)) soils.

From a mathematical formulation it appears more convenient (assuming incompressibility of individual grains) to re-plot Fig. 11.3(a) in $\varepsilon_v - \ln(-\sigma_m)$ space, ε_v being the total volumetric strain, see Figs. 11.4.
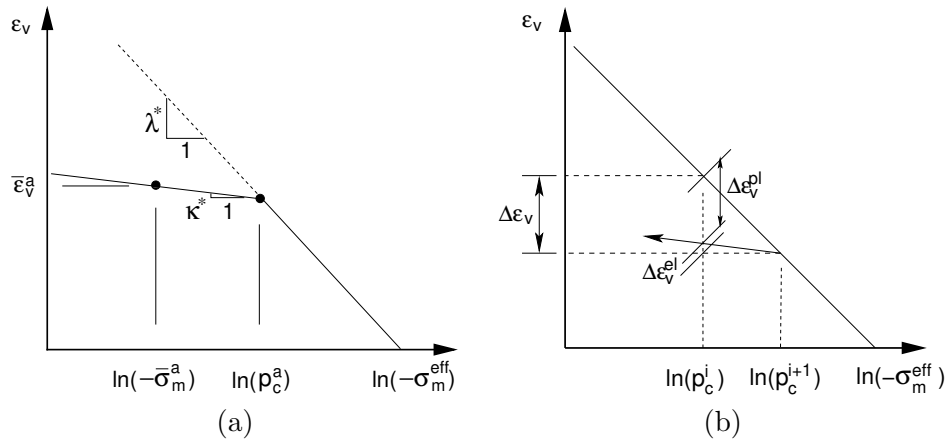
Figure 11.4: a) Behavior under isotropic compression, b) Elastic and plastic part of total strain increment

Note that the rate form of Eq. (11.2) is given by

$$\dot{e} = -\kappa \frac{\dot{\sigma}_m}{\sigma_m} \tag{11.4}$$

With reference to Eq. (1.75) and Fig. 11.4(b) we get the rate of elastic strain as

$$\dot{\varepsilon}_v^{el} = -\frac{\kappa}{1 + e} \frac{\dot{\sigma}_m}{\sigma_m} = -\kappa^* \frac{\dot{\sigma}_m}{\sigma_m} \tag{11.5}$$

Accepting linearization (1.77) provides

$$\dot{\varepsilon}_v^{el} = \frac{\dot{e}}{1 + e_{in}} \tag{11.6}$$

so that

$$\kappa^* = \frac{\kappa}{1 + e_{in}} \quad \text{and similarly} \quad \lambda^* = \frac{\lambda}{1 + e_{in}} \tag{11.7}$$

In summary, the rate form of a constitutive law when making difference between primary loading and unloading-reloading is given by

$$\dot{\sigma}_m = -\frac{\sigma_m}{\lambda^*}\dot{\varepsilon}_v \quad \text{– primary loading} \tag{11.8}$$

$$\dot{\sigma}_m = -\frac{\sigma_m}{\kappa^*}\dot{\varepsilon}_v^{el} \quad \text{– unloading-reloading} \tag{11.9}$$

$$\tag{11.10}$$

When moving along the $\lambda-$line the material point experiences plastic loading while elastic response is assumed inside the domain. During plastic loading the total volumetric strain increment $\Delta\varepsilon_v$ can be split into elastic and plastic parts. With reference to Fig. 11.4(b) we get

$$\Delta\varepsilon_v = -\lambda^* \left[\ln(p_c^{i+1}) - \ln(p_c^i)\right] \tag{11.11}$$

$$\Delta\varepsilon_v^{el} = -\kappa^* \left[\ln(p_c^{i+1}) - \ln(p_c^i)\right] \tag{11.12}$$

$$\Delta\varepsilon_v^{pl} = -(\lambda^* - \kappa^*) \left[\ln(p_c^{i+1}) - \ln(p_c^i)\right] \tag{11.13}$$

or in the rate form

$$\dot{\varepsilon}_v^{pl} = -(\lambda^* - \kappa^*)\frac{\dot{p}_c}{p_c} \tag{11.14}$$

Rearranging Eq. (11.13) then provides the evolution law for preconsolidation pressure p_c during primary loading in the form

$$p_c^{i+1} = p_c^i \exp\left[\frac{-\Delta\varepsilon_v^{pl}}{\lambda^* - \kappa^*}\right] \tag{11.15}$$

Eq. (11.15) thus gives a form of isotropic hardening/softening law for primary loading. During elastic unloading or reloading the preconsolidation pressure p_c remains constant. In analogy with Eq. (11.15) the evolution of mean effective stress σ_m is provided by

$$\sigma_m^{i+1} = \sigma_m^i \exp\left[\frac{-\Delta\varepsilon_v^{el}}{\kappa^*}\right] \tag{11.16}$$

which suggests a nonlinear elastic response.

11.1.2   Yield surface

Assuming a constant value of the void ratio e and following the work of Roscoe and Burland [67] the projection of the state boundary surface in $J - \sigma_m$ space is plotted as an ellipse given by

$$f^{MCC} = \frac{J^2}{M_{cs}^2} + \sigma_m^2 + \sigma_m p_c = 0 \tag{11.17}$$

where p_c is the current value of the preconsolidation pressure and M_{cs} is the slope of critical state line, see Fig. 11.2(a). Note that Eq. (11.17) represents a yield surface of the Modified Cam-clay model proposed in [67]. Its main advantage, apart from the ability to describe (at least qualitatively) the real response of clays (particularly those found in lightly overconsolidated state), is the simplicity in numerical implementation. In its original format the full surface is a surface of revolution about the J-axis thus giving a circular yield surface in the deviatoric plane. The allowable region for the material point to undergo only an elastic response depends solely on the value of M_{cs}, which is assumed to be

constant depending on the value of critical state angle φ_{cs}. As for the Drucker-Prager model it ranges between the values

$$
M_{cs}^{+30°}(\varphi_{cs}) = \frac{2\sqrt{3}\sin\varphi_{cs}}{3-\sin\varphi_{cs}} \quad \text{for triaxial compression} \tag{11.18}
$$

$$
M_{cs}^{-30°}(\varphi_{cs}) = \frac{2\sqrt{3}\sin\varphi_{cs}}{3+\sin\varphi_{cs}} \quad \text{for triaxial extension} \tag{11.19}
$$

It should be mentioned that the GEO5 FEM software adopts the first option, i.e., $M_{cs} = M_{cs}^{+30°}(\varphi_{cs})$.

With reference to Eq. (11.15) the size of the ellipse changes depending on the current value of the preconsolidation pressure p_c. For the material found on the subcritical side the yield surface expands with the direction of plastic strain normal to the yield surface (associated plasticity is assumed) until the point of intersection with the critical state line is reached. At this point (point 3 in Fig. 11.2(b)), the normal to the yield surface is vertical thus no plastic volumetric strain is predicted at this point. Hence, all the plastic strain is distortional. When further sheared under constant volume, the material point behaves as perfectly plastic with no change in stress. Such a response is consistent with what is observed in reality. When on the supercritical side, the constitutive model predicts softening. The amount of softening, however, is too excessive when compared to real soil behavior. In addition, for highly overconsolidated soils the model significantly overestimates the failure stresses. These drawbacks observed by many investigators led to the development of series of cam clay formulations in an attempt to modify the prediction of the clay response on the supercritical side. Mostly, combined yield surfaces were proposed. An overview of several such models is presented in [65]. Another possible modification is suggested in Chapter 12 describing the Generalized Cam-clay model.

11.2 Stress return mapping

With reference to Section 1.4 the yield function in Eq. (11.17) can be rewritten as

$$
\begin{aligned}
f^{MCC} &= \frac{J^2}{M_{cs}^2} + \sigma_m^2 + \sigma_m p_c = \frac{1}{2}\frac{\boldsymbol{s}^{\mathsf{T}}\mathbf{Q}^{-1}\boldsymbol{s}}{M_{cs}^2} + \sigma_m^2 + \sigma_m p_c \\
&= \frac{1}{2}\frac{\boldsymbol{s}^{\mathsf{T}}\mathbf{Q}^{-1}\boldsymbol{s}}{M_{cs}^2} + (\boldsymbol{m}^{\mathsf{T}}\boldsymbol{\sigma})^2 + \boldsymbol{m}^{\mathsf{T}}\boldsymbol{\sigma}p_c = \frac{1}{2}\frac{\boldsymbol{\sigma}^{\mathsf{T}}\mathbf{P}\boldsymbol{\sigma}}{M_{cs}^2} + (\boldsymbol{m}^{\mathsf{T}}\boldsymbol{\sigma})^2 + \boldsymbol{m}^{\mathsf{T}}\boldsymbol{\sigma}p_c
\end{aligned} \tag{11.20}
$$

Because the flow rule is assumed to obey associated plasticity ($f^{MCC} = g^{MCC}$) we get plastic strain increments in the form

$$
\Delta\varepsilon_v^{pl} = \Delta\lambda\frac{\partial f^{MCC}}{\partial\sigma_m} = \Delta\lambda(2\sigma_m + p_c) \tag{11.21}
$$

$$
\Delta\boldsymbol{e}^{pl} = \Delta\lambda\frac{\partial f^{MCC}}{\partial\boldsymbol{s}} = \Delta\lambda\frac{\mathbf{Q}^{-1}\boldsymbol{s}}{M_{cs}^2} = \Delta\lambda\frac{\mathbf{P}\boldsymbol{\sigma}}{M_{cs}^2} \tag{11.22}
$$

$$
\Delta\boldsymbol{\varepsilon}^{pl} = \Delta\lambda\frac{\partial f^{MCC}}{\partial\boldsymbol{\sigma}} = \Delta\lambda\left[\frac{\mathbf{P}\boldsymbol{\sigma}}{M_{cs}^2} + (2\sigma_m + p_c)\boldsymbol{m}\right] \tag{11.23}
$$

where $\Delta\lambda$ represents an increment of plastic multiplier. Starting from the above definitions the formulation of a stress return algorithm may proceed along two pathways:

- Variable elasticity return

- Constant elasticity return (currently implemented in GEO5 FEM)

11.2.1 Variable elasticity return

Recall Eq. (11.16) and write the increment of effective mean stress as

$$
\Delta\sigma_m = \sigma_m^{i+1} - \sigma_m^i = \sigma_m^i\left(\exp\left[\frac{-\Delta\varepsilon_v^{el}}{\kappa^*}\right] - 1\right) = K_s\Delta\varepsilon_v^{el} \tag{11.24}
$$

where superscripts (i) and $(i+1)$ represent to successive load steps. Noting that

$$\Delta\varepsilon_v^{el} = \Delta\varepsilon_v - \Delta\lambda(2\sigma_m^{i+1} + p_c^{i+1}) \tag{11.25}$$

provides the secant bulk modulus $\overline{K}_s$ as a function of the current stress state in the form

$$\overline{K}_s = \sigma_m^i \frac{\exp\left(-\dfrac{\Delta\varepsilon_v - \Delta\lambda(2\sigma_m^{i+1} + p_c^{i+1})}{\kappa^*}\right) - 1}{\Delta\varepsilon_v - \Delta\lambda(2\sigma_m^{i+1} + p_c^{i+1})} = \sigma_m^i \frac{\exp\left[-\dfrac{\Delta\varepsilon_v^{el}}{\kappa^*}\right] - 1}{\Delta\varepsilon_v^{el}} \tag{11.26}$$

The secant shear modulus $\overline{G}_s$ is usually written assuming a constant Poisson ratio ν as, see Section 1.8,

$$\overline{G}_s = \frac{3(1 - 2\nu)}{2(1 + \nu)}\overline{K}_s \tag{11.27}$$

Using a standard predictor corrector procedure described in Section 17.2.9 together with Eq. (11.22), the deviatoric stress at the end of the current load increment is provided by

$$\boldsymbol{s}^{i+1} = \frac{\boldsymbol{s}^i + 2\overline{G}_s\mathbf{Q}\Delta\boldsymbol{e}}{1 + \dfrac{2\overline{G}_s\Delta\lambda}{M_{cs}^2}} = \frac{\boldsymbol{s}^{tr}}{1 + \dfrac{2\overline{G}_s\Delta\lambda}{M_{cs}^2}} \tag{11.28}$$

where $\boldsymbol{s}^{tr}(\overline{G}_s)$ stands for the trial deviatoric stress. Adopting Eq. (1.24) finally gives

$$J^{i+1} = \frac{J^{tr}}{1 + \dfrac{2\overline{G}_s\Delta\lambda}{M_{cs}^2}} \tag{11.29}$$

where

$$J^{tr}(\overline{G}_s) = \sqrt{\frac{1}{2}(\boldsymbol{s}^{tr})^\mathsf{T}\mathbf{Q}^{-1}\boldsymbol{s}^{tr}} = \left[J_2^i + 2\overline{G}_s\Delta\boldsymbol{e}^\mathsf{T}\boldsymbol{s}^i + (\overline{G}_s)^2\Delta E_d^2\right]^{\frac{1}{2}} \tag{11.30}$$

$$J_2^i = \frac{1}{2}(\boldsymbol{s}^i)^\mathsf{T}\mathbf{Q}^{-1}\boldsymbol{s}^i \tag{11.31}$$

$$\Delta E_d = \sqrt{2\Delta\boldsymbol{e}^\mathsf{T}\mathbf{Q}\Delta\boldsymbol{e}} \tag{11.32}$$

It is evident that arriving at deviatoric stresses at the end of the $(i + 1)$ load step requires the knowledge of the mean stress σ_m^{i+1} (Eq. (11.16)), the preconsolidation pressure p_c^{i+1} (Eq. (11.15)), and the increment of plastic multiplier $\Delta\lambda$. To this end, the following set of residuals must be satisfied simultaneously

$$\boldsymbol{r} = \left\{ \begin{array}{c} \sigma_m^{i+1} - \sigma_m^i \exp\left[-\dfrac{\Delta\varepsilon_v^{el}}{\kappa^*}\right] \\[2mm] p_c^{i+1} - p_c^i \exp\left[-\dfrac{\Delta\lambda}{\lambda^* - \kappa^*}\left(2\sigma_m^{i+1} + p_c^{i+1}\right)\right] \\[2mm] \dfrac{\left(J^{i+1}\right)^2}{M_{cs}^2} + \left(\sigma_m^{i+1}\right)^2 + \sigma_m^{i+1}p_c^{i+1} \end{array} \right\} = \boldsymbol{r}(\boldsymbol{a}(\boldsymbol{\varepsilon}), \boldsymbol{\varepsilon}) \tag{11.33}$$

where the vector of primary variable $\boldsymbol{a}$ is reads

$$\boldsymbol{a}^\mathsf{T} = \{\sigma_m^{i+1}, p_c^{i+1}, \Delta\lambda\} \tag{11.34}$$

Such a system of implicit equations is solved with the help of Newton-Raphson method

$$\boldsymbol{a}_{j+1}^{i+1} = \boldsymbol{a}_j^{i+1} - \mathbf{H}^{-1}\boldsymbol{r}_j \tag{11.35}$$

supplemented by the initial condition

$$(\boldsymbol{a}_0^{i+1})^\mathsf{T} = \{\sigma_m^{tr}, p_c^i, 0\} \tag{11.36}$$

$$\boldsymbol{r}_0^\mathsf{T} = \{0, 0, \frac{(J^{tr})^2}{M_{cs}^2} + (\sigma_m^{tr})^2 + \sigma_m^{tr}p_c^i\} \tag{11.37}$$

With reference to Eq. (11.28) the Jacobian matrix $\mathbf{H}$ is then written as

$$\mathbf{H} = \frac{\partial \boldsymbol{r}}{\partial \boldsymbol{a}} + \frac{\partial \boldsymbol{r}}{\partial \boldsymbol{s}} \frac{\partial \boldsymbol{s}}{\partial \boldsymbol{a}} = \begin{bmatrix} \dfrac{\mathrm{d}r_1}{\mathrm{d}\sigma_m} & \dfrac{\mathrm{d}r_1}{\mathrm{d}p_c} & \dfrac{\mathrm{d}r_1}{\mathrm{d}\Delta\lambda} \\[2ex] \dfrac{\mathrm{d}r_2}{\mathrm{d}\sigma_m} & \dfrac{\mathrm{d}r_2}{\mathrm{d}p_c} & \dfrac{\mathrm{d}r_2}{\mathrm{d}\Delta\lambda} \\[2ex] \dfrac{\mathrm{d}r_3}{\mathrm{d}\sigma_m} & \dfrac{\mathrm{d}r_3}{\mathrm{d}p_c} & \dfrac{\mathrm{d}r_3}{\mathrm{d}\Delta\lambda} \end{bmatrix} \tag{11.38}$$

The components of matrix $\mathbf{H}$ are

- $\boldsymbol{H}_{1i}$

$$\frac{\mathrm{d}r_1}{\mathrm{d}\sigma_m} = \frac{\partial r_1}{\partial \sigma_m} = 1 - \frac{2\Delta\lambda}{\kappa^*}\overline{\sigma}_m \tag{11.39}$$

$$\frac{\mathrm{d}r_1}{\mathrm{d}p_c} = \frac{\partial r_1}{\partial p_c} = -\frac{\Delta\lambda}{\kappa^*}\overline{\sigma}_m \tag{11.40}$$

$$\frac{\mathrm{d}r_1}{\mathrm{d}\Delta\lambda} = \frac{\partial r_1}{\partial \Delta\lambda} = -\frac{2\sigma_m^{i+1} + p_c^{i+1}}{\kappa^*}\overline{\sigma}_m \tag{11.41}$$

- $\boldsymbol{H}_{2i}$

$$\frac{\mathrm{d}r_2}{\mathrm{d}\sigma_m} = \frac{\partial r_2}{\partial \sigma_m} = \frac{2\Delta\lambda}{\lambda^* - \kappa^*}\overline{p}_c \tag{11.42}$$

$$\frac{\mathrm{d}r_2}{\mathrm{d}p_c} = \frac{\partial r_2}{\partial p_c} = 1 + \frac{\Delta\lambda}{\lambda^* - \kappa^*}\overline{p}_c \tag{11.43}$$

$$\frac{\mathrm{d}r_2}{\mathrm{d}\Delta\lambda} = \frac{\partial r_2}{\partial \Delta\lambda} = \frac{2\sigma_m^{i+1} + p_c^{i+1}}{\lambda^* - \kappa^*}\overline{p}_c \tag{11.44}$$

- $\boldsymbol{H}_{3i}$

$$\frac{\mathrm{d}r_3}{\mathrm{d}\sigma_m} = \frac{\partial r_3}{\partial \sigma_m} + \left(\frac{\partial r_3}{\partial \boldsymbol{s}}\right)^{\mathsf{T}} \frac{\partial \boldsymbol{s}}{\partial \overline{G}_s} \frac{\partial \overline{G}_s}{\partial \sigma_m} \tag{11.45}$$

$$= \frac{\partial r_3}{\partial \sigma_m} + \frac{\partial r_3}{\partial J} \frac{\partial J}{\partial \overline{G}_s} \frac{\partial \overline{G}_s}{\partial \sigma_m} \tag{11.46}$$

$$\frac{\mathrm{d}r_3}{\mathrm{d}p_c} = \frac{\partial r_3}{\partial p_c} + \left(\frac{\partial r_3}{\partial \boldsymbol{s}}\right)^{\mathsf{T}} \frac{\partial \boldsymbol{s}}{\partial \overline{G}_s} \frac{\partial \overline{G}_s}{\partial p_c} \tag{11.47}$$

$$= \frac{\partial r_3}{\partial p_c} + \frac{\partial r_3}{\partial J} \frac{\partial J}{\partial \overline{G}_s} \frac{\partial \overline{G}_s}{\partial p_c} \tag{11.48}$$

$$\frac{\mathrm{d}r_3}{\mathrm{d}\Delta\lambda} = \left(\frac{\partial r_3}{\partial \boldsymbol{s}}\right)^{\mathsf{T}} \left(\frac{\partial \boldsymbol{s}}{\partial \Delta\lambda} + \frac{\partial \boldsymbol{s}}{\partial \overline{G}_s} \frac{\partial \overline{G}_s}{\partial \Delta\lambda}\right) \tag{11.49}$$

$$= \frac{\partial r_3}{\partial J} \left(\frac{\partial J}{\partial \Delta\lambda} + \frac{\partial J}{\partial \overline{G}_s} \frac{\partial \overline{G}_s}{\partial \Delta\lambda}\right) \tag{11.50}$$

where

$$\overline{\sigma}_m = \sigma_m^i \exp\left[-\frac{\Delta\varepsilon_v^{el}}{\kappa^*}\right] \tag{11.51}$$

$$\overline{p}_c = p_c^i \exp\left[-\frac{\Delta\varepsilon_v^{pl}}{\lambda^* - \kappa^*}\right] = p_c^i \exp\left[-\frac{\Delta\lambda}{\lambda^* - \kappa^*}\left(2\sigma_m^{i+1} + p_c^{i+1}\right)\right] \tag{11.52}$$

with partial derivatives in vector $\boldsymbol{H}_{3i}$ given by

$$
\frac{\partial r_3}{\partial \sigma_m} = 2\sigma_m^{i+1} + p_c^{i+1} \tag{11.53}
$$

$$
\frac{\partial r_3}{\partial p_c} = \sigma_m^{i+1} \tag{11.54}
$$

$$
\frac{\partial r_3}{\partial \boldsymbol{s}} = \frac{\mathbf{Q}^{-1}\boldsymbol{s}^{i+1}}{M_{cs}^2} \tag{11.55}
$$

$$
\frac{\partial \boldsymbol{s}}{\partial \Delta\lambda} = -\frac{\boldsymbol{s}^i + 2\overline{G}_s\mathbf{Q}\Delta\boldsymbol{e}}{\left(1 + \dfrac{2\overline{G}_s\Delta\lambda}{M_{cs}^2}\right)^2}\frac{2\overline{G}_s}{M_{cs}^2} = -\frac{\boldsymbol{s}}{1 + \dfrac{2\overline{G}_s\Delta\lambda}{M_{cs}^2}}\frac{2\overline{G}_s}{M_{cs}^2} \tag{11.56}
$$

$$
\frac{\partial \boldsymbol{s}}{\partial \overline{G}_s} = \frac{2\mathbf{Q}\Delta\boldsymbol{e} - \dfrac{2\Delta\lambda}{M_{cs}^2}\boldsymbol{s}^i}{\left(1 + \dfrac{2\overline{G}_s\Delta\lambda}{M_{cs}^2}\right)^2} = \frac{2\mathbf{Q}\Delta\boldsymbol{e} - \dfrac{2\Delta\lambda}{M_{cs}^2}\boldsymbol{s}}{1 + \dfrac{2\overline{G}_s\Delta\lambda}{M_{cs}^2}} \tag{11.57}
$$

$$
\frac{\partial r_3}{\partial J} = \frac{2J^{i+1}}{M_{cs}^2} \tag{11.58}
$$

$$
\frac{\partial J}{\partial \Delta\lambda} = -\frac{J^{tr}}{\left(1 + \dfrac{2\overline{G}_s\Delta\lambda}{M_{cs}^2}\right)^2}\frac{2\overline{G}_s}{M_{cs}^2} = -\frac{J}{1 + \dfrac{2\overline{G}_s\Delta\lambda}{M_{cs}^2}}\frac{2\overline{G}_s}{M_{cs}^2} \tag{11.59}
$$

$$
\frac{\partial J}{\partial \overline{G}_s} = \frac{\dfrac{\partial J^{tr}}{\partial \overline{G}_s}\left(1 + \dfrac{2\overline{G}_s\Delta\lambda}{M_{cs}^2}\right) - J^{tr}\dfrac{2\Delta\lambda}{M_{cs}^2}}{\left(1 + \dfrac{2\overline{G}_s\Delta\lambda}{M_{cs}^2}\right)^2} = \frac{\dfrac{\partial J^{tr}}{\partial \overline{G}_s} - J\dfrac{2\Delta\lambda}{M_{cs}^2}}{1 + \dfrac{2\overline{G}_s\Delta\lambda}{M_{cs}^2}} \tag{11.60}
$$

$$
\frac{\partial J^{tr}}{\partial \overline{G}_s} = \frac{1}{J^{tr}}\left(\Delta\boldsymbol{e}^{\mathsf{T}}\boldsymbol{s}^i + \overline{G}_s\Delta E_d^2\right) \tag{11.61}
$$

$$
\frac{\partial \overline{G}_s}{\partial \sigma_m} = \zeta\frac{\partial \overline{K}_s}{\partial \Delta\varepsilon_v^{el}}\frac{\partial \Delta\varepsilon_v^{el}}{\partial \sigma_m} = -2\Delta\lambda\zeta\frac{\partial \overline{K}_s}{\partial \Delta\varepsilon_v^{el}} \tag{11.62}
$$

$$
\frac{\partial \overline{G}_s}{\partial p_c} = \zeta\frac{\partial \overline{K}_s}{\partial \Delta\varepsilon_v^{el}}\frac{\partial \Delta\varepsilon_v^{el}}{\partial p_c} = -\Delta\lambda\zeta\frac{\partial \overline{K}_s}{\partial \Delta\varepsilon_v^{el}} \tag{11.63}
$$

$$
\frac{\partial \overline{G}_s}{\partial \Delta\lambda} = \zeta\frac{\partial \overline{K}_s}{\partial \Delta\varepsilon_v^{el}}\frac{\partial \Delta\varepsilon_v^{el}}{\partial p_c} = -(2\sigma_m^{i+1} + p_c^{i+1})\zeta\frac{\partial \overline{K}_s}{\partial \Delta\varepsilon_v^{el}} \tag{11.64}
$$

$$
\frac{\partial \overline{K}_s}{\partial \Delta\varepsilon_v^{el}} = -\frac{\overline{K}_s\kappa^* + \overline{\sigma}_m}{\kappa^*\Delta\varepsilon_v^{el}} \tag{11.65}
$$

11.2.2 Constant elasticity return

When keeping the bulk modulus constant within a given load step, i.e., $\overline{K}_s = K_s^i = -\dfrac{\sigma_m^i}{\kappa^*}$, we arrive at a simplified version of Eq. (11.16) in the form

$$\sigma_m^{i+1} = \sigma_m^i + K_s^i(\Delta\varepsilon_v - \Delta\varepsilon_v^{pl}) = \sigma_m^{tr} - K_s^i\Delta\varepsilon_v^{pl} \tag{11.66}$$

Next, substitute from Eq. (11.21) into Eq. (11.66) and suitably rearrange to get

$$\sigma_m^{i+1} = \frac{\sigma_m^{tr} - K_s^i\Delta\lambda p_c^{i+1}}{1 + 2K_s^i\Delta\lambda} = \frac{\sigma_m^i + K_s^i(\Delta\varepsilon_v - \Delta\lambda p_c^{i+1})}{1 + 2K_s^i\Delta\lambda} \tag{11.67}$$

Introducing Eq. (11.67) into Eq. (11.15) or Eq. (11.52) gives the preconsolidation pressure p_c^{i+1} as

$$
\begin{aligned}
p_c^{i+1} &= p_c^i \exp\left[-\frac{\Delta\lambda(2\sigma_m^{i+1} + p_c^{i+1})}{\lambda^* - \kappa^*}\right] = p_c^i \exp\left[-\frac{\Delta\lambda}{\lambda^* - \kappa^*}\frac{2\sigma_m^{tr} + p_c^{i+1}}{1 + 2K_s^i\Delta\lambda}\right] \\
&= p_c^i \exp\left[-\frac{\Delta\lambda}{\lambda^* - \kappa^*}\frac{2(\sigma_m^i + K_s^i\Delta\varepsilon_v) + p_c^{i+1}}{1 + 2K_s^i\Delta\lambda}\right]
\end{aligned}
\tag{11.68}
$$

Similar procedure yielding Eq. (11.67) can be exploited to provide the deviatoric stress $\boldsymbol{s}^{i+1}$

$$\boldsymbol{s}^{i+1} = \frac{\boldsymbol{s}^{tr}}{1 + \dfrac{2G_s^i\Delta\lambda}{M_{cs}^2}} = \frac{\boldsymbol{s}^i + 2G_s^i\mathbf{Q}\Delta\boldsymbol{e}}{1 + \dfrac{2G_s^i\Delta\lambda}{M_{cs}^2}} \tag{11.69}$$

and subsequently

$$J^{i+1} = \frac{J^{tr}}{1 + \dfrac{2G_s^i\Delta\lambda}{M_{cs}^2}} \tag{11.70}$$

Therefore, $\sigma_m^{i+1} = \sigma_m^{i+1}(p_c^{i+1}, \Delta\lambda)$, $\boldsymbol{s}^{i+1} = \boldsymbol{s}^{i+1}(p_c^{i+1}, \Delta\lambda)$, $J^{i+1} = J^{i+1}(p_c^{i+1}, \Delta\lambda)$ are functions p_c^{i+1} and $\Delta\lambda$ only. The latter two variables can be arranged in the vector of primary variables $\boldsymbol{a}$

$$\boldsymbol{a}^\mathsf{T} = \{p_c^{i+1}, \Delta\lambda\} \tag{11.71}$$

They follow from the solution of the following two residuals

$$\boldsymbol{r} = \left\{
\begin{array}{c}
p_c^{i+1} - p_c^i \exp\left[-\dfrac{\Delta\lambda}{\lambda^* - \kappa^*}\dfrac{2(\sigma_m^i + K_s^i\Delta\varepsilon_v) + p_c^{i+1}}{1 + 2K_s^i\Delta\lambda}\right] \\
\dfrac{\left(J^{i+1}\right)^2}{M_{cs}^2} + \left(\sigma_m^{i+1}\right)^2 + \sigma_m^{i+1}p_c^{i+1}
\end{array}
\right\} \tag{11.72}$$

employing the Newton-Raphson scheme (11.35) with

$$(\boldsymbol{a}_0^{i+1})^\mathsf{T} = \{p_c^i, 0\} \tag{11.73}$$

$$\boldsymbol{r}_0^\mathsf{T} = \left\{0, \frac{(J^{tr})^2}{M_{cs}^2} + (\sigma_m^{tr})^2 + \sigma_m^{tr}p_c^i\right\} \tag{11.74}$$

The 2×2 Jacobian matrix $\mathbf{H}$ now receives the form

$$\mathbf{H} = \frac{\partial\boldsymbol{r}}{\partial\boldsymbol{a}} + \frac{\partial\boldsymbol{r}}{\partial J}\left(\frac{\partial J}{\partial\boldsymbol{a}}\right)^\mathsf{T} + \frac{\partial\boldsymbol{r}}{\partial\sigma_m}\left(\frac{\partial\sigma_m}{\partial\boldsymbol{a}}\right)^\mathsf{T} = \begin{bmatrix} \dfrac{\mathrm{d}r_1}{\mathrm{d}p_c} & \dfrac{\mathrm{d}r_1}{\mathrm{d}\Delta\lambda} \\ \dfrac{\mathrm{d}r_2}{\mathrm{d}p_c} & \dfrac{\mathrm{d}r_2}{\mathrm{d}\Delta\lambda} \end{bmatrix}$$

where

- $\boldsymbol{H}_{1i}$

$$\frac{\mathrm{d}r_1}{\mathrm{d}p_c} = 1 + \frac{\overline{p}_c}{\lambda^* - \kappa^*}\frac{\Delta\lambda}{1 + 2K_s^i\Delta\lambda} \tag{11.75}$$

$$\frac{\mathrm{d}r_1}{\mathrm{d}\Delta\lambda} = \frac{\overline{p}_c}{\lambda^* - \kappa^*}\frac{2\sigma_m^{tr} + p_c^{i+1}}{(1 + 2K_s^i\Delta\lambda)^2} = \frac{\mathrm{d}p_c}{\lambda^* - \kappa^*}\frac{2\sigma_m^{i+1} + p_c^{i+1}}{1 + 2K_s^i\Delta\lambda} \tag{11.76}$$

- $\boldsymbol{H}_{2i}$

$$\frac{\mathrm{d}r_2}{\mathrm{d}p_c} = \frac{\partial f^{MCC}}{\partial p_c} + \frac{\partial f^{MCC}}{\partial \sigma_m}\frac{\partial \sigma_m}{\partial p_c} = \sigma_m^{i+1} - (2\sigma_m^{i+1} + p_c^{i+1})\frac{K_s^i\Delta\lambda}{1 + 2K_s^i\Delta\lambda} \tag{11.77}$$

$$\frac{\mathrm{d}r_2}{\mathrm{d}\Delta\lambda} = \frac{\partial f^{MCC}}{\partial J}\frac{\partial J}{\partial \Delta\lambda} + \frac{\partial f^{MCC}}{\partial \sigma_m}\frac{\partial \sigma_m}{\partial \Delta\lambda} \tag{11.78}$$

$$\frac{\partial f^{MCC}}{\partial J}\frac{\partial J}{\partial \Delta\lambda} = -\frac{2J^{i+1}}{M_{cs}^2}\frac{J^{tr}\dfrac{2G_s^i}{M_{cs}^2}}{\left(1 + \dfrac{2G_s^i\Delta\lambda}{M_{cs}^2}\right)^2} = -\frac{4G_s^i(J^{i+1})^2}{M_{cs}^2(M_{cs}^2 + 2G_s^i\Delta\lambda)} \tag{11.79}$$

$$\frac{\partial f^{MCC}}{\partial \sigma_m}\frac{\partial \sigma_m}{\partial \Delta\lambda} = -(2\sigma_m^{i+1} + p_c^{i+1})\frac{K_s^i(2\sigma_m^{tr} + p_c^{i+1})}{(1 + 2K_s^i\Delta\lambda)^2} = -K_s^i\frac{(2\sigma_m^{i+1} + p_c^{i+1})^2}{1 + 2K_s^i\Delta\lambda} \tag{11.80}$$

where we again introduced

$$\overline{p}_c = p_c^i \exp\left[-\frac{\Delta\lambda}{\lambda^* - \kappa^*}\frac{2(\sigma_m^i + K_s^i\Delta\varepsilon_v) + p_c^{i+1}}{1 + 2K_s^i\Delta\lambda}\right] \tag{11.81}$$

It is worth to remember that all derivatives are evaluated at the end of the $(i+1)$ load step, i.e., they are taken with respect to $p_c^{i+1}, \sigma_m^{i+1}, \boldsymbol{s}^{i+1}$, and J^{i+1}.

11.3   Algorithmic tangent stiffness matrix

Similarly to Section 4.3 we begin by writing the algorithmic tangent stiffness matrix $\boldsymbol{\mathcal{D}}$ as

$$\boldsymbol{\mathcal{D}} = \frac{\mathrm{d}\boldsymbol{\sigma}^{i+1}}{\mathrm{d}\boldsymbol{\varepsilon}^{i+1}} = 3\boldsymbol{m}\left(\frac{\mathrm{d}\sigma_m^{i+1}}{\mathrm{d}\boldsymbol{\varepsilon}^{i+1}}\right)^{\mathsf{T}} + \frac{\mathrm{d}\boldsymbol{s}^{i+1}}{\mathrm{d}\boldsymbol{\varepsilon}^{i+1}} \tag{11.82}$$

and consider the two stress return mapping approaches described in the above two sections separately. Taking into account the last sentence in the previous section we drop the superscripts $(i+1)$ to raise readability, so for example $\dfrac{\mathrm{d}\boldsymbol{\sigma}}{\mathrm{d}\boldsymbol{\varepsilon}} = \dfrac{\mathrm{d}\boldsymbol{\sigma}^{i+1}}{\mathrm{d}\boldsymbol{\varepsilon}^{i+1}}$.

11.3.1   Matrix $\boldsymbol{\mathcal{D}}$ based on variable elasticity stress return

The formulation proceeds closely in the footsteps of [14] with some minor simplifications attributed to omitting the residuum g_2 in Eq. (3.13b).

Given Eqs. (11.16) and (11.15) we first write

$$\begin{aligned}
\frac{\mathrm{d}\sigma_m}{\mathrm{d}\boldsymbol{\varepsilon}} &= \frac{\partial \sigma_m}{\partial \Delta\varepsilon_v^{el}}\frac{\mathrm{d}\Delta\varepsilon_v^{el}}{\mathrm{d}\boldsymbol{\varepsilon}} = -\frac{\sigma_m}{\kappa^*}\frac{\mathrm{d}\Delta\varepsilon_v^{el}}{\mathrm{d}\boldsymbol{\varepsilon}} = \tilde{\sigma}_m\frac{\mathrm{d}\Delta\varepsilon_v^{el}}{\mathrm{d}\boldsymbol{\varepsilon}} \\
&= \tilde{\sigma}_m\left[\frac{\partial \Delta\varepsilon_v^{el}}{\partial \boldsymbol{\varepsilon}} - \Delta\lambda\left(2\frac{\mathrm{d}\sigma_m}{\mathrm{d}\boldsymbol{\varepsilon}} + \frac{\mathrm{d}p_c}{\mathrm{d}\boldsymbol{\varepsilon}}\right) - (2\sigma_m^{i+1} + p_c^{i+1})\frac{\partial \Delta\lambda}{\partial \boldsymbol{\varepsilon}}\right]
\end{aligned} \tag{11.83}$$

$$\frac{\mathrm{d}p_c}{\mathrm{d}\boldsymbol{\varepsilon}} = -\frac{p_c^{i+1}}{\lambda^* - \kappa^*}\left[\Delta\lambda\left(2\frac{\mathrm{d}\sigma_m}{\mathrm{d}\boldsymbol{\varepsilon}} + \frac{\mathrm{d}p_c}{\mathrm{d}\boldsymbol{\varepsilon}}\right) + (2\sigma_m^{i+1} + p_c^{i+1})\frac{\partial \Delta\lambda}{\partial \boldsymbol{\varepsilon}}\right] \tag{11.84}$$

Next, rearrange Eq. (11.84) to get

$$\frac{\mathrm{d}p_c}{\mathrm{d}\boldsymbol{\varepsilon}} = -\frac{2\Delta\lambda p_c^{i+1}}{(\lambda^* - \kappa^*) + \Delta\lambda p_c^{i+1}}\frac{\mathrm{d}\sigma_m}{\mathrm{d}\boldsymbol{\varepsilon}} - \frac{p_c^{i+1}(2\sigma_m^{i+1} + p_c^{i+1})}{(\lambda^* - \kappa^*) + \Delta\lambda p_c^{i+1}}\frac{\partial\Delta\lambda}{\partial\boldsymbol{\varepsilon}} \tag{11.85}$$

Substituting from Eq. (11.85) into Eq. (11.83) and rearranging provides

$$\frac{\mathrm{d}\sigma_m}{\mathrm{d}\boldsymbol{\varepsilon}} = a_1 3\boldsymbol{m} + a_2\frac{\partial\Delta\lambda}{\partial\boldsymbol{\varepsilon}} \tag{11.86}$$

$$a_1 = \frac{\tilde{\sigma}_m}{a}\left(1 + \frac{\Delta\lambda p_c^{i+1}}{\lambda^* - \kappa^*}\right) = \tilde{\sigma}_m\left(1 - \frac{2\Delta\lambda\tilde{\sigma}_m}{a}\right) \tag{11.87}$$

$$a_2 = -\frac{\tilde{\sigma}_m}{a}\left(2\sigma_m^{i+1} + p_c^{i+1}\right) \tag{11.88}$$

$$a = 1 + \frac{\Delta\lambda p_c^{i+1}}{\lambda^* - \kappa^*} + 2\Delta\lambda\tilde{\sigma}_m \tag{11.89}$$

Similarly, substituting from Eq. (11.86) into Eq. (11.85) and rearranging yields

$$\frac{\mathrm{d}p_c}{\mathrm{d}\boldsymbol{\varepsilon}} = a_3 3\boldsymbol{m} + a_4\frac{\partial\Delta\lambda}{\partial\boldsymbol{\varepsilon}^{i+1}} \tag{11.90}$$

$$a_3 = -\frac{\tilde{\sigma}_m}{a}\frac{2\Delta\lambda p_c^{i+1}}{\lambda^* - \kappa^*} \tag{11.91}$$

$$a_4 = -\frac{p_c^{i+1}}{a}\frac{2\sigma_m^{i+1} + p_c^{i+1}}{\lambda^* - \kappa^*} \tag{11.92}$$

With reference to Eq. (11.28) the second term in Eq. (11.82) becomes

$$\frac{\mathrm{d}\boldsymbol{s}}{\mathrm{d}\boldsymbol{\varepsilon}} = \frac{\partial\boldsymbol{s}}{\partial\Delta\boldsymbol{e}}\frac{\partial\Delta\boldsymbol{e}}{\partial\boldsymbol{\varepsilon}} + \frac{\partial\boldsymbol{s}}{\partial\Delta\lambda}\left(\frac{\partial\Delta\lambda}{\partial\boldsymbol{\varepsilon}}\right)^{\mathsf{T}} + \frac{\partial\boldsymbol{s}}{\partial\overline{G}_s}\frac{\partial\overline{G}_s}{\partial\Delta\varepsilon_v^{el}}\left(\frac{\mathrm{d}\Delta\varepsilon_v^{el}}{\mathrm{d}\boldsymbol{\varepsilon}}\right)^{\mathsf{T}} \tag{11.93}$$

$$= \mathbf{E} + \frac{\partial\boldsymbol{s}}{\partial\Delta\lambda}\left(\frac{\partial\Delta\lambda}{\partial\boldsymbol{\varepsilon}}\right)^{\mathsf{T}} + \boldsymbol{\mu}\left(\frac{\mathrm{d}\Delta\varepsilon_v^{el}}{\mathrm{d}\boldsymbol{\varepsilon}}\right)^{\mathsf{T}} \tag{11.94}$$

The partial derivatives appearing in Eq. (11.94) are

$$\frac{\partial\boldsymbol{s}}{\partial\Delta\boldsymbol{e}} = \frac{2\overline{G}_s\mathbf{Q}}{1 + \dfrac{2\overline{G}_s\Delta\lambda}{M_{cs}^2}} \tag{11.95}$$

$$\frac{\partial\boldsymbol{s}}{\partial\Delta\lambda} = -\frac{\boldsymbol{s}^i + 2\mathbf{Q}\Delta\boldsymbol{e}}{\left(1 + \dfrac{2\overline{G}_s\Delta\lambda}{M_{cs}^2}\right)^2}\frac{2\overline{G}_s}{M_{cs}^2} = -\frac{\boldsymbol{s}}{1 + \dfrac{2\overline{G}_s\Delta\lambda}{M_{cs}^2}}\frac{2\overline{G}_s}{M_{cs}^2}, \quad \text{Eq. (11.56)} \tag{11.96}$$

$$\frac{\partial\boldsymbol{s}}{\partial\overline{G}_s} = \frac{2\mathbf{Q}\Delta\boldsymbol{e} - \dfrac{2\Delta\lambda}{M_{cs}^2}\boldsymbol{s}^i}{\left(1 + \dfrac{2\overline{G}_s\Delta\lambda}{M_{cs}^2}\right)^2} = \frac{2\mathbf{Q}\Delta\boldsymbol{e} - \dfrac{2\Delta\lambda}{M_{cs}^2}\boldsymbol{s}}{1 + \dfrac{2\overline{G}_s\Delta\lambda}{M_{cs}^2}}, \quad \text{Eq. (11.57)} \tag{11.97}$$

$$\frac{\partial\overline{G}_s}{\partial\Delta\varepsilon_v^{el}} = \zeta\frac{\partial\overline{K}_s}{\partial\Delta\varepsilon_v^{el}} = -\frac{\zeta}{\Delta\varepsilon_v^{el}}\left(\overline{K}_s + \frac{\sigma_m^{i+1}}{\kappa^*}\right) \tag{11.98}$$

$$\frac{\partial\Delta\boldsymbol{e}}{\partial\boldsymbol{\varepsilon}^{i+1}} = \mathbf{PQ} \tag{11.99}$$

With reference to Eq. (11.83) the last total derivative in Eq. (11.82) receives the form

$$\frac{\mathrm{d}\Delta\varepsilon_v^{el}}{\mathrm{d}\boldsymbol{\varepsilon}} = \frac{\partial\Delta\varepsilon_v^{el}}{\partial\boldsymbol{\varepsilon}} - \Delta\lambda\left(2\frac{\mathrm{d}\sigma_m}{\mathrm{d}\boldsymbol{\varepsilon}} + \frac{\mathrm{d}p_c}{\mathrm{d}\boldsymbol{\varepsilon}}\right) - (2\sigma_m^{i+1} + p_c^{i+1})\frac{\partial\Delta\lambda}{\partial\boldsymbol{\varepsilon}} \tag{11.100}$$

which upon substituting from Eqs. (11.86) and (11.90) rewrites as

$$\frac{\mathrm{d}\Delta\varepsilon_v^{el}}{\mathrm{d}\boldsymbol{\varepsilon}} = b_1 3\boldsymbol{m} + b_2 \frac{\partial\Delta\lambda}{\partial\boldsymbol{\varepsilon}^{i+1}} \tag{11.101}$$

$$b_1 = 1 - \Delta\lambda(2a_1 + a_3) = \frac{a_1}{\tilde{\sigma}_m} = 1 - \frac{2\Delta\lambda\tilde{\sigma}_m}{a} \tag{11.102}$$

$$b_2 = -\Delta\lambda(2a_2 + a_4) - (2\sigma_m^{i+1} + p_c^{i+1}) = \frac{a_2}{\tilde{\sigma}_m} = -\frac{1}{a}\left(2\sigma_m^{i+1} + p_c^{i+1}\right) \tag{11.103}$$

It now remains to determine the term $\dfrac{\partial\Delta\lambda}{\partial\boldsymbol{\varepsilon}}$. Following [14] we employ the consistency condition

$$\frac{\mathrm{d}f^{MCC}}{\mathrm{d}\boldsymbol{\varepsilon}} = \left[\frac{\mathrm{d}\boldsymbol{s}}{\mathrm{d}\boldsymbol{\varepsilon}}\right]^{\mathsf{T}} \frac{\partial f^{MCC}}{\partial\boldsymbol{s}} + (2\sigma_m^{i+1} + p_c^{i+1})\frac{\mathrm{d}\sigma_m}{\mathrm{d}\boldsymbol{\varepsilon}} + \sigma_m^{i+1}\frac{\mathrm{d}p_c}{\mathrm{d}\boldsymbol{\varepsilon}} = \boldsymbol{0} \tag{11.104}$$

where the first term on the on the right hand side of Eq. (11.104) is provided by (recall Eq. (11.94))

$$\left(\frac{\mathrm{d}f^{MCC}}{\mathrm{d}\boldsymbol{\varepsilon}}\right)_1 = \left[\left(\frac{\partial f^{MCC}}{\partial\boldsymbol{s}}\right)^{\mathsf{T}}\frac{\mathrm{d}\boldsymbol{s}}{\mathrm{d}\boldsymbol{\varepsilon}}\right]^{\mathsf{T}} = \left[\frac{\mathrm{d}\boldsymbol{s}}{\mathrm{d}\boldsymbol{\varepsilon}}\right]^{\mathsf{T}}\frac{\partial f^{MCC}}{\partial\boldsymbol{s}} =$$

$$= \left[\mathbf{E}^{\mathsf{T}} + \frac{\partial\Delta\lambda}{\partial\boldsymbol{\varepsilon}}\left(\frac{\partial\boldsymbol{s}}{\partial\Delta\lambda}\right)^{\mathsf{T}} + \frac{\mathrm{d}\Delta\varepsilon_v^{el}}{\mathrm{d}\boldsymbol{\varepsilon}}\boldsymbol{\mu}^{\mathsf{T}}\right]\frac{\partial f^{MCC}}{\partial\boldsymbol{s}} =$$

$$= \left[\mathbf{E}^{\mathsf{T}} + \frac{\partial\Delta\lambda}{\partial\boldsymbol{\varepsilon}}\left(\frac{\partial\boldsymbol{s}}{\partial\Delta\lambda}\right)^{\mathsf{T}} + \left(b_1 3\boldsymbol{m} + b_2\frac{\partial\Delta\lambda}{\partial\boldsymbol{\varepsilon}}\right)\boldsymbol{\mu}^{\mathsf{T}}\right]\frac{\partial f^{MCC}}{\partial\boldsymbol{s}} \tag{11.105}$$

Next, substitute from Eqs. (11.86), (11.90) and (11.105) into Eq. (11.104) to get

$$\frac{\mathrm{d}f^{MCC}}{\mathrm{d}\boldsymbol{\varepsilon}} = \left[\mathbf{E}^{\mathsf{T}} + \frac{\partial\Delta\lambda}{\partial\boldsymbol{\varepsilon}}\left(\frac{\partial\boldsymbol{s}}{\partial\Delta\lambda}\right)^{\mathsf{T}} + \left(b_1 3\boldsymbol{m} + b_2\frac{\partial\Delta\lambda}{\partial\boldsymbol{\varepsilon}}\right)\boldsymbol{\mu}^{\mathsf{T}}\right]\frac{\partial f^{MCC}}{\partial\boldsymbol{s}} +$$

$$+ (2\sigma_m^{i+1} + p_c^{i+1})\left(a_1 3\boldsymbol{m} + a_2\frac{\partial\Delta\lambda}{\partial\boldsymbol{\varepsilon}}\right) + \sigma_m^{i+1}\left(a_3 3\boldsymbol{m} + a_4\frac{\partial\Delta\lambda}{\partial\boldsymbol{\varepsilon}}\right) \tag{11.106}$$

$$= \boldsymbol{0}$$

Solving Eq. (11.106) for $\dfrac{\partial\Delta\lambda}{\partial\boldsymbol{\varepsilon}}$ finally gives

$$\frac{\partial\Delta\lambda}{\partial\boldsymbol{\varepsilon}} = \frac{1}{c}(\boldsymbol{f} + c_1 3\boldsymbol{m}) \tag{11.107}$$

$$\boldsymbol{f} = \left[\mathbf{E}^{\mathsf{T}} + b_1 3\boldsymbol{m}\boldsymbol{\mu}^{\mathsf{T}}\right]\frac{\partial f^{MCC}}{\partial\boldsymbol{s}}, \quad \frac{\partial f^{MCC}}{\partial\boldsymbol{s}} = \frac{1}{M_{cs}^2}\mathbf{Q}^{-1}\boldsymbol{s}^{i+1} = \frac{1}{M_{cs}^2}\mathbf{P}\boldsymbol{\sigma}^{i+1} \tag{11.108}$$

$$c_1 = a_1(2\sigma_m^{i+1} + p_c^{i+1}) + a_3\sigma_m^{i+1} \tag{11.109}$$

$$c = -\left[\left(\frac{\partial\boldsymbol{s}}{\partial\Delta\lambda}\right)^{\mathsf{T}} + b_2\boldsymbol{\mu}^{\mathsf{T}}\right]\frac{\partial f^{MCC}}{\partial\boldsymbol{s}} - a_2(2\sigma_m^{i+1} + p_c^{i+1}) - a_4\sigma_m^{i+1} \tag{11.110}$$

Introducing Eq. (11.107) back into Eqs. (11.101), (11.94), (11.90), and (11.86) suggests

$$\frac{\mathrm{d}\sigma_m}{\mathrm{d}\boldsymbol{\varepsilon}} = \left(a_1 + \frac{a_2 c_1}{c}\right)3\boldsymbol{m} + \frac{a_2}{c}\boldsymbol{f} \tag{11.111}$$

$$\frac{\mathrm{d}\boldsymbol{s}}{\mathrm{d}\boldsymbol{\varepsilon}} = \mathbf{E} + \frac{1}{c}\left(\frac{\partial\boldsymbol{s}}{\partial\Delta\lambda} + b_2\boldsymbol{\mu}\right)\boldsymbol{f}^{\mathsf{T}} + \left[\frac{c_1}{c}\frac{\partial\boldsymbol{s}}{\partial\Delta\lambda} + \left(b_1 + \frac{b_2 c_1}{c}\right)\boldsymbol{\mu}\right]3\boldsymbol{m}^{\mathsf{T}} \tag{11.112}$$

which when substituted back into Eq. (11.82) finally yields the algorithmic tangent stiffness matrix $\boldsymbol{\mathcal{D}}$ as (for $\dfrac{\partial\boldsymbol{s}}{\partial\Delta\lambda}$ refer to Eq. (11.56))

$$\boldsymbol{\mathcal{D}} = \mathbf{E} + \frac{1}{c}\left(\frac{\partial\boldsymbol{s}}{\partial\Delta\lambda} + 3a_2\boldsymbol{m} + b_2\boldsymbol{\mu}\right)\boldsymbol{f}^{\mathsf{T}} +$$

$$+ \frac{1}{c}\left[3c_1\frac{\partial\boldsymbol{s}}{\partial\Delta\lambda} + 9\left(a_1 c + a_2 c_1\right)\boldsymbol{m} + 3\left(b_1 c + b_2 c_1\right)\boldsymbol{\mu}\right]\boldsymbol{m}^{\mathsf{T}} \tag{11.113}$$

11.3.2 Matrix $\mathcal{D}$ based on constant elasticity stress return

In analogy with the previous section, see also [15], we start from Eqs. (11.67) and (11.68) and write

$$
\begin{aligned}
\frac{\mathrm{d}\sigma_m}{\mathrm{d}\varepsilon} &= \frac{\partial\sigma_m}{\partial\varepsilon} + \frac{\partial\sigma_m}{\partial p_c}\frac{\mathrm{d}p_c}{\mathrm{d}\varepsilon} + \frac{\partial\sigma_m}{\partial\Delta\lambda}\frac{\partial\Delta\lambda}{\partial\varepsilon} \\
&= \frac{1}{1+2K_s^i\Delta\lambda}\left(3K_s^i\boldsymbol{m} - K_s^i\Delta\lambda\frac{\mathrm{d}p_c}{\mathrm{d}\varepsilon} - K_s^i\left(2\sigma_m^{i+1}+p_c^{i+1}\right)\frac{\partial\Delta\lambda}{\partial\varepsilon}\right)
\end{aligned} \tag{11.114}
$$

$$
\begin{aligned}
\frac{\mathrm{d}p_c}{\mathrm{d}\varepsilon} &= -\frac{p_c^{i+1}}{(\lambda^*-\kappa^*)(1+2K_s^i\Delta\lambda)}\left[6K_s^i\Delta\lambda\boldsymbol{m} + \Delta\lambda\frac{\mathrm{d}p_c}{\mathrm{d}\varepsilon} + \frac{2\sigma_m^{tr}+p_c^{i+1}}{1+2K_s^i\Delta\lambda}\frac{\partial\Delta\lambda}{\partial\varepsilon}\right] \\
&= -\frac{p_c^{i+1}}{(\lambda^*-\kappa^*)(1+2K_s^i\Delta\lambda)}\left[6K_s^i\Delta\lambda\boldsymbol{m} + \Delta\lambda\frac{\mathrm{d}p_c}{\mathrm{d}\varepsilon} + (2\sigma_m^{i+1}+p_c^{i+1})\frac{\partial\Delta\lambda}{\partial\varepsilon}\right]
\end{aligned} \tag{11.115}
$$

Rearranging Eq. (11.115) gives

$$
\frac{\mathrm{d}p_c}{\mathrm{d}\varepsilon} = a_3 3\boldsymbol{m} + a_4\frac{\partial\Delta\lambda}{\partial\varepsilon} \tag{11.116}
$$

$$
a_3 = -\frac{2K_s^i\Delta\lambda p_c^{i+1}}{(\lambda^*-\kappa^*)(1+2K_s^i\Delta\lambda)+\Delta\lambda p_c^{i+1}} = -\frac{K_s^i}{a}\frac{2\Delta\lambda p_c^{i+1}}{\lambda^*-\kappa^*} \tag{11.117}
$$

$$
a_4 = -\frac{(2\sigma_m^{i+1}+p_c^{i+1})p_c^{i+1}}{(\lambda^*-\kappa^*)(1+2K_s^i\Delta\lambda)+\Delta\lambda p_c^{i+1}} = -\frac{p_c^{i+1}}{a}\frac{2\sigma_m^{i+1}+p_c^{i+1}}{\lambda^*-\kappa^*} \tag{11.118}
$$

$$
a = 1 + \frac{\Delta\lambda p_c^{i+1}}{\lambda^*-\kappa^*} + 2K_s^i\Delta\lambda \tag{11.119}
$$

Next, upon substituting from Eq. (11.116) into Eq. (11.114) we get

$$
\frac{\mathrm{d}\sigma_m}{\mathrm{d}\varepsilon} = a_1 3\boldsymbol{m} + a_2\frac{\partial\Delta\lambda}{\partial\varepsilon} \tag{11.120}
$$

$$
a_1 = \frac{K_s^i}{1+2K_s^i\Delta\lambda}(1-a_3\Delta\lambda) = \frac{K_s^i}{a}\left(1 + \frac{\Delta\lambda p_c^{i+1}}{\lambda^*-\kappa^*}\right) \tag{11.121}
$$

$$
a_2 = -\frac{K_s^i}{1+2K_s^i\Delta\lambda}\left(2\sigma_m^{i+1}+p_c^{i+1}+\Delta\lambda a_4\right) = -\frac{K_s^i}{a}\left(2\sigma_m^{i+1}+p_c^{i+1}\right) \tag{11.122}
$$

Point out the terms $a_1 - a_4$ are identical to those provided by Eqs. (11.87) - (11.92) once replacing K_s^i by $\tilde{\sigma}_m$ in Eqs. (11.117), (11.119), (11.121), and (11.122). The second term in in Eq. (11.82) now becomes

$$
\frac{\mathrm{d}\boldsymbol{s}}{\mathrm{d}\varepsilon} = \frac{\partial\boldsymbol{s}}{\partial\Delta\boldsymbol{e}}\frac{\partial\Delta\boldsymbol{e}}{\partial\varepsilon} + \frac{\partial\boldsymbol{s}}{\partial\Delta\lambda}\left(\frac{\partial\Delta\lambda}{\partial\varepsilon}\right)^{\mathsf{T}} = \mathbf{E} + \frac{\partial\boldsymbol{s}}{\partial\Delta\lambda}\left(\frac{\partial\Delta\lambda}{\partial\varepsilon}\right)^{\mathsf{T}} \tag{11.123}
$$

where

$$
\mathbf{E} = \frac{2G_s^i\mathbf{QPQ}}{1+\dfrac{2G_s^i\Delta\lambda}{M_{cs}^2}} \tag{11.124}
$$

$$
\frac{\partial\boldsymbol{s}}{\partial\Delta\lambda} = -\frac{2G_s^i}{M_{cs}^2}\frac{\boldsymbol{s}^{i+1}}{1+\dfrac{2G_s^i\Delta\lambda}{M_{cs}^2}} = -\frac{2G_s^i\boldsymbol{s}^{i+1}}{M_{cs}^2+2G_s^i\Delta\lambda} \tag{11.125}
$$

With the help of consistency condition, remember Eq. (11.106), in the form

$$
\begin{aligned}
\frac{\mathrm{d}f^{MCC}}{\mathrm{d}\varepsilon} &= \left[\mathbf{E}^{\mathsf{T}} + \frac{\partial\Delta\lambda}{\partial\varepsilon}\left(\frac{\partial\boldsymbol{s}}{\partial\Delta\lambda}\right)^{\mathsf{T}}\right]\frac{\partial f^{MCC}}{\partial\boldsymbol{s}} + \\
&\quad + (2\sigma_m^{i+1}+p_c^{i+1})\left(a_1 3\boldsymbol{m} + a_2\frac{\partial\Delta\lambda}{\partial\varepsilon}\right) + \sigma_m^{i+1}\left(a_3 3\boldsymbol{m} + a_4\frac{\partial\Delta\lambda}{\partial\varepsilon}\right) \\
&= \mathbf{0}
\end{aligned} \tag{11.126}
$$

we arrive at the searched term $\dfrac{\partial \Delta \lambda}{\partial \varepsilon}$ in the form

$$\frac{\partial \Delta \lambda}{\partial \varepsilon} = \frac{1}{c}(\boldsymbol{f} + c_1 3\boldsymbol{m}) \tag{11.127}$$

$$\boldsymbol{f} = \mathbf{E}^\mathsf{T} \frac{\partial f^{MCC}}{\partial \boldsymbol{s}}, \quad \frac{\partial f^{MCC}}{\partial \boldsymbol{s}} = \frac{1}{M_{cs}^2} \mathbf{Q}^{-1} \boldsymbol{s}^{i+1} = \frac{1}{M_{cs}^2} \mathbf{P}\boldsymbol{\sigma}^{i+1} \tag{11.128}$$

$$c_1 = a_1(2\sigma_m^{i+1} + p_c^{i+1}) + a_3\sigma_m^{i+1} \tag{11.129}$$

$$c = -\left(\frac{\partial \boldsymbol{s}}{\partial \Delta \lambda}\right)^\mathsf{T} \frac{\partial f^{MCC}}{\partial \boldsymbol{s}} - a_2(2\sigma_m^{i+1} + p_c^{i+1}) - a_4\sigma_m^{i+1} \tag{11.130}$$

As in the previous section we now substitute from Eq. (11.127) into Eqs. (11.120) and (11.123) to get

$$\frac{\mathrm{d}\sigma_m}{\mathrm{d}\varepsilon} = \left(a_1 + \frac{a_2 c_1}{c}\right) 3\boldsymbol{m} + \frac{a_2}{c}\boldsymbol{f} \tag{11.131}$$

$$\frac{\mathrm{d}\boldsymbol{s}}{\mathrm{d}\varepsilon} = \mathbf{E} + \frac{1}{c}\frac{\partial \boldsymbol{s}}{\partial \Delta \lambda}\left(\boldsymbol{f}^\mathsf{T} + c_1 3\boldsymbol{m}^\mathsf{T}\right) \tag{11.132}$$

and subsequently from Eqs. (11.131) and (11.132) into Eq. (11.82) to obtain the algorithmic tangent stiffness matrix $\boldsymbol{\mathcal{D}}$ in the form (for $\dfrac{\partial \boldsymbol{s}}{\partial \Delta \lambda}$ refer to Eq. (11.125))

$$\boldsymbol{\mathcal{D}} = \mathbf{E} + \frac{1}{c}\left(\frac{\partial \boldsymbol{s}}{\partial \Delta \lambda} + 3a_2\boldsymbol{m}\right)\boldsymbol{f}^\mathsf{T} + \frac{1}{c}\left[3c_1\frac{\partial \boldsymbol{s}}{\partial \Delta \lambda} + 9\left(a_1 c + a_2 c_1\right)\boldsymbol{m}\right]\boldsymbol{m}^\mathsf{T} \tag{11.133}$$

11.4   Note on numerical implementation

An important issue which requires our attention is the determination of initial preconsolidation pressure p_c^{in} and associated initial bulk modulus K_s^{in}. Limiting our attention to the GEO5 FEM program we note that these two parameters are not included in the standard material setting of the Modified Cam-clay model. Instead, their distributions are derived on the basis of the assumed geostatic stress profile.

The distribution of initial geostatic stress in GEO5 FEM is always calculated in the first calculation stage. The user may choose from the following three options:

K_0 procedure

The K_0 procedure is described in Section 1.14 suggesting the initial mean stress in the form

$$\overline{\sigma}_m^a = \frac{1}{3}\left(1 + 2K_0\right)\overline{\sigma}_z^a \tag{11.134}$$

where K_0 is the coefficient of lateral earth pressure at rest and $\overline{\sigma}_z^a$ is the vertical geostatic stress, recall Figs. 11.3(b,c) and the corresponding discussion in Section 11.1.1. In the most simple case we have $\overline{\sigma}_z^a = -\gamma h$, where γ is the bulk unit weight and h is the actual depth of a stress point in the soil profile.

If we assume that the clay did not experience greater vertical stresses in the past (normally consolidated clay) then the value of initial preconsolidation pressure is determined for the current stress to sit on the yield surface. This gives for the Modified Cam-clay model, recall Fig. 11.3(c),

$$p_c^{in} = p_c^a = -\frac{(\overline{J}^b)^2}{M_{cs}^2 \overline{\sigma}_m^a} - \overline{\sigma}_m^a \tag{11.135}$$

Initializaton of p_c^{in} for overconsolidated soils is described in Section 1.13.

The initial bulk modulus follows directly from

$$K_a^{in} = -\frac{1 + e_{in}}{\kappa}\overline{\sigma}_m^a = -\frac{\overline{\sigma}_m^a}{\kappa^*}, \quad K_{s,min} = \frac{1}{\kappa^*} \text{ for } \overline{\sigma}_m^a > -1\,\text{kPa} \tag{11.136}$$

where the initial void ratio e_{in} is provided by Eq. (11.3).

Elastic analysis

Note that the program GEO5 FEM allows us to switch from one material model to another between two calculation stages. This option can therefore be exploited in cases where K_0 procedure is not applicable. In particular, the soil to be represented by the Modified Cam-clay models is assumed to follow a linear Hooke's law in the first calculation stage. The corresponding initial stresses $\overline{\sigma}^a$ are then used in Eq. (11.135) in place of Eq. (11.134) to derive the desired distributions of p_c^{in} and K_s^{in}. Equation (11.3) still applies when setting the initial void ratio e_{in}. From the second construction stage the linear elastic model is substituted by an appropriate plastic one to obtain more realistic predictions of the soil behavior.

It is worth mentioning that in some cases both approaches may generate stresses found in the super-critical domain and consequently predicting too large values of p_c^{in} when introduced into Eq. (11.135). Also, the overconsolidation parameters $OCR = 1$ and $POP = 0$ are considered so the soil is assumed to be normally consolidated. To introduce overconsolidation a loading/unloading sequence would have to be introduced.

Plastic analysis

The plastic analysis involves plastic material models for clayey soils already in the first calculation stage. During calculation, the soil is thus assumed to move down the virgin consolidation line with the initial values of $p_c^{in} = 1$ kPa and $K_s^{in} = \dfrac{1}{\kappa^*}$. All plastic deformations that arise during the first calculation stage are set equal to zero before resuming any further calculations. The initial void ratio $e_{in} = e_0$ gradually evolves until arriving at the value of $e^{1^{st}stage}$ at the end of this first calculation stage. This value is then used to initialize parameters κ^*, λ^* adopted in subsequent calculation stages. Similarly to elastic step the overconsolidation parameters $OCR = 1$ and $POP = 0$ are considred so the soil is assumed to be normally consolidated. To introduce overconsolidation a loading/unloading sequence would have to be introduced.

11.4.1 Note on determination of parameters κ and λ

The input parameters for the present critical state models are listed in Table 11.1. Our experience indicates that unlike Young's modulus or Poisson's ratio the swelling modulus κ and the compression modulus λ in particular are, however, unknown to majority of practical users. This is also why the critical state models still receive much less attention in comparison with rather classical Mohr-Coulomb like models. Fortunately, we may direct the user to our calibration software ExCalibre [25] available free of charge which provides all data of the model such that numerical predictions fit the supplied laboratory measurements as close as possible. Application of this software typically requires data from oedometric and triaxial tests. When only data from an oedometric test are available one may proceed along the following lines to get a quick estimate of the stiffness parameters κ, λ.

To establish a link between the κ and λ moduli and the corresponding parameters derived we consider results of a typical oedometric test in Fig. 11.5. It is well known that the complete stress state of a sample in the oedometer apparatus in not known. Unlike the triaxial apparatus the oedometer apparatus provides only the axial stress σ_z and the total volumetric strain ε_v equal to the axial strain ε_z. Assuming undrained conditions the results from oedometer tests are often plotted in terms of $e - \log(-\sigma_z)$ diagram, see Fig. 11.5(a). This graph is very similar to $e - \ln(-\sigma_m)$ diagram plotted in Fig. 11.3(a). Owing to the geometrical constraints imposed by a standard oedometer apparatus the slope of the virgin consolidation line is called the one-dimensional compression index written as

$$C_c = \frac{\Delta e}{\Delta \log(-\sigma_z)} = \frac{\Delta e}{\log \dfrac{\sigma_z^{i+1}}{\sigma_z^i}} \tag{11.137}$$

To bring the compression modulus λ and the one-dimensional compression index C_c to the same footing we introduce the coefficient of lateral earth pressure at rest for normally consolidated soils
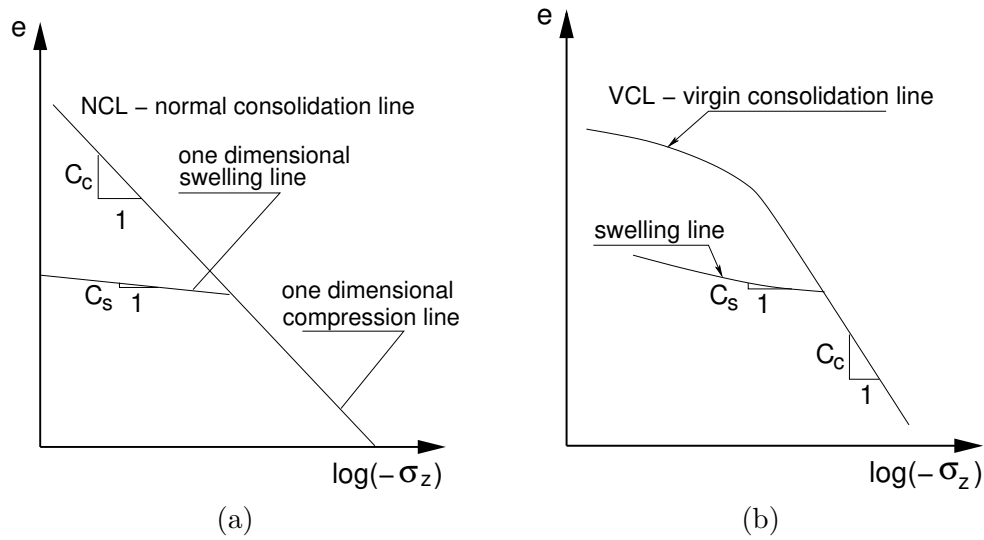
Figure 11.5: Behavior under one dimensional compression: a) idealization, b) typical result of an oedometer test

K_0^{NC} and write the effective mean stress as, recall Eq. (11.134),

$$\sigma_m = \frac{1}{3}(1 + 2K_0^{NC})\sigma_z \tag{11.138}$$

Note that K_0^{NC} is often estimated from Jaky's formula $K_0^{NC} = 1 - \sin\varphi$, where φ is the effective angle of internal friction. Since K_0^{NC} is approximately constant along the virgin compression line [66, Chapter 1] we get, recall Eq. (11.1),

$$\lambda = \frac{\Delta e}{\Delta \ln(-\sigma_m)} = \frac{\Delta e}{\ln \dfrac{\sigma_m^{i+1}}{\sigma_m^i}} = \frac{\Delta e}{\ln \dfrac{\sigma_z^{i+1}}{\sigma_z^i}} \tag{11.139}$$

Since $\ln x = 2.3 \log x$ we get after comparing Eqs. (11.137) and (11.139)

$$\lambda = \frac{C_c}{2.3} \tag{11.140}$$

Assuming that the swelling lines also plot as straight lines in both $e - \ln(-\sigma_m)$ and $e - \log(-\sigma_z)$ diagrams as shown in Figs. 11.3(a) and 11.5(a) we obtain a similar approximation of the swelling modulus κ in terms of the swelling index C_s as

$$\kappa \approx \frac{C_s}{2.3} \tag{11.141}$$

However, such an assumption is not valid in general. In fact, K_0 is not constant along the swelling line but rather increases during unloading as schematically demonstrated in Fig. 11.5(b). A modification to Eq. (11.141) is typically provided in the form

$$\kappa \approx 3\frac{1 - \nu_{ur}}{1 + \nu_{ur}}\frac{C_s}{2.3} \tag{11.142}$$

where ν_{ur} represents Poisson's ratio derived from the ratio of differences in the horizontal and vertical stress developed in oedometer during unloading and reloading

$$\Delta\sigma_x = \frac{\nu_{ur}}{1 - \nu_{ur}}\Delta\sigma_z = K_0\Delta\sigma_z \tag{11.143}$$

With this definition it is easy to show that

$$3\frac{1 - \nu_{ur}}{1 + \nu_{ur}} = \frac{3}{1 + 2K_0} \tag{11.144}$$

However, neither of the two approximate relations for the swelling modulus κ are universally accepted and should therefore be used with considerable caution. Finally note that Eq. (11.142) reduces to Eq. (11.141) under incompressibility condition since for $\nu_{ur} = 0.5$ the term $3\dfrac{1 - \nu_{ur}}{1 + \nu_{ur}} = 1$.

11.5 Testing implementation with simple laboratory tests

Two specific features of the Modified Cam-clay model concerning an initial stiffness and a hardening/softening behavior are addressed. While the current version of GEO5 FEM exploits the constant elasticity stress return algorithm, the following examples are presented for illustration in the framework of variable elasticity stress return mapping.

11.5.1 Influence of low initial stiffness

Regardless of the type of elasticity return, either variable (Section 11.2.1) or constant (Section 11.2.2), the initial value of the bulk modulus K_s^{in} in GEO5 FEM is calculated according to Eq. (11.136). With variable elasticity return it is subsequently updated with the help of Eq. (11.26). It is therefore clear that the initial stiffness might be quite low when starting the loading process from zero initial stress considering the initial preconsolidation pressure $p_c = 1$ kPa and the initial bulk modulus $K_s^{in} = \dfrac{1}{\kappa^*}$ kPa. Consequently, the initial load step considerably affects the resulting stress-strain response. Adopting data from Table 11.2 this issue is examined in Figs. 11.6 and 11.7. To this end, an axisymmetric analysis using two 3-node constant strain triangles displayed in Fig. 11.6(a) are used.

Table 11.2: Material properties of Modified Cam-clay model used in numerical tests

ν	κ	λ	e_{in}	M_{cs}
0.26	0.0077	0.066	0.788	0.693

Figure 11.6 shows the results from an isotropic compression test assuming $\sigma_v = \sigma_r$ in Fig. 11.6(a). Because starting from $\sigma_m = 0$ the initial bulk modulus is small, which in turn may considerably overestimates the volumetric strain for the 1st load increment providing its magnitude is insufficiently small. Such a result is represented by the black solid line derived for the load fraction $\zeta = 0.1$. The influence of small initial stiffness is reduced when decreasing the initial load increment, compare the red and blue lines in Fig. 11.6(b) corresponding to $\zeta = 0.01$ and $\zeta = 0.001$, respectively. To avoid large number of load steps, the program GEO5 FEM allows for a gradual increase of the load fraction in dependency on the number of iterations needed to achieve convergence for the previous load step. This option can be set by specifying the minimum number of iterations for a given load step in the "analysis settings". If the number of iterations does not exceed this value, the load fraction is increased for the next load step. In Fig. 11.6 this option corresponds to the response marked as VLF (variable load fraction). By default the minimum number of iterations is set equal to 1 thus enforcing the constant load step throughout the analysis. In this particular case, the VLF result was derived with the minimum number of iterations set equal to 5. While 1000 steps was considered to plot the blue line, the VLF plot needed 10 load steps only with no loss of accuracy. Point out that normal consolidation was considered moving down the λ-line with p_c gradually increasing from 1 kPa to 10 MPa in this particular example.

The second example illustrates the effect of low initial stiffness in the simulation of an oedometric test. To comply with the kinematic constrains imposed by an oedometer the traction boundary conditions in the radial direction are replaced by the kinematic boundary conditions evident in Fig. 11.6(a).

We begin with the results in Fig. 11.7 corresponding to pure nonlinear elastic response. Both loading and unloading branch is represented. Clearly, for constant load increment keeping the load fraction ζ constant throughout the analysis the loading and unloading response follows the same path, see the black and red lines. A noticeable deviation from this result occurs when allowing for a gradual increase of load increment, see the blue line. This is because of elasticity where the load increment is
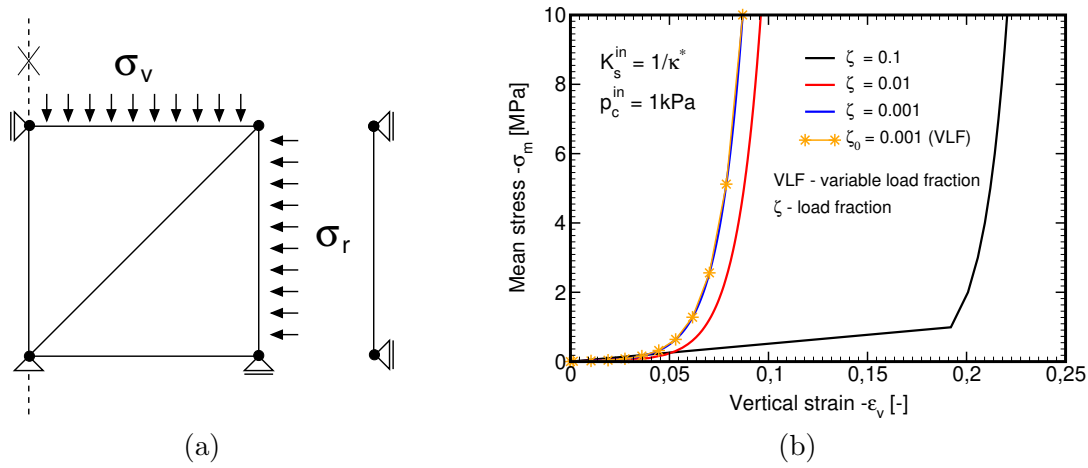
Figure 11.6: a) Axisymmetric FEM model, b) Nonlinear elastic response in isotropic compression

increased with every load step thus also at the initial stage of loading which was not the case in the previous example. Moreover, allowing for a variable load fraction also upon unloading may generate some permanent elastic strains as demonstrated by the green line.

On the other, running the analysis within a plastic regime provides almost negligible difference between the results associated with both constant variable load fraction options. This is attributed to the fact that at the initial loading stage the first few steps proceed with the same load increment. Upon unloading, artificial permanent strains due to nonlinearity are negligible compare to permanent plastic strains.
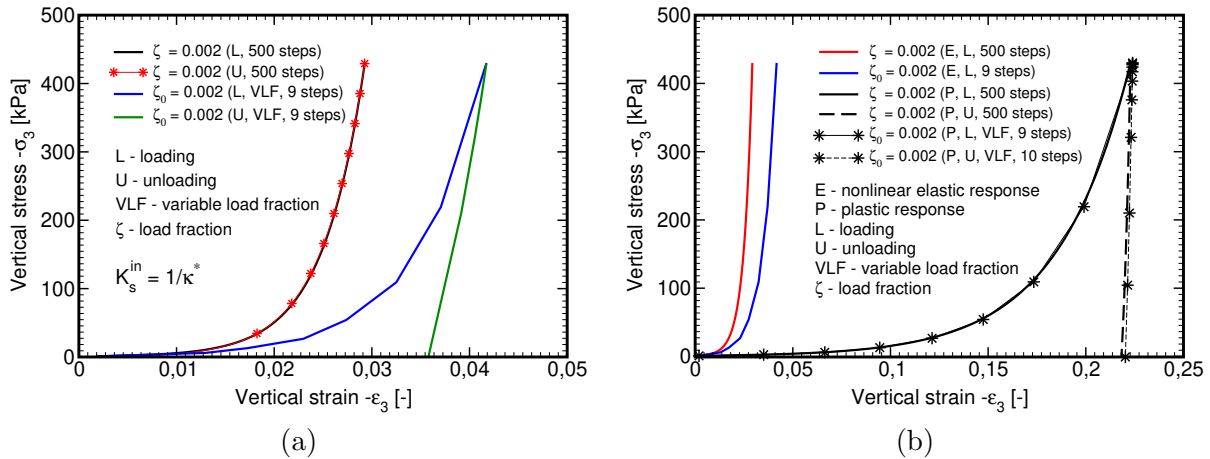
Figure 11.7: a) Nonlinear elastic response in oedometric compression, b) Comparing nonlinear elastic and elastic plastic response in oedometric compression

11.5.2 Effect of hardening/softening in triaxial loading conditions

We have already put forward that simulating a triaxial test with an elastic-perfectly plastic model may result in a singular stiffness matrix once first violating the failure criterion. This typically occurs when combining the Newton-Raphson method with the loading driven by applied tractions. With the Modified Cam-clay model, however, such a situation arises only when reaching the critical state. Prior to that the model predicts either hardening or softening in dependence on the current stress state as visualized in Fig. 11.2(b). To examine all these features we move back to triaxial loading conditions and consider a specific loading path presented in Fig. 11.8. Drained conditions are assumed with no evolution of pore pressure so all stresses are effective.

The entire analysis was split into four calculation stages:

1. Isotropic compression to set initial chamber pressure. The analysis started from a zero mean

(a)

(b)

(c)

Figure 11.8: a) Evolution of yield surface, b) Prescribed load path in terms vertical (σ_v) and radial (σ_r) pressure, c) Evolution of mean (σ_m) and equivalent deviatoric (J) stress measures as a function of vertical strain

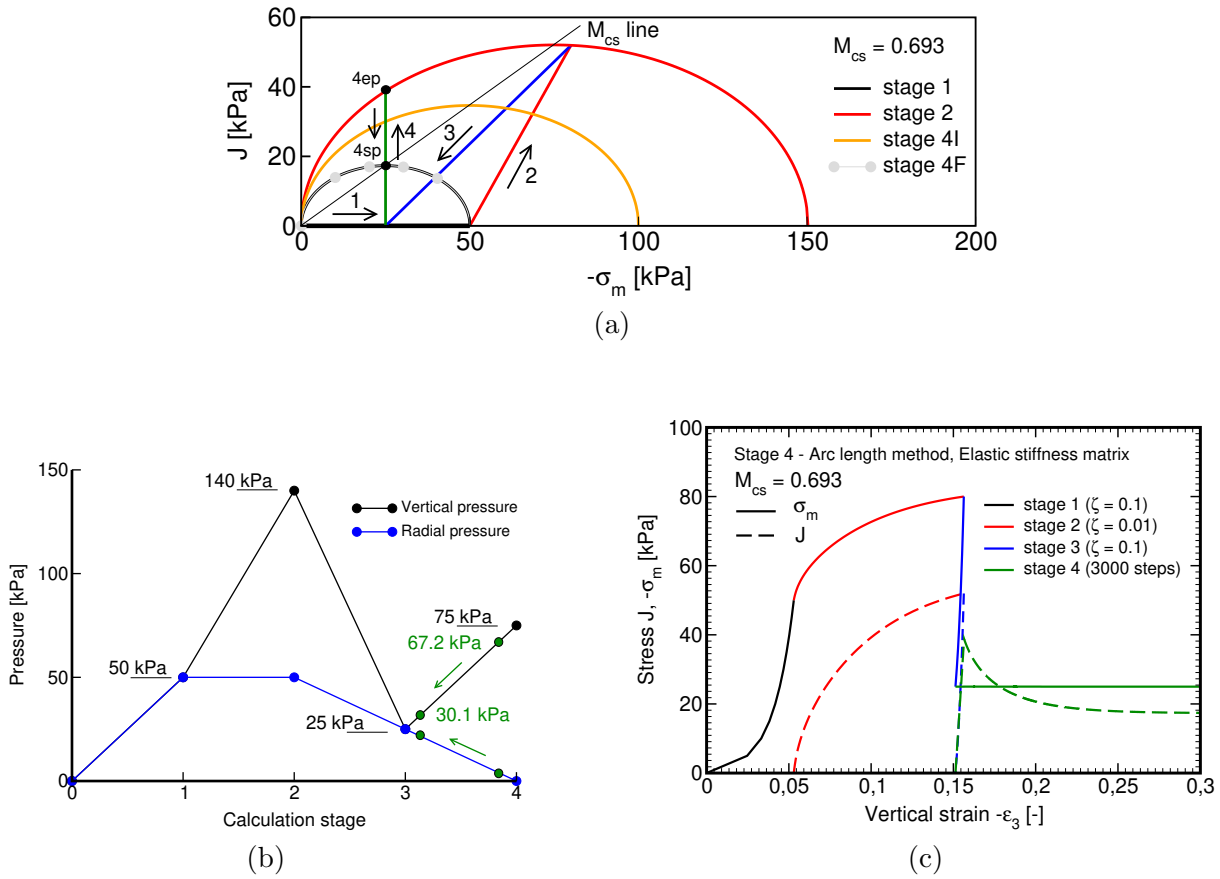pressure with $p_c^{in} = 1$ kPa and $K_s^{in} = 1/\kappa^* \approx 232$ kPa. As indicated in Fig. 11.8(b), the sample was isotropically normally consolidated to a mean stress $\sigma_m = p_c = 50$ kPa by proportionally increasing the vertical and radial stresses $\sigma_v = \sigma_r$. The resulting yield surface plots as the black ellipse in Fig. 11.8(a). The black arrow shows the corresponding loading path. The solid black line in Fig. 11.8(c) shows the evolution of the mean stress σ_m as a function of the vertical strain ε_v. Point out a relatively compliant behavior within the first load increment attributed to combination of a low initial stiffness and a large load fraction of $\zeta = 0.1$.

2. In the second calculation stage the sample was loaded in triaxial compression to arrive at the maximum vertical pressure $\sigma_v = 140$ kPa while keeping the radial pressure constant, see Fig. 11.8(b). In this calculation stage the preconsolidation pressure gradually increases according to Eq. (11.15). This hardening phase is manifested by a gradually expanding yield surface. The final state derived at end of loading is plotted as the red ellipse in Fig. 11.8(a). The arrow shows a standard triaxial compression loading path with the slope of $J/\sigma_m = \sqrt{3}$. Clearly, the critical state, defined as the intersection of the critical state (M_{cs}) line with the yield surface, was not reached during this stage. Consequently, no difficulty to converge was experienced with the application of *FULL* Newton-Raphson method, recall Section 17.2.6. This is also supported by the red stress-strain curves not reaching the plateau as typical of the critical state.

3. The third stage represents elastic unloading. The soil response, however, is still nonlinear. The unloading path, displayed both in Fig. 11.8(b) and Fig. 11.8(a) (blue line), was selected specifically to arrive at an overconsolidated state with a zero deviatoric stress J and the mean stress $\sigma_m = 25$ kPa being at the center of the original black yield surface, see also the resulting stress-strain curves (blue lines) in Fig. 11.8(c).

4. In the forth calculation stage the sample was loaded in pure shear while keeping the mean stress

constant at the level of $\sigma_m = 25$ kPa, see the green line in Fig. 11.8(a) The prescribed evolution of vertical and radial pressures appears in Fig. 11.8(b). Because expecting softening (the stress point appears in supercritical region of the yield surface, see Fig. 11.2(b)) the Arc-length method was adopted. In particular, the option with no update of a material stiffness matrix (update *NONE*, recall Section 17.2.6) was selected. It is seen that initially the response is elastic moving inside the current yield surface. Once violating the yield criterion (point 4ep on the red ellipse) the material begins to soften. Point out that this state corresponds to the vertical pressure of $\sigma_v = 67.2$ kPa, well below the preset value of 75 kPa as indicated in Fig. 11.8(b). The softening continues until arriving at a critical state (point 4sp on the final gray ellipse). Green arrows in Fig. 11.8(b) indicate a gradual change of both vertical and radial pressures being well identified by the Arc-length method. Once at the critical state there is no further evolution of p_c and thus no change in the equivalent deviatoric stress J. Also notice that in this particular case the increment of both total and elastic volumetric strain is equal to zero. In this case, the application of Eq. (11.26) is not applicable and the algorithm switches to constant elasticity return mapping. More specifically, this loading path keeps the bulk modulus constant equal to that at the end of the unloading stage 3. Notice that orange curve (stage 4I) represents an intermediate state obtained prior to arriving at the final critical state. Additionally, because the mean effective stress remains constant equal to half the preconsolidation pressure at the end of isotropic loading stage the final yield surface matches the one at the end of isotropic compression. Final comment concerns the large number of iterations observed in this calculation stage. This is clearly attributed to the application of elastic stiffness matrix within the Arc-length method as schematically illustrated in Fig. 17.9(c).

11.6 Modified Cam-model in undrained analysis

11.7 Modified Cam-clay model in stability analysis

The GEO5 FEM software allows for the application of the Modified Cam-clay model in stability analysis performed within a given calculation stage. As in standard analysis the solution procedure is based on the reduction of a shear strength parameter, i.e., the critical state friction angle φ_{cs}. Its initial value is derived from the current value of the critical state line M_{cs} as

$$\sin \varphi_{cs} = \frac{3M_{cs}}{2\sqrt{3} + M_{cs}} \tag{11.145}$$

Thus when starting from a certain equilibrium stress state $\overline{\overline{\sigma}}$ sitting on the current yield surface the reduction of φ_{cs} generates an inadmissible stresses which must be returned to the new yield surface, e.g. the one associated with the 1st reduction step, as indicated in Fig. 11.9(a).
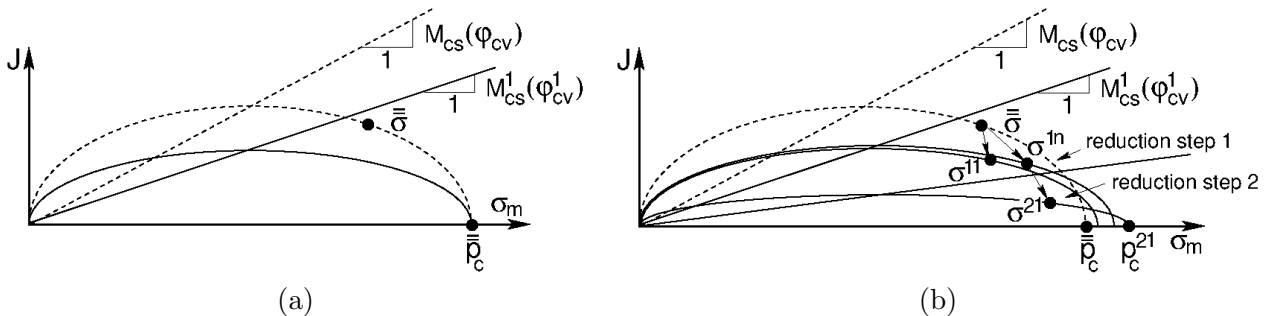
Figure 11.9: Illustration of reduction steps in stability analysis: a) initial yield surface associated with the 1st reduction step (solid line), b) evolution of yield surfaces within successive reduction steps

Unlike standard analysis, however, the stiffness $\overline{\overline{K}}$, associated with the stress state $\overline{\overline{\sigma}}$ at the end of the standard calculation stage, is kept constant throughout the whole reduction process. Note that keeping the initial preconsolidation pressure $\overline{\overline{p}}_c$ fixed corresponds to an elastic-perfectly plastic material. In such a case, one may experience convergences problems when returning from an inadmissible

stress state along the hydrostatic axis. Therefore, the preconsolidation pressure is allowed to evolve as displayed in Fig. 11.9(b). Therein, the stress $\boldsymbol{\sigma}^{11}$ sits on a yield surface that evolves during the 1st local stress update $\bar{\bar{p}}_c \to p_c^{11}$ and the stress $\boldsymbol{\sigma}^{1n}$ is the stress at convergence of the 1st reduction step. The corresponding yield surface is the initial yield surface for the next reduction step as again indicated in Fig. 11.9(b).

From numerical point of view the local stress return algorithm and the algorithmic tangent stiffness matrix are therefore described in Sections 11.2.2 and 11.3.2, respectively.

Chapter 12

Generalized Cam-clay model

The last paragraph in Section 11.1.2 put forward several drawbacks associated with the formulation of the Modified Cam-clay (MCC) model. To overcome these drawbacks, e.g., prediction of the excessive shear strength on the supercritical side, a new model, termed the Generalized Cam-clay (GCC) model henceforth, has been proposed. Similar to existing formulations the yield function is composed of two smoothed functions continuously connected at the point of intersection with the critical state line. Graphical representation is displayed in Fig. 12.1. The list of material parameters describing the associated stress-strain response is provided in Table 12.1.
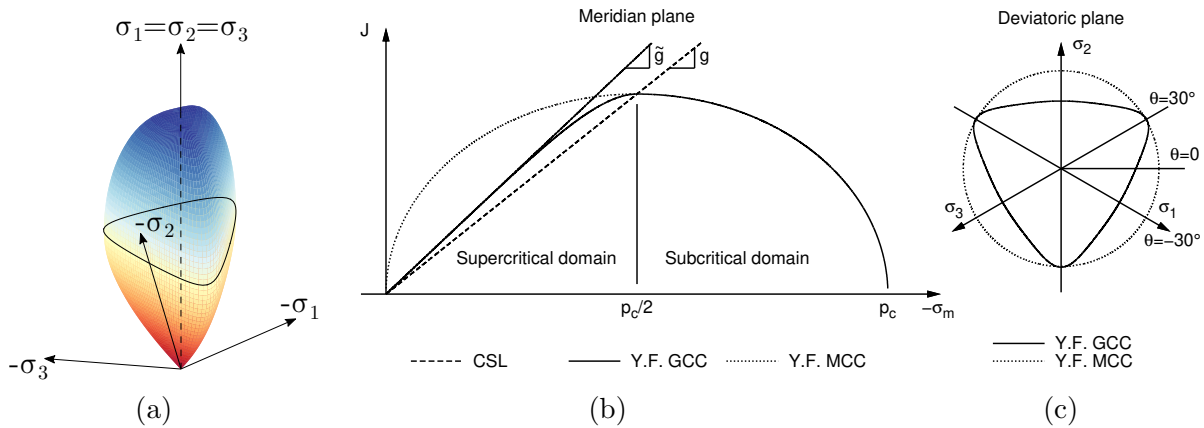
Figure 12.1: Generalized Cam-clay yield surface: a) plot in effective principal stress space, b) plot in meridian plane, c) plot in deviatoric plane

Table 12.1: Parameters of Generalized Cam-clay plasticity model

Symbol	Units	Description
κ	[-]	Slope of swelling line (swelling modulus)
λ	[-]	Slope of normal consolidation line (isotropic NCL, compression modulus)
e_0	[-]	Maximum void ratio
ν	[-]	Poisson's ratio
φ_{cs}	[°]	Critical state friction angle
φ	[°]	Peak friction angle
OCR	[-]	Overconsolidation ratio
POP	[kPa]	Preoverburden pressure
α	[1/°C]	Coefficient of thermal expansion
p_c	[kPa]	Preconsolidation pressure ($p_c^{min} = 1$kPa), calculated

12.1   Formulation of Generalized Cam-clay yield criterion

Since falling into a family of critical state models we refer the reader to Chapter 11 for a general introduction to individual model parameters and to Section 11.1.1, in particular, for the formulation of constitutive (stress-strain) equations. Reformulation of the original Modified Cam-clay yield surface is presented next.

12.1.1   Yield and plastic potential surface

Mathematically, the two functions governing the soil behavior in the subcritical and supercritical domains, recall Fig. 12.1, are written as

$$f^{GCC} = \begin{cases} f_d^{GCC}, & \text{for } \sigma_m > -p_c/2 \quad \text{(supercritical side)} \\ f_c^{GCC}, & \text{for } \sigma_m \le -p_c/2 \quad \text{(subcritical side)} \end{cases} \tag{12.1}$$

$$f_d^{GCC} = \frac{J^2}{g^2(\theta, \varphi_{cs})} - \beta \left[\sigma_m^2 - (-\sigma_m)^{1+\alpha} (\gamma p_c)^{1-\alpha} \right] \tag{12.2}$$

$$f_c^{GCC} = \frac{J^2}{g^2(\theta, \varphi_{cs})} + \sigma_m^2 + \sigma_m p_c \tag{12.3}$$

where

$$\widetilde{g}(\theta, \varphi_{cs}, \varphi) = g(\theta, \varphi_{cs})\sqrt{\beta} \tag{12.4}$$

$$g(\theta, \varphi_{cs}) = \chi(\theta, \varphi_{cs}) M_{\varphi_{cs}} \tag{12.5}$$

$$M_{\varphi_{cs}}^{TC} = \frac{2\sqrt{3}\sin\varphi_{cs}}{3 - \sin\varphi_{cs}} \quad \text{for triaxial compression} \tag{12.6}$$

$$M_{\varphi_{cs}}^{TE} = \frac{2\sqrt{3}\sin\varphi_{cs}}{3 + \sin\varphi_{cs}} \quad \text{for triaxial extension} \tag{12.7}$$

$$\beta = \left(\frac{\sin\varphi}{\sin\varphi_{cs}} \frac{3 - \sin\varphi_{cs}}{3 - \sin\varphi} \right)^2 \tag{12.8}$$

$$\gamma = \left(\frac{2^\alpha}{1 + \alpha} \right)^{\frac{1}{1-\alpha}} \tag{12.9}$$

$$\alpha = \frac{\beta + 1}{\beta - 1} \tag{12.10}$$

Function $\chi(\theta, \varphi_{cs})$ depends on the current value of Lode's angle θ and describes the shape of the projection of GCC yield surface into a deviatoric plane, which in the present formulation assumes the form provided by the Matsuoka-Nakai yield surface outlined in detail in Section 8.1.2. Also point out that $M_{\varphi_{cs}} = M_{\varphi_{cs}}^{TC}$ is actually used in GEO5 FEM. Parameters α, β, γ are defined such as to give a vertical normal to the yield surface at the joint point of the two functions and to maintain compatibility of both yield functions for any value of Lode's angle. As plotted in Fig. 12.1(b), at zero deviatoric stress ($J = 0$) they suggest a common tangent of the function f_d^{GCC} with the limit function of Hardening soil model, see Chapter 8, or the Soft soil model, see Chapter 9.

Note that no changes with respect to the MCC model are introduced on the subcritical side. The smooth transition from one surface to the other not only considerably simplifies the numerical implementation, but also ensures fulfilling the critical state condition already predicted by the Modified Cam-clay model. Furthermore, the model also predicts a unique state boundary surface and the consolidation/swelling behavior. Unlike for the MCC model, the swelling behavior and the failure stresses, in particular, are considerably suppressed. Such a behavior is in better accordance with reported experimental results.

Formulation of the plastic potential surface is again consistent with the Hardening and Soft soil models as it considers a circular projection of the plastic potential surface into a deviatoric plane. This

is achieved by fixing the current value of Lode's angle to the one associated with the trial stresses, i.e., $\tilde{\theta} = \theta^{tr}$, recall Section 8.3. This gives the plastic potential surfaces in the form

$$g_d^{GCC} = \frac{J^2}{g_G^2(\tilde{\theta}, \varphi_{cs})} - \beta\left[\sigma_m^2 - (-\sigma_m)^{1+\alpha}(\gamma p_c)^{1-\alpha}\right] \tag{12.11}$$

$$g_c^{GCC} = \frac{J^2}{g_G^2(\tilde{\theta}, \varphi_{cs})} + \sigma_m^2 + \sigma_m p_c \tag{12.12}$$

$$g_G(\tilde{\theta}, \varphi_{cs}) = \tilde{\chi}^2(\tilde{\theta}, \varphi_{cs})M_{\varphi_{cs}}^2 \tag{12.13}$$

With this definition the flow rule becomes, unlike the MCC model, a non-associated.

12.2 Stress return mapping

With reference to Eqs. (12.11) and (12.12) the volumetric $\Delta\varepsilon_v^{pl}$ and deviatoric e^{pl} plastic strain increments are given by

$$\Delta\varepsilon_{vd}^{pl} = \Delta\lambda\frac{\partial g_d^{GCC}}{\partial\sigma_m} = \Delta\lambda\beta\left[-2\sigma_m - (1+\alpha)(-\sigma_m)^\alpha(\gamma p_c)^{1-\alpha}\right] \tag{12.14}$$

$$\Delta\varepsilon_{vc}^{pl} = \Delta\lambda\frac{\partial g_c^{GCC}}{\partial\sigma_m} = \Delta\lambda\left(2\sigma_m + p_c\right) \tag{12.15}$$

$$\Delta e_d^{pl} = \Delta\lambda\frac{\partial g_d^{GCC}}{\partial s} = \Delta\lambda\frac{\mathbf{P}\sigma}{g_G^2} = \Delta\lambda\frac{\mathbf{Q}^{-1}s}{g_G^2} \tag{12.16}$$

$$\Delta e_c^{pl} = \Delta\lambda\frac{\partial g_c^{GCC}}{\partial s} = \Delta\lambda\frac{\mathbf{P}\sigma}{g_G^2} = \Delta\lambda\frac{\mathbf{Q}^{-1}s}{g_G^2} \tag{12.17}$$

so the elastic volumetric strain increments read

$$\Delta\varepsilon_{vd}^{el} = \Delta\varepsilon_v - \Delta\lambda\beta\left[-2\sigma_m - (1+\alpha)(-\sigma_m)^\alpha(\gamma p_c)^{1-\alpha}\right] \tag{12.18}$$
$$\Delta\varepsilon_{vc}^{el} = \Delta\varepsilon_v - \Delta\lambda\left(2\sigma_m + p_c\right) \tag{12.19}$$

Recall that $\Delta\lambda$ represents an increment of plastic multiplier. Similar to Section 11.2 (MCC model) the two stress return mapping algorithms are considered

- Variable elasticity return

- Constant elasticity return (currently implemented in GEO5 FEM)

12.2.1 Variable elasticity return

Because a detailed derivation of stress-strain equations, representing the current values of preconsolidation pressure p_c^{i+1}, mean σ_m^{i+1} and deviatoric s^{i+1} stresses and the corresponding equivalent stress deviatoric stress measure J^{i+1} and the increment of equivalent deviatoric strain ΔE at $(i+1)$ load increment, is presented in Section 11.2.1 we only list the final expressions for the sake of conciseness:

- Preconsolidation pressure

$$p_c^{i+1} = p_c^i \exp\left[-\frac{\Delta\varepsilon_v^{pl}}{\lambda^* - \kappa^*}\right] \tag{12.20}$$

- Mean stress

$$\sigma_m^{i+1} = \sigma_m^i \exp\left[-\frac{\Delta\varepsilon_v^{el}}{\kappa^*}\right] \tag{12.21}$$

- Deviatoric stress

$$s^{i+1} = \frac{s^i + 2\overline{G}_s\mathbf{Q}\Delta e}{1 + \frac{2\overline{G}_s\Delta\lambda}{g_G^2}} = \frac{s^{tr}}{1 + \frac{2\overline{G}_s\Delta\lambda}{g_G^2}} \tag{12.22}$$

- Equivalent deviatoric stress

$$J^{i+1} = \frac{J^{tr}}{1 + \dfrac{2\overline{G}_s \Delta\lambda}{g_G^2}} \tag{12.23}$$

$$J^{tr}(\overline{G}_s) = \sqrt{\frac{1}{2}(s^{tr})^\mathsf{T}\mathbf{Q}^{-1}s^{tr}} = \left[J_2^i + 2\overline{G}_s\Delta e^\mathsf{T}s^i + (\overline{G}_s)^2\Delta E_d^2\right]^{\frac{1}{2}} \tag{12.24}$$

$$J_2^i = \frac{1}{2}(s^i)^\mathsf{T}\mathbf{Q}^{-1}s^i \tag{12.25}$$

$$\Delta E_d = \sqrt{2\Delta e^\mathsf{T}\mathbf{Q}\Delta e} \tag{12.26}$$

where the secant shear modulus $\overline{G}_s$ is provided by Eqs. (11.27) and (11.26).

As already indicated in Section 11.2.1 arriving at updated stress values at the end of the $(i+1)$ load increment requires satisfying a certain set of residuals which now receive the form

$$\mathbf{r} = \left\{ \begin{array}{c} \sigma_m^{i+1} - \overline{\sigma}_m \\ p_c^{i+1} - \overline{p}_c \\ (f_d^{GCC})^{i+1} \text{ or } (f_c^{GCC})^{i+1} \end{array} \right\} = \mathbf{r}(\mathbf{a}(\varepsilon), \varepsilon) \tag{12.27}$$

where $\overline{\sigma}_m, \overline{p}_c$ are given by Eqs. (12.21) and (12.20), respectively. The vector of primary variables $\mathbf{a}$ is identical to that of Eq. (11.34) and is found employing the Newton-Raphson method

$$\mathbf{a}_{j+1}^{i+1} = \mathbf{a}_j^{i+1} - \mathbf{H}^{-1}\mathbf{r}_j \tag{12.28}$$

together with the initial condition

$$(\mathbf{a}_0^{i+1})^\mathsf{T} = \{\sigma_m^{tr}, p_c^i, 0\} \tag{12.29}$$

$$\mathbf{r}_0^\mathsf{T} = \{0, 0, (f_d^{GCC})^{tr} \text{ or } (f_c^{GCC})^{tr}\} \tag{12.30}$$

Individual components of the Jacobian matrix $\mathbf{H}$, recall Eq. (11.38), are given by

- $\mathbf{H}_{1i}$

$$H_{11} = \frac{\mathrm{d}r_1}{\mathrm{d}\sigma_m} = 1 + \frac{\overline{\sigma}_m}{\kappa^*}\frac{\partial\Delta\varepsilon_v^{el}}{\partial\sigma_m} = 1 - \frac{\overline{\sigma}_m}{\kappa^*}\frac{\partial\Delta\varepsilon_v^{pl}}{\partial\sigma_m} \tag{12.31}$$

$$H_{12} = \frac{\mathrm{d}r_1}{\mathrm{d}p_c} = \frac{\overline{\sigma}_m}{\kappa^*}\frac{\partial\Delta\varepsilon_v^{el}}{\partial p_c} = -\frac{\overline{\sigma}_m}{\kappa^*}\frac{\partial\Delta\varepsilon_v^{pl}}{\partial p_c} \tag{12.32}$$

$$H_{13} = \frac{\mathrm{d}r_1}{\mathrm{d}\Delta\lambda} = \frac{\overline{\sigma}_m}{\kappa^*}\frac{\partial\Delta\varepsilon_v^{el}}{\partial\Delta\lambda} = -\frac{\overline{\sigma}_m}{\kappa^*}\frac{\partial\Delta\varepsilon_v^{pl}}{\partial\Delta\lambda} \tag{12.33}$$

- $\mathbf{H}_{2i}$

$$H_{21} = \frac{\mathrm{d}r_2}{\mathrm{d}\sigma_m} = \frac{\overline{p}_c}{\lambda^* - \kappa^*}\frac{\partial\Delta\varepsilon_v^{pl}}{\partial\sigma_m} \tag{12.34}$$

$$H_{22} = \frac{\mathrm{d}r_2}{\mathrm{d}p_c} = 1 + \frac{\overline{p}_c}{\lambda^* - \kappa^*}\frac{\partial\Delta\varepsilon_v^{pl}}{\partial p_c} \tag{12.35}$$

$$H_{23} = \frac{\mathrm{d}r_2}{\mathrm{d}\Delta\lambda} = \frac{\overline{p}_c}{\lambda^* - \kappa^*}\frac{\partial\Delta\varepsilon_v^{pl}}{\partial\Delta\lambda} \tag{12.36}$$

- $\boldsymbol{H}_{3i}$

$$
\begin{aligned}
H_{31} &= \frac{\mathrm{d}r_3}{\mathrm{d}\sigma_m} = \frac{\partial f^{GCC}}{\partial \sigma_m} + \frac{\partial f^{GCC}}{\partial J}\frac{\partial J}{\partial \overline{G}_s}\frac{\partial \overline{G}_s}{\partial \sigma_m} + \\
&+ \frac{\partial f^{GCC}}{\partial g}\frac{\partial g}{\partial \sin 3\theta}\left(\frac{\partial \sin 3\theta}{\partial J}\frac{\partial J}{\partial \overline{G}_s}\frac{\partial \overline{G}_s}{\partial \sigma_m} + \frac{\partial \sin 3\theta}{\partial I_{3s}}\left(\frac{\partial I_{3s}}{\partial \boldsymbol{s}}\right)^{\mathsf{T}}\frac{\partial \boldsymbol{s}}{\partial \overline{G}_s}\frac{\partial \overline{G}_s}{\partial \sigma_m}\right) \quad (12.37)
\end{aligned}
$$

$$
\begin{aligned}
H_{32} &= \frac{\mathrm{d}r_3}{\mathrm{d}p_c} = \frac{\partial f^{GCC}}{\partial p_c} + \frac{\partial f^{GCC}}{\partial J}\frac{\partial J}{\partial \overline{G}_s}\frac{\partial \overline{G}_s}{\partial p_c} + \\
&+ \frac{\partial f^{GCC}}{\partial g}\frac{\partial g}{\partial \sin 3\theta}\left(\frac{\partial \sin 3\theta}{\partial J}\frac{\partial J}{\partial \overline{G}_s}\frac{\partial \overline{G}_s}{\partial p_c} + \frac{\partial \sin 3\theta}{\partial I_{3s}}\left(\frac{\partial I_{3s}}{\partial \boldsymbol{s}}\right)^{\mathsf{T}}\frac{\partial \boldsymbol{s}}{\partial \overline{G}_s}\frac{\partial \overline{G}_s}{\partial p_c}\right) \quad (12.38)
\end{aligned}
$$

$$
\begin{aligned}
H_{33} &= \frac{\mathrm{d}r_3}{\mathrm{d}\Delta\lambda} = \frac{\partial f^{GCC}}{\partial J}\left(\frac{\partial J}{\partial \Delta\lambda} + \frac{\partial J}{\partial \overline{G}_s}\frac{\partial \overline{G}_s}{\partial \Delta\lambda}\right) + \\
&+ \frac{\partial f^{GCC}}{\partial g}\frac{\partial g}{\partial \sin 3\theta}\left(\frac{\partial \sin 3\theta}{\partial J}\left[\frac{\partial J}{\partial \Delta\lambda} + \frac{\partial J}{\partial \overline{G}_s}\frac{\partial \overline{G}_s}{\partial \Delta\lambda}\right] + \right. \\
&\left. \frac{\partial \sin 3\theta}{\partial I_{3s}}\left(\frac{\partial I_{3s}}{\partial \boldsymbol{s}}\right)^{\mathsf{T}}\left[\frac{\partial \boldsymbol{s}}{\partial \Delta\lambda} + \frac{\partial \boldsymbol{s}}{\partial \overline{G}_s}\frac{\partial \overline{G}_s}{\partial \Delta\lambda}\right]\right) \quad (12.39)
\end{aligned}
$$

where

$$
\frac{\partial \overline{G}_s}{\partial \sigma_m} = \zeta\frac{\partial \overline{K}_s}{\partial \Delta\varepsilon_v^{el}}\frac{\partial \Delta\varepsilon_v^{el}}{\partial \sigma_m} = -\zeta\frac{\partial \overline{K}_s}{\partial \Delta\varepsilon_v^{el}}\frac{\partial \Delta\varepsilon_v^{pl}}{\partial \sigma_m} \tag{12.40}
$$

$$
\frac{\partial \overline{G}_s}{\partial p_c} = \zeta\frac{\partial \overline{K}_s}{\partial \Delta\varepsilon_v^{el}}\frac{\partial \Delta\varepsilon_v^{el}}{\partial p_c} = -\zeta\frac{\partial \overline{K}_s}{\partial \Delta\varepsilon_v^{el}}\frac{\partial \Delta\varepsilon_v^{pl}}{\partial p_c} \tag{12.41}
$$

$$
\frac{\partial \overline{G}_s}{\partial \Delta\lambda} = \zeta\frac{\partial \overline{K}_s}{\partial \Delta\varepsilon_v^{el}}\frac{\partial \Delta\varepsilon_v^{el}}{\partial \Delta\lambda} = -\zeta\frac{\partial \overline{K}_s}{\partial \Delta\varepsilon_v^{el}}\frac{\partial \Delta\varepsilon_v^{pl}}{\partial \Delta\lambda} \tag{12.42}
$$

$$
\frac{\partial \overline{K}_s}{\partial \Delta\varepsilon_v^{el}} = -\frac{\overline{K}_s\kappa^* + \overline{\sigma}_m}{\kappa^*\Delta\varepsilon_v^{el}} \tag{12.43}
$$

where

$$
\frac{\partial \Delta\varepsilon_{vd}^{pl}}{\partial \sigma_m} = \Delta\lambda\beta\left[-2 + \alpha(1+\alpha)(-\sigma_m^{i+1})^{\alpha-1}(\gamma p_c^{i+1})^{1-\alpha}\right] \tag{12.44}
$$

$$
\frac{\partial \Delta\varepsilon_{vc}^{pl}}{\partial \sigma_m} = 2\Delta\lambda \tag{12.45}
$$

$$
\frac{\partial \Delta\varepsilon_{vd}^{pl}}{\partial p_c} = \Delta\lambda\beta\left[-(1+\alpha)(1-\alpha)\gamma(-\sigma_m^{i+1})^{\alpha}(\gamma p_c^{i+1})^{-\alpha}\right] \tag{12.46}
$$

$$
\frac{\partial \Delta\varepsilon_{vc}^{pl}}{\partial p_c} = \Delta\lambda \tag{12.47}
$$

$$
\frac{\partial \Delta\varepsilon_{vd}^{pl}}{\partial \Delta\lambda} = \beta\left[-2\sigma_m^{i+1} - (1+\alpha)(-\sigma_m^{i+1})^{\alpha}(\gamma p_c^{i+1})^{1-\alpha}\right] \tag{12.48}
$$

$$
\frac{\partial \Delta\varepsilon_{vc}^{pl}}{\partial \Delta\lambda} = 2\sigma_m^{i+1} + p_c^{i+1} \tag{12.49}
$$

The remaining partial derivatives are

$$\frac{\partial f_d^{GCC}}{\partial \sigma_m} = \beta \left[-2\sigma_m - (1+\alpha)(-\sigma_m^{i+1})^\alpha (\gamma p_c^{i+1})^{1-\alpha} \right] \tag{12.50}$$

$$\frac{\partial f_c^{GCC}}{\partial \sigma_m} = 2\sigma_m^{i+1} + p_c^{i+1} \tag{12.51}$$

$$\frac{\partial f_d^{GCC}}{\partial p_c} = \beta\gamma(1-\alpha)(-\sigma_m^{i+1})^{1+\alpha}(\gamma p_c^{i+1})^{-\alpha} \tag{12.52}$$

$$\frac{\partial f_c^{GCC}}{\partial p_c} = \sigma_m^{i+1} \tag{12.53}$$

$$\frac{\partial f_d^{GCC}}{\partial J} = \frac{\partial f_c^{GCC}}{\partial J} = \frac{2J^{i+1}}{g^2} \tag{12.54}$$

$$\frac{\partial f_d^{GCC}}{\partial g} = \frac{\partial f_c^{GCC}}{\partial g} = -\frac{2(J^{i+1})^2}{g^3} \tag{12.55}$$

$$\frac{\partial g}{\partial \sin 3\theta} = \frac{\partial g}{\partial \chi}\frac{\partial \chi}{\partial \vartheta}\frac{\partial \vartheta}{\partial \sin 3\theta} \tag{12.56}$$

$$\frac{\partial g}{\partial \chi} = M_{\varphi_{cs}} \tag{12.57}$$

All other derivatives have already been defined either in Section 11.2.1 when replacing M_{cs} by g_G or in Section 8.3.2 within the formulation of the Hardening soil model.

12.2.2 Constant elasticity return

Similarly to the previous section and with reference to Section 11.2.2 we first summarize the governing equations of the local stress update

- Preconsolidation pressure

$$p_c^{i+1} = p_c^i \exp\left[-\frac{\Delta \varepsilon_v^{pl}}{\lambda^* - \kappa^*} \right] \tag{12.58}$$

- Mean stress

$$\sigma_m^{i+1} = \sigma_m^i + K_s^i(\Delta \varepsilon_v - \Delta \varepsilon_v^{pl}) \tag{12.59}$$

- Deviatoric stress

$$\boldsymbol{s}^{i+1} = \frac{\boldsymbol{s}^i + 2G_s^i \mathbf{Q}\Delta \boldsymbol{e}}{1 + \dfrac{2G_s^i \Delta\lambda}{g_G^2}} = \frac{\boldsymbol{s}^{tr}}{1 + \dfrac{2G_s^i \Delta\lambda}{g_G^2}} \tag{12.60}$$

- Equivalent deviatoric stress

$$J^{i+1} = \frac{J^{tr}}{1 + \dfrac{2G_s^i \Delta\lambda}{g_G^2}} \tag{12.61}$$

$$J^{tr} = \left[J_2^i + 2G_s^i \Delta \boldsymbol{e}^\mathsf{T} \boldsymbol{s}^i + (G_s^i)^2 \Delta E_d^2 \right]^{\frac{1}{2}} \tag{12.62}$$

where in analogy with Section 11.2.2 the secant bulk modulus $K_s^i = -\dfrac{\sigma_m^i}{\kappa^*}$ is kept constant with the plastic corrector step. The variables J^i and ΔE_d are provided by Eqs. (12.25) and (12.26), respectively. Because the local stress update follows entirely in the footsteps of Section 12.2.1, Eqs. (12.27) - (12.30), we present only the relevant derivatives that appear in definition of the Jacobian matrix **H**.

The components of **H** now receive the following simplified forms

- $\boldsymbol{H}_{1i}$

$$H_{11} = 1 + K_s^i \frac{\partial \Delta \varepsilon_v^{pl}}{\partial \sigma_m} \tag{12.63}$$

$$H_{12} = K_s^i \frac{\partial \Delta \varepsilon_v^{pl}}{\partial p_c} \tag{12.64}$$

$$H_{13} = K_s^i \frac{\partial \Delta \varepsilon_v^{pl}}{\partial \Delta \lambda} \tag{12.65}$$

- $\boldsymbol{H}_{2i}$ - given by Eqs. (12.34) - (12.36)

- $\boldsymbol{H}_{3i}$

$$H_{31} = \frac{\mathrm{d}r_3}{\mathrm{d}\sigma_m} = \frac{\partial f^{GCC}}{\partial \sigma_m} \tag{12.66}$$

$$H_{32} = \frac{\mathrm{d}r_3}{\mathrm{d}p_c} = \frac{\partial f^{GCC}}{\partial p_c} \tag{12.67}$$

$$\begin{aligned} H_{33} = \frac{\mathrm{d}r_3}{\mathrm{d}\Delta\lambda} &= \frac{\partial f^{GCC}}{\partial J} \frac{\partial J}{\partial \Delta\lambda} + \\ &+ \frac{\partial f^{GCC}}{\partial g} \frac{\partial g}{\partial \sin 3\theta} \left(\frac{\partial \sin 3\theta}{\partial J} \frac{\partial J}{\partial \Delta\lambda} + \frac{\partial \sin 3\theta}{\partial I_{3s}} \left(\frac{\partial I_{3s}}{\partial \boldsymbol{s}} \right)^{\mathsf{T}} \frac{\partial \boldsymbol{s}}{\partial \Delta\lambda} \right) \end{aligned} \tag{12.68}$$

where

$$\frac{\partial J}{\partial \Delta\lambda} = -\frac{J^{tr}}{\left(1 + \frac{2G_s^i \Delta\lambda}{g_G^2}\right)^2} \frac{2G_s^i}{g_G^2} = -\frac{J}{1 + \frac{2G_s^i \Delta\lambda}{g_G^2}} \frac{2G_s^i}{g_G^2} \tag{12.69}$$

$$\frac{\partial \boldsymbol{s}}{\partial \Delta\lambda} = -\frac{\boldsymbol{s}^{tr}}{\left(1 + \frac{2G_s^i \Delta\lambda}{g_G^2}\right)^2} \frac{2G_s^i}{g_G^2} = -\frac{\boldsymbol{s}}{1 + \frac{2G_s^i \Delta\lambda}{g_G^2}} \frac{2G_s^i}{g_G^2} \tag{12.70}$$

All other derivatives were already defined either in the previous section or in Section 8.3.2.

12.3 Algorithmic tangent stiffness matrix

Although the Generalized Cam-clay model is a two-yield surface plasticity model, the derivation of the algorithmic tangent stiffness matrix is analogous to the procedure described in Section 11.3 as only one yield surface can be active at a given time (load step). So there is no need to consider the concept of multisurface plasticity as was the case of the Hardening soil model in Chapter 8 or the Soft soil model in Chapter 9. From what was presented in the previous sections it is also obvious that the derivation of algorithmic tangent stiffness matrix $\boldsymbol{\mathcal{D}}$ given by

$$\boldsymbol{\mathcal{D}} = \frac{\mathrm{d}\boldsymbol{\sigma}^{i+1}}{\mathrm{d}\boldsymbol{\varepsilon}^{i+1}} = 3\boldsymbol{m} \left(\frac{\mathrm{d}\sigma_m^{i+1}}{\mathrm{d}\boldsymbol{\varepsilon}^{i+1}} \right)^{\mathsf{T}} + \frac{\mathrm{d}\boldsymbol{s}^{i+1}}{\mathrm{d}\boldsymbol{\varepsilon}^{i+1}} \tag{12.71}$$

is common to both yield surfaces with some minor differences pertinent to their specific formulations, regardless of the type of returning mapping algorithm. Similarly to Section 11.3 we shall drop the superscript $(i+1)$ and consider all derivatives to be taken at the end of the $(i+1)$ load increment, so for example the notation $\frac{\mathrm{d}\boldsymbol{\sigma}}{\mathrm{d}\boldsymbol{\varepsilon}} = \frac{\mathrm{d}\boldsymbol{\sigma}^{i+1}}{\mathrm{d}\boldsymbol{\varepsilon}^{i+1}}$ will be used.

12.3.1 Matrix $\mathcal{D}$ based on variable elasticity stress return

Similarly with other sections, see also [14], we start from Eqs. (12.21) - (12.20) and Eqs. (12.14) - (12.15) to write

$$\frac{\mathrm{d}\sigma_m}{\mathrm{d}\varepsilon} = -\frac{\sigma_m^{i+1}}{\kappa^*}\left(3\boldsymbol{m} - \frac{\mathrm{d}\Delta\varepsilon_v^{pl}}{\mathrm{d}\varepsilon}\right) = \tilde{\sigma}_m\left(3\boldsymbol{m} - \frac{\mathrm{d}\Delta\varepsilon_v^{pl}}{\mathrm{d}\varepsilon}\right) \tag{12.72}$$

$$\frac{\mathrm{d}p_c}{\mathrm{d}\varepsilon} = -\frac{p_c^{i+1}}{\lambda^* - \kappa^*}\frac{\mathrm{d}\Delta\varepsilon_v^{pl}}{\mathrm{d}\varepsilon} \tag{12.73}$$

$$\begin{aligned}
\frac{\mathrm{d}\Delta\varepsilon_v^{pl}}{\mathrm{d}\varepsilon} &= \frac{\partial\Delta\varepsilon_v^{pl}}{\partial\sigma_m^{i+1}}\frac{\mathrm{d}\sigma_m}{\mathrm{d}\varepsilon} + \frac{\partial\Delta\varepsilon_v^{pl}}{\partial p_c}\frac{\mathrm{d}p_c}{\mathrm{d}\varepsilon} + \frac{\partial\Delta\varepsilon_v^{pl}}{\partial\Delta\lambda}\frac{\partial\Delta\lambda}{\partial\varepsilon} \\
&= a_1\frac{\mathrm{d}\sigma_m}{\mathrm{d}\varepsilon} + a_2\frac{\mathrm{d}p_c}{\mathrm{d}\varepsilon} + a_3\frac{\partial\Delta\lambda}{\partial\varepsilon}
\end{aligned} \tag{12.74}$$

where the terms a_1, a_2, a_3 follow from Eqs. (12.44) (12.49) depending on the active yield surface. Therefore

$$\begin{aligned}
\frac{\mathrm{d}\sigma_m}{\mathrm{d}\varepsilon} &= \tilde{\sigma}_m\left(3\boldsymbol{m} - a_1\frac{\mathrm{d}\sigma_m}{\mathrm{d}\varepsilon} - a_2\frac{\mathrm{d}p_c}{\mathrm{d}\varepsilon} - a_3\frac{\partial\Delta\lambda}{\partial\varepsilon}\right) = \\
&= \frac{\tilde{\sigma}_m}{1 + a_1\tilde{\sigma}_m}\left(3\boldsymbol{m} - a_2\frac{\mathrm{d}p_c}{\mathrm{d}\varepsilon} - a_3\frac{\partial\Delta\lambda}{\partial\varepsilon}\right)
\end{aligned} \tag{12.75}$$

$$\begin{aligned}
\frac{\mathrm{d}p_c}{\mathrm{d}\varepsilon} &= -\frac{p_c^{i+1}}{\lambda^* - \kappa^*}\left(a_1\frac{\mathrm{d}\sigma_m}{\mathrm{d}\varepsilon} + a_2\frac{\mathrm{d}p_c}{\mathrm{d}\varepsilon} + a_3\frac{\partial\Delta\lambda}{\partial\varepsilon}\right) = \\
&= -\frac{p_c}{(\lambda^* - \kappa^*)(1 + a_1\tilde{\sigma}_m)}\left(a_1\tilde{\sigma}_m3\boldsymbol{m} + a_2\frac{\mathrm{d}p_c}{\mathrm{d}\varepsilon} + a_3\frac{\partial\Delta\lambda}{\partial\varepsilon}\right)
\end{aligned} \tag{12.76}$$

Rearranging Eq. (12.76) gives

$$\frac{\mathrm{d}p_c}{\mathrm{d}\varepsilon} = a_6 3\boldsymbol{m} + a_7\frac{\partial\Delta\lambda}{\partial\varepsilon^{i+1}} \tag{12.77}$$

$$a_6 = -\frac{p_c^{i+1}a_1\tilde{\sigma}_m}{(\lambda^* - \kappa^*)(1 + a_1\tilde{\sigma}_m) + a_2 p_c^{i+1}}, \quad \text{compare with Eq. (11.117)} \tag{12.78}$$

$$a_7 = -\frac{p_c^{i+1}a_3}{(\lambda^* - \kappa^*)(1 + a_1\tilde{\sigma}_m) + a_2 p_c^{i+1}}, \quad \text{compare with Eq. (11.118)} \tag{12.79}$$

Finally, substituting from Eq. (12.77) back to Eq. (12.75) yields

$$\frac{\mathrm{d}\sigma_m}{\mathrm{d}\varepsilon} = a_4 3\boldsymbol{m} + a_5\frac{\partial\Delta\lambda}{\partial\varepsilon} \tag{12.80}$$

$$a_4 = \frac{\tilde{\sigma}_m}{1 + a_1\tilde{\sigma}_m}(1 - a_2 a_6), \quad \text{compare with Eq. (11.121)} \tag{12.81}$$

$$a_5 = -\frac{\tilde{\sigma}_m}{1 + a_1\tilde{\sigma}_m}(a_3 + a_2 a_7), \quad \text{compare with Eq. (11.122)} \tag{12.82}$$

Recall Eq. (12.22) to write the second term in Eq. (12.71) in the form, compare with Eq (11.94),

$$\begin{aligned}
\frac{\mathrm{d}\boldsymbol{s}}{\mathrm{d}\varepsilon} &= \frac{\partial\boldsymbol{s}}{\partial\varepsilon} + \underbrace{\frac{\mathrm{d}\boldsymbol{s}}{\mathrm{d}\tilde{\chi}}\left(\frac{\mathrm{d}\tilde{\chi}}{\mathrm{d}\varepsilon}\right)^{\mathsf{T}}}_{\boldsymbol{\mathsf{E}}_2} + \frac{\partial\boldsymbol{s}}{\partial\Delta\lambda}\left(\frac{\partial\Delta\lambda}{\partial\varepsilon}\right)^{\mathsf{T}} + \frac{\partial\boldsymbol{s}}{\partial\overline{G}_s}\frac{\partial\overline{G}_s}{\partial\Delta\varepsilon_v^{el}}\left(3\boldsymbol{m} - \frac{\mathrm{d}\Delta\varepsilon_v^{pl}}{\mathrm{d}\varepsilon}\right)^{\mathsf{T}} = \\
&= \boldsymbol{\mathsf{E}}_1 + \boldsymbol{\mathsf{E}}_2 + \boldsymbol{s}_1\left(\frac{\partial\Delta\lambda}{\partial\varepsilon}\right)^{\mathsf{T}} + \boldsymbol{\mu}\left(3\boldsymbol{m} - \frac{\mathrm{d}\Delta\varepsilon_v^{pl}}{\mathrm{d}\varepsilon}\right)^{\mathsf{T}}
\end{aligned} \tag{12.83}$$

where the total and partial derivatives that enter Eq. (12.83) are provided by

$$\frac{\partial s}{\partial \varepsilon} = \frac{\partial s}{\partial \Delta e}\frac{\partial \Delta e}{\partial \varepsilon} = \mathbf{E}_1 \tag{12.84}$$

$$\frac{\partial s}{\partial \Delta e} = \frac{2\overline{G}_s\mathbf{Q}}{1 + \dfrac{2\overline{G}_s\Delta\lambda}{g_G^2}} \tag{12.85}$$

$$\frac{\partial \Delta e}{\partial \varepsilon} = \mathbf{PQ} \tag{12.86}$$

$$\frac{\mathrm{d}s}{\mathrm{d}\tilde{\chi}} = \frac{\partial s}{\partial g_G}\frac{\partial g_G}{\partial \tilde{\chi}} = \frac{s^{i+1}}{1 + \dfrac{2\overline{G}_s\Delta\lambda}{g_G^2}}\frac{4\overline{G}_s\Delta\lambda}{\tilde{\chi}^3 M_{\varphi_{cs}}^2} \tag{12.87}$$

$$\frac{\mathrm{d}\tilde{\chi}}{\mathrm{d}\varepsilon} = \left[\frac{\mathrm{d}\tilde{s}}{\mathrm{d}\varepsilon}\right]^\mathsf{T}\frac{\partial \tilde{\chi}}{\partial \tilde{s}} \tag{12.88}$$

$$\frac{\mathrm{d}\tilde{s}}{\mathrm{d}\varepsilon} = \frac{\partial \tilde{s}}{\partial \Delta e}\frac{\partial \Delta e}{\partial \varepsilon} + \frac{\partial \tilde{s}}{\partial \Delta\varepsilon_v}\frac{\partial \Delta\varepsilon_v}{\partial \varepsilon} \tag{12.89}$$

$$\frac{\partial \tilde{\chi}}{\partial \tilde{s}} = \frac{\partial \tilde{\chi}}{\partial \vartheta}\frac{\partial \vartheta}{\partial \sin 3\tilde{\theta}}\left(\frac{\partial \sin 3\tilde{\theta}}{\partial \tilde{J}}\frac{\partial \tilde{J}}{\partial \tilde{s}} + \frac{\partial \sin 3\tilde{\theta}}{\partial \tilde{I}_{3s}}\frac{\partial \tilde{I}_{3s}}{\partial \tilde{s}}\right) \tag{12.90}$$

$$\frac{\partial \tilde{s}}{\partial \Delta e} = 2\tilde{\overline{G}}_s\mathbf{Q} \tag{12.91}$$

$$\frac{\partial \tilde{s}}{\partial \Delta\varepsilon_v} = \frac{\partial \tilde{s}}{\partial \tilde{\overline{G}}_s}\frac{\partial \tilde{\overline{G}}_s}{\partial \Delta\varepsilon_v} = 2\mathbf{Q}\Delta e\,\zeta\frac{\partial \tilde{\overline{K}}_s}{\partial \Delta\varepsilon_v} \tag{12.92}$$

$$\frac{\partial \tilde{\overline{K}}_s}{\partial \Delta\varepsilon_v} = -\frac{1}{\Delta\varepsilon_v}\left(\tilde{\overline{K}}_s - \frac{\tilde{\sigma}_m}{\kappa^*}\right) \tag{12.93}$$

The term $\dfrac{\mathrm{d}\Delta\varepsilon_v^{pl}}{\mathrm{d}\varepsilon}$ is given by Eq. (12.74), which can be rearranged with the help of Eqs. (12.80) and (12.77) to get

$$\frac{\mathrm{d}\Delta\varepsilon_v^{pl}}{\mathrm{d}\varepsilon} = b_1 3m + b_2\frac{\partial \Delta\lambda}{\partial \varepsilon^{i+1}} \tag{12.94}$$

$$b_1 = a_1a_4 + a_2a_6 \tag{12.95}$$

$$b_2 = a_1a_5 + a_2a_7 + a_3 \tag{12.96}$$

Adopting Eq. (12.74) in Eq. (12.83) we finally arrive at its simplified version

$$\frac{\mathrm{d}s}{\mathrm{d}\varepsilon} = \mathbf{E}_1 + \mathbf{E}_2 + 3(1 - b_1)\boldsymbol{\mu}m^\mathsf{T} + (s_1 - b_2\boldsymbol{\mu})\left(\frac{\partial \Delta\lambda}{\partial \varepsilon}\right)^\mathsf{T} = \mathbf{F} + f\left(\frac{\partial \Delta\lambda}{\partial \varepsilon}\right)^\mathsf{T} \tag{12.97}$$

In analogy with previous sections the term $\dfrac{\partial \Delta\lambda}{\partial \varepsilon}$ (see, e.g., Section 11.3.1, Eq. (11.104)) is derived from the consistency condition written as

$$\frac{\mathrm{d}f^{GCC}}{\mathrm{d}\varepsilon} = \frac{\mathrm{d}r_3}{\mathrm{d}\varepsilon} = \frac{\partial r_3}{\partial J}\frac{\mathrm{d}J}{\mathrm{d}\varepsilon} + \frac{\partial r_3}{\partial g}\frac{\partial g}{\partial \sin 3\theta}\frac{\mathrm{d}\sin 3\theta}{\mathrm{d}\varepsilon} + \frac{\partial r_3}{\partial \sigma_m}\frac{\mathrm{d}\sigma_m}{\mathrm{d}\varepsilon} + \frac{\partial r_3}{\partial p_c}\frac{\mathrm{d}p_c}{\mathrm{d}\varepsilon} = \mathbf{0} \tag{12.98}$$

Remember Section 8.4 where the terms $\dfrac{\mathrm{d}J}{\mathrm{d}\varepsilon}$ (Eq. (8.222)) and $\dfrac{\mathrm{d}\sin 3\theta}{\mathrm{d}\varepsilon}$ (Eq. (8.237)) were derived to give

$$\frac{\mathrm{d}J}{\mathrm{d}\varepsilon} = \left[\frac{\mathrm{d}s}{\mathrm{d}\varepsilon}\right]^\mathsf{T}\frac{\partial J}{\partial s} \tag{12.99}$$

$$\frac{\mathrm{d}\sin 3\theta}{\mathrm{d}\varepsilon} = \frac{\partial \sin 3\theta}{\partial J}\left[\frac{\mathrm{d}s}{\mathrm{d}\varepsilon}\right]^\mathsf{T}\frac{\partial J}{\partial s} + \frac{\partial \sin 3\theta}{\partial I_{3s}}\left[\frac{\mathrm{d}s}{\mathrm{d}\varepsilon}\right]^\mathsf{T}\frac{\partial I_{3s}}{\partial s} \tag{12.100}$$

With these definitions we may expand Eq. (12.98) as

$$
\begin{aligned}
\frac{\mathrm{d}r_3}{\mathrm{d}\varepsilon} &= \frac{\partial r_3}{\partial \sigma_m}\frac{\mathrm{d}\sigma_m}{\mathrm{d}\varepsilon} + \\
&+ \left(\frac{\partial r_3}{\partial J} + \frac{\partial r_3}{\partial g}\frac{\partial g}{\partial \sin 3\theta}\frac{\partial \sin 3\theta}{\partial J}\right)\left[\frac{\mathrm{d}s}{\mathrm{d}\varepsilon}\right]^{\mathsf{T}}\frac{\partial J}{\partial s} + \\
&+ \frac{\partial r_3}{\partial g}\frac{\partial g}{\partial \sin 3\theta}\frac{\partial \sin 3\theta}{\partial I_{3s}}\left[\frac{\mathrm{d}s}{\mathrm{d}\varepsilon}\right]^{\mathsf{T}}\frac{\partial I_{3s}}{\partial s} + \\
&+ \frac{\partial r_3}{\partial p_c}\frac{\mathrm{d}p_c}{\mathrm{d}\varepsilon} \quad\quad\quad\quad\quad\quad\quad (12.101)\\
&= c_1\frac{\mathrm{d}\sigma_m}{\mathrm{d}\varepsilon} + c_2\left[\frac{\mathrm{d}s}{\mathrm{d}\varepsilon}\right]^{\mathsf{T}}\boldsymbol{j}_1 + c_3\left[\frac{\mathrm{d}s}{\mathrm{d}\varepsilon}\right]^{\mathsf{T}}\boldsymbol{j}_2 + c_4\frac{\mathrm{d}p_c}{\mathrm{d}\varepsilon} = \boldsymbol{0} \quad (12.102)
\end{aligned}
$$

where the terms $c_1 = \dfrac{\partial r_3}{\partial \sigma_m} = \dfrac{\partial f}{\partial \sigma_m}$ and $c_4 = \dfrac{\partial r_3}{\partial p_c} = \dfrac{\partial f}{\partial p_c}$ are given by Eqs. (12.50) - (12.53) depending on the active yield surface. Substituting from Eqs. (12.80), (12.97) and (12.77) into Eq. (12.102) gives

$$
\begin{aligned}
\frac{\mathrm{d}r_3}{\mathrm{d}\varepsilon} &= \boldsymbol{g} + h\frac{\partial \Delta\lambda}{\partial \varepsilon} = \boldsymbol{0} \longrightarrow \frac{\partial \Delta\lambda}{\partial \varepsilon} = -\frac{1}{h}\boldsymbol{g} = \boldsymbol{q} & (12.103)\\
\boldsymbol{g} &= (c_1 a_4 + c_4 a_6)3\boldsymbol{m} + \mathbf{F}^{\mathsf{T}}(c_2\boldsymbol{j}_1 + c_3\boldsymbol{j}_2) & (12.104)\\
h &= c_1 a_5 + c_4 a_7 + \boldsymbol{f}^{\mathsf{T}}(c_2\boldsymbol{j}_1 + c_3\boldsymbol{j}_2) & (12.105)
\end{aligned}
$$

The consistent tangent stiffness matrix $\boldsymbol{\mathcal{D}}$ is finally obtained by substituting back from Eq. (12.103) into Eqs. (12.80), (12.97) and (12.77). This yields

$$
\boldsymbol{\mathcal{D}} = \mathbf{F} + 9a_4\boldsymbol{m}\boldsymbol{m}^{\mathsf{T}} + (3a_5\boldsymbol{m} + \boldsymbol{f})\boldsymbol{q}^{\mathsf{T}} \quad\quad\quad (12.106)
$$

12.3.2   Matrix $\boldsymbol{\mathcal{D}}$ based on constant elasticity stress return

The general procedure is identical to that in the previous section taking into account some simplifications introduced already in Section 12.2.2, the constant stiffness within the stress return mapping algorithm in particular. With that and in light of Eqs. (12.59) - (12.58) and Eqs. (12.14) - (12.15) the first two equations in the previous section become

$$
\frac{\mathrm{d}\sigma_m}{\mathrm{d}\varepsilon} = K_s^i\left(3\boldsymbol{m} - \frac{\mathrm{d}\Delta\varepsilon_v^{pl}}{\mathrm{d}\varepsilon}\right) \quad\quad\quad (12.107)
$$

$$
\frac{\mathrm{d}p_c}{\mathrm{d}\varepsilon} = -\frac{p_c^{i+1}}{\lambda^* - \kappa^*}\frac{\mathrm{d}\Delta\varepsilon_v^{pl}}{\mathrm{d}\varepsilon} \qu\quad\quad\quad (12.108)
$$

Unlike the previous section we now treat the term $\dfrac{\mathrm{d}\Delta\varepsilon_v^{pl}}{\mathrm{d}\varepsilon}$ for individual domains separately. Thus starting with the subcritical domain, recall Section 11.3.2 and Eqs. (11.114) and (11.115), we get

$$
\begin{aligned}
\frac{\mathrm{d}\sigma_m}{\mathrm{d}\varepsilon} &= K_s^i\left[3\boldsymbol{m} - \Delta\lambda\left(2\frac{\mathrm{d}\sigma_m}{\mathrm{d}\varepsilon} + \frac{\mathrm{d}p_c}{\mathrm{d}\varepsilon}\right) - (2\sigma_m + p_c)\frac{\partial \Delta\lambda}{\partial \varepsilon}\right] \\
&= \frac{K_s^i}{1 + 2\Delta\lambda K_s^i}\left[3\boldsymbol{m} - \Delta\lambda\frac{\mathrm{d}p_c}{\mathrm{d}\varepsilon} - (2\sigma_m^{i+1} + p_c^{i+1})\frac{\partial \Delta\lambda}{\partial \varepsilon}\right] & (12.109)
\end{aligned}
$$

$$
\begin{aligned}
\frac{\mathrm{d}p_c}{\mathrm{d}\varepsilon} &= -\frac{p_c^{i+1}}{\lambda^* - \kappa^*}\left[\Delta\lambda\left(2\frac{\mathrm{d}\sigma_m}{\mathrm{d}\varepsilon} + \frac{\mathrm{d}p_c}{\mathrm{d}\varepsilon}\right) + (2\sigma_m^{i+1} + p_c^{i+1})\frac{\partial \Delta\lambda}{\partial \varepsilon}\right] \\
&= -\frac{p_c^{i+1}}{(\lambda^* - \kappa^*)(1 + 2\Delta\lambda K_s^i)}\left[2\Delta\lambda K_s^i 3\boldsymbol{m} + \Delta\lambda\frac{\mathrm{d}p_c}{\mathrm{d}\varepsilon} + (2\sigma_m^{i+1} + p_c^{i+1})\frac{\partial \Delta\lambda}{\partial \varepsilon}\right] & (12.110)
\end{aligned}
$$

As expected the terms $\dfrac{\mathrm{d}p_c^{+1}}{\mathrm{d}\varepsilon^{i+1}}$ and $\dfrac{\mathrm{d}\sigma_m^{i+1}}{\mathrm{d}\varepsilon^{i+1}}$ are, therefore, given by Eqs. (11.116) - (11.122). Now, considering the supercritical domain, we first write

$$
\begin{aligned}
\frac{\mathrm{d}\Delta\varepsilon_v^{pl}}{\mathrm{d}\varepsilon} &= \frac{\partial\Delta\varepsilon_{vd}^{pl}}{\partial\sigma_m}\frac{\mathrm{d}\sigma_m}{\mathrm{d}\varepsilon} + \frac{\partial\Delta\varepsilon_{vd}^{pl}}{\partial p_c}\frac{\mathrm{d}p_c}{\mathrm{d}\varepsilon} + \frac{\partial\Delta\varepsilon_{vd}^{pl}}{\partial\Delta\lambda}\frac{\partial\Delta\lambda}{\partial\varepsilon} \\
&= a_1\frac{\mathrm{d}\sigma_m}{\mathrm{d}\varepsilon} + a_2\frac{\mathrm{d}p_c}{\mathrm{d}\varepsilon} + a_3\frac{\partial\Delta\lambda}{\partial\varepsilon}
\end{aligned} \tag{12.111}
$$

where the terms a_1, a_2, a_3 are given by Eqs. (12.44), (12.46) and (12.48), respectively. Therefore

$$
\begin{aligned}
\frac{\mathrm{d}\sigma_m}{\mathrm{d}\varepsilon} &= K_s^i\left(3\boldsymbol{m} - a_1\frac{\mathrm{d}\sigma_m}{\mathrm{d}\varepsilon} - a_2\frac{\mathrm{d}p_c}{\mathrm{d}\varepsilon} - a_3\frac{\partial\Delta\lambda}{\partial\varepsilon}\right) = \\
&= \frac{K_s^i}{1 + a_1 K_s^i}\left(3\boldsymbol{m} - a_2\frac{\mathrm{d}p_c}{\mathrm{d}\varepsilon} - a_3\frac{\partial\Delta\lambda}{\partial\varepsilon}\right)
\end{aligned} \tag{12.112}
$$

$$
\begin{aligned}
\frac{\mathrm{d}p_c}{\mathrm{d}\varepsilon} &= -\frac{p_c^{i+1}}{\lambda^* - \kappa^*}\left(a_1\frac{\mathrm{d}\sigma_m}{\mathrm{d}\varepsilon} + a_2\frac{\mathrm{d}p_c}{\mathrm{d}\varepsilon} + a_3\frac{\partial\Delta\lambda}{\partial\varepsilon}\right) = \\
&= -\frac{p_c^{i+1}}{(\lambda^* - \kappa^*)(1 + a_1 K_s^i)}\left(a_1 K_s^i 3\boldsymbol{m} + a_2\frac{\mathrm{d}p_c}{\mathrm{d}\varepsilon} + a_3\frac{\partial\Delta\lambda}{\partial\varepsilon}\right)
\end{aligned} \tag{12.113}
$$

Point out that setting $a_1 = 2\Delta\lambda$ (Eq. (12.45)), $a_2 = \Delta\lambda$ (Eq. (12.47)) and $a_3 = 2\sigma_m^{i+1} + p_c^{i+1}$ (Eq. (12.49)) in Eqs. (12.112) and (12.113) yields Eqs. (12.109) and (12.110), respectively. Next, rearrange Eq. (12.113) to get

$$
\frac{\mathrm{d}p_c}{\mathrm{d}\varepsilon} = a_6 3\boldsymbol{m} + a_7\frac{\partial\Delta\lambda}{\partial\varepsilon} \tag{12.114}
$$

$$
a_6 = -\frac{p_c^{i+1}a_1 K_s^i}{(\lambda^* - \kappa^*)(1 + a_1 K_s^i) + a_2 p_c^{i+1}}, \quad \text{compare with Eqs. (11.117), (12.78)} \tag{12.115}
$$

$$
a_7 = -\frac{p_c^{i+1}a_3}{(\lambda^* - \kappa^*)(1 + a_1 K_s^i) + a_2 p_c^{i+1}}, \quad \text{compare with Eqs. (11.118), (12.79)} \tag{12.116}
$$

Finally, substituting from Eq. (12.114) back to Eq. (12.112) provides

$$
\frac{\mathrm{d}\sigma_m}{\mathrm{d}\varepsilon} = a_4 3\boldsymbol{m} + a_5\frac{\partial\Delta\lambda}{\partial\varepsilon} \tag{12.117}
$$

$$
a_4 = \frac{K_s^i}{1 + a_1 K_s^i}(1 - a_2 a_6), \quad \text{compare with Eqs. (11.121), (12.81)} \tag{12.118}
$$

$$
a_5 = -\frac{K_s^i}{1 + a_1 K_s^i}(a_3 + a_2 a_7), \quad \text{compare with Eqs. (11.122), (12.82)} \tag{12.119}
$$

Similarly to the Modified Cam-clay model these equations are identical to those derived in the previous section if replacing K_s^i by $\tilde{\sigma}_m$. We have also confirmed that no specific distinction between subcritical and supercritical regions is needed providing the terms a_1, a_2, a_3 are associated with the correct derivatives. In what follows we thus proceed in a general way and if needed the differences between supercritical and subcritical regions will be mentioned. Therefore, with reference to the previous section, the next step is to derive the term $\dfrac{\mathrm{d}\boldsymbol{s}}{\mathrm{d}\varepsilon}$ which in the case of constant elasticity return receives this simplified form

$$
\frac{\mathrm{d}\boldsymbol{s}}{\mathrm{d}\varepsilon} = \frac{\partial\boldsymbol{s}}{\partial\varepsilon} + \underbrace{\frac{\mathrm{d}\boldsymbol{s}}{\mathrm{d}\tilde{\chi}}\left(\frac{\mathrm{d}\tilde{\chi}}{\mathrm{d}\varepsilon}\right)^{\mathsf{T}}}_{\mathbf{E}_2} + \frac{\partial\boldsymbol{s}}{\partial\Delta\lambda}\left(\frac{\partial\Delta\lambda}{\partial\varepsilon}\right)^{\mathsf{T}} = \underbrace{\mathbf{E}_1 + \mathbf{E}_2}_{\mathbf{E}} + s_1\left(\frac{\partial\Delta\lambda}{\partial\varepsilon}\right)^{\mathsf{T}} \tag{12.120}
$$

where the corresponding total and partial derivatives are now provided by

$$\frac{\partial s}{\partial \varepsilon} = \frac{\partial s}{\partial \Delta e}\frac{\partial \Delta e}{\partial \varepsilon} = \mathbf{E}_1 \tag{12.121}$$

$$\frac{\partial s}{\partial \Delta e} = \frac{2G_s^i \mathbf{Q}}{1 + \dfrac{2G_s^i \Delta\lambda}{g_G^2}} \tag{12.122}$$

$$\frac{\partial \Delta e}{\partial \varepsilon} = \mathbf{PQ} \tag{12.123}$$

$$\frac{\mathrm{d}s}{\mathrm{d}\tilde\chi} = \frac{\partial s}{\partial g_G}\frac{\partial g_G}{\partial \tilde\chi} = \frac{s^{i+1}}{1 + \dfrac{2G_s^i\Delta\lambda}{g_G^2}}\frac{4G_s^i\Delta\lambda}{\tilde\chi^3 M_{\varphi_{cs}}^2} \tag{12.124}$$

$$\frac{\mathrm{d}\tilde\chi}{\mathrm{d}\varepsilon} = \left[\frac{\mathrm{d}\tilde s}{\mathrm{d}\varepsilon}\right]^{\mathsf{T}}\frac{\partial \tilde\chi}{\partial \tilde s} \tag{12.125}$$

$$\frac{\mathrm{d}\tilde s}{\mathrm{d}\varepsilon} = \frac{\partial \tilde s}{\partial \Delta e}\frac{\partial \Delta e}{\partial \varepsilon} \tag{12.126}$$

$$\frac{\partial \tilde\chi}{\partial \tilde s} = \frac{\partial \tilde\chi}{\partial \vartheta}\frac{\partial \vartheta}{\partial \sin 3\theta}\left(\frac{\partial \sin 3\theta}{\partial \tilde J}\frac{\partial \tilde J}{\partial \tilde s} + \frac{\partial \sin 3\theta}{\partial \tilde I_{3s}}\frac{\partial \tilde I_{3s}}{\partial \tilde s}\right) \tag{12.127}$$

$$\frac{\partial \tilde s}{\partial \Delta e} = \frac{\partial s^{tr}}{\partial \Delta e} = 2G_s^i \mathbf{Q} \tag{12.128}$$

To obtain the term $\dfrac{\partial \Delta\lambda}{\partial \varepsilon}$ we invoke again the consistency condition

$$\frac{\mathrm{d}f^{GCC}}{\mathrm{d}\varepsilon} = \frac{\mathrm{d}r_3}{\mathrm{d}\varepsilon} = \frac{\partial r_3}{\partial J}\frac{\mathrm{d}J}{\mathrm{d}\varepsilon} + \frac{\partial r_3}{\partial g}\frac{\partial g}{\partial \sin 3\theta}\frac{\mathrm{d}\sin 3\theta}{\mathrm{d}\varepsilon} + \frac{\partial r_3}{\partial \sigma_m}\frac{\mathrm{d}\sigma_m}{\mathrm{d}\varepsilon} + \frac{\partial r_3}{\partial p_c}\frac{\mathrm{d}p_c}{\mathrm{d}\varepsilon} = \mathbf{0} \tag{12.129}$$

which, with the help of Eqs. (12.99) and (12.100), rewrites as

$$\frac{\mathrm{d}r_3}{\mathrm{d}\varepsilon} = \frac{\partial r_3}{\partial \sigma_m}\frac{\mathrm{d}\sigma_m}{\mathrm{d}\varepsilon} +$$

$$+ \left(\frac{\partial r_3}{\partial J} + \frac{\partial r_3}{\partial g}\frac{\partial g}{\partial \sin 3\theta}\frac{\partial \sin 3\theta}{\partial J}\right)\left[\frac{\mathrm{d}s}{\mathrm{d}\varepsilon}\right]^{\mathsf{T}}\frac{\partial J}{\partial s} +$$

$$+ \frac{\partial r_3}{\partial g}\frac{\partial g}{\partial \sin 3\theta}\frac{\partial \sin 3\theta}{\partial I_{3s}}\left[\frac{\mathrm{d}s}{\mathrm{d}\varepsilon}\right]^{\mathsf{T}}\frac{\partial I_{3s}}{\partial s} +$$

$$+ \frac{\partial r_3}{\partial p_c}\frac{\mathrm{d}p_c}{\mathrm{d}\varepsilon} \tag{12.130}$$

$$= c_1\frac{\mathrm{d}\sigma_m}{\mathrm{d}\varepsilon} + c_2\left[\frac{\mathrm{d}s}{\mathrm{d}\varepsilon}\right]^{\mathsf{T}}\boldsymbol{j}_1 + c_3\left[\frac{\mathrm{d}s}{\mathrm{d}\varepsilon}\right]^{\mathsf{T}}\boldsymbol{j}_2 + c_4\frac{\mathrm{d}p_c}{\mathrm{d}\varepsilon} = \mathbf{0} \tag{12.131}$$

where the terms $c_1 = \dfrac{\partial r_3}{\partial \sigma_m} = \dfrac{\partial f}{\partial \sigma_m}$ and $c_4 = \dfrac{\partial r_3}{\partial p_c} = \dfrac{\partial f}{\partial p_c}$ are given by Eqs. (12.50) - (12.53) depending on the active yield surface. Substituting from Eqs. (12.117), (12.120) and (12.114) into Eq. (12.131) gives

$$\frac{\mathrm{d}r_3}{\mathrm{d}\varepsilon} = \boldsymbol{g} + h\frac{\partial \Delta\lambda}{\partial \varepsilon} = \mathbf{0} \longrightarrow \frac{\partial \Delta\lambda}{\partial \varepsilon} = -\frac{1}{h}\boldsymbol{g} = \boldsymbol{q} \tag{12.132}$$

$$\boldsymbol{g} = (c_1 a_4 + c_4 a_6)3\boldsymbol{m} + \mathbf{E}^{\mathsf{T}}(c_2\boldsymbol{j}_1 + c_3\boldsymbol{j}_2) \tag{12.133}$$

$$h = c_1 a_5 + c_4 a_7 + \boldsymbol{s}_1^{\mathsf{T}}(c_2\boldsymbol{j}_1 + c_3\boldsymbol{j}_2) \tag{12.134}$$

The consistent tangent stiffness matrix $\mathcal{D}$ follows again from substituting back from Eq. (12.132) into Eqs. (12.117), (12.120) and (12.114). This gives, compare with Eq. (12.106),

$$\mathcal{D} = \mathbf{E} + 9a_4\boldsymbol{m}\boldsymbol{m}^{\mathsf{T}} + (3a_5\boldsymbol{m} + \boldsymbol{s}_1)\boldsymbol{q}^{\mathsf{T}} \tag{12.135}$$

12.4 Note on numerical implementation

Recall Eq. (12.2) to realize that neither function f_d^{GCC} nor its derivatives with respect to σ_m can be evaluated when the mean effective stress becomes positive, e.g. the value of the trial stress $\sigma_m^{tr} > 0$ attained during the elastic predictor step. In such a case the stress is first brought back to the yield surface represented by the Matsuoka-Nakai model, see the relevant section in Chapter 8 devoted to the Hardening soil model, and subsequently adjusted using the implicit integration scheme described next. When this return is not permitted, the apex problem must be solved as discussed for example in Section 4.4. Because all issues pertinent to the Matsuoka-Nakai yield surface are thoroughly discussed in Section 8.1.2 we again limit out attention to essential steps associated with the formulation of the Matsuoka-Nakai yield surface within the GCC model. We begin with writing the yield and plastic potential surfaces as

$$
\begin{aligned}
f_{MN}^{GCC} &= I_\sigma(\boldsymbol{\sigma}) - \sin^2\varphi & (12.136)\\
g_{MN}^{GCC} &= J + \sigma_m g_G(\tilde{\theta}, \varphi_{cs}) & (12.137)
\end{aligned}
$$

where the invariant stress measure I_σ is given by Eq. (8.24). The plastic volumetric and deviatoric strains are then provided by

$$
\Delta\varepsilon_v^{pl} = \Delta\lambda\frac{\partial g_{MN}^{GCC}}{\partial\sigma_m} = \Delta\lambda g_G \tag{12.138}
$$

$$
\Delta\boldsymbol{e}^{pl} = \Delta\lambda\frac{\partial g_{MN}^{GCC}}{\partial\boldsymbol{s}} = \Delta\lambda\frac{\mathbf{Q}^{-1}\boldsymbol{s}^{i+1}}{2J^{i+1}} \tag{12.139}
$$

and the current stress measures follow from

$$
\begin{aligned}
\sigma_m^{i+1} &= \sigma_m^{tr} - K_s^i\Delta\lambda g_G & (12.140)\\
J^{i+1} &= J^{tr} - G_s^i\Delta\lambda & (12.141)
\end{aligned}
$$

$$
\boldsymbol{s}^{i+1} = \boldsymbol{s}^{tr} - 2G_s^i\Delta\lambda\frac{\boldsymbol{s}^{i+1}}{2J^{i+1}} = \frac{\boldsymbol{s}^{tr}}{1 + \dfrac{G_s^i\Delta\lambda}{J^{i+1}}} = \boldsymbol{s}^{tr}\left(1 - \frac{G_s^i\Delta\lambda}{J^{tr}}\right), \quad \frac{\boldsymbol{s}^{i+1}}{J^{i+1}} = \frac{\boldsymbol{s}^{tr}}{J^{tr}} \tag{12.142}
$$

An indicator that turns on the apex problem, recall Eq. (4.44), is now given by

$$
g_G(\tilde{\theta}, \varphi_{cs})\frac{J^{tr}}{G_s^i} - \frac{\sigma_m^{tr}}{K_s^i} < 0 \tag{12.143}
$$

Assuming that neither the preconsolidation pressure ($p_c = p_c^i$) nor the bulk modulus ($K_s = K_s^i$) evolves within the plastic corrector step leaves the plastic multiplier $\Delta\lambda$ the only unknown to be determined such that the residuum $r = (f_{MN}^{GCC})^{i+1} \to 0$. The associated Newton-Raphson scheme then reads

$$
\Delta\lambda_{j+1} = \Delta\lambda_j - \frac{r_j}{\dfrac{\mathrm{d}r_j}{\mathrm{d}\Delta\lambda}} \tag{12.144}
$$

$$
r_0 = f_{MN}^{GCC}(\boldsymbol{\sigma}^{tr}), \quad \Delta\lambda_0 = 0 \tag{12.145}
$$

$$
\begin{aligned}
\frac{\mathrm{d}r}{\mathrm{d}\Delta\lambda} &= \frac{\mathrm{d}I_\sigma}{\mathrm{d}\Delta\lambda} = \left(\frac{\partial I_\sigma}{\partial I_{1\sigma}}\frac{\partial I_{1\sigma}}{\partial\sigma_m} + \frac{\partial I_\sigma}{\partial I_{2\sigma}}\frac{\partial I_{2\sigma}}{\partial\sigma_m} + \frac{\partial I_\sigma}{\partial I_{3\sigma}}\frac{\partial I_{3\sigma}}{\partial\sigma_m}\right)\frac{\partial\sigma_m}{\partial\Delta\lambda} + \\
&+ \frac{\partial I_\sigma}{\partial I_{2\sigma}}\frac{\partial I_{2\sigma}}{\partial J}\frac{\partial J}{\partial\Delta\lambda} + \frac{\partial I_\sigma}{\partial I_{3\sigma}}\left(\frac{\partial I_{3\sigma}}{\partial J}\frac{\partial J}{\partial\Delta\lambda} + \frac{\partial I_{3\sigma}}{\partial I_{3s}}\frac{\mathrm{d}I_{3s}}{\mathrm{d}\Delta\lambda}\right)
\end{aligned} \tag{12.146}
$$

where the not yet defined partial derivatives receive the forms, otherwise refer to Section 8.3.2,

$$
\frac{\partial\sigma_m}{\partial\Delta\lambda} = -K_s^i g_G \tag{12.147}
$$

$$
\frac{\partial J}{\partial\Delta\lambda} = -G_s^i \tag{12.148}
$$

$$
\frac{\mathrm{d}I_{3s}}{\mathrm{d}\Delta\lambda} = \left(\frac{\partial I_{3s}}{\partial\boldsymbol{s}}\right)^{\mathsf{T}}\frac{\mathrm{d}\boldsymbol{s}}{\mathrm{d}\Delta\lambda} = -\left(\frac{\partial I_{3s}}{\partial\boldsymbol{s}}\right)^{\mathsf{T}}\frac{\boldsymbol{s}^{tr}G_s^i}{J^{tr}} \tag{12.149}
$$

Further comments concerning initialization of the preconsolidation pressure p_c^{in} and the bulk modulus K_s^{in} are consistent with Section 11.4.

12.5   Testing implementation with simple laboratory tests

Simple laboratory tests are again simulated to test the model implementation. Herein, the material parameters summarized in Table 12.2 are used. Depending on the initial stress and the volumetric strain increment, the algorithm switches between the constant and variable elasticity return mapping, recall Section 11.5. Nevertheless, the version grounding on the constant elasticity return mapping is implemented in the current version of GEO5 FEM. Because the effect of initial stiffness on the predicted stress-strain response is comparable to the MCC model, recall Section 11.5.1, we focus on the issue of softening, which is the essential difference between the GCC and MCC models. In all numerical experiments only the triaxial loading conditions are be examined.

Table 12.2: Material properties used for triaxial test

ν	κ	λ	e_{in}	M_{cs}	φ [°]	φ_{cs} [°]
0.26	0.025	0.181	1.67	0.794	40	34

The first test considers an undrained triaxial test. The sample is first stressed in isotropic compression (IC) to the value of mean effective stress $\sigma_m = -100$ kPa starting with $p_c^{in} = 1$ kPa and $K_s^{in} = \dfrac{1}{\kappa^*}$ kPa. The second load stage assumes an undrained triaxial compression (TC). The results are plotted in Fig. 12.2. Is is seen that the critical state was eventually reached. This example is selected primarily to show agreement between the Modified and the Generalized Cam-clay models as in triaxial compression the variable $\chi(\theta = 30°) = 1$. Also because $\Delta\varepsilon_v = \Delta\varepsilon_v^{el}$, the analysis adopts the constant elasticity return mapping algorithm with both the bulk (K_s) and shear (G_s) moduli being constant equal to their values at the end of the isotropic compression state.
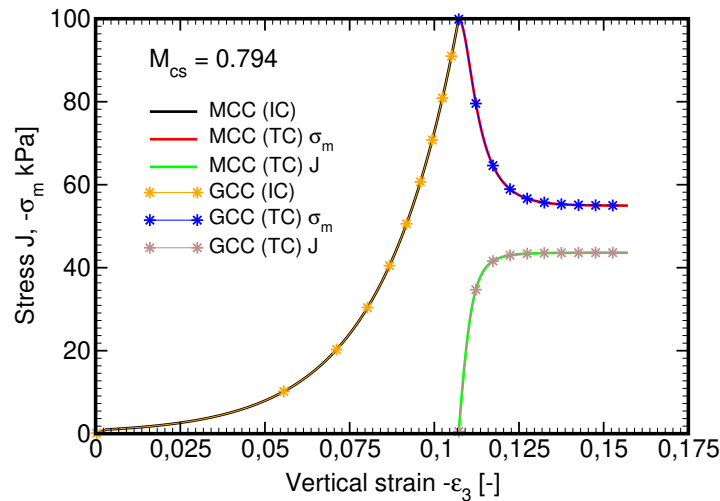

Figure 12.2: Undrained triaxial test - comparing cam-clay and generalized cam-clay model

The second example aims to test the response upon softening. A similar loading/unloading sequence as plotted in Fig. 11.8(a) is again examined. Since the shear strength is now controlled by the angle of internal friction φ rather than by the M_{cs}-line the onset of plasticity appears much sooner resulting also in much less of softening in comparison to the prediction provided by the MCC model. With the MCC model the shear strength is significantly overestimated. Note that the onset of softening with the MCC model would be associated with the red bullet on the dashed red line in Fig. 12.3(a). Again, the orange yield surface in 12.3(a) represents an intermediate state evolving prior to finally arriving at the critical state.

Similarly to the Modified Cam-clay model, modeling softening with triaxial compression (constant stress state) required application of the Arc length method in the stress loading regime. To avoid this, the loading via prescribed displacements only would be required. More detailed discussion on this numerical experiment is available in Section 11.5.2.
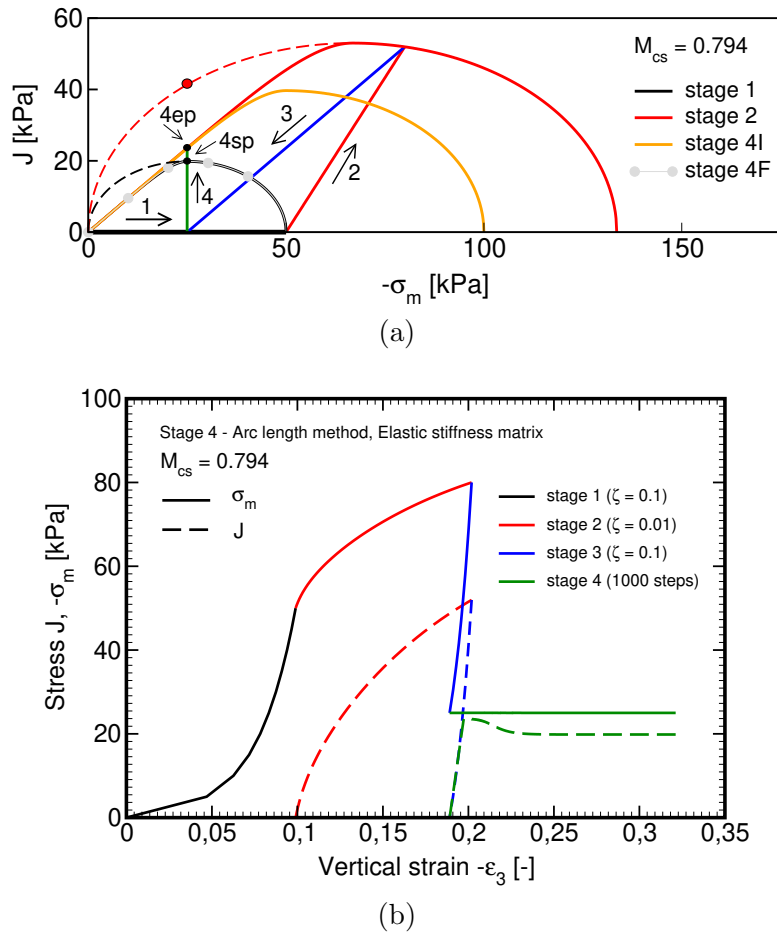

(a)

(b)

Figure 12.3: Drained triaxial test: a) loading path and evolution of yield surface, b) evolution of mean (σ_m) and equivalent deviatoric (J) stress measures as a function of vertical strain

12.5.1   Comparing GCC and MCC models in triaxial compression and extension

It has been found that predictions based on circular yield surface in the deviatoric plane (Drucker-Prager, Modified Cam-clay models) do not agree well with experimental observations. The literature further advocates the use of yield surfaces that plot somewhere in between circle and Mohr-Coulomb hexagon in the deviatoric plane. Finally, the comments on the shape of plastic potential in the deviatoric plane, see [65], support the implementation of the Generalized Cam-clay model in the framework of non-associated plasticity with a circular shape of plastic potential and rounded triangular shape of yield surface in the deviatoric plane.

In all experiments the sample was first isotropically stressed to arrive at the mean stress $\sigma_m = -200$ kPa. When interested in the effect of highly overconsolidated states the sample was then isotropically unloaded to reach the initial overconsolidated stress $\sigma_m = -20$ kPa prior to shearing. The results appears in Figs. 12.4 - 12.7. Note that CDP stands for a circular shape while RTDP for a triangular shape of the yield surface in the deviatoric plane. As seen, formulation of the GCC model assuming a circular shape in the deviatoric plane (GCC$_{\text{CDP}}$) is also examined. It is worth mentioning that when testing overconsolidated soils the soil within the yield surface was considered a linear elastic for simplicity.

Fig. 12.4 shows the results for a normally consolidated sample loaded in triaxial compression. Both the initial and final (critical state) yield surface is displayed in Fig. 12.4(a). As expected, for

this particular example all models deliver the same response. Recall that for triaxial compression the initial yield stress coincides for all yield surfaces and in correspondence with the formulation evolves in the same way for all models, recall Fig. 12.2.

The results for overconsolidated soils are plotted in Fig. 12.5 together with those derived from the GCC$_{\text{CDP}}$ model. Clearly, the same response is predicted by both Generalized Cam-clay models. Fig. 12.5 shows again evolution of the yield surface. Arrows along the loading path indicate the softening regime after the first yielding is met. Normals to the yield surface confirm an initial steeper slope of a descending part of the curves plotted for the GCC models in Fig. 12.5(c) when compared to the evolution of volumetric strain predicted by the MCC model. As for normally consolidated soils, all predictions eventually arrive at the same critical state.

An expected difference between both formulations of GCC models becomes visible when examining the triaxial extension tests. Fig. 12.6 shows the results for normally consolidated soils. Note that the GCC$_{\text{RTDP}}$ model (the one implemented in GEO5 FEM) delivers a considerably softer response when compared to the predictions provided by the MCC and GCC$_{\text{CDP}}$ models. This fact is further explained in Fig. 12.6(a), which shows that the critical yield surface for the GCC$_{\text{RTDP}}$ model is reached at much lower stresses than for the other two models (not shown). Such a critical comparison also suggests that the use of critical state models requires some caution as the formulations based on the constant slope of the critical state line (CDP) may significantly overestimate the final failure, see also discussion in [65] on the problem of a rigid strip footing.

Perhaps the most interesting results are presented for overconsolidated soils loaded in triaxial extension, see Fig. 12.7. Note that for the assumed loading path the MCC and GCC$_{\text{CDP}}$ predict hardening while softening is observed for the GCC$_{\text{RTDP}}$ model. So not only quantitatively, but also a qualitatively different behavior of clayey soils can be predicted with different formulations of critical state models.

12.6 Generalized Cam-clay model in stability analysis

Similarly to the Modified Cam-clay model the strength reduction procedure corresponds to a simultaneous reduction of both the peak φ and critical φ_{cs} friction angles while keeping the stiffness $\overline{\overline{K}}$ constant, while the preconsolidation pressure p_c is allowed to evolve, recall Fig. 11.9. Implementation of the stress return algorithm within a given reduction step and the formulation of the algorithmic tangent stiffness matrix thus follows Sections 12.2.2 and 12.3.2, respectively.
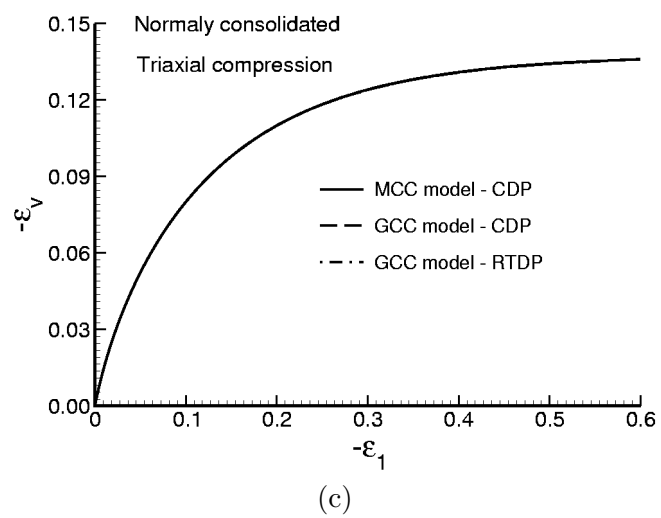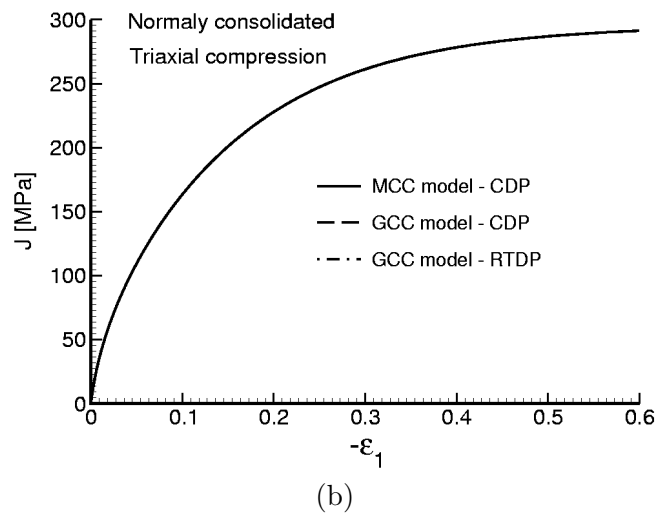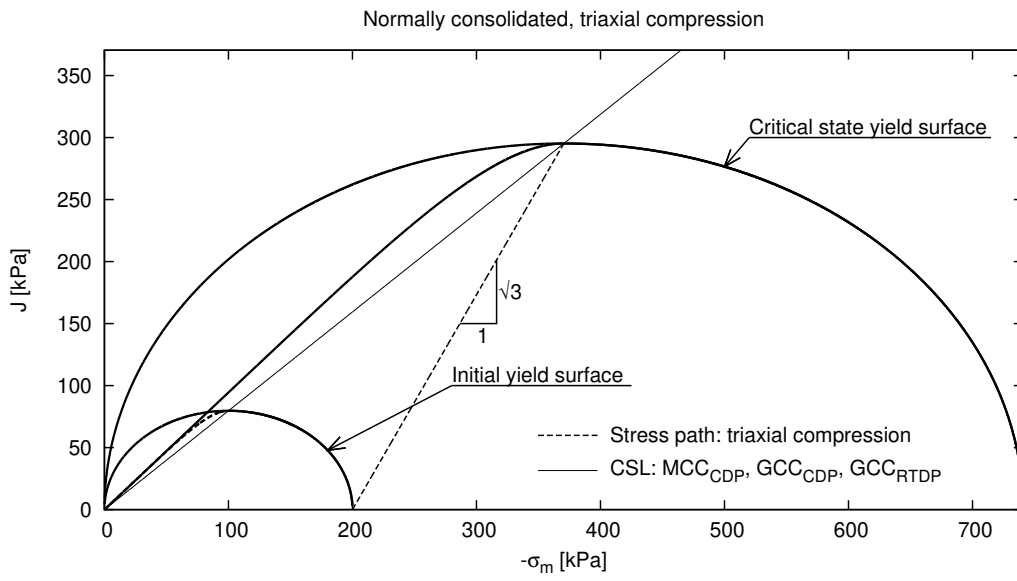
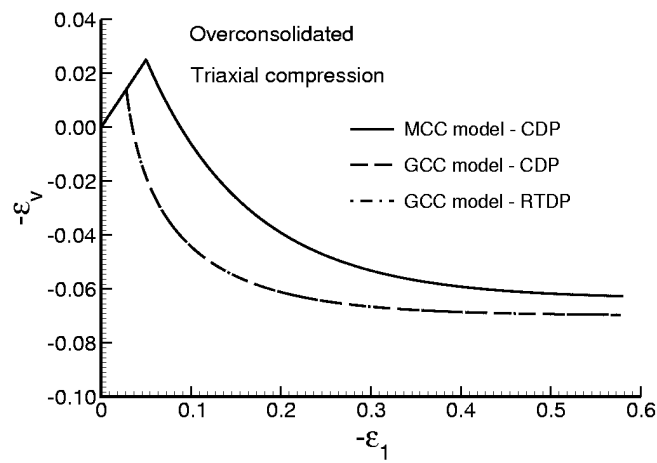Figure 12.4: Drained triaxial compression test - NC

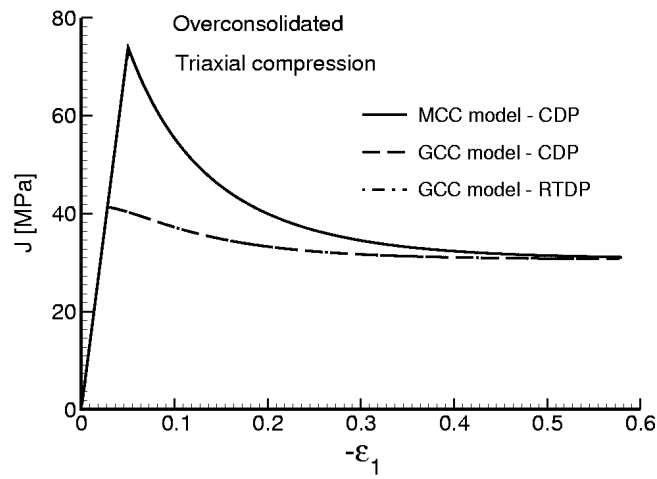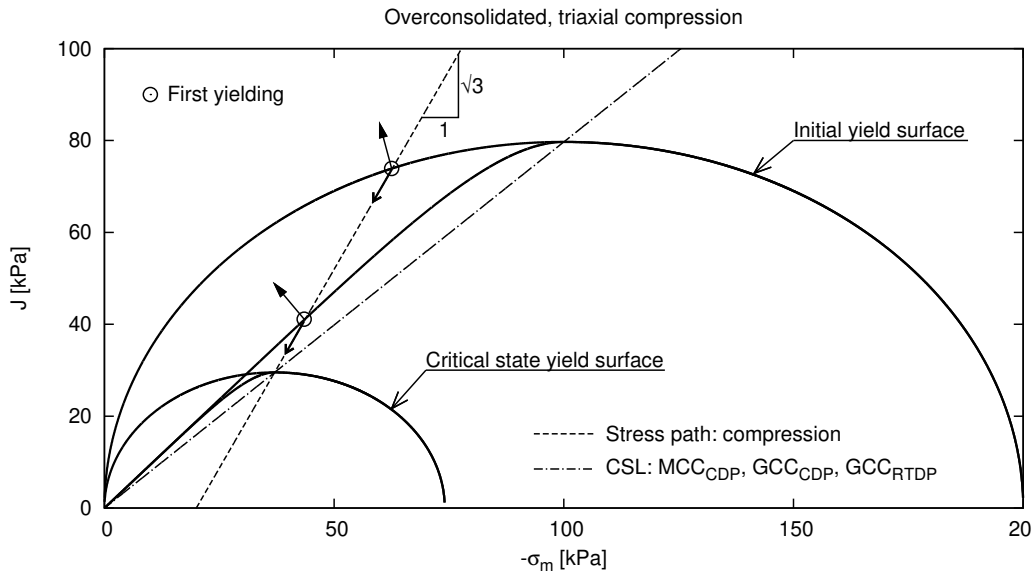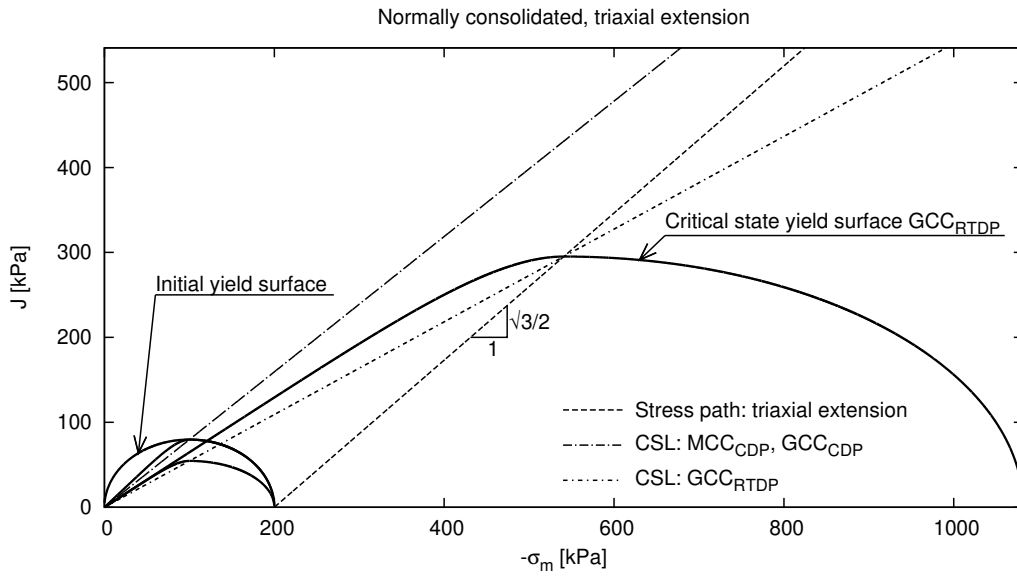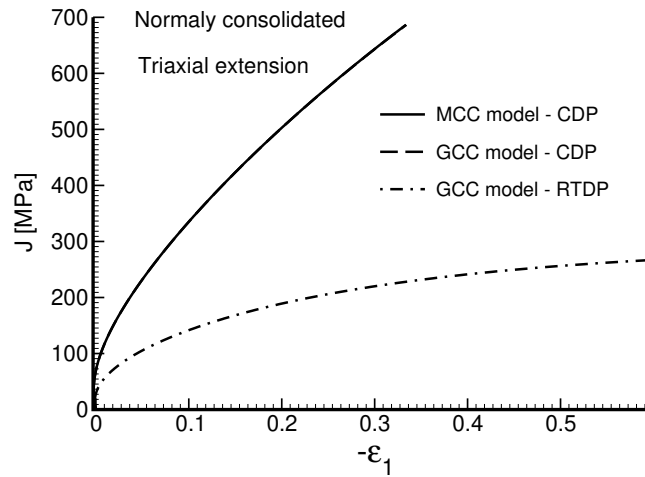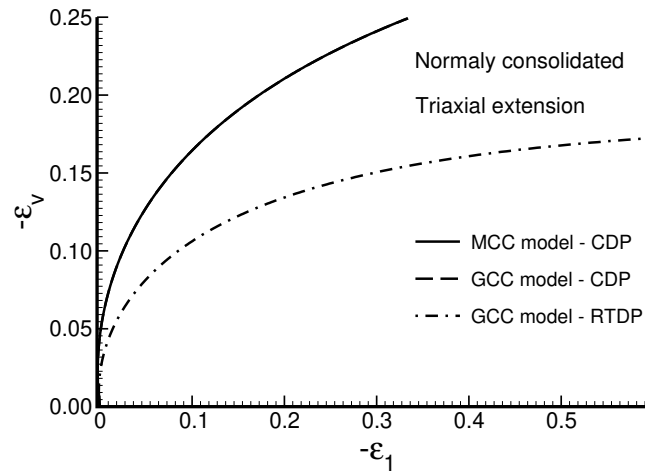Figure 12.5: Drained triaxial compression test - OC

Figure 12.6: Drained triaxial extension test - NC

(a)

(b)

(c)
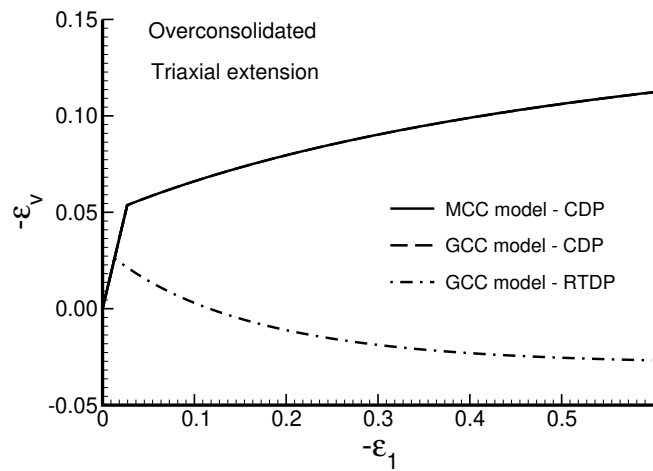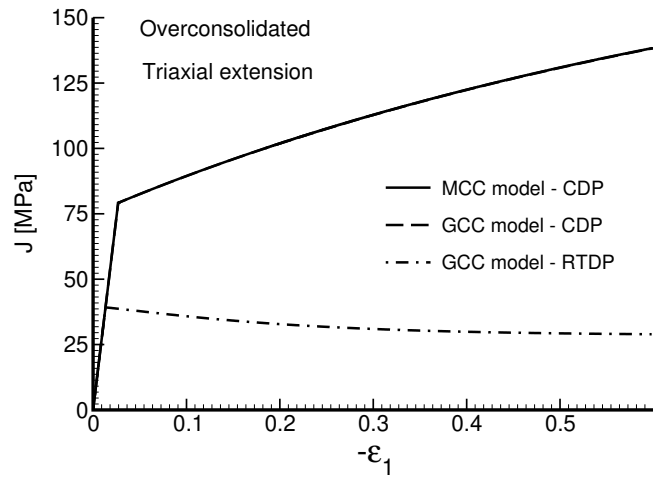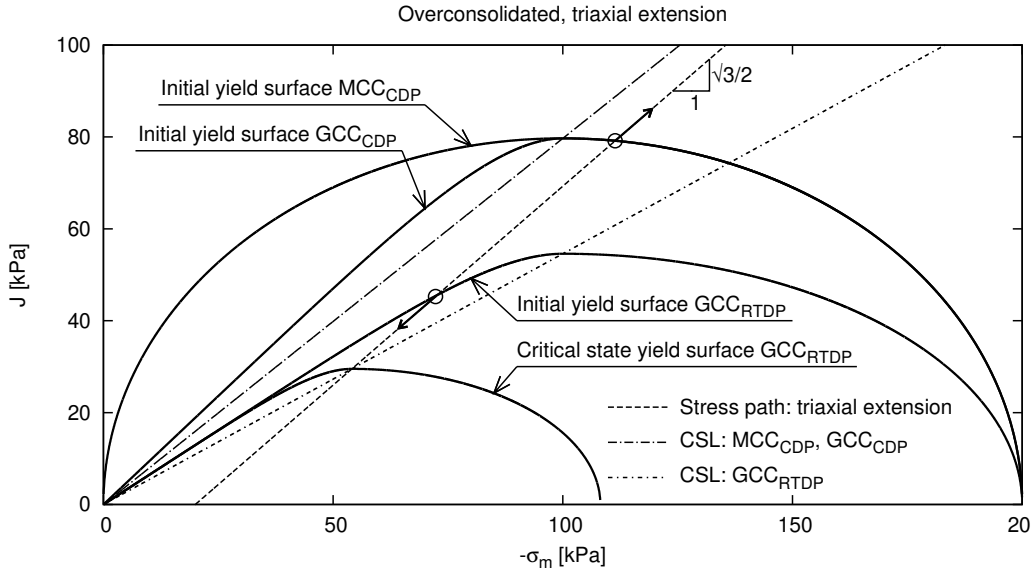
Figure 12.7: Drained triaxial extension test - OC

Chapter 13

Hypoplastic clay model

Chapter 14

Hypoplastic sand model

Chapter 15

Interface constitutive model

A proper modeling of soil–structure interaction requires a suitable treatment of relative movement of the structure with respect to the soil that usually occurs. In the framework of continuum mechanics, the most appealing way of treating interfaces is the use of interface elements discussed in Section 17.2.5. This section introduces an interface material model that can be used to simulate contact between two materials, e.g., a concrete pile and soil.

Table 15.1: Parameters of interface constitutive model

Symbol	Units	Description
K_n	[MN/m^3]	Normal stiffness
K_s	[MN/m^3]	Tangential stiffness
μ	[-]	Interface friction ($\mu = \tan \varphi$)
c	[kPa]	Cohesion
φ	[°]	Angle of internal friction
ψ	[°]	Angle of dilation ($\psi = 0$)
σ_t	[kPa]	Tensile strength
δ_c	[-]	Cohesion reduction factor ($c = \delta_c \cdot c_{soil}$)
δ_φ	[-]	Friction reduction factor ($\tan \varphi = \delta_\varphi \cdot \tan \varphi_{soil}$)

The material parameters of the interface model are listed in Table 15.1. Similarly to material models of the Mohr-Coulomb type the nonlinear response is controlled by the interface shear strength parameters c and φ. The model also allows us to reduce or completely exclude tension by specifying the tensile strength $\sigma_t < c \cot \varphi$ in the direction normal to the interface. The elastic response is driven by normal and tangential stiffnesses K_n and K_s representing the relation between interface tensile σ (normal) and shear τ (longitudinal) stresses and normal $\llbracket u \rrbracket$ and shear $\llbracket v \rrbracket$ relative displacements (jumps), respectively, developed along the interface.

Figure 15.1: Failure surface for interface model

The interface material is assumed in GEO5 FEM to be well represented by the Mohr-Coulomb failure criterion with tension cut off as seen in Fig. 15.1.

An elastic – perfectly plastic response of the interface material in shear is assumed. Such a behavior is schematically illustrated in Fig. 15.2(a) showing a variation of the shear stress as a function of the relative tangential displacement. In tension or compression a purely elastic response of the interface material is considered. When the tensile stress σ exceeds a certain allowable strength limit σ_t, the initial yield surface collapses to a residual surface which corresponds to dry friction, see Figs. 15.1 and 15.2(b).
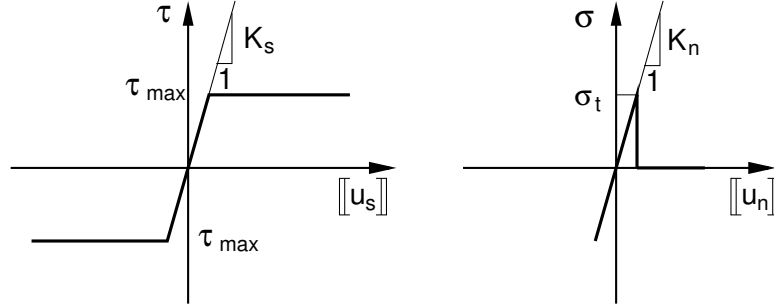

Figure 15.2: Constitutive model for interface

15.1   Yield surface and stress update procedure

The mathematical representation of the initial yield surface displayed in Fig. 15.1 is given by

$$f^{INT} = |\tau| + \sigma \tan \varphi - c \tag{15.1}$$

where φ and c are the angle of internal friction and cohesion of the interface material, respectively. The direction of the plastic flow depends on the shape of the plastic potential surface. Here, a non-associated plastic flow rule is assumed with the plastic potential function written as

$$g^{INT} = |\tau| + \sigma \tan \psi \tag{15.2}$$

where ψ is the angle of dilation. In analogy to material models described in the previous sections, the angle of dilation controls the magnitude of the irreversible (plastic) volume expansion. As stated in the previous paragraph, the plastic response is limited to shear only which corresponds to the value of the dilation angle ψ equal to zero (volume preserving return mapping), see Fig. 15.1. Thus, setting $\psi = 0$ gives the normals to the yield and potential surfaces in the form, recall for example the Mohr-Coulomb model in Chapter 5 and the corresponding equations (5.17) - (5.22),

$$\boldsymbol{n} = \frac{\partial f^{INT}}{\partial \boldsymbol{\sigma}} = \left\{ \begin{array}{c} \tau/|\tau| \\ \tan \varphi \end{array} \right\} \qquad \boldsymbol{n_g} = \frac{\partial g^{INT}}{\partial \boldsymbol{\sigma}} = \left\{ \begin{array}{c} \tau/|\tau| \\ 0 \end{array} \right\} \tag{15.3}$$

where the stress vector $\boldsymbol{\sigma}$ follows from Eq. (17.43)

$$\boldsymbol{\sigma}^{\mathsf{T}} = \{\tau, \sigma\}$$

The normal to the plastic potential function $\boldsymbol{n}_g$ then provides the direction of the plastic flow governing the return mapping algorithm. This algorithm is schematically depicted in Fig. 15.1. In particular, when solving a plasticity problem the analysis is carried out in several load increments. To that end, suppose that stresses at state i are known and we wish to proceed to a new stress state $i + 1$ by applying a new load increment. This step results into an increment of the vector of relative displacements $\Delta \llbracket \boldsymbol{u} \rrbracket^{\mathsf{T}} = \{\Delta \llbracket u \rrbracket, \Delta \llbracket v \rrbracket\}$. The elastic "trial" stresses are provided by

$$
\begin{aligned}
\tau^{tr} &= \tau^i + K_s \Delta \llbracket u \rrbracket^{i+1} \tag{15.4} \\
\sigma^{tr} &= \sigma^i + K_n \Delta \llbracket v \rrbracket^{i+1} \tag{15.5}
\end{aligned}
$$

The particular form of $\boldsymbol{n}_g$ just confirms the elastic response in the normal direction so that

$$\sigma^{i+1} = \sigma^{tr}$$

as evident from Figs. 15.1 and 15.2. The shear stress then follows from the yield condition (15.1). Note that during plastic flow the stresses must remain on the yield surface. Therefore

$$(f^{INT})^{i+1} = |\tau^{i+1}| + \sigma^{i+1} \tan\varphi - c = 0 \tag{15.6}$$

Next, multiplying both sides of Eq. (15.6) by the first component of $\boldsymbol{n}_g$, noting that $\tau^{i+1}/|\tau^{i+1}| = \tau^{tr}/|\tau^{tr}|$ and then solving for τ^{i+1} gives

$$\tau^{i+1} = \left(-\sigma^{tr}\tan\varphi + c\right) \frac{\tau^{tr}}{|\tau^{tr}|}$$

Thus, in the absence of pore pressure the stresses at the end of the $i+1$ load increment are given by

$$\left\{ \begin{array}{c} \tau \\ \sigma \end{array} \right\}^{i+1} = K_n \, [\![v]\!]^{i+1} \left\{ \begin{array}{c} 0 \\ 1 \end{array} \right\} + \left(-\sigma^{tr}\tan\varphi + c\right) \left\{ \begin{array}{c} \tau^{tr}/|\tau^{tr}| \\ 0 \end{array} \right\} \tag{15.7}$$

15.2   Tangent stiffness matrix

Following [73] the algorithmic tangent stiffness matrix $\boldsymbol{D}$ can be found from the expression, recall for example Eq. (4.19),

$$\boldsymbol{D} = \frac{\partial \boldsymbol{\sigma}^{i+1}}{\partial [\![\boldsymbol{u}]\!]^{i+1}} \tag{15.8}$$

Referring to Eq. (15.7) it becomes evident that

$$\frac{\partial \left(K_n \, [\![v]\!]^{i+1} \left\{ \begin{array}{c} 0 \\ 1 \end{array} \right\} \right)^{\mathsf{T}}}{\partial \left\{ \begin{array}{c} [\![u]\!]^{i+1} \\ [\![v]\!]^{i+1} \end{array} \right\}} = K_n \begin{bmatrix} 0 & 0 \\ 0 & 1 \end{bmatrix} \tag{15.9}$$

$$\frac{\partial \left(\left(-\sigma^{tr}\tan\varphi + c\right) \left\{ \begin{array}{c} \tau^{tr}/|\tau^{tr}| \\ 0 \end{array} \right\} \right)^{\mathsf{T}}}{\partial \left\{ \begin{array}{c} [\![u]\!]^{i+1} \\ [\![v]\!]^{i+1} \end{array} \right\}} = \begin{bmatrix} a_{11} & a_{12} \\ 0 & 0 \end{bmatrix} \tag{15.10}$$

where

$$a_{11} = \left(-\sigma^{tr}\tan\varphi + c\right) \frac{\partial}{\partial\tau^{tr}} \left(\frac{\tau^{tr}}{|\tau^{tr}|} \right) \frac{\partial\tau^{tr}}{\partial [\![u]\!]^{i+1}}$$

$$a_{12} = \frac{\partial(-\sigma^{tr}\tan\varphi + c)}{\partial\sigma^{i+1}} \frac{\tau^{tr}}{|\tau^{tr}|} \frac{\partial\sigma^{i+1}}{\partial [\![v]\!]^{i+1}}$$

After expanding individual derivatives in the above expressions we get

$$\frac{\partial}{\partial\tau^{tr}} \left(\frac{\tau^{tr}}{|\tau^{tr}|} \right) = \frac{1}{|\tau^{tr}|} \left(1 - \frac{\tau^{tr}\tau^{tr}}{|\tau^{tr}||\tau^{tr}|} \right) = 0$$

$$\frac{\partial(-\sigma^{tr}\tan\varphi + c)}{\partial\sigma^{i+1}} = -\tan\varphi$$

$$\frac{\partial\tau^{tr}}{\partial [\![u]\!]^{i+1}} = K_s$$

$$\frac{\partial\sigma^{i+1}}{\partial [\![v]\!]^{i+1}} = K_n$$

Finally, introducing the above expressions back into Eq. (15.10) and then adding to Eq. (15.9) yields the desired tangent stiffness matrix in the form

$$\mathcal{D} = \begin{bmatrix} 0 & -K_n \tan \varphi \left(\tau^{tr} / |\tau^{tr}| \right) \\ 0 & K_n \end{bmatrix} \tag{15.11}$$

It is interesting to see that with $\psi = 0$ the algorithmic tangent stiffness matrix does not depend on the shear stiffness K_s. So when moving beyond the elastic limit, the choice of K_s is irrelevant. This observation will be addressed in subsequent section with regard to a practical application of interface elements.

15.3   Application of interface elements in structural analysis

It has been demonstrated in a number of practical applications that meaningful results can only be obtained providing the interface elements are adopted to allow for the evolution of relative displacements along the soil-structure interface. While simple from an implementation point of view, this step introduces a number of modeling as well as computational complications the user should be aware of. Some of the more important ones will now be discussed in greater detail.
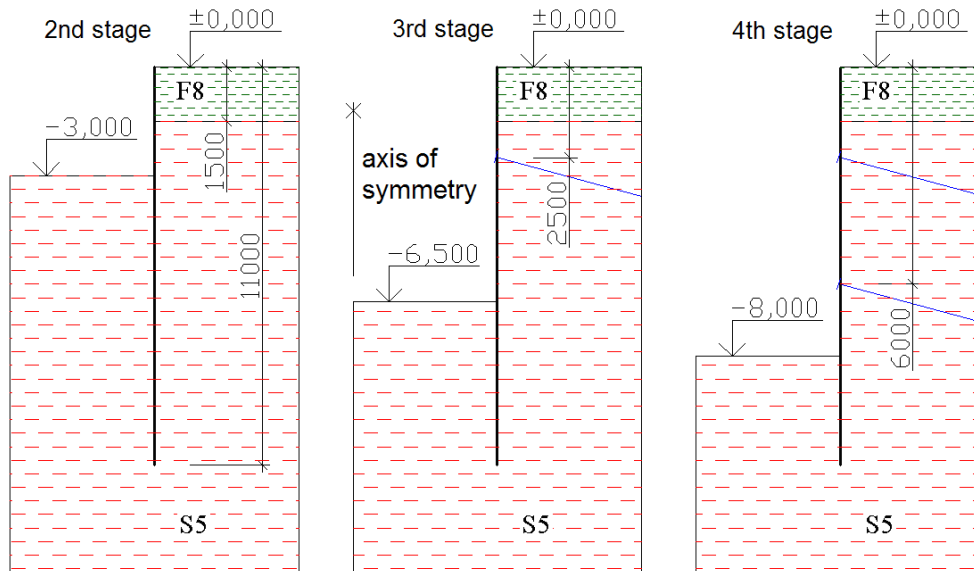

Figure 15.3: Topology, soil profile and construction stages

As a suitable example we consider an analysis of a sheeting wall performed in several calculation stages as schematically shown in Fig. 15.3. Point out that the initial stresses were generated with the help of K_0 procedure described in Section 1.14. For simplicity, the analysis was performed using elastic perfectly plastic Mohr-Coulomb model with material parameters listed in Table 15.2.

Table 15.2: Material properties of selected soils

soil	$E = E_{ur}$ [MPa]	ν	c [MPa]	φ [^{0}]	ψ [^{0}]	γ [kN/m^3]
F8 - CH	4	0.42	8	17	0	20.5
S5 - SC	12	0.35	12	28	0	18.5

Choice of nonlinear constitutive model

Here, the previously developed Mohr-Coulomb failure criterion is adopted to simulate an imperfect bonding between the retaining structure and soil, Fig. 15.1. A tension cut-off condition with $\sigma_t = 0$ is invoked to limit tensile stresses immediately adjacent to the retaining wall. Also, plastic volumetric

strains are excluded by setting the dilation angle $\psi = 0$. Consequently, the elastic interface response in tension/compression is a priori predicted. Once tensile tractions are developed at any point along the interface the initial yield surface is abruptly switched to the final one, the dashed line in Fig. 15.1. The new yield surface thus becomes active whenever the interface closes upon compression.
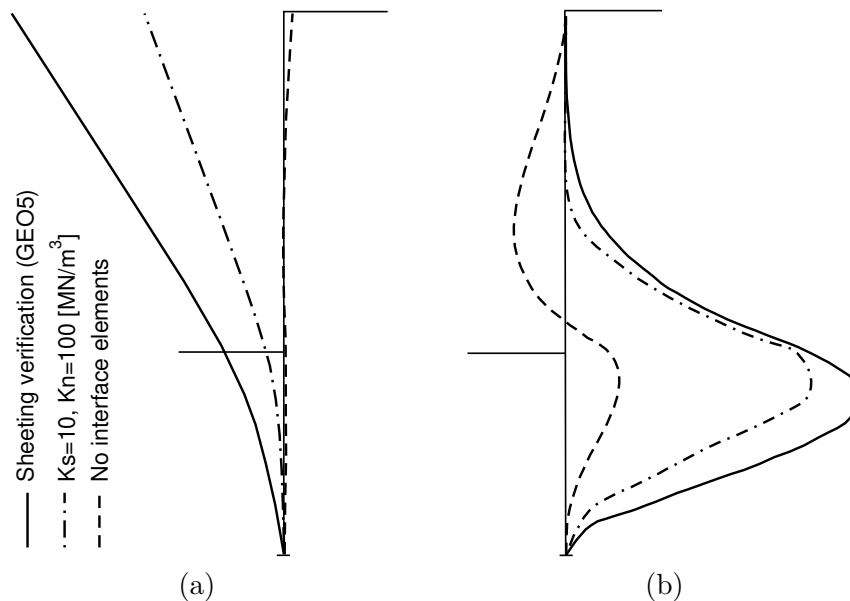

Figure 15.4: Influence of interface elements: predicted deformations of embedded wall and distributions of bending moments

The importance of interface elements to predict realistic behavior is clearly seen from Fig. 15.4. If the perfect bonding is assumed (analysis without interface elements) the condition of zero shear stress at the ground surface (condition to maintain right angle between the earth retaining structure and ground surface) produces an unacceptable deformation of the structure into the soil - the structure is essentially pulled by the adjacent soil. This results in an unrealistic prediction of bending moment, the dashed line in Fig. 15.4. The dot-dashed lines then represent the results derived with the use of interface elements and the Mohr-Coulomb plasticity model driving the evolution of mutual displacements along the soil-structure interface. These results are at least qualitatively close to those predicted by the GEO5 Sheeting verification program based on the theory of dependent pressures. Here it is worth to recall a rather problematic determination of the modulus of subsoil reaction, which greatly influences the resulting deformations of the wall estimated by the program Sheeting verification. Similarly, a less severe disagreement between the results can be expected upon modifying the initial elastic modulus of the soil and when adopting a stiffness increasing with depth in finite element simulations. This will be partly examined in the last paragraph of this section.

Influence of elastic stiffnesses of interface model

As outlined at the beginning of this chapter, see also Section 17.2.5, the interface tractions that do not violate the yield condition (15.1) are proportional to the relative displacements of the top and button of the interface according to Eq. (17.43). However, in the elastic regime a perfect bonding is generally assumed suggesting the displacement jumps $[\![u]\!]$ and $[\![v]\!]$ be equal to zero. The elastic stiffnesses K_s and K_n in Eq. (17.44) can thus be thought as certain penalty terms of no particular physical meaning, as long as they are sufficiently high, to allow for the introduction of these constraints into the principle of virtual work.

It is generally recognized that very high values of the elastic stiffnesses (of several orders of magnitude larger than the elastic moduli of the adjacent soil) may cause ill-conditioning of the resulting system of algebraic equations owing to the large differences between the diagonal and off-diagonal terms in the global stiffness matrix. This is often manifested by oscillations of interface tractions in the interface elements [3], which may eventually result in the loss of convergence of the solution of

the underlying nonlinear problem. It has been shown that this undesirable effect is not satisfactorily solved when using the Newton-Cotes integration scheme in place of a more standard Gauss integration scheme. On the other hand, when allowing for a certain "small" displacement jump along the interface by reducing the interface stiffness the correct (smooth) representation of interfacial tractions is recovered. Similar and perhaps an even more clean effect can be achieved with a sufficiently fine finite element mesh. It has been numerically proven that refining the finite element mesh offers an elegant way for avoiding numerical problems associated with ill-conditioning of the global (structural) stiffness matrix.

(a)   (b)   (c)
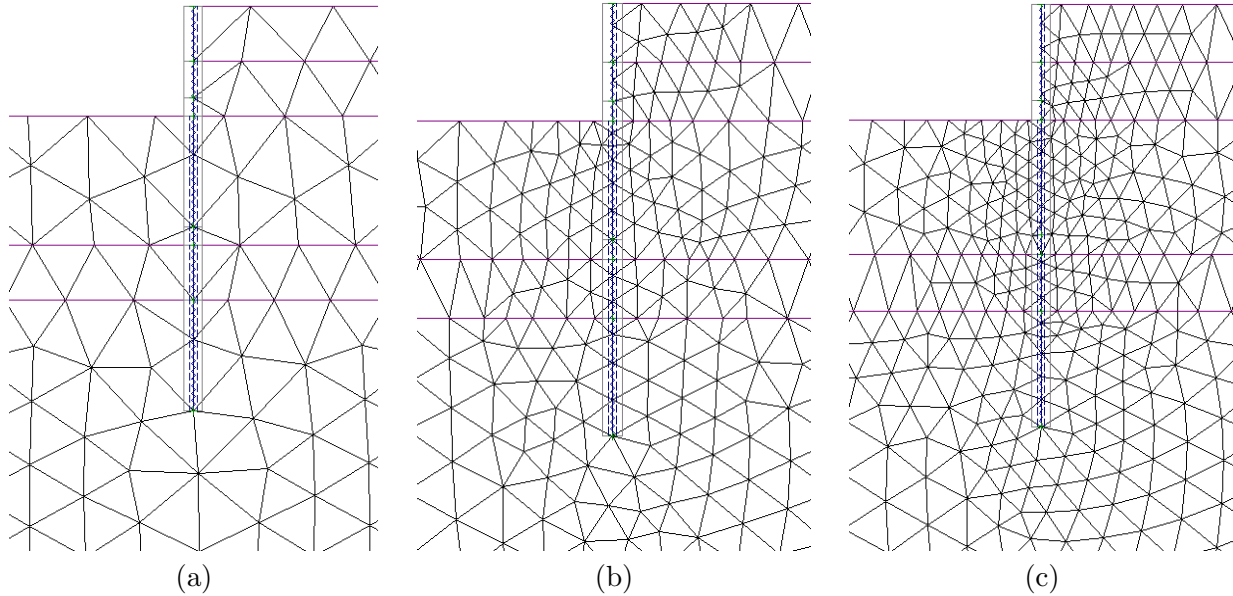
Figure 15.5: Influence of finite element mesh on the solution convergence characteristics: a) coarse mesh, b) medium mesh, c) fine mesh

To confirm the above statements we considered the embedded cantilever wall in Fig. 15.3. The analysis was performed for three different meshes with a variable degree of refinement as shown in Fig. 15.5. The soil was excavated in two stages up to a depth of 6,5 m. The normal stiffness $K_n = 1000$ [MN/m^3] was used in all analyses. The shear stiffness, on the other hand, was assigned the maximum value for which the analysis was successfully completed. These values are stored in Table 15.3.

mesh	max K_s [MN/m^3]	K_n [MN/m^3]
a	60	1000
b	80	1000
c	175	1000

Table 15.3: Maximum allowable shear interface stiffness K_s to reach convergence

When attempting to proceed with the third excavation step we experienced the loss of convergence even when using a very low shear stiffness $K_s = 5$ [MN/m^3]. This result, however, cannot be attributed to poor behavior of the interface elements but rather to a loss of overall stability due to the evolution of a critical slip surface. The need for a support system is therefore obvious. Henceforth, all analyses were performed assuming an anchored cantilever wall supported by ground anchors as schematically shown in Fig. 15.3. The results presented in Figs. 15.6 and 15.7 and also stored in Tables 15.4 - 15.7 were derived by considering the finest mesh and a point-to-point anchor (only a free length is modeled).

Distributions of bending moments in Fig. 15.6 together with their maximal values listed in Tables 15.4 and 15.6 clearly demonstrate the significance of high values of normal interface stiffness on the reliable prediction of bending moments especially when compared with the results provided by GEO5 Sheeting verification, see also Tables 15.4 and 15.5. Fortunately, the high value of K_n is likely to have a smaller influence on the stability of the numerical solution as opposed to the shear stiffness K_s.
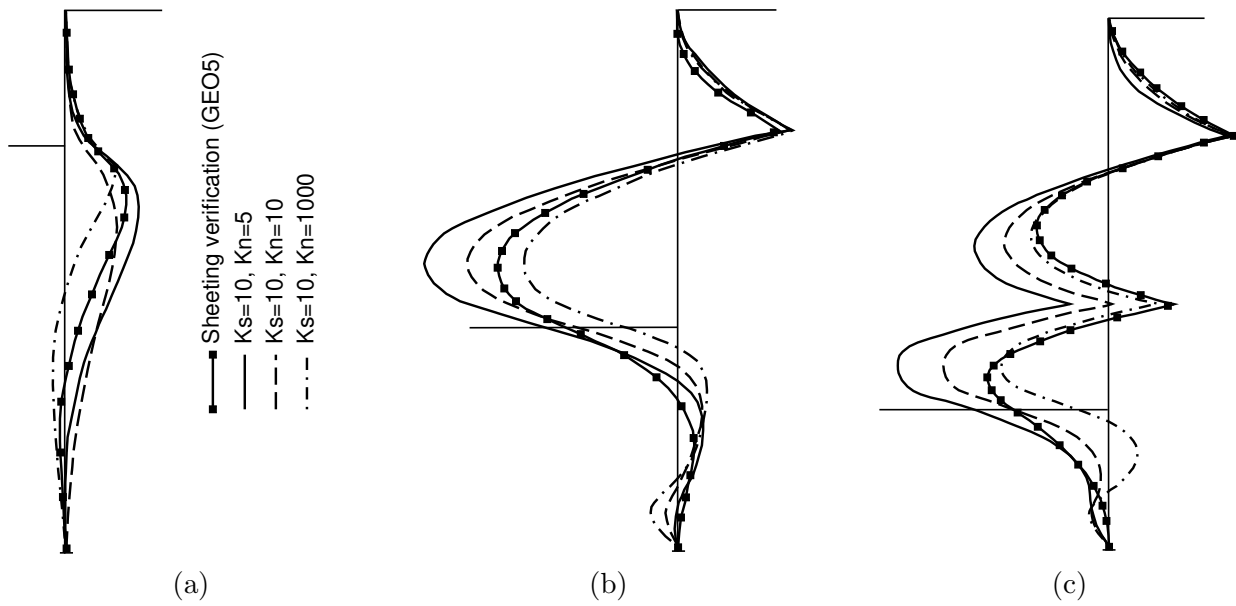
Figure 15.6: Influence of initial stiffness of interface elements (K_s, K_n in [MN/m^3]): a) 2nd stage, b) 3rd stage, c) 4th stage

Moreover, the results in Table 15.6 indicate that even a relatively low value of K_s needed to maintain a smooth convergence of the numerical solution allows for acceptable predictions. One explanation arises from the fact that once at yielding the shear interface traction does no longer depend on the initial elastic stiffness K_s as evident from Eq. (15.11).

Table 15.4: Maximum values of bending moments - influence of elastic stiffnesses

Stiffness		2nd stage	3rd stage		4th stage			
K_s	K_n	M [kNm]	M [kNm]	M [kNm]	M [kNm]	M [kNm]	M [kNm]	M [kNm]
[MN/m^3]		field	anchor	field	anchor 1	field 1	anchor 2	field 2
10	5	16.02	22.78	-57.20	27.84	-30.94	-9.27	-48.71
10	10	13.26	25.68	-47.63	29.03	-24.05	-0.34	-37.93
10	100	10.90	26.58	-34.90	28.00	-17.82	10.08	-24.87
100	100	10.96	26.78	-34.80	27.75	-18.35	9.44	-25.64
100	1000	10.68	26.60	-32.86	27.44	-17.37	10.76	-23.71

Table 15.5: Maximum values of bending moments - influence of normal stiffness K_n

Stiffness		2nd stage	3rd stage		4th stage			
K_s	K_n	M [kNm]	M [kNm]	M [kNm]	M [kNm]	M [kNm]	M [kNm]	M [kNm]
[MN/m^3]		field	anchor	field	anchor 1	field 1	anchor 2	field 2
10	5	16.02	22.78	-57.20	27.84	-30.94	-9.27	-48.71
10	10	13.26	25.68	-47.63	29.03	-24.05	-0.34	-37.93
10	50	11.38	26.71	-36.74	28.27	-18.55	9.06	-26.43
10	100	10.90	26.58	-34.90	28.00	-17.82	10.08	-24.87
10	1000	10.90	26.33	-33.09	27.64	-17.19	10.90	-23.39

Table 15.6: Maximum values of bending moments - influence of shear stiffness K_s

Stiffness		2nd stage	3rd stage		4th stage			
K_s	K_n	M [kNm]	M [kNm]	M [kNm]	M [kNm]	M [kNm]	M [kNm]	M [kNm]
[MN/m^3]		field	anchor	field	anchor 1	field 1	anchor 2	field 2
5	1000	11.12	26.04	-33.13	27.58	-17.13	11.04	-23.22
10	1000	10.90	26.33	-33.09	27.64	-17.19	10.90	-23.39
50	1000	10.73	26.60	-32.88	27.53	-17.27	10.80	10.76
100	1000	10.68	26.60	-32.86	27.44	-17.37	10.76	-23.71

Influence of shear strength parameters of interface model

Unlike the elastic stiffnesses K_s and K_n, the interface strength parameters c and φ can be derived from standard laboratory experiments. For preliminary designs theses values are often sought in terms of fractions of the strength parameters of the adjacent soil, recall Table 15.1,

$$c = \delta_c \cdot c_{soil} \qquad \varphi = \delta_\varphi \cdot \varphi.$$

Fig. 15.7 provides a certain notion as to the influence of $\delta_{c,\varphi}$ on the degree of soil-structure interaction. Clearly, the higher the value of $\delta \leq 1$ the stronger the interface resistance, which essentially increases the resistance of the ground below excavation and consequently also the bending moments. Obviously, there is a family of construction materials which require different values of the reduction parameter δ. While $\delta = 1$ might be acceptable for concrete, for steel the value of $\delta = 0.3$ would be perhaps more appropriate.

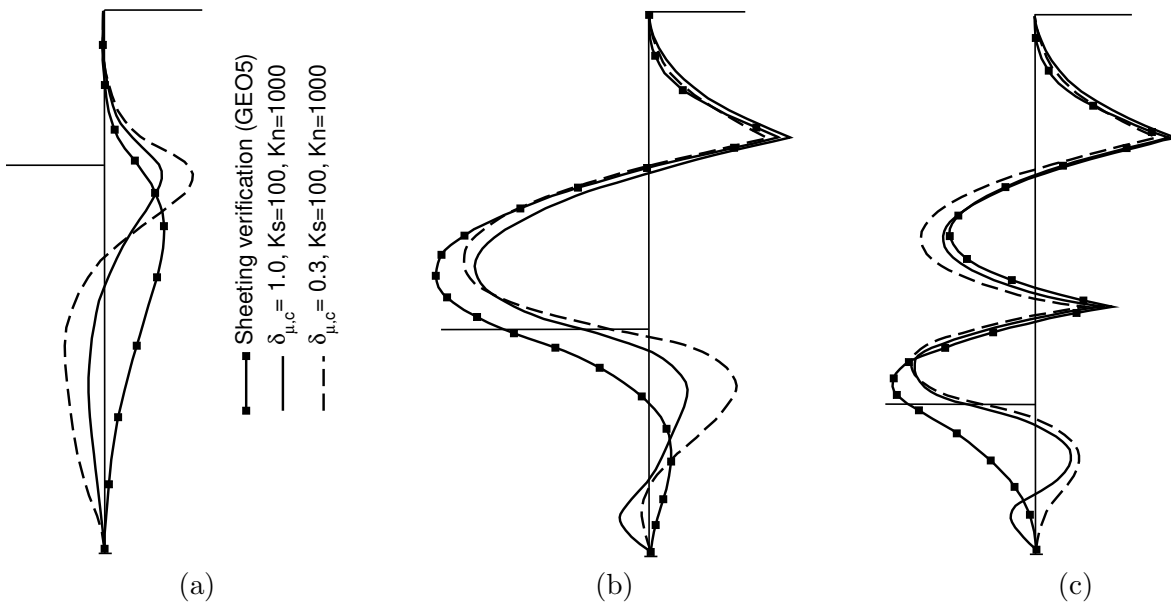(a)   (b)   (c)

Figure 15.7: Influence of shear strength parameters (K_s, K_n in [MN/m^3]): a) 2nd stage, b) 3rd stage, c) 4th stage

Influence of initial elastic modulus of soil

It is well documented that the soil stiffness may have a considerable influence not only on the surface settlement behind the wall but also on the behavior of the wall itself. This can be seen from Table 15.7 summarizing the results from two analyses with variable stiffness of the soil.

Table 15.7: Maximum values of bending moments - influence of shear stiffness K_s

Stiffness		2nd stage	3rd stage		4th stage			
Soil Modulus	K_s [MN/m^3]	M [kNm] field	M [kNm] anchor	M [kNm] field	M [kNm] anchor 1	M [kNm] field 1	M [kNm] anchor 2	M [kNm] field 2
E	50	11.12	26.04	-33.13	27.58	-17.13	11.04	-23.22
$3E$	100	11.12	26.04	-33.13	27.58	-17.13	11.04	-23.22
GEO5 Sheeting		11.12	26.04	10.68	26.60	-32.86	27.44	-17.37

Chapter 16

Water flow models

To better understand the application of water flow models in steady state and transient seepage problems we start from the formulation of constitutive model analogous to Hooke's law used in the previous chapters. In seepage analysis such a constitutive model is known as Darcy's.
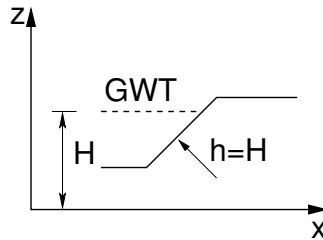

Figure 16.1: Coordinate system

As a point of departure, consider the coordinate system in Fig. 16.1 and define the total (piesometric) head h in terms of the pressure head $h_p = p/\gamma_w$ (recall that the pore pressure p is positive when in compression) and the elevation head h_e as

$$h = h_p + h_e = \frac{p}{\gamma_w} + z, \qquad \gamma_w = \rho^w g \approx 10 [\text{kNm}^{-3}] \qquad (16.1)$$

The generalized form of Darcy's law describing the flow in a porous medium then reads [65, 50, 45]

$$n S \boldsymbol{v}^{ws} = -K_r \mathbf{K}_{sat} \boldsymbol{\nabla} h, \qquad \boldsymbol{v}^{ws} = \boldsymbol{v}^w - \boldsymbol{v}^s \qquad (16.2)$$

where, $\boldsymbol{v}^r$ stores the components of the velocity vector of a given phase $r = w, s$ and $\mathbf{K}_{sat}$ [ms^{-1}] is the permeability matrix for $S = 1$ (fully saturated soil). Limiting attention to an orthotropic material the permeability matrix is diagonal and in two-dimensional space pertinent to Fig. 16.1 is written in terms of directional permeabilities as

$$\mathbf{K}_{sat} = \left[\begin{array}{cc} k_{x,sat} & 0 \\ 0 & k_{z,sat} \end{array} \right] \qquad (16.3)$$

Note that in GEO5 FEM the porosity n is calculated from the initial void ratio adopting Eq. (2.4). Table 16.1 stores the basic parameters needed in the description of seepage in a fully saturated medium.

Table 16.1: Material parameters to define flow in fully saturated medium

Symbol	Units	Description
$k_{x,sat}$	[m/day]	Saturated permeability along x-axis
$k_{z,sat}$	[m/day]	Saturated permeability along z-axis
e^{in}	[-]	Initial void ratio

Several relationships are available in the literature to define the dimensionless relative permeability $K_r \in \langle 0, 1 \rangle$ for the modeling of unsaturated flow. The models implemented in GEO5 FEM are:
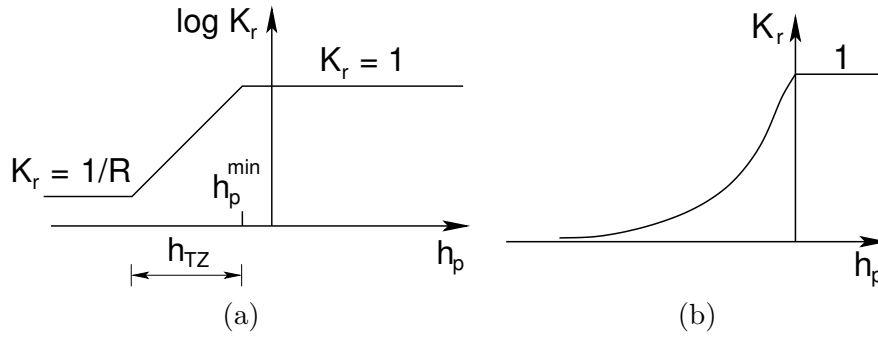

Figure 16.2: Variation of permeability with pore fluid pressure: a) Log-linear model [51, 65] , b) Gardner's and van Genuchten's model [26, 82]

16.1   Log-linear model

Table 16.2 lists material parameters needed by the Log-linear model.

Table 16.2: Parameters of Log-linear model

Symbol	Units	Description
R	[-]	Reduction factor (sufficiently large number)
h_{TZ}	[m]	Pressure head transition zone
$h_p^{\min}$	[m]	Minimum pressure head
S_r	[-]	Residual (irreducible) degree of saturation
b	[-]	Model parameter

When the soil is assumed to be above the phreatic surface (ground water table) the permeability is reduced by a large factor R. A transition zone between the fully saturated ($S = K_r = 1$) and fully unsaturated ($S, K_r \to 0$) soil is then represented by the pressure head transition zone h_{TZ} [m]. Introducing such a zone not only supports the laboratory observations but also stabilizes the required iterative algorithm typically based on the modified Newton-Raphson scheme with the permeability matrix being kept constant during iterations. According to Fig. 16.2(a) the relative permeability K_r is then given by

$$K_r(h_p) = 10^{\frac{(h_p - h_p^{\min}) \log R}{h_{TZ}}}, \qquad h_p^{\min} \leq 0 \qquad (16.4)$$

where $h_p^{\min}$ is the minimum pressure head associated with $S_{sat} = 1$ in GEO5 FEM (typically $h_p^{\min} = 0$).

In transient flow analysis the evolution of degree of saturation S is assumed in the form

$$S = S_r + (S_{sat} - S_r)\,\Theta \qquad (16.5)$$

$$S = (1 - \Theta)S_r, \quad \text{GEO5 FEM} \qquad (16.6)$$

$$\Theta = K_r^b \qquad (16.7)$$

where Θ is the normalized water content, see e.g. [82], b is a fitting parameter, and S_r represents an irreducible limit of saturation defined as the value of S for which capacity, the gradient dS/dh_p, becomes zero. The two parameters b and S_r can be deduced from the soil water retention curve [82]. A linear relationship between Θ and K_r with $b = 1$ was considered for example in Warrick [84]. Note that unlike van Genuchten's model described in Section 16.3 Eq. (16.7) fails to predict zero capacity at $h_p \to 0$, see also Figs. 16.3(c) and 16.4(g,h,i).

16.2 Gardner's model

Table 16.3 lists material parameters needed by Gardner's model.

Table 16.3: Parameters of Gardner's model

Symbol	Units	Description
a	[1/m]	Model parameter
S_r	[-]	Residual (irreducible) degree of saturation
b	[-]	Model parameter

A somewhat simpler variant of Eq. (16.4) plotted in Fig. 16.2(b) was introduced by Gardner already in 1958 [26] in the form

$$K_r(h_p) = e^{ah_p} = 10^{ah_p \log e} \qquad (16.8)$$

where a [m^{-1}] is the model parameter. Parameters b and S_r needed in transient flow analysis are decribed in Section 16.1, see Eqs. (16.5) - (16.7).

16.3 Van Genuchten's model

Table 16.4 lists material parameters needed by the Van Genuchten model.

Table 16.4: Parameters of van Genuchten's model

Symbol	Units	Description
α	[1/m]	Model parameter
n	[-]	Model parameter (do not match with porosity n in Eq. (16.2))
S_r	[-]	Residual (irreducible) degree of saturation

The van Genuchten model [82] is the most advanced water flow model implemented in GEO5 FEM. It suggests the variation between the relative permeability and the pore fluid pressure, see graphical representation in Fig. 16.2(b), in the form

$$K_r(h_p) = \frac{\left\{ 1 - (-\alpha h_p)^{n-1} \left[1 + (-\alpha h_p)^n \right]^{-m} \right\}^2}{\left[1 + (-\alpha h_p)^n \right]^{m/2}}, \qquad h_p < 0 \qquad (16.9)$$

where $\alpha > 0$ [m^{-1}], $n > 1$ [-], $m = 1 - 1/n$ are model parameters to be estimated from observed soil water retention data. In van Genuchten's model [82] the normalized water content Θ in Eq. (16.5) is provided by

$$\Theta = [1 + (-\alpha h_p)^n]^{-m}, \qquad h_p < 0 \qquad (16.10)$$

16.4 Comparing performance of individual water flow models

Individual models are compared in Figure 16.3. The following material and model parameters were assumed: $S_{sat} = 1.0, S_r = 0.1, a = 5$ [m^{-1}], $R = 1000, h_p^{\min} = 0, h_{TZ} = 1.4$ [m], $n = 2, \alpha = 2$ [m^{-1}]. Parameters a, R, h_{TZ} and α were selected to match the relative permeability provided by Equations (16.4) - (16.9) as close as possible. Clearly, the Gardner and Log-linear models are essentially equivalent.

In addition, Figures 16.4 help to identify the influence of these parameters on the corresponding model performance. Regarding this, it has been suggested in [72] that for example in estimation of ground water table via steady state water flow analysis the choice of a particular model does not play a

significant role. This could be exploited in situations where a highly nonlinear variation of K_r does not allow for a smooth convergence of the iteration process. On the contrary, reasonable predictions, both in terms of the overall flux and location of ground water table, can be found with the application of the most simple Gardner's model with a suitably adjusted value of a (e.g., $a \approx 1$) resulting in considerably more favorable convergence characteristics, compare distributions in Fig. 16.4(a) for $a = 1$ and $a = 5$.
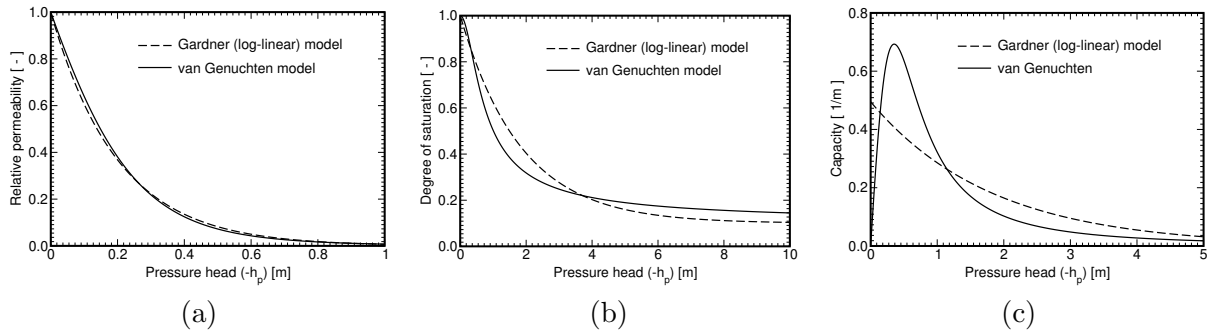

Figure 16.3:   Comparison of various models: a) relative permeability, b) degree of saturation, c) capacity ($\mathrm{d}S/\mathrm{d}h_p$)
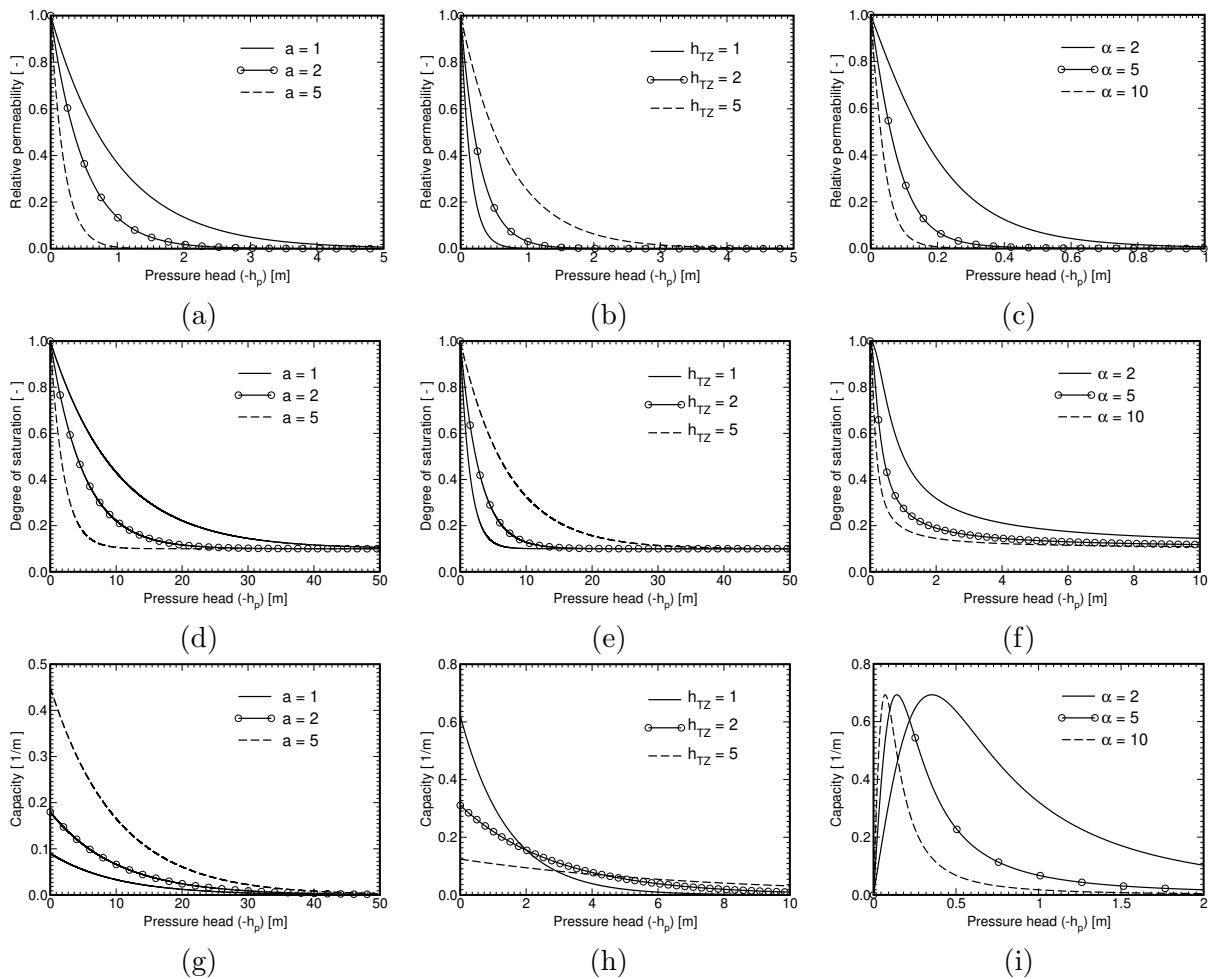

Figure 16.4:   Influence of model parameters - Relative permeability: a) Gardner, b) Log-linear, c) van Genuchten; Degree of saturation: d) Gardner, e) Log-linear, f) van Genuchten; Capacity $\mathrm{d}S/\mathrm{d}h_p$: g) Gardner, h) Log-linear, i) van Genuchten

Chapter 17

Governing equations of finite element method, Finite element types, Earthquake, Consolidation, Water flow

17.1 Governing equations of finite element method

This section provides a brief introduction to finite element method (FEM) aiming to introduce some basic definitions associated with the solution of a general nonlinear problem at a structural level. Such an issue arises with the application of any of the plasticity models introduced in the previous Sections. Further details can be found in one of the famous FEM books, e.g., [36, 6, 10].

Implementation in GEO5 FEM grounds on the principle of virtual displacements. Because the material response is expected to be nonlinear, we present this principle in incremental (linearized) form as

$$\delta E_i \;=\; \delta E_e \tag{17.1}$$

$$\delta E_i \;=\; \int_\Omega \delta \Delta \boldsymbol{\varepsilon}^\mathsf{T} \Delta \boldsymbol{\sigma} \, \mathrm{d}\Omega = \delta \Delta \boldsymbol{r}^\mathsf{T} \underbrace{\int_\Omega \mathbf{B}^\mathsf{T} \boldsymbol{\mathcal{D}} \mathbf{B} \, \mathrm{d}\Omega}_{\boldsymbol{\mathcal{K}}} \Delta \boldsymbol{r} + \delta \Delta \boldsymbol{r}^\mathsf{T} \int_\Omega \mathbf{B}^\mathsf{T} \Delta \boldsymbol{\sigma}_{in} \, \mathrm{d}\Omega \tag{17.2}$$

$$\delta E_e \;=\; \int_\Omega \delta \Delta \boldsymbol{u}^\mathsf{T} \Delta \boldsymbol{X} \, \mathrm{d}\Omega + \int_{\Gamma_t} \delta \Delta \boldsymbol{u}^\mathsf{T} \Delta \bar{\boldsymbol{t}} \, \mathrm{d}\Gamma = \delta \Delta \boldsymbol{r}^\mathsf{T} \int_\Omega \mathbf{N}^\mathsf{T} \Delta \boldsymbol{X} \, \mathrm{d}\Omega + \delta \Delta \boldsymbol{r}^\mathsf{T} \int_{\Gamma_t} \mathbf{N}^\mathsf{T} \Delta \bar{\boldsymbol{t}} \, \mathrm{d}\Gamma \tag{17.3}$$

where δE_i is a virtual work of internal forces, δE_i is a virtual work of external forces, Ω and Γ_t stand for an analysis domain and a portion of external boundary with the prescribed tractions, respectively, $\boldsymbol{X}$ is a vector of body forces (e.g., bulk weight of soil), $\bar{\boldsymbol{t}}$ represents applied surface tractions (e.g., surcharge distributed over the terrain boundary), $\boldsymbol{\sigma}_{in}$ is an initial stress (e.g., prestress in anchors, stress due to thermal effects, etc.), $\mathbf{N}$ is a matrix of standard nodal shape functions and $\mathbf{B}$ is a geometric matrix to approximate the distribution of displacements $\boldsymbol{u}$ and strains $\boldsymbol{\varepsilon}$ in an analysis domain via nodal displacements $\boldsymbol{r}$ as

$$\boldsymbol{u}(\boldsymbol{x}) \;=\; \mathbf{N}(\boldsymbol{x})\boldsymbol{r} \tag{17.4}$$

$$\boldsymbol{\varepsilon}(\boldsymbol{x}) \;=\; \mathbf{B}(\boldsymbol{x})\boldsymbol{r} \tag{17.5}$$

and $\boldsymbol{\mathcal{D}}$ is the elastoplastic (algorithmic) tangent stiffness matrix consistent with integration of local constitutive equations pertinent to a given material model as described in subsequent chapters. Because Eq. (17.1) must be satisfied for an arbitrary kinetically admissible virtual displacements $\delta \boldsymbol{r}$ and strains $\delta \boldsymbol{\varepsilon}$ we get

$$\boldsymbol{\mathcal{K}} \Delta \boldsymbol{r} = \Delta \boldsymbol{f}, \qquad \boldsymbol{\mathcal{K}} = \mathop{\mathsf{A}}_{e=1}^{N_e} \boldsymbol{\mathcal{K}}_e, \qquad \Delta \boldsymbol{f} = \mathop{\mathsf{A}}_{e=1}^{N_e} \Delta \boldsymbol{f}_e \tag{17.6}$$

where $\boldsymbol{\mathcal{K}}$ is the tangent stiffness matrix at a structural level, $\Delta \boldsymbol{r}$ collects the increment of nodal displacements and $\Delta \boldsymbol{f}$ represents the increment of external load. The symbol A represents standard

localization step of element quantities (e) into their structural counterparts with N_e being the total number of elements.

Figure 17.1 provides a graphical representation of various types of elements used in the current two-dimensional version of GEO5 FEM in standard stress (static) and earthquake (dynamic) analyses, where u, v are the nodal displacements and φ is the nodal rotation. Elements used with consolidation and water flow analyses are presented separately in the corresponding sections.

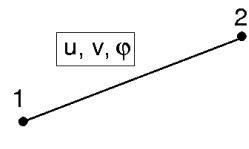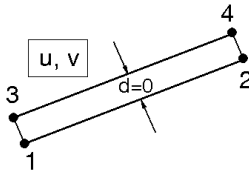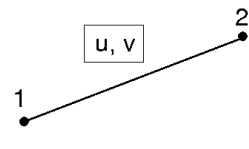Figure 17.1: List of finite elements implemented in GEO5 FEM

17.2   Finite elements for soil and compatible structural members

The following section provides a brief overview of finite elements implemented in GEO5 FEM. The presented elements can be divided into two groups: two-dimensional plane strain or axisymmetric elements (3-node and 6-node triangular elements, 4-node and 8-node quadrilateral elements) and special elements such as the 2-node rod element to model anchors props, and geotextiles, 2-node and 3-node beam elements to model supporting walls, tunnel linings or foundations and the 4-node and 6-node interface elements to model relative movement of the structure with respect to the soil. Typically, such finite elements are constructed within the framework of isoparametric formulation, which means that the same interpolation functions are used to approximate geometry as well as the displacement field in standard analysis, excess pore pressure in consolidation, or pressure head in water flow analysis. Because all primary variables can be are treated identically, we limit attention to the approximation of displacement field via nodal displacements a potentially also nodal rotations in the case of beam elements.

17.2.1   2-node rod element

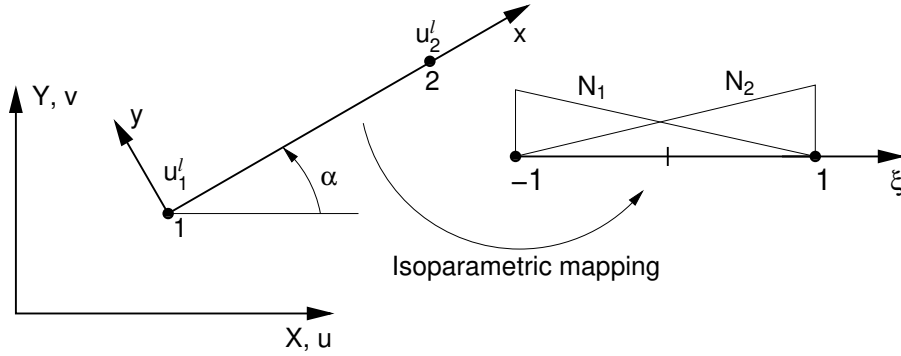The 2-node rod element with the linear interpolation of the displacement field is shown in Fig. 17.2.

Figure 17.2: 2-node rod element

Kinematics

The local displacement u^l written in terms of the global degrees of freedom, two for each node, $\boldsymbol{r}_e = \{u_1, v_1, u_2, v_2\}^\mathsf{T}$ reads

$$u^l = N_1 \underbrace{(u_1 \cos\alpha + v_1 \sin\alpha)}_{u_1^l} + N_2 \underbrace{(u_2 \cos\alpha + v_2 \sin\alpha)}_{u_2^l} \tag{17.7}$$

where the isoparametric element shape functions N_1, N_2 are given by

$$N_1 = \frac{1}{2}(1 - \xi)$$
$$N_2 = \frac{1}{2}(1 + \xi)$$

Element stiffness matrix

Taking the derivative of Eq. (17.7) with respect to the local x axis gives the axial strain in the form

$$\varepsilon = \mathbf{B}\boldsymbol{r} \tag{17.8}$$

where the (1×4) matrix $\mathbf{B}$ attains the following form

$$\mathbf{B} = \frac{1}{L}\{-\cos\alpha, -\sin\alpha, \cos\alpha, \sin\alpha\} \tag{17.9}$$

where L is the element length. To conclude the derivation of the element stiffness matrix we introduce the constitutive law in the form

$$\sigma = E\varepsilon \tag{17.10}$$

where E is the Young modulus. Finally, making use of Eq. (17.2) on the element level provides the element stiffness matrix $\mathbf{K}_e$ as

$$\mathbf{K}_e = \frac{EA}{L}\begin{bmatrix} \cos\alpha\cos\alpha & \cos\alpha\sin\alpha & -\cos\alpha\cos\alpha & -\cos\alpha\sin\alpha \\ \cos\alpha\sin\alpha & \sin\alpha\sin\alpha & -\cos\alpha\sin\alpha & -\sin\alpha\sin\alpha \\ -\cos\alpha\cos\alpha & -\cos\alpha\sin\alpha & \cos\alpha\cos\alpha & \cos\alpha\sin\alpha \\ -\cos\alpha\sin\alpha & -\sin\alpha\sin\alpha & \cos\alpha\sin\alpha & \sin\alpha\sin\alpha \end{bmatrix} \tag{17.11}$$

where EA/L represents the element axial stiffness; A is the the element cross-sectional area.
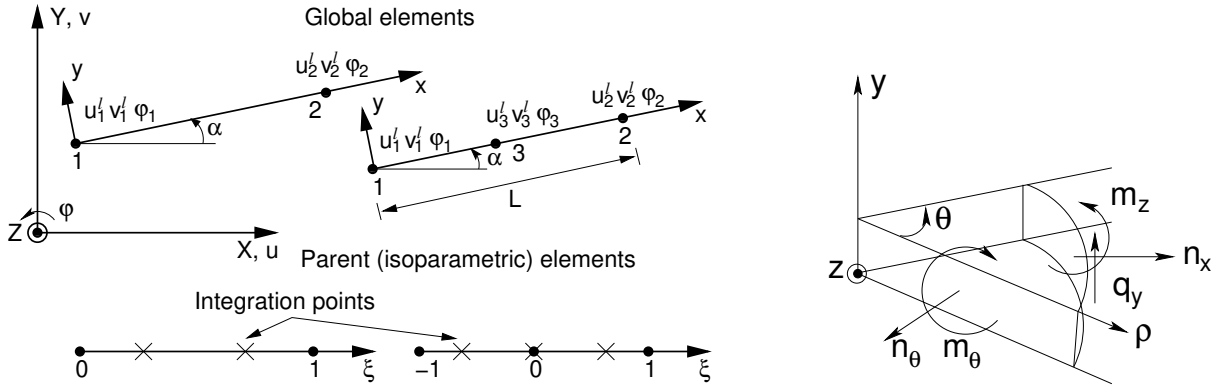
Figure 17.3: a) 2-node and 3-node beam elements, b) Stress resultants

17.2.2   2-node and 3-node beam elements

The 2-node and 3-node beam elements with three degrees of freedom (two translations and one rotation) in each node appear in Fig. 17.3(a).

Kinematics

In plane strain or axisymmetric analysis the beam elements can be introduced to represent, e.g., a retaining wall or a circular foundation slab. The generalized stress resultants shown in Fig. 17.3(b)

$$\boldsymbol{\sigma}^{\mathsf{T}} = \{n_x, m_z, q_y, n_\theta, m_\theta\} \tag{17.12}$$

are then assumed per 1m run. While the first three components appear only in the plane strain analysis, the other two arise when axisymmetric conditions apply. In particular, n_x, m_z, q_y represent the membrane (normal) force, bending moment and shear force, whereas n_θ and m_θ are the circumferential (hoop) membrane force and circumferential (hoop) bending moment. For an isotropic beam element the above stress resultants are related to the generalized strains, that now involve extension and curvatures of the middle surface, through the material stiffness matrix **D** in the form

$$\left\{ \begin{array}{c} n_x \\ m_z \\ q_y \\ n_\theta \\ m_\theta \end{array} \right\} = \frac{Eh}{1-\nu^2} \begin{bmatrix} 1 & 0 & 0 & \nu & 0 \\ 0 & \dfrac{h^2}{12} & 0 & 0 & \dfrac{\nu h^2}{12} \\ 0 & 0 & \dfrac{k(1-\nu)}{2} & 0 & 0 \\ \nu & 0 & 0 & 1 & 0 \\ 0 & \dfrac{\nu h^2}{12} & 0 & 0 & \dfrac{h^2}{12} \end{bmatrix} \left\{ \begin{array}{c} \dfrac{\mathrm{d}u^l}{\mathrm{d}x} \\ -\dfrac{\mathrm{d}\varphi_z}{\mathrm{d}x} \\ -\varphi_z + \dfrac{\mathrm{d}v^l}{\mathrm{d}x} \\ \dfrac{v^l \sin\alpha - u^l \cos\alpha}{\rho} \\ -\dfrac{\theta\cos\alpha}{\rho} \end{array} \right\} \tag{17.13}$$

where h is the plate thickness and ρ is the circumferential radius. The material parameters E, ν stand as usual for Young's modulus and Poisson's ratio. The constant k can be determined from the condition that the work of the actual stresses must be equal to the work of the averaged stresses. Note that for a rectangular cross-section, $k = 5/6$. Further details are available in [10]. Finally, the unknown functions in the local displacement field $\boldsymbol{u}^l = \left\{u^l, \varphi_z, v^l\right\}^{\mathsf{T}}$ stand for the longitudinal displacement, rotation about the z-axis and vertical displacement given in the local coordinate system, respectively. For plane strain analysis the last two rows in Eq. (17.13) are not included.

The components of the local displacement field follow from the standard finite element approximation using the element shape functions and the nodal degrees of freedom

$$\boldsymbol{u}^l = \mathbf{N}\boldsymbol{r}^l \tag{17.14}$$

Table 17.1: Shape functions for 2-node beam element

Node i	Function N_i
1	$1 - \xi$
2	ξ
3	$\dfrac{1}{L(1 + 2\kappa)} \left[6\xi - 6\xi^2 \right]$
4	$\dfrac{1}{1 + 2\kappa} \left[(1 + 2\kappa) - 2(2 + \kappa)\xi + 3\xi^2 \right]$
5	$\dfrac{1}{L(1 + 3\kappa)} \left[-6\xi + 6xi^2 \right]$
6	$\dfrac{1}{1 + 2\kappa} \left[-2(1 - \kappa)\xi + 3\xi^2 \right]$
7	$\dfrac{1}{1 + 2\kappa} \left[(1 + 2\kappa) - 2\kappa\xi - 3\xi^2 + 2\xi^3 \right]$
8	$\dfrac{L}{1 + 2\kappa} \left[-(1 + \kappa)\xi + (2 + \kappa)\xi^2 - \xi^3 \right]$
9	$\dfrac{1}{1 + 2\kappa} \left[2\kappa\xi + 3\xi^2 - 2\xi^3 \right]$
10	$\dfrac{L}{1 + 2\kappa} \left[\kappa\xi + (1 - \kappa)\xi^2 - \xi^3 \right]$

2-node beam element: Detailed derivation of the finite element matrices for the 2-node beam element is given in [10]. Here we present only the most essential part. In particular, the matrix **N** in Eq. (17.14) assumes the form

$$\mathbf{N} = \begin{bmatrix} N_1 & 0 & 0 & N_2 & 0 & 0 \\ 0 & -N_3 & N_4 & 0 & -N_5 & N_6 \\ 0 & N_7 & -N_8 & 0 & N_9 & -N_{10} \end{bmatrix} \tag{17.15}$$

where individual shape functions are listed in Table 17.1. The variable κ that appears in individual terms of the shape functions is given by

$$\kappa = \frac{6EI_z}{k\mu AL^2} \tag{17.16}$$

where k is the shear correction factor, I_z is the moment of inertia with respect to z axis and μ is the elastic shear modulus. The finite element representation of the strain field

$$\varepsilon^{\mathsf{T}} = \left\{ \frac{\mathrm{d}u^l}{\mathrm{d}x}, -\frac{\mathrm{d}\varphi_z}{\mathrm{d}x}, -\varphi_z + \frac{\mathrm{d}v^l}{\mathrm{d}x}, \frac{v^l \sin\alpha - u^l \cos\alpha}{\rho}, -\frac{\theta \cos\alpha}{\rho} \right\} \tag{17.17}$$

calls for the introduction of the strain matrix **B**. Using Eq. (17.15) and taking into account the transformation of coordinates from the local to the global coordinate system it is easy to see that

$$
\mathbf{B} = \begin{bmatrix}
CN_1' & SN_1' & 0 & CN_2' & SN_2' & 0 \\[2mm]
-SN_3' & CN_3' & -N_4' & -SN_5' & CN_5' & -N_6' \\[2mm]
-S(N_3 + N_7') & C(N_3 + N_7') & -N_4 - N_8' & -S(N_5 + N_9') & C(N_5 + N_9') & -N_6 - N_{10}' \\[2mm]
\dfrac{N_1}{\rho} & 0 & 0 & \dfrac{N_2}{\rho} & 0 & 0 \\[3mm]
0 & \dfrac{CN_3}{\rho} & -\dfrac{CN_4}{\rho} & 0 & \dfrac{CN_2}{\rho} & -\dfrac{CN_1}{\rho}
\end{bmatrix}
\tag{17.18}
$$

where

$$
C = \cos(\alpha), \quad S = \sin(\alpha), \qquad N_i' = \frac{1}{J}\frac{\mathrm{d}N_i}{\mathrm{d}\xi} \tag{17.19}
$$

The angle α in the above equation is defined in Fig. 17.3 and the Jacobian J follows from Eq. (17.26). The current radius is given by

$$
\rho = \sum_{i=1}^{2} N_i x_i \tag{17.20}
$$

Table 17.2: Shape functions for 3-node beam element

Node i	Regular function N_i	Substitute function $\overline{N}_i$
1	$\dfrac{1}{2}\xi(\xi - 1)$	$\dfrac{1}{2}\left(\dfrac{1}{3} - \xi\right)$
2	$\dfrac{1}{2}\xi(\xi - 1)$	$\dfrac{1}{2}\left(\dfrac{1}{3} + \xi\right)$
3	$(1 - \xi^2)$	$\dfrac{2}{3}$

3-node beam element: Assuming the standard isoparametric shape functions listed in Table 17.2 to approximate the displacement field gives the matrix **N** in the form

$$
\mathbf{N} = \begin{bmatrix}
N_1 & 0 & 0 & N_2 & 0 & 0 & N_3 & 0 & 0 \\
0 & N_1 & 0 & 0 & N_2 & 0 & 0 & N_3 & 0 \\
0 & 0 & N_1 & 0 & 0 & N_2 & 0 & 0 & N_3
\end{bmatrix}
\tag{17.21}
$$

Next, recall the representation of the strain field (17.17) and use Eq. (17.21) to arrive at

$$
\mathbf{B} = \begin{bmatrix}
CN_1' & SN_1' & 0 & CN_2' & SN_2' & 0 & CN_3' & SN_3' & 0 \\[2mm]
0 & -N_1' & 0 & 0 & -N_2' & 0 & 0 & -N_3' & 0 \\[2mm]
-SN_1' & CN_1' & \overline{N}_1 & -SN_2' & CN_2' & \overline{N}_2 & -SN_3' & CN_3' & \overline{N}_3 \\[2mm]
\dfrac{\overline{N}_1}{\rho} & 0 & 0 & \dfrac{\overline{N}_2}{\rho} & 0 & 0 & \dfrac{\overline{N}_3}{\rho} & 0 & 0 \\[3mm]
0 & 0 & -\dfrac{C\overline{N}_1}{\rho} & 0 & 0 & -\dfrac{C\overline{N}_2}{\rho} & 0 & 0 & -\dfrac{C\overline{N}_3}{\rho}
\end{bmatrix}
\tag{17.22}
$$

The standard **B** matrix was again augmented to account for the transformation of coordinates. Parameters C, S, N_i' receive the same meaning as in Eq. (17.19) with the Jacobian J found from Eq. (17.27). For the circumferential strain terms the current radius r now becomes [65]

$$\rho = \sum_{i=1}^{3} \overline{N}_i x_i \tag{17.23}$$

In addition, substitute shape functions $\overline{N}_i$ were used to define the variation of φ in the definition of shear strain $-\varphi_z + \dfrac{\mathrm{d}v^l}{\mathrm{d}x}$ to avoid shear force locking. Note that the substitute shape functions coincide with the regular shape functions at the reduced Gaussian integration points. Details can be found in [21, 65].

Element stiffness matrix

Derivation of the stiffness matrix follows Eq. (17.2). After applying standard numerical integration, e.g., the Gaussian quadrature with r_j being the location of an integration point and w_j the associated weight, the result becomes

- Plane strain analysis

$$\mathbf{K}_e = \sum_{j=1}^{N} w_j \mathbf{B}^{\mathsf{T}}(\xi_j)\mathbf{D}\mathbf{B}(\xi_j) J \tag{17.24}$$

- Axisymmetric analysis

$$\mathbf{K}_e = \sum_{j=1}^{N} w_j \mathbf{B}^{\mathsf{T}}(\xi_j)\mathbf{D}\mathbf{B}(\xi_j)\rho(\xi_j) J \tag{17.25}$$

where the Jacobian J reads

$$J \;=\; L \qquad \text{for} \quad 2-\text{node element} \tag{17.26}$$

$$J \;=\; \frac{L}{2} \qquad \text{for} \quad 3-\text{node element} \tag{17.27}$$

Locations of integration points within parent elements also shown in Fig. 17.3 are stored in Table 17.3.

Table 17.3: Integration points for 2-node and 3-node beam elements

Integration	2-node beam		3-node beam	
point	coordinate ξ	weight w	coordinate ξ	weight w
1	0.211324865	0.5	-0.774596669241483	5/9
2	0.788675131	0.5	0.0	8/9
3			0.774596669241483	5/9

17.2.3   Plane 3-node and 6-node triangular elements

This section presents derivation of element stiffness matrix of 3-node and 6-node triangular isoparametric elements plotted in Fig. 17.4. These are the only triangular elements implemented in GEO5 FEM.
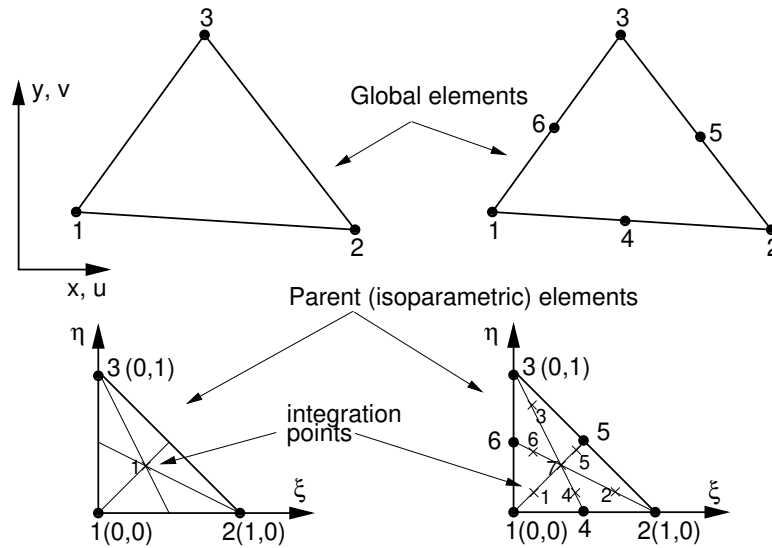
Figure 17.4: 3-node and 6-node triagular elements

Kinematics

The displacement interpolation functions are listed in Table 17.4. The element degrees of freedom (two translational degrees of freedom for each node) are

$$\boldsymbol{r}^{\mathsf{T}} = \{u_1, v_1, u_2, v_2, u_3, v_3\} \qquad \qquad 3-\text{node elem} \qquad (17.28)$$

$$\boldsymbol{r}^{\mathsf{T}} = \{u_1, v_1, u_2, v_2, u_3, v_3, u_4, v_4, u_5, v_5, u_6, v_6\} \quad 6-\text{node elem} \qquad (17.29)$$

The displacement field inside the element is uniquely described by the above nodal parameters

$$u = \sum_{i=1}^{n} N_i u_i, \qquad \qquad v = \sum_{i=1}^{n} N_i v_i \qquad (17.30)$$

where n is the number of element nodes.

Element stiffness matrix

The components of the strain tensor follow from Eq. (17.5). The element stiffness matrix is then defined by Eq. (17.2). Here, the integral is again evaluated by the Gaussian quadrature so that

- Plane strain analysis

$$\mathbf{K}_e = \sum_{j=1}^{N} w_j \mathbf{B}^{\mathsf{T}}(\xi_j, \eta_j, \frac{1}{J}) \mathbf{D} \mathbf{B}(\xi_j, \eta_j, \frac{1}{J}) J(\xi_j, \eta_j) \qquad (17.31)$$

- Axisymmetric analysis

$$\mathbf{K}_e = \sum_{j=1}^{N} w_j \mathbf{B}^{\mathsf{T}}(\xi_j, \eta_j, \frac{1}{J}) \mathbf{D} \mathbf{B}(\xi_j, \eta_j, \frac{1}{J}) \rho(\xi_j, \eta_j) J(\xi_j, \eta_j) \qquad (17.32)$$

where w_j is the weight for a given integration point j, N is the number of integration points and J is the Jacobian of the transformation given by

$$J(\xi, \eta) = \frac{\partial x}{\partial \xi} \frac{\partial y}{\partial \eta} - \frac{\partial x}{\partial \eta} \frac{\partial y}{\partial \xi} \qquad (17.33)$$

The linear 3-node element is integrated at one integration point, while $N = 7$ is assumed for the quadratic 6-node element, see Fig. 17.4. Locations of integration points within parent elements are stored in Tables 17.5 and 17.6. Further details on the evaluation of the element stiffness matrix can be found in [10].

Table 17.4: Interpolation functions for 3-node and 6-node triangular elements

Node i	Function N_i	Included only if node i is defined		
		$i = 4$	$i = 5$	$i = 6$
1	$1 - \xi - \eta$	$-\dfrac{1}{2}N_4$		$-\dfrac{1}{2}N_6$
2	ξ	$-\dfrac{1}{2}N_4$	$-\dfrac{1}{2}N_5$	
3	η		$-\dfrac{1}{2}N_5$	$-\dfrac{1}{2}N_6$
4	$4\xi(1 - \xi - \eta)$			
5	$4\xi\eta$			
6	$4\eta(1 - \xi - \eta)$			

Table 17.5: Integration points for a 3-node triangular element

Integration point	Coordinate ξ	Coordinate η	Weight w
1	1/3	1/3	1/2

Table 17.6: Integration points for a 6-node triangular element

Integration point	Coordinate ξ	Coordinate η	Weight w
1	0.1012865073235	0.1012865073235	0.06296959027240
2	0.7974269853531	0.1012865073235	0.06296959027240
3	0.1012865073235	0.7974269853531	0.06296959027240
4	0.4701420641051	0.0597158717898	0.06619707639425
5	0.4701420641051	0.4701420641051	0.06619707639425
6	0.0597158717898	0.4701420641051	0.06619707639425
7	0.3333333333333	0.3333333333333	0.11250000000000

17.2.4   Plane 4-node and 8-node quadrilateral elements

This section presents derivation of element stiffness matrix of 4-node and 8-node quadrilateral isoparametric elements plotted in Fig. 17.5. These are the only quadrilateral elements implemented in GEO5 FEM.
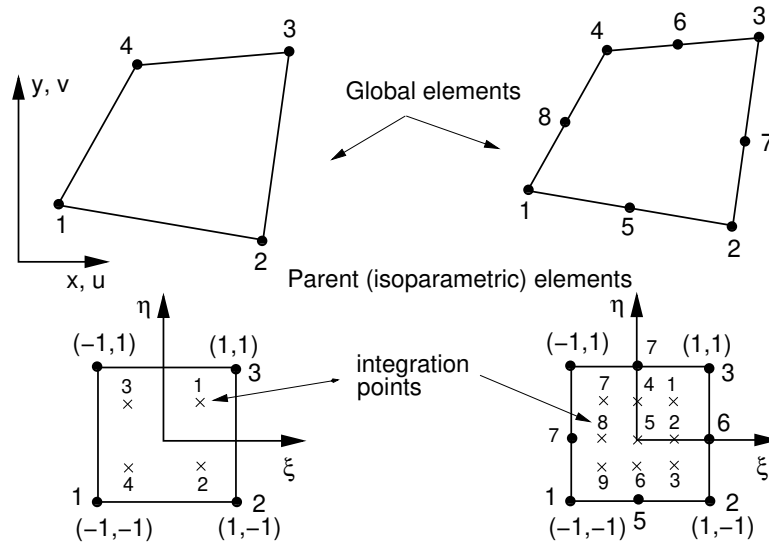

Figure 17.5: 4-node and 8-node quadrilateral elements

Kinematics

The displacement interpolation functions are listed in Table 17.7. Similarly to triangular elements we consider only translational degrees of freedom, two for each node, so that

$$
\begin{aligned}
\boldsymbol{r}^\mathsf{T} &= \{u_1, v_1, u_2, v_2, u_3, v_3, u_4, v_4\} & 4 - \text{node} \quad \text{elem} & \quad (17.34)\\
\boldsymbol{r}^\mathsf{T} &= \{u_1, v_1, u_2, v_2, u_3, v_3, u_4, v_4, u_5, v_5, u_6, v_6, u_7, v_7, u_8, v_8\} & 8 - \text{node} \quad \text{elem} & \quad (17.35)
\end{aligned}
$$

The displacement field inside the element is again uniquely described by the above nodal parameters

$$
u = \sum_{i=1}^{n} N_i u_i, \qquad\qquad v = \sum_{i=1}^{n} N_i v_i \tag{17.36}
$$

where n is the number of element nodes.

Element stiffness matrix

In analogy to triangular elememts the components of the strain tensor follow from Eq. (17.5) and the element stiffness matrix is then provided by Eq. (17.2). Here, the integral is again evaluated by the Gaussian quadrature, which, however, takes a slightly different form in comparison to Eqs. (17.31) and (17.32)

- Plane strain analysis

$$
\mathbf{K}_e = \sum_{i=1}^{N} \sum_{j=1}^{N} w_i w_j \mathbf{B}^\mathsf{T}(\xi_i, \eta_j, \tfrac{1}{J}) \mathbf{D} \mathbf{B}(\xi_i, \eta_j, \tfrac{1}{J}) J(\xi_j, \eta_j) \tag{17.37}
$$

- Axisymmetric analysis

$$
\mathbf{K}_e = \sum_{i=1}^{N} \sum_{j=1}^{N} w_i w_j \mathbf{B}^\mathsf{T}(\xi_i, \eta_j, \tfrac{1}{J}) \mathbf{D} \mathbf{B}(\xi_i, \eta_j, \tfrac{1}{J}) \rho(\xi_i, \eta_j) J(\xi_i, \eta_j) \tag{17.38}
$$

where w_i, w_j are the weights for a given integration point i, j. The Jacobian J follows from (17.33), see [10] for further details. The 2×2 ($N = 2$) and 3×3 ($N = 3$) Gaussian integration rules are considered for 4-node and 8-node elements, respectvely. Locations of integration points within parent elements are stored in Table 17.8.

Table 17.7: Interpolation functions for 4-node and 8-node quadrilateral elements

Node i	Function N_i	Included only if node i is defined			
		$i = 5$	$i = 6$	$i = 7$	$i = 8$
1	$\frac{1}{4}(1+\xi)(1+\eta)$	$-\frac{1}{2}N_5$			$-\frac{1}{2}N_8$
2	$\frac{1}{4}(1-\xi)(1+\eta)$	$-\frac{1}{2}N_5$	$-\frac{1}{2}N_6$		
3	$\frac{1}{4}(1-\xi)(1-\eta)$		$-\frac{1}{2}N_6$	$-\frac{1}{2}N_7$	
4	$\frac{1}{4}(1+\xi)(1-\eta)$			$-\frac{1}{2}N_7$	$-\frac{1}{2}N_8$
5	$\frac{1}{2}(1-\xi^2)(1+\eta)$				
6	$\frac{1}{2}(1-\eta^2)(1-\xi)$				
7	$\frac{1}{2}(1-\xi^2)(1-\eta)$				
8	$\frac{1}{2}(1-\eta^2)(1+\xi)$				

Table 17.8: Integration points for a 4-node and 8-node quadrilateral element

Integration order	Coordinate ξ, η_i	Weight w_i
2×2	$\pm\ 0.577350269189626$	1.0
3×3	$\pm\ 0.774596669241483$ 0.0	0.555555555555555 0.888888888888888

17.2.5 4-node and 6-node interface elements

This section presents the derivation of the element stiffness matrix for the 4-node and 6-node interface elements that are compatible with the previously discussed 3-node and 6-node triangular elements. Both elements are displayed in Fig. 17.6.
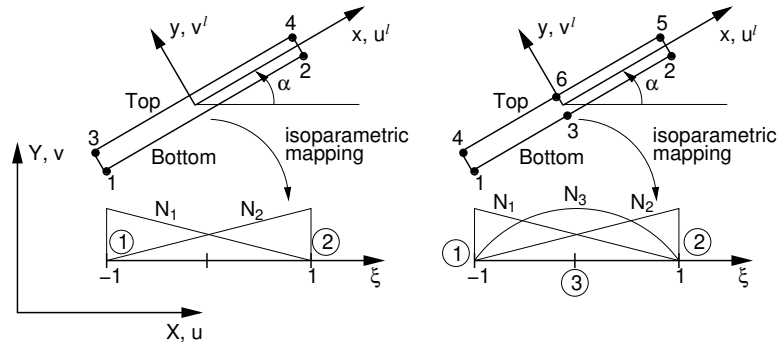

Figure 17.6: 4-node and 6-node interface elements

Kinematics

In the finite element framework the global displacements are approximated using the standard element shape functions listed in Table 17.9. Referring to Fig 17.6 the displacement field for the 4-node interface element receives the form

$$
\begin{aligned}
u^{top} &= N_1 u_3 + N_2 u_4 \\
u^{bot} &= N_1 u_1 + N_2 u_2 \\
v^{top} &= N_1 v_3 + N_2 v_4 \\
v^{bot} &= N_1 v_1 + N_2 v_2
\end{aligned}
\tag{17.39}
$$

In the compact form the global nodal degrees of freedom u_i, v_i are

$$
\boldsymbol{r}^{\mathsf{T}} = \{u_1, v_1, u_2, v_2, u_3, v_3, u_4, v_4\}
\tag{17.40}
$$

Similarly for the 6-node interface element we get

$$
\begin{aligned}
u^{top} &= N_1 u_4 + N_2 u_5 + N_3 u_6 \\
u^{bot} &= N_1 u_1 + N_2 u_2 + N_3 u_3 \\
v^{top} &= N_1 v_4 + N_2 v_5 + N_3 v_6 \\
v^{bot} &= N_1 v_1 + N_2 v_2 + N_3 v_3
\end{aligned}
\tag{17.41}
$$

and

$$
\boldsymbol{r}^{\mathsf{T}} = \{u_1, v_1, u_2, v_2, u_3, v_3, u_4, v_4, u_5, v_5, u_6, v_6\}
\tag{17.42}
$$

Element stiffness matrix

The stress-displacement relationship of the interface model assumes the form

$$
\left\{ \begin{array}{c} \tau \\ \sigma \end{array} \right\} = \mathbf{D} \left\{ \begin{array}{c} [\![u]\!]^l \\ [\![v]\!]^l \end{array} \right\}
\tag{17.43}
$$

where $[\![u]\!]^l$ and $[\![v]\!]^l$ represent the relative displacements of the top and bottom of the interface element in the local coordinate system, Fig. 17.6. For isotropic linear elastic behavior the interface material stiffness matrix $\mathbf{D}$ takes the form

$$
\mathbf{D} = \left[\begin{array}{cc} K_s & 0 \\ 0 & K_n \end{array} \right]
\tag{17.44}
$$

Table 17.9: Interpolation functions for 4-node and 6-node interface elements

Node i	Function N_i	Included only if node 3 is defined
1	$\frac{1}{2}(1 - \xi)$	$-\frac{1}{2}N_3$
2	$\frac{1}{2}(1 + \xi)$	$-\frac{1}{2}N_3$
3	$(1 - \xi^2)$	

where K_s and K_n are the elastic shear and normal stiffnesses, respectively. They can be related to the interface shear and Young's moduli G_{int}, E_{int} as

$$K_s = \frac{G_{int}}{t}$$
$$K_n = \frac{E_{int}}{t}$$

where t represents the interface thickness. It should be noted here that setting the interface stiffnesses K_s, K_n to low values may lead to excessively large elastic displacements. However, if the elastic parameters are too large (attempt to model a perfect bond), then the numerical ill-conditioning may occur. This is usually manifested by the oscillation of interface stresses. It has been argued that such unwanted oscillatory behavior can be reduced by using the Newton-Cotes integration scheme (integration points coincide with the element nodes) when computing the element stiffness matrix [24, 34]. On the contrary, the results presented in [22] suggest that the use of the Newton-Cotes integration scheme has no benefit over the Gaussian quadrature.

The global degrees of freedom in Eqs. (17.40) and (17.42) are related to local displacements in the form

$$\left\{ \begin{array}{c} [\![u]\!]^l \\ [\![v]\!]^l \end{array} \right\} = \mathbf{B}r \tag{17.45}$$

where the matrix **B** is written as

$$\mathbf{B} = [-\mathbf{TB}_1 \ -\mathbf{TB}_2 \ \mathbf{TB}_1 \ \mathbf{TB}_2] \qquad\qquad 4 - \text{node elem} \tag{17.46}$$
$$\mathbf{B} = [-\mathbf{TB}_1 \ -\mathbf{TB}_2 \ -\mathbf{TB}_3 \ \mathbf{TB}_1 \ \mathbf{TB}_2 \ \mathbf{TB}_3] \quad 6 - \text{node elem} \tag{17.47}$$

and

$$\mathbf{T} = \left[\begin{array}{cc} \cos\alpha & \sin\alpha \\ -\sin\alpha & \cos\alpha \end{array} \right] \qquad \mathbf{B}_i = \left[\begin{array}{cc} N_i & 0 \\ 0 & N_i \end{array} \right] \tag{17.48}$$

The element stiffness matrix $\mathbf{K}_e$ then follows from

$$\mathbf{K}_e = \frac{L}{2} \int_{-1}^{1} \mathbf{B}^\mathsf{T} \mathbf{D} \mathbf{B} \, \mathrm{d}r \tag{17.49}$$

where L is the element length.

17.2.6   Solution strategies

As typical for the analysis of nonlinear problems a standard step by step incremental procedure (the total load can be split into a set of increments) is adopted. Equation $(17.6)_1$ then receives the form

$$\mathcal{K}_j^i \Delta u_j^i = \Delta f_j^i \tag{17.50}$$

where the scripts i and j stand for the current load increment and the current iteration step, respectively. Schematic representation of this procedure is evident from Fig. 17.7, in which $\Delta\lambda$ is the coefficient of proportionality and the term $\boldsymbol{F} - \boldsymbol{R}$ represents a vector of out-of-balanced forces. It arises as a direct consequence of the nonlinear behavior. Here, the attention is limited to standard plasticity only.
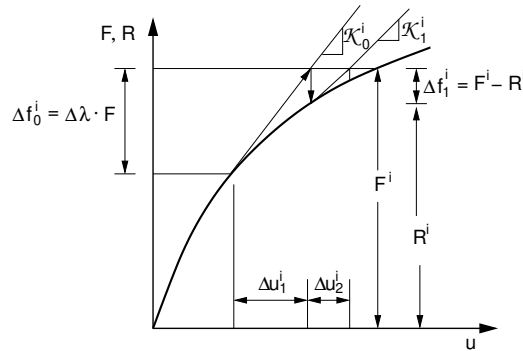

Figure 17.7: Incremental procedure: reason for out-of balanced forces

The GEO5 FEM software offers two methods to solve the system of nonlinear equations:

1. Newton-Raphson method

2. Arc-length method

As indicated in Figs. 17.8 and 17.9 both methods are implemented in three potential variants:

1. *FULL* - tangent stiffness matrix $\mathcal{K}$ is updated after each iteration step (default setting)

2. *STEP* - tangent stiffness matrix $\mathcal{K}$ is updated after each load step

3. *NONE* - the elastic stiffness matrix $\mathcal{K} = \mathsf{K}^{el}$ is used

Newton-Raphson method

To shortly introduce this method we accord our attention to *FULL* Newton-Raphson method plotted in Fig. 17.8(a). When referring to imbalance forces the basic equations to be solved in nonlinear
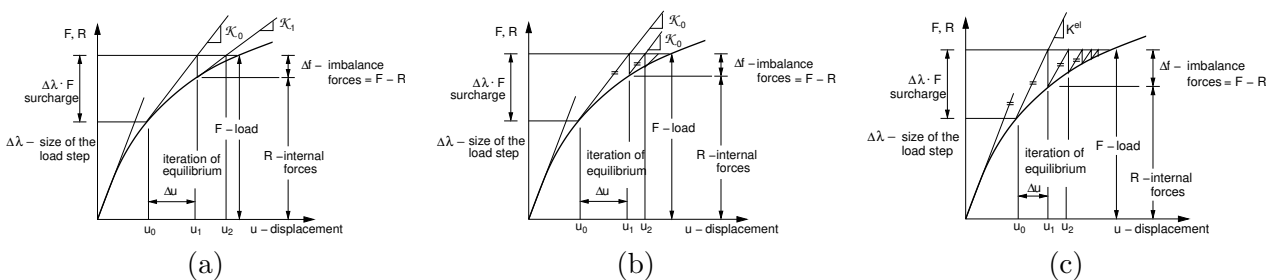

Figure 17.8: Newton-Raphson method: a) update full, b) update step, c) update none

analysis are

$$\boldsymbol{F}^i - \boldsymbol{R}^i = 0 \tag{17.51}$$

where $\boldsymbol{F}^i$ is the vector of externally applied nodal forces at the end of the i-th loading step and $\boldsymbol{R}^k$ is the vector of nodal forces found from the element stresses such that

$$\boldsymbol{R}^i = \mathop{\textbf{A}}_{e=1}^{N_e} \int_{\Omega_e} \mathbf{B}^{\mathsf{T}} \boldsymbol{\sigma}_e^i \, \mathrm{d}V \tag{17.52}$$

Figure 17.8 suggests that Eq. (17.51) might not in general be fulfilled at every step of the solution process, because the nodal forces $\boldsymbol{R}^i$ depend nonlinearly on the nodal displacements. Therefore, an iteration is required within a given load increment. The iterative procedure as shown in Fig. 17.8(a) arises from the consistent linearization of the nonlinear response of the finite element equations at iteration $j-1$. The consistently linearized tangent stiffness matrix is therefore formed at the beginning of every iteration step. The resulting iterative scheme reads

$$\begin{aligned}
\boldsymbol{r}_0^i &= \boldsymbol{r}^{i-1}, \quad \boldsymbol{R}_0^i = \boldsymbol{R}^{i-1} \Longrightarrow \Delta \boldsymbol{f}_0 = \boldsymbol{F}^i - \boldsymbol{F}^{i-1} + \Delta \boldsymbol{f}_\epsilon^{i-1} & (17.53) \\
\Delta \boldsymbol{f}_{j-1} &= \boldsymbol{F}^i - \boldsymbol{R}_{j-1}^i & (17.54) \\
\mathcal{K}_{j-1}^i \Delta \boldsymbol{r}_j &= \Delta \boldsymbol{f}_{j-1} & (17.55) \\
\boldsymbol{r}_j^i &= \boldsymbol{r}_{j-1}^i + \Delta \boldsymbol{r}_j & (17.56)
\end{aligned}$$

Vector $\Delta \boldsymbol{f}_\epsilon^{i-1}$ represents the out-of-balance forces found at the end of the previous loading increment that are linked to the selected solution accuracy ϵ, see Section 17.2.7.

Note that the Newton-Raphson method is a locally convergent method. Consequently, the method might not converge if the load increment is too large. In such a case, the load increment is progressively reduced depending on the "analysis settings".

Arc-length method

In situations where we seek for the unknown collapse load, e.g., stability analysis of earth slopes, the Newton-Raphson method introduced in the previous sections may experience rather poor behavior. This can be attributed to the fact that the solutions by the Newton-Raphson method and closely related techniques are driven by load increments. The difficulty that arises around the collapse point can be overcome when driving the solution by displacement increments. This is the essential ingredient of the Arc-length method discussed hereafter. In particular, the method fixes both the loading and displacement at the end of the current load increment by introducing a scalar multiplier that controls the magnitude of the applied load. The load multiplier λ now becomes an additional unknown and calls for the introduction of an additional equation for its determination. There exist several constraint equations in the literature employed for the evaluation of λ. In what follows the constraint equations that arise from the so-called spherical (Crisfield) and linearized arc-length methods are reviewed.
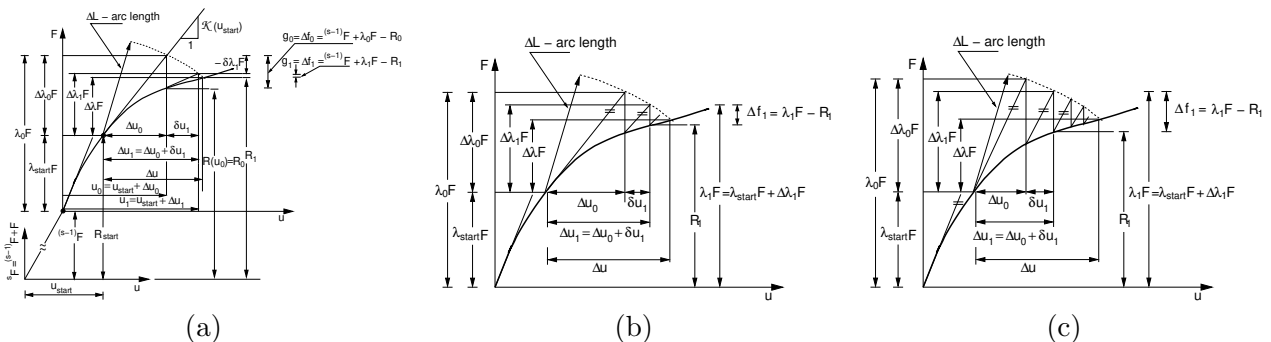

Figure 17.9: Arc-length method: a) update full, b) update step, c) update none

For illustration, we limit out attention to *FULL* Spherical Arc-length method proposed by Crisfield [20]. The basic idea behind the Arc-length method is best understood from Fig. 17.9(a). A fundamental assumption of the method is that the load vector varies proportionally during the analysis. To that end, suppose that the solution process is split into several construction stages and denote

the external load applied up to the beginning of the current construction stage s as $^{s-1}\boldsymbol{F}$. The total load $^{s}\boldsymbol{F} = {}^{s-1}\boldsymbol{F} + \boldsymbol{F}$ represents a certain "reference" or expected load vector at the end of the current load stage s and $\boldsymbol{F}$ is the corresponding reference load increment applied at the beginning of the s-stage. The goal now becomes to determine a fraction λ of the applied load $\boldsymbol{F}$ such that the vector of out-of-balanced forces $\Delta\boldsymbol{f} = \boldsymbol{g}$ converges again to zero in some appropriate measure ϵ, see Section 17.2.7. Individual vectors and parameters introduced in Fig. 17.9 are:

- $\boldsymbol{F}$ – total load applied in a given solution stage.

- $^{s}\boldsymbol{F} = {}^{s-1}\boldsymbol{F} + \boldsymbol{F}$ – total load expected at the end of a given solution stage.

- $^{s-1}\boldsymbol{F}$ – load applied up to stage $(s-1)$.

- λ_{start} – fraction of $\boldsymbol{F}$ at the beginning of a new load increment.

- $\lambda_j^i = \lambda_{start}^i + \Delta\lambda_j^i$ – fraction of $\boldsymbol{F}$ at the end of the j-th iteration within the i-th load increment.

- $\boldsymbol{R}_{start} = \lambda_{start}^i \boldsymbol{F} + {}^{s-1}\boldsymbol{F}$ – internal forces at the beginning of a new load increment.

- $\boldsymbol{g}_j$ – out-of-balanced forces at the end of the j-th iteration.

- $\widehat{\boldsymbol{g}}_j = \boldsymbol{g}_{j-1} + \delta\lambda_j \boldsymbol{F}$ – load increment in the j-th iteration.

The starting point of the method is an incremental expression of a differential of the arc-length that provides the additional constraint equation given by

$$\eta^2 \Delta\boldsymbol{r}_j{}^{\mathsf{T}} \Delta\boldsymbol{r}_j + \beta^2 \Delta\lambda_j^2 \boldsymbol{F}^{\mathsf{T}} \boldsymbol{F} = \Delta L^2 \tag{17.57}$$

where

- ΔL – represents a radius of a spherical hyper-surface in $(\boldsymbol{r}, \lambda)$ (standard Arc-length method as introduced by Crisfield in [20]; when setting $\beta = 0 \rightarrow \Delta L$ becomes a radius of a cylinder (Cylindrical ALM). This parameter is an a priori set step length and serves to evaluate the corresponding fraction of the current load increment $\Delta\lambda$. Note that the selection of this parameter is essential for the success of the solution. By default, $\beta = 0$ in GEO5 FEM.

- β – is a scalar parameter describing the ratio of selected scales for λ and $\boldsymbol{r}$.

- η – is a scalar parameter which comes from the line search method, see Section 17.2.8

With the help of Eq. (17.57) the graphical representation of the iterative procedure displayed in Fig. 17.8(a) can be put forward in mathematical terms as follows. Suppose you wish to determine $\delta\boldsymbol{r}_j$, in the i-th load increment. Referring to Fig. 17.8(a) we have

$$\delta\boldsymbol{r}_j = \mathcal{K}^{-1}(\boldsymbol{r}_{j-1})\big(\underbrace{\boldsymbol{g}_{j-1} + \delta\lambda_j \boldsymbol{F}}\big) \tag{17.58}$$

$$\underbrace{{}^{s-1}\boldsymbol{F} + \lambda_{j-1}\boldsymbol{F} - \boldsymbol{R}_{j-1}}_{\text{mechanical part of the total applied load}}$$

$$= \underbrace{\mathcal{K}^{-1}(\boldsymbol{r}_{j-1})\boldsymbol{g}_{j-1}}_{\delta\boldsymbol{w}_j} + \delta\lambda_j \underbrace{\mathcal{K}^{-1}(\boldsymbol{r}_{j-1})\boldsymbol{F}}_{\delta\boldsymbol{v}_j}, \tag{17.59}$$

$$\delta\boldsymbol{r}_j = \delta\boldsymbol{w}_j + \delta\lambda_j \delta\boldsymbol{v}_j \implies \Delta\boldsymbol{r}_j = \Delta\boldsymbol{r}_{j-1} + \delta\boldsymbol{r}_j \tag{17.60}$$

Next, set

$$\Delta\lambda_j = \Delta\lambda_{j-1} + \delta\lambda_j \tag{17.61}$$

and introduce Eq. (17.61) into Eq. (17.57) to get

$$\begin{aligned} \Delta L^2 &= \eta^2 \left\{\Delta\boldsymbol{r}_{j-1} + \delta\boldsymbol{w}_j + \delta\lambda_j \delta\boldsymbol{v}_j\right\}^{\mathsf{T}} \left\{\Delta\boldsymbol{r}_{j-1} + \delta\boldsymbol{w}_j + \delta\lambda_j \delta\boldsymbol{v}_j\right\} \\ &+ \beta^2 \left\{\Delta\lambda_{j-1}\boldsymbol{F} + \delta_j \boldsymbol{F}\right\}^{\mathsf{T}} \left\{\Delta\lambda_{j-1}\boldsymbol{F} + \delta_j \boldsymbol{F}\right\} \end{aligned} \tag{17.62}$$

Rearranging the above equation to collect the terms $\delta\lambda_j$ with the same power gives

$$a_2\delta\lambda_j^2 + a_1\delta\lambda_j + a_0 = 0, \tag{17.63}$$

where

$$
\begin{aligned}
a_2 &= \eta^2\delta\boldsymbol{v}_j{}^{\mathsf{T}}\delta\boldsymbol{v}_j + \beta^2\boldsymbol{F}^{\mathsf{T}}\boldsymbol{F} \tag{17.64}\\
a_1 &= \eta^2\underbrace{\left(\{\Delta\boldsymbol{r}_{j-1} + \delta\boldsymbol{w}_j\}{}^{\mathsf{T}}\delta\boldsymbol{v}_j + \delta\boldsymbol{v}_j{}^{\mathsf{T}}\{\Delta\boldsymbol{r}_{j-1} + \delta\boldsymbol{w}_j\}\right)}_{2\delta\boldsymbol{v}_j{}^{\mathsf{T}}\{\Delta\boldsymbol{r}_{j-1} + \delta\boldsymbol{w}_j\}} + 2\Delta\lambda_{j-1}\beta^2\boldsymbol{F}^{\mathsf{T}}\boldsymbol{F} \tag{17.65}\\
a_0 &= \eta^2\{\Delta\boldsymbol{r}_{j-1} + \delta\boldsymbol{w}_j\}{}^{\mathsf{T}}\{\Delta\boldsymbol{r}_{j-1} + \delta\boldsymbol{w}_j\} + \Delta\lambda_{j-1}^2\beta^2\boldsymbol{F}^{\mathsf{T}}\boldsymbol{F} - \Delta L^2 \tag{17.66}
\end{aligned}
$$

Two cases are possible when solving Eq. (17.63) for unknown $\delta\lambda_j$.

- Both roots $\delta\lambda_j^1, \delta\lambda_j^2$ are real, or

- both roots $\delta\lambda_j^1, \delta\lambda_j^2$ are imaginary, see [10].

When the latter possibility occurs, the computation must be restarted with a shorter step ΔL. As for the real roots it is necessary to choose which one to use. The one which maximizes the angle ϑ found from

$$\cos\vartheta = \frac{\Delta\boldsymbol{r}_{j-1}^{\mathsf{T}}\Delta\boldsymbol{r}_j}{\Delta L} \tag{17.67}$$

is typically used. A complete algorithm requires determining a starting value of ΔL_0. The magnitude of ΔL_0 must be either prescribed manually, or depending on the prior history of iterations the value of ΔL found at the end of stage $s-1$ can be used as a initial value of the arc-length step in the stage s or it can be estimated from the prescribed load increment $\Delta\lambda_0$. The latter procedure is presented next. To begin set

$$\delta\lambda_0 = 0 \qquad \delta\boldsymbol{w}_0 = \boldsymbol{0}$$

and write

$$\delta\boldsymbol{r}_0 = \Delta\boldsymbol{r}_0 = \Delta\lambda_0\mathcal{K}^{-1}(\boldsymbol{r}_{start})\boldsymbol{F} \tag{17.68}$$

From Eq. (17.63) it follows that

$$
\begin{aligned}
a_0 &= a_1 = 0\\
a_2 &= \eta^2\underbrace{\overbrace{\Delta\boldsymbol{r}_0{}^{\mathsf{T}}\Delta\boldsymbol{r}_0}^{\Delta\lambda_0\delta\boldsymbol{v}_1}}_{\mathcal{K}^{-1}(\boldsymbol{r}_{start})\boldsymbol{F}} + \Delta\lambda_0^2\beta^2\boldsymbol{F}^{\mathsf{T}}\boldsymbol{F} - \Delta L_0^2 = 0
\end{aligned}
$$

Finally, solving for ΔL_0 from Eq. (17.63) we get

$$\Delta L_0 = \Delta\lambda_0\sqrt{\eta^2\delta\boldsymbol{v}_1{}^{\mathsf{T}}\delta\boldsymbol{v}_1 + \beta^2\boldsymbol{F}^{\mathsf{T}}\boldsymbol{F}} \tag{17.69}$$

The subsequent magnitude of ΔL depends on the history of iteration and may either increase or be reduced if convergence difficulties are encountered.

Several modifications are available depending on the "analysis setting". To this end, the interested reader is refereed to [10]. In addition, it worth pointing out certain drawbacks as well as advantageous when using the Arc-length method in geotechnical engineering.

Drawbacks: recall that the application of Arc-length method requires the load to change proportionally. This means that a load increment or a portion of the total applied load can be written as

$$
\begin{aligned}
\Delta\boldsymbol{F} &= \Delta\lambda\boldsymbol{F}\\
\boldsymbol{F}_j &= \lambda_j\boldsymbol{F}
\end{aligned}
$$

Although in static problems such requirement does not usually cause any trouble, it becomes a severe limitation in the time dependent problems such as consolidation. In particular, this method becomes inappropriate when assigning different time histories to various loads within a single construction stage. Such a task can be satisfactorily solved only with the Newton-Raphson method.

Advantages: the Arc-length method is particularly useful in problems that involve the search for the collapse load as typical of stability problems. Note that in stability problems the load leading to instability is not known a priori.

17.2.7   Convergence criteria

An additional ingredient of the successful implementation of iterative methods are realistic convergence criteria to terminate the iterative process. In particular, at the end of each iteration step, it should be checked whether Eq. (17.51) is satisfied within the preset convergence criteria, e.g., given by

$$\sqrt{\frac{(\Delta \boldsymbol{r}_j)^\mathsf{T} \Delta \boldsymbol{r}_j}{\displaystyle\sum_{m=1}^{j} (\Delta \boldsymbol{r}_m)^\mathsf{T} \Delta \boldsymbol{r}_m}} \quad \leq \quad \epsilon_d, \tag{17.70}$$

$$\sqrt{\frac{(\Delta \boldsymbol{f}_j)^\mathsf{T} \Delta \boldsymbol{f}_j}{(\Delta \boldsymbol{f}_0)^\mathsf{T} \Delta \boldsymbol{f}_0}} \quad \leq \quad \epsilon_f, \tag{17.71}$$

$$\sqrt{\frac{(\Delta \boldsymbol{u}_j)^\mathsf{T} \Delta \boldsymbol{f}_{j-1}}{|\displaystyle\sum_{m=1}^{i} (\Delta \boldsymbol{r}_m)^\mathsf{T} \Delta \boldsymbol{f}_0|}} \quad \leq \quad \epsilon_e, \tag{17.72}$$

where $\epsilon_d, \epsilon_f, \epsilon_e$ are the preset displacement, out-of-balance forces and energy convergence tolerance, respectively. The first criterion naturally requires the displacement at the end of iteration to be found within a certain tolerance, while the second criterion is a measure of the state of equilibrium at the end of the iteration given in terms of out-of-balance forces. The precision can also be measured by the work of out-of-balance forces on the current displacement increment as suggested by the third criterion. This is a rather appealing criterion as it is written in terms of both the displacements and forces. Similar convergence criteria are proposed in [6].

Note that the selection of values for individual tolerances may be crucial for the success of computation. Setting these tolerances to too large values may lead to inaccurate results, while selecting rather small values may result in time consuming iterative process in search for unnecessary accuracy. Also note that there is no guarantee that the process will converge either due to the excessive number of iterations or due to the divergence. Therefore, an appropriate divergence check to terminate the iterative process and then restarting should be built into the solver, so that it is possible to repeat a failed increment with a shorter step.

In particular, the solution is started with some preset increment of the applied load. If the solution diverges or fails to converge for a given number of step iterations, the load increment is reduced and the solution is restarted from the last converged step. The divergence can be checked, e.g., against the out-of-balance forces. If the norm of out-of-balance forces increases in two successive iterations, the iterative process is thought to diverge, the iteration is terminated and the solution is restarted. Similarly, if the number of iterations needed for the convergence is less than a certain preset number, the load increment can be increased to accelerate the solution process. This option, however, should be used with caution. All the mentioned options to control an iterative process are defined in the "analysis settings".

The above criteria apply to standard stress analysis. In flow analysis, for example, the vector $\boldsymbol{r}$ corresponds to values of nodal excess pore pressures and the energy error is not activated.

17.2.8 Line search method

Principal idea behind the line search method is to find a scaling factor η of the current increment of the displacement field Δr_j^i such that the stationarity of the total energy functional is preserved at the end of each iteration step. Suppose that a new displacement r_j^i at the end of the iteration step j is expressed as

$$r_j^i = r_{j-1}^i + \eta \Delta r_j \tag{17.73}$$

Recall Eq. (17.56) in which η is assumed to be equal to one. Next, introducing Eq. (17.73) into the stationary condition of the total potential energy at the end of the j-th step gives

$$\delta \Pi(r_j^i(\eta)) = \delta \Pi(r_{j-1}^i + \eta \Delta r_j) = \frac{\partial \Pi(r_j^i(\eta))}{\partial r_j^i(\eta)} \frac{\partial r_j^i}{\partial \eta} \delta \eta = 0 \tag{17.74}$$

Because

$$\frac{\partial \Pi(r_j^i(\eta))}{\partial r_j^i(\eta)} = \Delta f_j(\eta) \tag{17.75}$$

$$\frac{\partial r_j^i}{\partial \eta} = \Delta r_j \tag{17.76}$$

we get

$$\delta \Pi(r_j^i(\eta)) = \Delta f_j(\eta) \Delta r_j \delta \eta = 0 \tag{17.77}$$

Thus the stationary condition (17.74) corresponds to the condition of zero work of out-of-balance forces on the displacement increment Δr_j. Eq. (17.77) does not need to be solved exactly. An estimate of
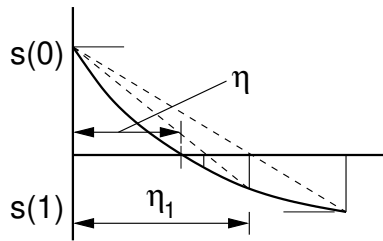

Figure 17.10: Line search method

the scaling parameter η can be found from a simple linear interpolation as displayed in Fig. 17.10. The first estimate of η is then provided by

$$\eta_1 = \frac{-s(0)}{s(1) - s(0)} \tag{17.78}$$

A recursive application of Eq. (17.78) then leads to a more accurate value of η, see Fig. 17.10,

$$\eta_{k+1} = \eta_k \frac{-s(0)}{s(i) - s(0)} \tag{17.79}$$

The iterations in Eq. (17.79) are usually terminated when the ratio

$$\frac{|s_{k+1}|}{|s_0|} < 0.8,$$

is reached. Clearly, the line search method can either dampen ($\eta < 1$) or accelerate ($\eta > 1$) the speed of the analysis. The latter option, however, is not recommended. Details can be found in [20]. By default, the GEO5 FEM software locates the scaling parameter according to Eq. (17.78) .

17.2.9   Stress return mapping

Chapters devoted to individual models describe procedures that allow us to maintain the stress point either below or on the yield surface formulated in the general stress space $\boldsymbol{\sigma}$ as

$$f(\boldsymbol{\sigma}, \boldsymbol{\kappa}) \leq 0 \tag{17.80}$$

where $\boldsymbol{\kappa}$ represents certain parameters which drive evolution of the yield surface (either expansion or contraction) with the evolution of plastic strains. The yield surface is thus a boundary between elastic and plastic response.
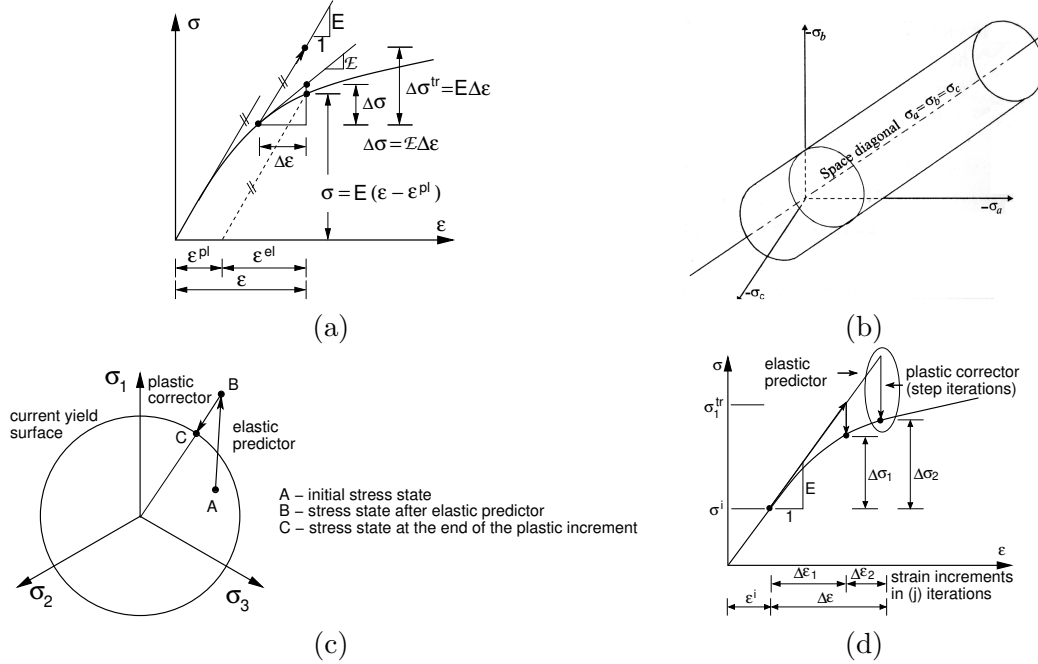

Figure 17.11: Stress return mapping: a) stress-strain law, b) von Mises yield surface in principal stress space, c) elastic predictor - plastic corrector steps presented in deviatoric, d) iteration process at material point

As an example we may consider the most simple von Mises yield criterion plotted in Fig. 17.11(b,c). For points located on the yield surface the constitutive law (1.40) modifies as

$$\boldsymbol{\sigma} = \mathbf{D}(\boldsymbol{\varepsilon} - \boldsymbol{\varepsilon}^{pl}) \tag{17.81}$$

where $\boldsymbol{\varepsilon}^{pl}$ is an accumulated plastic strain, see Fig. 17.11(a). Calculation of plastic strain is usually carried out following standard elastic predictor - plastic corrector approach as evident in Fig. 17.11(c). We see that after completing the elastic step we arrive at a state of stress lying outside the yield surface. Note that the circle represents projection of the von Mises yield surface into a deviatoric plane. Such a stress state is not admissible and the plastic corrector step has to be applied to bring the stress back to the yield surface. This step in general may call for the solution of a nonlinear problem constructed at a material point. In Fig. 17.11(d) this step is hidden within the bubble. Mathematically, we may write the stress at the end of the $i + 1$ load increment and j-th iteration performed at a structural level, recall Fig. 17.7, as

$$\boldsymbol{\sigma}_j^{i+1} = \boldsymbol{\sigma}^i + \Delta\boldsymbol{\sigma}_j = \boldsymbol{\sigma}^i + \mathbf{D}\sum\Delta\boldsymbol{\varepsilon}_j - \mathbf{D}\Delta\boldsymbol{\varepsilon}_j^{pl} = \boldsymbol{\sigma}^{tr} - \mathbf{D}\Delta\boldsymbol{\varepsilon}_j^{pl} \tag{17.82}$$

where $\boldsymbol{\sigma}^i$ satisfies equilibrium condition (17.51), $\boldsymbol{\sigma}^{tr}$ is called the trial stress derived at the end of the elastic predictor step associated with the j-th iteration and $\Delta\boldsymbol{\varepsilon}_j^{pl}$ is the corresponding plastic strain increment to be predicted via the plastic corrector step. This procedure is presented for individual material models in subsequent chapters. This step also drives the calculation of the algorithmic tangent stiffness matrix $\boldsymbol{\mathcal{K}}_j^{i+1}$.

17.3 Earthquake analysis

The previous section described some of the solution strategies associated with the analysis of a general nonlinear problem while limiting attention to a static loading. However, modeling the response of a structure subjected to earthquake requires introduction of inertia forces and more advanced boundary conditions. This topic is addressed next (Section 17.3.1) providing also the basic theoretical grounds to the solution of an eigenvalue problem (Section 17.3.2), generation of artificial accelerograms (Section 17.3.3), and formulation of a material damping (Section 17.3.4). The entire solution process is finally summarized in Section 17.3.5.

17.3.1 Governing equations of finite element method accounting for seismic events

The basic equation describing the vibration of a discrete system with N degrees of freedom written as, compare with Eq. $(17.6)_1$,

$$\mathsf{M}\ddot{r}(t) + \mathsf{C}\dot{r}(t) + \mathsf{K}r(t) = \boldsymbol{F}(t) \tag{17.83}$$

Equation (17.83) represents a system of N second order differential equations of motion, where $\dot{r} = \dfrac{\mathrm{d}r}{\mathrm{d}t}$ and $\ddot{r} = \dfrac{\mathrm{d}^2 r}{\mathrm{d}t^2}$ represent the velocity and acceleration in the direction of the i-th degree of freedom $(i = 1, \ldots, N)$. In the framework of the finite element method (FEM), the $N \times 1$ vector $\boldsymbol{r}$ stores the components of unknown nodal displacements. The $N \times N$ matrices M, C and K stand for the mass, damping and stiffness matrix, respectively. The $N \times 1$ vector $\boldsymbol{F}$ stores the nodal components of the external actions.

Henceforth, we limit attention to seismic actions caused by earthquake in the form of prescribed acceleration of underground longitudinal (pressure P) and transverse (shear S) waves. It is assumed that these waves travel from the bottom boundary of the FEM model towards the terrain surface. The resulting acceleration field in space and time $\ddot{\boldsymbol{u}}(\boldsymbol{x}, t)$[1] can be conveniently expressed as a sum of the acceleration prescribed to all nodes of the numerical model $\overline{\boldsymbol{a}}(t)$ and a component $\ddot{\boldsymbol{u}}_R(\boldsymbol{x}, t)$ relative to $\overline{\boldsymbol{a}}(t)$ as

$$\ddot{\boldsymbol{u}}(\boldsymbol{x}, t) = \overline{\boldsymbol{a}}(t) + \ddot{\boldsymbol{u}}_R(\boldsymbol{x}, t) \tag{17.84}$$

How to introduce $\overline{\boldsymbol{a}}(t)$ into analysis

The overall displacement at an arbitrary point of the model is equal to the sum of the displacement u_u corresponding to a wave traveling upwards and the displacements u_d associated with a wave traveling downwards

$$\boldsymbol{u}(\boldsymbol{x}, t) = \boldsymbol{u}_u(\boldsymbol{x}, t) + \boldsymbol{u}_d(\boldsymbol{x}, t) \tag{17.85}$$

The seismic motion is typically monitored on the free surface. Such a motion is denoted as the *outcrop motion*, see Fig. 17.12. To correctly predict the acceleration measured on the terrain (target motion) requires the acceleration $\overline{\boldsymbol{a}}(t)$, prescribed on the bottom boundary, be suitably adjusted to the recover the corresponding outcrop motion for given types of layers representing the subsoil.

Considering the monitoring point m_1 and the bottom boundary in the bedrock (point a_1) or at the soil-bedrock interface (point a_2) would probably allow us to assume $\overline{\boldsymbol{a}}_{1,2} \approx \ddot{\boldsymbol{u}}_1$.[2] Providing the bottom boundary is located at points b_1 a b_2, the value of displacement $\boldsymbol{u}_{b1,2}$ may considerably differ from both $\boldsymbol{u}_1$ and $\boldsymbol{u}_2$, i.e. $\overline{\boldsymbol{a}}_{b1,2} \neq \ddot{\boldsymbol{u}}_{1,2}$. For point m_2 one may even expect $\overline{\boldsymbol{a}}_{a1,2} \neq \ddot{\boldsymbol{u}}_2$. To correctly adjust the prescribed acceleration $\overline{\boldsymbol{a}}(t)$ so that the predicted motion approximates the target motion with sufficient accuracy, it is possible to employ the SHAKE software [71]. Further details are available in [55].

---

[1] In the case of 2D analysis the vector $\boldsymbol{u} = \{u, v\}$ represents displacements in the direction of coordinate axes x, y.

[2] The speed of a seismic wave is proportional to the stiffness of a soil/rock layer through which it propagates. In the rock layer the wave velocity can be of the order of magnitude higher in comparison to the soft soil layer.
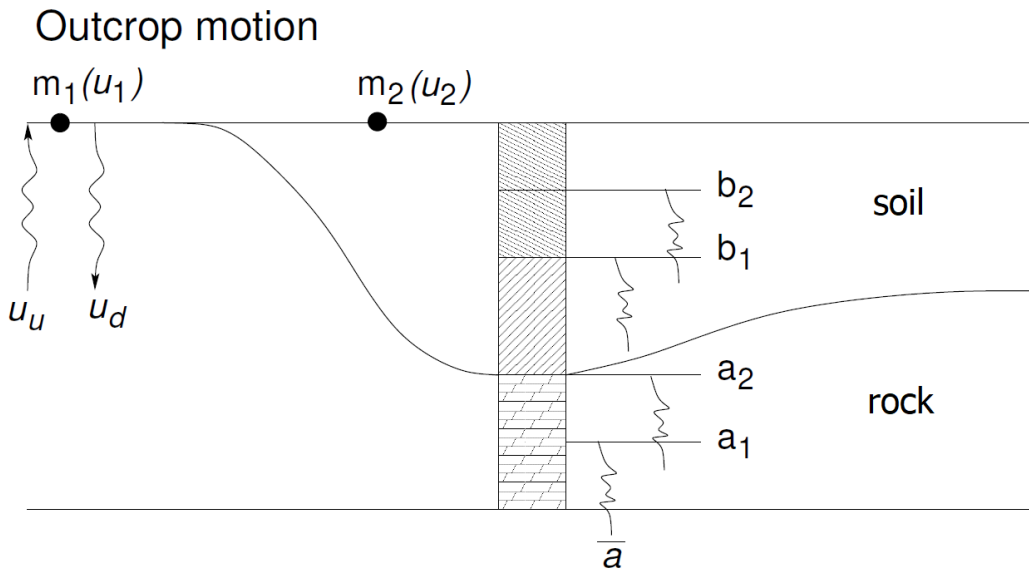
Outcrop motion

$m_1(u_1)$ $m_2(u_2)$

Figure 17.12: Prescribing acceleration

Definition of boundary conditions on model bottom boundary

Given the fact that on free surface the amplitude of the upcoming wave equals the one of the reflected wave allows us to write the overall displacement on the terrain surface as twice the displacement of the upcoming wave $\boldsymbol{u}(\boldsymbol{x},t) = 2\boldsymbol{u}_u(\boldsymbol{x},t)$. For a general point within a soil body one may adopt Eq. (17.85). If limiting attention to the bottom boundary this equation receives the form

$$\boldsymbol{u}(\boldsymbol{x},t)|_{\boldsymbol{x}=\boldsymbol{x}_{BB}} = \boldsymbol{u}_I(\boldsymbol{x},t)|_{\boldsymbol{x}=\boldsymbol{x}_{BB}} + \boldsymbol{u}_O(\boldsymbol{x},t)|_{\boldsymbol{x}=\boldsymbol{x}_{BB}} \tag{17.86}$$

where BB denotes the bottom boundary of the numerical model, $\boldsymbol{u}_I$ and $\boldsymbol{u}_O$ represent the incoming wave (wave entering the model) and outgoing wave (wave leaving the model), respectively.

The above relations will be now exploited to define the prescribed acceleration $\overline{\boldsymbol{a}}$ depending on the choice of the boundary conditions specified on the bottom boundary of the numerical model. The GEO5 FEM program allows the user to define two types of boundary conditions, i.e., fixed and absorbing (quiet) boundary conditions.
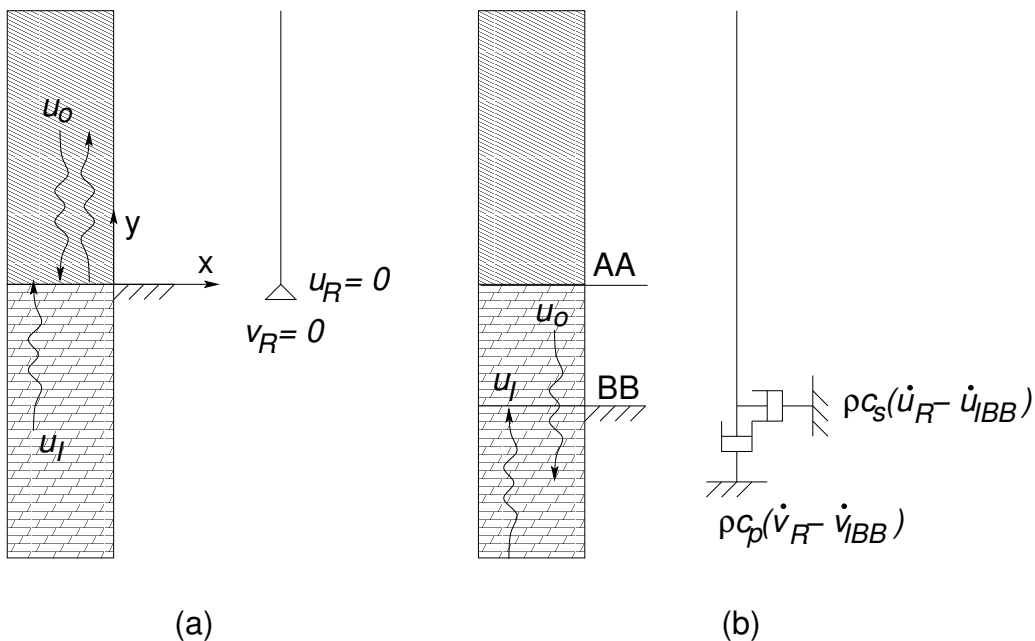

Figure 17.13: a) Fixed (kinematic) boundary conditions, b) Absorbing (traction) boundary conditions

Fixed boundary conditions

The fixed boundary condition can be safely used only in the case when the bottom boundary is found at soft soil/stiff rock interface. Then the incoming wave is "fully" reflected back into the model. Taking into account Eqns. (17.86) and (17.84) gives

$$\boldsymbol{u}(\boldsymbol{x}, t) = \boldsymbol{u}(t)|_{\boldsymbol{x}=\boldsymbol{x}_{BB}} + \boldsymbol{u}_R(\boldsymbol{x}, t), \quad \boldsymbol{u}_R(\boldsymbol{x} = \boldsymbol{x_{BB}}, t) = 0, \quad \bar{a}(t) = \ddot{\boldsymbol{u}}(t)_{\boldsymbol{x}=\boldsymbol{x}_{BB}} \tag{17.87}$$

As evident from Fig. 17.13(a) the value of a relative displacement at the bottom boundary BB is equal to zero. Therefore, the fixed boundary conditions are prescribed along this boundary. The magnitude of the prescribed acceleration $\bar{a}$ thus corresponds to the total motion at BB given by Eq. (17.85). Recall that for the monitoring point m_1 and the bottom boundary located at point a_2 in Fig. 17.12 it is possible to consider the *outcrop motion* as the prescribed motion, i.e., $\bar{a} \approx \ddot{\boldsymbol{u}}_1$.

Absorbing boundary conditions

Consider Fig. 17.13(b) with the bottom boundary within a layer below the AA interface. In accord with Eqns. (17.85) and (17.84) the value of the displacement at an arbitrary point of the layer bounded by the AA and BB interfaces is given by

$$\boldsymbol{u}(\boldsymbol{x}, t) = \boldsymbol{u}_I(\boldsymbol{x}, t) + \boldsymbol{u}_O(\boldsymbol{x}, t) = \boldsymbol{u}_{IBB}(t) + \boldsymbol{u}_R(\boldsymbol{x}, t) \tag{17.88}$$

where $\boldsymbol{u}_{IBB}$ represents the incoming wave at the bottom boundary BB. Because this interface is found within a homogeneous layer the outgoing wave must freely pass this interface. The theoretical model assumes an infinite half-space below this interface. Therefore, the outgoing wave will never return and must be on the BB boundary fully damped. The outgoing wave $\boldsymbol{u}_O$

$$\boldsymbol{u}_O(\boldsymbol{x}, t) = \boldsymbol{u}_{IBB}(t) + \boldsymbol{u}_R(\boldsymbol{x}, t) - \boldsymbol{u}_I(\boldsymbol{x}, t) \tag{17.89}$$

satisfies on the BB boundary the radiation condition

$$\left\{ \begin{array}{c} \dfrac{\partial u_O(\boldsymbol{x}, t)}{\partial x} \\ \dfrac{\partial v_O(\boldsymbol{x}, t)}{\partial y} \end{array} \right\}_{\boldsymbol{x}=\boldsymbol{x}_{BB}} = \left[\begin{array}{cc} \dfrac{1}{c_s} & 0 \\ 0 & \dfrac{1}{c_p} \end{array} \right] \left\{ \begin{array}{c} \dfrac{\mathrm{d}u_O(\boldsymbol{x}, t)}{\mathrm{d}t} \\ \dfrac{\mathrm{d}v_O(\boldsymbol{x}, t)}{\mathrm{d}t} \end{array} \right\}_{\boldsymbol{x}=\boldsymbol{x}_{BB}} \tag{17.90}$$

where c_p a c_s represent the velocities of the propagating P and S waves and are provided by

$$c_p = \sqrt{\dfrac{E_{oed}}{\rho}}, \quad c_s = \sqrt{\dfrac{G}{\rho}} \tag{17.91}$$

where ρ, E_{oed}, G are the density, the oedometric modulus and the shear modulus of a given subsoil layer. With reference to Eqns. (17.88) and (17.84) it is, however, necessary to express condition (17.90) in terms of a relative displacement $\boldsymbol{u}_R$. Approach described in [86] introduces a static boundary condition in the form

$$\left\{ \begin{array}{c} \bar{p}_x = \tau_{xy} \\ \bar{p}_y = \sigma_y \end{array} \right\}_{\boldsymbol{x}=\boldsymbol{x}_{BB}} = \left[\begin{array}{cc} G & 0 \\ 0 & E_{oed} \end{array} \right] \left\{ \begin{array}{c} \dfrac{\partial u_R(\boldsymbol{x}, t)}{\partial x} \\ \dfrac{\partial v_R(\boldsymbol{x}, t)}{\partial y} \end{array} \right\}_{\boldsymbol{x}=\boldsymbol{x}_{BB}}$$

$$= \left[\begin{array}{cc} \rho c_s & 0 \\ 0 & \rho c_p \end{array} \right] \left\{ \begin{array}{c} \dfrac{\mathrm{d}u_R(\boldsymbol{x}, t)}{\mathrm{d}t} - \dfrac{\mathrm{d}u_{IBB}(t)}{\mathrm{d}t} \\ \dfrac{\mathrm{d}v_R(\boldsymbol{x}, t)}{\mathrm{d}t} - \dfrac{\mathrm{d}v_{IBB}(t)}{\mathrm{d}t} \end{array} \right\}_{\boldsymbol{x}=\boldsymbol{x}_{BB}} \tag{17.92}$$

A graphical representation of this conditions is seen in Fig. 17.13(b) as a dashpot with the viscosity ρc_s and ρc_p, respectively. Given Eqns. (17.88) and (17.84) the prescribed acceleration reads

$$\bar{a}(t) = \ddot{\boldsymbol{u}}_{IBB}(t) \tag{17.93}$$

Thus if limiting attention to the monitoring point m_1 in Fig. 17.12 and the bottom boundary at point a_1 it appears possible to consider the prescribed acceleration to the half of the *outcrop motion*, i.e., $\overline{a} \approx \frac{1}{2}\ddot{u}_1$. It is also worth noting that the definition of absorbing boundary conditions assumes that the layer immediately above the BB boundary behaves linearly elastic. Therefore, the nonlinear response should be allowed for the top layers only.
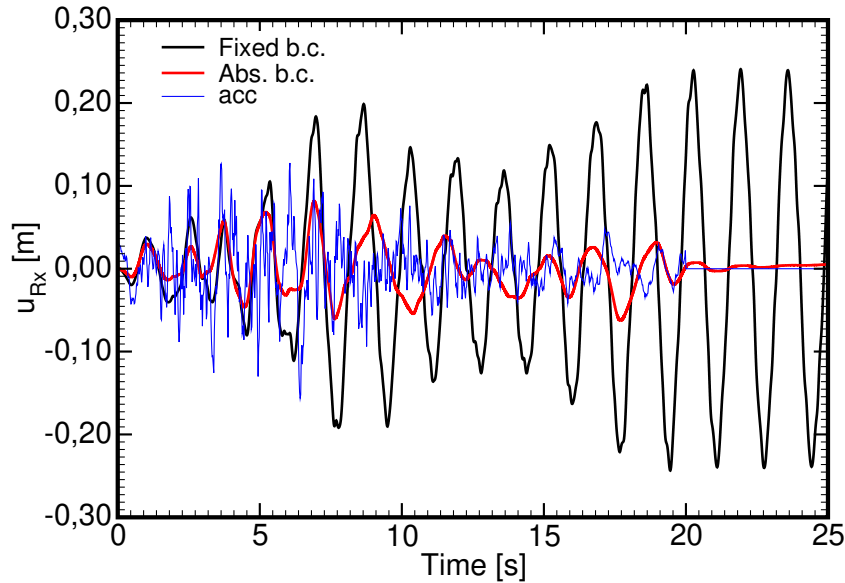

Figure 17.14: Comparing response of homogeneous layer generated by fixed and absorbing boundary conditions

For illustration, we compare in Fig. 17.14 the response of a homogeneous 50 m thick layer with either fixed or absorbing boundary conditions subjected to the prescribed horizontal acceleration. Clearly, when the fixed boundary conditions are used the outgoing wave is trapped in the model. Thus for and undamped system the vibration will continue infinitely long. On the other hand, the absorbing boundary will damp the outgoing wave and once the prescribed acceleration ceases, the vibration gradually stops. Further details regarding the influence of boundary conditions on the subsoil response can be found in [61, 62].

Definition of boundary conditions along lateral boundaries

Suppose that both geometrical and material properties of the subsoil do not change in the horizontal direction, see Fig. 17.15. The response of such a system to the prescribed seismic action will be the same along any vertical section. This corresponds to so called Free field conditions. Such a task can be solved with the help of a one-dimensional (1D) *Free field column* (FF) model.
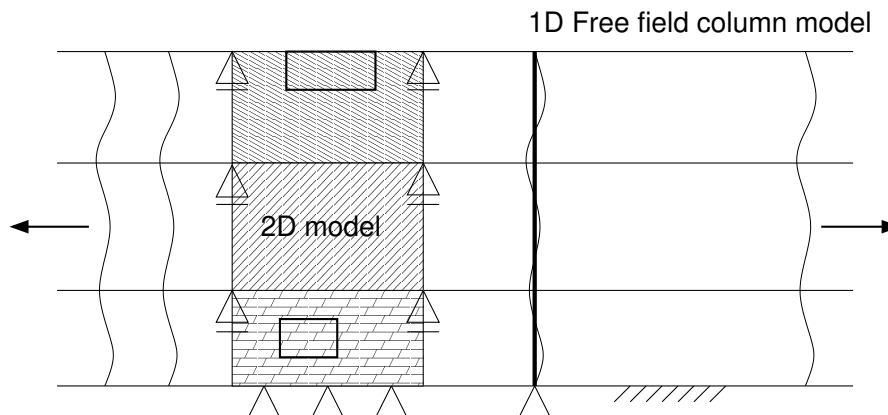

Figure 17.15: 2D infinite strip of subsoil and 1D Free field model

Solving such a task using a two-dimensional (2D) model truncated in the horizontal direction by lateral boundaries (LB), see Fig. 17.15, calls for introducing suitable boundary conditions along these boundaries to force the response predicted by the 2D model be identical to that of the 1DFF model. In a special case of horizontal motion generating S waves only, the use of standard kinematic conditions in Fig. 17.15 would be sufficient. However, this is no longer possible when the P and S waves interact. In this general case, the static (traction) boundary condition in terms of the prescribed vertical tractions corresponding to the shear stress τ_{xy}^{FF} provided by the 1DFF analysis proved useful, see Fig. 17.16.
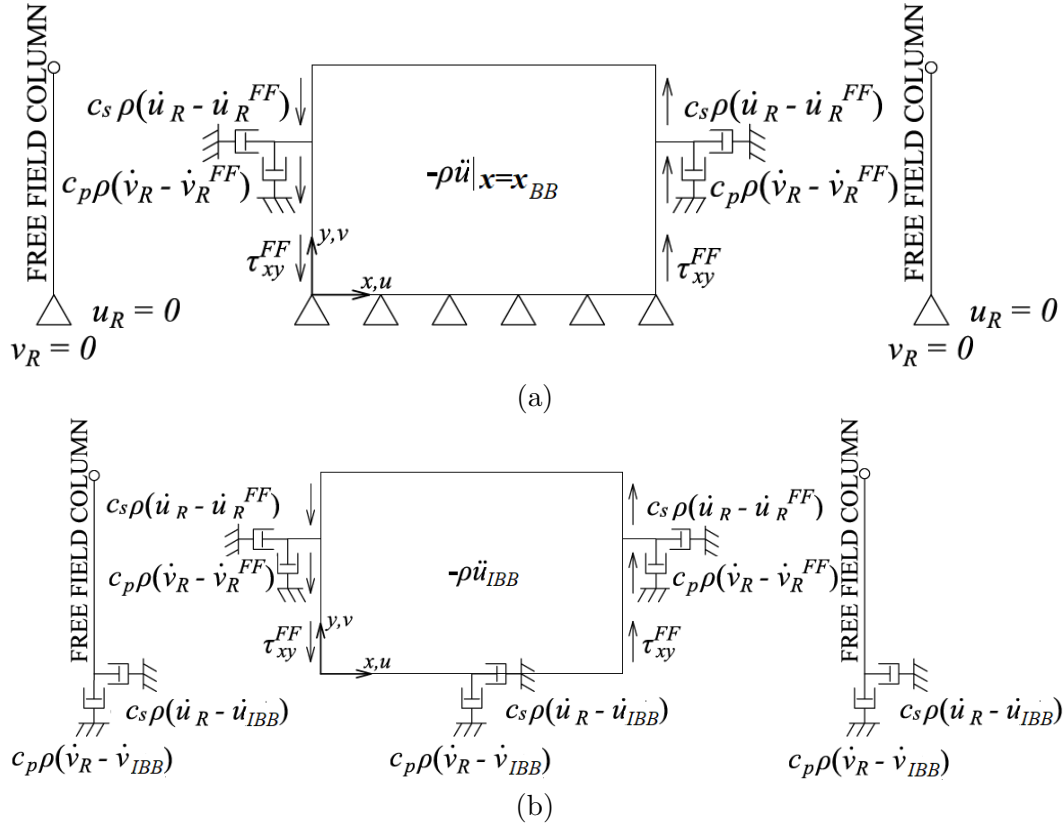

Figure 17.16: Boundary conditions on lateral boundaries assuming a) fixed and b) absorbing boundary conditions on bottom boundary. 1D Free field column model and 2D model

Providing the Free field conditions are disturbed due to, e.g., excavation (Fig. 17.15), the part of the motion, corresponding to the difference between the real incoming wave and the one produced by the FF analysis, will have to be damped. This is achieved similarly to the absorbing boundary conditions on the BB boundary (Section 17.3.1) by introducing radiation (static) boundary conditions as displayed in Fig. 17.16[3]. For more details the interested reader is referred to [86]. A detailed study of the influence of boundary conditions prescribed on lateral boundaries is discussed in [61].

Assuming the fixed boundary conditions and a 2D analysis, Fig. 17.16(a), yields the resulting form of Eq. (17.83) as

$$\mathbf{M}\ddot{u}_R + \mathbf{C}^M \dot{u}_R + \boldsymbol{K} u_R + \mathbf{C}^{LB} \dot{u}_R|_{x=0,L}$$
$$= -\mathbf{M}\ddot{u}_0 - \mathbf{C}^M \dot{u}_0 + \mathbf{C}^{LB} \dot{u}_R^{FF}|_{x=0,L} - \boldsymbol{R}_\tau|_{x=0} + \boldsymbol{R}_\tau|_{x=L} \tag{17.94}$$

where $\boldsymbol{u}_0 = \boldsymbol{u}(\boldsymbol{x_{BB}})$. For absorbing boundary conditions, Fig. 17.16(b), we get

$$\mathbf{M}\ddot{u}_R + \mathbf{C}^M \dot{u}_R + \boldsymbol{K} u_R + \mathbf{C}^{BB} \dot{u}_R|_{y=0} + \mathbf{C}^{LB} \dot{u}_R|_{x=0,L}$$
$$= -\mathbf{M}\ddot{u}_{IBB} - \mathbf{C}^M \dot{u}_{IBB} + \mathbf{C}^{BB} \dot{u}_{IBB}|_{y=0} + \mathbf{C}^{LB} \dot{u}_R^{FF}|_{x=0,L} - \boldsymbol{R}_\tau|_{x=0} + \boldsymbol{R}_\tau|_{x=L} \tag{17.95}$$

The damping matrix will thus split into the contribution due to material damping ($\mathbf{C}^M$) and the influence of absorbing boundary conditions along the BB ($\mathbf{C}^{BB}$) and LB ($\mathbf{C}^{LB}$) boundaries, respectively.

---

[3]Waves approaching the LB boundary in a certain angle not equal to $90°$ will be damped only partially.

The load vector $\boldsymbol{F}(t)$ corresponds to the action of inertia forces, the first term on the right hand side of Eqns. (17.94) and (17.95).

Direct integration of equations of motion

To determine unknown displacements $\boldsymbol{r}$ requires integrating Eq. (17.83) in time[4]. The GEO5 FEM program employs the implicit Newmark method, which gives the following relationship between displacements, velocities, and accelerations at $i+1$ integration step ($i+1$ load increment in static analysis assumed in Section 17.1) providing they are known at step i [11, 37]

$$
\begin{aligned}
\boldsymbol{r}^{i+1} &= \boldsymbol{r}^i + \Delta t\dot{\boldsymbol{r}}^i + \frac{\Delta t^2}{2}\left[(1-2\beta)\ddot{\boldsymbol{r}}^i + 2\beta\ddot{\boldsymbol{r}}^{i+1}\right] & (17.96) \\
\dot{\boldsymbol{r}}^{i+1} &= \dot{\boldsymbol{r}}^i + \Delta t\left[(1-\gamma)\ddot{\boldsymbol{r}}^i + \gamma\ddot{\boldsymbol{r}}^{i+1}\right] & (17.97)
\end{aligned}
$$

where Δt represents the time step and β, γ the method parameters to specify the displacement and velocity vectors, respectively. In light of standard incremental solution in static analysis we modify Eqns.(17.96) and (17.97) by introducing the increment of the displacement vector $\Delta\boldsymbol{r} = \boldsymbol{r}^{i+1} - \boldsymbol{r}^i$ as

$$
\begin{aligned}
\ddot{\boldsymbol{r}}^{i+1} &= b_1\Delta\boldsymbol{r} - b_2\dot{\boldsymbol{r}}^i - b_3\ddot{\boldsymbol{r}}^i & (17.98) \\
\dot{\boldsymbol{r}}^{i+1} &= b_4\Delta\boldsymbol{r} - b_5\dot{\boldsymbol{r}}^i - b_6\ddot{\boldsymbol{r}}^i & (17.99) \\
\boldsymbol{r}^{i+1} &= \boldsymbol{r}^i + \Delta\boldsymbol{r} & (17.100)
\end{aligned}
$$

where parameters $b_1 - b_6$ are provided by

$$
\begin{aligned}
b_1 &= \frac{1}{\beta\Delta t^2}, & b_2 &= \frac{1}{\beta\Delta t}, & b_3 &= \frac{1-2\beta}{2\beta}, \\
b_4 &= \frac{\gamma}{\beta\Delta t}, & b_5 &= \frac{\gamma}{\beta} - 1, & b_3 &= \frac{\gamma-2\beta}{2\beta}\Delta y
\end{aligned}
\tag{17.101}
$$

Adopting the above equations renders the incremental form of Eq. (17.83)

$$
(b_1\mathsf{M} + b_4\mathsf{C} + \mathsf{K}_j)\,\Delta\boldsymbol{r} = \boldsymbol{F}^{i+1} + (b_2\mathsf{M} + b_5\mathsf{C})\,\dot{\boldsymbol{r}}^i + (b_3\mathsf{M} + b_6\mathsf{C})\,\ddot{\boldsymbol{r}}^i - \boldsymbol{R}_j \tag{17.102}
$$

where $\boldsymbol{F}^{i+1}$ represents the loading at $i+1$ integration step and $\boldsymbol{R}_j\,(\boldsymbol{R}_0 = \boldsymbol{R}^i)$ is the vector of internal nodal forces in the j-th iteration of a given step. The parameters β, γ can be chosen such that the method is stable. Providing the stability does not depend on the size of Δt the method is *unconditionally* stable. It then holds [37]

$$
2\beta \le \gamma \le \frac{1}{2} \tag{17.103}
$$

One of the most widely used methods is the *average acceleration method* obtained by setting

$$
\beta = \frac{1}{4}, \quad \gamma = \frac{1}{2} \tag{17.104}
$$

This setting is also generally recommended.

Apart from stability, one should also be concerned with the accuracy of integration. In [37] two specific accuracy measures are introduced to address numerical dissipation and dispersion. The measure of numerical dissipation is the algorithmic damping ratio $\bar{\xi} = \xi + \text{AD}$ and the measure of dispersion is the relative period error $RPE = (\overline{\text{T}} - \text{T})/\text{T}$. The parameter ξ is the material damping ratio, see Section 17.3.4), AD represents the amplitude decay attributed to the selected numerical integration scheme, T is the real period of vibration and $\overline{\text{T}}$ is the period associated with the discrete system. Providing $\gamma = 0.5$, we get AD=0. In such a case, the amplitude decay, if not assuming the absorbing boundary conditions, will be caused by the material damping only (the matrix C^{M}, e.g., in Eq. (17.94)) driven by the value of ξ.

---

[4]In GEO5 FEM we solve Eq. (17.94) or (17.95) for unknown displacements $\boldsymbol{u}_R$.

However, in the solution of a discrete system it is often desirable to have AD $\neq 0$ to filter out high-frequency modes, which are artifacts of the discretization into finite elements, while keeping good accuracy in the load modes. To that end, the algorithm introduced in [28] and termed the α-method deserves particular attention. This method modifies the original Eq. (17.102) as

$$[b_1\mathbf{M} + (1+\alpha)b_4\mathbf{C} + (1+\alpha)\mathbf{K}_j]\,\Delta\boldsymbol{r} = \tag{17.105}$$
$$\boldsymbol{F}^{i+1} + [b_2\mathbf{M} + ((1+\alpha)b_5 + \alpha)\,\mathbf{C}]\,\dot{\boldsymbol{r}}^i + [b_3\mathbf{M} + (1+\alpha)b_6\mathbf{C}]\,\ddot{\boldsymbol{r}}^i - \boldsymbol{R}_j$$

where $t^{i+\alpha} = t^{i+1} + \alpha\Delta t$. For $\alpha = 0$ we recover Eq. (17.102). The method to be unconditionally stable and second order accurate requires

$$\alpha \in \left[-\frac{1}{3}, 0\right], \quad \beta = \frac{1-\alpha^2}{4}, \quad \gamma = \frac{1-2\alpha}{2} \tag{17.106}$$

Clearly, increasing α decreases the amount of numerical damping. For $\alpha = 0$ we get $\gamma = \frac{1}{2}$, i.e. AD=0.

Both the average acceleration method and α-method are unconditionally stable. The selected integration time step thus determines the accuracy, or vice versa. To a large extent, this is affected by material properties and the type of finite element mesh (type and size of the element, local mesh refinement). Thus in general settings, to define an optimal time step is not an easy task.

For conditionally stable Newmark method ($\gamma \leq \frac{1}{2}$, $\beta \leq \gamma$), the time step Δt must comply with the following condition [37]

$$\Delta t \leq \Delta t_{crit}, \quad \Delta t_{crit} = \frac{\Omega_{crit}}{\omega_{eq}} \tag{17.107}$$

$$\Omega_{crit} = \frac{\xi\left(\gamma - \frac{1}{2}\right) + \left[\frac{\gamma}{2} - \beta + \xi^2\left(\gamma - \frac{1}{2}\right)^2\right]^{\frac{1}{2}}}{\frac{\gamma}{2} - \beta} \tag{17.108}$$

where Ω_{crit} is the critical sampling frequency and ω_{eq} is the maximum natural frequency of the discrete system, which can be bounded by the maximum frequency of individual elements[5]. Perhaps the most widely used unconditionally stable Newmark method is the *central difference scheme* ($\beta = 0$, $\gamma = \frac{1}{2}$ and for $\xi = 0$ is $\Omega_{crit} = 2$). For the diagonal mass and damping matrices, this method is explicit. To minimize the period error it is recommended to combine the diagonal mass matrix (lumped mass matrix) with the central scheme, while the consistent mass matrix should be used with the average acceleration method [37]. Because the GEO5 FEM program assumes the consistent mass matrix for all types of elements, the use of central difference scheme is not recommended.

The list of Δt_{crit} for the 1D linear and quadratic rod elements considering both the lumped and consistent mass matrices is available, e.g. in [37]. Further examples can be found in [7].

To conclude, point out that in the case of earthquake the maximum time step depends on the acceleration record, which in general assumes sampling in the interval of $\Delta t \in [0.005, 0.01]$ s.

17.3.2 Solution of eigenvalue problem

The GEO5 FEM program allows for the determination of eigenvalues (natural frequencies) and eigenvectors (mode shapes) of a discrete problem by solving the generalized eigenvalue problem of an undamped system in the form

$$(\mathbf{M} - \lambda_\alpha\mathbf{K})\,\phi_\alpha = \mathbf{0}, \quad \lambda_\alpha = \omega_\alpha^2 \tag{17.109}$$

where ϕ_α is the eigenvector associated with the eigenvalue λ (natural frequency ω_α). During analysis, the eigenvectors are normalized with respect to the mass matrix as

$$\overline{\phi}_\alpha = \frac{\phi_\alpha}{\left[\phi_\alpha^\mathsf{T}\mathbf{M}\phi_\alpha\right]^{\frac{1}{2}}} \qquad \text{unit} \left[\frac{1}{\sqrt{t}}\right] \tag{17.110}$$

---

[5]It is seen that for $\gamma = \frac{1}{2}$, the viscous damping has no effect on stability.

For the sake of visual presentation, the eigenvectors are further scaled by the maximum total nodal displacement (k-node number, Nn-total number of nodes) as

$$\overline{\overline{\phi}}_\alpha = \frac{\overline{\phi}_\alpha}{A_\alpha^{max}} \ [-], \qquad A_\alpha^{max} = \max_{k=1}^{Nn} \left(\sqrt{(\phi_{\alpha,k}^x)^2 + (\phi_{\alpha,k}^y)^2} \right) \tag{17.111}$$

The GEO5 FEM program solves Eq. (17.109) for the selected number of the lowest eigenvalues using standard method of subspace iteration [11, 37, 10]. To solve this task one may choose either the Jacobi method or the Gram Schmidt orthogonalization method. In each iteration step, the Jacobi method solves the reduced eigenvalue problem. This analysis is, however, very effective and the total number of required global iterations is typically less than when using the Gram Schmidt orthogonalization method. However, the Jacobi method does not guarantee that the first K eigenvalues will always be found.
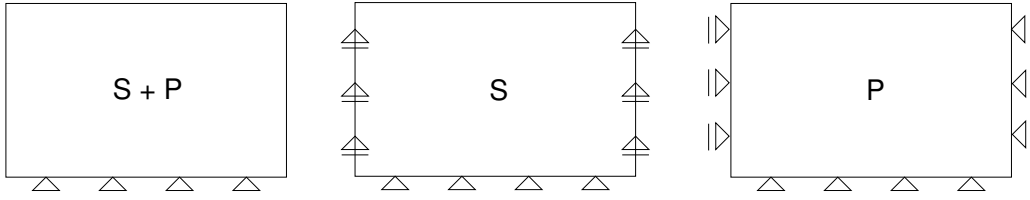

Figure 17.17: Kinematic boundary conditions available for solving the eigenvalue problem

When solving the eigenvalue problem the GEO5 FEM program allows the user to consider three types of kinematic boundary conditions, see Fig. 17.17. The first case (S+P) does not account for a specific vibration mode. On the contrary, the second and the third option makes preference of a horizontal (S) and vertical (P) vibration mode, respectively. Nevertheless, it is recommended to make a visual check prior to selecting the desired vibration mode, e.g., for the calculation of parameters of material damping described in Section 17.3.4. An additional hint for choosing the vibration mode might the *Modal participation factor* and *Modal effective mass*.

Modal participation factor

We limit our attention to 2D plane-strain analysis with no account for rotational degrees of freedom. The modal participation factor $\Gamma_{\alpha,i}$ for mode α in the direction ($i \equiv x$ or $i \equiv y$) is given by

$$\Gamma_{\alpha,i} = \frac{\{\overline{\phi}_\alpha\}^\mathsf{T} [\mathsf{M}] \{I_i\}}{m_\alpha} \qquad \text{unit } \left[\sqrt{t}\right] \tag{17.112}$$

and indicates how strongly the motion in the direction of the coordinate axis x, y is represented in the eigenvector $\{\phi_\alpha\}$. The vector $\{I_i\}$ is the influence vector associated with either the horizontal ($i \equiv x, \{I_x\}^\mathsf{T} = \{1, 0, 1, 0, \ldots, 1, 0\}$) or vertical ($i \equiv y, \{I_y\}^\mathsf{T} = \{0, 1, 0, 1, \ldots, 0, 1\}$) component of the vibration. The generalized mass m_α is written as

$$m_\alpha = \{\overline{\phi}_\alpha\}^\mathsf{T} [\mathsf{M}] \{\overline{\phi}_\alpha\} \ [-] \tag{17.113}$$

Because the eigenvectors in GEO5 FEM are normalized with respect to the mass matrix, we get $m_\alpha = 1$.

Modal effective mass

Another parameter representing participation of a given eigenvector in either horizontal or vertical component of the vibration is the modal effective mass

$$m_{\alpha,i} = (\Gamma_{\alpha,i})^2 m_\alpha \qquad \text{unit } [t] \tag{17.114}$$

This parameter can be adopted to determine the minimum number of eigenvectors to be used in application of modal analysis to solve Eq. (17.83). It holds that the sum of modal effective masses

$m_{\alpha,i}$ of all modes in any particular direction ($i \equiv x$ or $i \equiv y$) is equal to the total mass, except for the mass associated with kinetically constrained degrees of freedom. The program provides the total modal effective mass in either direction as

$$\text{TMEM}_i = \sum_{\alpha=1}^{M} m_{\alpha,i} \tag{17.115}$$

where M is the number of adopted (determined) modes. The minimum number of eigenvectors is typically determined such as the TMEM_i value exceeds the 90% of the total mass. If this value is considerably smaller than the total mass, it means that the modes that have a significant participation in that direction, have not been extracted.

17.3.3 Response spectrum - generation of artificial accelerograms

To describe a seismic motion we generally use accelerograms, i.e., the time variation of ground acceleration. In 2D analysis, such a motion considers two components of the acceleration vector. One component serves to describe motion in the horizontal direction, the other one in the vertical direction. The Eurocode 8 (EC8) allows us, for the description of seismic motion, to adopt artificial, real, or simulated accelerograms.

The real accelerograms follow from the measurements of real earthquakes by seismographic stations installed all over the world. Simulated accelerograms are obtained by simulating both the source of a seismic activity and mechanism of transport of seismic waves. However, the interest of structural engineers is usually shifted towards artificial accelerograms. This is why we address this issue in the next subsections in more details.

Elastic response spectrum

The elastic response spectrum of an accelerogram is represented by the graph of a function $a(T)$ the value of which is defined as the maximum acceleration of a harmonic oscillator with a single degree of freedom having the natural period T and being exited by this accelerogram. The physical model adopted to compute the response spectrum is plotted in Fig. 17.18. Each oscillator i with the mass m_i, the spring stiffness k_i, and the coefficient of viscous damping c_i has the natural frequency $\omega_{0,i} = \sqrt{k_i/m_i}$ and the coefficient of proportional damping $\xi_i = c_i/(2\sqrt{m_i k_i})$. Providing its base is exited by the acceleration, the corresponding mass will move with the acceleration $a_i(t)$. The maximum absolute value of $a_i(t)$ represents the value of response spectrum $S_e(a_i)$ plotted as a function of $T_i = 2\pi/\omega_{0,i}$. An example of the design response spectrum appears in Fig. 17.19.
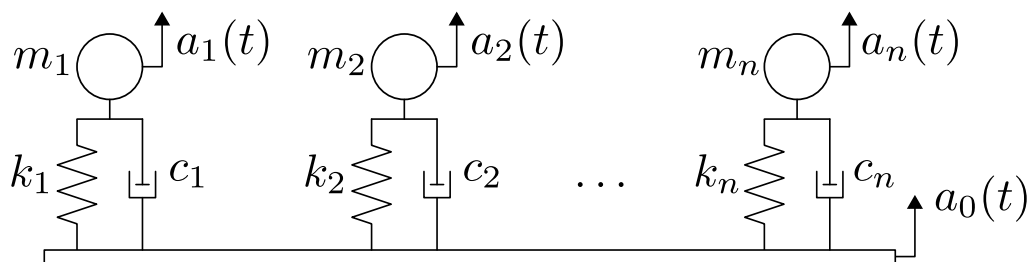

Figure 17.18: Principle of computation of elastic response spectrum: harmonic oscillators with various natural frequencies exited by accelerogram $a_0(t)$ and monitored response $a_i(t)$

Artificial accelerograms

An artificial accelerogram has to be generated such as to correspond to the elastic response spectrum with the viscous damping $\xi = 0.05$ defined in the Eurocode 8. This standard further determines the minimum duration of the acceleration and minimum number of accelerations used to address the response of a structure to seismic actions.
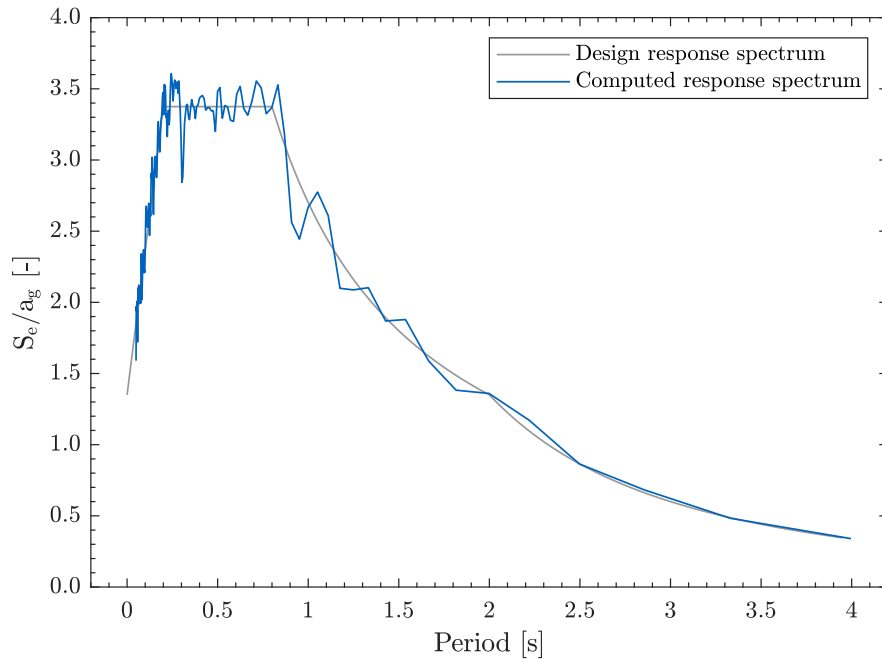
Figure 17.19: Comparing design response spectrum defined by EC8 and response spectrum extracted from generated accelerogram, adopted from [62]

The algorithm to generate artificial accelerograms is taken from [46] and assumes the following steps:

1. The Fourier spectrum with constant spectral amplitudes and random phase shifts is generated.

2. The Fourier transform is then used to get the corresponding time variation of acceleration.

3. For this accelerogram, the elastic response spectrum of single degree of freedom systems with frequencies corresponding to frequencies used in the Fourier spectrum is computed.

4. The contribution of the design elastic response spectrum specified by EC8 and the contribution due to the generated accelerogram are computed for each frequency.

5. Spectral amplitudes of the original Fourier spectrum are adjusted based on the contributions acquired in the previous step. The phase shifts remain the same.

6. The steps 2–5 are repeated for the adjusted Fourier spectrum until the calculated response spectrum matches the design elastic response spectrum due to EC8 up to an error less than 10 %, see Fig. 17.19.

The accelerogram obtained from this algorithm complies with the EC8 conditions, but it is stationary and lacks characteristic stages typical of real measured accelerograms, see the stationary distribution in Fig. 17.20. For this accelerogram to contain an amplification stage, a region of strong motion followed by a gradual decay, it is necessary to multiply the stationary accelerogram by an envelope function $E(t)$ [13]
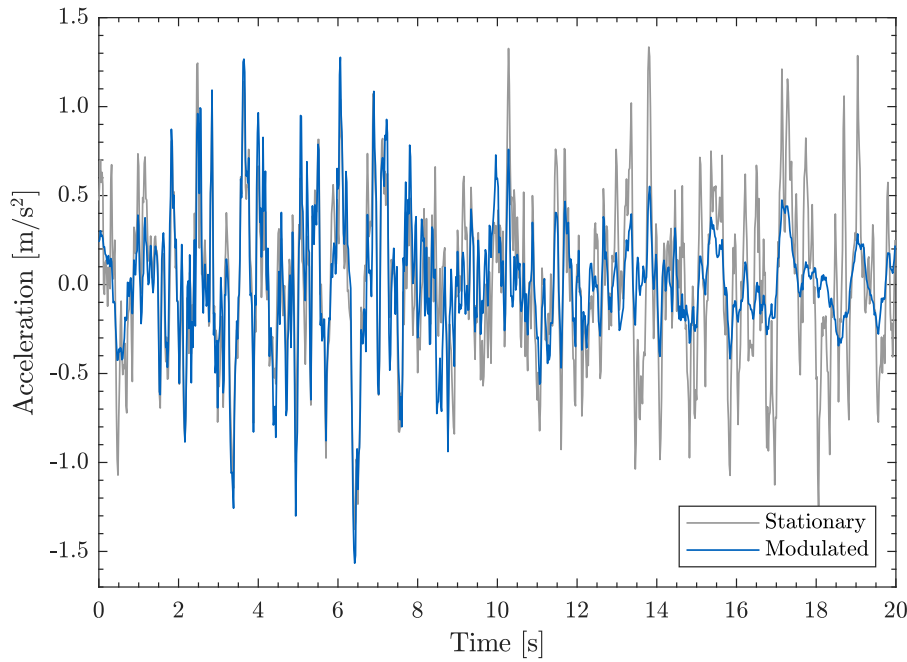
$$E(t) = at^b e^{-ct} \tag{17.116}$$

Figure 17.20: Comparing stationary and non-stationary (modulated) artificial accelerograms, adopted from [62]

with coefficients

$$a = \left(\frac{e}{\varepsilon T_w}\right)^b \tag{17.117}$$

$$b = \frac{-\varepsilon \ln \mu}{1 + \varepsilon(\ln \varepsilon - 1)} \tag{17.118}$$

$$c = \frac{b}{\varepsilon T_w} \tag{17.119}$$

where T_w is the specific earthquake duration. The parameter ε determines at what time instant of T_w the envelope function attains its maximum value. The parameter μ determines the reduction factor of the envelope function at time T_w with respect to its maximum value.

The accelerogram is generated such to get zero velocity and displacement at time T_w, while zero initial velocity and displacement contained already by the stationary accelerogram are retained. The impact of the application of envelope function on the time variation of the generated acceleration is illustrated in Fig. 17.20, compare stationary and non-stationary accelerograms. Further details regarding the response spectrum and accelerograms in connection to EC8 are available in [57, 42]. For details on the use of envelope function the interested reader is referred to [46].

17.3.4 Introducing material damping

The most simple approach to constructing the damping matrix $\mathbf{C}^M$, adopted also in GEO5 FEM, is based on the assumption of proportional damping. In such a case it holds

$$\mathbf{\Phi}^\mathsf{T}\mathbf{C}^M\mathbf{\Phi} = 2\mathbf{\Omega}^d \tag{17.120}$$

where $\mathbf{\Phi}$ is the modal matrix the columns of which are represented by individual eigenvectors of the vibrating system, recall Section 17.3.2. The matrix $\mathbf{\Omega}^d$ is diagonal with the components $\omega_i^d = \xi_i \omega_i$, where ω_i^d denotes the damped frequency and ξ_i is the coefficient of proportional damping associated with the natural frequency ω_i. Then, the eigenvectors are orthogonal also to the damping matrix $\mathbf{C}^M$.

In the case of modal decomposition the solution of Eq. (17.83) splits into the system of n independent differential equations, where n is the number of used eigenvectors. This considerably simplifies the analysis.

Formulation of proportional damping (17.120) is very simple, but it assumes the knowledge of the coefficients of proportional damping ξ_i for all the frequencies. This can hardly be achieved in practice. Additional hypothesis allowing for the determination of all ξ_i on the basis of just a few constants is therefore needed. In this regard, it is convenient to consider in most practical applications the Rayleigh damping which assumes the damping matrix $\mathbf{C}^M$ in the form of a linear combination of the mass and stiffness matrices as

$$\mathbf{C}^M = \alpha\mathbf{M} + \beta\mathbf{K} \tag{17.121}$$

where α, β are the parameters of proportional damping[6]. The fact that the eigenvectors in GEO5 FEM are normalized with respect to the mass matrix provides upon multiplying Eq (17.121) from the left by $\mathbf{\Phi}^\mathsf{T}$ and from the right by $\mathbf{\Phi}$

$$2\mathbf{\Omega}^d = \alpha\mathbf{I} + \beta\mathbf{\Omega}^2 \longrightarrow 2\omega_i^d = 2\xi_i\omega_i = \alpha + \beta\omega_i^2 \tag{17.122}$$

where $\mathbf{I}$ is the identity matrix. The spectral matrix $\mathbf{\Omega}$ is similar to $\mathbf{\Omega}^d$ diagonal and collects on the diagonal the squares of natural frequencies.

It is evident from Eq. (17.122) that to determine parameters α, β it is sufficient to know two eigenfrequencies ω_i and their corresponding coefficients ξ_i. If we accept that both frequencies ω_a and ω_b are damped by the same coefficient of proportional damping, i.e., $\xi_a = \xi_b = \xi$, we get

$$\alpha = \frac{2\xi\omega_a\omega_b}{\omega_a + \omega_b}, \qquad \beta = \frac{2\xi}{\omega_a + \omega_b} \tag{17.123}$$

However, most often we have at our disposal only one value of the coefficient of proportional damping for the lowest natural frequency ω_1. If we accept the hypothesis that this frequency is damped the least, then using Eq. (17.122) gives

$$\frac{d\xi}{d\omega_i} = \frac{1}{2}\left(-\frac{\alpha}{\omega_i^2} + \beta\right) = 0 \tag{17.124}$$

Introducing $\omega_i = \omega_1$ into Eq. (17.124) yields

$$\alpha = \omega_1^2\beta \tag{17.125}$$

Back substitution for α from Eq. (17.125) into Eq. (17.122) finally provides

$$\alpha = \xi_1\omega_1, \qquad \beta = \frac{\xi_1}{\omega_1} \tag{17.126}$$

Further details can be found in [11].

Example of calculating α, β

Details regarding the presented example including the geometry of the numerical model and material properties of individual layers of subsoil are available in [62]. Hence, we provide only a brief description of the potential way of calculating the parameters of Rayleigh damping α, β.

Eurocode 8 offers a single values of proportional damping $\xi = 0.05$ (5%) only. The presented example will show, how strongly are individual natural frequencies damped in dependence on the way of calculating the parameters α, β. For illustration, we consider a simple model displayed in Fig. 17.21(a). The impact of material damping is best evaluated on the basis of fixed boundary conditions on the BB boundary (FBB). To allow for relating the natural frequencies of the system to the prescribed acceleration we shall consider the accelerogram in Fig. 17.14 generated on the grounds of the design reponse spectrum plotted in Fig. 17.21(b), recall Section 17.3.3.

---

[6]These parameters should not be confused with the parameters α, β, γ introduced in Section 17.3.1.
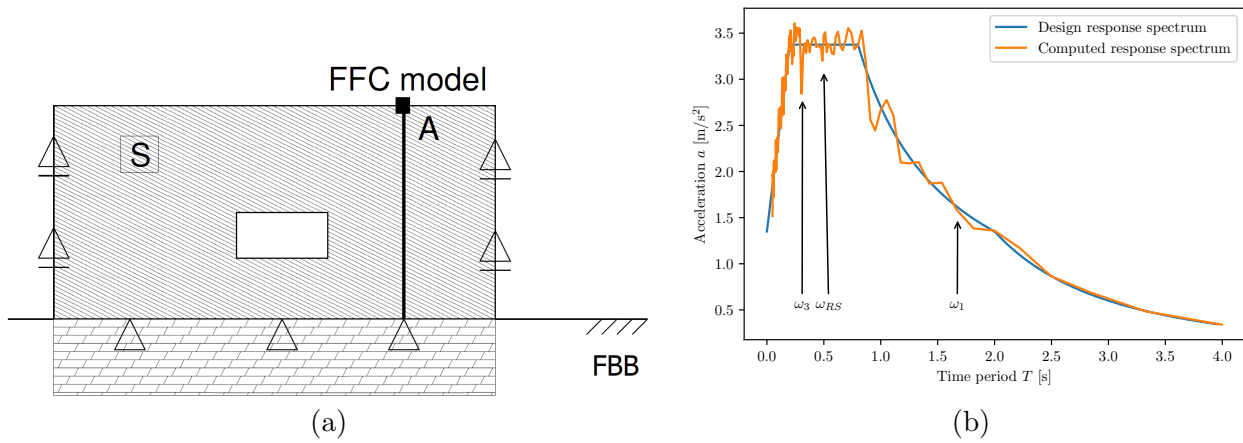
Figure 17.21: a) Subsoil model, b) Response spectrum

This accelerogram introduces the horizontal (shear) seismic waves only. Thus to determine the first few natutral frequencies, we considered the kinematic boundary conditons on the lateral boundaries in accordance with Fig. 17.21(a), recall also Section 17.3.2 and Fig. 17.17. To identify purely shear dominated mode shapes we employed the *Modal participation factor* $\Gamma_{\alpha,x}$.

The following three variants of the calculation of parameters α, β are presented for illustration:

1. The least damped is the first natural frequency. The parameters α, β follow from Eq. (17.126).

2. The least damped frequecies are found between the first and third[7] natural frequency. The third natural frequency was adopted according to recommendations presented in [17]. The parameters α, β follow from Eq. (17.123).

3. The least damped frequencies are found between the first and the the most dominant frequency ω_{RS} of the design response spectrum, see Fig. 17.21(b). The parameters α, β follow from Eq. (17.123).

Table 17.10: Parameters of Rayleigh damping for $\xi = 5\%$, adopted from 17.10

Damping	ω	α	β
Typ 1	ω_1	0.1875	0.0133
Typ 2	$\omega_1 + \omega_3$	0.3143	0.0043
Typ 3	$\omega_1 + \omega_{RS}$	0.2888	0.0061

The resulting values of natural frequencies and parameters α, β are summarized in Table 17.10. A graphical representation of the amount of damping is provided in Fig. 17.22. Clearly, only the chosen frequncies are damped with $\xi = 5\%$. Apart from identifying the domain of the least damped frequecies we also observe that particularly high frequecies of the design spectrum are damped the most[8].

Finally, to judge the influence of material damping we compare the influnce of fixed and absorbing (ABB) bounary conditions on the response of a homogeneous layer exited by the horizontal seismic waves generated from the design response spectrum in Fig. 17.21(b). For simplicity, we consider the *Free field column* analysis depicted in Fig. 17.21(a). The resulting distributions of the relative horizontal displacement at point A are seen in Fig. 17.23. The impact of material damping is evident and in the case of FBB conditions it repersents the only way how to bring he vibrating system to rest once the applied acceleration ceases. For ABB conditions, the material damping does not play a significant role.

---

[7]More specifically, the third frequency from the list of purely shear mode shapes.

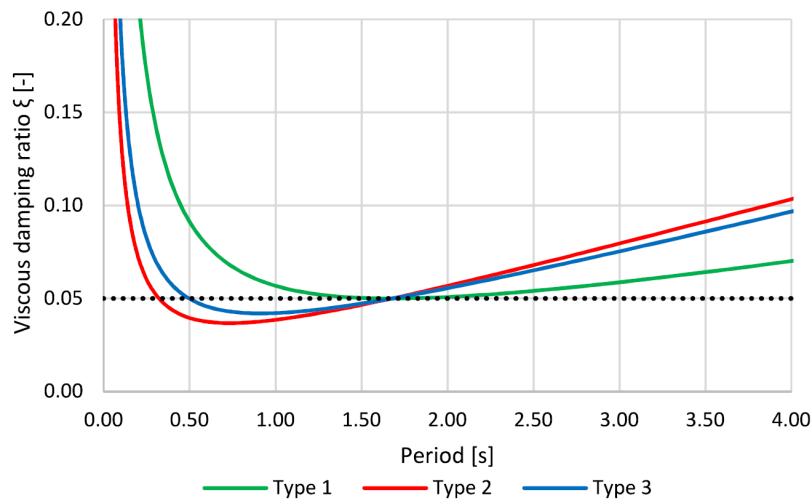[8]The abscissa represents natural periods $T = \dfrac{2\pi}{\omega}$.

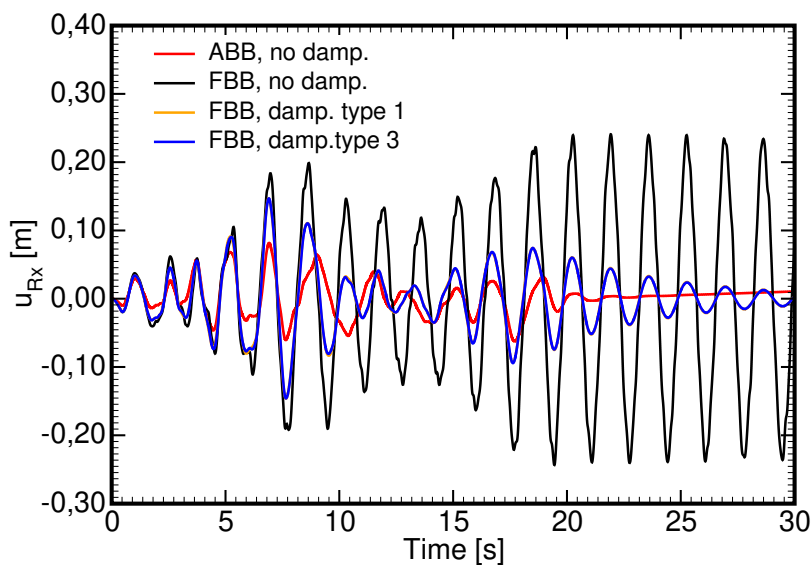Figure 17.22: Proportional damping ratio as a function natural period

Figure 17.23: Comparing response of homogeneous layer assuming fixed and absorbing boundary conditions to evaluate influnce of material damping

17.3.5   Solution process

It is clear from the previous text that earthquake analysis requires a certain sequence of calculations. In particular:

1. **Static analysis** in a given stage to get the initial stress state prior to application of dynamic load (prescribed acceleration).

2. **Solution of the eigenvalue problem to acquire natural frequencies and mode shapes**. The program determines the first M eigenfrequencies $\omega_1 < \omega_2 < \ldots < \omega_M$, where M is the required number set by the user. Depending on the solution setting it may happen that not all requested eigenfrequencies are extracted or some of them are missed. When employing the Jacobi method the program searches for more frequencies than requested so that the number frequencies found typically exceeds the number specified by the user. The program offers a table collecting not only all converged frequencies but also the ones found with the error larger than the one specified in the solution setting. The maximum error associated with the highest frequency is provided. The table also lists for each eigenfrequency the *Modal participation factor* and *Modal effective mass* identifying which of the basic vibration modes (vibration either horizontal

or vertical directions) prevails in the given eigenvector. A visual check is available by animating the particular eigenvector.

The extracted eigenfrequencies can be used to determine the parameters α, β of the Rayleigh damping when specifying the coefficient of proportional damping ξ in the material setting. The solution process can be terminated after completing the eigenvalue analysis to verify, either visually or numerically, the expected range of frequencies used in the calculation of α, β, recall Section 17.3.4.

3. **Free field column analysis**. The Free field column analysis provides the time variation of traction boundary conditions prescribed on lateral boundaries of the computational model, see Section 17.3.1. On both boundaries, the analysis is carried out simultaneously. The material models in individual layers, boundary conditions on the BB boundary, the prescribed acceleration, and the initial time step comply with the 2D analysis. The results of this analysis cannot be visualized.

4. **Two-dimensional earthquake analysis pertinent to given calculation stage**. The analysis provides a time variation of all quantities. These can be presented in an arbitrary time step, visualized step by step or animated.

17.4 Consolidation

Section 2.1 opened the discussion to the modeling of ground water pressure and its action on a soil body. Undrained conditions in particular assumed impermeable external boundaries of a computational model which resulted in an instantaneous development of an excess pore pressure in a body if subjected to loading. Switching to permeable boundaries then allows for a gradual dissipation of this excess pore pressure arriving finally at drained conditions, when the pore pressure is no longer affected by the soil body deformation. The transition from undrained to drained conditions in addressed in the theory of consolidation.

The presented theoretical formulations and their implementation in GEO5 FEM grounds on several simplifying assumptions:

- Attention is accorded to a primary consolidation manifested by the reduction of pore space due to loading while pushing water out of pores.

- The soil body is assumed to be fully saturated, i.e., using the notation introduced in Section 2.1 we consider $p = p^w, p^g = 0$, and $S = 1$ both below and above the ground water table (GWT), see Fig. 17.24(b). With this simplification we arrive at a one phase flow in a fully saturated medium.

- The pore pressure distribution at the beginning and at the end of consolidation is the same. The the steady state pore pressure is prescribed as the initial pore pressure, i.e., $p_{in} = p^{ss}$. It can be obtained either by specifying the ground water table or by running the steady state flow analysis with given flow boundary conditions as illustrated in Fig. 17.24(a). The interested reader is referred to Section 17.5 for more details.

- During consolidation the boundary conditions are, however. limited to either zero flux (closed boundary) or zero excess pore pressure (open boundary) boundary conditions. This is schematically demonstrated in Fig. 17.24(b).

- The excess pore pressure p^{ex} rather then the actual pore pressure $p = p^{ss} + p^{ex}$ is the primary unknown to be determined during consolidation. This is because the change in p expressed in terms of the time derivative $\dot{p} = \dot{p}^{ex}, \dot{p}^{ss} = 0$, where $\dot{p} = \dfrac{\mathrm{d}p}{\mathrm{d}t}$.

Figure 17.24 shows the flow boundary conditions adopted in steady state seepage analysis and consolidation, respectively. Therein, Γ_q represents the boundary with the prescribed flux q whereas Γ_p stands for the boundary with the prescribed pore pressure. Further details are provided in Section 17.5.
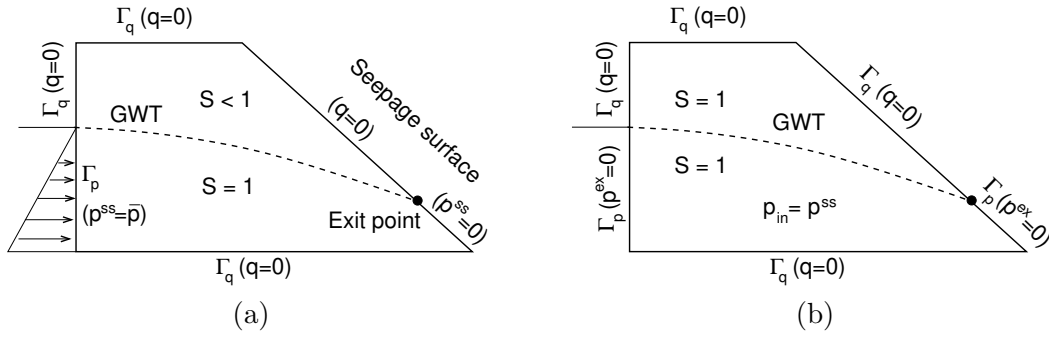
Figure 17.24: Example of flow boundary conditions adopted in the consolidation analysis: a) steady state step to generate the initial steady state pressure p^{ss}, b) consolidation step to generate the time dependent variation of excess pore pressure p^{ex}.

To simplify further reading we briefly review some of the notation introduced previously in Section 2.1 and Chapter 16:

- Biot coefficient α provided by Eq. (2.11) in terms of the bulk modulus of the porous skeleton K_{sk} and the bulk modulus of water K_w in the form

$$\alpha = 1 - \frac{K_{sk}}{K_m} < 1$$

- Biot modulus M introduced in Eq. (2.15) in terms of the porosity n, the bulk modulus of the solid grains K_m and the bulk modulus of water K_w as

$$\frac{1}{M} = \frac{\alpha - n}{K_m} + \frac{n}{K_w}$$

- Terzaghi's concept of effective stresses given by Eq. (2.10) is now presented also in the rate form

$$\boldsymbol{\sigma} = \boldsymbol{\sigma}^{eff} - 3\boldsymbol{m}p = \boldsymbol{\sigma}_\varepsilon - \alpha 3\boldsymbol{m}p, \qquad \dot{\boldsymbol{\sigma}}_\varepsilon = \mathbf{D}^{ep}\dot{\boldsymbol{\varepsilon}} \qquad (17.127)$$

$$\dot{\boldsymbol{\sigma}} = \mathbf{D}^{ep}\dot{\boldsymbol{\varepsilon}} - \alpha 3\boldsymbol{m}\dot{p}^{ex}, \qquad \dot{p}^{ss} = 0 \qquad (17.128)$$

- Darcy's flow is now presented in a slightly different form given the fact that the relative permeability $S = 1, K_r = 1$. Thus combining Eqs. (16.1) and (16.2) we get the flux $\boldsymbol{q} = n\boldsymbol{v}^{ws}$ in terms of the permeability matrix $\mathbf{K}_{sat}$, recall Eq. (16.3), and the bulk weight of water γ_w in the form

$$\boldsymbol{q} = \underbrace{-\frac{\mathbf{K}_{sat}}{\gamma_w}\left(\nabla p^{ss} + \gamma_w z\right)}_{q^{ss}} \underbrace{-\frac{\mathbf{K}_{sat}}{\gamma_w}\nabla p^{ex}}_{q^{ex}} = -\frac{\mathbf{K}_{sat}}{\gamma_w}\left(\nabla p + \gamma_w z\right) \qquad (17.129)$$

We now proceed with the formulation of fundamental equations governing the one phase flow in a fully saturated medium.

17.4.1   Flow - mass conservation law

In general, the mass conservation law or the equation of continuity for one phase flow in a fully saturated medium attains the following form, see for example [50, 72],

$$\frac{1}{M}\dot{p} + \alpha\dot{\varepsilon}_v + \boldsymbol{\nabla}^{\mathsf{T}}\left(-\frac{\mathbf{K}_{sat}}{\gamma_w}\boldsymbol{\nabla}(p + \gamma_w z)\right) = m(t) \qquad (17.130)$$

where ε_v is the volumetric strain and m represents any internal sources ($m > 0$) and/or sinks ($m < 0$), e.g., the volume of water removed per unit time from a unit volume of soil due to evaporation or due to plant water uptake. Next, suppose that the source term $m(t) = 0$. As already pointed out

$$p = p^{ss} + p^{ex}, \qquad \dot{p} = \dot{p}^{ex} \text{ or } \Delta p = \Delta p^{ex} \qquad (17.131)$$

This gives the steady state condition in the form

$$\boldsymbol{\nabla}^{\mathsf{T}} \left(-\frac{\mathbf{K}_{sat}}{\gamma_w} \boldsymbol{\nabla}(p^{ss} + \gamma_w z) \right) = 0 \tag{17.132}$$

Eq. (17.130) then simplifies

$$\frac{1}{M}\dot{p}^{ex} + \alpha\dot{\varepsilon}_v + \boldsymbol{\nabla}^{\mathsf{T}} \left(-\frac{\mathbf{K}_{sat}}{\gamma_w} \boldsymbol{\nabla}p^{ex} \right) = 0 \tag{17.133}$$

It is interesting to point out that writing the time derivative $\dot{a}$ as $\dot{a} = \dfrac{\Delta a}{\Delta t}$, then multiplying through by Δt, and letting $\Delta t \to 0$ yields Eq. (2.15) derived already for undrained conditions for time $t = 0$ in Section 2.1 from pure volume averaging.

Solving Eq. (17.133) requires introduction of boundary conditions as mentioned already with reference to Fig. 17.24 The Neumann (prescribed normal flux $\overline{q}_n$ on Γ_q) and the Dirichlet (prescribed pore pressure $\overline{p}$ on Γ_p) boundary conditions can in general be written as

$$\boldsymbol{n}^{\mathsf{T}} \left(\frac{\mathbf{K}_{sat}}{\gamma_w} \boldsymbol{\nabla}(p(t) + \gamma_w y) \right) + \overline{q}_n(t) = 0 \qquad \text{on } \Gamma_q, \qquad \text{Neumann b.c.} \tag{17.134}$$

$$p(t) - \overline{p}(t) = 0 \qquad \text{on } \Gamma_p, \qquad\qquad\qquad \text{Dirichlet b.c} \tag{17.135}$$

However, the present implementation is limited to either closed or open boundaries only. Thus the following boundary conditions apply when solving Eq. (17.133) in the consolidation step, recall Fig. 17.24,

$$\boldsymbol{n}^{\mathsf{T}} \left(\frac{\mathbf{K}_{sat}}{\gamma_w} \boldsymbol{\nabla}p^{ex}(t) \right) = 0 \qquad \text{on } \Gamma_q \tag{17.136}$$

$$p^{ex}(t) = 0 \qquad \text{on } \Gamma_p \tag{17.137}$$

Time discretization of equation (17.133)

In the present implementation in GEO5 FEM the time derivatives in Eq. (17.133) are approximated employing the fully explicit Euler backward integration scheme which, in light of potentially nonlinear analysis, gives

$$\dot{p}^{ex} = \frac{p^{ex}_{i+1,j+1} - p^{ex}_i}{\Delta t} = \frac{p^{ex}_{i+1,j} + \Delta p - p^{ex}_i}{\Delta t} = \frac{\Delta p}{\Delta t} + \frac{p^{ex}_{i+1,j} - p^{ex}_i}{\Delta t} \tag{17.138}$$

$$\dot{\boldsymbol{\varepsilon}} = \frac{\boldsymbol{\varepsilon}_{i+1,j+1} - \boldsymbol{\varepsilon}_i}{\Delta t} = \frac{\boldsymbol{\varepsilon}_{i+1,j} + \Delta\boldsymbol{\varepsilon} - \boldsymbol{\varepsilon}_i}{\Delta t} = \frac{\Delta\boldsymbol{\varepsilon}}{\Delta t} + \frac{\boldsymbol{\varepsilon}_{i+1,j} - \boldsymbol{\varepsilon}_i}{\Delta t} \tag{17.139}$$

where

$$p^{ex}_{i+1,j+1} = p^{ex}_{i+1,j} + \Delta p, \qquad p_{i+1,j+1} = p^{ex}_{i+1,j+1} + p^{ss} \tag{17.140}$$

$$\boldsymbol{\varepsilon}_{i+1,j+1} = \boldsymbol{\varepsilon}_{i+1,j} + \Delta\boldsymbol{\varepsilon} \tag{17.141}$$

$$i \quad - \quad \text{stands for the i-th integration step (load increment)}$$

$$j \quad - \quad \text{stands for the j-th iteration within the i-th integration step}$$

Equation (17.133) then becomes

$$\frac{1}{\Delta t M}\Delta p + \frac{\alpha 3 \boldsymbol{m}^{\mathsf{T}}}{\Delta t}\Delta\boldsymbol{\varepsilon} + \boldsymbol{\nabla}^{\mathsf{T}} \left(-\frac{\mathbf{K}_{sat}}{\gamma_w} \boldsymbol{\nabla}(\Delta p) \right) =$$
$$-\frac{1}{\Delta t M}(p^{ex}_{i+1,j} - p^{ex}_i) - \frac{\alpha 3 \boldsymbol{m}^{\mathsf{T}}}{\Delta t}(\boldsymbol{\varepsilon}_{i+1,j} - \boldsymbol{\varepsilon}_i) - \boldsymbol{\nabla}^{\mathsf{T}} \left(-\frac{\mathbf{K}_{sat}}{\gamma_w} \boldsymbol{\nabla}p^{ex}_{i+1,j} \right) \tag{17.142}$$

Note that in general the permeability matrix $\mathbf{K}_{sat}$ might be function of the current void ratio $e(\varepsilon_v)$, see for example [41]. This option, however, is not implemented in the current version of GEO5 FEM.

17.4.2   Mechanics - momentum balance

In analogy to mass balance equation (17.130) we write the Cauchy equations of equilibrium driving the state of deformation of a soil body as

$$\partial\dot{\boldsymbol{\sigma}} + \dot{\boldsymbol{X}} = \mathbf{0} \tag{17.143}$$

where $\dot{\boldsymbol{\sigma}}$ is the rate of total stresses and $\boldsymbol{X}$ is the vector of body forces. In soil mechanics, a typical example of a vertical component of $\boldsymbol{X}$ in static analysis is the soil density.

The corresponding Neumann and Dirichlet boundary conditions are now the prescribed surface tractions and displacements on external boundaries of a computational model, respectively.

Time discretization of equation (17.133)

Adopting Eqs. (17.138) and (17.139) gives the time derivative of total stresses at $(i+1)$ integration step in the form

$$\dot{\boldsymbol{\sigma}}|_{i+1} = \frac{1}{\Delta t}\mathbf{D}^{ep}\Delta\boldsymbol{\varepsilon} - \frac{\alpha 3\boldsymbol{m}}{\Delta t}\Delta p + \frac{1}{\Delta t}\mathbf{D}^{ep}(\boldsymbol{\varepsilon}_{i+1,j} - \boldsymbol{\varepsilon}_i) - \frac{\alpha 3\boldsymbol{m}}{\Delta t}(p^{ex}_{i+1,j} - p^{ex}_i) \tag{17.144}$$

17.4.3   Finite element discretization

Unlike formulations outlined in Section 17.1, where the generalized displacements (displacements and rotations) were considered as the only primary variables, we now search for a simultaneous evolution of displacements and excess pore pressure both in time and space.

To this end, we invoke the principal of virtual work presented in Section 17.1 in the form Eq. (17.1) to get the discretized version of the continuity and equilibrium equations. In the framework of finite element method we start from finite element discretization of both displacements $\boldsymbol{u}$ and excess pore pressure p^{ex} in terms of their nodal representations $\boldsymbol{r}^u$ and $\boldsymbol{r}^p$ (or their increments $\Delta\boldsymbol{r}^u, \Delta\boldsymbol{r}^p$) to get

$$\begin{aligned}
p^{ex} &= \mathbf{N}^p\boldsymbol{r}^p, & \Delta p &= \mathbf{N}^p\Delta\boldsymbol{r}^p & (17.145) \\
\boldsymbol{u} &= \mathbf{N}^u\boldsymbol{r}^u, & \Delta\boldsymbol{u} &= \mathbf{N}^u\Delta\boldsymbol{r}^u & (17.146) \\
\boldsymbol{\varepsilon} &= \mathbf{B}^u\boldsymbol{r}^u, & \Delta\boldsymbol{\varepsilon} &= \mathbf{B}^u\Delta\boldsymbol{r}^u & (17.147)
\end{aligned}$$

where indexes (p, u) identify the approximations associated with the excess pore pressure and displacements, respectively.

Finite element discretization of equation (17.142)

Introducing the above approximations together with the flow type of Neumann boundary conditions, Eq. (17.136), in Eq. (17.1) gives the discretized form of Eq. (17.142) as

$$(\mathbf{C} + \Delta t\mathbf{H})\,\Delta\boldsymbol{r}^p + \mathbf{Q}\Delta\boldsymbol{r}^u = -\Delta t\mathbf{H}\boldsymbol{r}^p_{i+1,j} - \mathbf{C}(\boldsymbol{r}^p_{i+1,j} - \boldsymbol{r}^i_p) - \mathbf{Q}(\boldsymbol{r}^u_{i+1,j} - \boldsymbol{r}^u_i) \tag{17.148}$$

where

$$\begin{aligned}
\mathbf{C} &= \mathop{\mathbf{A}}_{e=1}^{N_e} \int_{\Omega_e} \frac{1}{M}(\mathbf{N}^p)^\mathsf{T}\mathbf{N}^p \, \mathrm{d}\Omega, & \text{Compressibility matrix} & & (17.149) \\
\mathbf{H} &= \mathop{\mathbf{A}}_{e=1}^{N_e} \int_{\Omega_e} (\mathbf{B}^p)^\mathsf{T}\frac{\mathbf{K}_{sat}}{\gamma_w}\mathbf{B}^p \, \mathrm{d}\Omega, & \text{Permeability matrix} & & (17.150) \\
\mathbf{Q} &= \mathop{\mathbf{A}}_{e=1}^{N_e} \int_{\Omega_e} (\mathbf{N}^p)^\mathsf{T}3\boldsymbol{m}^\mathsf{T}\mathbf{B}^u \, \mathrm{d}\Omega, & \text{Coupling matrix} & & (17.151)
\end{aligned}$$

The right hand side of Eq. (17.148) can be written as

$$
{}^P\boldsymbol{f}^{i+1,j} = \; + \; \underbrace{\Delta t \; \mathop{\mathbf{A}}_{e=1}^{N_e} \int_{\Omega_e} (\mathbf{B}^p)^\mathsf{T} \boldsymbol{q}_{i+1,j} \, \mathrm{d}\Omega}_{-\Delta t \mathbf{H} \boldsymbol{r}^p_{i+1,j}}
$$

$$
- \; \underbrace{\mathop{\mathbf{A}}_{e=1}^{N_e} \int_{\Omega_e} \frac{1}{M} (\mathbf{N}^p)^\mathsf{T} (p^{ex}_{i+1,j} - p^{ex}_i) \, \mathrm{d}\Omega}_{\mathbf{C}(\boldsymbol{r}^p_{i+1,j} - \boldsymbol{r}^p_i)}
$$

$$
- \; \underbrace{\mathop{\mathbf{A}}_{e=1}^{N_e} \int_{\Omega_e} (\mathbf{N}^p)^\mathsf{T} \alpha 3 \boldsymbol{m}^\mathsf{T} (\boldsymbol{\varepsilon}_{i+1,j} - \boldsymbol{\varepsilon}_i) \, \mathrm{d}\Omega}_{\mathbf{Q}(\boldsymbol{r}^u_{i+1,j} - \boldsymbol{r}^u_i)} . \tag{17.152}
$$

Note that at equilibrium, converged solution (one step in case of linear analysis), the vector ${}^P\boldsymbol{f}$ should be equal to zero.

Finite element discretization of equation (17.143)

The principal of virtual work, Eq. (17.1), together with Eq. (17.144) now gives the discrete system of equations of equilibrium in the form

$$
\mathbf{K}_T \Delta \boldsymbol{r}^u - \mathbf{Q}^\mathsf{T} \Delta \boldsymbol{r}^p = -\mathbf{K}_T (\boldsymbol{r}^u_{i+1,j} - \boldsymbol{r}^u_i) + \mathbf{Q}^\mathsf{T} (\boldsymbol{r}^p_{i+1,j} - \boldsymbol{r}^p_i) + \Delta \boldsymbol{F} \tag{17.153}
$$

where

$$
\mathbf{K}_T = \mathbf{K}_{i+1,j} = \mathop{\mathbf{A}}_{e=1}^{N_e} \int_{\Omega_e} (\mathbf{B}^u)^\mathsf{T} \mathbf{D}^{ep}_{i+1,j} \mathbf{B}^u \, \mathrm{d}\Omega, \qquad \text{Stiffness matrix} \tag{17.154}
$$

$$
\mathbf{Q}^\mathsf{T} = \mathop{\mathbf{A}}_{e=1}^{N_e} \int_{\Omega_e} (\mathbf{B}^u)^\mathsf{T} 3 \boldsymbol{m} \mathbf{N}^p \, \mathrm{d}\Omega, \qquad \text{Coupling matrix} \tag{17.155}
$$

$$
\Delta \boldsymbol{F} = \boldsymbol{F}^{i+1} - \underbrace{\mathop{\mathbf{A}}_{e=1}^{N_e} \int_{\Omega_e} (\mathbf{B}^u)^\mathsf{T} \boldsymbol{\sigma}_i \, \mathrm{d}\Omega}_{\boldsymbol{F}_i = \mathbf{K}_T \boldsymbol{r}^u_i - \mathbf{Q}^\mathsf{T} \boldsymbol{r}^p_i}, \qquad \text{Vector of applied load} \tag{17.156}
$$

With reference to Eq. (17.51) and similarly to Eq. (17.152) we may write the right hand side of Eq. (17.153) as

$$
{}^M\boldsymbol{f}_{i+1,j} = \boldsymbol{F}_{i+1} - {}^M\boldsymbol{R}_{i+1,j} \tag{17.157}
$$

$$
{}^M\boldsymbol{R}_{i+1,j} = \underbrace{\mathop{\mathbf{A}}_{e=1}^{N_e} \int_{\Omega_e} (\mathbf{B}^u)^\mathsf{T} \boldsymbol{\sigma}_{i+1,j} \, \mathrm{d}\Omega}_{\mathbf{K}_T \boldsymbol{r}^u_{i+1,j} - \mathbf{Q}^\mathsf{T} \boldsymbol{r}^p_{i+1,j}}
$$

where $\boldsymbol{\sigma}_{i+1,j}$ represents the current vector of total stresses given by

$$
\boldsymbol{\sigma}_{i+1,j} = (\boldsymbol{\sigma}_\varepsilon)_{i+1,j} - 3\alpha \boldsymbol{m} (p^{ss} + p^{ex}_{i+1,j}) \tag{17.158}
$$

17.4.4 Coupled system of equations

Combining Eqs. (17.148), (17.153), (17.152) and (17.158) provides the incremental form of the coupled consolidation, with limitation to one-phase flow in a fully saturated medium, as

$$
\begin{bmatrix} -\mathbf{K}_{i+1,j} & \mathbf{Q}^\mathsf{T} \\ \mathbf{Q} & \mathbf{C} + \Delta t \mathbf{H} \end{bmatrix} \left\{ \begin{array}{c} \Delta \boldsymbol{r}^u \\ \Delta \boldsymbol{r}^p \end{array} \right\} = \left\{ \begin{array}{c} -({}^M\boldsymbol{f}_{i+1,j}) \\ {}^P\boldsymbol{f}_{i+1,j} \end{array} \right\} \tag{17.159}
$$

The updated variables at $i + 1$ load increment and $j + 1$ iteration are

$$\boldsymbol{r}^p_{i+1,j+1} = \boldsymbol{r}^p_{i+1,j} + \Delta\boldsymbol{r}^p, \qquad \boldsymbol{r}^u_{i+1,j+1} = \boldsymbol{r}^u_{i+1,j} + \Delta\boldsymbol{r}^u \tag{17.160}$$

At the beginning of each iteration within a given time integration step we have

$$\boldsymbol{r}^p_{i+1,0} = \boldsymbol{r}^p_i, \qquad \boldsymbol{r}^u_{i+1,0} = \boldsymbol{r}^u_i, \qquad \boldsymbol{q}_{i+1,0} = \boldsymbol{q}_i, \qquad \boldsymbol{\sigma}_{i+1,0} = \boldsymbol{\sigma}_i \tag{17.161}$$

Thus at the beginning of each new time integration step we receive the right hand side of Eq. (17.159) in the form

$$\boldsymbol{f}^{i+1,0} = \left\{ \begin{array}{c} -(\boldsymbol{F}^{i+1} - \boldsymbol{F}^i) \\ \Delta t \, \mathsf{A}^{N_e}_{e=1} \int_{\Omega_e} \mathbf{B}_p{}^\mathsf{T} \boldsymbol{q}^i \, \mathrm{d}\Omega = -\Delta t \mathbf{H} \boldsymbol{r}^i_p \end{array} \right\} \tag{17.162}$$

Solving the coupled system of equations (17.159) requires, apart from the application of Dirichlet boundary conditions (prescribed nodal excess pore pressures and displacements) also the introduction of initial conditions, i.e., the distribution of initial stress and steady state pore pressure at the onset of consolidation at time $t = 0$. In GEO5 FEM this step is performed in the 1st computational stage. The consolidation analysis is carried out from the 2nd stage on. At time $t = 0$ (beginning of consolidation) the initial conditions are

$$p_{in} \;=\; p^{ss}, \quad p^{ex}|_{t=0} = 0 \quad (\boldsymbol{r}^p_0 = \mathbf{0}) \tag{17.163}$$
$$\boldsymbol{\sigma}|_{t=0} \;=\; \boldsymbol{\sigma}_{1st\,stage} \tag{17.164}$$

17.4.5   Limiting cases - undrained and drained conditions

It is interesting to show that the limiting cases representing the beginning (time $t = 0$) and the end (time $t \to \infty$) of consolidation essentially correspond to the undrained and drained conditions discussed already in Section 2.1.

Undrained conditions from Eq. (17.159)

Consider Eq. (17.159) together with the specific format of Eq. (17.152) (remember that $p^{ex}|_{t=0} = 0, \Delta\boldsymbol{\varepsilon} = \mathbf{0}$) and let $\Delta t \to 0$. This gives

$$\begin{bmatrix} -\mathbf{K} & \mathbf{Q}^\mathsf{T} \\ \mathbf{Q} & \mathbf{C} \end{bmatrix} \left\{ \begin{array}{c} \Delta\boldsymbol{r}^u \\ \Delta\boldsymbol{r}^p \end{array} \right\} = \left\{ \begin{array}{c} -({}^M\boldsymbol{f}) \\ \mathbf{0} \end{array} \right\} \tag{17.165}$$

This system of coupled equations can be solved by first solving the 2nd equation of system (17.165) for pore pressures $\boldsymbol{r}^p$ in terms of displacements $\boldsymbol{r}^u$ as (compare with Eq. (2.15))

$$\Delta\boldsymbol{r}^p = -\mathbf{C}^{-1}\mathbf{Q}\Delta\boldsymbol{r}^u = - \mathop{\mathsf{A}}^{N_e}_{e=1} \Big(\int_{\Omega_e} \alpha M 3 \boldsymbol{m}^\mathsf{T} \mathbf{B}^u \, \mathrm{d}\Omega \Big) \boldsymbol{r}^u \tag{17.166}$$

Substitution from (17.166) back into the 1st equation of system (17.165) yields

$$\underbrace{\Big(\mathbf{K} + \mathbf{Q}^\mathsf{T}\mathbf{C}^{-1}\mathbf{Q} \Big)}_{\mathbf{K}_{eff}} \Delta\boldsymbol{r}^u = {}^M\boldsymbol{f} \tag{17.167}$$

or (compare with Eq. (2.17))

$$\mathop{\mathsf{A}}^{N_e}_{e=1} \Big(\int_{\Omega_e} (\mathbf{B}^u)^\mathsf{T} \Big(\mathbf{D} + \alpha^2 M 9 \boldsymbol{m}\boldsymbol{m}^\mathsf{T} \Big) \mathbf{B}^u \, \mathrm{d}\Omega \Big) \boldsymbol{r}^u = {}^M\boldsymbol{f} \tag{17.168}$$

Drained conditions from Eq. (17.159)

First rewrite Eq. (17.159) as

$$\begin{bmatrix} -\mathbf{K} & \mathbf{Q}^{\mathsf{T}} \\ \dfrac{\mathbf{Q}}{\Delta t} & \dfrac{\mathbf{C}}{\Delta t} + \mathbf{H} \end{bmatrix} \left\{ \begin{array}{c} \Delta \boldsymbol{r}^u \\ \Delta \boldsymbol{r}^p \end{array} \right\} = \left\{ \begin{array}{c} -({}^M\boldsymbol{f}) \\ \dfrac{{}^P\boldsymbol{f}}{\Delta t} \end{array} \right\} \tag{17.169}$$

and let $\Delta t \to \infty$ to get

$$\begin{bmatrix} -\mathbf{K} & \mathbf{Q}^{\mathsf{T}} \\ \mathbf{0} & \mathbf{H} \end{bmatrix} \left\{ \begin{array}{c} \Delta \boldsymbol{r}^u \\ \Delta \boldsymbol{r}^p \end{array} \right\} = \left\{ \begin{array}{c} -({}^M\boldsymbol{f}) \\ {}^P\boldsymbol{f} = \mathsf{A}_{e=1}^{N_e} \int_{\Omega_e} (\mathbf{B}^p)^{\mathsf{T}} \boldsymbol{q} \, d\Omega \end{array} \right\} \tag{17.170}$$

This system of equations is already decoupled and can be split into the solution of two independent problems

- Steady state water flow (see Section 17.5 for more details)

$$\mathbf{H} \Delta \boldsymbol{r}^p = {}^P\boldsymbol{f} \tag{17.171}$$

- Mechanical problem with known distribution of pore pressures found from the solution of steady state water flow

$$\mathbf{K} \Delta r^u = ({}^M\boldsymbol{f}) + \mathbf{Q}^{\mathsf{T}} \Delta \boldsymbol{r}^p \tag{17.172}$$

17.4.6 Types of finite elements

The strain-displacement relation calls for a different order of interpolation for strains and displacements. Clearly, the displacements should be approximated by an order of higher polynomial degree than the strains. Equation (17.128), or its discretized version Eq. (17.144), further suggests the same order of approximation for strains and pore pressure. To comply with these requirements, the GEO5 FEM program offers two types of elements both with quadratic interpolation of displacements and linear interpolation of pore pressure, see Fig. 17.25.
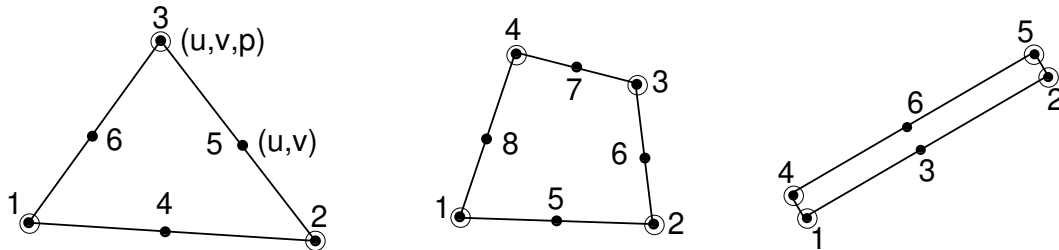

Figure 17.25: Element types used in consolidation analysis with GEO5 FEM

17.4.7 Example of one-dimensional consolidation

To test implementation of the presented theoretical grounds into GEO5 FEM we perform analysis of a simple one-dimensional (1D) consolidation problem which allows us to compare numerical predictions with analytical solution.

Analytical solution

Although the analytical solution to 1D consolidation, also implemented in GEO5 Settlement, is generally available in literature, see for example [45], we briefly address this issue here for the sake of clarity.

For simplicity, attention will be further accorded to constant loading $q(t) = -\sigma_z(t) = const$, where σ_z is the total stress in a given soil layer with the thickness H, see Fig. 17.26. The soil is
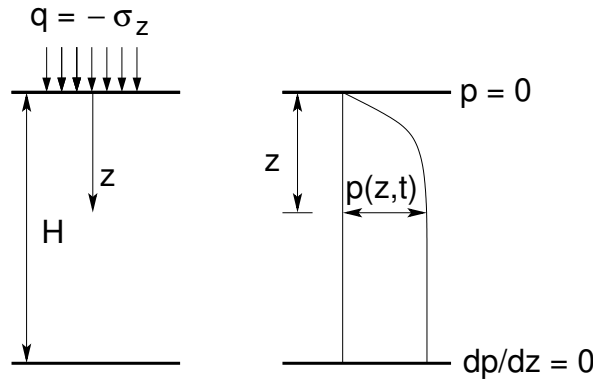
Figure 17.26: One-dimensional consolidation – soil layer permeable at $z = 0$

considered to be permeable at the top base $z = 0$. This corresponds to the flow boundary condition of the Dirichlet type with the zero excess pore pressure prescribed over the entire time domain, i.e., $\overline{p}^{ex} = p^{ex}(t, z = 0) = 0$, recall Eq. (17.135) or Eq. (17.137). We shall further assume that both the solid grains and pore water are incompressible, i.e., $\alpha = 1, M \to \infty$. These assumptions then yield a simplified version of equation of continuity (17.133) in the form

$$\dot{\varepsilon}_v = \frac{K_{sat}}{\gamma_w} \frac{\partial^2 p^{ex}}{\partial z^2} \tag{17.173}$$

and because $\alpha = 1$ and $\sigma_z(t) = const$ we get

$$\dot{\sigma}_m = \dot{\sigma}_m^{eff} - \dot{p}^{ex} = 0 \tag{17.174}$$

Next suppose that the kinematic boundary conditions comply with the oedometric test to arrive at

$$\varepsilon_x = \varepsilon_y = 0 \tag{17.175}$$

$$\varepsilon_v = \varepsilon_z = \frac{\sigma_z^{eff}}{E_{oed}} \tag{17.176}$$

Combining Eqs. (17.173)–(17.176) gives after some manipulations

$$\dot{p}^{ex} = c_v \frac{\partial^2 p^{ex}}{\partial z^2} \tag{17.177}$$

where the coefficient of consolidation c_v is given in terms of oedometric modulus E_{oed} by

$$c_v = \frac{K_{sat} E_{oed}}{\gamma_w} \tag{17.178}$$

The flow boundary conditions in Fig. 17.26 indicated that at time $t = 0$ the whole loading is taken by pore water promoting the initial conditions in the form

$$\sigma_z^{eff}(z, t = 0) = 0 \to \varepsilon_z(z, t = 0) = 0, \qquad w(z, t = 0) = 0 \tag{17.179}$$

The solution of Eq, (17.177) is then provided by

$$p(z, t) = 2q \sum_{n=0}^{\infty} \frac{1}{N} \sin \frac{Nz}{H} \exp\left(-N^2 T\right) \tag{17.180}$$

where

$$N = (2n + 1)\frac{\pi}{2} \tag{17.181}$$

and T is the reduced time written as

$$T = \frac{c_v t}{H^2} \tag{17.182}$$

The strain-displacement relation together with constitutive equation (17.176)

$$\varepsilon_z = \frac{\partial u_z}{\partial z} = \frac{\sigma_z^{eff}}{E_{oed}} = \frac{p-q}{E_{oed}}, \qquad p = p^{ss} + p^{ex}$$

provide the time evolution of settlement $w(t)$ in the form

$$w(z=0,t) = \int_0^H \frac{q-p}{E_{oed}} \, dz = w^{ss}(z=0)W(t) \qquad (17.183)$$

$$W(t) = \left(1 - \sum_{n=0}^{\infty} \frac{2}{N^2} \exp\left(-N^2 T\right)\right) \qquad (17.184)$$

where function $W(t)$ is termed the degree of consolidation and

$$w^{ss}(0) = qH/E_{oed} \qquad (17.185)$$

represents the terrain settlement at the end of consolidation at $t \to \infty$, i.e., the steady state.

Numerical solution and discussion

To be consistent with analytical solution we consider a linearly elastic material model with material parameters listed in Table 17.11.

Table 17.11: Material parameters

E_{oed} [MPa]	K_{sat} [m/den]	ν [–]	M [MPa]	α [–]	γ_w [kN/m^3]
10	10^{-3}	$\approx 0{,}0$	10^3	1	10

The geometrical model including the loading and flow boundary conditions is plotted in Fig. 17.27(a), where (N) represents an impermeable boundary, i.e., the Neumann boundary conditions with the prescribed zero normal flux ($\bar{q}_n = 0$). On the other hand, the letter (P) indicates permeable boundary allowing for free outflow, i.e., the Dirichlet boundary conditions with the zero prescribed excess pore pressure ($\bar{p}^{ex} = 0$). Note that in GEO5 FEM this is the default setting for all boundaries so it is up to the user to specify the impermeable (N) boundaries manually. The kinematic boundary conditions, zero horizontal displacements along vertical edges and zero vertical displacements along the horizontal base, are evident in Fig. 17.27(d). As for the initial conditions at time $t = 0$ we set both stresses and steady state pore pressure to zero ($\boldsymbol{\sigma}(t=0)\mathbf{0}, p^{ss} = 0$).
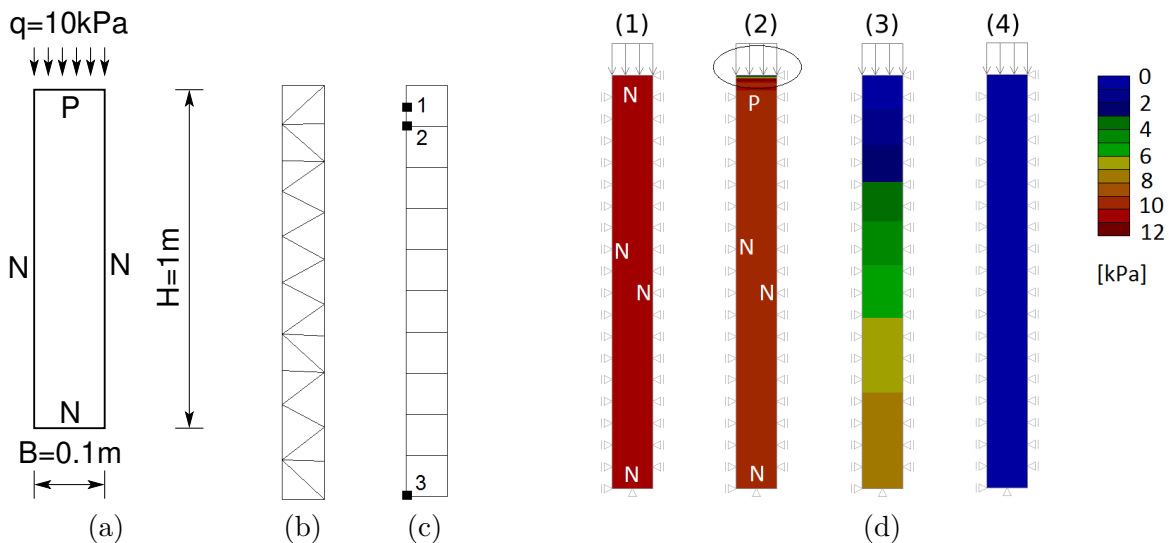

Figure 17.27: 1D consolidation: a) geometry, loading and flow boundary conditions, b,c) finite element mesh, d) kinematic boundary conditions and evolution of excess pore pressure - 1) undrained conditions, 2) T= 10^-6, 3) T= 0.1, 4) T= 1

Figure 17.28 shows evolution of excess pore pressure both in space and time for two types of meshes in Fig. 17.27(b,c) predicted numerically as well as analytically. The vertical dashed line identifies the solution at time $t = 0$ when the entire load is taken by pore water. This state is represented by the excess pore pressure distribution in Fig. 17.27(a1) obtained via standard analysis with undrained conditions confirming the correctly determined value of $p^{ex}(t = 0) = 10$ kPa. However, when running consolidation analysis the smallest time to display available results is given by the initial time step which was set to $\Delta t = 10^{-5}$ [day] in our simulation. The corresponding results appear in Fig. 17.27(a2). We observe some differences localized in the vicinity of the top boundary where $p^{ex} = 0$ is prescribed. This can partly be attributed to numerical solution and partly to a relatively course meshes. This numerical error, relevant for the smallest reduced time $T = 10^{-6}$ only, is also clearly evident in Fig. 17.28 for both meshes. This error gradually disappears with increasing time and for larger reduced times the numerical and analytical results essentially coincide.
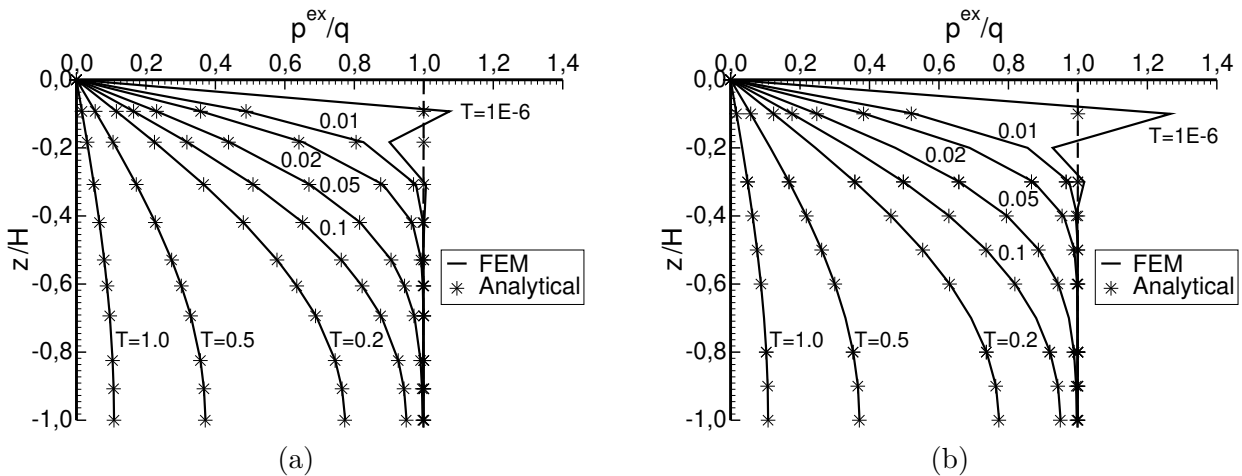

Figure 17.28: Distribution of excess pore pressure – numerical vs. analytical solution: a) triangular mesh, b) quadrilateral mesh

Almost perfect match between numerical and analytical predictions is also seen for terrain settlement $w(t, z = 0)$ in Fig. 17.29(a) asymptotically arriving at the steady state solution $w^{ss}(t \to \infty, z = 0)$ given by Eq. (17.185).
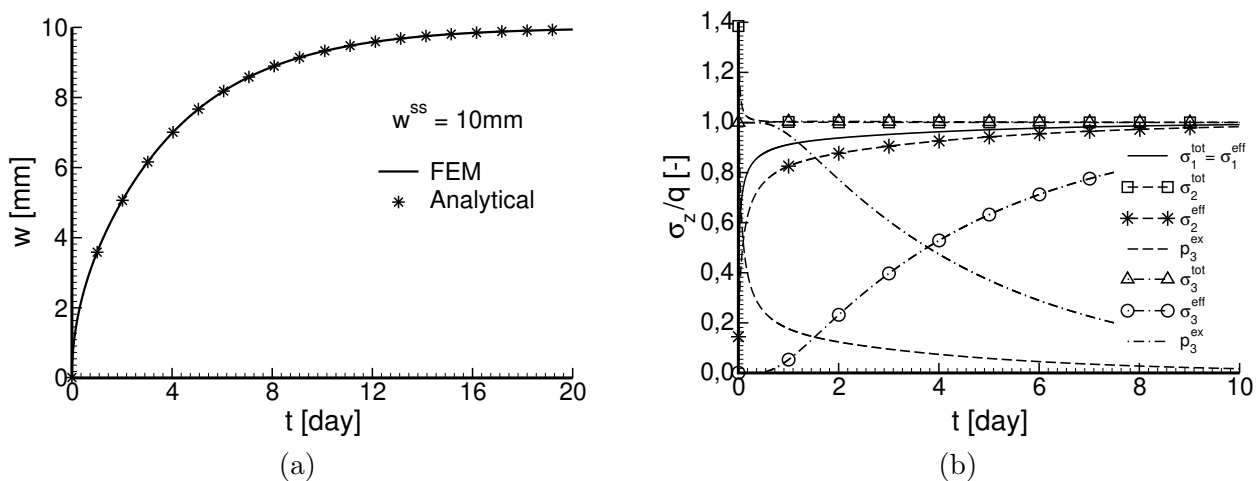

Figure 17.29: a) Terrain settlement w, b) evolution of total stress σ_z^{tot}, effective stress σ_z^{eff} and excess pore pressure p^{ex} at selected points

Figure 17.29(b) finally illustrates time evolution of total (σ_z^{tot}) and effective (σ_z^{eff}) vertical stresses at selected points shown in Fig. 17.27(c) in dependence on the dissipation of excess pore pressure (p^{ex}).

It is seen that with increasing time all excess pore pressure in the entire domain is gradually dissipated while effective stresses are approaching the total stress in correspondence with Eq. (17.127). It is also evident that the conventional assumption about the constant total stress is more or less fulfilled. This, however, is no longer valid when considering a multi-dimensional analysis as demonstrated for example in [72]. In this regard, the application of analytical solution of 1D consolidation in 2D space, such as the one implemented in GEO5 Settlement, should be approached with care.

17.5 Water flow analysis

Section 17.4.1 introduced the mass conservation law in terms of contnuity equation (17.130) to describe the flow of water in a fully saturated (degree of saturation $S = 1$ in the entire domain) deformable porous medium. When allowing for water flow through a partially saturated medium (region with positive pore pressure representing suction and $S < 0$) this equation receives an advanced format in terms of the bulk moduli of the solid phase (K_m) and water (K_w), the porosity n, and Biot parameter α, recall Section 2.1,

$$\frac{(\alpha - n)S}{K_m}(\dot{S}p + S\dot{p}) + \frac{nS}{K_w}\dot{p} + \alpha S \text{div}(\boldsymbol{v}^s) + n\dot{S} + \text{div}\left(-K_r\mathbf{K}_{sat}\boldsymbol{\nabla}h(p)\right) = m(t) \qquad (17.186)$$

Taking this equation as a point of departure and then neglecting the skeleton deformation and the compressibility of pore fluid ($\text{div}\boldsymbol{v}^s = 0, K_m \to \infty, K_w \to \infty$) in Eq. (17.186) we arrive at the general version of Richards' equation for unsaturated flow in the absence of internal sources in the form

$$n\dot{S} + \text{div}\left(-K_r\mathbf{K}_{sat}\boldsymbol{\nabla}h\right) = 0 \qquad \text{in } \Omega \qquad (17.187)$$

In analogy to Section 17.4.1 solving Eq. (17.187) calls for the introduction of hydraulic boundary conditions. These are either imposed fluxes (Neumann or natural boundary conditions) or prescribed changes in pore fluid pressure (Dirichlet or essential boundary conditions). They are essentially anal-
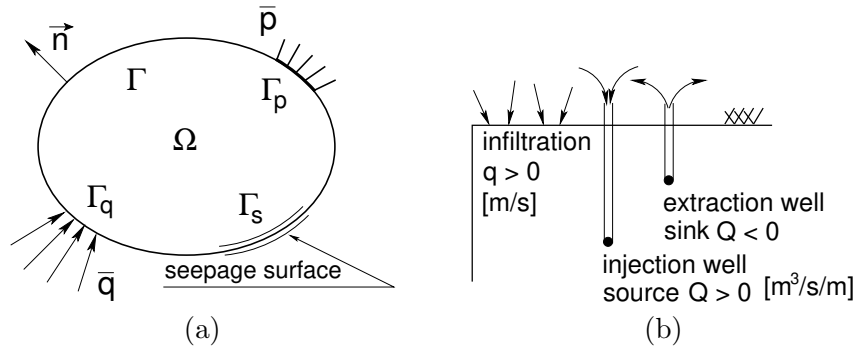

Figure 17.30: a) Hydraulic boundary conditions, b) Infiltration, sources and sinks

ogous to prescribed traction and displacement boundary conditions mentioned, e.g., in Section 17.4.2. In particular, see Fig. 17.30(a), we have (the seepage boundary conditions on Γ_s are treated separately in Section 17.5.5)

- Imposed flux density $\bar{q}_n$ normal to the boundary Γ_q; $\boldsymbol{n}$ is the outward unit normal, $\bar{q}_n$ is assumed positive when in the direction parallel to $\boldsymbol{n}$ (outflow), see Fig. 17.30 and Eq. (16.2))

$$\boldsymbol{n}^\mathsf{T}(n\boldsymbol{v}^{ws}) = -\boldsymbol{n}^\mathsf{T}\left(K_r\mathbf{K}_{sat}\boldsymbol{\nabla}h\right) = \bar{q}_n \qquad \text{on } \Gamma_q \qquad (17.188)$$

- Prescribed pore pressure $\bar{p}$ or total head $\bar{h}$ on the boundary Γ_p

$$p = \bar{p} \qquad \text{or} \qquad h = \bar{h} \qquad \text{on } \Gamma_p \qquad (17.189)$$

Apart from the boundary flux density q_n [m/s] the program GEO FEM allows for introducing the point sources or sinks Q [m³s⁻¹]. The sign convention, evident from Fig. 17.30 is identical with the boundary flux.

17.5.1   Temporal discretization of Equation (17.187)

Defining the specific water content capacity $C = \mathrm{d}S/\mathrm{d}h_p$ [m^{-1}], so that $\dot{S} = C\dot{h}$, provides the so called h-based version of the Richards equation. On the contrary, introducing the pore fluid diffusivity $D = K/C$ [m^{2}s^{-1}] allows us to write Eq. (17.187) solely in terms of the degree of saturation. Although both versions require to deal with a single variable only, they experience certain drawbacks when solved numerically. While the h-based formulation is known to fail in preserving mass in some applications, the S-based formulation although mass-conservative cannot be adopted for describing the fully saturated flow [18, 35].

To overcome these difficulties Celia et al. [18] proposed a fully explicit mass-conservative scheme to solve the original mixed form of Richards' equation (17.187) directly by adopting the modified Picard iteration scheme to get

$$n\frac{S^{i+1,j+1} - S^i}{\Delta t} - \boldsymbol{\nabla}^\mathsf{T} K_r(h_p^{i+1,j})\mathbf{K}_{sat}\boldsymbol{\nabla} h^{i+1,j+1} = 0 \tag{17.190}$$

where i stands for a given time (load) increment and j represents the current iteration step. Next, write $S^{i+1,j+1}$ with the help of Taylor's series expansion as

$$S^{i+1,j+1} = S^{i+1,j} + \left(\frac{\mathrm{d}S}{\mathrm{d}h_p}\right)^{i+1,j}\left(h_p^{i+1,j+1} - h_p^{i+1,j}\right) \tag{17.191}$$

and define

$$\begin{aligned}
\Delta h &= h_p^{i+1,j+1} - h_p^{i+1,j} = h^{i+1,j+1} - h^{i+1,j} \\
\left(\frac{\mathrm{d}S}{\mathrm{d}h_p}\right)^{i+1,j} &= C^{i+1,j} \\
S^{i+1,j+1} &= S^{i+1,j} + C^{i+1,j}\Delta h \\
\mathbf{K}^{i+1,j} &= K_r^{i+1,j}\mathbf{K}_{sat}
\end{aligned}$$

Substituting the above terms into Eq. (17.190) then gives

$$\frac{1}{\Delta t}nC^{i+1,j}\Delta h - \boldsymbol{\nabla}^\mathsf{T}\mathbf{K}^{i+1,j}\boldsymbol{\nabla}(\Delta h) = \boldsymbol{\nabla}^\mathsf{T}\mathbf{K}^{i+1,j}\boldsymbol{\nabla} h^{i+1,j} - \frac{1}{\Delta t}n(S^{i+1,j} - S^i) \tag{17.192}$$

17.5.2   Finite element approximation of Equation (17.192)

Note that a closed form solution of Eq. (17.192) together with boundary conditions (17.188) and (17.189) is not generally available. A natural step is therefore to rewrite Eq. (17.192) in the context of the principle of virtual work. To do so, we begin with the dervation of principal of virtual work, Eq. (17.1), pertinent to the present task by first combining Eqns. (17.192) and (17.188) to get

$$\begin{aligned}
&\frac{1}{\Delta t}\int_\Omega \delta h \left(nC^{i+1,j}\right)\Delta h\,\mathrm{d}\Omega - \int_\Omega \delta h \left[\boldsymbol{\nabla}^\mathsf{T}\mathbf{K}^{i+1,j}\boldsymbol{\nabla}(\Delta h)\right]\mathrm{d}\Omega \\
&- \int_\Omega \delta h \left[\boldsymbol{\nabla}^\mathsf{T}\mathbf{K}^{i+1,j}\boldsymbol{\nabla} h^{i+1,j}\right]\mathrm{d}\Omega + \frac{1}{\Delta t}\int_\Omega \delta h \left[n(S^{i+1,j} - S^i)\right]\mathrm{d}\Omega \\
&+ \int_{\Gamma_q} \delta h \left[\boldsymbol{n}^\mathsf{T}\mathbf{K}^{i+1,j}\boldsymbol{\nabla}(\Delta h + h^{i+1,j}) + \bar{q}_n^{i+1}\right]\mathrm{d}\Gamma = 0
\end{aligned} \tag{17.193}$$

Next, integrating Eq. (17.193) by parts and realizing that $\delta h = 0$ on Γ_p gives

$$\begin{aligned}
&\frac{1}{\Delta t}\int_\Omega \delta h \left(nC^{i+1,j}\right)\Delta h\,\mathrm{d}\Omega + \int_\Omega (\delta\boldsymbol{\nabla} h)^\mathsf{T}\mathbf{K}^{i+1,j}\boldsymbol{\nabla}(\Delta h)\,\mathrm{d}\Omega = \\
&- \int_\Omega (\delta\boldsymbol{\nabla} h)^\mathsf{T}\mathbf{K}^{i+1,j}\boldsymbol{\nabla} h^{i+1,j}\,\mathrm{d}\Omega - \frac{1}{\Delta t}\int_\Omega \delta h \left[n(S^{i+1,j} - S^i)\right]\mathrm{d}\Omega \\
&- \int_{\Gamma_q} \delta h\,\bar{q}_n^{i+1}\,\mathrm{d}\Gamma
\end{aligned} \tag{17.194}$$

This equation now can be solved easily using the finite element method. In such a case the distribution of the total head can be approximated using standard element shape functions from Sections 17.2.3 or 17.2.4 as

$$\Delta h = \sum_{i=1}^{n} N_i \Delta r_i = \mathbf{N}\Delta\boldsymbol{r} \tag{17.195}$$

where Δr_i represents the increment of nodal total heads and n is the number of nodes. The finite element equations derived by substituting for Δh from Eq. (17.195) into Eq. (17.194) and taking into account the boundary conditions (17.189) now become

$$
\begin{bmatrix}
\frac{1}{\Delta t}\mathbf{C}_{11} + \mathbf{H}_{11} & \frac{1}{\Delta t}\mathbf{C}_{12} + \mathbf{H}_{12} \\[2mm]
\left(\frac{1}{\Delta t}\mathbf{C}_{12} + \mathbf{H}_{12}\right)^{\mathsf{T}} & \frac{1}{\Delta t}\mathbf{C}_{22} + \mathbf{H}_{22}
\end{bmatrix}^{i+1,j}
\left\{ \begin{array}{c} \Delta\boldsymbol{r} \\ \mathbf{0} \end{array} \right\}
$$
$$
= \left\{ \begin{array}{c} \boldsymbol{f}_{\text{ext}}^{i+1} \\ \mathbf{0} \end{array} \right\}
- \begin{bmatrix} \mathbf{H}_{11} & \mathbf{H}_{12} \\[1mm] (\mathbf{H}_{12})^{\mathsf{T}} & \mathbf{H}_{22} \end{bmatrix}^{i+1,j}
\left\{ \begin{array}{c} \boldsymbol{r}^{i+1,j} \\ \overline{\boldsymbol{r}}^{i+1} \end{array} \right\}
- \frac{1}{\Delta t}\left\{ \begin{array}{c} \boldsymbol{S}_1^{i+1,j} \\ \boldsymbol{S}_2^{i+1,j} \end{array} \right\}
\tag{17.196}
$$

Point out that the 2nd equation allows us to calculate fluxes at nodes with the prescribed nodal pressure heads $\overline{\boldsymbol{r}}^{i+1}$ (notice analogy with reactions at nodes with prescribed displacements). The first equation thus gives the unknown nodal increments of total head $\Delta\boldsymbol{r}$ at the end of the current time step as

$$\left[\frac{1}{\Delta t}\mathbf{C}_{11}^{i+1,j} + \mathbf{H}_{11}^{i+1,j}\right]\Delta\boldsymbol{r} = \boldsymbol{f}_{\text{ext}}^{i+1} - \mathbf{H}_{12}^{i+1,j}\overline{\boldsymbol{r}}^{i+1} - \mathbf{H}_{11}^{i+1,j}\boldsymbol{r}^{i+1,j} - \frac{1}{\Delta t}\boldsymbol{S}_1^{i+1,j} \tag{17.197}$$

where the matrices $\mathbf{C}_{11}^{i+1,j}$ and $\mathbf{H}_{12}^{i+1,j}$ read (N_e stands for the number of elements)

$$\mathbf{C}_{11}^{i+1,j} = \mathop{\mathbf{A}}_{e=1}^{N_e} \int_{\Omega_e} \mathbf{N}^{\mathsf{T}}(nC^{i+1,j})\mathbf{N}\,\mathrm{d}\Omega \tag{17.198}$$

$$\mathbf{H}_{11}^{i+1,j} = \mathop{\mathbf{A}}_{e=1}^{N_e} \int_{\Omega_e} \mathbf{B}^{\mathsf{T}}\mathbf{K}^{i+1,j}\mathbf{B}\,\mathrm{d}\Omega \tag{17.199}$$

$$\boldsymbol{S}_1^{i+1,j} = \mathop{\mathbf{A}}_{e=1}^{N_e} \int_{\Omega_e} \mathbf{N}^{\mathsf{T}}\left[n(S^{i+1,j} - S^i)\right]\,\mathrm{d}\Omega \tag{17.200}$$

For the purpose of numerical stability a diagonal format of the capacity matrix $\mathbf{C}_{\text{diag}}$ is usually adopted in place of the consistent matrix $\boldsymbol{C}$ given by Eq. (17.198). For low order elements, i.e., 3-node triangular or 4-node quadrilateral element, the diagonal terms of $\mathbf{C}_{\text{diag}}$ are equal to the sum of all terms in the corresponding row of $\mathbf{C}$. So these are the only elements available in GEO5 FEM to perform the transient water flow analysis.

The right hand side of Eq. (17.197) represents a vector of out-of-balanced loads

$$\boldsymbol{R}^{i+1,j} = \boldsymbol{f}_{\text{ext}}^{i+1} - \boldsymbol{f}_{\text{int}}^{i+1,j} \tag{17.201}$$

where the vector of external loads $\boldsymbol{f}_{\text{ext}}^{i+1}$ is provided by

$$\boldsymbol{f}_{\text{ext}}^{i+1} = \boldsymbol{f}_q^{i+1} + \boldsymbol{Q}^{i+1} \tag{17.202}$$

$$\boldsymbol{f}_q^{i+1} = -\mathop{\mathbf{A}}_{e=1}^{N_E} \int_{\Gamma_{qE}} \mathbf{N}^{\mathsf{T}}\overline{q}_n^{i+1}\,\mathrm{d}\Gamma, \qquad \overline{q}_n = \mathbf{N}\overline{\boldsymbol{q}}$$

where N_E stands for the number of loaded element edges on the boundary. $\boldsymbol{Q}^{i+1}$ is the vector of nodal values of prescribed sources and/or sinks, which may correspond to injection or pumping rates representing for example the effect of injection or extraction wells as shown schematically in Fig. 17.30(b). Similarly, prescribing the nodal intensities $\overline{\boldsymbol{q}}^{i+1}$ allows for simulating pore fluid flows

across a boundary of the finite element mesh, e.g., infiltration rate as seen in Fig. 17.30(b). In the simplest case, in which no fluid is transferred across the boundary Γ_q, the imposed flux density $\bar{q}_n = 0$. In comparison with the solution of pure deformation of a soil body these boundary conditions correspond to prescribed surface tractions.

The vector of generalized internal loads $\boldsymbol{f}_{\text{int}}^{i+1,j}$ can be formally written as

$$\boldsymbol{f}_{\text{int}}^{i+1,j} = \overset{N_e}{\underset{e=1}{\text{A}}} \int_{\Omega_e} \mathbf{B}^\mathsf{T} \boldsymbol{q}^{i+1,j} \, \mathrm{d}\Omega + \frac{1}{\Delta t} \boldsymbol{S}_1^{i+1,j} \tag{17.203}$$

where the flux vector $\boldsymbol{q}^{i+1,j}$ is given by

$$\boldsymbol{q}^{i+1,j} = \mathbf{K}^{i+1,j} \mathbf{B} \boldsymbol{r}^{i+1,j} \tag{17.204}$$

Note that the 1st term on the right hand side of Eq. (17.203) derives from the second two terms on the right hand side of Eq. (17.197).

17.5.3   Iteration within a given time step

Solving the system of nonlinear equations (17.197) typically employs the Newton-Raphson method. Assigning $\boldsymbol{r}^\mathrm{I}$ the initial value of total nodal heads at time $t = 0$ and defining $\mathcal{K}^{i+1,j}$ the matrix of the global system of equations (17.197) as

$$\mathcal{K}^{i+1,j} = \frac{1}{\Delta t} \mathbf{C}_{11}^{i+1,j} + \mathbf{H}_{11}^{i+1,j}$$

allows us to consider the following three cases:

- 1st loading increment - state at the end of the initializing stage I
  $(i = j = 0, t_0 = 0, t_1 = \Delta t)$

$$\mathcal{K}^1(\boldsymbol{h}_p^1)\Delta\boldsymbol{r} = \boldsymbol{f}_{\text{ext}}^1 - \mathbf{H}_{12}(K_{sat})\bar{\boldsymbol{r}}^1, \quad \boldsymbol{r}^1 = \boldsymbol{r}^\mathrm{I} + \Delta\boldsymbol{r}$$

- $i + 1$ loading incremen - state at the end of the ith loading step
  $(j = 0, t_{i+1} = t_i + \Delta t)$

$$\mathbf{C}^{i+1,0} = \mathbf{C}^i, \quad \mathbf{H}^{i+1,0} = \mathbf{H}^i, \quad \boldsymbol{S}_1^{i+1,0} = \boldsymbol{S}_1^i, \quad \boldsymbol{r}^{i+1,0} = \boldsymbol{r}^i$$

$$\boldsymbol{f}_{\text{int}}^{i+1,0} = \overset{N_e}{\underset{e=1}{\text{A}}} \int_{\Omega_e} \mathbf{B}^\mathsf{T} \boldsymbol{q}^i \, \mathrm{d}\Omega + \frac{1}{\Delta t} \boldsymbol{S}_1^i$$

$$\boldsymbol{R}^{i+1,0} = \boldsymbol{f}_{\text{ext}}^{i+1} - \boldsymbol{f}_{\text{int}}^{i+1,0} = \underbrace{(\boldsymbol{f}_{\text{ext}}^{i+1} - \boldsymbol{f}_{\text{ext}}^i)}_{\Delta\boldsymbol{f}} + \underbrace{(\boldsymbol{f}_{\text{ext}}^i - \boldsymbol{f}_{\text{int}}^{i+1,0})}_{=\boldsymbol{\epsilon}}$$

$$\mathcal{K}^{i+1,0}\Delta\boldsymbol{r} = \Delta\boldsymbol{f} + \boldsymbol{\epsilon}, \quad \boldsymbol{r}^{i+1,1} = \boldsymbol{r}^i + \Delta\boldsymbol{r}$$

  If $\Delta\boldsymbol{f} = \mathbf{0}$ then the new total head increment is estimated as $\Delta\boldsymbol{r}^0 = (\boldsymbol{r}^i - \boldsymbol{r}^{i-1})\dfrac{\Delta t^{i+1}}{\Delta t^i}$ where $\Delta t^i, \Delta t^{i+1}$ represent the two successive time steps.

- $i + 1$ loading increment - state at the end of jth iteration step $(t_{i+1} = t_i + \Delta t)$

$$\boldsymbol{R}^{i+1,j+1} = \boldsymbol{f}_{\text{ext}}^{i+1} - \boldsymbol{f}_{\text{int}}^{i+1,j+1},$$

$$\boldsymbol{f}_{\text{int}}^{i+1,j+1} = \overset{N_e}{\underset{e=1}{\text{A}}} \int_{\Omega_e} \mathbf{B}^\mathsf{T} \boldsymbol{q}^{i+1,j+1} \, \mathrm{d}\Omega + \frac{1}{\Delta t} \boldsymbol{S}_1^{i+1,j+1}$$

$$\mathcal{K}^{i+1,j+1}\Delta\boldsymbol{r} = \boldsymbol{R}^{i+1,j+1}, \quad \boldsymbol{r}^{i+1,j+2} = \boldsymbol{r}^{i+1,j+1} + \Delta\boldsymbol{r}$$

Suitable convergence criteria to terminate the iteration process are discussed in Section 17.2.7. Some useful information on the comparison of various convergence criteria with possible acceleration of the iteration process particularly in the simulation of infiltration in initially dry soils can be found in [35].

17.5.4 Steady state water flow

When the soil saturation S no longer evolves with time ($\dot{S} = 0$), we arrive at the steady state solution and Eq. (17.187) reduces to

$$\text{div}\,(-K_r \mathbf{K}_{sat} \boldsymbol{\nabla} h) = 0 \qquad (17.205)$$

After discretization, compare with Eq. (17.197) and also with Eq. (17.171), we get

$$\mathbf{H}^j \Delta \boldsymbol{r} = \boldsymbol{R}^j, \qquad \mathbf{H}^j = \mathop{\mathbf{A}}_{e=1}^{N_e} \int_{\Omega_e} \mathbf{B}^{\mathsf{T}} K_r^j \mathbf{K}_{sat} \mathbf{B}\,\mathrm{d}\Omega \qquad (17.206)$$

When the permeability matrix $K_r \mathbf{K}_{sat}$ is constant and the flow is confined (the phreatic surface is known), the solution of Eq. (17.206) reduces to a single inversion of the matrix $\mathbf{H}$. If, on the other hand, the flow is unconfined (the phreatic surface is unknown), an iterative scheme must be employed to solve Eq. (17.206). For example, in the framework of the modified Newton-Raphson method we proceed as follows. Define a vector of out-of-balanced loads at the beginning of the j-th iteration, recall Eq. (17.201),

$$\boldsymbol{R}^j = \boldsymbol{f}_{\text{ext}} - \boldsymbol{f}_{\text{int}}^j \qquad (17.207)$$

where

$$\boldsymbol{f}_{\text{int}}^j = \mathbf{H}^j \boldsymbol{r}^j, \qquad \boldsymbol{r}^j = \boldsymbol{r}^{j-1} + \Delta \boldsymbol{r} \qquad \Delta \boldsymbol{r} = (\mathbf{H}^{j-1})^{-1} \Delta \boldsymbol{R}^{j-1} \qquad (17.208)$$

Therefore, at each iteration the increments of total heads are calculated for a given increment of the out-of-balanced loads found from Eq. (17.207) and added to the total heads. This procedure is repeated until a certain convergence criterion from Section 17.2.7. is reached. Further details can be found in [4].

17.5.5 Seepage surface

To introduce the subject consider two examples of a rectangular dam in Fig. 17.31. It is a relatively complex problem as it involves both a phreatic surface separating saturated and unsaturated zones inside the dam and a seepage surface on the right hand side of the dam where the characteristic hydraulic conditions are not known a priori. While $\overline{q}_n = 0$ is a correct boundary condition above the point where the phreatic surface touches the seepage surface ($S < 1, h < 0$ inside the domain), below this point along the seepage surface the pore fluid pressure becomes zero (it should rather be in equilibrium with the atmospheric pressure, but that is taken as a reference pressure) since water is free to flow across the boundary ($S = 1, h = y$). This problem was studied, e.g., in [4] by changing the boundary conditions during an iterative solution (either prescribed flux or prescribed total head) whenever necessary owing to the fact that the exit point is not known in advance.
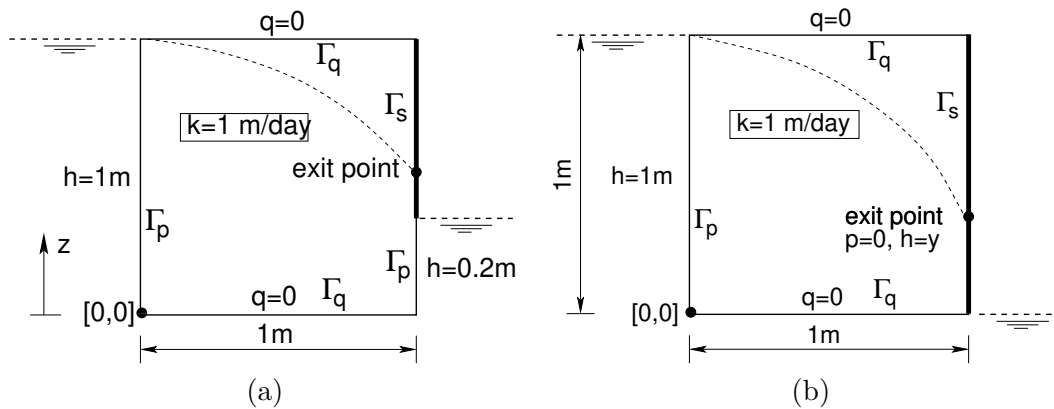

Figure 17.31: Example of unconfined flow: modeling of flow through a seepage surface: a) h=0.2m, b) h=0

Switching from one type of boundary condition to the other may cause substantial difficulty in coding the finite element program. While the flux boundary condition Eq. (17.188) is automatically

satisfied by the weak formulation the imposed total head boundary condition , Eq. (17.189), reduces the number of active degrees of freedom. An elegant way to deal with these seepage boundary conditions was suggested in [2] by formulating special seepage interface elements in the framework of the penalty method. The main advantage of these elements is the possibility of distinguishing between internal and external hydraulic conditions. When introduced along a boundary inside the domain it further allows us to simulate a constant pore pressure jump across the interface.

The use of these special interface elements can be avoided providing the Newton-Cotes integration scheme is assumed. The seepage boundary conditions apply directly to the boundary nodes and can be introduced through a nonlinear spring model by defining a point flux through the surface in the form

$$\overline{Q} = k_v(h - h_{ext}) \tag{17.209}$$

where k_v is a fictitious permeability (a spring constant) that must be sufficiently large to ensure that $h = h_{ext}$ at the boundary nodes where a nonzero external pressure is prescribed. Imposing external pressures through Eq. (17.209) appears useful when the location of zero external pressure changes with time, which may occur not only on the downstream face of the dam but also on the upstream face during filling or drawdown. Since only steady state flow is considered herein the external pressure does not change with time and can be imposed directly on the respective degrees of freedom. The seepage surface then becomes adequate only for that part of the boundary where $p_{ext} = 0$ (flow at atmospheric pressure). The seepage boundary conditions on Γ_s can then be written as

$$\overline{Q} = k_v(h - y), \qquad \text{if } h > y \ (S = 1) \text{ in the domain and } p_{ext} = 0 \tag{17.210}$$
$$\overline{Q} = 0, \qquad\qquad \text{if } h < y \ (S < 1) \text{ in the domain and } p_{ext} = 0 \tag{17.211}$$

where the zero flux boundary condition Eq. (17.211) is generated by setting $k_v = 0$. Note that this is exactly the same approach as used with tension excluded spring supports in purely mechanical analyses. The weak form of Eq. (17.205) when combined with Eq. (17.210) becomes

$$f_{\text{int}} + \sum_{i=1}^{M_s} k_v h_i|_{\Gamma_s} = f_{\text{ext}} + \sum_{i=1}^{M_s} k_v z_i|_{\Gamma_s} \tag{17.212}$$

where M_s is the number of nodes on the seepage surface and z_i is the z-coordinate of the node i.

This particular approach was employed to solve the two problems in Fig. 17.31. Note that for boundaries well above the phreatic surface where no seepage is expected it may be more appropriate to directly prescribe the no flow conditions $\overline{q}_n = 0$ rather then let this condition be generated through the seepage surface Eq. (17.211). The results are plotted in Fig. 17.32. The applied boundary conditions as well as isolines of velocity v_x clearly show the difference between the two example problems. The total discharge through individual boundaries is also shown.
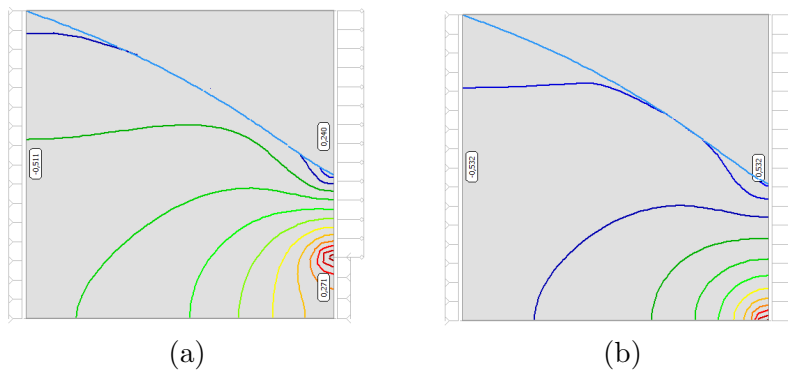

(a)   (b)

Figure 17.32: Modeling of seepage surface: distribution of velocity v_x (van Genuchten model with $n = 2, \alpha = 2\text{m}^{-1}$): a) h=0.2m, b) h=0

It is worth noting that the solution is not as much dependent on the penalty stiffness k_v as it is on the parameters of the van Genuchten model and the density of finite element mesh in the vicinity of the expected exit point. In GEO5 FEM, this point will coincide with a particular node of the finite element mesh owing to Eq. (17.210) being enforced only in the nodes, recall Eq. (17.212).

17.5.6 Flow through a thin zone - modeling of interfaces

In many real situations we often need to deal with flow across or along an interface of two layers having marginally different permeabilities. Although two nodes, one for each layer, are generated along the common boundary in some commercial codes by default a fully permeable boundary condition is generally assumed by tying the corresponding total head degrees of freedom of the adjacent nodes. Treating impermeable or partially permeable boundaries on the other hand requires the introduction of interface elements into the finite element model. Interface elements can also be used to either block the flow across an impermeable sheeting wall or to represent a drain by easing flow along the longitudinal direction of the interface.
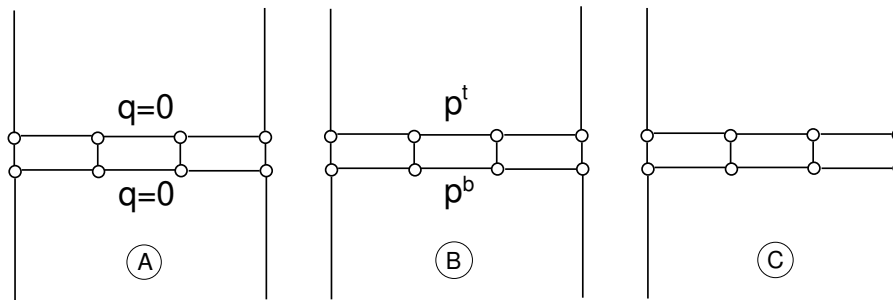
Figure 17.33: Hydraulic boundary conditions on interface

Figure 17.33 shows three particular conditions which may occur when simulating flow through a thin interfacial zone. Example A represents a fully impermeable boundary. This is the most simple case when interface elements essentially do not contribute to the governing system of equations which in turn results into a discontinuous pore pressure field. To enforce pore pressure continuity ($p_t = p_b$) in the case of a fully permeable boundary, example B, it is sufficient to tie the corresponding total head (pore pressure) degrees of freedom along the interface without actually formulating interface elements to account for flow. The intermediate boundary conditions (example C), which may include both the above two extremes, must however be handled by interface elements.
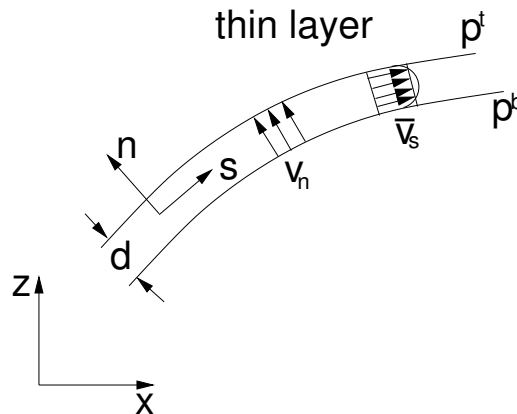

Figure 17.34: Flow through a thin zone

Figure 17.34 shows a simplified representation of flow both in the longitudinal (s) and normal (n) directions of a thin interfacial zone with s, n representing the local coordinate system. Since interface elements have zero thickness we get (for the local coordinate system)

$$h = \frac{p}{\gamma_w} \tag{17.213}$$

Darcy's law then assumes the following form

$$n\boldsymbol{v}^{ws} = -\boldsymbol{\mathsf{K}}_{sat}\boldsymbol{\nabla}h = -\frac{\boldsymbol{K}_{sat}}{\gamma_w}\boldsymbol{\nabla}p \tag{17.214}$$

Because this topic is also common to consolidation described in Section 17.4 and has not be specifically addressed yet, we start from continuity equation (17.130) which in this particular case reads

$$\frac{n}{K_w}\dot{p} + \dot{\varepsilon}_v + \text{div}(-\mathbf{K}_{sat}\boldsymbol{\nabla}h) = 0 \tag{17.215}$$

The 2×2 permeability matrix $\mathbf{K}_{sat}$ now reads

$$\mathbf{K}_{sat} = \left[\begin{array}{cc} k_s & 0 \\ 0 & k_n \end{array} \right] \tag{17.216}$$

where k_s, k_n are the permeabilities in the longitudinal and normal directions, respectively. The corresponding fluxes are given by, see Figure 17.34,

$$q_s = -k_s\frac{1}{2}\frac{\partial(h^t + h^b)}{\partial s} \tag{17.217}$$

$$q_n = -k_n\frac{h^t - h^b}{d} \tag{17.218}$$

where d is a virtual thickness of the interface. Similarly we define the velocity components of the solid phase so that

$$\dot{\varepsilon}_v = \text{div}(\boldsymbol{v}^s) = v_s^s + v_n^s = \frac{1}{2}\frac{\partial((\dot{u}_s^s)^t + (\dot{u}_s^s)^b)}{\partial s} + \frac{(\dot{u}_n^s)^t - (\dot{u}_n^s)^b}{d} \tag{17.219}$$

Admitting steady state conditions only Equation (17.215) considerably simplifies (note the similarity with Equation (17.205))

$$\text{div}(-\mathbf{K}_{sat}\boldsymbol{\nabla}h) = 0 \tag{17.220}$$

A weak form of Equation (17.220) leads again, after finite element discretization, to Equation $(17.206)_1$ where the $\mathbf{B}$ matrix in Equation $(17.206)_2$ is now provided by

- 4-node interface element

$$\mathbf{B} = \left[\begin{array}{cccc} \dfrac{1}{2J}\dfrac{\partial N_1}{\partial r} & \dfrac{1}{2J}\dfrac{\partial N_2}{\partial r} & \dfrac{1}{2J}\dfrac{\partial N_1}{\partial r} & \dfrac{1}{2J}\dfrac{\partial N_2}{\partial r} \\[3mm] -\dfrac{N_1}{d} & -\dfrac{N_2}{d} & \dfrac{N_1}{d} & \dfrac{N_2}{d} \end{array} \right] \tag{17.221}$$

- 6-node interface element

$$\mathbf{B} = \left[\begin{array}{cccccc} \dfrac{1}{2J}\dfrac{\partial N_1}{\partial r} & \dfrac{1}{2J}\dfrac{\partial N_2}{\partial r} & \dfrac{1}{2J}\dfrac{\partial N_3}{\partial r} & \dfrac{1}{2J}\dfrac{\partial N_1}{\partial r} & \dfrac{1}{2J}\dfrac{\partial N_2}{\partial r} & \dfrac{1}{2J}\dfrac{\partial N_3}{\partial r} \\[3mm] -\dfrac{N_1}{d} & -\dfrac{N_2}{d} & -\dfrac{N_3}{d} & \dfrac{N_1}{d} & \dfrac{N_2}{d} & \dfrac{N_3}{d} \end{array} \right] \tag{17.222}$$

where N_i are the element shape functions for either 2-node or 3-node rod elements discussed already in Section 17.2.5, Table 17.9, and J is the Jacobian equal to L for 4-node and $L/2$ for 6-node interface elements, respectively, with L being the element length.

An example illustrating the use of interface elements is shown in Figure 17.35. For simplicity a confined flow through a triangular dam was considered. A sealing membrane at the bottom of the dam and an impermeable curtain were introduced to simulate drain and flow around an impermeable wall. Both a membrane and a grout curtain are modeled by interface elements. Their contribution to the finite element equations then depends on the values assigned to interfacial permeabilities k_s, k_n.

If no restriction to flow through interface elements is assumed, the interface elements are either excluded from the finite element mesh or their permeabilities are assigned very high values (1000 times the permeability of the soil was used in this example) resulting, in both cases, in a continuous pore pressure distribution. This option is examined in Figures 17.36(a)(b) considering the dam to represent a fully impermeable concrete block. The part of boundary on the bottom of the dam is then assigned a zero flux boundary condition $\bar{q}_n = 0$ by default. When on the other hand the interface elements are

used to block the flow (impermeable wall) then the values of both k_s and k_n are set to zero producing a discontinuous distribution of pore pressures. This is evident from Figures 17.36(d)(e). Compare then with Figure 17.36(c) where no restrictions to flow were imposed. Intermediate conditions can also be specified to simulate specific drain conditions by allowing for fluid to flow freely in the longitudinal direction while blocking the flow in the perpendicular direction. Such conditions were assigned to a sealing membrane by setting $k_s = 1000\times$ the soil permeability and $k_n = 0$. The corresponding results are plotted in Figures 17.36(e)(f). Notice again the discontinuity in the pore pressure isolines.
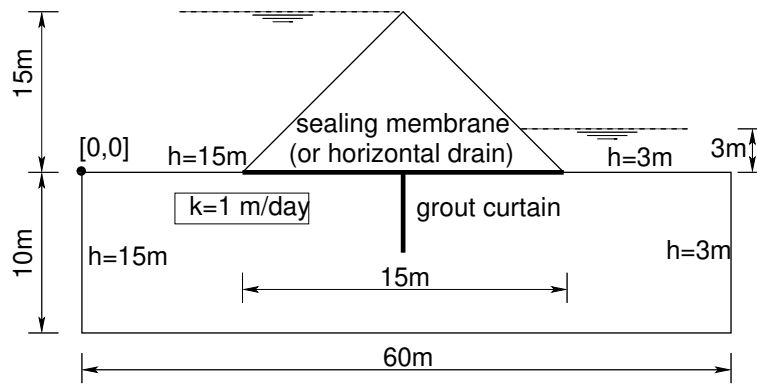
Figure 17.35: Modeling of confined interfacial flow: geometry and boundary conditions
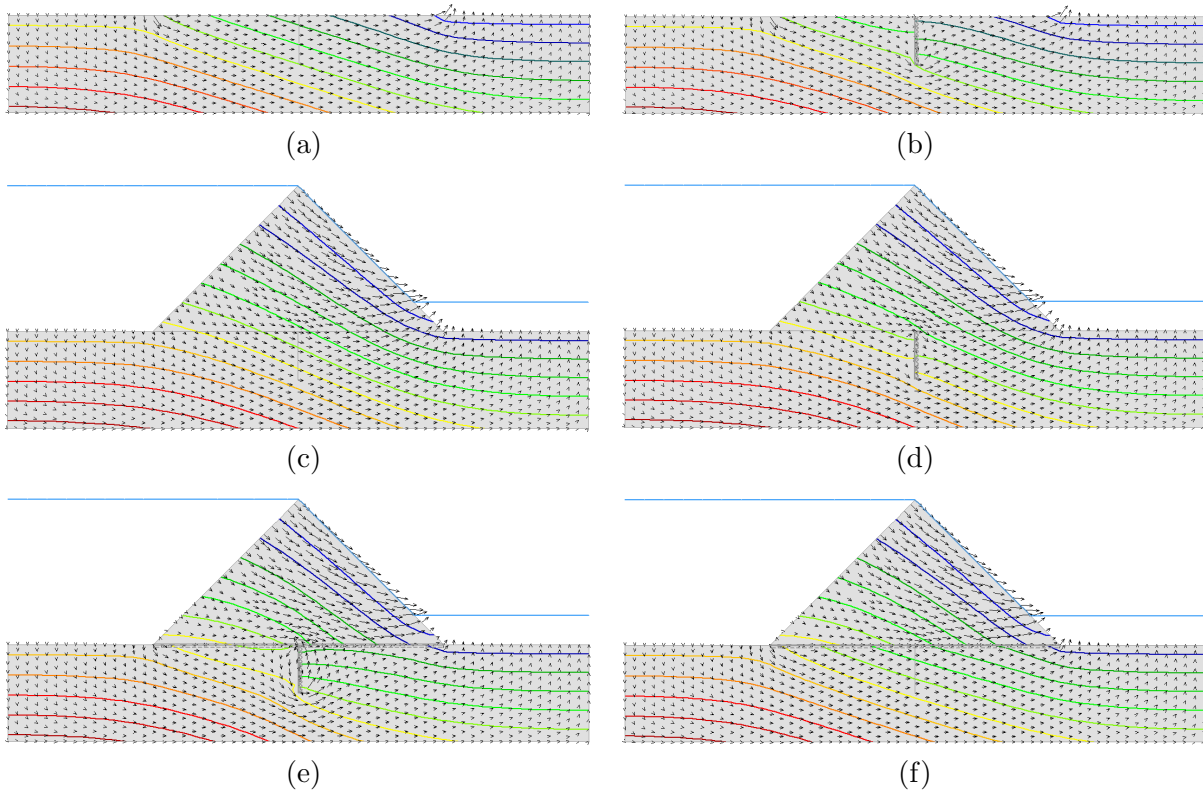
Figure 17.36: Modeling of interfacial flow - results: a) impermeable dam, permeable curtain, no interface elements, b) impermeable dam, permeable curtain - interface elements, c) membrane and curtain fully permeable, d) permeable membrane and impermeable curtain, e) drain and impermeable curtain, f) drain and permeable curtain

17.5.7   Testing implementation of transient flow analysis

The present section summarizes analytical solutions of the one- and two-dimensional Green-Ampt problem [27] provided in a series of papers by Tracy [78, 79, 80, 81]. Such analytical solutions can be used not only to check the accuracy of numerical solution of a generally highly nonlinear Richards' equation but also to compare predictions and stability of numerical solver associated with various models presented in the previous sections.

Analytical solutions

Graphical representation of the 1D and 2D Green-Ampt problem is shown in Figure 17.37. The soil is assumed initially dry with pressure head $h_p = h_p^{in}$. The rainfall (rather ponding boundary condition) is then applied to bring the pressure head to zero at the top boundary while maintaining the initial conditions at the bottom boundary.
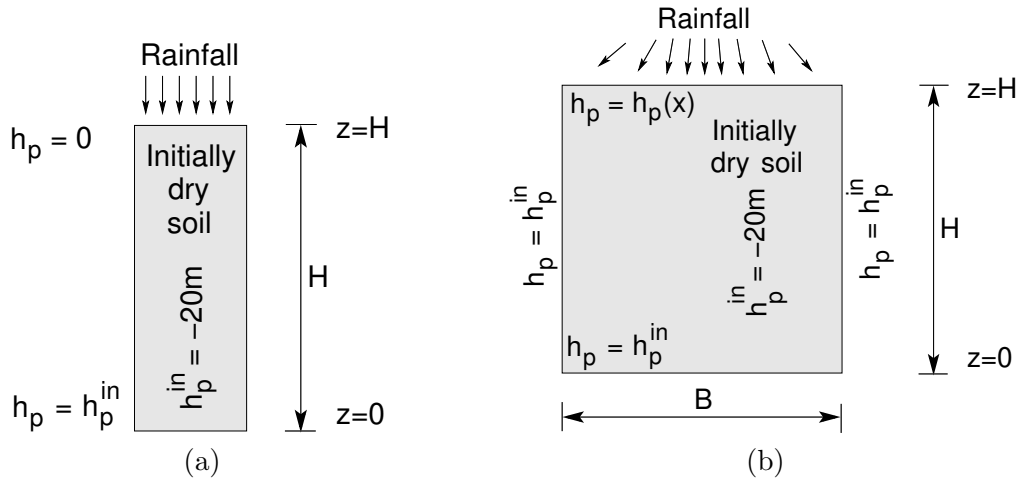
Figure 17.37: Green-Ampt problem - geometry, initial, boundary conditions: (a) 1D, (b) 2D

In the case of 1D problem we consider an initially dry column of soil infiltrated by water. The corresponding initial and boundary conditions are plotted in Figure 17.37(a).

- Initial conditions

$$h_p(y, 0) = h_p^{in} = -20 \text{ [m]} \tag{17.223}$$

- Boundary conditions

$$h_p(0, t) = h_p^{in}, \qquad h_p(H, t) = 0 \tag{17.224}$$

The analytical solution of this problem can be found in Tracy [78, 79] assuming the relative permeability K_r and the degree of saturation S for $h_p < 0$ in the form, recall Equations (16.8), (16.5) and (16.7),

$$K_r = \exp(ah_p) \tag{17.225}$$

$$S = S_r + (S_{sat} - S_r)K_r \tag{17.226}$$

- Steady state solution

$$h_p(y, t \to \infty) = \frac{1}{a} \ln \left[(1 - \varepsilon) \exp \left(\frac{a}{2}(H - y) \right) \frac{\sinh \left(\frac{a}{2}y \right)}{\sinh \left(\frac{a}{2}H \right)} + \varepsilon \right] \tag{17.227}$$

where

$$\varepsilon = \exp(ah_p^{in}) \tag{17.228}$$

- Transient solution

$$h_p(y,t) = \frac{1}{a} \ln \left[\overline{h}_p + \varepsilon \right] \tag{17.229}$$

where

$$\overline{h}_p = (1-\varepsilon) \exp\left(\frac{a}{2}(H-y)\right) \left[\frac{\sinh\left(\frac{a}{2}y\right)}{\sinh\left(\frac{a}{2}H\right)} + \frac{2}{cH} \sum_{k=1}^{\infty} (-1)^k \frac{\lambda_k}{\mu_k} \sin(\lambda_k y) \exp(-\mu_k t) \right] \tag{17.230}$$

$$c = \frac{na}{K_{sat}}(S_{sat} - S_r) = \frac{a}{K_{sat}}(\theta_s - \theta_r) \tag{17.231}$$

$$\mu_k = \frac{1}{c}\left(\frac{a^2}{4} + \lambda_k^2\right) \tag{17.232}$$

$$\lambda_k = \frac{\pi}{H}k \tag{17.233}$$

The results for $H = 6$m and $H = 50$m appear in Figure 17.38. The steady state solution is reached approximately at the time of $t = 6$ days for $H = 6$m and $t = 300$ days for $H = 50$m. The adopted material parameters are listed in Table 17.12.

Table 17.12: Material parameters (recall definitions in Section 2.1 and Chapter 16

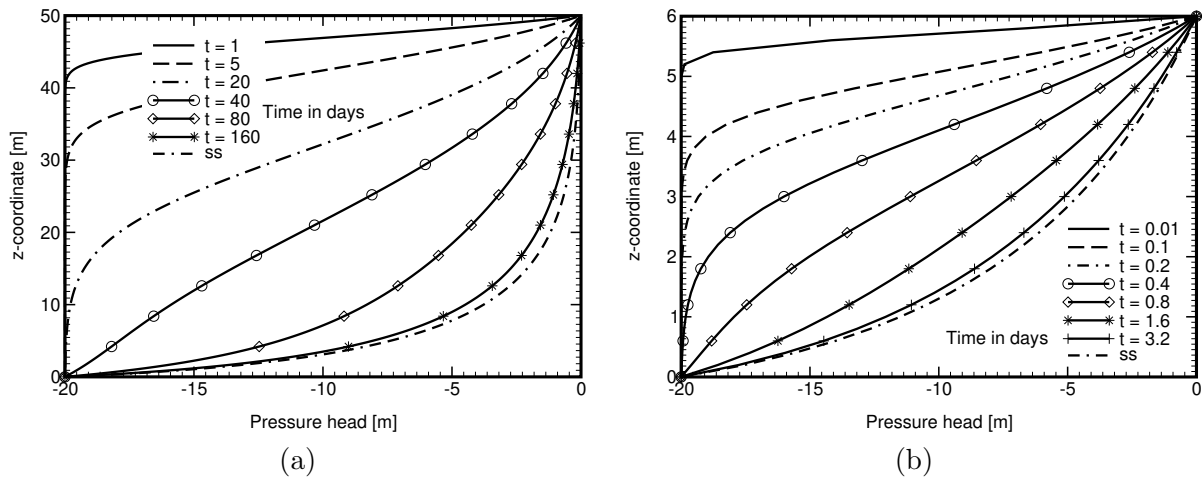| θ_s (S_{sat})	θ_r (S_r)	n	a [1/m]	K_{sat} [m/day]
0.45 (1.0)	0.15 (0.33)	0.45	0.1	0.1

Figure 17.38: Analytical solution of 1D Green-Ampt problem - pressure head distribution vs depth: (a) H = 50m, (b) H=6m, (ss stands for steady state conditions)

In the case of 2D problem we consider a rectangular region with initial and boundary conditions shown in Figure 17.37(b). The variation of the pressure head boundary conditions, Equation (17.236), applied along the top edge of the soil sample are depicted in Figure 17.39(a).

- Initial conditions

$$h_p(x,z,0) = h_p^{in} = -20 \ [\text{m}] \tag{17.234}$$

- Boundary conditions

$$h_p(0,y,t) = h_p(B,y,t) = h_p(x,0,t) = h_p^{in} \tag{17.235}$$

$$h_p(x,H,t) = \frac{1}{a} \ln \left\{ \varepsilon + (1-\varepsilon)\left[\frac{3}{4}\sin\left(\frac{\pi}{B}x\right) - \frac{1}{4}\sin\left(\frac{3\pi}{B}x\right)\right] \right\} \tag{17.236}$$

The analytical solution is again provided by Tracy [78, 79] and is given by

- Steady state solution

$$h_p(x, z, t \to \infty) = \frac{1}{a} \ln \left[\overline{h}_{ss} + \varepsilon \right] \tag{17.237}$$

where

$$\overline{h}_{ss} = \eta \left[\frac{3}{4} \sin \left(\frac{\pi}{B} x \right) \frac{\sinh(\beta_1 y)}{\sinh(\beta_1 H)} - \frac{1}{4} \sin \left(\frac{3\pi}{B} x \right) \frac{\sinh(\beta_3 y)}{\sinh(\beta_3 H)} \right] \tag{17.238}$$

$$\eta = (1 - \varepsilon) \exp \left(\frac{a}{2} (H - y) \right) \tag{17.239}$$

$$\beta_k = \sqrt{\frac{a^2}{4} + \lambda_k^2}, \quad \lambda_k = \frac{\pi}{H} k \tag{17.240}$$

- Transient solution

$$h_p(x, z, t) = \frac{1}{a} \ln \left[\overline{h}_p + \varepsilon \right] \tag{17.241}$$

where

$$\begin{aligned}
\overline{h}_p = \eta \Bigg\{ \frac{3}{4} \sin \left(\frac{\pi}{B} x \right) \left[\frac{\sinh(\beta_1 y)}{\sinh(\beta_1 H)} + \frac{2}{cH} \sum_{k=1}^{\infty} (-1)^k \frac{\lambda_k}{\gamma_{1k}} \sin(\lambda_k y) \exp(-\gamma_{1k} t) \right] - \\
\frac{1}{4} \sin \left(\frac{3\pi}{B} x \right) \left[\frac{\sinh(\beta_3 y)}{\sinh(\beta_3 H)} + \frac{2}{cH} \sum_{k=1}^{\infty} (-1)^k \frac{\lambda_k}{\gamma_{3k}} \sin(\lambda_k y) \exp(-\gamma_{3k} t) \right] \Bigg\}
\end{aligned} \tag{17.242}$$

$$\gamma_{ik} = \frac{1}{c} \left(\beta_i^2 + \lambda_k^2 \right) \tag{17.243}$$

The resulting variation of pressure head $h_p(x = 25\text{m}, y, t)$ appears in Figure 17.39(b). The same material parameters as in the case of 1D problem were adopted.
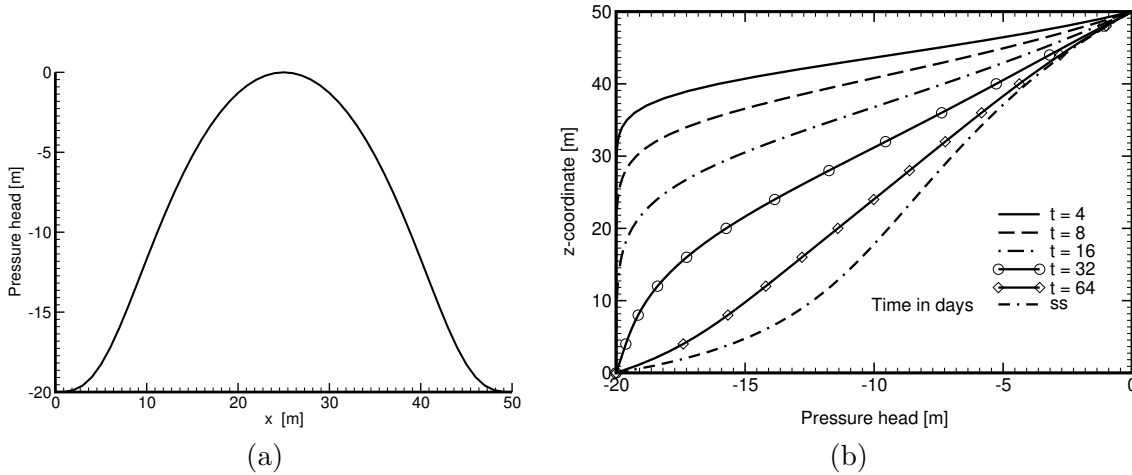

Figure 17.39: a) Pressure head boundary conditions applied at the top of the soil sample, b) Analytical solution of 2D Green-Ampt problem calculated at $x = 25\text{m}$ (ss stands for steady state conditions)

Numerical results

Henceforth we present the results of numerical solution of the Green-Ampt problem. Both 1D and 2D problem was solved with two-dimensional 3-node triangular elements. Note that the GEO5 FEM program allows for the linear variation of boundary pressure heads only, Figure 17.40. Thus for numerical calculations, the boundary conditions in Figure 17.39(a) had to be introduced directly into the finite element source code.
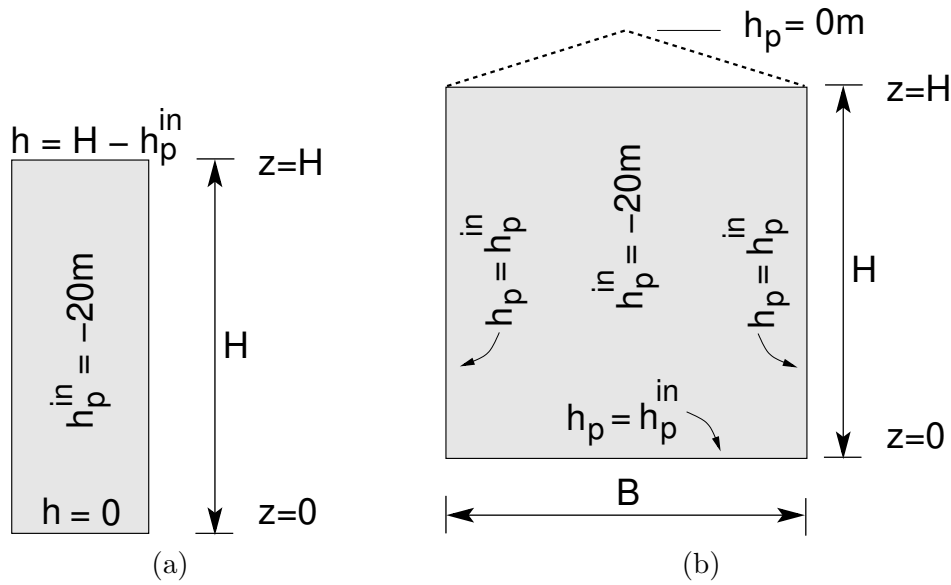
Figure 17.40: Boundary conditions in GEO5 FEM: a) 1D, b) 2D

In the case of 1D problem the $0, 4 \times 6$m domain was considered with an average element edge equal to 0.2m. The 50×50m domain with element edge equal to ≈ 2.5m was analyzed in the case of 2D problem. Figure 17.41 compares the analytical and numerical results of both problems. The time step $\Delta t = 0.1$ day was used to solve Equation (17.197). Both predictions match the analytical results relatively well.
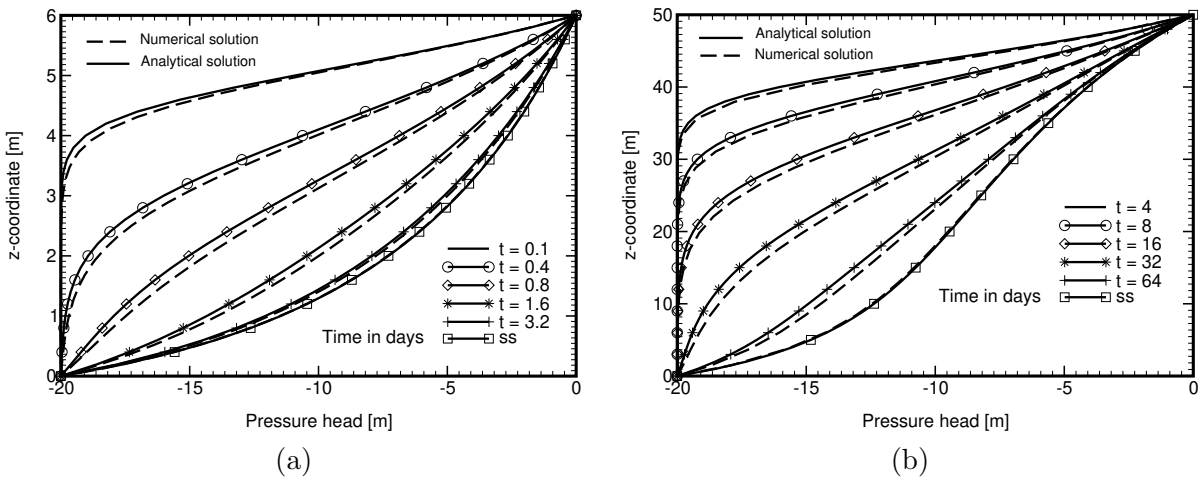

Figure 17.41: Comparing analytical and numerical results (ss stands for steady state conditions): a) 1D problem (0.4×6m), b) 2D problem (50×50m, $x = 25$m)
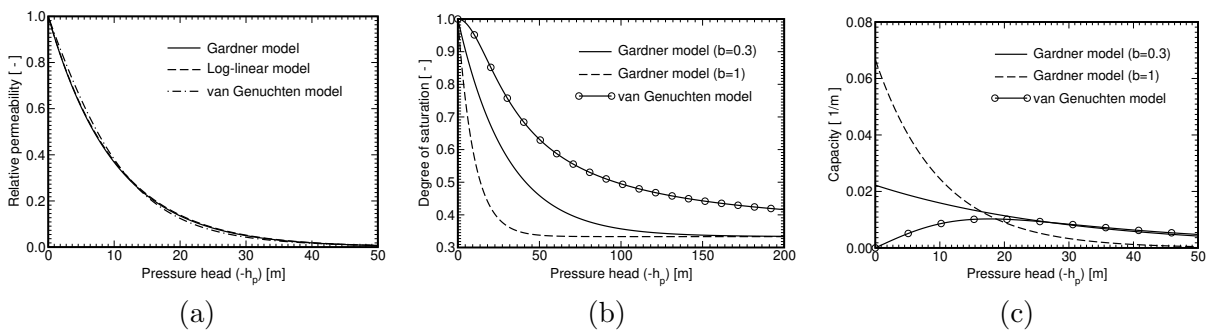

Figure 17.42: a) Relative permeability, b) degree of saturation, c) capacity ($\mathrm{d}S/\mathrm{d}h_p$)

The final set of results compares predictions of the time dependent pressure head evolution at-

tributed to individual models. The following material and model parameters were assumed: $S_{sat} = 1.0, S_r = 0.33, a = 0.1$ [m^{-1}], $R = 100, h_p^{\min} = 0, h_{TZ} = 45$ [m], $n = 2, \alpha = 0.04$ [m^{-1}]. Parameters a, R, h_{TZ} and α were again selected such as to provide the same steady state solution. Since this is driven by a relative permeability only it is sufficient to enforce the same evolution of $K_r(h_p)$, see Figure 17.42(a). This also renders the same predictions provided by the Gardner and log-linear models. Thus only the Gardner and van Genuchten models are considered next.

First notice considerable differences in the variation of degree of saturation $S(h_p)$ provided by Equations (16.5) - (16.7) and the associated capacity $C(h_p) = \mathrm{d}S/\mathrm{d}h_p$ terms, respectively. Expected differences in the pressure head time history predicted by individual equations appear in Figures 17.43(a)(b) also suggesting a shorter time to reach the steady state solution for the van Genuchten model in comparison to the Gardner model based formulations for the selected model parameters.
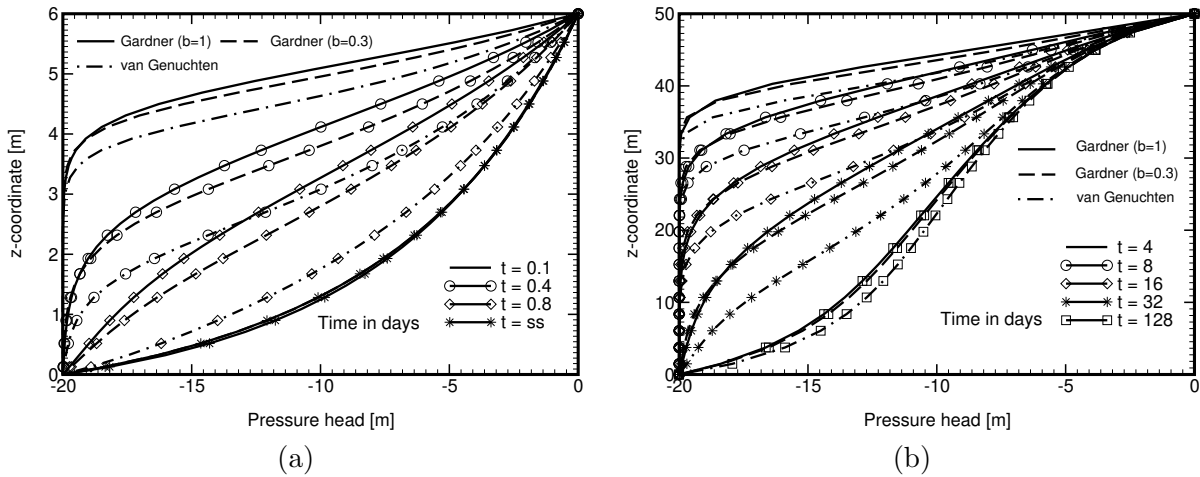

Figure 17.43: Comparing numerical results provided by Gardner and van Genuchten models: a) 1D problem (0.4 × 6m), b) 2D problem (50 × 50m, $x = 25$m)

Bibliography

[1] Material models manual 2d. Technical report, Bentley Advancing Infrastructure, 2023. Available at `https://communities.bentley.com/cfs-file/__key/communityserver-wikis-components-files/00-00-00-05-58/PLAXIS_5F00_2D_5F00_2023.2_5F00_2D_5F00_3_5F00_Material-Models-Manual.pdf`.

[2] D. Aubry and O. Ozanam. Free-surface tracking through non-saturated models. In Swoboda, editor, *International Conference on Numerical Methods in Geomechanics, Innsbruck*, pages 757–763. Balkema, Rotterdam, 1988.

[3] M. Audy, J. Krček, J. Zeman, and M. Šejnoha. Constant strain triangular element with embedded discontinuity based on partition of unity. *Building Research Journal*, 51(3):172–185, 2003.

[4] K. J. Bakker. Analysis of groundwater flow through revetments. In *3rd International Symposium on Numerical Methods in Geomechanics, Niagara Falls, Canada*, pages 367–734, 1989.

[5] J.P. Bardet. Lode Dependence for Isotropic Pressure-Sensitive Elastoplastic Materials. *Transactions of ASME*, 57:497–506, 1990.

[6] K. J. Bathe. *Finite Element Procedures*. Prentice Hall, second edition, 1995.

[7] T. Belytschko. An Overview of Semidiscretization and Time Integration Procedures. In T. Belytschko & T.J.R. Hughes, editor, *Computational Methods for Transient Analysis*, pages 1–65, 1983.

[8] T. Benz, R. Schwab, R.A. Kauther, and P. A. Vermeer. A Hoek-Brown Criterion with instrinsic material strength factorization. *International Journal of Rock Mechanics and Mining Sciences*, 45:210–222, 2008.

[9] Thomas Benz. *Small-Strain Stiffness of Soils and its Numerical Consequences*. Phd thesis, University of Stuttgart, 2007. Available at `https://www.igs.uni-stuttgart.de/dokumente/Mitteilungen/55_Benz`.

[10] Z. Bittnar and J. Šejnoha. *Numerical methods in structural engineering*. ASCE Press, 1996.

[11] Zdeněk Bittnar and Petr Řeřicha. *Metoda konečných prvků v dynamice konstrukcí*. SNTL, 1981.

[12] J. Boháč, D. Mašín, R. Malát, V. Novák, and J. Rott. Methods of determination of K_0 in overconsolidated clay. In *Proceedings of the 18 th International Conference on Soil Mechanics and Geotechnical Engineering*, pages 1–4. Paris, 2013.

[13] David M Boore. Stochastic simulation of high-frequency ground motions based on seismological models of the radiated spectra. *Bulletin of the Seismological Society of America*, 73(6A):1865–1894, 1983.

[14] R.I. Borja. Cam-Clay plastitcity, Part II: Implicit integration of constitutive equation based on a nonlinear elastic stress predictor. *Computer Methods in Applied Mechanics and Engineering*, 88:225–240, 1991.

[15] R.I. Borja and S.R. Lee. Cam-Clay plastitcity, Part I: Implicit integration of elasto-plastic constitutve relations. *Computer Methods in Applied Mechanics and Engineering*, 78:49–72, 1990.

[16] R. B. J. Brinkgreve. *Geomaterial Models and Numerical Analysis of Softening*. Phd thesis, Technische Universiteit Delft, 1994. Available at https://repository.tudelft.nl/record/uuid:6738de62-4dde-45b0-b3bd-3635504767c2.

[17] RBJ Brinkgreve, E Engin, and WM Swolfs. Plaxis 2D manual. http://www.plaxis.nl, *Rotterdam, Netherlands, Balkema*, 2017.

[18] M. A. Celia and E. T. Bouloutas. A general mass-conservative numerical solution for the unsaturated flow equation. *Water Resources Research*, 26(7):1483–1496, 1990.

[19] L.J. Cocco and M.E. Ruiz. *Numerical Methods in Geotechnical Engineering IX*, chapter Numerical implementation of hardening soil model, pages 195–203. 2018.

[20] M. A. Crisfield. A fast incremental/iterative solution procedure that handles snap-through. *Computers and Structures*, 13:55–62, 1981.

[21] R. A. Day and D. M. Potts. Curved mindlin beam and axi-symmetric shell elements - A new approach. *International Journal for Numerical Methods in Engineering*, 30:1263–1274, 1990.

[22] R. A. Day and D. M. Potts. Zero thickness interface elements - numerical stability and applications. *International Journal for Numerical and Analytical Methods in Geomechanics*, 18:689–708, 1994.

[23] E.A. de Souza Neto, D. Perič, and D.R.J. Owen. *Computational Methods for Plasticity: Theory and Applications*. John Wiley & Sons, Ltd, 2008.

[24] J. M. Dluzewski. Nonlinear consolidation in finite element modeling. In *Proceedings of the IX International Conference on Computer Methods and Advances in Geomechanics, Wuhan, China*, pages 1089–1094, 1997.

[25] ExCalibre team. https://soilmodels.com/excalibre/.

[26] W. R. Gardner. Some steady-state solutions of the unsaturated moisture flow equation to evaporation from a water table. *Soil Science*, 85(4):228–232, 1958.

[27] W Green and G. Ampt. Studies on soil physics, part I, the flow of air and water through soils. *Journal of Agricultural Science*, 4:1–24, 1911.

[28] H.M. Hilber, T.J.R Hughes, and R.L Taylor. Improved numerical dissipation for time integration algorithms in structural dynamics. *Earthquake Engineering and Structural Dynamics*, 5, 1977.

[29] M. Hjiaj, J. Fortin, and G. de Saxce. A complete stress update algorithm for the non-associated Drucker-Prager model including treatment of apex. *International Journal of Engineering Science*, 41:1109–1143, 2003.

[30] E. Hoek and E. T. Brown. *Underground excavations in rock*. London: Institution of Mining and Metallurgy, 1980.

[31] E. Hoek and E. T. Brown. Practical estimates of rock mass strength. *International Journal of Rock Mechanics and Mining Sciences*, 34.8:1165–1186, 1997.

[32] E. Hoek, C. Carranza-Torres, and B. Corkum. Hoek-Brown failure criterion - 2002 edition. *Proceedings of the 5th North American symposium - NARMS-TAC*, 2002.

[33] E. Hoek and M.S. Diederichs. Empirical estimation of rock mass modulus. *International Journal of Rock Mechanics & Mining Sciences*, 43:203–215, 2006.

[34] J. M. Hohberg. A note on spurious oscillations in FEM joint elements. *Earthquake Engineering and Structural Dynamics*, 19(5):773–779, 1990.

[35] K. Huang, B. P. Mohanty, and M. Th. van Genuchten. A new convergence criterion for the modified picard iteration method to solve the variably saturated flow equation. *Journal of Hydrology*, 178:69–91, 1996.

[36] J. R. Hughes. *The Finite Element Method. Linear Static and Dynamic Finite Element Method.* Prentice-Hall, Inc., Englewoods Cliffs, New Jersey 07632, 1987.

[37] T.J.R. Hughes. *The Finite Eelement Method: Linear Static and Dynamic Finite Element Analysis.* Prentice Hall, INC., Englewood Clifts, New Jersey 07632, 1987.

[38] M. J. Hvorslev. On the physical properties of disturbed cohesive soils. *Ingeniorvidenskabelige Skrifter A*, 45, 1937.

[39] J. Jáky. Pressure in silos. In *Proceedings of 2nd ICSMFE*, volume 1, pages 103–107. Rotterdam, 1948.

[40] N. Janbu. Soil compressibility as determined by oedometer and triaxial tests. In *3rd FCSMFE, Wiesbaden*, volume 1, pages 19–25, 1963.

[41] T. Janda, P. Kuklík, and M. Šejnoha. Mixed experimental numerical approach to evaluation of material parameters of clayey soils. *International Journal of Geomechanics*, 4(3):199–206, 2004.

[42] Lenka Janošková. Dynamická analýza konstrukce zatížené seismickým zatížením. diplomová práce, *Vysoké učení technické v Brně*, 2013.

[43] W. T. Koiter. Stress-strain relations, uniqueness and variatonal theorems for elasto-plastic materials with a singular yield surface. *Quarterly of Applied Mathematics*, 11:350–354, 1953.

[44] R.L. Kondner and J.S. Zelasko. A hyperbolic stress-strain formulation for sands. In *2nd PanAmerican Conference on Soil Mechechanics and Foundation Engineering, Brazil*, volume 1, pages 289–394, 1963.

[45] T. Krejčí, T. Nový, L. Sehnoutek, and J. Šejnoha. *Structure - subsoil interaction in view of transport processes in porous media*, volume 5 of *CTU Reports*. CTU in Prague, 2001.

[46] Ashok Kumar. Software for generation of spectrum compatible time history. In *Proceedings of 13th World Conference on Earthquake Engineering*, pages 1–6, 2004.

[47] S. Lacasse, M. Jamiolkowski, R. Lancellotta, and T. Lunne. In situ characteristics of two norwegian clays. In *Proceedings of 10th European Conference of Soil Mechanics and Foundation Engineering*, volume 2, pages 91–125. Stockholm, 1981.

[48] S. Lacasse and T. Lunne. Calibration of dilatometer correlations. In *Penetration Testing 88, ISOPT-1*, pages 539–548. Orlando, Florida, 1988.

[49] R. Lagioia, A. Panteghini, and A.M. Puzrin. The I_3 generalization of the Galileo-Rankine tension criterion. *Proceedings of the Royal Society A*, 470:20140568, 2014.

[50] R. W. Lewis and B. A. Schrefler. *The Finite Element Method in the Static and Dynamic Deformation and Consolidation of Porous Media.* John Wiley&Sons, Chichester, England, 2nd edition, 1999.

[51] G. C. Li and C. S. Desai. Stress and seepage analysis of earth dams. *Journal of Geotechnical Engineering*, 109(7):946–960, 1983.

[52] ZSOIL Ltd. http://www.zsoil.info/.

[53] S. Marchetti. In situ tests by flat dilatometer. *Journal of the Geotechnical Engineering Division, ASCE*, 106:299–321, 1980.

[54] P.W. Mayne and F.H. Kulhawy. $K_0 - OCR$ relationship in clay. *Journal of the Geotechnical Engineering Division, ASCE*, 108(6):851–870, 1982.

[55] L.H. Mejia and E.M. Dawson. Earthquake deconvolution for FLAC. In Hart & Varona, editor, *4th International FLAC Symposium on Numerical Modeling in Geomechanics*, pages 4–10, 2006.

[56] G.G. Meyerhof. Bearing capacity and settlement of pile foundations (11th Terzaghi Lecture). *Journal of the Geotechnical Engineering Division, ASCE*, 102(3):195–228, 1976.

[57] J. Máca and K. Pohl. Seizmická odolnost stavebních konstrukcí. https://docplayer.cz/15128735-Seizmicka-odolnost-stavebnich-konstrukci.html, Workshop 2005 – VZ "Udržitelná výstavba". [Online; cit. 2019-11-03].

[58] R.F. Obrzud and A. Truty. The hardening soil model - a practical guidebook. Technical report, Z Soil.PC 100701 report, 2020. Available at `https://www.zsoil.com/zsoil_manual/Rep-HS-model.pdf`.

[59] M. Ortiz and J. C. Simo. An analysis of a new class of integration algorithms for elastoplastic constitutive relations. *International Journal for Numerical Methods in Engineering*, 23:353–366, 1986.

[60] Pankaj and N. Bičanič. Detection of multiple active yield conditions for Mohr-Coulomb elasto-plasticity. *Computers and Structures*, 62:51–61, 1997.

[61] Veronika Pavelcová, Tereza Poklopová, Tomáš Janda, and Michal Šejnoha. The influence of boundary conditions on the response of underground structures subjected to earthquake. *Acta Polytechnica CTU Proceedings*, 15:74–80, 2018.

[62] Veronika Pavelcová, Tereza Poklopová, Tomáš Janda, and Michal Šejnoha. Influence of material damping on the response of underground structures subjected to earthquake. *Acta Polytechnica CTU Proceedings*, 26:64–70, 2020.

[63] PLAXIS. http://www.plaxis.nl/.

[64] T. Poklopová and M. Šejnoha. Comparing the Hoek-Brown and Mohr-Coulomb failure criteria in FEM analysis. In *Acta Polytechnica CTU Proceedings*, volume 30, pages 69–75, 2021.

[65] D. M. Potts and L. Zdravkovič. *Finite element analysis in geotechnical engineering – theory*. Thomas Telford, London, 1999.

[66] D. M. Potts and L. Zdravkovič. *Finite element analysis in geotechnical engineering – application*. Thomas Telford, London, 2001.

[67] K. H. Roscoe and J. B. Burland. On the generalised stress-strain behaviour of 'wet' clay. In J. Heyman and F. A. Lechie, editors, *Engineering plasticity*, pages 535–609. Cambridge University Press, 1968.

[68] K. H. Roscoe, A. N. Schofield, and C. P. Wroth. On the yielding of soils. *Geotechnique*, 8:22–52, 1958.

[69] P.W. Rowe. The stress-dilatancy relation for static equilibrium of an assembly of particles in contact. In *Royal Society of London. Series A, Mathematical and Physical Sciences*, volume 269, pages 500–527, 1962.

[70] T. Schanz, P.A. Vermeer, and P.G. Bonnier. The hardening soil model: Formulation and verification. In Ronald B. J. Brinkgreve, editor, *Beyond 2000 in Computational Geotechnics*, pages 281–296. Routledge, 1 edition, January 2019.

[71] P.B Schnabel, J. Lysmer, and B.H. Seed. SHAKE, a computer program for earthquake response analysis of horizontally layered sites. Technical report, Earthquake Engineering Re-search Center, University of California, Berkeley. Report No. EERC 72-12, 1972.

[72] M. Šejnoha, J. Pruška, T. Janda, and M. Brouček. *Metoda konečných prvků v geomechanice: teoretické základy a inženýrské aplikace.* V Praze České vysoké učení technické, 2015.

[73] J. C. Simo and R. L. Taylor. Consistent tangent operators for rate-independent elastoplasticity. *Computer Method in Applied Mechanics and Engineering*, 48:101–118, 1985.

[74] B. Simpson. Retaining structures: displacement and design. *Géotechnique*, 42(4):541–576, 1992.

[75] B. Simpson, G. Calabresi, H. Sommer, and M. Wallays. Design parameters for stiff clays. In *Proceedings of 7th European Conference of Soil Mechanics and Foundation Engineering*, volume 5, pages 91–125. Brighton, British Geotechnical Association, London, UK, 1980.

[76] V. Sirakumar, I. G. Doran, J. Graham, and T. Navaneethan. Relationship between K_0 and overconsolidation ratio: A theoretical approach. *Géotechnique*, 52(3):225–230, 2001.

[77] G. Totani, S. Marchetti, P. Monaco, , and M. Calabrese. Use of the flat dilatometer test (DMT) in geotechnical design. In *IN SITU 2001 Int Conf In Situ Measurement of Soil Properties and Case Histories*. Bali, Indonesia, 2001.

[78] F. T. Tracy. 1-D, 2-D, and 3-D analytical solutions of unsaturated flow in groundwater. *Journal of Hydrology*, 4:199–214, 1995.

[79] F. T. Tracy. Clean two- and three-dimensional analytical solution of richard's equation for testing numerical solvers. *Water Resources Research*, 42:W08503, 2006.

[80] F. T. Tracy. Three-dimensional analytical solutions of richards' equation for a box-shaped soil sample with piecewise-constant head boundary conditions on the top. *Journal of Hydrology*, 336:391–400, 2007.

[81] F. T. Tracy. Testing computational algorithms for unsaturated flow. *The Open Hydrology Journal*, 170:227–235, 2010.

[82] M. Th. van Genuchten. A closed-form equation for predicting the hydraulic conductivity of unsaturated soils. *Journal Soil Science Society of America*, 44:892–898, 1980.

[83] T. Žalská and M. Šejnoha. Return mapping scheme for the Hoek-Brown model witch tension cut-off. In *Acta Polytechnica CTU Proceedings*, volume 40, pages 117–122, 2023.

[84] A. Warrick. *Soil Water Dynamics.* Oxford University Press, New York., 2003.

[85] S. Wu, S. Zhang, and G. Zhang. Three-dimensional strength estimation of intact rocks using a modified Hoek-Brown criterion based on a new deviatoric function. *International Journal of Rock Mechanics and Mining Sciences*, 107:181–190, 2018.

[86] O. C Zienkiewicz, N Bicanic, and F Q Shen. Generalized Smith boundary – – a transmitting boundary for dynamic computation. *Institute for Numerical Methods in Engineering, University College of Swansea*, 207, 1986.